Novel Modified Optical Fibers for High Temperature In-Situ Miniaturized Gas Sensors in Advanced Fossil Energy Systems

Final Technical Report

DOE Award Number: DE-FC26-05NT42441

Recipient Organization: Virginia Polytechnic Institute & State University
Office of Sponsored Programs
460 Turner Street, Suite 306 (0170)
Blacksburg, VA 24061

Principal Investigator: Dr. Gary R. Pickrell

Reporting Period Start Date: July 1, 2005

Reporting Period End Date: June 30, 2014

Report Issued: September 30, 2014

Report Prepared by: Dr. Brian Scott

CPT
CENTER FOR PHOTONICS TECHNOLOGY

Disclaimer:

Abstract

This report covers the technical progress on the program "Novel Modified Optical Fibers for High Temperature In-Situ Miniaturized Gas Sensors in Advanced Fossil Energy Systems", funded by the National Energy Technology Laboratory of the U.S. Department of Energy, and performed by the Materials Science & Engineering and Electrical & Computer Engineering Departments at Virginia Tech, and summarizes technical progress from July 1st, 2005 –June 30th, 2014. The objective of this program was to develop novel fiber materials for high temperature gas sensors based on evanescent wave absorption in optical fibers.

This project focused on two primary areas: the study of a sapphire photonic crystal fiber (SPCF) for operation at high temperature and long wavelengths, and a porous glass based fiber optic sensor for gas detection. The sapphire component of the project focused on the development of a sapphire photonic crystal fiber, modeling of the new structures, fabrication of the optimal structure, development of a long wavelength interrogation system, testing of the optical properties, and gas and temperature testing of the final sensor. The fabrication of the 6 rod SPCF gap bundle (diameter of 70μm) with a hollow core was successfully constructed with lead-in and lead-out 50μm diameter fiber along with transmission and gas detection testing. Testing of the sapphire photonic crystal fiber sensor capabilities with the developed long wavelength optical system showed the ability to detect CO_2 at or below 1000ppm at temperatures up to 1000°C.

Work on the porous glass sensor focused on the development of a porous clad solid core optical fiber, a hollow core waveguide, gas detection capabilities at room and high temperature, simultaneous gas species detection, suitable joining technologies for the lead-in and lead-out fibers and the porous sensor, sensor system sensitivity improvement, signal processing improvement, relationship between pore structure and fiber geometry to optical properties, and the development of a sensor packaging prototype for laboratory testing. Analysis and experiments determined that a bonding technique using a CO_2 laser is the most suitable joining technique. Pore morphology alteration showed that transmission improved with increasing annealing temperature (producing smaller pores), while the sensor response time increased and the mechanical strength decreased with increasing annealing temperature. Software was developed for data acquisition and signal processing to collect and interpret spectral gas absorption data. Gas detection on porous glass sensors was completed and the detection limit was evaluated using acetylene and was found to be around 1- 200ppm. A complete materials package for porous glass sensors was manufactured for testing.

Table of Contents

1 Introduction:

Energy from coal fired power plants will continue to play a dominant role in the energy landscape well into the next century. Accurate and reliable detection of various gases is necessary for emissions monitoring and advanced process control in the coal fired power plants of today as well as the FutureGen advanced power generation systems of the future. Ideal gas sensors in these processes would operate in situ, exposed to the high temperatures and harsh environments, where many conventional sensors cannot operate. Very few sensors are commercially available for high temperature ($\geq$ 1000ºC) and harsh environment monitoring of gases such as NO_x, SO_x, CO, H_2, O_2, CH_4, NH_3, etc., which are present in coal and coal-derived syngas applications. These sensors suffer from a number of major limitations including rather limited accuracy, extremely short lifetimes and unexpected failure, and intensive maintenance. The objective of this program is to develop novel modified fiber materials for high temperature gas sensors based on evanescent wave absorption in standing hole optical fibers. Gas molecules have a number of characteristic vibrational absorption bands in the near-IR region, corresponding to the transmission window for silica optical fiber. Gas molecules in the holey fiber pores can be interrogated through the evanescent field of the guided mode, and their presence will appear as a loss at wavelengths characteristic to the gas species, as described below in the preliminary data for acetylene gas.

2 Approach

Optical fiber-based sensors have been demonstrated to be attractive for measurement of a variety of physical and chemical parameters. Especially in the past five years, due to the sharp increase in investment in the development of a range of industrial sensors, fiber sensor R&D has become more active than ever before. In parallel with the increased fiber sensor research, the recent invention and development of holey fibers have had profound impacts in many fields, including sensors. However, all of the holey fibers used in past gas detection demonstrations o involve longitudinal holes. Because of the long thin holes, it is difficult for gas molecules to get in and out freely, resulting in response times as long as hours or even days. One of the objectives of this program is to develop a novel process to produce holey fibers with radial holes – holes perpendicular to the fiber axis. Figure 2-1 shows schematic representations of longitudinal hole fibers (the only type of holey fibers available today), as well as the standing hole fibers that will be developed in this program.

With longitudinal hole fibers, the gas molecules must diffuse through the length of the fiber in order to interact with the evanescent field propagating through the fiber. The length of the holey fiber used must be long enough to allow a sufficient optical interaction with the propagating light signal. This poses a severe limitation on the response time of the fiber since the gas molecules must permeate (through a gas phase diffusion) over long lengths (on the order of many centimeters) of fiber.

In order to eliminate this problem and the closing off of the holes when the fibers are spliced, a novel process will be developed in this project to produce optical fibers with holes perpendicular to the fiber axis. This will be accomplished by a spinodal phase separation process of the cladding glass (after fiber drawing has been completed), with subsequent leaching to produce the three dimensionally interconnected porous cladding phase. In general, phase separation in glasses occurs by one of two processes, nucleation and growth or spinodal decomposition. The process of nucleation and growth can be characterized by the formation of

nuclei with compositional differences that are large over a small spatial extent. In contrast, spinodal decomposition occurs by a process whereby the compositional differences are small but these compositional differences occur over a large spatial extent. The resulting microstructures are quite different for these two processes. The second phase which forms from spinodal decomposition in borosilicate glasses (with compositions that fall within the spinodal region) is three dimensionally interconnected, which allows easy removal of the second phase through a simple leaching process. [1] [2] [3] It also ensures that during the operation of the fiber optic gas sensor, the gas phase molecules can easily penetrate through the large amount of porosity present since the diffusion distance is minimized.

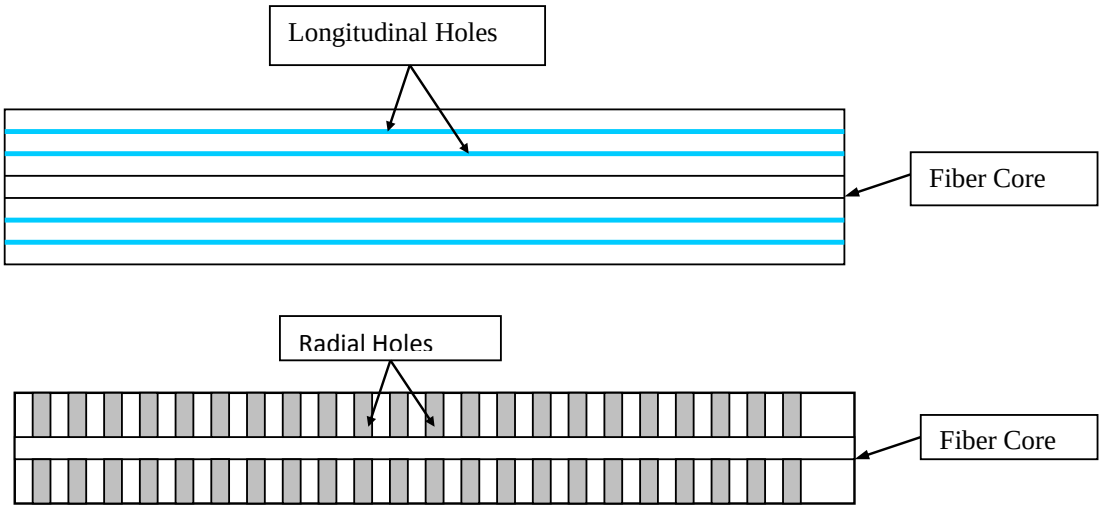

Figure 2-1. **Schematic representation of a porous fiber with longitudinal holes (top) and standing holes (bottom).**

The amount and size distribution of the porosity can be adjusted by controlling the composition of the original glass, the conditions of the leaching process, and also the conditions of a final etching step that may be employed. After the spinodal phase separation is performed by heat-treating in the appropriate temperature range, the second phase can be leached from the first phase. In the case of borosilicates, the second phase that forms is composed almost entirely of soda and boron. When this soda and boron rich phase is leached from the glass, what is left is an approximately 96% silica glass with the spaces the leached phase occupied being empty – forming porosity. This process has been used quite extensively in industry to form porous articles (such as porous Glass) or to produce high silica content glasses at much lower temperatures than would be required to melt the high silica glass.

From a thermodynamic perspective [1-3], the free energy of mixing for the solution may be given by

$$\Delta G_m = \Delta H_m - T\Delta S_m \qquad \textit{(2-1)}$$

where ΔH_m is the enthalpy change of mixing given by

$$\Delta H_m = \Omega\, X_1 X_2 \qquad \textit{(2-2)}$$

(where X_1X_2 are the mole fractions and Ω is a constant related to bond energies) and ΔS_m is the entropy change of mixing given by

$$\Delta S_m = -R(X_1 \ln X_{1+} X_2 \ln X_2). \quad \textit{(2-3)}$$

When ΔH_m is negative, ΔG_m as a function of composition will always be negative since $-T\Delta S_m$ is always negative. However, when ΔH_m is positive, ΔG_m as a function of composition will become positive since $-T\Delta S_m$ will become increasingly less important as the temperature decreases. This in general will be true, except at the ends of the binary. Close to the binary ends, the change in free energy is dominated by the entropy, since a very large change in the configurational arrangements of the binary constituents is possible when adding a small amount of one component to an almost pure second component. Since ΔG_m is always negative near the ends of the binary, this will cause an inflection point in the ΔG_m versus composition curve as the temperature drops. [3]

The temperature at which the phase separation becomes thermodynamically preferred is called the consolute temperature. Below the consolute temperature, for a given composition C, the curvature of the free energy versus composition is negative ($\delta^2G/\delta^2C<0$). This produces a miscibility gap or region of immiscibility. Therefore, within this miscibility gap the free energy of the system is lowered by separating into two phases, which have a lower average free energy than the parent phase. The two new phases can form by a nucleation and growth process. However, in order to form nuclei of the second phase in the parent phase, energy must be supplied to form the interfacial region between the two phases due to the required surface energy. Assuming a spherical particle for simplicity, the energy required to create the new surface would be ($4\pi r^2\gamma$), the surface area times the surface energy (γ). Also, the volume free energy available from the phase separation (into the two lower average free energy phases) is given by $4/3\pi r^3\Delta G_v$, where ΔG_v is the volume free energy difference between the parent phase free energy and the average free energy of the two separated phases per unit volume. The total free energy change as a function of the radius of the particle then is given by

$$\Delta G_r = 4\pi r^2\gamma + 4/3\pi r^3\Delta G_v \quad \textit{(2-4)}$$

When the energy term based upon the volume of the new nuclei exceeds the energy term based upon the surface area of the new nuclei, the nuclei will be stable and has no thermodynamic barrier to further growth. However, before the volume energy term becomes larger than the surface energy term, the nuclei is unstable and (thermodynamically speaking) prefers to shrink away. Therefore, the critical radius of a stable nuclei will be given by [1]

$$r^* = (-2\gamma)/\Delta G_{v.} \quad \textit{(2-5)}$$

If we allow g(C) to be the free energy per molecule of the uniform solution, it is apparent that ΔG is positive if $\delta^2g/\delta^2C>0$. In this case, the system is stable against small fluctuations in composition. Only large fluctuations in composition such as encountered with a nucleation and growth process will be stable. In contrast, when $\delta^2g/\delta^2C<0$ then ΔG is negative, which results in the system being unstable against small fluctuations in composition, and this comprises the spinodal region. Therefore, in the spinodal region, phase separation occurs by a process whereby the compositional fluctuations are small in magnitude, but large in spatial extent. This produces a morphology that is three dimensionally interconnected and occurs over a fine dimensional scale. In borosilicate glasses with compositions within the spinodal region, this phase separation scale range may be on the order of tens to hundreds of nanometers.

New types of optical fibers have recently been developed which promise to play an important role in both sensing and communication applications. Photonic crystal fibers (PCF), which belong to the class known as “microstructured optical fibers” (MOF) or “holey fibers,” were first reported in the 1990s and have been the subject of intensive research ever since. Most PCF’s

consist of a pure silica core surrounded by ordered longitudinal air holes in the cladding region. Many PCF structures have been proposed (mainly differing in the size, spacing, and number of air holes present in the cladding region), including hollow core PCFs.

Photonic crystal fibers or "ordered hole" fibers have generated a significant amount of interest due to the unique properties exhibited by these fibers including large single mode core size, single mode guidance over a very large wavelength range and guidance through a hollow core. If the size and spacing of the "holes" in the fiber are controlled properly, a photonic band gap fiber can be produced.

If the size and/or spacing of the holes does not permit a photonic band gap to exist, the fiber can still guide light by lowering of the average effective index in the cladding region. Many useful fibers and devices have been developed based upon these "ordered hole" PCF's. However, these are all based on silica fibers, which limit the maximum use temperature due to fiber crystallization, fiber reactions with the environment, or glass creep under stress. Many industrial applications require sensors to be able to withstand high temperatures and harsh environments. In addition, the transmission of silica drops off rapidly above about 1.6 μm, but many sensing applications require longer wavelength detection capability.

Single-crystal sapphire has a high melting point, approximately 2054°C, which provides a high laser damage threshold. It also has superior mechanical characteristics, excellent chemical resistance in corrosive environments, high hardness, and reasonably good optical propagation. The transmission window for single crystal sapphire extends beyond 5 μm (with about a 20% transmission at wavelengths as long as 6 μm). Other important properties of single crystal sapphire include good nonlinearity in the $n_2 \approx 3 \times 10^{-20}$ m^2/W range and highly availability since single crystal sapphire can be easily be grown by the laser heated pedestal growth (LHPG) method. Extensive research has been performed to develop sapphire fiber-based sensors. Various sensors including intrinsic and extrinsic interferometers, polarimetric devices, and birefringence-balanced lead-insensitive sensors have been demonstrated for measurement of various physical parameters at high temperatures.

However, full utilization of these devices has not been realized in large part due to the lack of appropriate high temperature claddings on sapphire optical fibers. The lack of cladding on the single crystal sapphire fibers results in higher environmental vulnerability of the single crystal sapphire fibers due to fluctuations in the optical signal as a result of materials adsorbed onto the fiber surface or reactions at the sapphire surface; higher modal volume resulting in higher phase difference between low and high order modes; and increased sensitivity to the effects of fiber bending due to the loss of the higher order modes.

3 Porous clad solid core optical fiber structure

Fabrication of the porous optical fiber can be broken down into two parts, fabrication of the porous clad fiber and alteration of the morphology of the pore structure through additional processing. Fabrication of the fiber is described in two parts, with the first section describing the preform fabrication and fiber drawing and the second section describing the phase separation and leaching of the fiber cladding. Two experiments were done to explore the achievable pore sizes in the cladding. The first of these experiments looked at the use of an alkaline treatment to remove the silica gel from the pore structure. Removal of the silica gel allows for the maximum pore size as determined by the phase separation temperature while leaving the silica skeleton

intact. Retaining as much of the skeleton as possible ensures that the fiber maintains as much mechanical integrity as possible. In the second experiment three processing variables are investigated. The first variable is the temperature at which the phase separation is carried out. Second is the use of an alkaline treatment on the porous glass. The third variable investigated is a heat treatment on the porous glass, where different temperatures and times were used in the heat treatment. Due to the extent of the second experiment, samples were prepared from bulk samples of the phase separating glass. These experiments are detailed in the second section with each experiment treated independently.

Characterization of the fibers and bulk glass samples is treated in the last section and includes both material characterizations and optical and functional characterization. The methods to do the material characterizations were the use of scanning electron microscopy, nitrogen adsorption, and optical microscopy.

3.1 Fiber fabrication

3.1.1 Preform manufacture

The fibers that have been fabricated have a two part structure, a porous cladding surrounding a solid core. Making of the fiber begins with construction of a preform from which the fibers are pulled. To make the preform, a glass tube of a phase separable sodium borosilicate composition is collapsed around a rod made of a non-phase separable borosilicate glass composition. The phase separable glass portion of the preform was obtained in the form of tubes from the Corning glass plant in Danville, Virginia. The starting glass composition is proprietary, but is within the spinodal phase separation region of the sodium borosilicate system. The tubes were pulled from the Vycor production line prior to the phase separating heat treatment. The core region of the fiber is made from a different glass composition that does not phase separate and has been made using a borosilicate comparable to the Corning code 7740, although many other non-phase separating glass compositions can be used. A borosilicate glass was chosen so that the glass softening points of the core and cladding region would be close enough to allow for reduction of both regions during the pulling of the fibers. Figure 3-1details the beginning process to make the preform. First a length of glass tubing is taken and a section on either end of the tube is collapsed on a glass lathe so that there is opening at the center slightly larger than the diameter of the core rod to be used. The initial diameter of the core rod will partially determine the core diameter of the fiber. Once the tubing section is collapsed, a borosilicate core rod is inserted into the tube which is then fully collapsed, beginning at one end and working toward the other collapsed section. The preform manufacture is carried out on a glass lathe with the glass being worked using an oxygen-hydrogen torch.

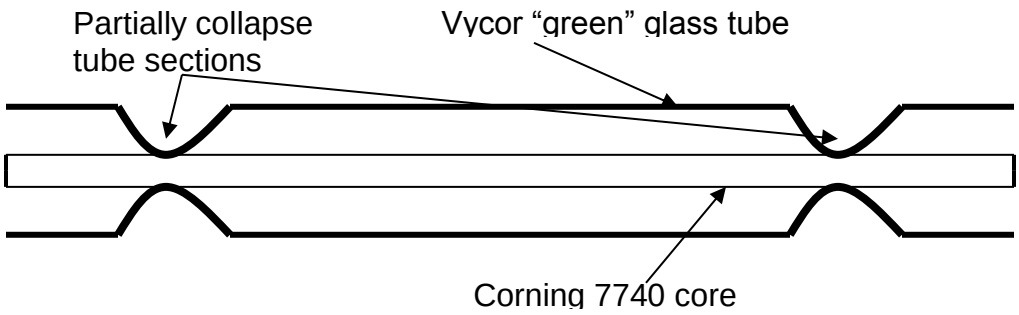

Figure 3-1: Schematic of perform manufacture

3.2 Fabrication of the initial glass fiber

With the preform manufactured the fibers are pulled from the end of the preform. The preform is worked with an oxygen-hydrogen torch to lower the viscosity of the preform tip to a suitable range to pull fibers. Random lengths and diameters were produced using this process. The following procedure was used for pulling fibers.

I. The preform is secured in both chucks on a glass lathe and rotated while the one of the necked-down section is flame worked to ensure even heating.

II. After the preform has reached a sufficient viscosity the chucks are moved apart drawing the necked-down section out into a fiber

A. This step prepares the preform end for fiber pulling

III. The end of the preform is then heated using a hydrogen-oxygen torch until the end of the preform has a low enough viscosity to begin pulling fibers

A. Viscosity is approximated visually

IV. After the end of the tube is at a sufficient viscosity a rod of borosilicate is attached to the molten mass of glass at the end of the preform.

A. Prior to the rod being attached the following steps are taken.

1. The end of the fused silica rod to be attached is heated to ensure bonding to the borosilicate glass.
2. The rotation of the lathe is stopped to prevent any twisting of the glass during the fiber drawing process.

V. With the borosilicate rod attached to the molten, glass the flame from the torch is removed from the vicinity of the preform to prevent differential heating of the glass during the fiber drawing process.

VI. Once the flame is removed from the end of the preform, a fiber is drawn by pulling the borosilicate rod away from the end of the tube.

A. The speed of the pull will determine the diameter of the fiber produced

B. Viscosity of the glass at the end of the preform will also determine the diameter and length of the fiber produced.

3.2.1 Phase Separation

In order to produce the porosity within the fibers, the glass needs to be heat treated to induce the phase separation. This phase separation allows for one of the phases to be preferentially leached out of the glass, leaving the cladding porous. The fibers were heat treated as follows:

I. Fibers produced from the heating and pulling process using the lathe were separated into fiber lengths of approximately 9 inches to accommodate the size of the furnace that was used. The furnace that was used is a Thermolyne 1500.

II. Fiber lengths were placed on an alumina plate that was then placed in the furnace.

III. The furnace was set at a temperature of 565˚C and the fibers were held at this temperature for 20 hours followed by a furnace cool. These were the heat treatment conditions given by Corning for this glass.

IV. After the dwell time was reached the furnace was switched off and allowed to cool to room temperature.

3.2.2 Leaching process to produce the porous clad fiber

Fibers that are produced and heat treated as previously described are leached using a surface etching treatment and then an acid bath leaching treatment. The surface etching treatment is done using a 5% solution of ammonium biflouride. Fibers are surface etched for a duration of 5 minutes. Fibers are then subjected to the acid bath immediately upon completion of the surface etching treatment. The acid bath is done with a 3N concentration of HNO_3 at a temperature of 80˚C. Fibers are processed according to the following procedure:

I. The fibers are immersed into a 5% ammonium biflouride solution bath for five minutes.

II. After a fiber is in the surface etching solution for its allotted time the etching solution is drained off.

III. The fiber is then immediately immersed in a bath of a 3N solution of nitric acid that is at a temperature of 80˚C. Fibers are left in the acid solution over night to ensure complete dissolution of the secondary phase.

IV. After the fibers have been in the acid solution for a sufficient time, the container is emptied of the nitric acid.

V. Fibers are rinsed in the containers which then filled with distilled water and left overnight to wash any contaminates from the pores within the fibers. Fibers are left in the container during the rinsing process.

VI. Once the washing process was completed, the fibers were removed from the containers and placed on paper towels and allowed to dry in air under ambient conditions.

3.3 Experiments to affect pore size of cladding region

3.3.1 Removal of colloidal silica with an alkaline solution to increase pore size

This portion of the research was conducted to determine the treatment time necessary to remove all of the silica gel from the pore structure. Treatment times for fibers in the solution ranged from 15 minutes to 60 minutes due to the small diameter of the fibers. Solution to glass ratio was well over 10:1 to ensure a stable alkaline environment. Experimental procedure was as follows:

I Surface etching -Fiber immersed in 5% ammonium biflouride solution

1) Immersed for 30 seconds

II Leaching of fibers

2) Placed in glass test tube containing 3N HNO_3 directly from surface etching process
3) Tubes placed in beaker of water that is heated to 90˚C
4) Fibers left in solution for 18-24 hours to ensure complete dissolution of secondary phase
5) Fibers washed by empting HNO_3 from tubes and replaced with 18.2 MΩ deionized water and replaced in heated beaker
6) Fibers washed for 18-24 hours
7) Fibers removed from water

II. Removal of colloidal silica

1) Fibers immersed in 0.5N solution of NaOH
    a. Immersion times of 15, 30, 45, and 60 minutes
2) Fibers removed from NaOH bath and placed in 3N solution of HNO_3 for 3 hours
3) Fibers were removed from the HNO_3 solution and rinsed in 18.2 MΩ deionized water for 12-18 hours
4) Fibers removed from water and air dried.

3.3.2 Phase separation temperature and post heat treatment of bulk glass experiment

Glass samples for this experiment were all prepared for processing on the same day from the same batch of tubes that were received from Corning. The processing of the tubes involved crushing the tubes into large fragments of about 1 cm^2. Glass fragments were placed in an alumina crucible and heat treated at one of the three phase separation temperatures. The temperature of the crucible was monitored through the placement of a thermocouple at the crucible location in the furnace. All three phase separation temperature groups were heat treated in the same location in the furnace with the phase separation temperature monitored and adjusted so that the thermocouple was touching the alumina crucible.

Once the glass had cooled it was then leached to make the glass porous. Fragments were initially placed in a 5% solution of ammonium biflouride for 5 minutes. This initial immersion removes the silica rich layer that forms during the making of the tubes and heat treatment process. Without this initial step, the leaching process is inhibited and there is no visible porosity in the glass. After removal of the surface layer the glass was immediately placed in a 3N solution of nitric acid. The fragments were left in solution for 72 hours to ensure that complete leaching of the secondary phase is accomplished. A volume ratio of 50 ml glass to 500 ml of nitric acid solution was used during the leaching of the glass fragments to provide a more adequate supply of H^+ during the leaching.

Experimental groups were classified by the initial phase separation temperature and were grouped and processed accordingly. All surface etching, leaching, and washing was done for a phase separation temperature group. After the group was leached and washed the total amount of fragments in a group were divided in half, with one group receiving the post heat treatment as the next step and the other group undergoing a treatment with a 0.5 N NaOH solution. After the fragments underwent the NaOH treatment they were washed in a 3N nitric acid solution for 24 hours to remove any contamination and residue during the NaOH treatment. Following the acid wash the fragments were washed in DI water for 24 hours and then air dried. The NaOH treated fragments received the post heat treatments after the air drying. A flow chart of the experimental process is shown in Figure 3-2.

Treatment time for the NaOH was determined by assuming that the diffusion condition of the NaOH was the same for both the fibers as for the bulk glass pieces. If the conditions are the same then the diffusion distance is the only adjustment that needs to be taken into account. Since the NaOH treatment involves the dissolution of the silica gel in the pore structure and its transport out of the glass then the diffusion distance affects the time needed for the treatment. Time in solution was calculated as follows with D being the diffusion distance, t is the time in solution and α all other factors effecting diffusion. Diffusion in the fibers is denoted by an f subscript and in the bulk by b. Glass thickness is 1.4 mm and the average fiber diameter is 200 μm.

$$D_f = \alpha\sqrt{t_f} \qquad D_b = \alpha\sqrt{t_b}$$

$$D_b = 7\, D_f = 7\alpha\sqrt{t_f} = \alpha\sqrt{t_b}$$

$$t_b = 49\, t_f = 49 * 30 \text{ min}$$

$$t_b = 1470 \text{ min} = 24.5 \text{ hours}$$

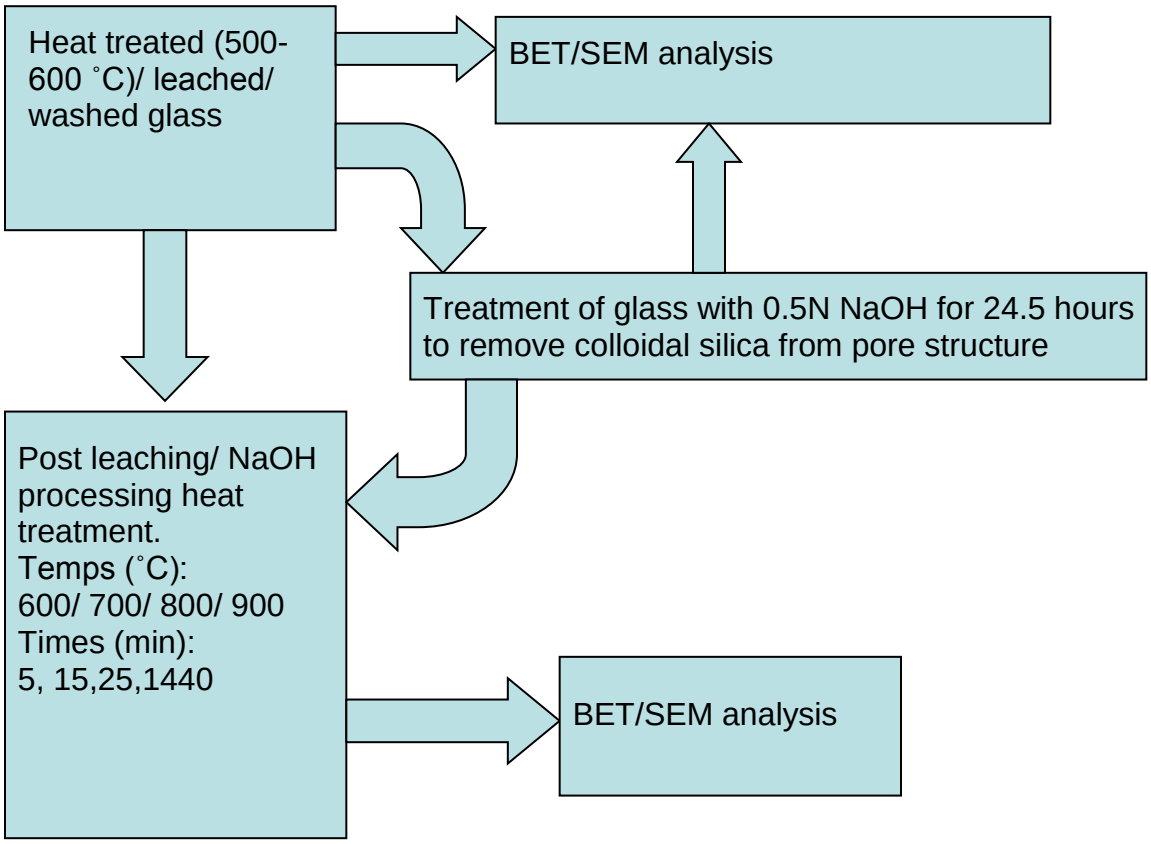

Figure 3-2: Phase separation temperature and post heat treatment experimental schematic

3.4 Materials characterization

Materials characterization done on the fibers investigated the overall structure of the fiber and the morphology and pore characteristics of the cladding region. The methods used were primarily scanning electron microscopy (SEM, LEO 1550) and nitrogen adsorption (BET, Quantachrome autosorb 1-c).

Samples prepared for the SEM were done in two different ways depending on which type of sample was imaged. Fibers were prepared by mounting onto a sample stub with a colloidal silver paint. Mounting with the silver paint ensures an ample conduction path that is usually absent due to the size of the fiber and the curvature of the surface. Bulk glass samples were mounted onto the stubs with carbon tape. Both the fiber and bulk samples were coated with 10 nm of gold using a sputter coater. When imaged in the SEM the accelerating voltage was set to 5 KV so that only the surface of the glass would be imaged.

Pore structure was characterized through the use of a nitrogen adsorption technique. The samples for the analysis were placed in a 9mm sample holder. Samples were then out gassed for a minimum of 24 hours at a heating cuff setting of 300˚C. Time and temperature of the outgas step was chosen to ensure that all adsorbed water was removed from the glass samples. Weights of the samples were taken before and after out gassing and the samples were placed into the machine immediately after the final weight was taken. The produced isotherms were analyzed through the use of a Monte Carlo analysis program supplied with the instrument. Parameters

chosen for the analysis were nitrogen adsorption onto oxygen and the analysis was applied to the adsorption branch of the isotherm. The model used was for nitrogen adsorption onto silica with a cylindrical pore structure.

Some fibers that have been fabricated and subjected to the leaching process have not been able to sense gas. However fibers that have been treated with a 0.5 N NaOH solution for 30 minutes will sense acetylene gas. As a starting point the initial fiber characterization is presented for comparison to the remainder of the experimental results. An optical micrograph of the end face of the fiber is shown in

Figure 3-3. The cladding region is visible and distinct from the core in the micrograph.

Figure 3-4 is an SEM micrograph of the surface of the fiber and

Figure 3-5 is an SEM micrograph of the interface between the core and the cladding of the fiber. Both of the micrographs show porosity on the surface of the fiber and the interface between the core and cladding regions. The interface between the core and cladding can be clearly seen in the SEM micrograph in Figure 19. Nitrogen adsorption characterization is detailed in Figure which shows the pore distribution profile for the initial fibers. The fiber sample amounts were small and were close to the resolution of the scale used for weighing. An accurate measure of the sample weight was difficult. This produces an incorrect specific pore size distribution and the amounts on the y-axis should be taken only as a relative measure. However, the actual distribution of the pore sizes is not affected by an incorrect sample weight. Nitrogen adsorption shows that the mode 1 pore size is 6 nm with an average pore size of 10.9 nm.

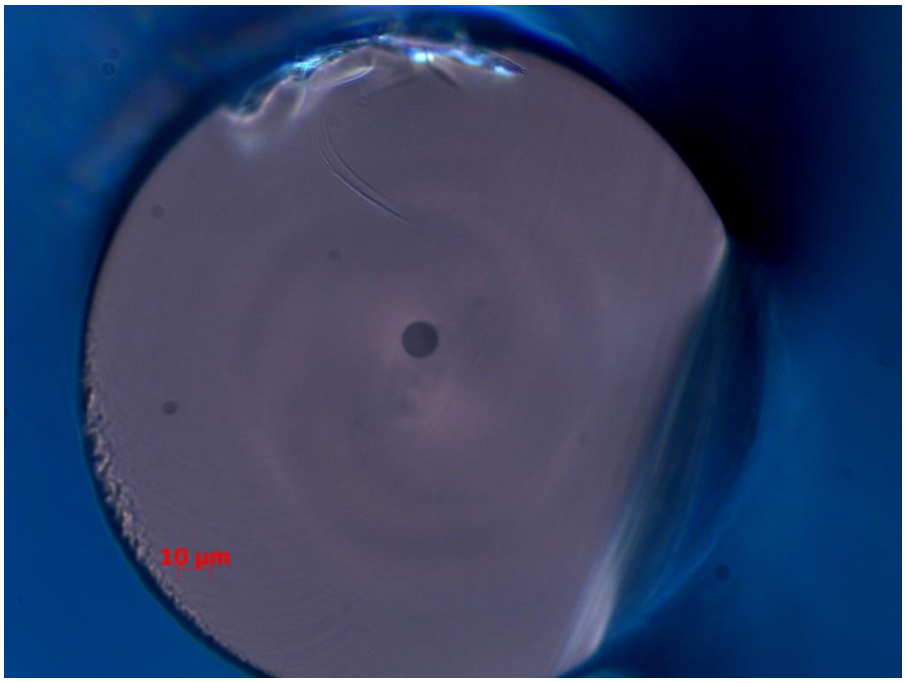

Figure 3-3: Optical micrograph of a fracture surface of the end face of a leached only optical fiber

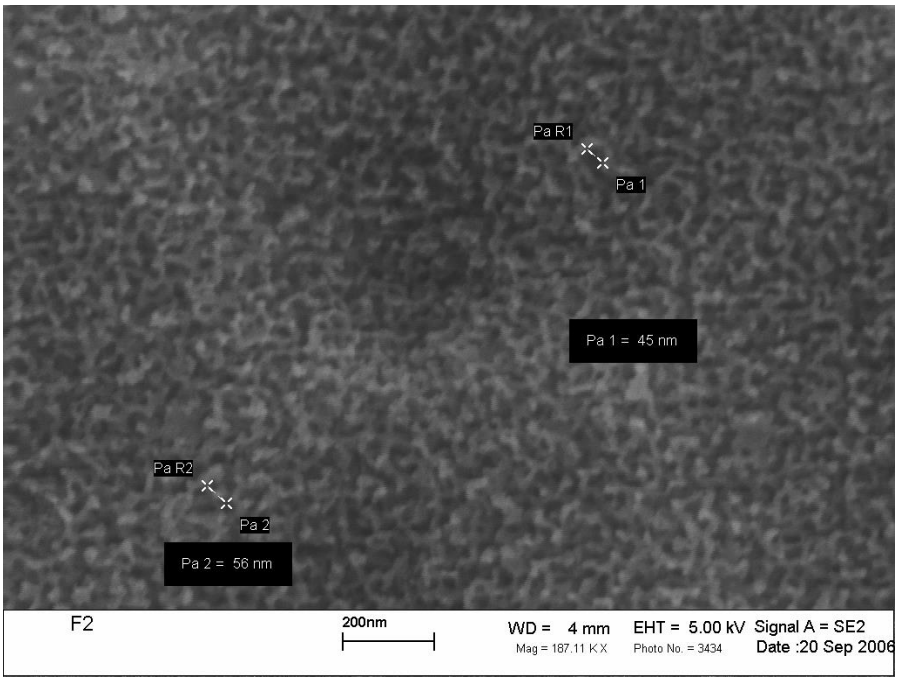

Figure 3-4: SEM micrograph of leached only optical fiber surface

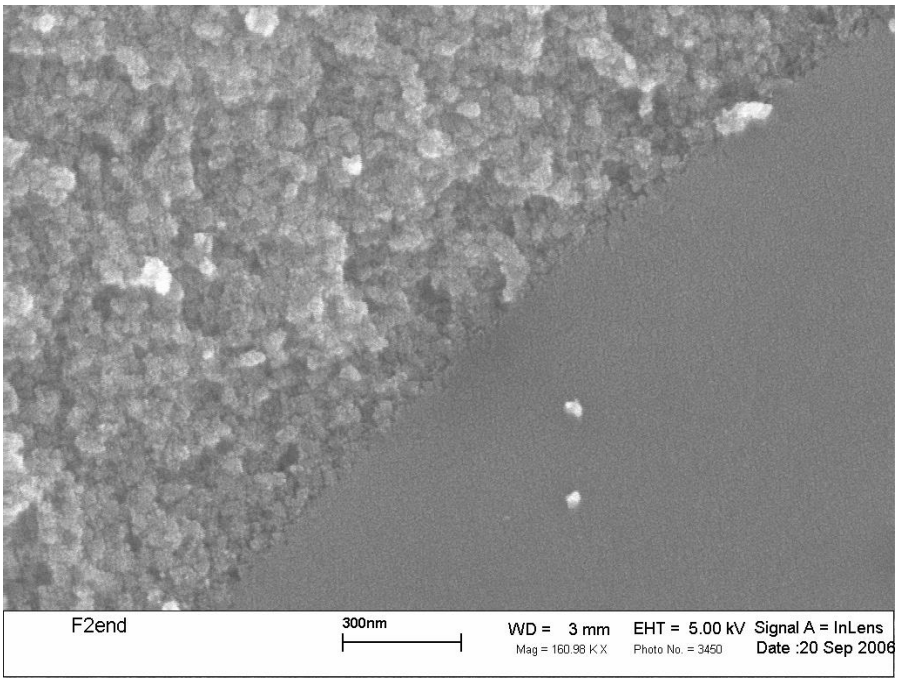

Figure 3-5: SEM micrograph of core-cladding interface of leached only optical fiber

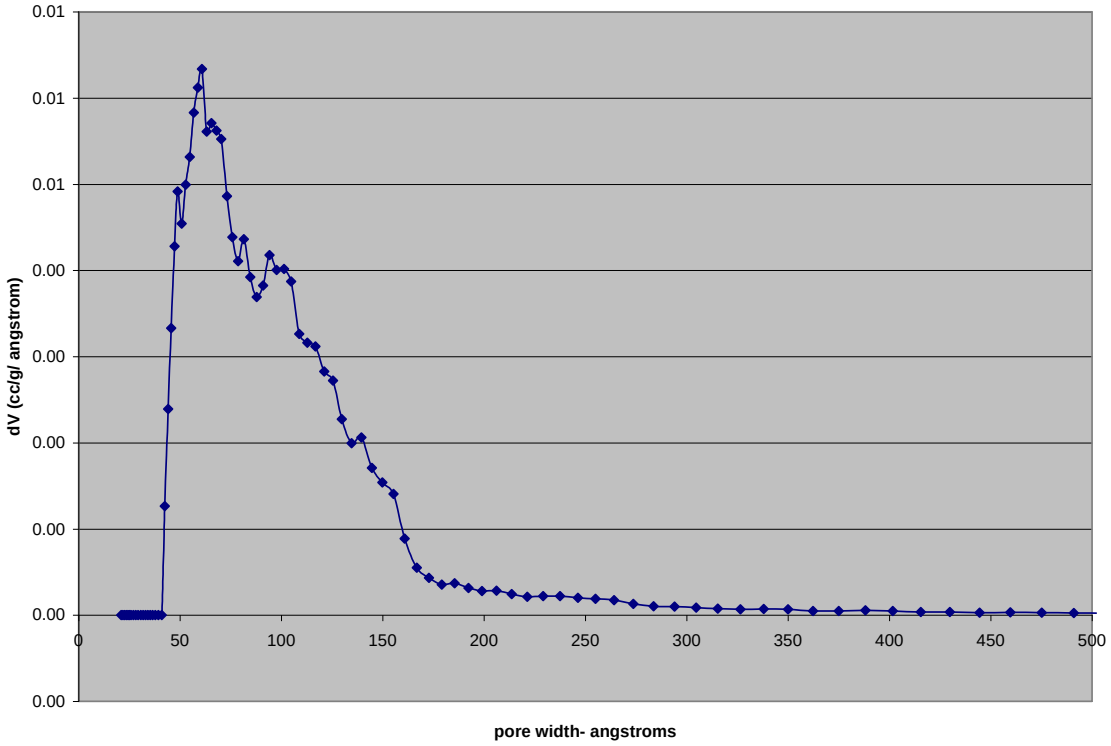

Figure 3-6: Pore size distribution of leached only optical fiber

3.4.1 Removal of colloidal silica to increase pore size with alkaline solution

The processing of fibers to remove the colloidal silica from the pore structure resulted in a maximum average pore size of approximately 30 nm after a processing time of 30 minutes. This is supported by SEM micrographs of the fibers. In
Figure 3-7and
Figure 3-8 the SEM micrographs show the interface between the core and cladding region of the fibers treated for 15 and 30 minutes respectively. The increase in the pore size is visible in the micrograph as the processing time changes. Pore size distributions from characterizing the fibers through nitrogen adsorption is shown in
Figure 3-9 and a plot of the average pore size as a function of processing time is in
Figure 3-10. From
Figure 3-9, it can be seen that the maximum shift in the pore distribution occurs at 30 minutes and that the 45 and 60 minutes treated fibers have the same distribution as the fiber that was treated for 30 minutes. The nitrogen adsorption characterization shows that maximum average pore size is achieved after 30 minutes of treating the fibers with a NaOH solution. Enlargement of the pore structure is confirmed by the SEM micrographs in
Figure 3-7 and
Figure 3-8 when compared against the SEM micrograph of the as-leached fiber in
Figure 3-5.

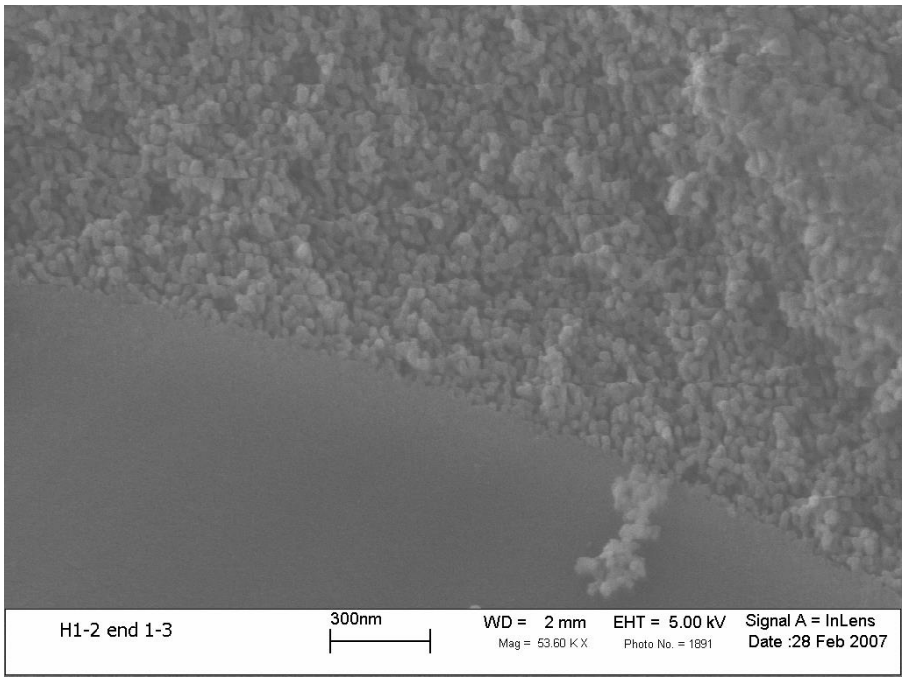

Figure 3-7: SEM micrograph of core-cladding interface of fiber treated with 0.5 N NaOH for 15 minutes

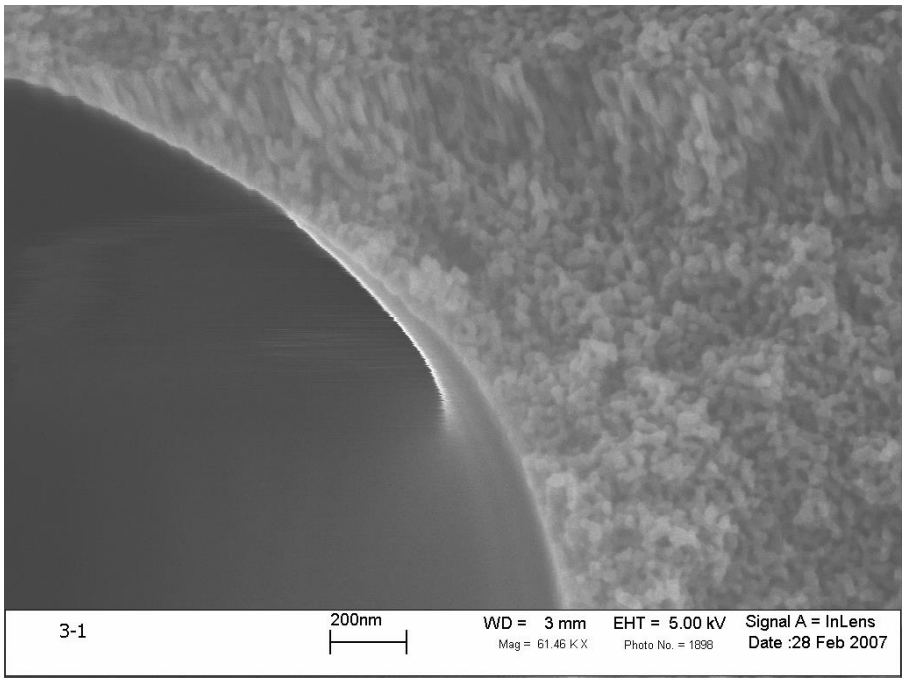

Figure 3-8: SEM micrograph of core-cladding interface of fiber treated with 0.5 N NaOH for 30 minutes

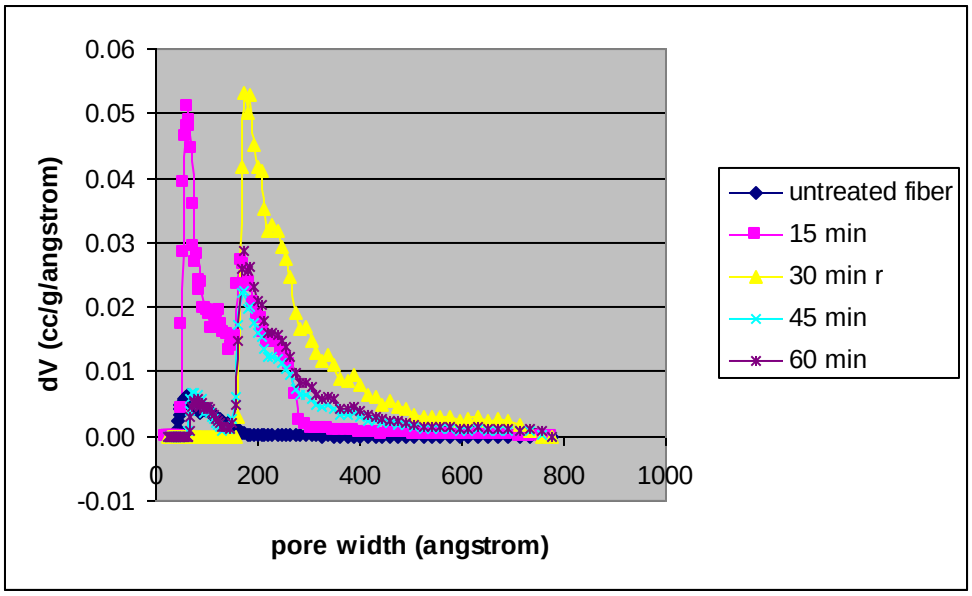

Figure 3-9: Pore size distribution for fibers treated with NaOH

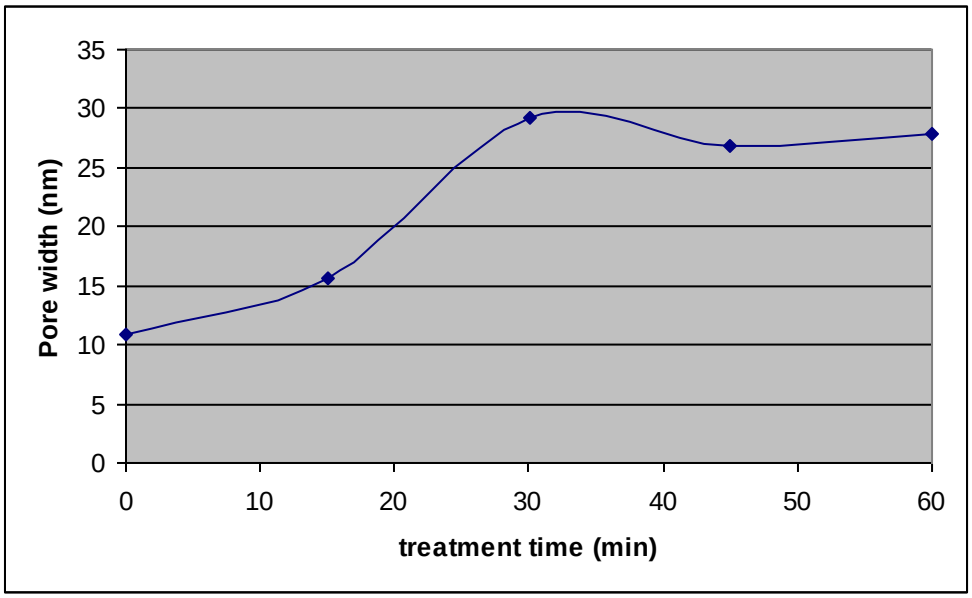

Figure 3-10: Average pore size of fibers treated with NaOH

3.5 Phase separation temperature and post heat treatment of bulk glass experiment

The purpose of this experiment was to investigate if certain factors would affect the pore size of the cladding region of the optical fiber. It is desirable to be able to control the pore size of the cladding so that the sensor can be optimized for a particular application. The factors that were chosen were the temperature at which the cladding region was phase separated, treatment of the fiber with sodium hydroxide after the fiber had undergone the initial leaching stage, and

the use of a heat treatment of the fiber after all other processing was done. Phase separation temperature was chosen because the size of the phase regions has a dependence on the temperature at which the phase separation is allowed to proceed. Pore size of this glass type can be altered by treating the porous glass with a solution of sodium hydroxide. Immersing the fibers in the sodium hydroxide removes the colloidal silica that is present in the pore structure after the leaching process is completed. Previous experiments have shown that the pore size reaches a maximum when the fibers have been in solution for 30 minutes. The treatment time in the NaOH solution was adjusted for the increased diffusion lengths in the bulk glass. Typical diameters of the fibers are around 200 microns and the thickness of the bulk glass is 1.7 mm. Treating the glass with sodium hydroxide after the leaching process was done to show the maximum pore size for a particular phase separation temperature and to understand how this would affect the pore size after post heat treatment. The pore structure of this porous glass can be consolidated at temperatures above 600˚C. It is thought that during the process of consolidation the smaller pores initially consolidate in order to reduce the surface area of the glass. After the small pores consolidate, the larger pores will begin to consolidate and collapse and make the glass solid. By heat treating the fibers at temperatures of 600˚C and above, and for different times the process of consolidation of the cladding region can be understood. In understanding the process a heat treatment schedule can be chosen that will give a pore structure that is chosen.

The glass that is used for the cladding region was obtained from Corning and the phase separation schedule that the plant uses is a temperature of 565˚C for a duration of 20 hours. This heat treatment schedule ensures that the resultant glass articles are stress free during the leaching process. Since this is the heat treatment schedule for this glass composition, temperatures of 500, 550, and 600˚C were chosen to bracket the temperature used industrially. By heat treating the glass at temperatures close to that used to maintain a stress free porous glass some exchange of pore size for stress within the glass is made. Temperatures above 600˚C were attempted but fibers treated at those temperatures softened and bonded to the alumina plate the fibers were on when heat treated. Heat treating the glass after it was made porous was done to increase the pore size and possibly increase the mechanical strength of the fibers. Temperatures for the post heat treatment were 600-900 ˚C in 100˚C increments. This temperature range was chosen because 600˚C is the maximum continuous service temperature that is recommended by Corning and 900˚C is the temperature above which rapid sintering starts. The samples were post heat treated for 25 minutes and 24 hours.

The data that was accumulated during the analysis of these glass samples included the adsorption and desorption isotherms of the glass samples, the output from the Monte-Carlo analysis and the data that was derived from the Monte-Carlo outputs. The total amount of data is large, so the only data that will be presented is the average pore size, median pore size, pore volume, surface area, and the widths of the pore distributions. The range of pore size for this type of analysis is from 2.5 nm up to 77 nm with the full width of the distribution being 75.19 nm.

Figure 3-11 through

Figure 3-14detail the differences that are produced due to different phase separation temperatures and the use of the 0.5 N NaOH treatments. In Figures 28-31 there is not a large change in the response variables between the phase separation groups, with the exception of the NaOH treated group at 550 and 600˚C.

Figure 3-11 also shows that the distribution of pore widths changes by the separation of the median pore width from the average pore width in both the 550 and 600˚C samples.

Figure 3-11 shows the change in the average and median pore size as a function of the phase separation temperature for both the as-leached and NaOH treated samples. The average and median pore widths increase by a few nanometers in the as-leached samples as the phase separation temperature increases. When the samples are treated with the NaOH solution the pore widths for the 550˚C and 600˚C samples have a much larger pore width increase over the 500˚C sample. The purpose of the NaOH treatment is to remove the silica gel that is deposited in the pore structure during leaching. The change in pore widths would indicate that the 550 and 600˚C samples have a higher amount of silica gel deposited in the pores. It should also be noted that the median and average pore widths are significantly different in the NaOH treated samples. These values are almost identical in the as-leached samples. This would indicate that the silica gel is removed mainly from the larger pores.

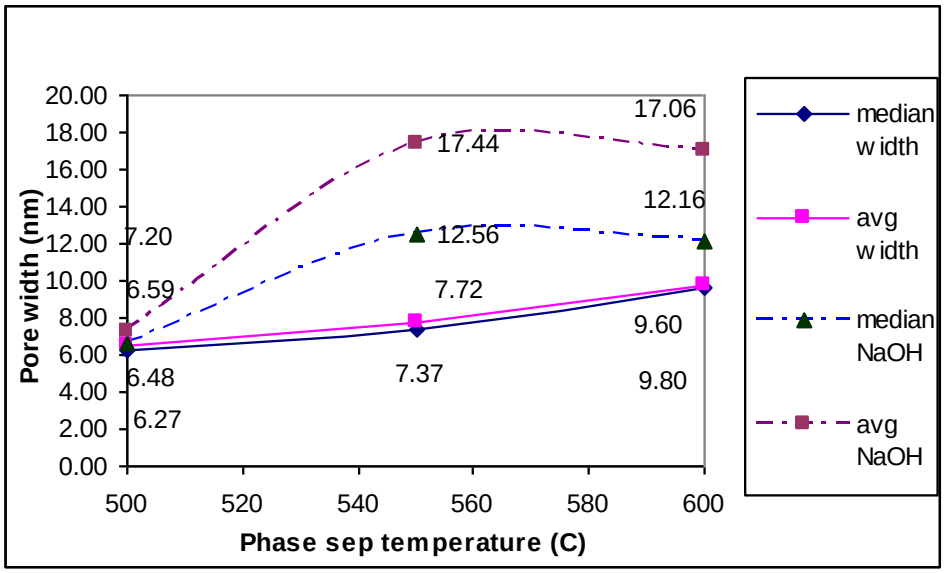

Figure 3-11: Average and median pore size for different phase separation temperatures

Figure 3-12 is the change in pore volume for both the as leached and NaOH treated samples. The as leached samples show a slight decrease in the pore volume as the phase separation temperature is increased, while the NaOH treated samples have maximum pore volume in the 550˚C sample. This would support the conclusion that the 550 and 600˚C samples have a higher amount of silica gel deposited in the pores during leaching. Since the gel deposited is primarily produced from the silica in the secondary phase, it can be concluded that the secondary phase in the 550 and 600˚C samples have higher silica content than the samples phase separated at 500°C, with the largest amount of silica in the secondary phase existing in the glass phase separated at 550°C.

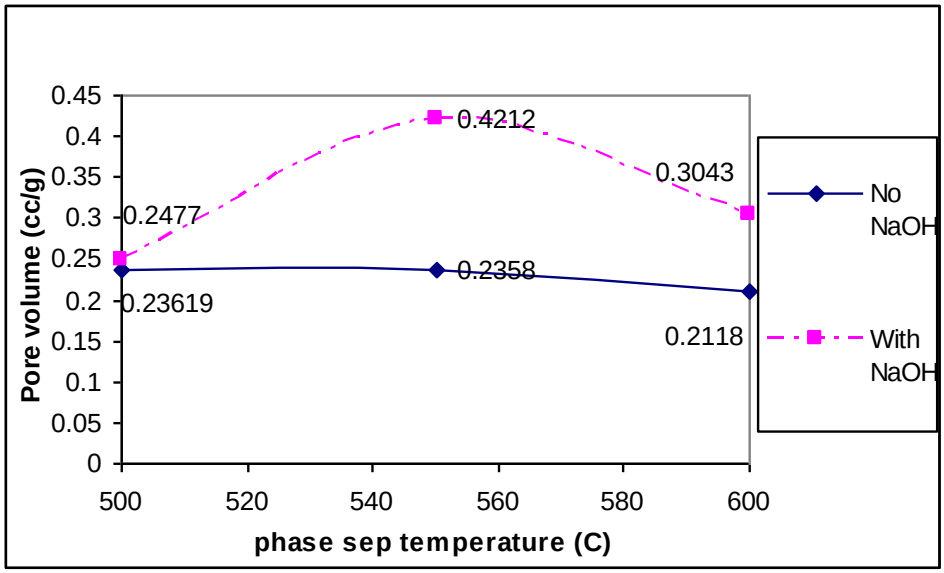

Figure 3-12: **Pore volume for different phase separation temperatures**

Figure 3-13 is the change in surface area of the samples. The surface area decreases in the as-leached samples as the phase separation temperature increases. Maximum increase in the surface area is found in the 550˚C sample that was treated with NaOH. When this trend is taken together with the trends from

Figure 3-11 and

Figure 3-12, one conclusion that can be made is that the pore morphologies produced by the phase separation temperatures are quite different. The average pore size is similar in the NaOH treated 550 and 600˚C samples but the pore volumes and surface areas do not increase at the same magnitude. This can be explained by different pore geometries and the amount of tortuosity present in the samples.

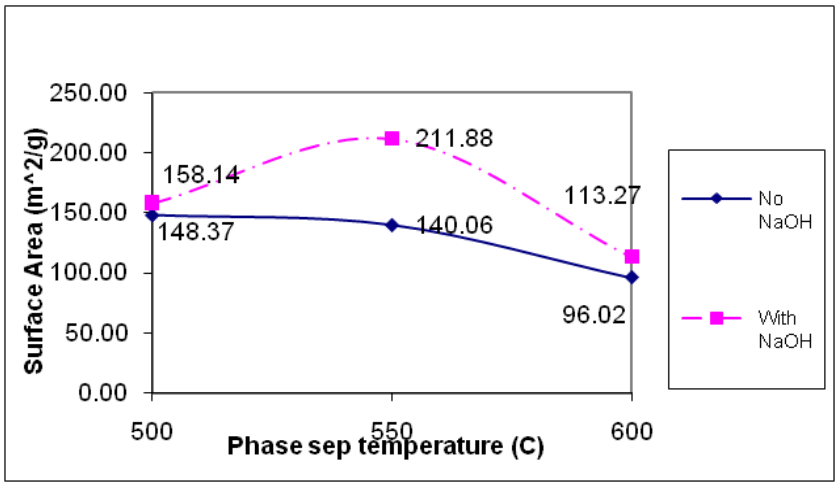

Figure 3-13: Surface area for different phase separation temperatures

Figure 3-14 is the change in the pore distribution width as a function of the phase separation temperature. The pore distributions for the as-leached samples do not change much with an increase in phase separation temperature. With a NaOH treatment, the distribution of the pore widths for the 550 and 600˚C samples reaches the maximum that can be analyzed by the nitrogen adsorption technique. This is another indication that the silica gel fills the larger pores in the material, since the greatest amount of increase in the distribution is in the larger pore widths.

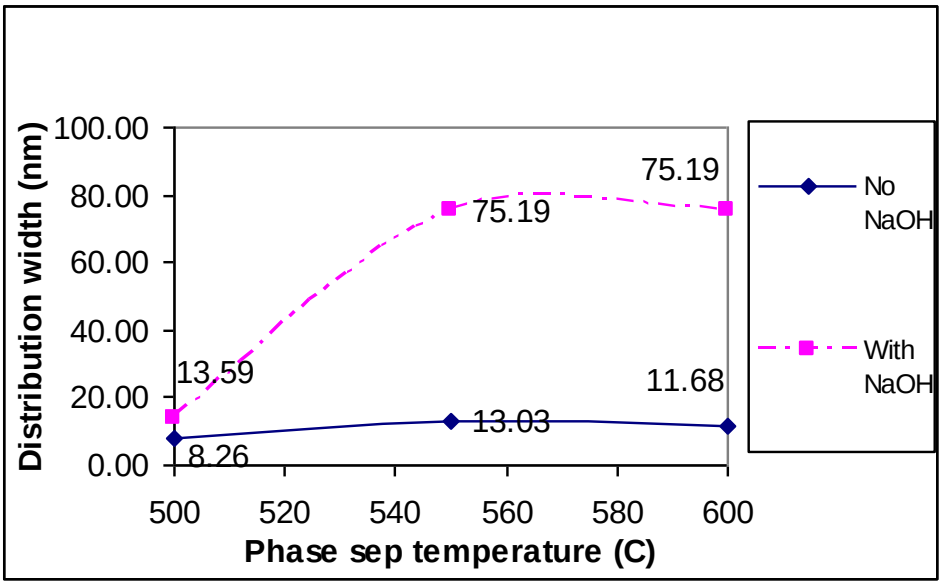

Figure 3-14: Pore size distribution widths for different phase separation temperatures

The analysis of the 25 minute and 24 hour samples shows a range of average pore width, pore volume, surface area and distribution widths. The starting treatment condition is the glass prior to post heat treatment, but having been phase separated, leached and treated with NaOH if required. The naming convention for the groups follows the pattern of first stating the phase separation temperature, then if the sample was treated with NaOH (y for yes), the temperature at which the sample was post heat treated, and finally the length of the post heat treatment. An example would be 550N900-25min, which is a sample that was phase separated at 550˚C, did not undergo treatment with NaOH, and was post heat treated at 900˚C for 25 minutes. Table 3 details the naming convention and processing conditions used in the experiment for each sample.

Table 3-1: Experimental sample notation and processing conditions

Sample name	Phase separation temperature	Treated with 0.5 N NaOH for 24.5 hrs	Post heat treatment temperature	Post heat treatment time
500n	500 ° C	no	none	None
500n600-25min	500 ° C	no	600	25 minutes

500n700-25min	500 ° C	no	700	25 minutes
500n800-25min	500 ° C	no	800	25 minutes
500n900-25min	500 ° C	no	900	25 minutes
500n600-24 hr	500 ° C	no	600	24 hours
500n700-24 hr	500 ° C	no	700	24 hours
500n800-24 hr	500 ° C	no	800	24 hours
500n900-24 hr	500 ° C	no	900	24 hours
500y	500 ° C	yes	none	None
500y600-25min	500 ° C	yes	600	25 minutes
500y700-25min	500 ° C	yes	700	25 minutes
500y800-25min	500 ° C	yes	800	25 minutes
500y900-25min	500 ° C	yes	900	25 minutes
500y600-24 hr	500 ° C	yes	600	24 hours
500y700-24 hr	500 ° C	yes	700	24 hours
500y800-24 hr	500 ° C	yes	800	24 hours
500y900-24 hr	500 ° C	yes	900	24 hours
550n	550 ° C	no	none	None
550n600-25min	550 ° C	no	600	25 minutes
550n700-25min	550 ° C	no	700	25 minutes
550n800-25min	550 ° C	no	800	25 minutes
550n900-25min	550 ° C	no	900	25 minutes
550n600-24 hr	550 ° C	no	600	24 hours
550n700-24 hr	550 ° C	no	700	24 hours
550n800-24 hr	550 ° C	no	800	24 hours
550n900-24 hr	550 ° C	no	900	24 hours
550y	550 ° C	yes	none	None
550y600-25min	550 ° C	yes	600	25 minutes
550y700-25min	550 ° C	yes	700	25 minutes
550y800-25min	550 ° C	yes	800	25 minutes
550y900-25min	550 ° C	yes	900	25 minutes
550y600-24 hr	550 ° C	yes	600	24 hours
550y700-24 hr	550 ° C	yes	700	24 hours
550y800-24 hr	550 ° C	yes	800	24 hours
550y900-24 hr	550 ° C	yes	900	24 hours
600n	600 ° C	no	none	None
600n600-25min	600 ° C	no	600	25 minutes
600n700-25min	600 ° C	no	700	25 minutes
600n800-25min	600 ° C	no	800	25 minutes
600n900-25min	600 ° C	no	900	25 minutes
600n600-24 hr	600 ° C	no	600	24 hours
600n700-24 hr	600 ° C	no	700	24 hours
600n800-24 hr	600 ° C	no	800	24 hours
600n900-24 hr	600 ° C	no	900	24 hours
600y	600 ° C	yes	none	None
600y600-25min	600 ° C	yes	600	25 minutes

600y700-25min	600 ° C	yes	700	25 minutes
600y800-25min	600 ° C	yes	800	25 minutes
600y900-25min	600 ° C	yes	900	25 minutes
600y600-24 hr	600 ° C	yes	600	24 hours
600y700-24 hr	600 ° C	yes	700	24 hours
600y800-24 hr	600 ° C	yes	800	24 hours
600y900-24 hr	600 ° C	yes	900	24 hours

The ranges of values for the pore characteristics are shown in Figures 32-35. In these range graphs, the value that the groups started off with is marked with a horizontal dash upon the vertical line above the starting treatment condition. Vertical lines on the graphs are the range of values that the treatment groups have due to the various heat treatment conditions for that group.
Figure 3-15 shows the range of average pore widths for the major treatment groups.
Figure 3-16 shows the pore volume ranges for the treatment groups.
Figure 3-17 shows the surface area ranges for the major treatment groups.
Figure 3-18 shows the ranges of pore size distributions for the major treatment groups. These range graphs show that the pore morphology of the glass can have a wide range of values for the various pore characteristics depending on the processing conditions.

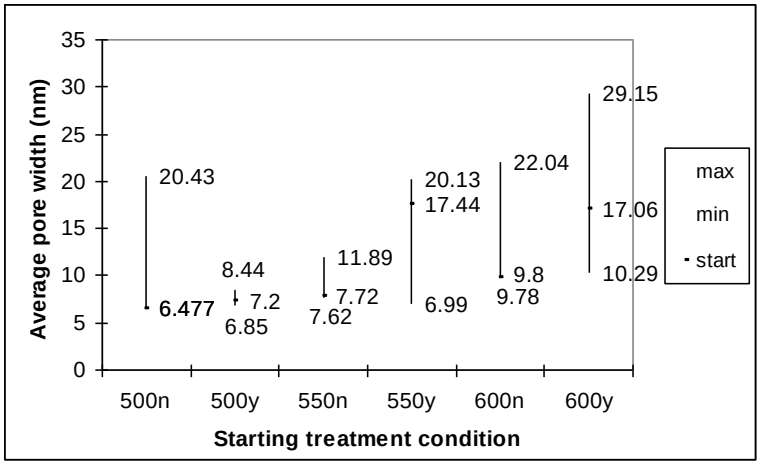

Figure 3-15: **Average pore width range for major treatment groups**

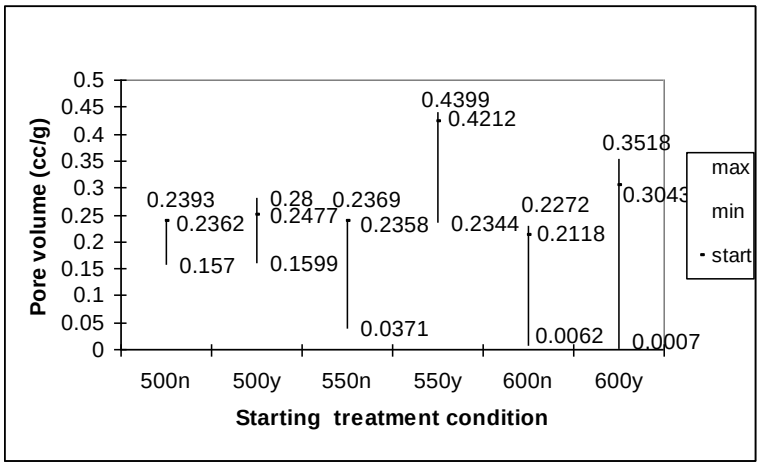

Figure 3-16: Pore volume range for major treatment groups

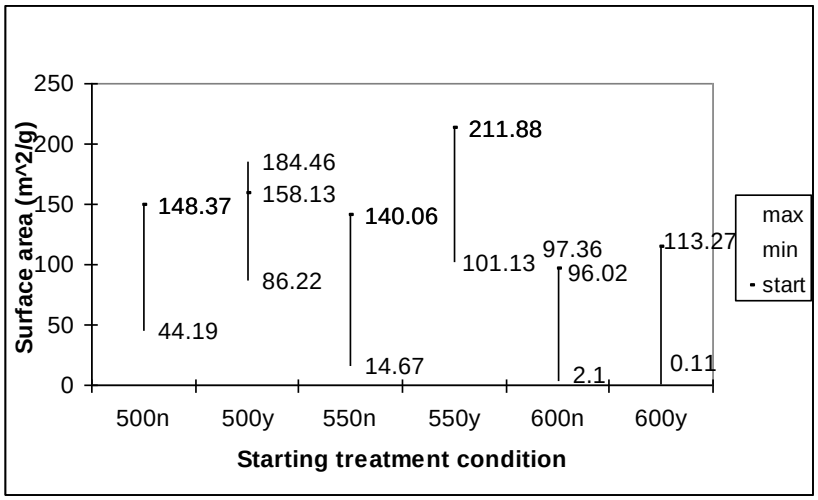

Figure 3-17: Surface area range for major treatment groups

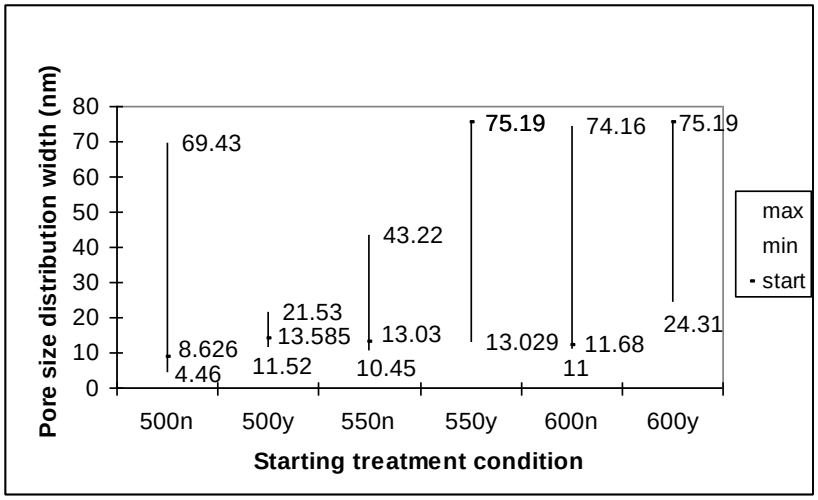

Figure 3-18: Pore size distribution width range for major treatment groups

To determine the useable parts of the pore experiment the average pore width and pore volume was graphed together for each starting treatment group. Graphs of the surface area (SA) are grouped together with the pore width-pore volume (PVPW) graphs. Changes in the pore characteristics indicate what type of morphological changes are taking place. The two types of changes that are considered in the analysis of the data are the coarsening of pores into larger pores and the consolidation of the pores to form a more dense glass. Coarsening of pores from small pores into larger pores shows up as an increase in the average pore width. Accompanied with the increase in pore width is a decrease in surface area while the pore volume will show very little change. The small pores coalesce into larger pores, with the surface area decreasing because the separation between the pores is removed. In this process, the pore volume should change very little because any reduction in the pore volume would be due to shrinking of the

pores. Any shrinkage of the pores should be considered consolidation and would be driven by the reduction of surface area through reduction in pore volume. Consolidation of the pore structure shows up as a change in the average pore width, accompanied by a decrease in pore volume and surface area of the glass. The change in the average pore width will be determined by the size of the pores that are consolidating. If small pores are the primary ones that are consolidating, then the average pore width will increase. If the average pore width decreases, this will be due to consolidation of large pores. If both large and small pores are consolidating then the average pore width will change very little. With consolidation of the pores there will be a decrease in the pore volume and surface area of the glass. It is also possible for there to be a combination of coarsening and consolidation. Where the samples show a large increase in pore width, with a pore volume change similar to samples with smaller pore width changes, indicates that some amount of consolidation is occurring during the coarsening of the pores.

Figure 3-19 and

Figure 3-20 are the PVPW and SA graphs for the 500N group. All of the samples in the 500N group had an increase in pore width. Most samples also had a decrease of pore volume and surface area, while none of the samples were fully consolidated during processing. The 600˚C shows little pore width or pore volume shift within the time of treatment, while the amount of the shift increases with temperature. The surface area for the 600˚C sample shows an overall decrease; however the decrease is 11% for 25 minutes and 5 % at 24 hours. This indicates that the 600°C sample initially undergoes coarsening followed by consolidation of the pores. Shifts in the pore width and pore volume are accompanied by a significant decrease in the surface area for the 700, 800, and 900˚C samples. In the 24 hour, 800°C and 25 minute, 900°C samples, the amount of increase in pore width is accompanied by a relatively small decrease in pore volume. With a small pore volume change and larger pore width increase, these samples are undergoing a mixed coarsening and consolidation process. In the 500N group the average pore widths are enlarged through a post leaching heat treatment for all treatment times. Pore volumes of the samples change slightly for treatments longer than 25 minutes, while the average pore widths of the 700, 800, and 900˚C samples continue to change. None of the samples in the 500N group had greater than 40% consolidation. Overall changes in the 500N group are summarized in Table 3-2 as the percent change in the pore characteristics and the type of process involved in the change. The primary change in pore structure is due to consolidation of the pores. The exception to this is the coarsening in the 600°C, 25 minutes sample and a mixed coarsening and consolidation process in the 800°C, 24 hour sample and the 900°C, 25 minute sample.

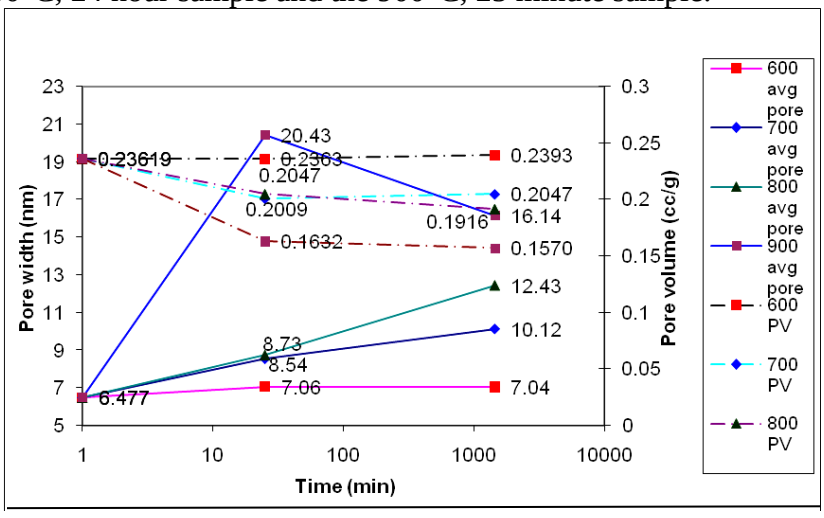

Figure 3-19: Average pore width and pore volume of 500N group

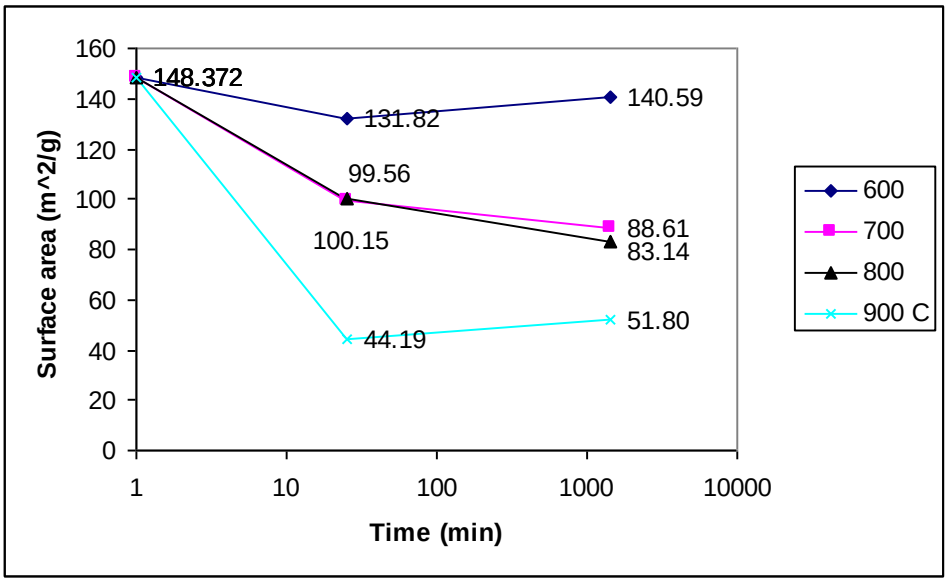

Figure 3-20: Surface area of 500N group

Table 3-2: Percent change of pore characteristics of the 500N group

	Percent change from base sample value			
Sample	Average Pore width (nm)	Pore volume (cc/g)	Surface Area (m^2/g)	Type of pore change
500N600-25	9.02%	0.05%	-11.16%	Coarsening
500N600-24H	8.68%	1.32%	-5.25%	Consolidation
500N700-25	31.81%	-14.94%	-32.90%	Consolidation
500N700-24 H	56.31%	-13.33%	-40.28%	Consolidation
500N800-25	23.57%	-13.33%	-32.50%	Consolidation
500N800-24H	91.85%	-18.88%	-43.97%	Mixed
500N900-25	189.27%	-30.90%	-70.22%	Mixed
500N900-24H	149.23%	-33.53%	-65.09%	Consolidation

Group 500Y PVPW and SA graphs are shown in Figure 3-21 and
Figure 3-22. The pore morphology changes have a different pattern than the 500N group. In this group, the 800 and 900˚C groups have a pore width increase, while the 600 and 700˚C groups have a decrease in the pore width for the 24 hour heat treatment times. In some of the samples there is an increase in the pore volume with a decrease in the pore width. The increase in pore volume is possibly due to the consolidation of silica gel that is blocking or filling a large number of small pores in the base sample. The 500Y group is treated with sodium hydroxide to remove the silica gel that is deposited in the pores during the leaching process. Time in solution was calculated to duplicate the conditions for the fibers. The unblocking effect would indicate that not all of the silica gel is removed and is possibly deposited in a manner to seal off or fill pores in the base sample. This explains the decrease in the average pore width with an increase in pore volume and surface area. Samples in the 500Y group primarily underwent pore consolidation with the unblocking of pores occurring in four of the samples. Unblocking of pores is a consolidation process where the silica gel is condensed to fully dense silica, so consolidation

can be considered to have occurred in all of the samples in the group. None of the samples in the group underwent complete consolidation. The changes in the 500Y group is summarized in Table 3-3 as the percent change in the pore characteristics with the type of process involved in the change. The samples in the 500Y group underwent consolidation with 4 samples showing signs of unblocking of the pores.

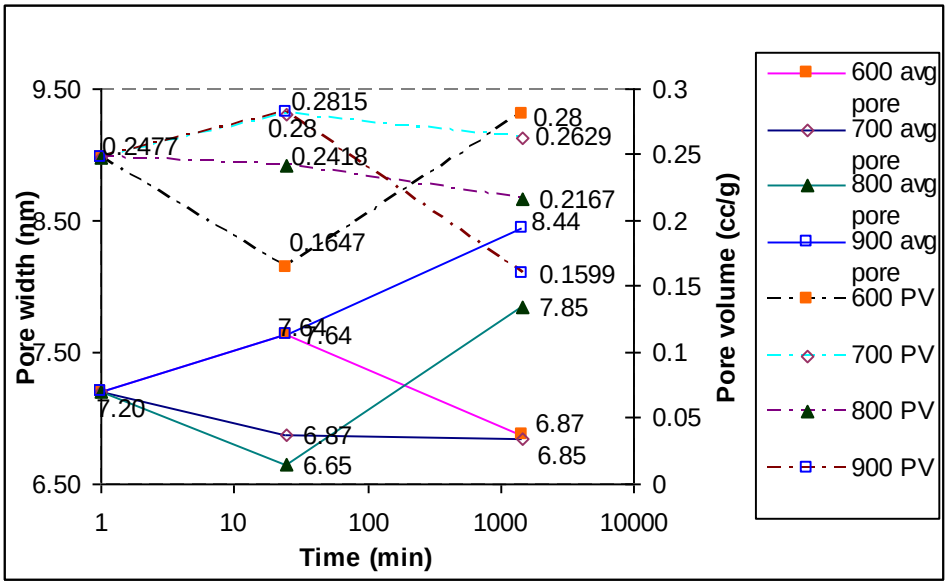

Figure 3-21: Average pore width and pore volume of 500Y group

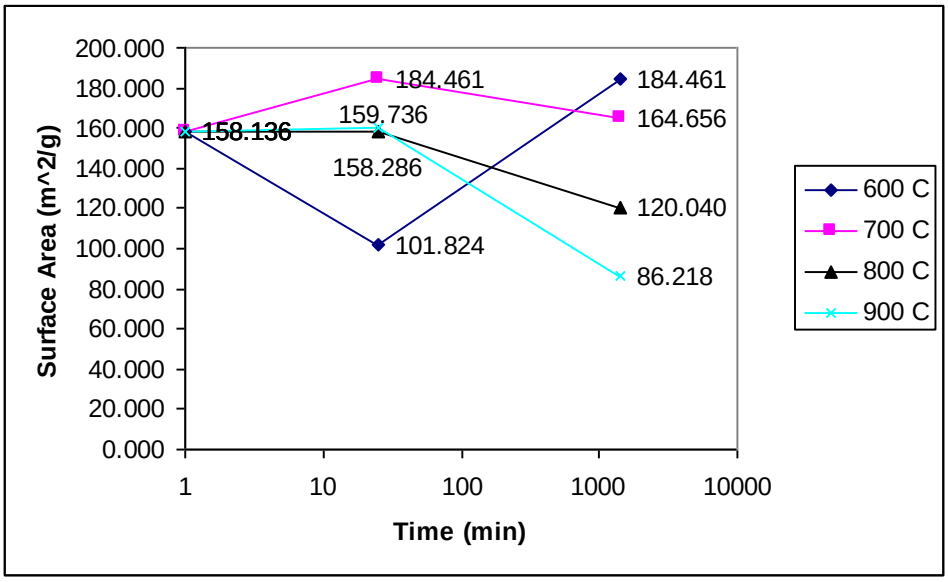

Figure 3-22: Surface area of 500Y group

Table 3-3: Percent change of pore characteristics for 500Y group

	Percent change from base sample value			
sample	Average Pore width (nm)	Pore volume (cc/g)	Surface Area (m^2/g)	Type of pore change
500Y600-25	6.11%	-33.51%	-35.61%	Consolidation
500Y600-24H	-4.60%	13.04%	16.65%	Unblocking
500Y700-25	-4.60%	13.04%	16.65%	Unblocking
500Y700-24H	-4.87%	6.14%	4.12%	Unblocking
500Y800-25	-7.58%	-2.38%	0.09%	Consolidation
500Y800-24H	9.01%	-12.52%	-24.09%	Consolidation
500Y900-25	6.08%	13.65%	1.01%	Unblocking
500y900-24H	17.30%	-35.45%	-45.48%	Consolidation

Figure 3-24 are the PVPW and SA graphs for the 550N group respectively. The PVPW graph shows an increasing pore width trend for most heat treatment conditions and a decreasing pore volume trend for most conditions. The SA graph also shows a general decreasing trend for most of the samples. All of the samples except the 900˚C have little change in pore width, while the pore volume and surface area decreases in all samples. Extensive consolidation does not happen in the sample until the sample is heat treated at 900°C for 24 hours. At 900˚C, the sample in this group has a high degree of consolidation at the end of the post heat treatment time. This sample has a pore volume consolidation of 84% from the base sample. Pore volumes and surface areas decrease less than 30% for all other samples. Coarsening is present in only the 600°C sample treated for 25 minutes; all other samples appear to undergo consolidation of the pore structure. Table 3-4 summarizes these changes in the pore characteristics and the type of process involved in the pore evolution.

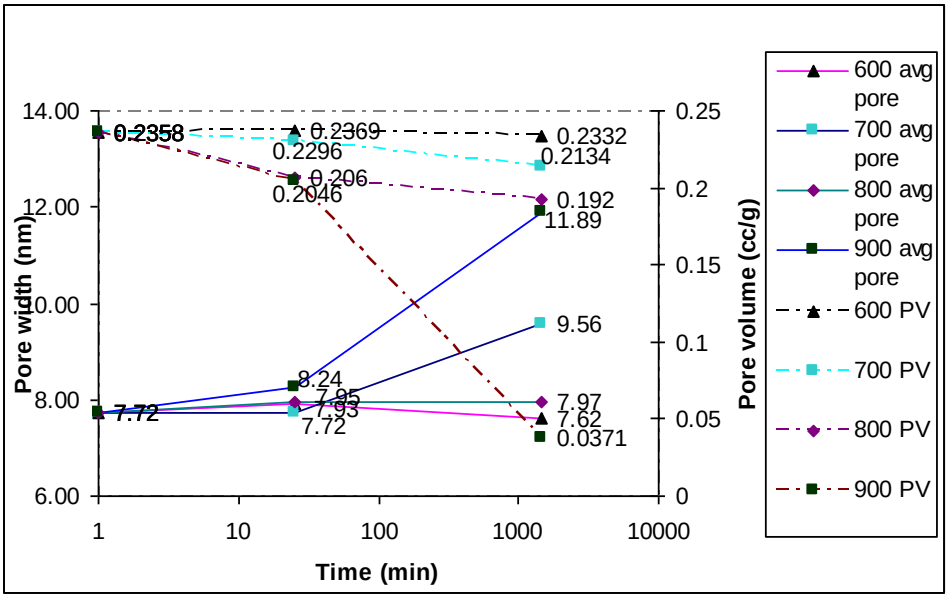

Figure 3-23: Average pore width and pore volume of 550N group

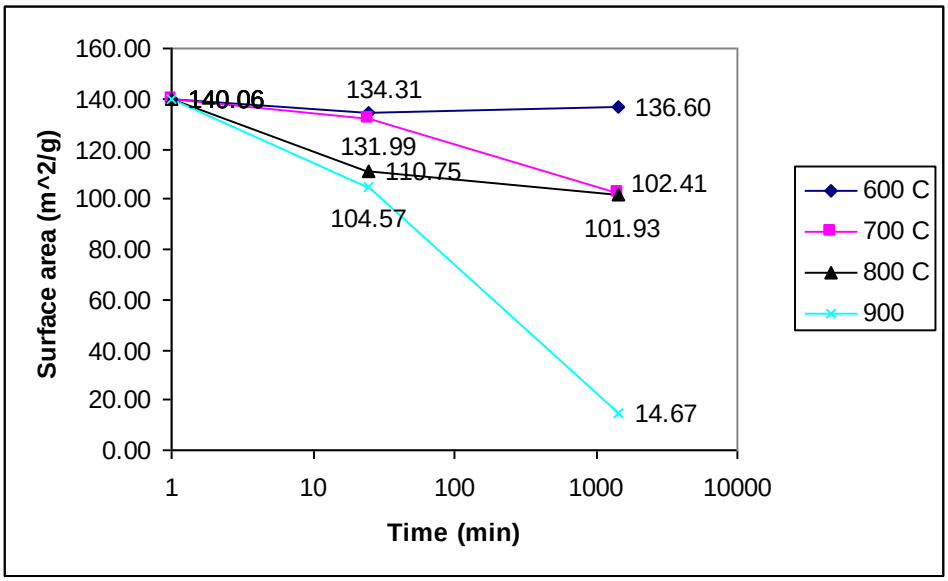

Figure 3-24: Surface area of 550N group

Table 3-4: Percent change of pore characteristics for 550N group

	Percent change from base sample value			
sample	Average Pore width (nm)	Pore volume (cc/g)	Surface Area (m^2/g)	Type of pore change
550N600-25	2.67%	0.47%	-4.10%	Coarsening
550N600-24H	-1.24%	-1.10%	-2.47%	Consolidation
550N700-25	0.06%	-2.63%	-5.76%	Consolidation
550N700-24H	23.80%	-9.50%	-26.88%	Consolidation
550N800-25	3.01%	-12.64%	-20.93%	Consolidation
550N800-24H	3.23%	-18.58%	-27.23%	Consolidation
550N900-25	6.78%	-13.23%	-25.34%	Consolidation
550N900-24H	53.98%	-84.27%	-89.53%	Consolidation

Group 550Y graphs are shown in Figure 3-25 and Figure 3-26. The general trend in the pore volume and the pore width is a decrease with exception of the 800°C sample. The surface area graph also shows a general decreasing trend for the samples with the exception of the 900°C, 24 hour sample. The graphs show both coarsening and consolidation of the pore structure. Coarsening is present in the sample treated for 25 minutes at 800°C. This is evidenced by the increase in an average pore width of 15% with only a 4% decrease in pore volume and a 22% decrease in surface area. Most of the other samples show a decrease in all of the pore characteristics. This would indicate that that the larger pores in the glass are consolidating which moves the average pore width down, along with the pore volumes and surface areas. Samples in this group do not consolidate to a high degree. The greatest amount of consolidation happens with the 900°C when treated for 24 hours. At this condition the consolidation of the sample only reaches a 44% decrease in the pore volume, but with a large decrease in the average pore width. Consolidation in the 550Y group appears to proceed through primarily shrinking of the larger pores. Percent changes in the group, along with the type of process involved in the pore change,

are given in Table 3-5 Samples in the 550Y group had pore consolidation occur with the exception of the 25 minute, 800°C sample, which underwent pore coarsening.

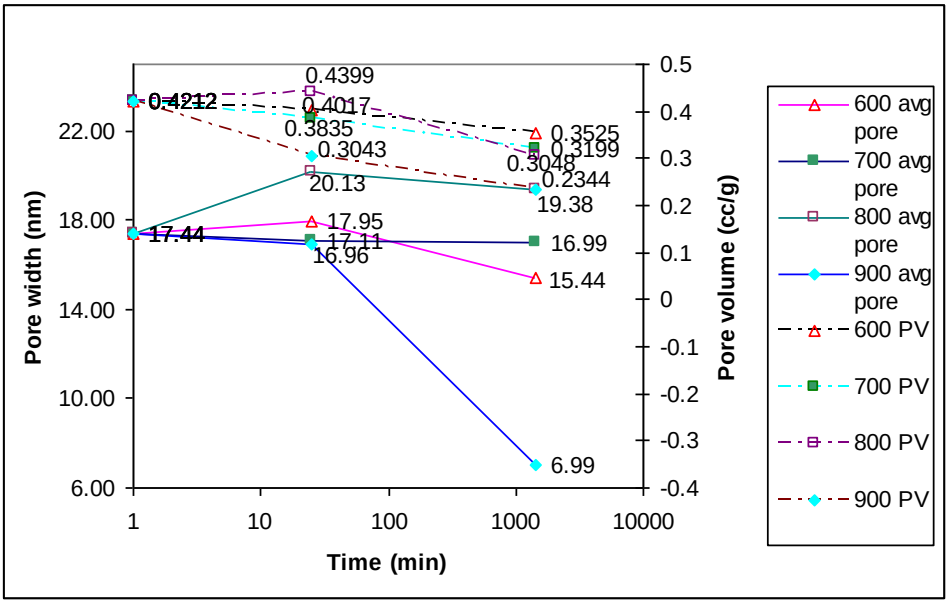

Figure 3-25: Average pore width and pore volume of 550Y group

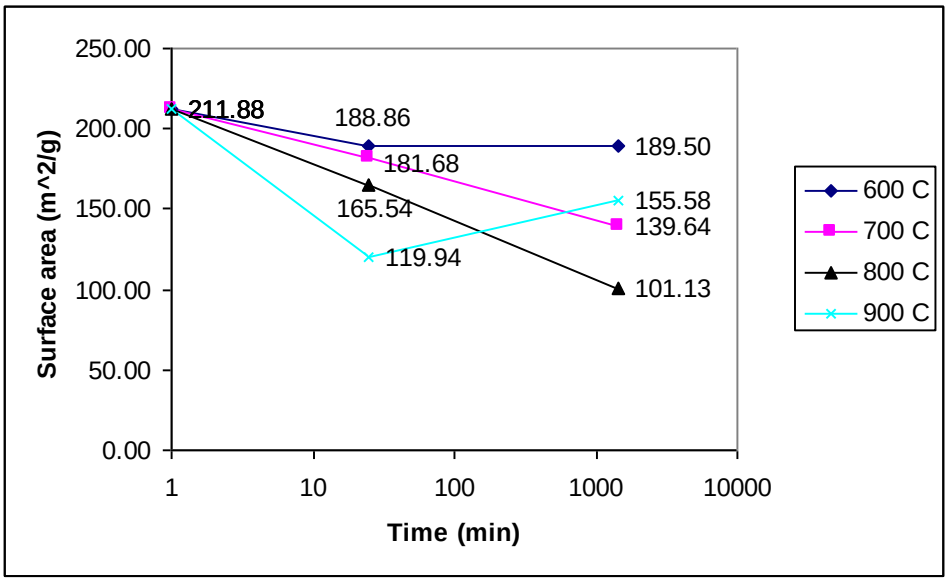

Figure 3-26: Surface area of 550Y group

Table 3-5: Percent change of pore characteristics for 550Y group

	Percent change from base sample value			
sample	Average Pore width (nm)	Pore volume (cc/g)	Surface Area (m^2/g)	Type of pore change
550Y600-25	2.96%	-4.63%	-10.87%	Consolidation
550Y600-24H	-11.47%	-16.31%	-10.57%	Consolidation
550Y700-25	-1.86%	-8.95%	-14.26%	Consolidation
550Y700-24H	-2.54%	-24.05%	-34.10%	Consolidation
550Y800-25	15.46%	4.44%	-21.87%	Coarsening
550Y800-24H	11.13%	-27.64%	-52.27%	Consolidation
550Y900-25	-2.73%	-27.75%	-43.40%	Consolidation
550Y900-24H	-59.91%	-44.35%	-26.57%	Consolidation

Figure 3-27 and Figure 3-28 are the PVPW and SA graphs for the 600N group. The 600N group is similar in pattern to the 550N group. There is a greater amount of consolidation for the 900˚C samples in the 600N group, while the changes in the pore width and pore volumes for the 600-800˚C samples show less change over the duration of the post heat treatment. Unblocking of pores is present in the 25 minute treated 600°C sample followed by consolidation when heat treated for 24 hours. Coarsening in the 25 minute 700°C sample is followed by consolidation when treated for 24 hours. The 900˚C sample is almost completely consolidated at 24 hours of heat treatment as is evidenced by the low pore volume and surface area. Consolidation in the 600N group proceeds with an increase in the average pore width, which indicates a small pore consolidation process. Table 3-6summarizes the changes in the pore characteristics.

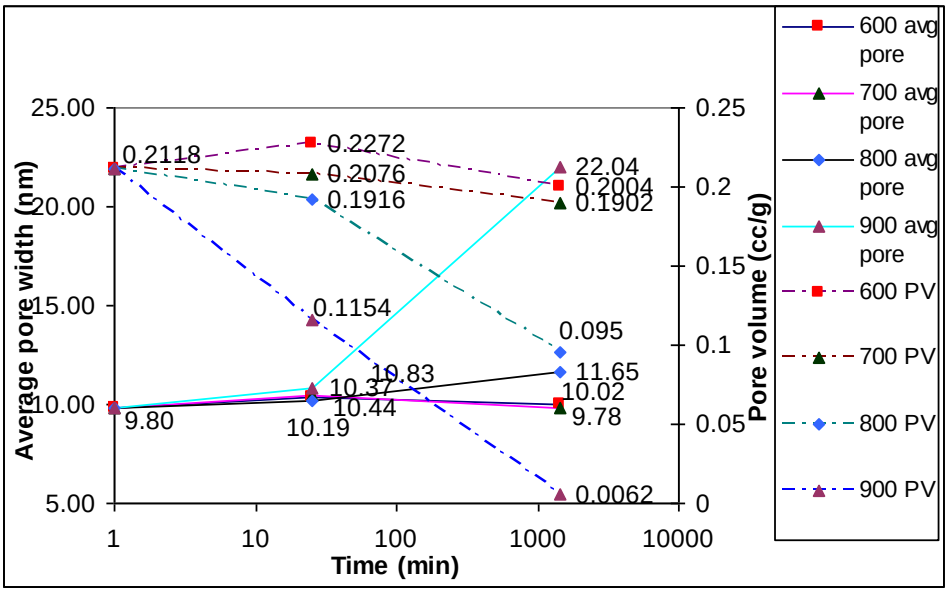

Figure 3-27: Average pore width and pore volume of 600N group

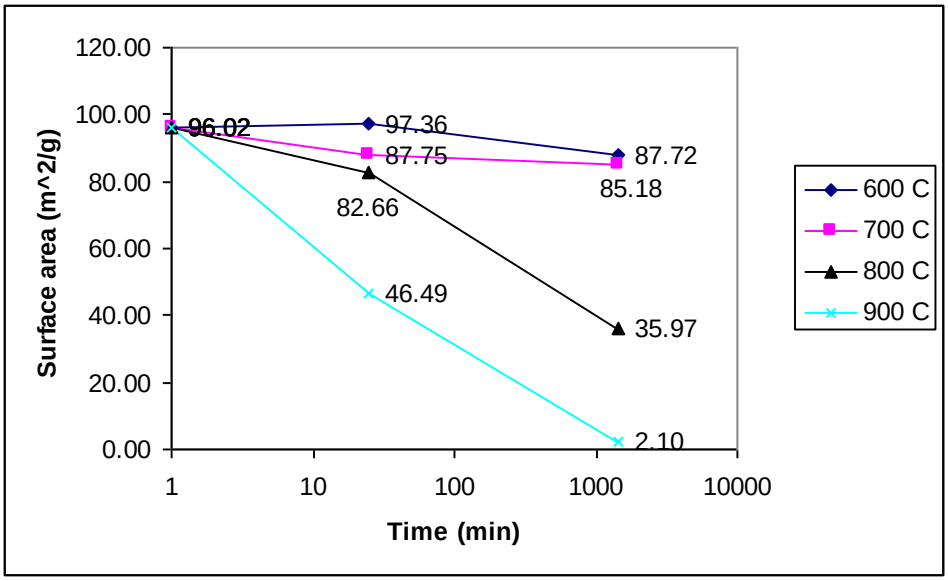

Figure 3-28: Surface area of 600N group

Table 3-6: Percent change of pore characteristics for 600N group

	Percent change from base sample value			
sample	Average Pore width (nm)	Pore volume (cc/g)	Surface Area (m^2/g)	Type of pore change
600N600-25	5.81%	7.27%	1.39%	Unblocking
600N600-24H	2.27%	-5.38%	-8.64%	Consolidation
600N700-25	6.59%	-1.98%	-8.62%	Coarsening
600N700-24 H	-0.14%	-10.20%	-11.29%	Consolidation
600N800-25	3.96%	-9.54%	-13.92%	Consolidation
600N800-24H	18.93%	-55.15%	-62.54%	Consolidation
600N900-25	10.56%	-45.51%	-51.59%	Consolidation
600N900-24H	124.97%	-97.07%	-97.82%	Consolidation

The PVPW and SA graphs for the 600Y group are shown in Figure 3-29 and Figure 3-30. The PVPW graph shows increasing and decreasing pore volumes and pore widths as the heat treatment time is increased, while the surface area graph shows a general decrease for the samples. The 600Y group has a greater amount of consolidation for the 800 and 900˚C samples than any of the previous groups. After 24 hours of heat treatment the 900˚C are fully consolidated. The 600°C sample initially undergoes consolidation during the first 25 minutes of heat treatment followed by unblocking of large pores or coarsening of the pore structure. This is evidenced by the 25 minute sample having a decrease in all of the pore characteristics and the 24 hour sample having an increase in all of the values in comparison to the 25 minute sample. Unblocking is also present in the 800°C sample heat treated for 25 minutes. Average pore width and pore volume increases with a decrease in the surface area of the sample. This would indicate that some pores are being opened while other pores are consolidating. The 700°C samples show an initial coarsening of the sample within the first 25 minutes followed by a process of consolidation of large and small pores in such a way to keep the average pore width unchanged in comparison to the 25 minute sample. Most of the samples in the 600Y group experience

consolidation of the pore structure at heat treatment above 600°C in as little as 25 minutes. This is summarized in Table 3-7 as the percent change in the pore characteristic and the of type process involved in the change.

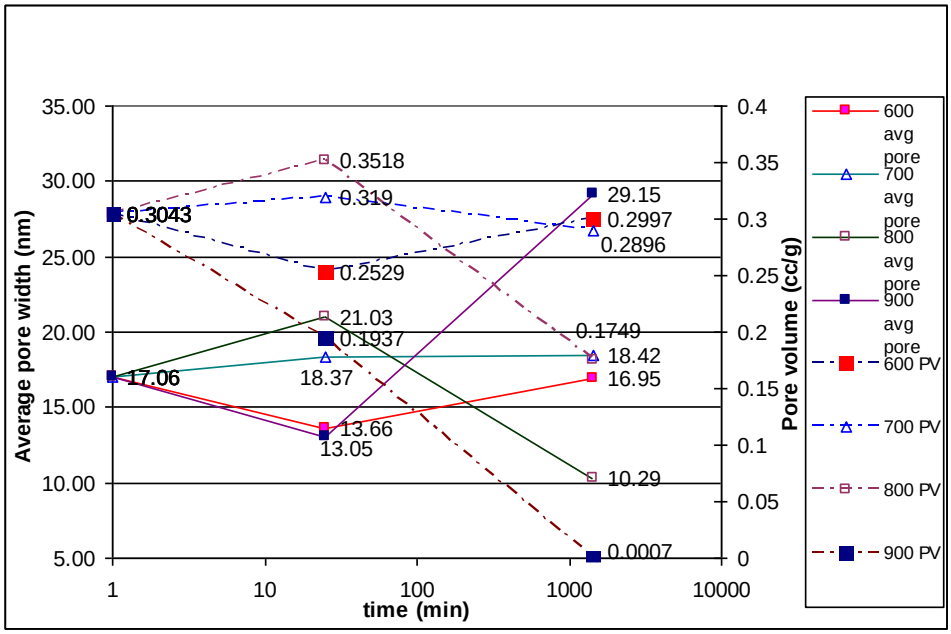

Figure 3-29: Average pore width and pore volume of 600Y group

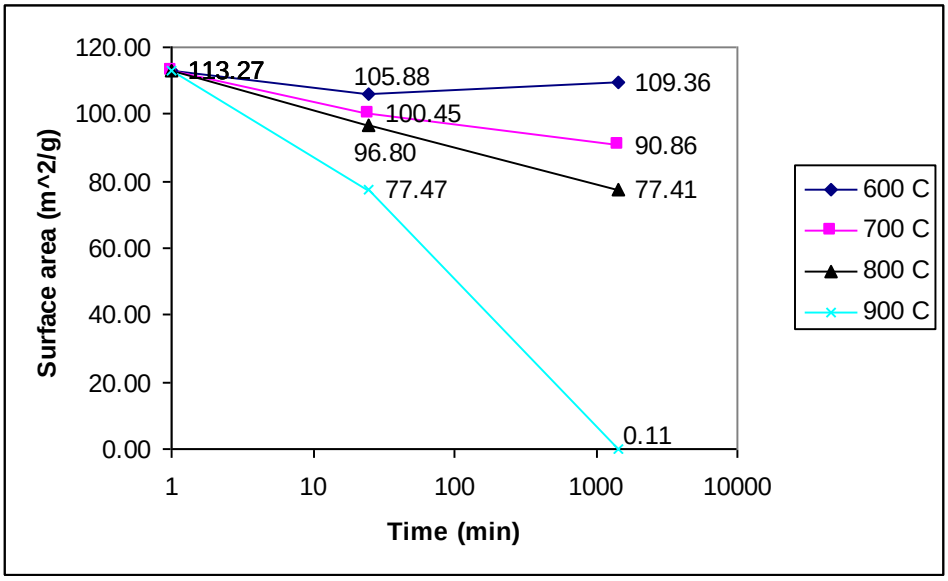

Figure 3-30: Surface area of 600Y group

Table 3-7: Percent change of pore characteristics for 600Y group

	Percent change from base sample value			
Sample	Average Pore width (nm)	Pore volume (cc/g)	Surface Area (m^2/g)	Type of pore change
600Y600-25	-19.94%	-16.89%	-6.52%	Consolidation
600Y600-24H	-0.65%	-1.51%	-3.45%	Unblocking
600Y700-25	7.69%	4.83%	-11.32%	Coarsening
600Y700-24H	7.98%	-4.83%	-19.78%	Consolidation
600Y800-25	23.28%	15.61%	-14.54%	Unblocking
600Y800-24H	-39.68%	-42.52%	-31.66%	Consolidation
600Y900-25	-23.49%	-36.35%	-31.60%	Consolidation
600y900-24H	70.88%	-99.77%	-99.91%	Consolidation

In the first experiment, a time study was done to determine how long the fibers would need to be in solution in order for all of the silica gel to be removed. The results show that after 30 minutes in solution the average pore size reaches a maximum. A further 30 minutes did not result in an appreciable increase in the average pore width. From this, it can be concluded that the silica gel is removed within 30 minutes of being in solution and that the etching of the pore surface or silica skeleton was not taking place in any significant amount. The maximum average pore size was around 29 nm for the 30 minute and above treatment groups. When the fibers were tested for gas sensing the initial fibers that were not treated with a sodium hydroxide solution did not sense gas, while the fibers that were treated with NaOH for 30 minutes did sense gas. The average pore size for the initial fibers is around 10 nm. This would indicate that for the particular gas being used, the pore size is too small in the initial fibers for the gas to diffuse quickly into the fiber core region. None of the fibers that were treated for less time have been tested for gas sensing capabilities. The first experiment imparts two items of information, first that the sensor works and that a treatment of 30 minutes for this diameter fiber removes all of the silica gel from the pore structure, which is the starting point for the NaOH treatment in the second experiment. Due to the size of the samples and the sample sizes, the results from first and second experiment should not be compared because the values are relative only to that experimental group.

The second experiment done on the bulk glass samples has detailed a range of pore morphologies that are achievable. In addition to this, the potential of long term stability of the fibers is explored. Within this experiment, the glass has an overall range of average pore width up to 29 nm, a range of pore volume up to 0.4399 cc/g, and a maximum surface area of 211.88 m^2/g. The lower end of these values would be zero with complete consolidation, so any value in between should be achievable. None of the porous samples remained unchanged during the heat treatment process. The operational definition of stability for the fibers will determine how much change is acceptable and would qualify the pore structure as stable.

The process involved in making the starting groups produces different pore morphologies. In the non-NaOH treated groups the average pore width and pore volume of the samples do not differ by much, it is only by the treatment with the NaOH solution that the 550 and 600˚C groups show a large change in these values. Pore size distributions in the non-NaOH treated samples have a much tighter distribution than the NaOH treated samples. Treatment of the glass with a NaOH solution is primarily done to remove a silica gel that is deposited within the larger pore structure during the initial leaching process. This would indicate that the pores in these two groups have a higher amount of silica gel deposited during the leaching process than

the glass phase separated at 500˚C. This is not surprising, because the phase separation temperature determines the composition and size of the two phases that form. All of the groups that were treated with a NaOH solution exhibited signs that some pores are blocked with silica gel, which are then opened during the heat treatment of the porous glass. This is probably due to the larger size of the bulk glass pieces, which allows for some of the silica gel to be deposited during the treatment with NaOH. The increased diffusion distances could result in the changing of the pH of the solution in regions of the porous glass, resulting in the silica precipitating out of solution while still in the glass.

This difference in composition most likely explains the higher amounts of consolidation in the 900˚C samples in the 550 ˚C and 600˚C groups. Composition will affect the viscosity of the glass at any given temperature and consolidation of the pore structure will occur through viscous flow. The composition is such that above 900˚C, the viscosity is low enough to have consolidation. This is contraindicated in the 900˚C sample in the 550Y group, but this is probably due to the large relative pore volume and surface area. The 900˚C sample reduces approximately the same amount of pore volume as in the 600N starting sample. Within the graphs there appears to be conflicting patterns of pore morphology changes. This is seen in the PVPW graph of the 500Y group in Figure 3-21. The pore width for the 600-25 minute sample is larger than the 800-25 minute sample, while the 24 hour samples have the opposite result. This can be explained though the idea of the process rate being temperature dependent. The higher temperature samples that exhibit this behavior could have undergone the increase in pore width in time before the 25 minute period while the lower temperature samples will exhibit the pore width increase at longer times than 24 hours. Other temperature dependent mechanisms for the pore width changes and sample variability should also be considered.

These types of changes in the pore structure of the groups are driven by the reduction of free energy of the glass. In doing a post heat treatment of the glass, the pore morphology should change through the coarsening of smaller pores into larger pores or the consolidation of pores. This consolidation is driven by the reduction in the total surface area, thereby reducing the free energy of the glass. In most of the samples the surface area of the glass is reduced throughout all ranges of the post heat treatment. There are a few examples where the pore width decreases with an increase in surface area. One of the mechanisms for this increase in surface area or pore volume with a decrease in pore width would be the consolidation of silica gel that is filling or blocking small pores in the glass. The most notable example is the 550Y900-24 hour sample. This sample goes from average pore width of 16.96 nm to 6.99 nm with a surface area change of 119.94 m^2/g to155.58 m^2/g. The mechanism for this type of change is not clear and duplication is appropriate to verify the result.

As can be seen in the all of the graphs of the pore volumes, a slight consolidation occurs through all parts of the post heat treatment of the glass. This heat treatment has the benefit of both enlarging the existing pore width in a large portion of the cases. One of the possible benefits of the increasing pore width is an increase in the wall thickness of the silica skeletal structure. This increased wall thickness is postulated by the general decrease in pore volume and surface area of the glass, which would require the glass to surround less pore volume. With less pore volume to surround the skeleton structure between the pores should increase in thickness. A change of this type in the skeleton should increase the mechanical integrity by increasing the wall thickness and by reducing crack nucleation points. Reduction in the crack nucleation points would also be a result as the glass reduces the surface area. Since crack tips have a high surface area for the volume, they should consolidate out as the surface area is reduced. This reduction

will blunt the crack tips within the pore matrix. Increasing the mechanical integrity in this fashion should also lead to the ability to do further chemical treatment to enlarge the pore widths further if necessary. The matrix of the starting groups is too fragile to receive any chemical processing to enlarge the pore width by removing matrix material. Removal of silica matrix material at this point will produce a wall thickness that is too small, in addition to sharpening any crack tips already present. Through a series of post heat treatments followed by chemical etching any pore width and volume necessary should be achievable.

3.6 Porous glass sensor gas sensing

3.6.1 Single gas detection testing

To facilitate the sensitivity test, the following vacuum bell jar system was designed and manufactured. Without such a system, a fiber sample needs to be connected with lead in/out fibers to be able to seal it inside the vacuum chamber (stainless steel tubing) for static sensitivity testing. This requires a relatively large amount of time for every single fiber sample. The idea for the vacuum bell jar system is to encompass the whole fiber alignment system inside a big bell jar, after alignment, the system can be quickly vacuumed without the necessity to connect the fibers. This is a much easier way to test the static sensitivity of the fiber sample, it may save a lot of time and realize mass sample testing. The design of the vacuum bell jar system is shown in Figure 3-31below.

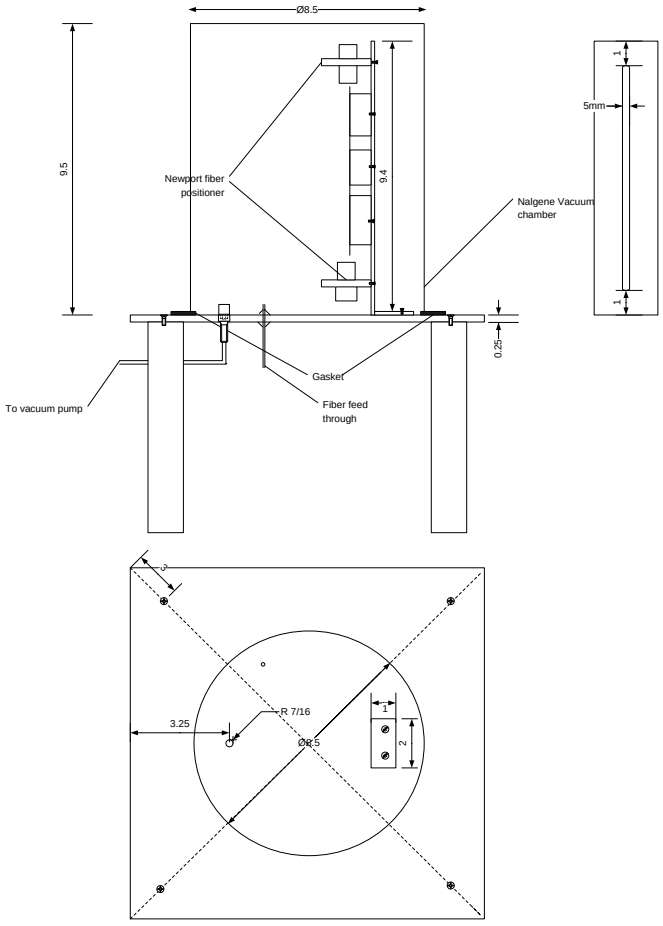

Figure 3-31: Design of the vacuum bell jar system

The jar used is the bell jar of the 8½" Nalgene Vacuum Chamber system, Nalge Company. The base plate is a 12"×12" quarter inch aluminum plate (aluminum 6061) from MACO Tool. The system is connected to vacuum pump and gas chamber by a 7/16 to 1/4" connector. The lead in/out fibers go into the system from an 0.5mm feed through. An aluminum plate 9.4" × 2" is mounted onto the base plate as the platform of the fiber alignment system. The Newport 5-D fiber positioners and the fiber sample holders can be easily skew-fastened through the 5mm slab opening on the aluminum platform, their position can be easily tuned according to the fiber sample's length. The system is lifted by 4 wooden legs to a height perfect for connecting to the duo-chamber system described in section 1. The vacuum bell jar system which is connected to the duo-chamber concentration control system is shown in Figure 3-32.

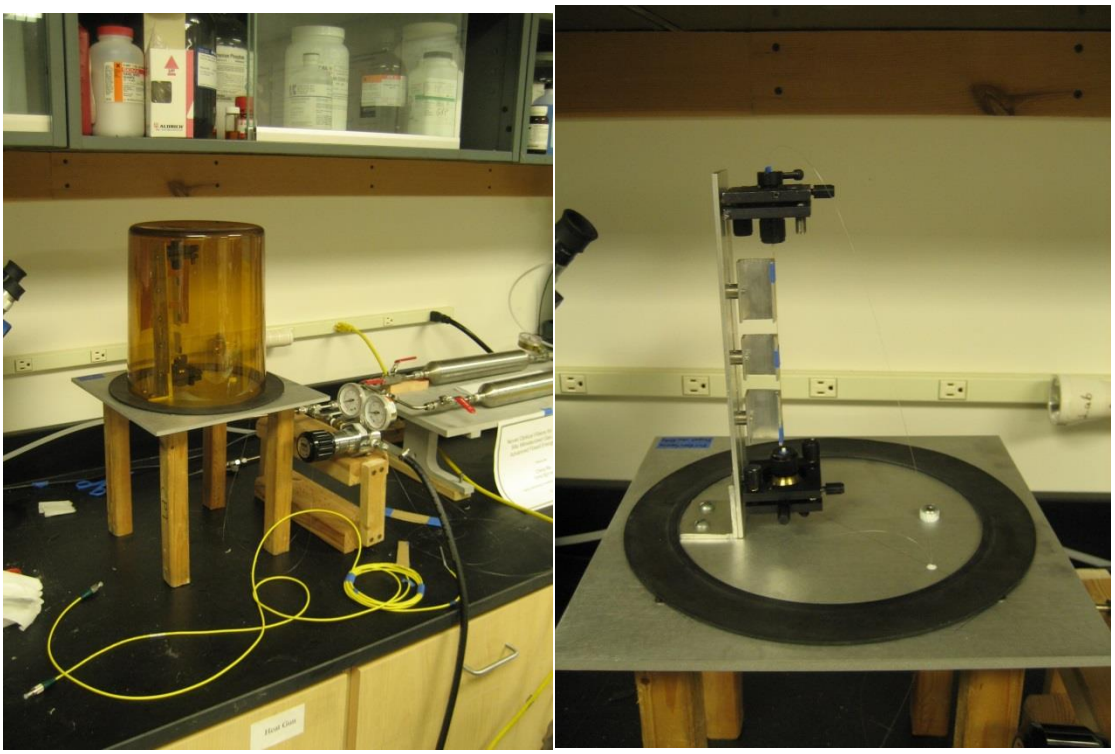

(a) (b)

Figure 3-32: The vacuum bell jar system (a) enclosed (b) fiber alignment platform

A fiber capillary tubing with I.D.=150 μm and length = 130 mm is chosen to test the system. The tubing is mounted onto the aluminum holders and pre-aligned using the lead in/out fiber positioners. After alignment, the platform was mounted onto the base plate, the lead in/out fiber go through the feed-through hole on the base plate and the feed-through was sealed with wax. The system was then enclosed by the bell jar without any vacuum grease. Then, the system is vacuumed for 5 minutes and acetylene was filled in to normal pressure. The transmission spectrum of the capillary tubing before, after vacuum and after acetylene exposure were taken and plotted below in Figure 3-33.

The deep absorption lines (about 20 dB) indicate that this system is suitable for the quick testing of the sensor's sensitivity. It holds a static and high target gas concentration in the surrounding of the sensor while does not require the sensor to be connected to the lead in/out

fibers, thusly much easier for the static sensitivity test compared to the steel vacuum tubing system. Two distinct groups of fibers were characterized during the reporting period. The first group consists of fibers manufactured using varied processing parameters, all of which included a post heat treatment process. In Group 1, the phase separation temperature of the samples varied from 500 to 600°C. Two of the fibers were placed in a 0.5 N NaOH bath for 30 minutes followed by an acid wash prior to heat treatment. Post heat treatment times varied from 5 to 15 minutes, and temperature from 600 to 900°.

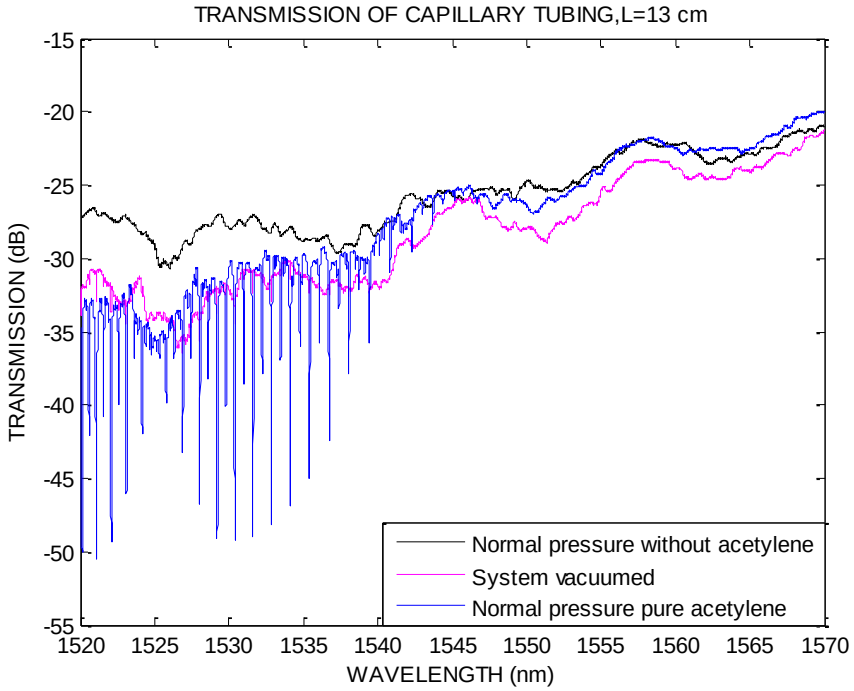

Figure 3-33: Transmission of the capillary tubing inside the vacuum bell jar system

Test 1 was simply a measurement to ensure the fiber length was adequate for insertion into the optical characterization setup. A minimum length of 48.08 mm was required. In Test 2, the optical transmission was observed using an optical microscope. Only two samples were found to have good transmission and were selected for gas sensing testing. The transmission of fiber sample G1-2 was about -40dB after both ends were cleaved. Both pure acetylene and acetylene/nitrogen mixture at 100 ppm were used for gas sensing. The fiber and the gas were confined inside a small metal box which slows the diffusion of gas into free air for better gas concentration. Absorption peaks were not observed in either case. In this group, many fibers were either too curved or too short for measurement. After refinement of the fiber drawing skills, newer fibers exhibited both better mechanical and optical quality. Group 1 characterization results are summarized in Table 3-8

Group 2 were a standard group of fibers that had only been acid leached. They were tested before and after treatment in 0.5 N NaOH for 30 min in order to enlarge the pore size. The same set of tests was performed as on Group 1. About half the samples were too curved and had poor outer diameter consistency. The cores of such fibers were discontinuous. Twenty good fibers were selected for observation of the fiber end through an optical microscope. Both ends of the fiber samples were cleaved prior to the next test. The fiber end faces were inspected while the

far end was illuminated using white light. Ten fibers were found to have bright cores, although some had relatively bright claddings as well. These ten pieces were selected for the transmission and gas sensing experiment in the next step.

Table 3-8: Fiber group 1 characterization results

Subgroup	t_{post}	#	$T_{ph\text{-}sep}$	NaOH	T_{post}	TEST 1 (length, mm)	TEST 2	TEST3
G1	5	G1-1	500	N	800	57.46		
		G1-2	550	N	600	77.76	Bright core	No peaks
			550	N	700	46.66		
			550	N	900	43.73		
		G1-3	600	N	600	63.30		
			600	N	800	C		
G2	15	G2-2	500	N	800	60.07		
		G2-3	550	N	600	53.54		
		G2-1	550	N	700	60.48	Bright core, small	No peaks
		G2-4	550	N	800	69.80		
			550	Y	800	44.04		
			600	N	600	76.89		
			600	N	900	C		
G3	25		500	N	700	44.89		
		G3-2	500	N	800	48.17		
			550	N	600	47.71		
		G3-1	550	N	800	73.10		
		G3-4	600	Y	600	55.38		
		G3-3	600	N	800	59.57		

The optical transmission of each sample was characterized. The fiber was confined within a small aluminum box with its ends outside for lead-in and lead-out alignment in order to slow gas diffusion into the open air during the gas sensing experiment. The transmission of each fiber is shown in Figure 3-34 through Figure 3-42, but none of the fibers were able to sense gas prior to NaOH treatment. Samples 1-10 were returned to processing and following treatment in 0.5 N NaOH, five were tested for optical transmission and gas sensing characteristics.

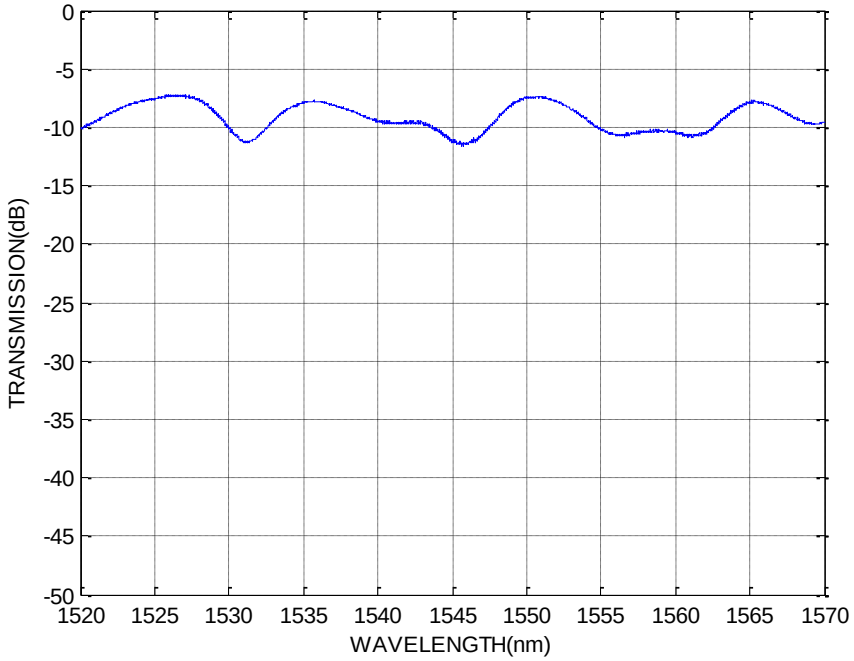

Figure 3-34: Optical transmission of fiber Group 2, Sample 1.

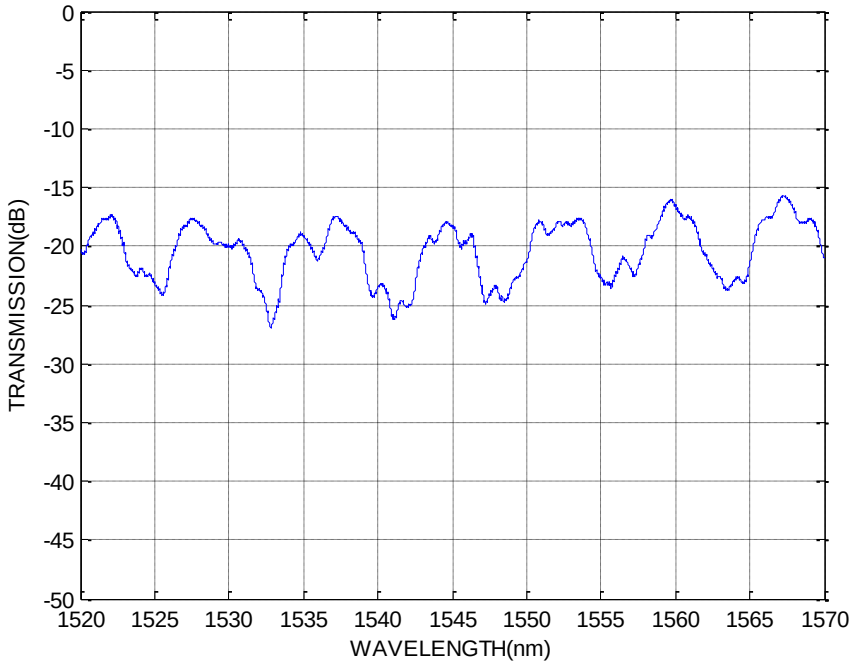

Figure 3-35: Optical transmission of fiber Group 2, Sample 2.

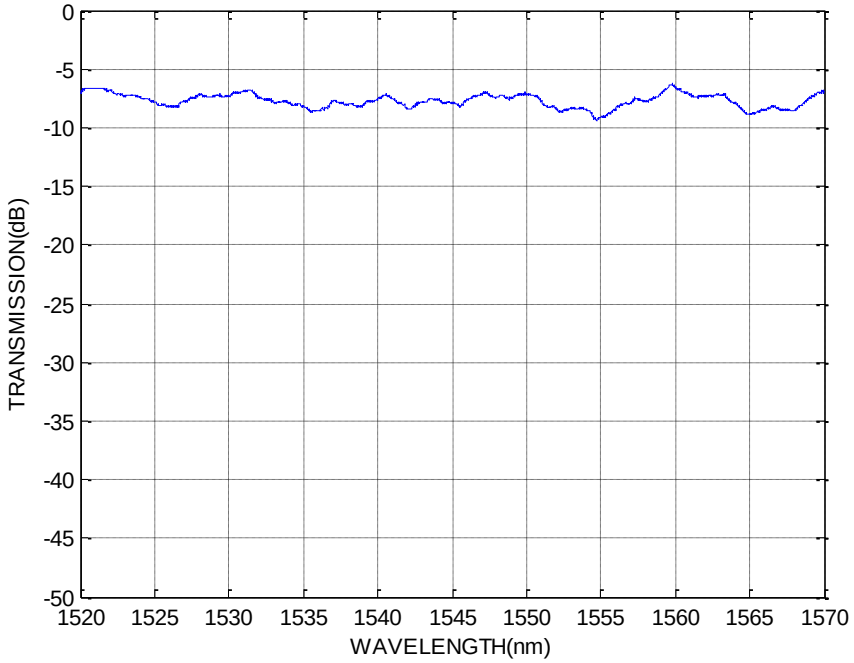

Figure 3-36: Optical transmission of fiber Group 2, Sample 3.

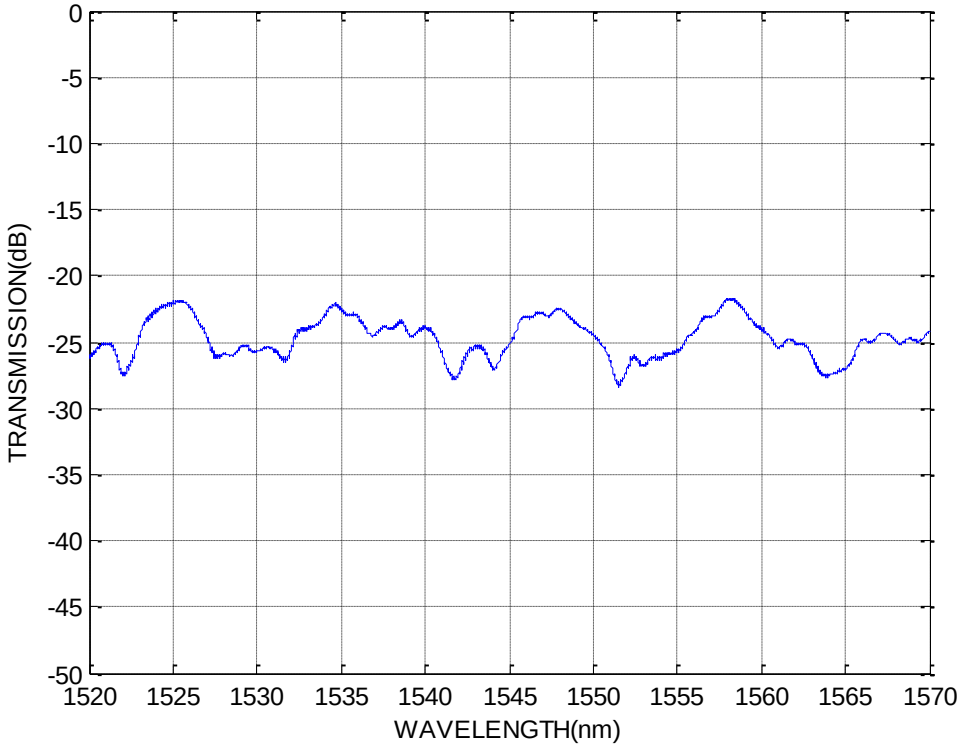

Figure 3-37: Optical transmission of fiber Group 2, Sample 4.

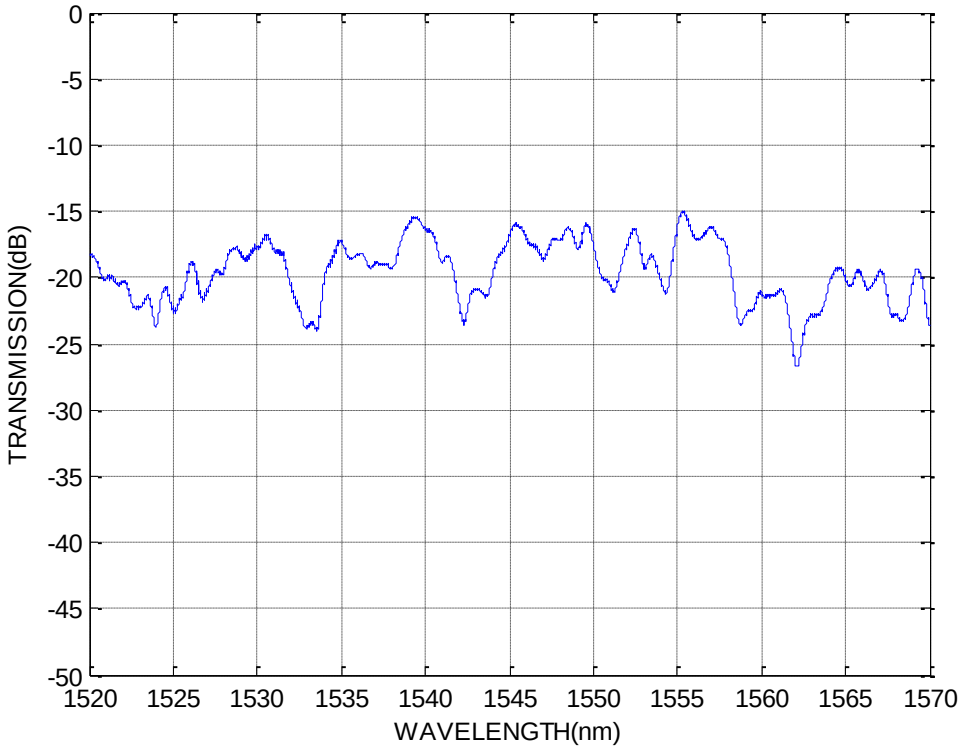

Figure 3-38: Optical transmission of fiber Group 2, Sample 5

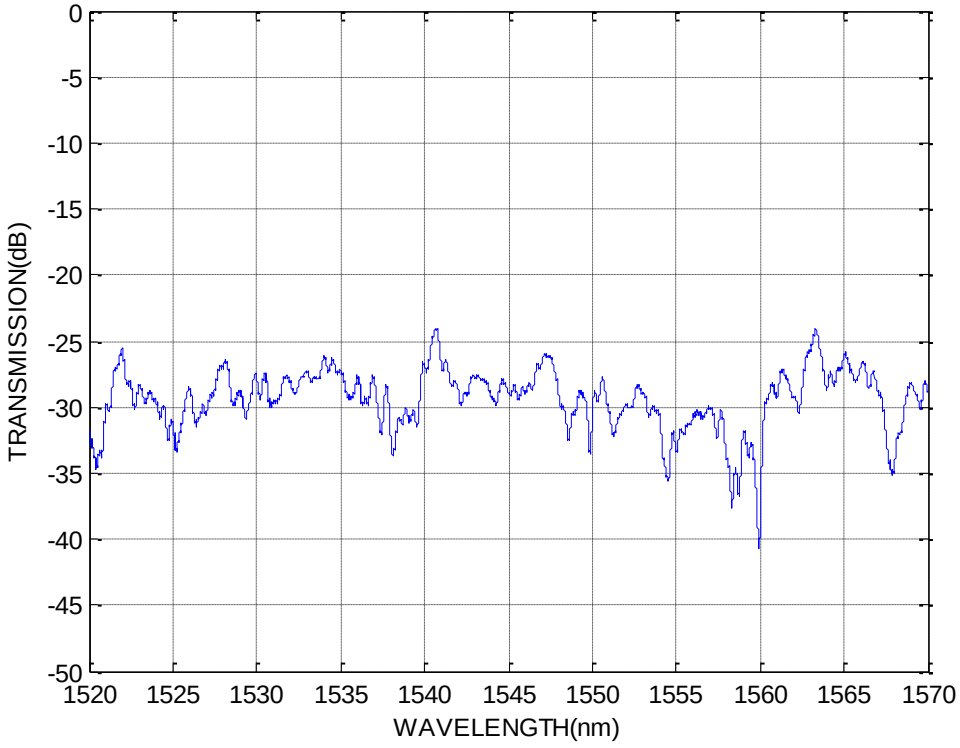

Figure 3-39: Optical transmission of fiber Group 2, Sample 6.

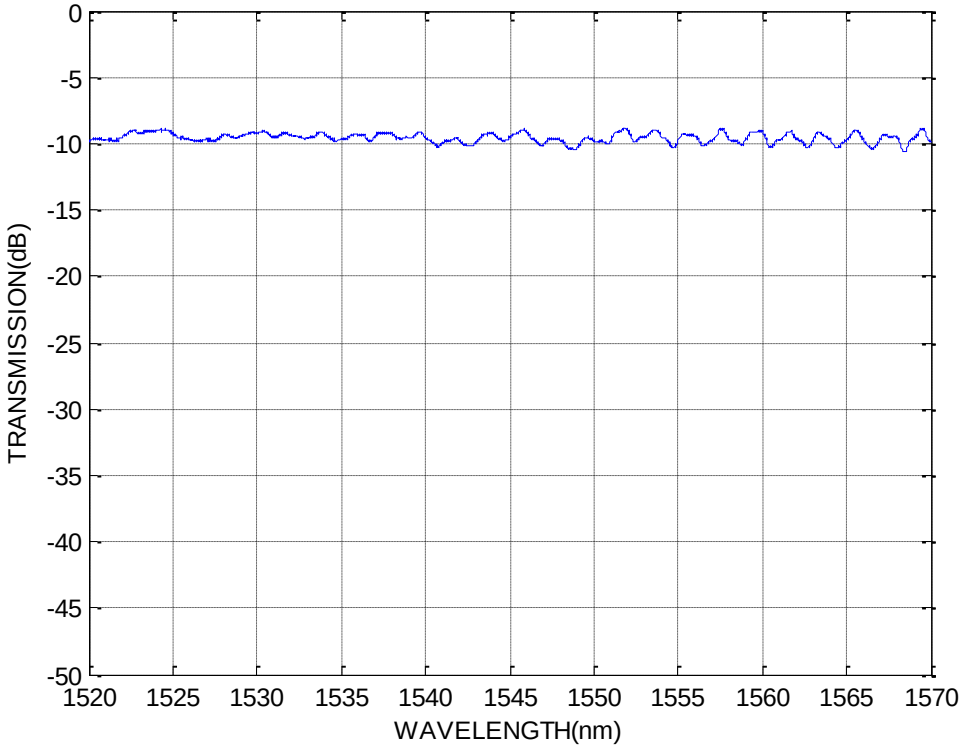

Figure 3-40: Optical transmission of fiber Group 2, Sample 7.

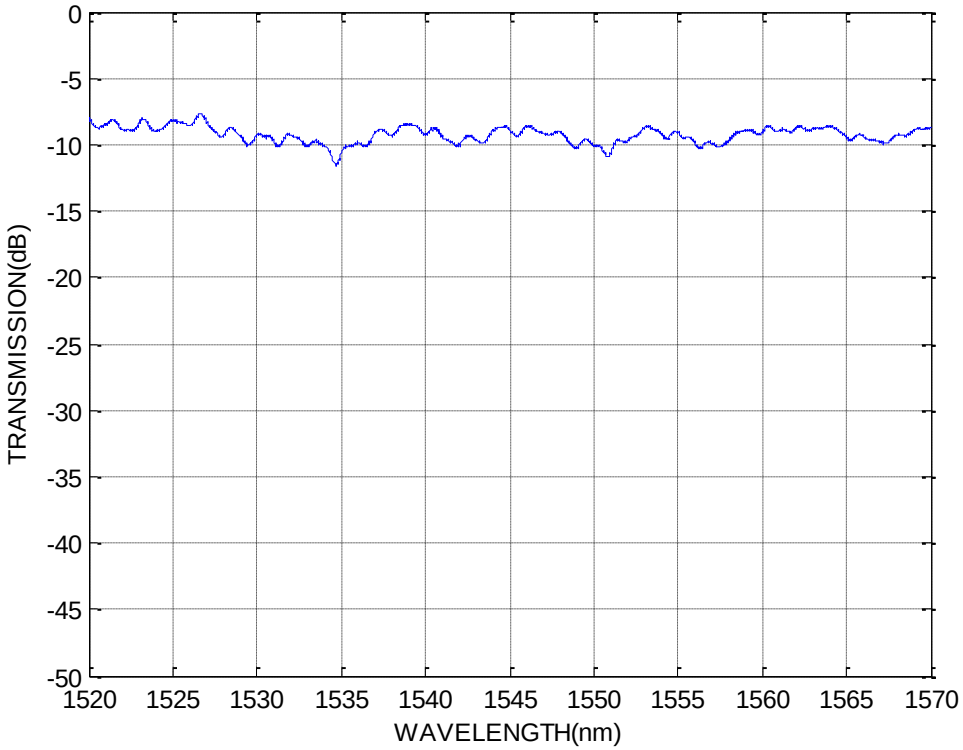

Figure 3-41: Optical transmission of fiber Group 2, Sample 8.

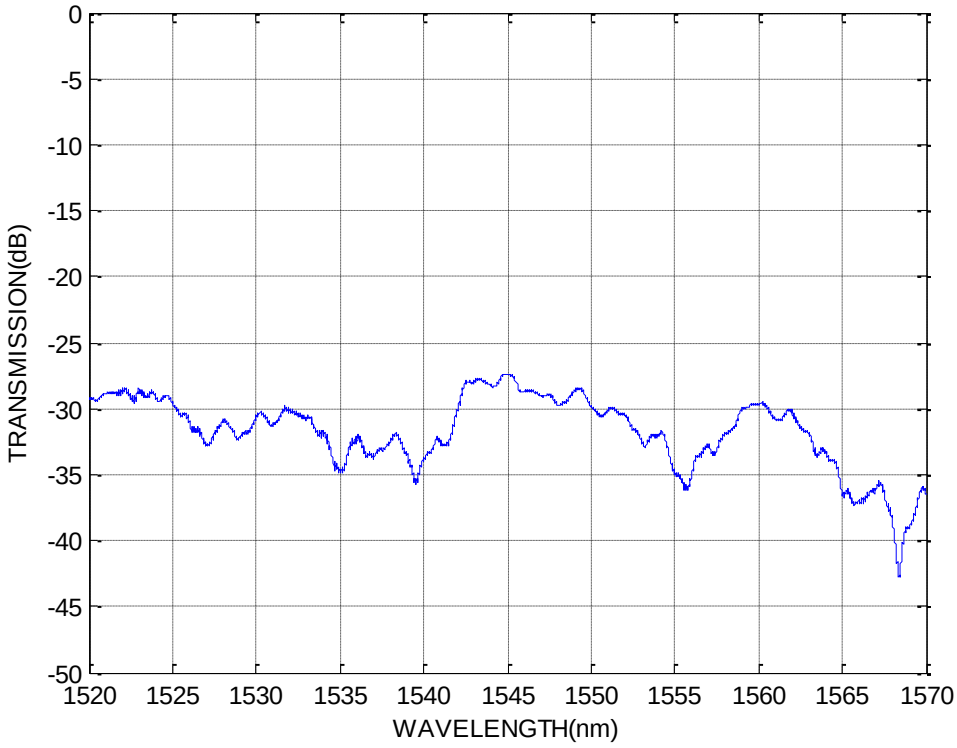

Figure 3-42: Optical transmission of fiber Group 2, Sample 9.

6.4 Fiber NaOH post treatments

Following NaOH treatment, Tests 2 and 3 were repeated for fiber Group 2. The optical transmission of all five fibers was evaluated; the gas sensing capability of fibers with transmission above -40 dB was then evaluated. For each sample, the transmission before and after treatment, on exposure to pure acetylene, and on exposure to 100 ppm acetylene (balance nitrogen), are plotted together in Figure 3-43 through Figure 3-47.

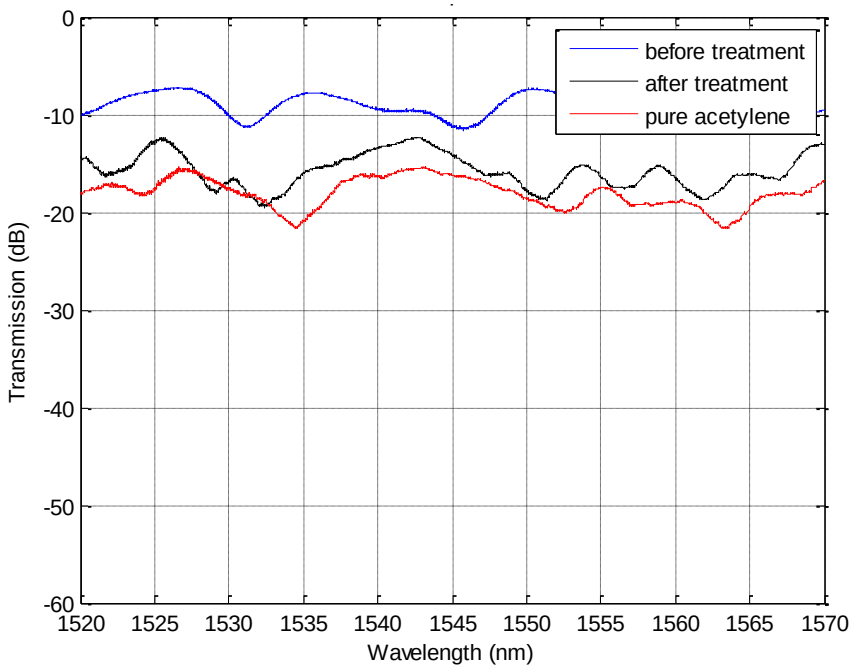

Figure 3-43: Optical transmission of fiber Group 2, Sample 1, before and after NaOH treatment and on exposure to pure acetylene.

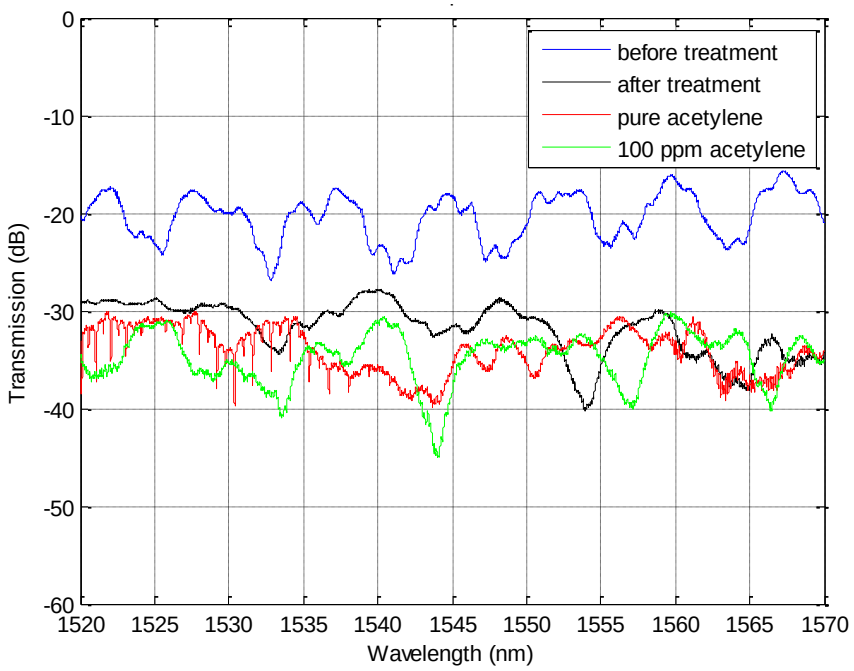

Figure 3-44: Optical transmission of fiber Group 2, Sample 2, before and after NaOH treatment and on exposure to pure and 100 ppm acetylene

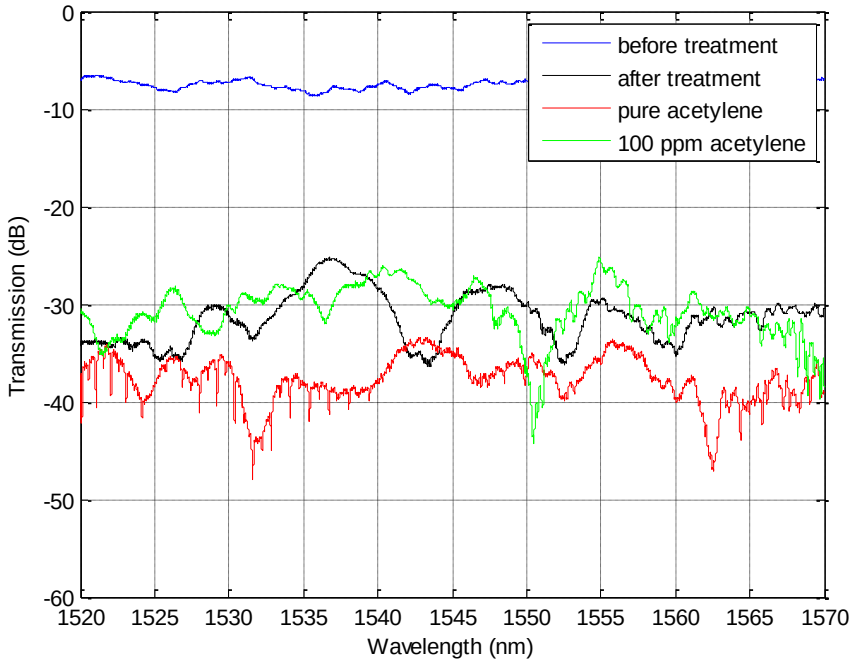

Figure 3-45: Optical transmission of fiber Group 2, Sample 3, before and after NaOH treatment and on exposure to pure and 100 ppm acetylene

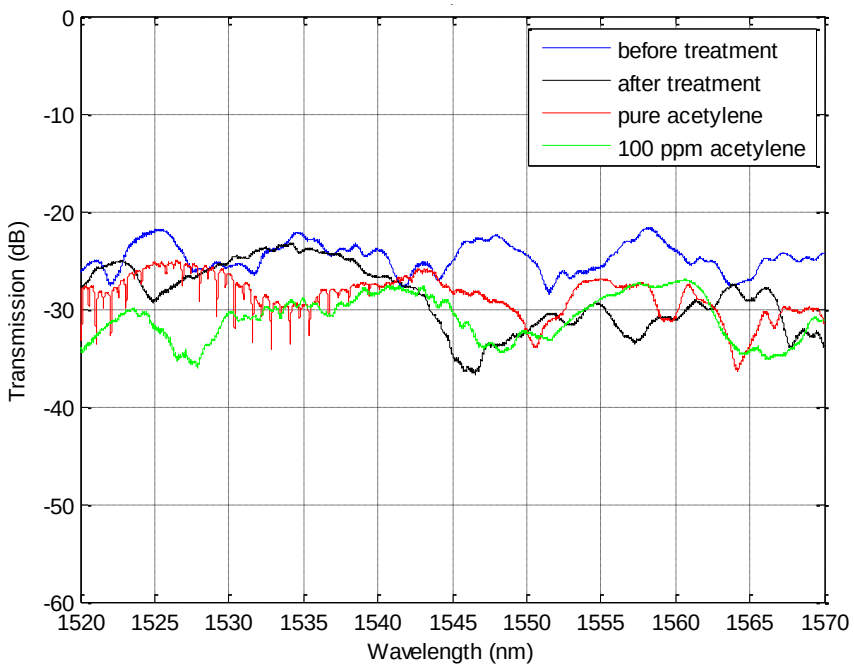

Figure 3-46: Optical transmission of fiber Group 2, Sample 4, before and after NaOH treatment and on exposure to pure and 100 ppm acetylene

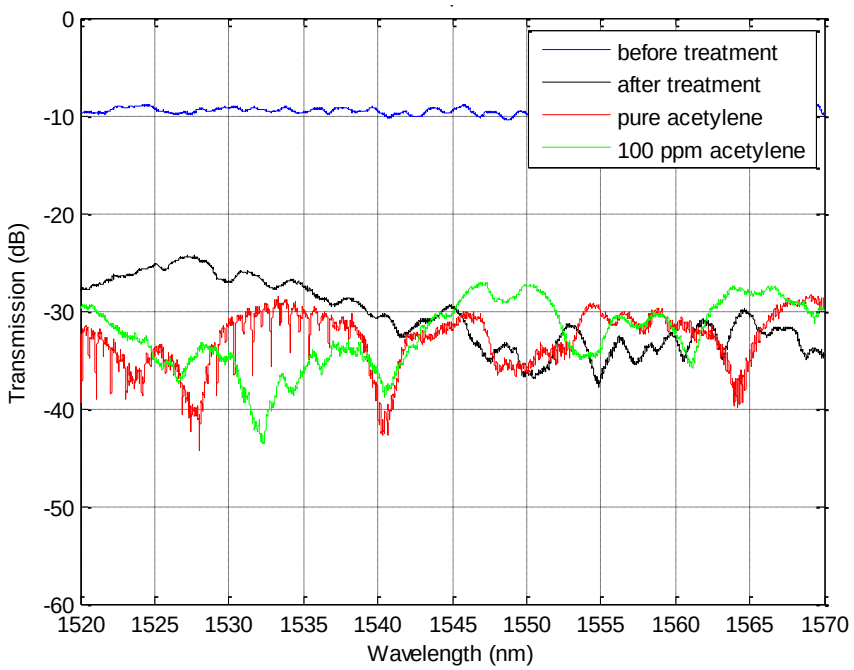

Figure 3-47: Optical transmission of fiber Group 2, Sample 7, before and after NaOH treatment and on exposure to pure and 100 ppm acetylene

The fibers were not recleaved following NaOH treatment. The transmission drop after treatment is believed to be due to destruction of the fiber ends during treatment, resulting in high coupling loss. The fiber body was also influenced by the treatment. For example, Figure 3-48 shows a portion of the cladding completely removed from the core. The results from this group of fibers was compared to tests performed in 2007. For the same test conditions (pure acetylene, sample confined in box), the absorption was 7.88 dB in the 2007 tests and 6.16 dB for this group, a reduction of 1.5 – 2 dB in the absorption strength(Figure 3-49). These issues were resolved through modification of the fiber treatment technique.

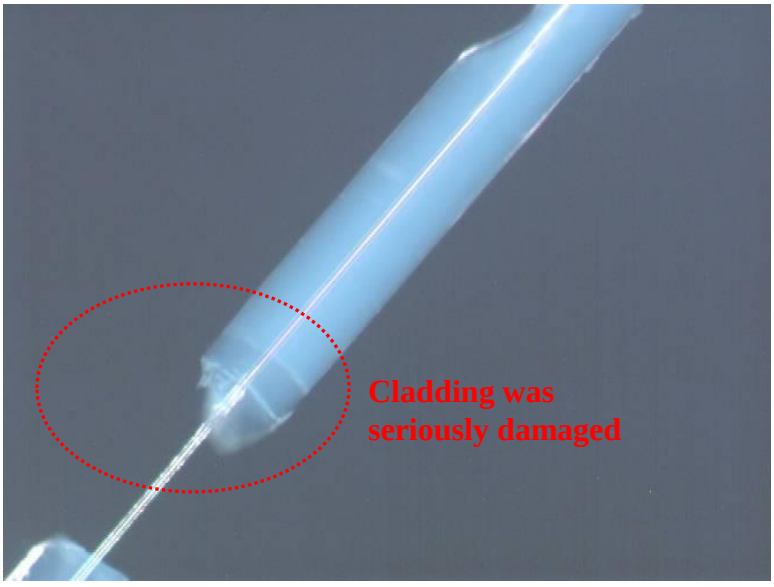

Figure 3-48: 6 Fiber side view; cladding damaged during NaOH treatment.

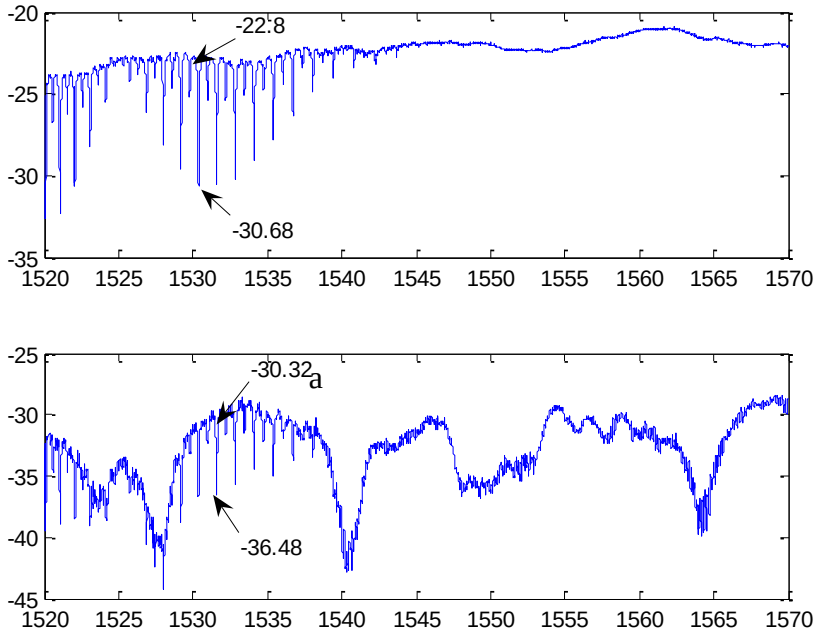

Figure 3-49: Transmission of fiber samples in pure acetylene environment a. Sample 3 (in Oct 2007 report) b. Sample 7

3.6.2 High temperature testing

The goal of this phase of experiments was to test the sensor under high temperatures (500 ℃). To verify the feasibility of our sensors at temperatures up to 500°C, a preliminary experiment was designed as follows: porous clad fiber samples were exposed to high temperatures (600, 700, 800℃) for different periods of time (25 and 50 minutes) as described above. These samples are grouped according to their heat exposure conditions and were tested for gas sensing capability after the high temperature exposures. The gas sensing capability testing done after the high temperature exposures was conducted in order to determine if changes in the glass pore morphology would affect the gas sensing capability. The fibers were initially processed in exactly the same way with the only significant change being the temperature of exposure and the time of exposure. Fiber characterization and gas sensing results are shown below in Table 3-9. (The fiber samples are labeled as follows: 550Y 700-25, in which, 700-25 means the sample was exposed to high temperature of 700℃ for 25 minutes; the 550 means that it was phase separated to 550°C during initial processing). Optical micrographs fiber end faces showing the transmission of the white light are shown in Figure 3-50 through Figure 3-55.

Table 3-9: Sample characterization results

No.	Size (μ m)(clad/core)	Treatment cond.	Transmission/Core/Clad	Sense?
1	180/9.8	550Y Base	-33/B/D	Y(-5)
2	140/6.4	550Y 600-25	-20/B/D	Y(-3)
3	90/6.0	550Y 600-50	-25/B/D	Y(-5)
4	100/6.6	550Y 700-25	-30/B/(Semi D)	Y(-5)
5	100/6.1	550Y 700-50	-23/B/D	Y(-4)
6	80/4.0	550Y 800-25	-15/B/D	**N**

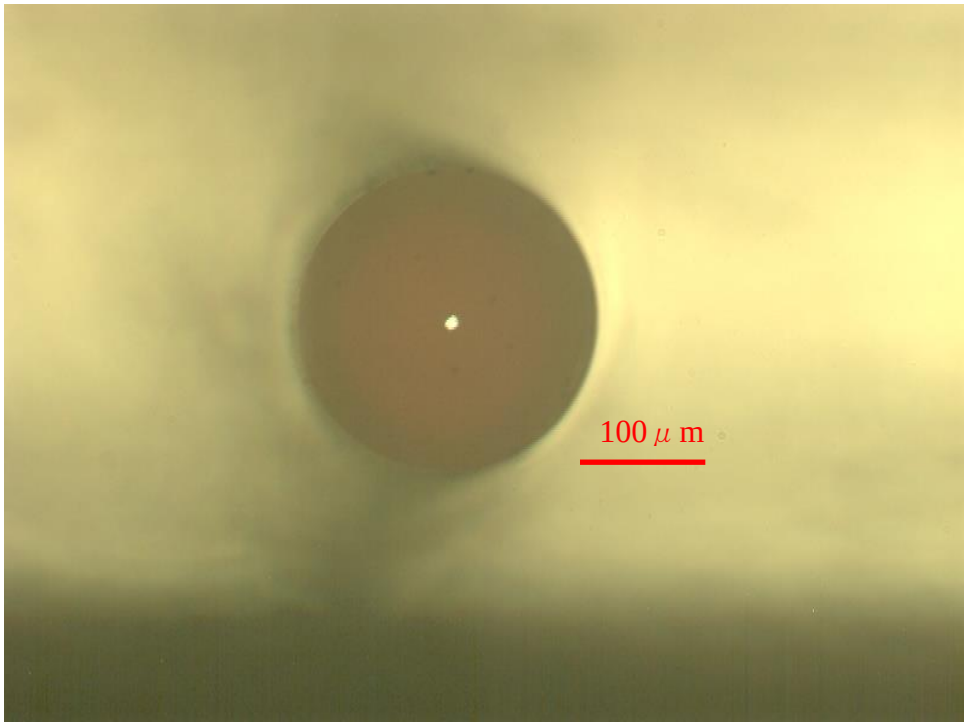

Figure 3-50: Fiber end-view 500Y Base

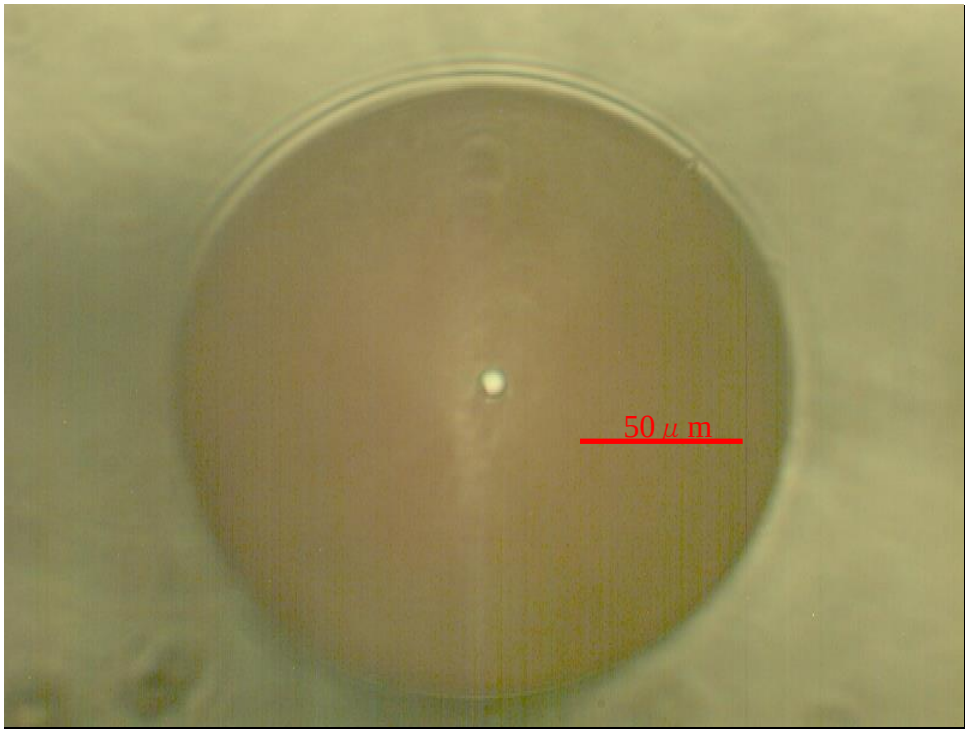

Figure 3-51: Fiber end-view 500Y 600-25

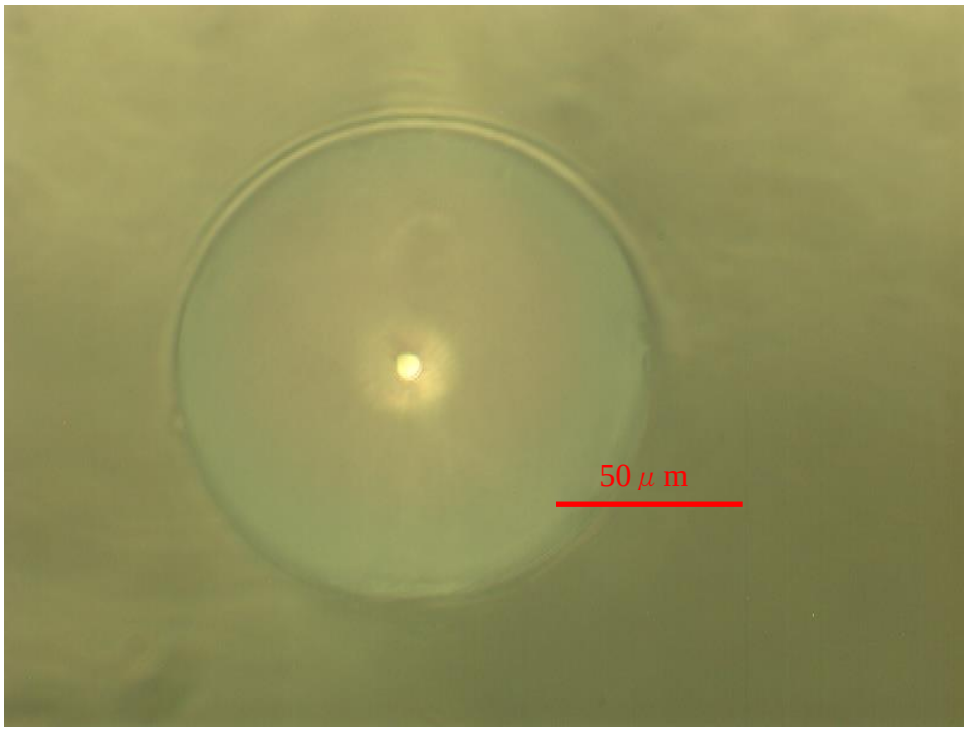

Figure 3-52: Fiber end-view 550Y 600-50

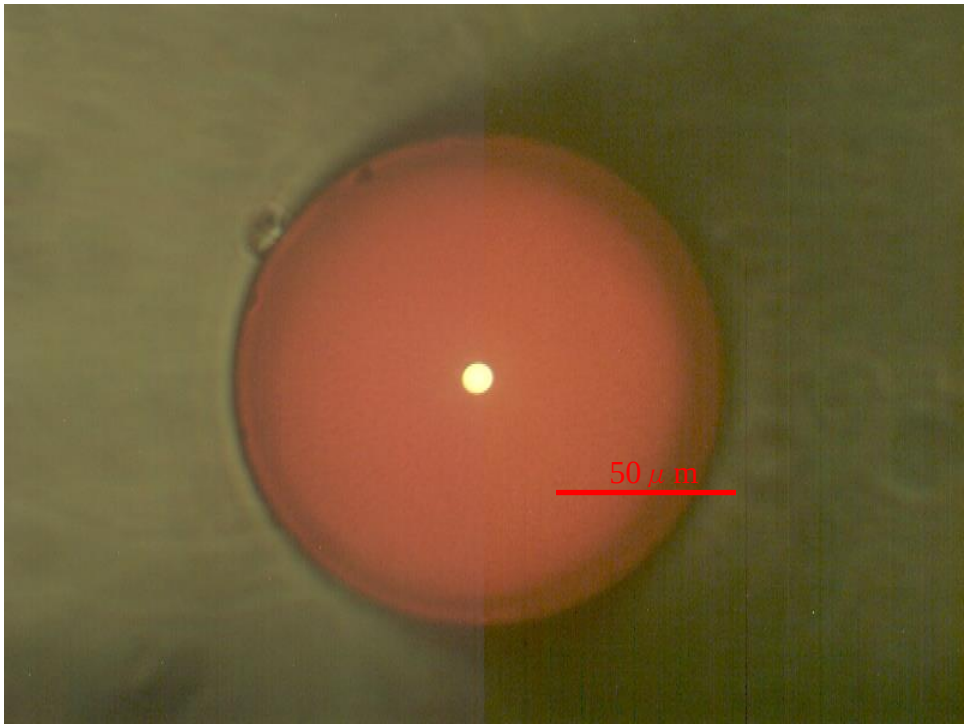

Figure 3-53: Fiber end-view 550Y 700-25

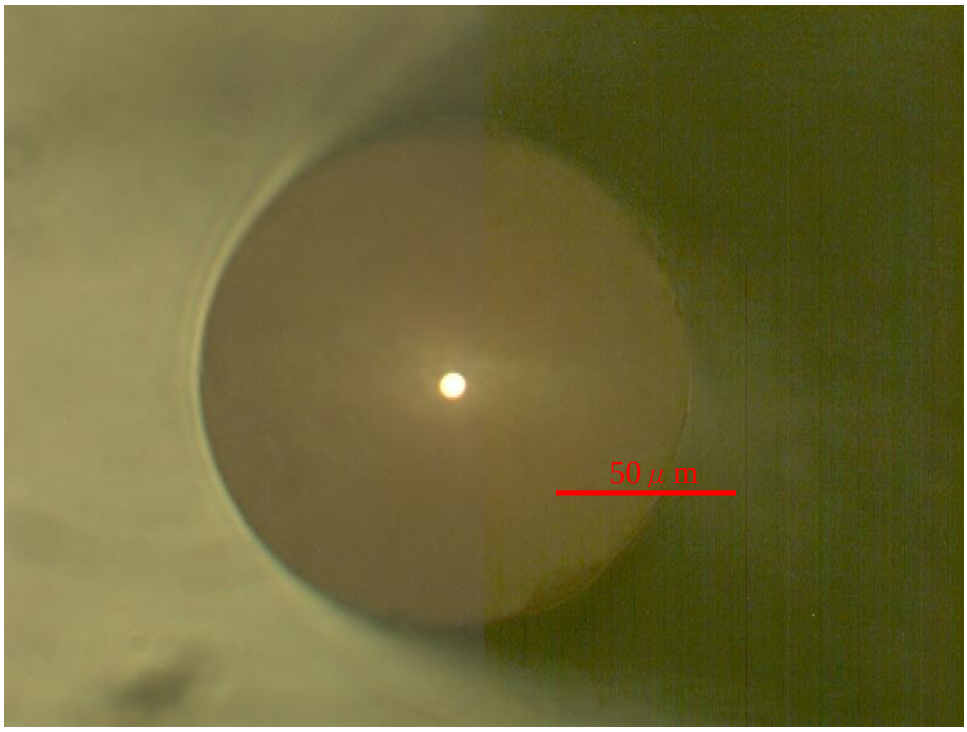

Figure 3-54: Fiber end-view 550Y 700-50

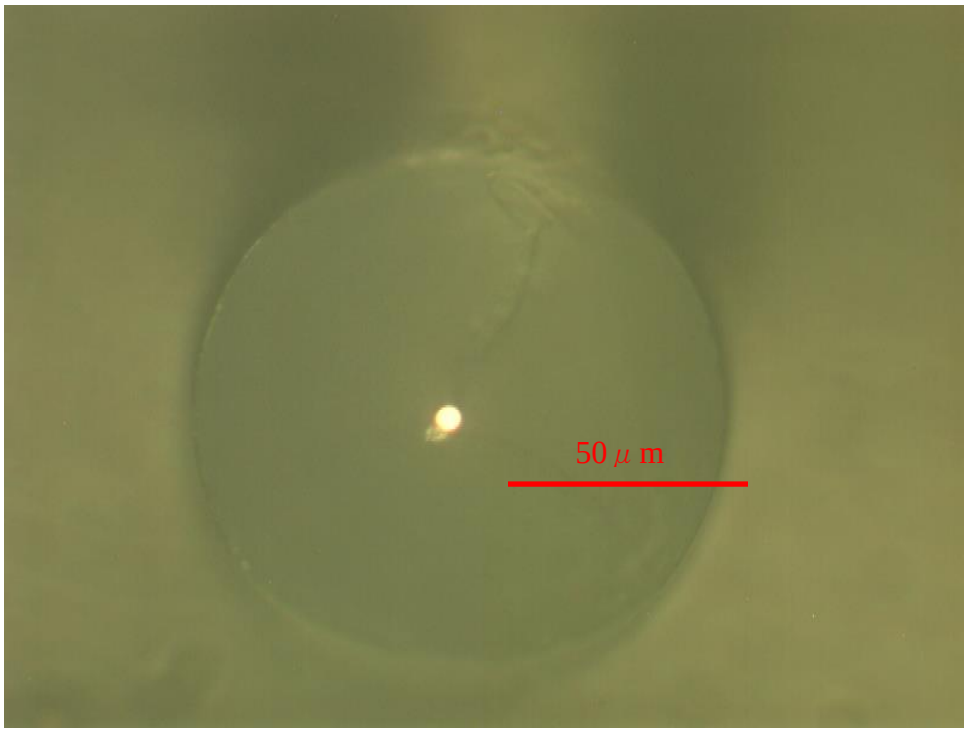

Figure 3-55: Fiber end-view 550Y 800-25

Transmission was tested under normal pressure, air environment; The length of the samples are 6cm, 6cm, 5.2cm, 5.6cm, 5.6cm, 5.7cm, for Base, 600-25, 600-50, 700-25, 700-50, 800-25 respectively. Gas was directly blown onto the sensor, with a low flow rate of

approximately ~1.5 slpm. Transmission spectra of the tested fibers are shown in Figure 3-56 through Figure 3-61.

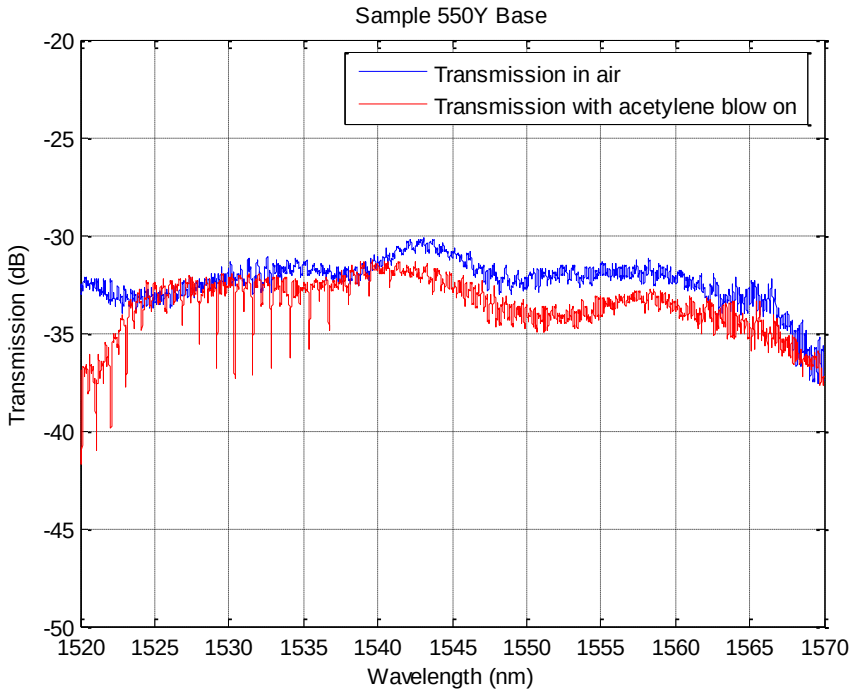

Figure 3-56: Transmission of sample 550Y Base

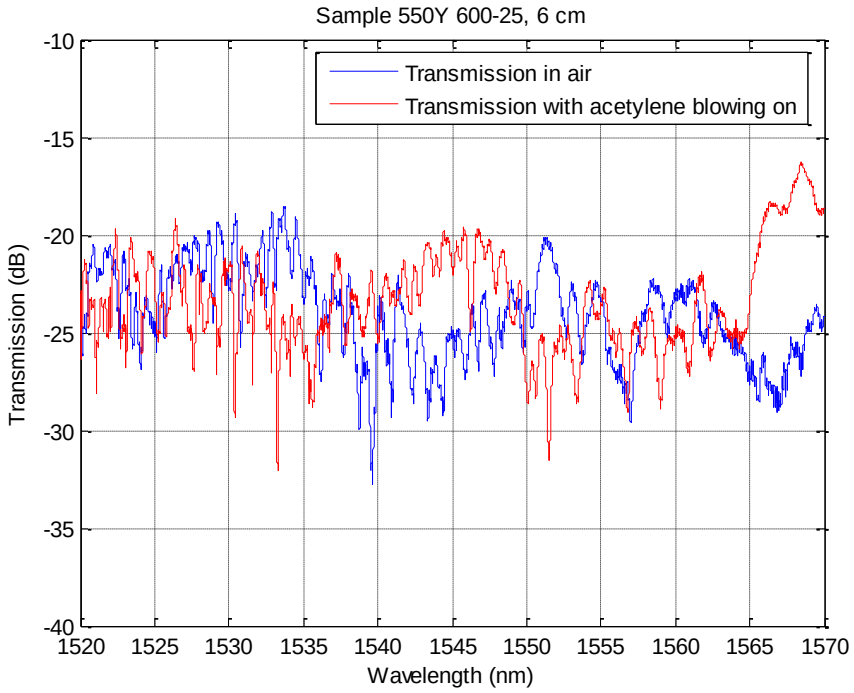

Figure 3-57: Transmission of sample 550Y 600-25

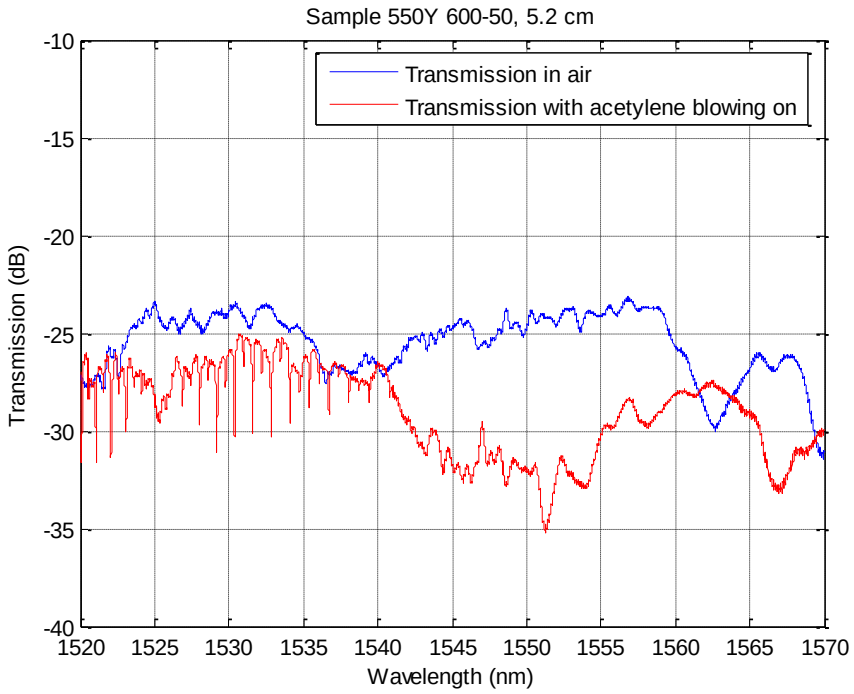

Figure 3-58: Transmission of sample 550Y 600-50

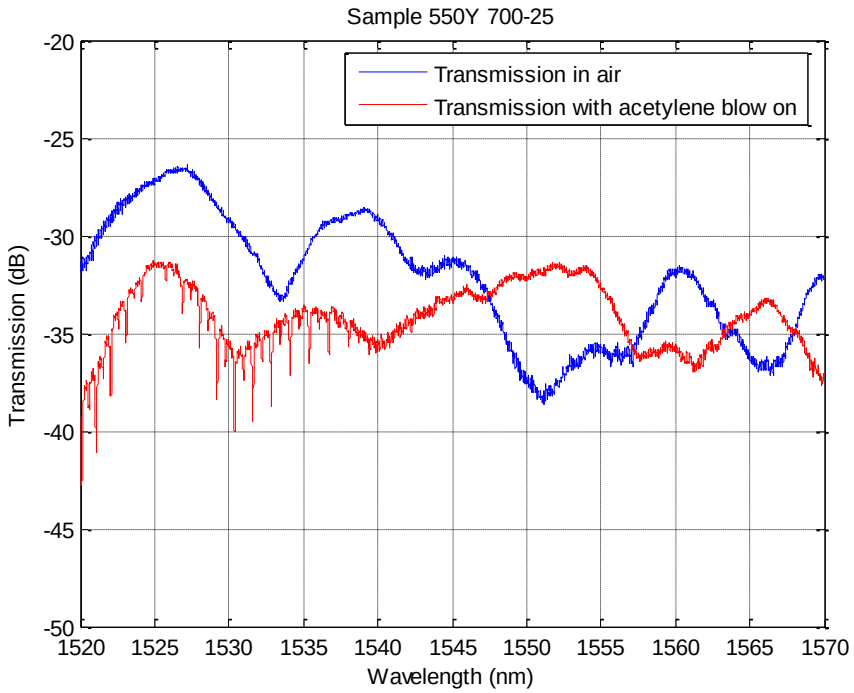

Figure 3-59: Transmission of sample 550Y 700-25

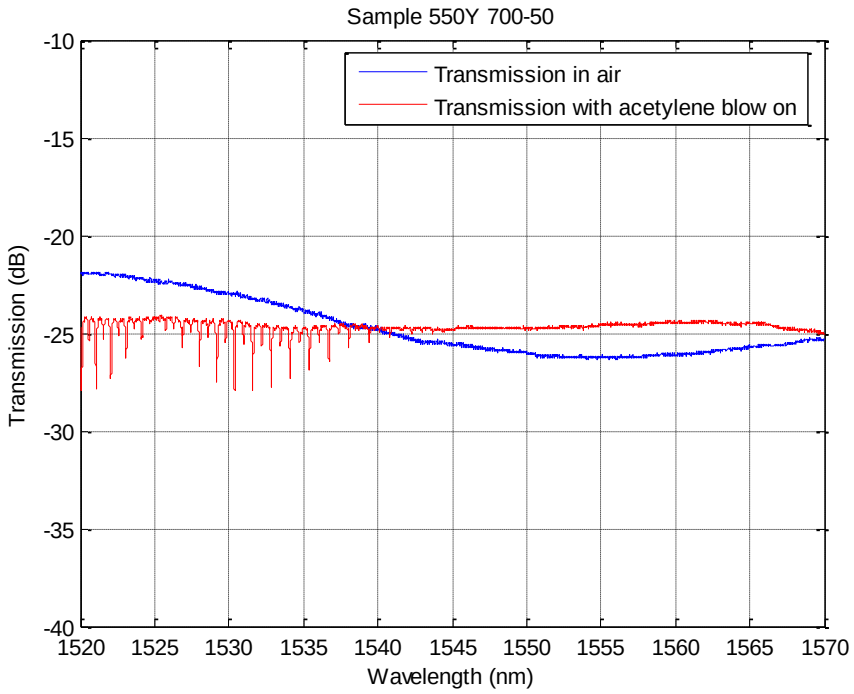

Figure 3-60: Transmission of sample 550Y 700-50

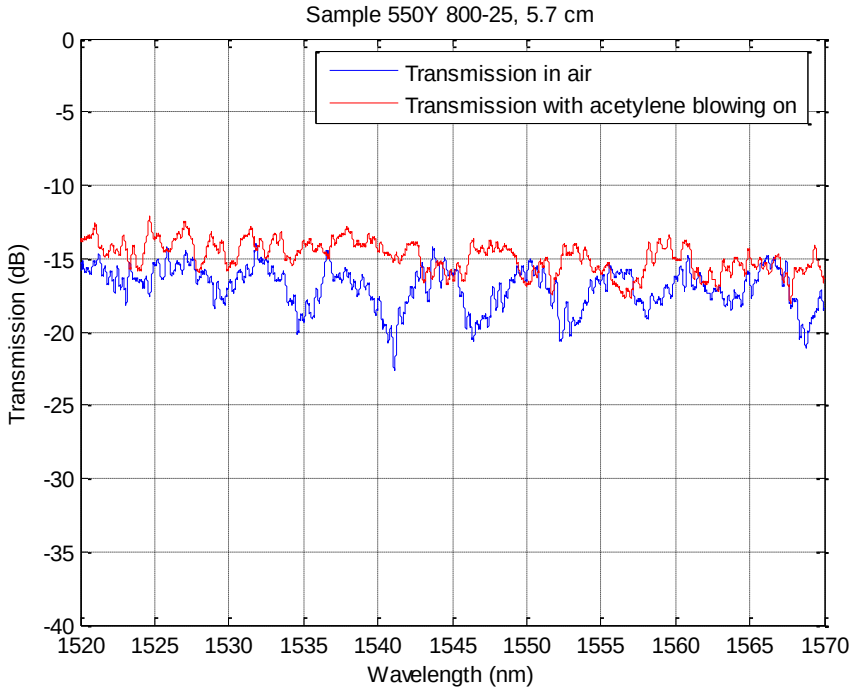

Figure 3-61: Transmission of sample 550Y 800-25

The absorption depths of the samples were measured at the 1530.4nm absorption line as shown in Figure 3-62. The following figure shows how the absorption depth is defined. Figure 3-63 shows a magnified view of the y axis to see if absorption peaks exist for the 800°C exposure, no

peaks can be seen at 1530.4 nm (where should be a strong absorption line, and which is used to calculate the sensitivity of the sensor).

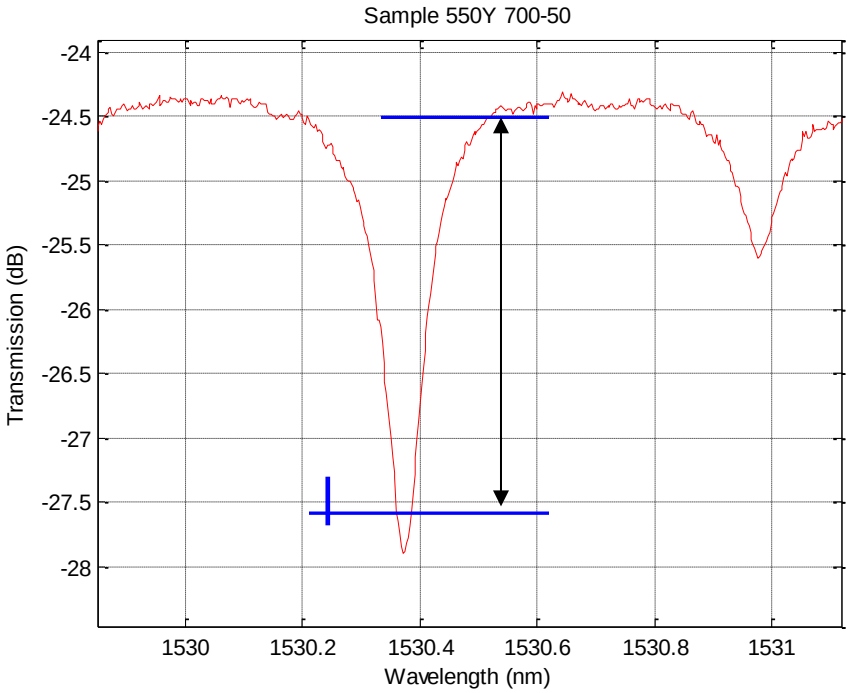

Figure 3-62: The measurement of the absorption depth

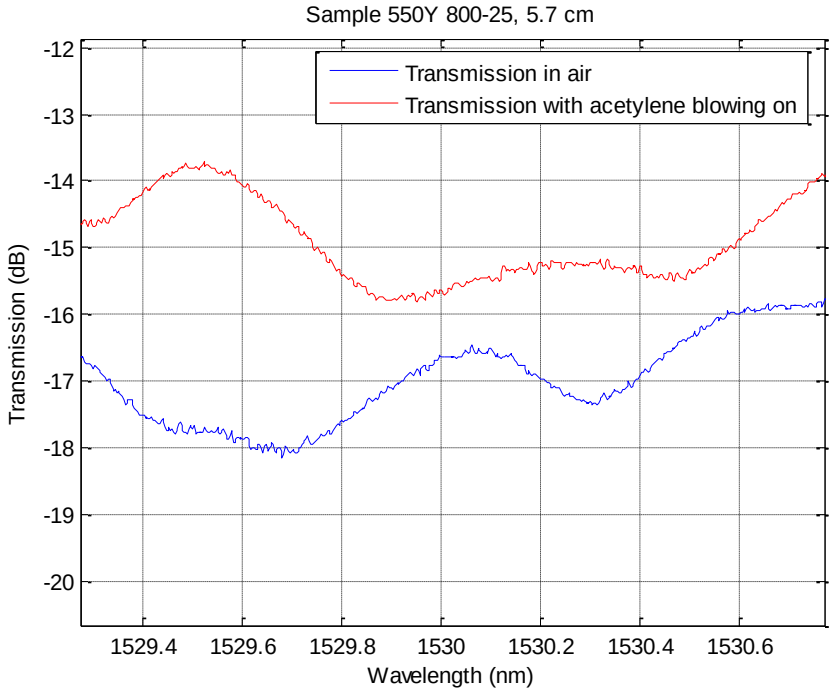

Figure 3-63: Magnified transmission of sample 550Y 800-25

Table 3-10 lists the absorption depths measured versus the sample treatment conditions and the relationship is plotted in Figure 3-64: Absorption depth as a function of heat exposure conditions:

Table 3-10: Fiber absorption depth as a function of heat exposure conditions

Sample #	1	2	3	4	5	6
Exposure condition	Base	600-25	600-50	700-25	700-50	800-25
Absorption depth (dB)	-4.98	-3.23	-4.30	-4.09	-3.52	0

Taking into account the experimental data above, the exposure conditions are well above 500℃, the time that the samples being exposed were as long as 50 minutes. Experiment results show that even exposed to 700℃ for 50 minutes, the porous fibers were still capable of sensing gas, even with a slow blow rate of 1.5 slpm, the sensitivity was as high as 3.5 dB. Since the process driving the morphological changes are expected to be exponentially temperature dependent, the time needed to achieve the same degree of morphological change will be much longer at 700℃ than at 800℃ and much longer at 600℃ than 700℃, and again much longer at 500℃ than at 600℃, this indicates that the fiber's capability of high-temperature gas sensing at up to 500℃ should have a very long lifetime with respect to the mechanisms active in this study.

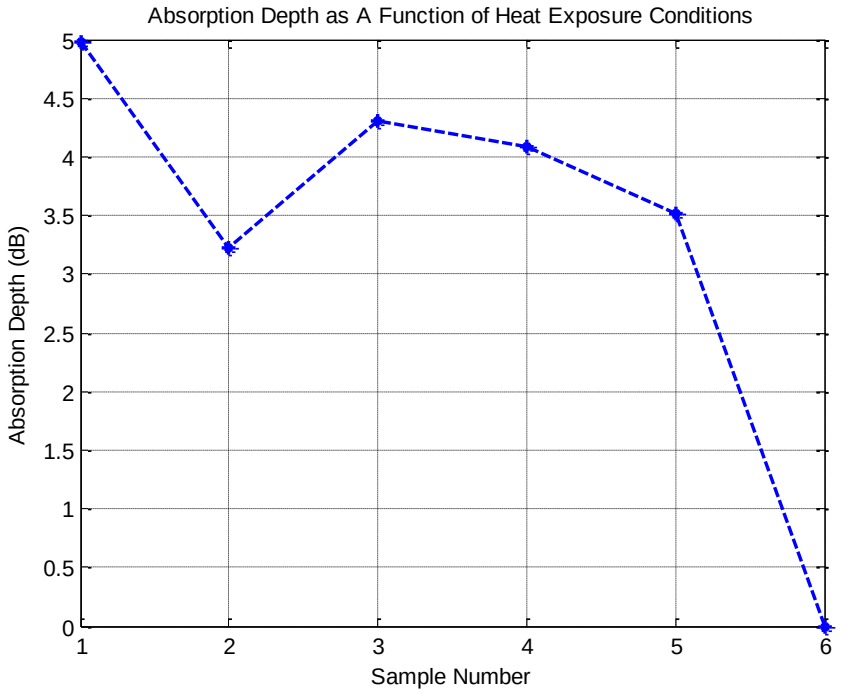

Figure 3-64: Absorption depth as a function of heat exposure conditions

3.6.2.1 500°C carbon monoxide (CO) detection:

The milestone for this quarterly reporting period was to detect carbon monoxide gas (CO) at 500ºC. In the designed experiments, only the high temperature working feasibility of the porous fiber is tested and verified, the whole sensor, however, with epoxy whose working temperature is lower than 500 ºC for sensor packaging is not tested at that temperature. This means we only heat the porous fiber section to 500 ºC, but the ends of the fiber and the ends of the packaged sensor are in an environment much lower than 500 ºC. By changing the epoxy attaching the lead-in and lead-out fiber with the V-groove to high temperature epoxy, the whole sensor can work under high temperature, as indicated by the experiments detailed below.

Experimental setup

The sensor was sealed inside the stainless steel chamber, and only the middle section was heated. This required that the chamber section where the sensor is to be heated should be enclosed by a furnace. The length of the heated region was 1 inch. Also, the exact temperature of the heated area inside the chamber was monitored using a thermocouple. The thermal couple is a 12-inch long shielded probe with outer diameter 0.02" (Super OMEGACLAD® Thermocouple Probe, Product number: KMQXL-020G-12). The furnace was made from electric heating wire wound around a glass tubing, and the furnace was heat-isolated from the outer environment by a thick ceramic tube. By changing the current applied on the heating wire, the inner temperature of the chamber can be adjusted continuously. It was determined that the stainless steel chamber itself provided a large enough temperature gradient that no cooling was needed for the whole system.

The sensor is a section of porous hollow tubing waveguide with inner diameter 170 μm and outer diameter 300μm. The fiber is cleaved to 6.5" with single mode fiber (Corning SMF-28) as lead in and multimode fiber (Thorlabs 105Core) as lead-out inserted into the center hollow core. The sensor is packaged by a v-groove with the lead-in and lead-out fiber attached to the v-groove using epoxy. The middle section of length 1" is where heat is applied. The sensor package is shown in Figure 3-65.

The optical source of Micron Optics Si-720 Component Testing System (CTS) was used as a swept laser ranging 1520-1570nm with 2.5pm wavelength resolution. The output light was coupled into a standard single mode optical fiber. The lead-in fiber was directly inserted into the porous hollow tubing waveguide (PHTW) for approximately 0.5". The light inside the waveguide will be partially reflected by its side-wall, the portion of confined light then will be collected by the lead-out fiber, in our case a 105μm core 125μm O.D. multimode fiber (MMF). Using the MMF as the lead-out fiber and a PIN photodetector provided mainly two advantages: 1. It collects more light taking advantage of the MMF's larger core; 2. It eliminates modal interference when a single mode fiber exists on the detection port. The photo current is then detected and captured bya high-speed oscilloscope (LeCroy WavePro 725Zi). The schematic plot and real photo of the system setup is shown in Figure 3-66 and Figure 3-67, respectively.

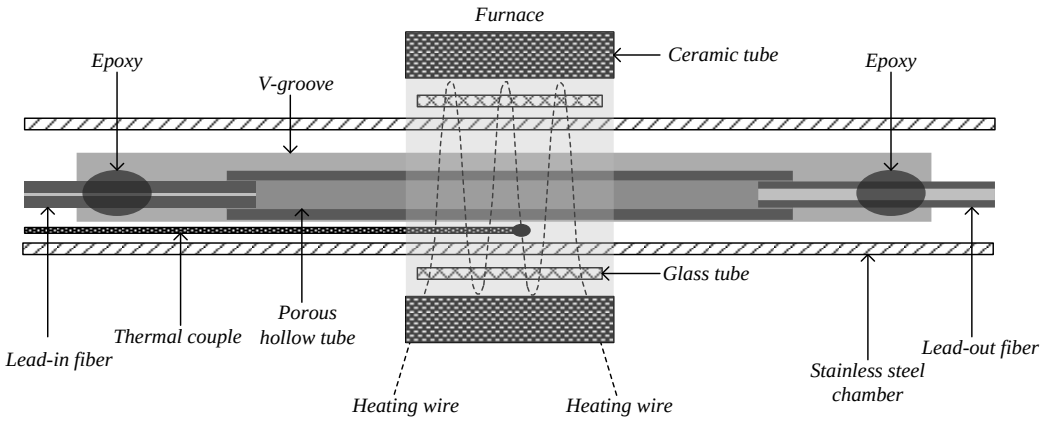

Figure 3-65: Sensor package

The chamber system was made up of a set of stainless steel tubes, connectors and valves. A vacuum pump and a CO tank were connected to the chamber system providing the ability of evacuating and CO pressurizing the system (in our case the chamber pressure is a maximum of 20Psi above ambient). The furnace and thermal couple were permanently mounted to the chamber system.

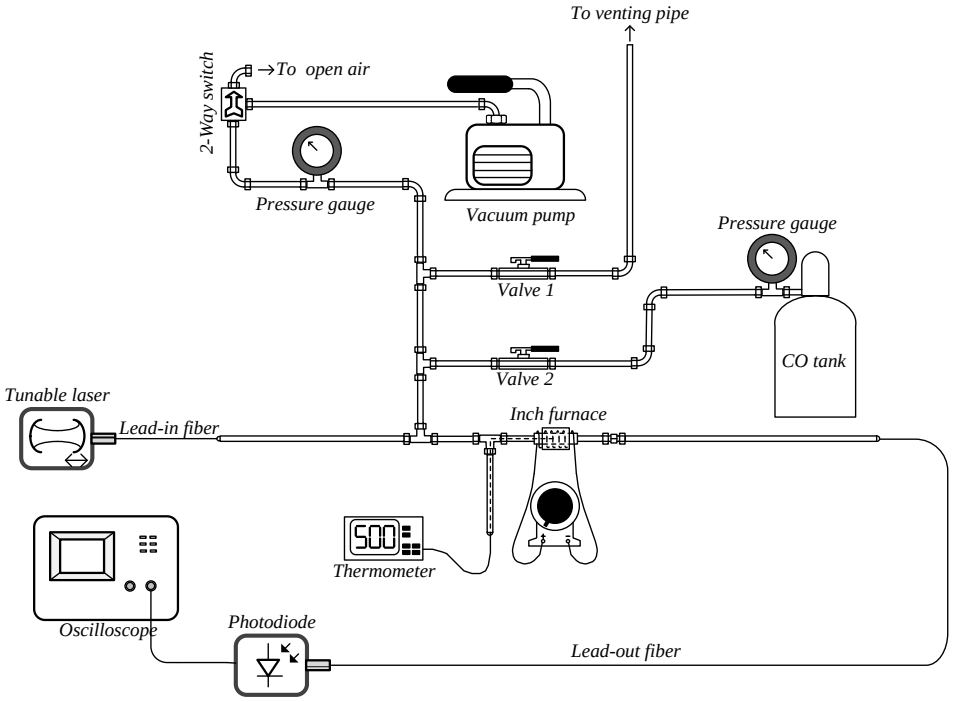

Figure 3-66: Schematic of the system setup

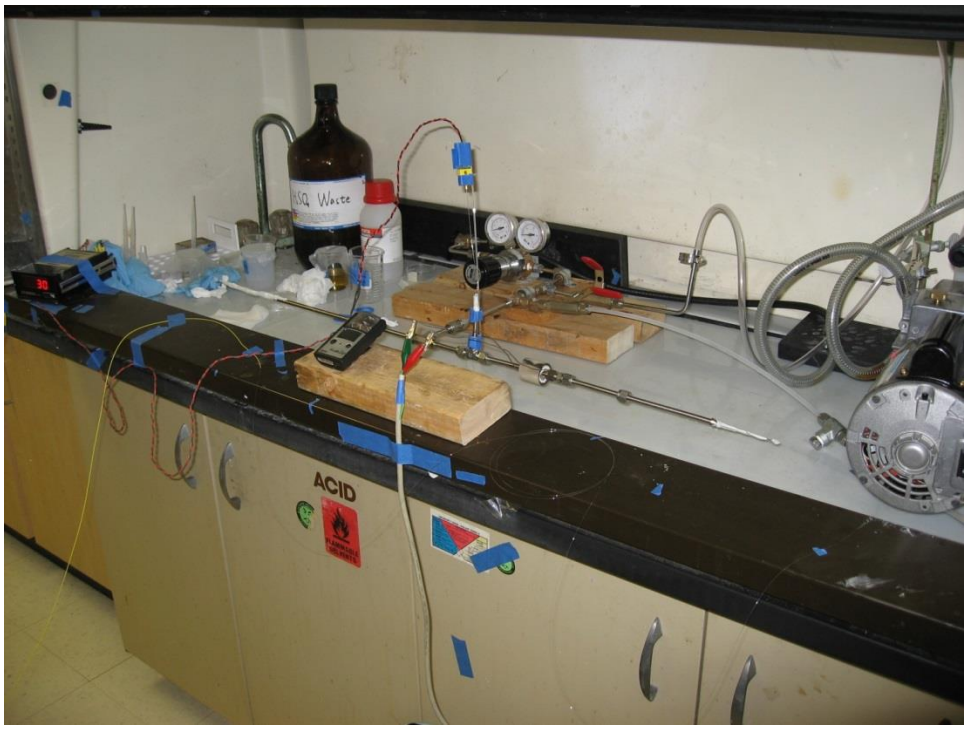

Figure 3-67: Photography of the system setup

Experimental procedure

Experiments were performed under 100 ºC, 200 ºC, 300 ºC, 400 ºC, 500 ºC. For each group, 5-10 sets of data were obtained and then averaged. Because the temperature for each group is not completely stable, an average of the temperature data was also performed after obtaining each group of data. To collect one set of data, two steps should be taken: 1. Vacuum the system, then take the data of the transmission spectrum of the sensor; 2. Pressurize the system, then take the data of the transmission spectrum of the sensor. The vacuum data is generated as a baseline which was subtracted from the data with the absorption features. Please refer to Table 3-11 (a)-(e) for the temperatures at which the data was taken. For each set of data, the following settings were used for the oscilloscope: C1: raw data channel, 50mV/div, 10ms/div, 100kS@1MS/s, 1μs/pt for 100ms, total sample 100kS; F1: averaged data channel, 1000 averaging times, 2mV/div, 2ms/div.

Table 3-11: (a) Group 1 temperatures

Data set	1	2	3	4	5
vacuum	108	103	104	100	110
CO	104	102	104	96	113

(b) Group 2 temperatures

Data set	1	2	3	4	5

vacuum	201	214	194	211	209
CO	197	201	207	210	210

(c) Group 3 temperatures

Data set	1	2	3	4	5
vacuum	294	301	293	295	290
CO	301	301	293	294	293

(d) Group 4 temperatures

Data set	1	2	3	4	5
vacuum	404	409	408	402	398
CO	409	406	405	403	397

(e) Group 5 temperatures

Data set	1	2	3	4	5
vacuum	495	505	514	515	508
CO	495	505	514	518	506

For each group of data, a Matlab program was used to process the data and plot the absorption spectra of the sensor. The program took several steps to complete the work:

a. Read from the computer hard drive all 10 sets of data (5 sets for vacuum and 5 sets for CO). Respectively average both vacuum spectrum and CO spectrum to produce baseline and CO raw spectrum.

b. Subtract the baseline from the CO raw spectrum to get an averaged CO spectrum. There will be low frequency noise added on the spectrum.

c. To eliminate the low frequency noise, a moving average window filter with window size of 500 data points will be applied to smooth the spectrum. After filtering, the low frequency noise will be suppressed dramatically.

d. To finalize the plotting of the CO spectrum, a wavelength calibration algorithm was employed. The basic idea is to identify the wavelengths of the two absorption peaks. The standard wavelengths of these peaks can be found in the HITRAN database. In our case, the two peaks selected are: absorption line at 6385.7715cm^{-1}, and 6374.4058cm^{-1}, and correspondingly, their datapoint numbers are: 9718 and 13476. After identifying these two peaks, all the datapoints on the spectrum will be linearly fitted to wavelength using the slope defined by the two points. Also the standard HITRAN absorption positions will be indicated as dotted vertical lines on the spectrum, to verify the absorption positions.

Using the above algorism, all the data groups were treated, and the absorption spectra of CO under 100 ºC, 200 ºC, 300 ºC, 400 ºC, 500 ºC are plotted. Also labeled on the plots are the average temperatures at which the experiments were performed. The plots, especially the 510 ºC one, demonstrated that our sensor can work above 500 ºC. The plots are provided in Figure 3-68 (a)-(e).

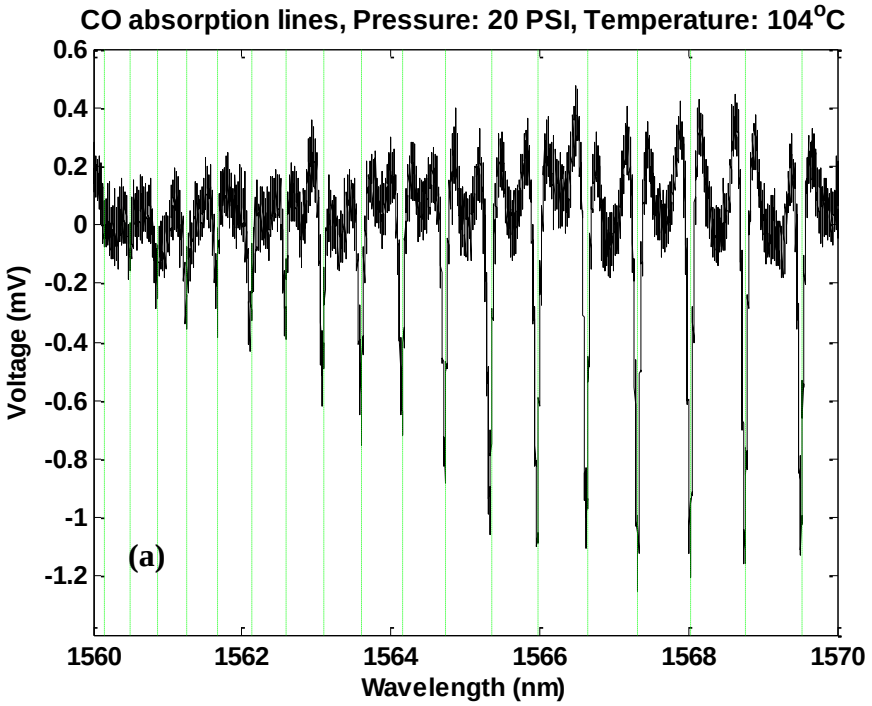

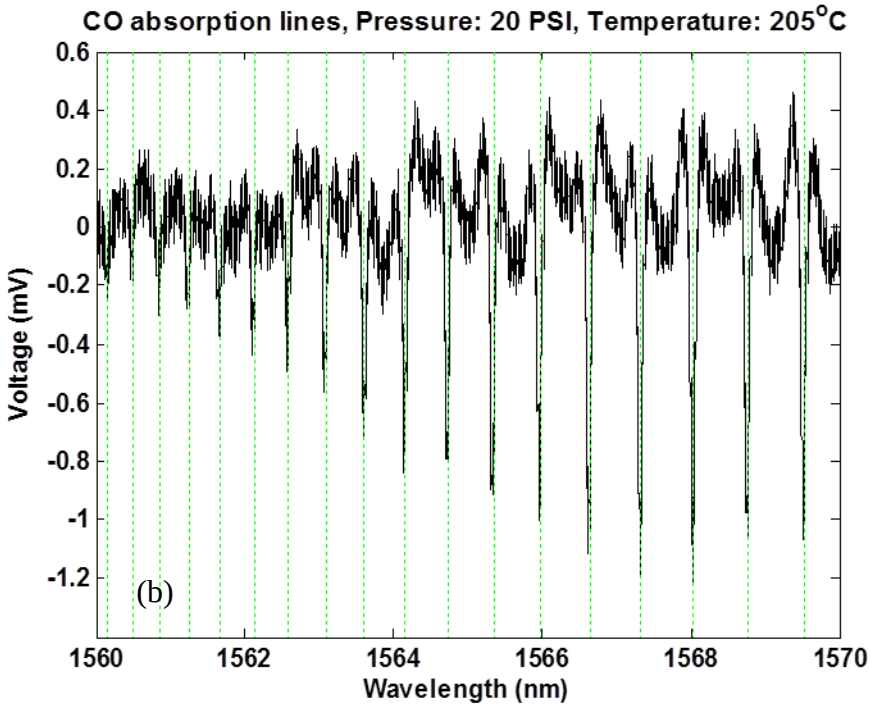

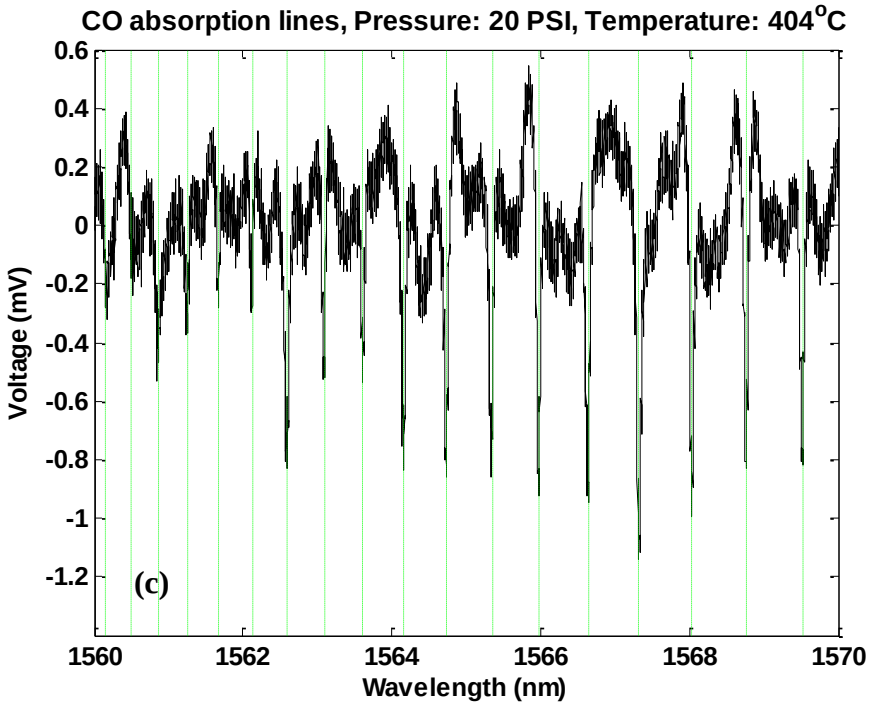
CO absorption lines, Pressure: 20 PSI, Temperature: 404°C
0.6
0.4
0.2
0
-0.2
-0.4
-0.6
-0.8
-1
-1.2
Voltage (mV)
(c)
1560
1562
1564
1566
1568
1570
Wavelength (nm)

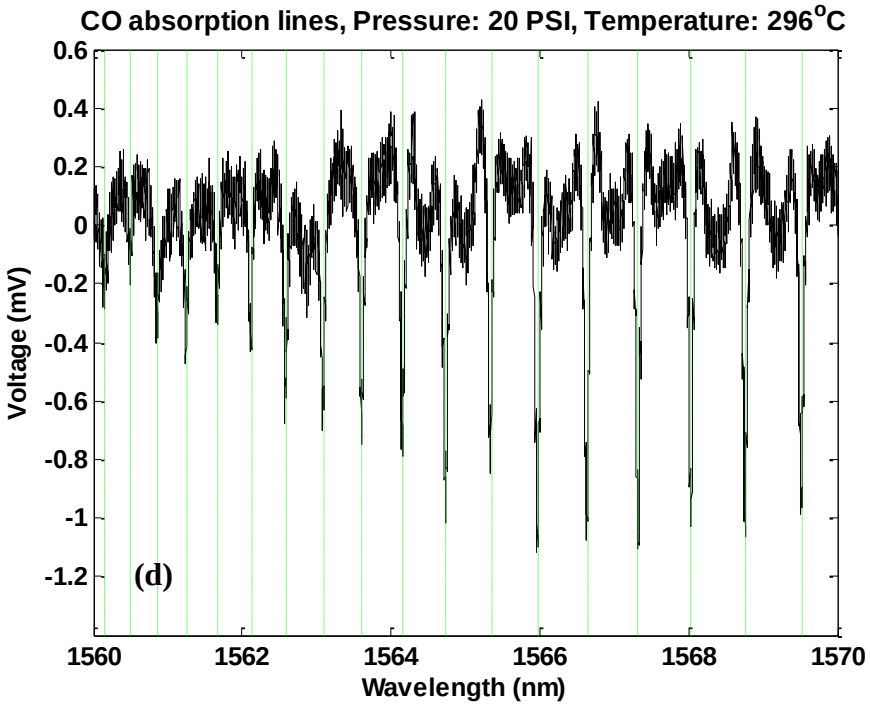
CO absorption lines, Pressure: 20 PSI, Temperature: 296°C
0.6
0.4
0.2
0
-0.2
-0.4
-0.6
-0.8
-1
-1.2
Voltage (mV)
(d)
1560
1562
1564
1566
1568
1570
Wavelength (nm)

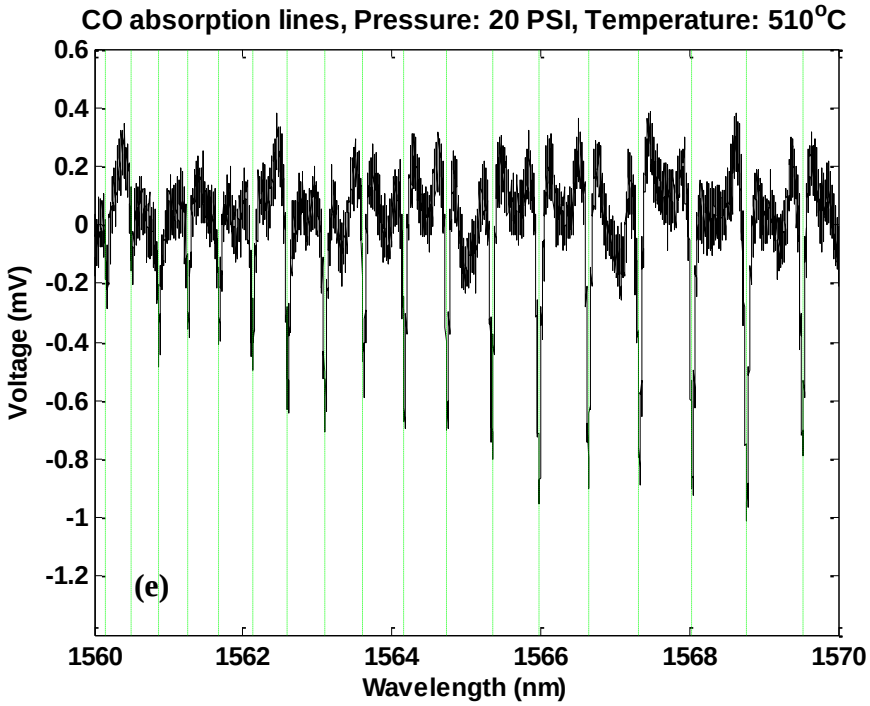

Figure 3-68: CO absorption at (a) 100 (b) 200 (c) 300 (d) 400 and (e) 500 ºC

Line broadening effect

The lineshape function Γ(v) of molecular absorption cross-section depends largely on two external factors for its linewidth: thermal motion and molecular collisions. At high temperature, the line-broadening is Gaussian according to the formula:

$$\Gamma_D(\nu) = \frac{1}{\gamma_D}\sqrt{\frac{ln2}{\pi}}\, e^{-\left(\frac{\nu-\nu_0}{\gamma_D}\right)^2 \ln 2} \qquad (1)$$

In Equ.1, $\nu_0$is the center of the absorption line, $\gamma_D = 3.58 \times 10^{-7}\nu_0\sqrt{\frac{T}{M}}$ is the thermal motion broadening coefficient, *T* is the temperature and *M* is the molecular weight.

The broadening will result in diminishing of the absorption intensity at higher temperature. Although in our case only part of the sensor was heated, the decreasing trend of the absorption depth was obvious, as shown in Figure 3-69. To plot the absorption intensity vs. temperature curve, five strongest absorption peaks were selected; their absorption intensities were calculated and averaged for each temperature. The wavenumber of the selected absorption peaks were: 6374.4058cm^{-1}, 6377.4066cm^{-1}, 6380.3013cm^{-1}, 6383.0896cm^{-1} and 6385.7715cm^{-1}.

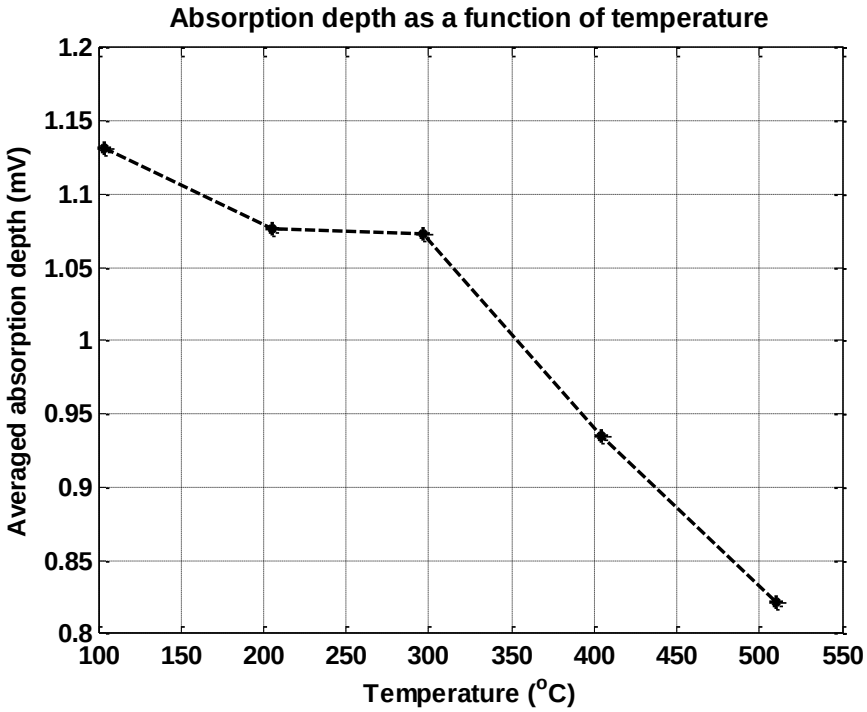

Figure 3-69: Absorption depth as a function of temperature

3.6.3 Simultaneous dual gas detection:

3.6.3.1 Experiment Setup Overview:

Porous hollow core fiber with an I.D.=170um was cut into length=16cm. SMF was used as the lead in fiber and 105/125 MMF was used as the lead out fiber. These were directly inserted into the center hole of the hollow core porous fiber. Using MMF as the lead out fiber takes advantage of the large core of the fiber to collect more power in the central core region to enhance the signal-to-noise ratio (SNR). Because of the use of MMF, the multiple optical transmission modes within the multimode fiber will interfere with each other at the output port of the CTS (Miron Optics *Si-720*) which uses an SMF-pigtailed detector. The modal interference manifests in a noise-like pattern superimposed on the transmission baseline of the sensor, which will overwhelm the small signal from the weakly absorbing species such as carbon monoxide (CO). Instead, the wavelength sweeping laser output from the CTS (linearly sweeping from 1520 to 1570nm) is coupled to an SMF, which goes through the porous hollow core fiber sensor and is collected by the MMF. The returning light is detected using an PIN photo-detector, which converts the impinging light energy into photocurrent and finally a voltage whose magnitude is linearly related to the detected light intensity, the time-varying voltage is then analyzed and displayed by an oscilloscope (LeCroy *LT342*). Because this setup avoids using a SMF immediately before the detector, which when connecting to a multimode fiber will bring in a significant amount of modal interference, the oscilloscope displays a time-varying output (which corresponds to the spectrum of the sensor) with only very little ripples due to the interference. One difficulty of the current setup is the final wavelength calibration of the spectrum. This is

solved in the gas sensing application by the absorption-peak tracking technique which will be discussed later.

3.6.3.2 Experimental Details:

The sensor is packaged by a 21 cm long metal V-groove, with part of the lead-in and lead-out fiber, and these were attached permanently to the V-groove by a small amount of epoxy. The packaged sensor was sealed inside the vacuum/pressure chamber, which is designed to work in the range from -100 VAC to 100 Psi above normal pressure.

Experiment 1: carbon monoxide detection at 20Psi

According to the HITRAN database, the absorption cross sections of carbon monoxide in the range of 1560-1570 nm are three orders less (one over thousands) than the absorption cross sections of acetylene at 1520-1530 nm range. The key point of the simultaneous detection of acetylene and carbon monoxide is thusly the detection of carbon monoxide at normal or low pressures. The first set of experiments is designed to detect CO at 20 Psi.

At first, the chamber is evacuated, and a section from a single period from the spectrum trace obtained by the oscilloscope is recorded which corresponds to the spectrum range where CO absorption is expected to occur. The recorded spectrum is named ‘Baseline 1’. Then, the chamber is pressurized with CO to 20 Psi above ambient pressure, and the same section of the spectrum is recorded and named ‘CO 20Psi 1’. The next step is to simply repeat the first step, which includes the recording of the same spectrum section at vacuum and at CO 20Psi, the spectra recorded are named ‘Baseline 2’ and ‘CO 20Psi 2’, respectively. In a similar manner, the evacuation and CO pressurization to the vacuum/pressure chamber are practiced for ten times, with a set of data recorded with name ‘Baseline 1’ to ‘Baseline 10’ and ‘CO 20Psi 1’ to ‘CO 20Psi 10’. The baseline and the spectrum with CO exposure are recorded for multiple times to average out fluctuations on the transmission spectrum due to temporal instability. The baseline spectrum, as well as the spectrum with CO exposure, is plotted in Figure 3-70 after averaging.

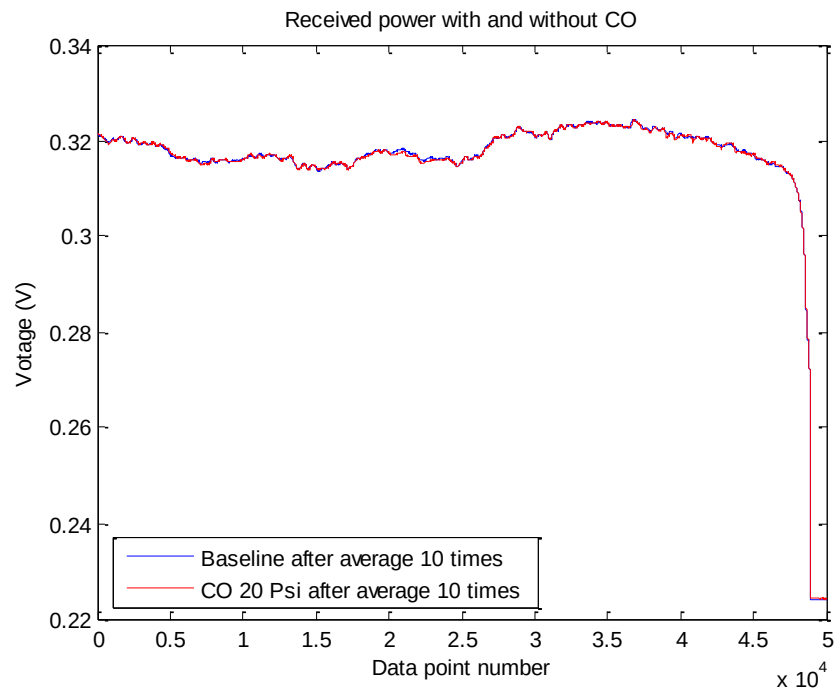

(a)

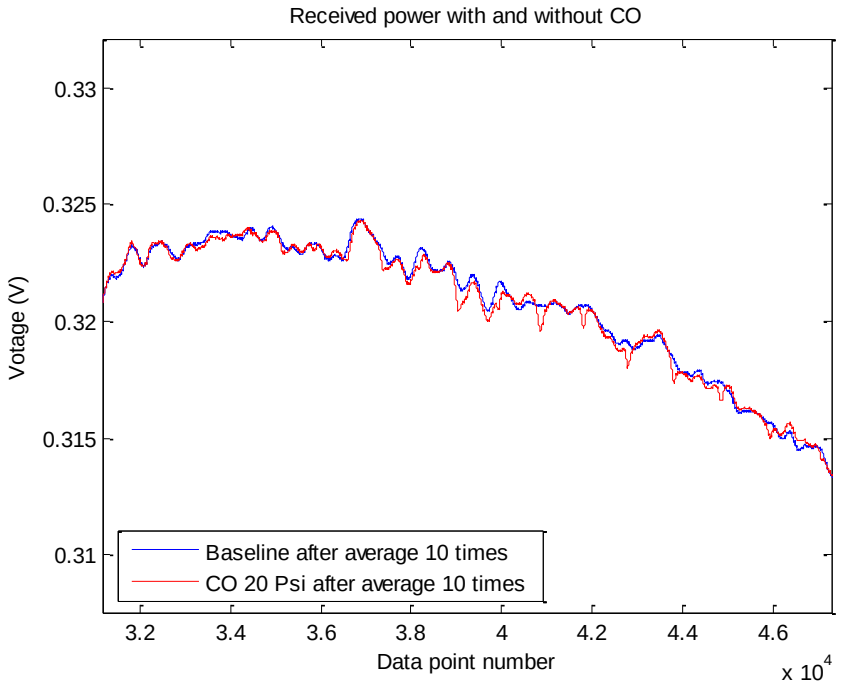

(b)

Figure 3-70: Average baseline and spectrum with CO exposure (a) Full spectrum (b) Zoomed in spectrum where CO absorptions occur

Then the baseline is subtracted from the spectrum with CO absorptions, as shown in Figure 3-71. By using a moving average filtering technique (with window size 500 data points) the baseline of the figure is generated (shown in the red curve).

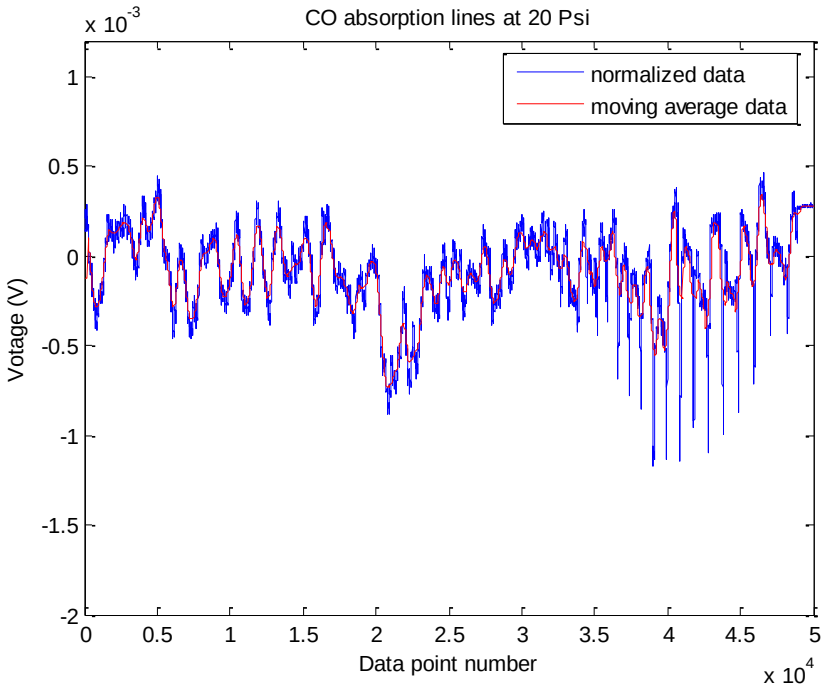

(a)

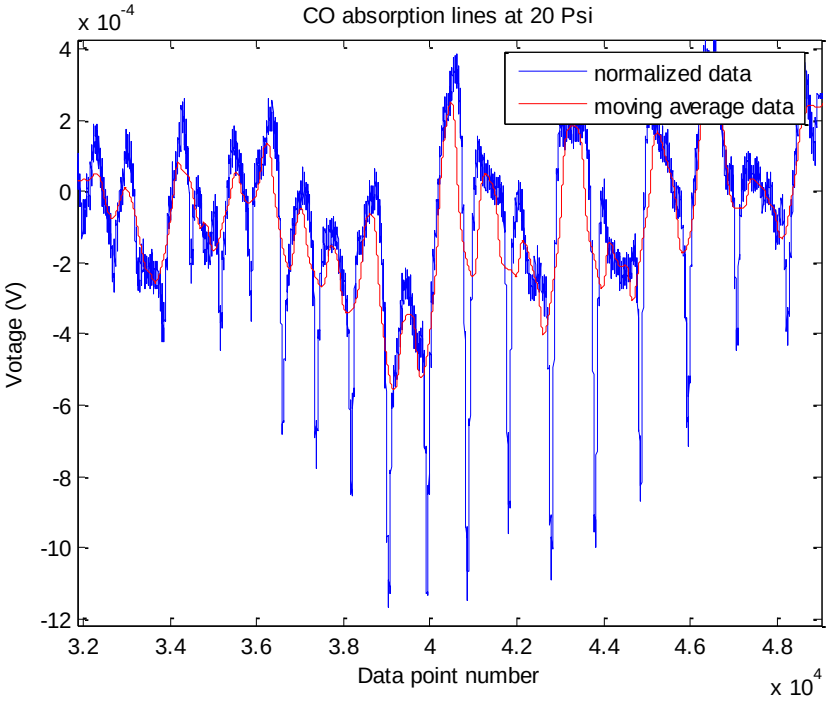

(b)

Figure 3-71: Absolute absorption and the moving average fitting to the baseline (a) Full spectrum (b) zoomed in view

By subtracting the moving-average fitting baseline from the original spectrum the CO absorption lines are more visible as shown in Figure 3-72. A main difficulty of this detection scheme is to calibrate the wavelength for the obtained spectrum. This task can be done in this

application by the absorption line position tracking technique. Because the absorption lines should be at very specific wavenumber positions published by the HITRAN database, it is possible to identify from the obtained spectrum at least two absorption lines (stronger absorptions are preferred). In the above figure, the circled 7 absorption lines are identified using HITRAN data and the first and third line from left are used to calibrate the spectrum.

For the first absorption line:

Data point number : **n1**

Published wavelength: λ_1

For the third absorption line:

Data point number: **n2**

Published wavelength: λ_2

So the wavelength resolution of the obtained spectrum can be calculated as $\Delta\lambda = \frac{\lambda_2 - \lambda_1}{n_2 - n_1}$.

The beginning wavelength can be calculated as $\lambda_{\min} = \lambda_1 - (n_1 - 1)\Delta\lambda$, and the ending wavelength should be $\lambda_{\max} = \lambda_{\min} + (N-1)\Delta\lambda$ where N is the total number of points in the spectrum. After calibration, the spectrum is plotted in the next figure. Also the published HITRAN data are marked with red vertical lines indicating the position of CO lines.

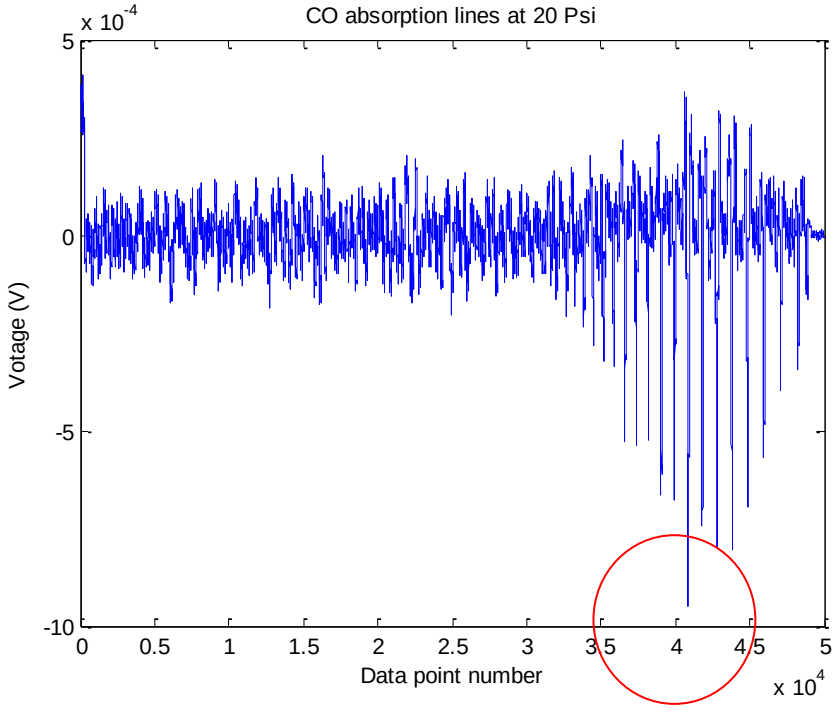

Figure 3-72: CO absorption spectrum obtained by subtracting the moving-average fitting baseline from the original data

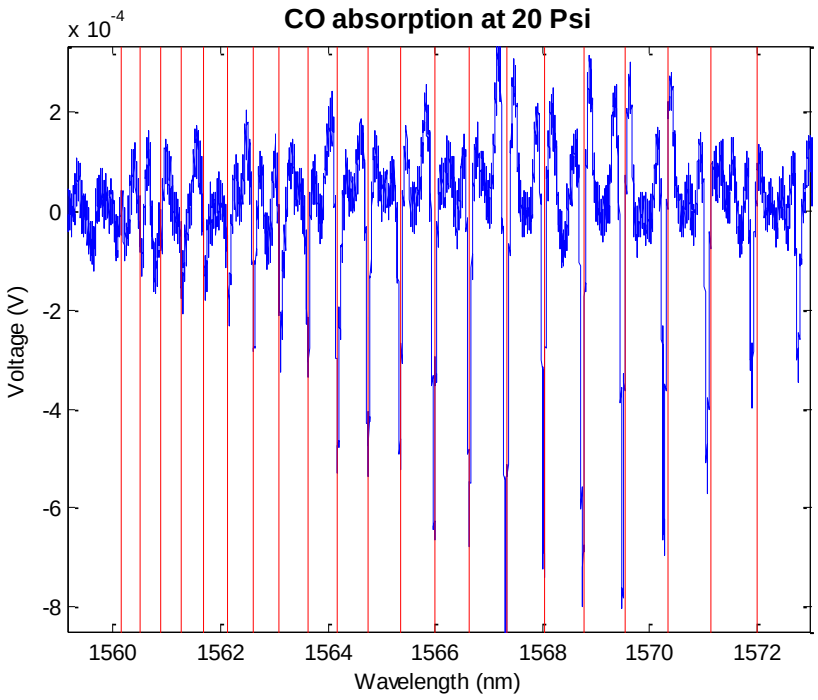

Figure 3-73: Wavelength calibrated CO absorption spectrum: zoomed in spectrum

The wavelength above 1570 nm is not accurate in Figure 3-73because the sweeping speed of the laser in CTS changes after 1570nm which is the detection limit of the CTS (out of detection range of CTS).

Experiment 2: spontaneous detection of acetylene and carbon monoxide

This experiment was designed to simultaneously detect acetylene and carbon monoxide in the vacuum/pressure chamber. At first, the chamber was evacuated to -100VAC vacuum and the spectrum 'Baseline 1' is recorded. The spectrum range should cover both acetylene and CO absorption bands (from 1520nm to 1570nm). Then, acetylene gas was admitted to the chamber to a pressure of -50VAC, and CO gas was filled in afterward to 25Psi. The spectrum named 'Acetylene and CO 1' was recorded. In the following steps, the evacuation and pressurization of the chamber with acetylene and CO would be performed for multiple times and several spectra were recorded. In the experiment, totally four sets of data (eight spectra) were taken and averaged to cancel the temporal interference noises. The baseline and the spectrum with acetylene and carbon monoxide are plotted in Figure 3-74.

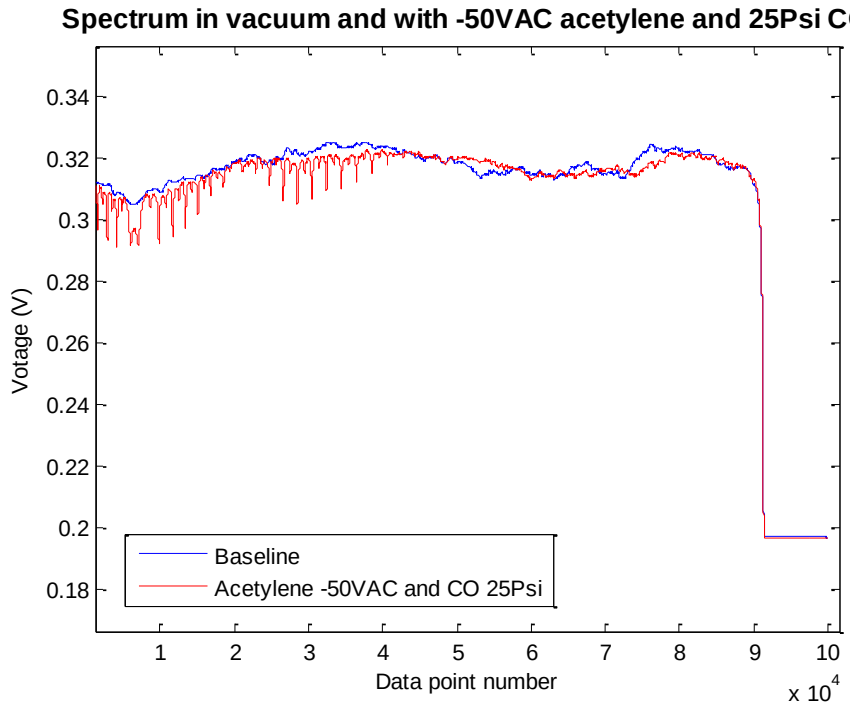

(a)

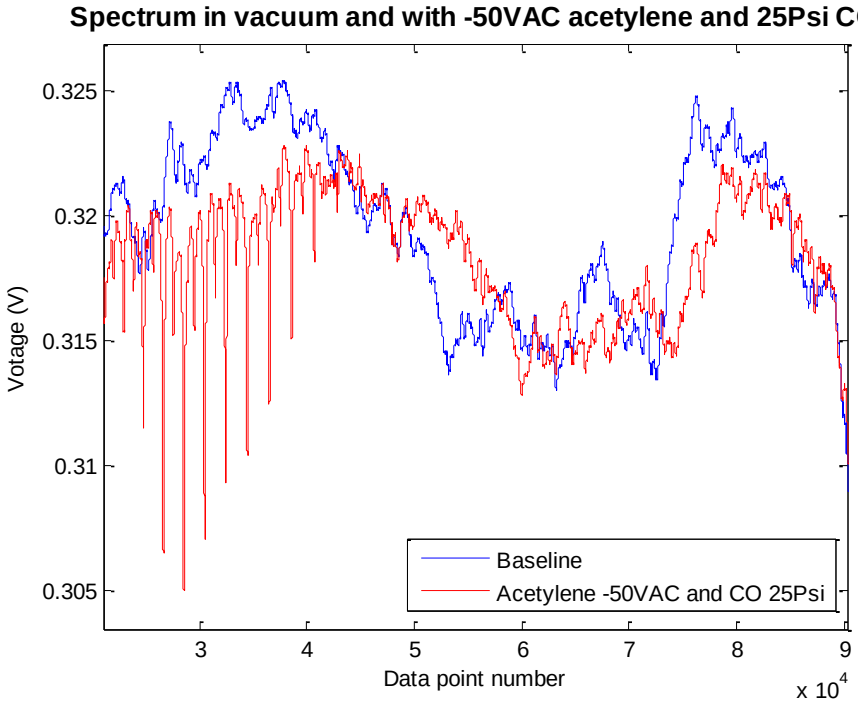

(b)

Figure 3-74: Baseline and transmission spectrum when sensor exposed to acetylene -50VAC and CO 25 Psi (a) Full spectrum (b) zoomed in view

Then the baseline (blue curve) is subtracted from the spectrum with acetylene and CO absorptions, as shown Figure 3-75. By using the same moving average filtering technique (with window size 500 data points) the baseline of the figure is generated (shown in the red curve

above). By subtracting the moving-average fitting baseline from the original spectrum absorption spectrum is obtained as shown in Figure 3-76.

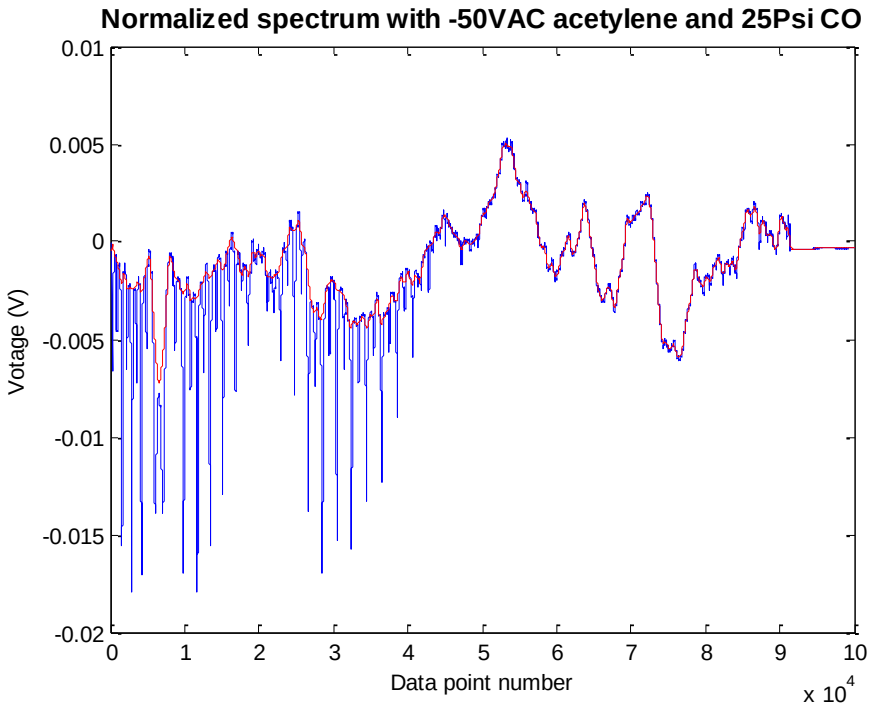

(a)

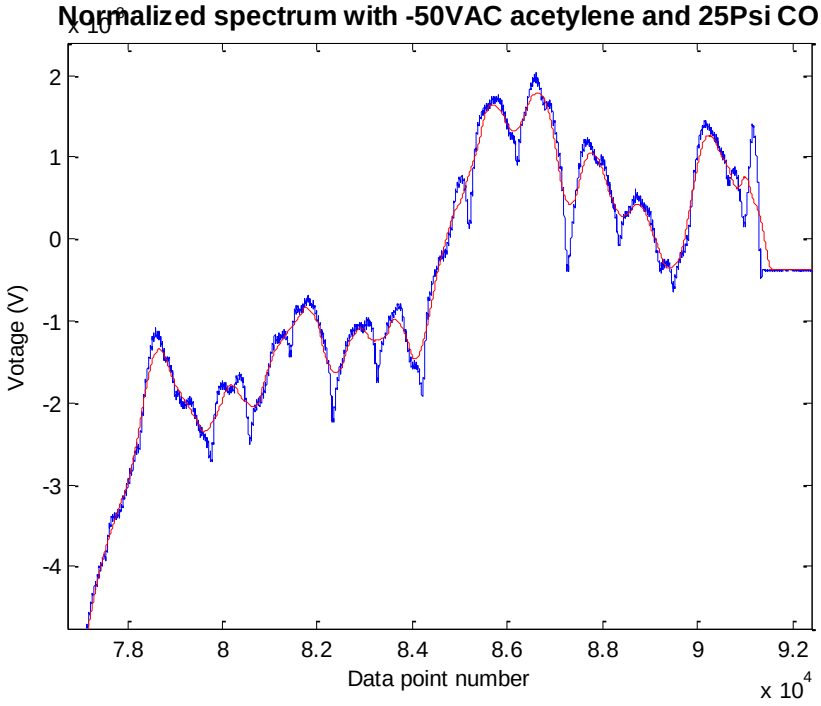

(b)

Figure 3-75: Spectrum of sensor after normalization and the red curve is the moving average fitting (a) Full spectrum (b) zoomed in view

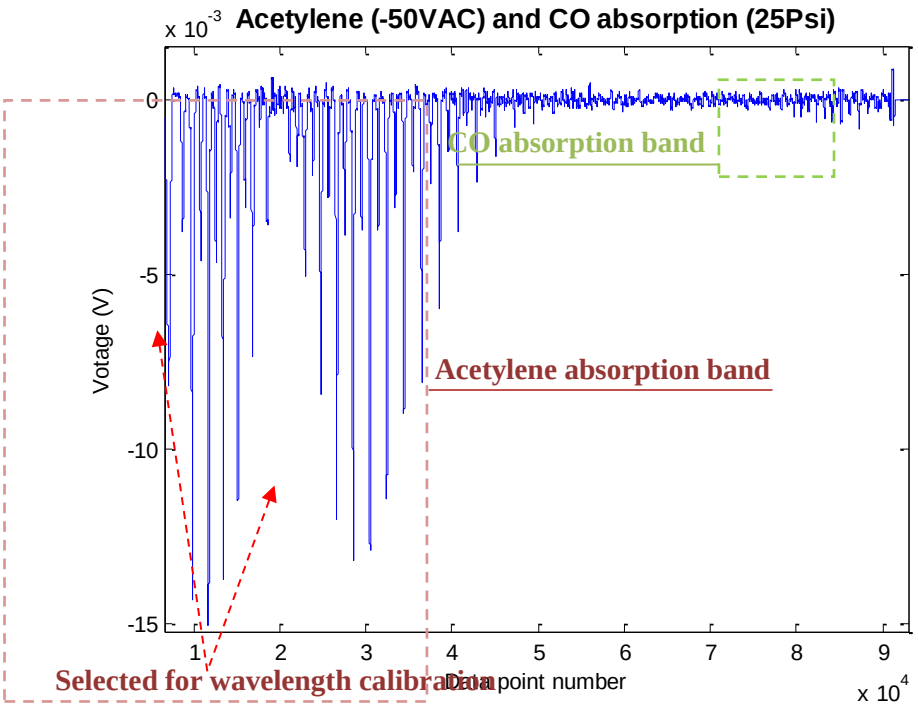

(a)

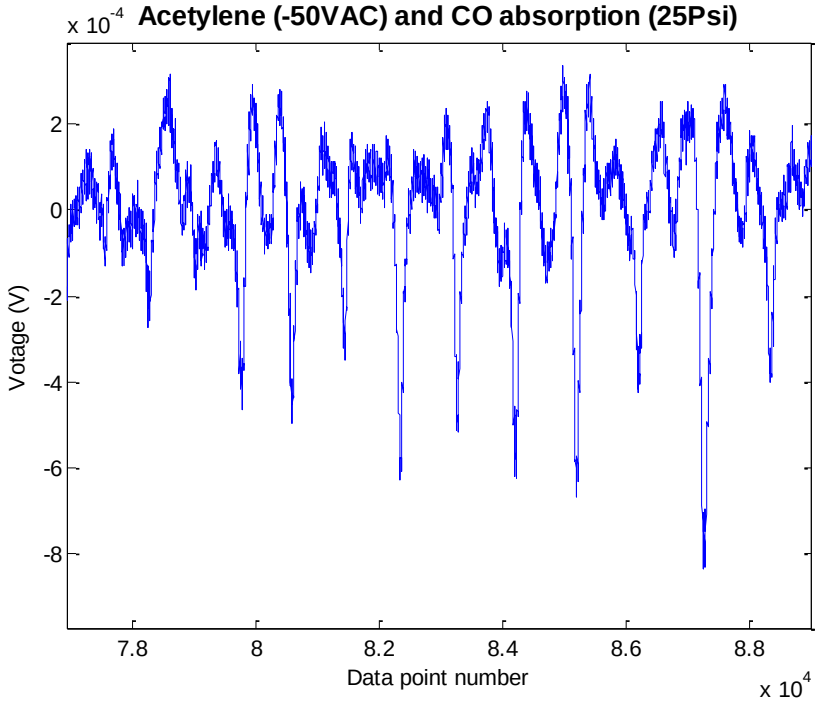

(b)

Figure 3-76: Absorption spectrum obtained by subtracting the moving average fitted baseline from the original data (a) full spectrum (b0 zoomed in view

To perform the wavelength calibration, two peaks from acetylene absorption lines are selected (acetylene line at 6549.328 cm-1 and 6518.486cm-1). The spectrum after wavelength calibration is shown in Figure 3-77.

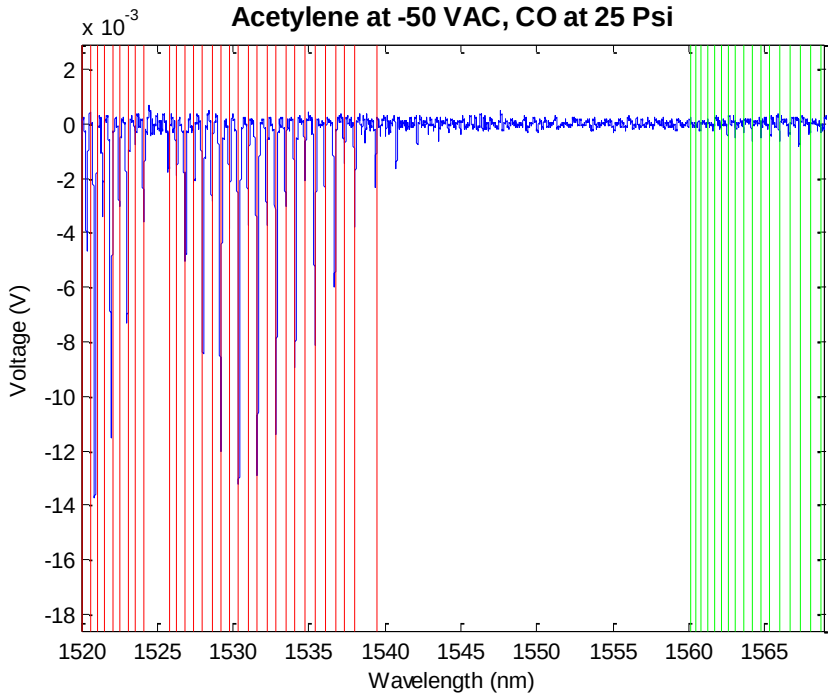

(a)

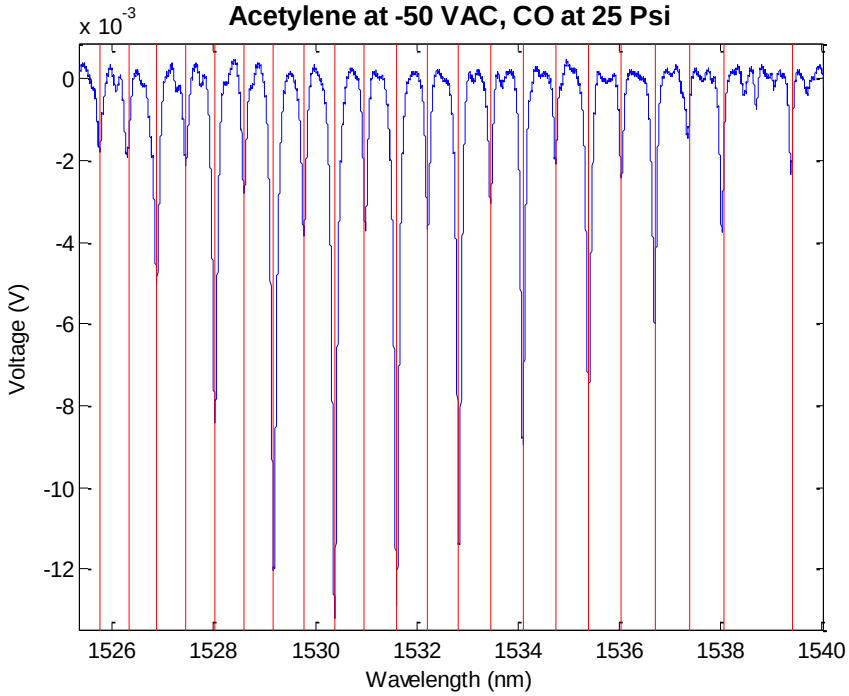

(b)

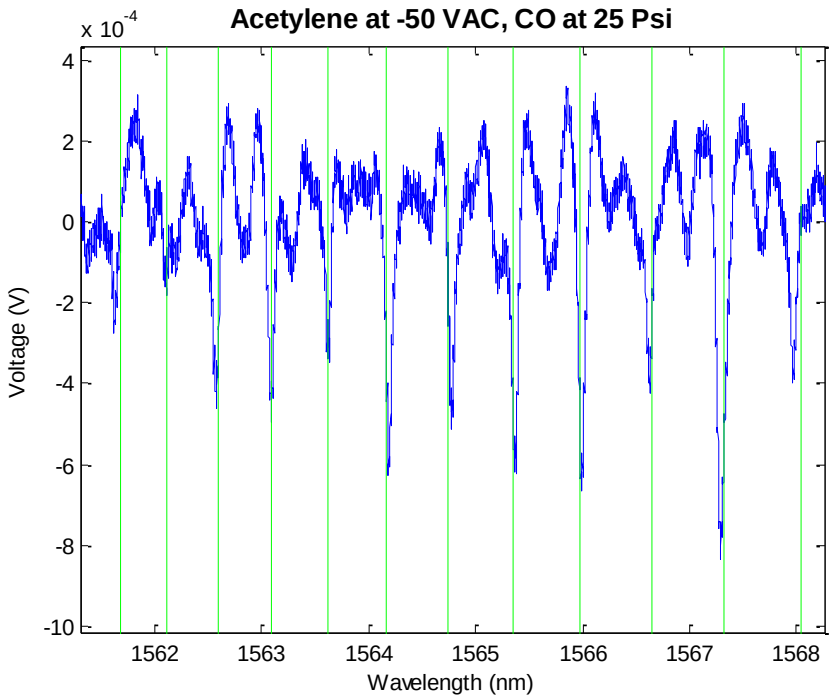

(c)

Figure 3-77: Wavelength calibrated absorption spectrum and the HITRAN absorption position; Red : HITRAN acetylene absorptions, Green: HITRAN CO absorptions (a) full spectrum (b) zoomed in acetylene absorption (c) zoomed in CO absorption

Experiment 3: sensor response time characterization

While the exact definition of what the response time is may be debated (for example return to ½ the intensity, 1/3, 1/e, etc. of the initial intensity may be defined as the response time), this set of experiments focused on measuring the response of the fiber to the presence of gas molecules. The porous structure allows gas molecules to penetrate into and out of the hollow-core tubing more easily, which is one of the main designed advantages of this kind of fiber. To measure the response of the new fibers, the following experiments were carried out.

A section of porous hollow-core fiber waveguide of length ~ 7cm was aligned by single-mode fibers as lead-in and lead-out. The alignment was achieved by two 5 dimensional optical stages. The transmission of the waveguide was obtained using a CTS. A gas pipe connecting to the gas cylinder conducts acetylene gas on top of the porous fiber. The on/off of the gas can be manually controlled by the gas valve on the cylinder. A computer program takes data every second from the CTS to record the transmission spectra of the sensor during a gas on/off cycle, then another computer program helps to average over several absorption peaks aimed at finding the averaged absorption intensity, which gives the concentration of gas molecules surrounding the waveguide. The averaged absorption intensity in log form is then converted to a concentration of gas molecules and displayed as a function of time (See Figure 3-78).

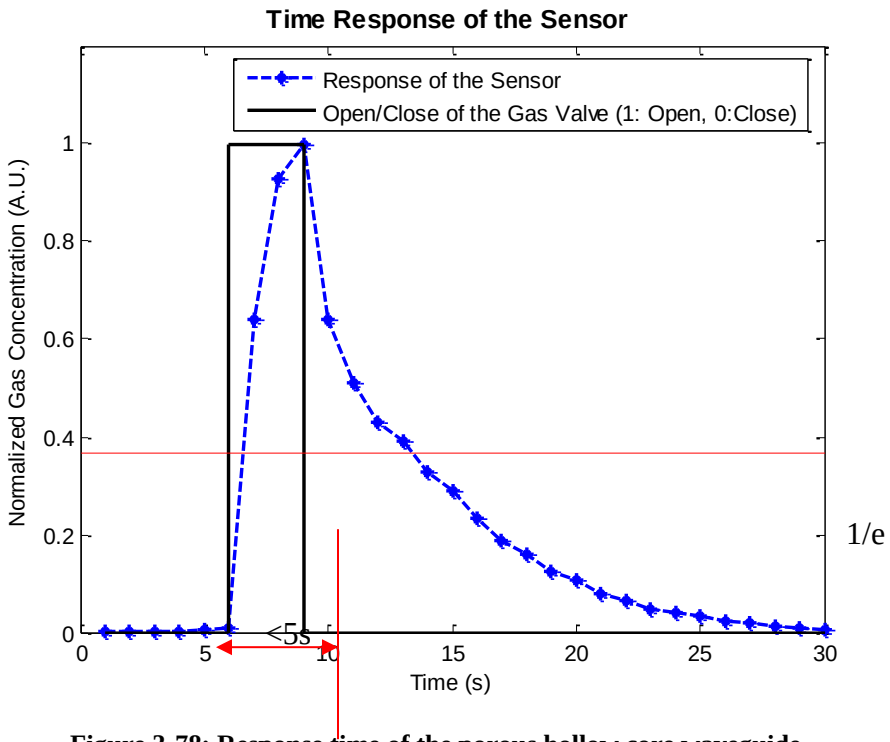

Figure 3-78: Response time of the porous hollow core waveguide

As Figure 3.23 shows, the response time of the porous hollow core waveguide is not symmetric for ascending and descending gas flow signals. For the 'switch-on' signal, the response time is within three seconds, which is pretty fast; for the 'switch-off' signal, the sensor signal (the concentration of gas molecules in the hollow core region) experiences an exponential decay, and with an definition for the response time as the time taken for the sensor from full response to reach 1/e value of the full response, the response time at a release state is roughly 5 seconds. What has not been measured in this set of experiments is actually how fast the gas molecules move away from the surface. It is possible that the residence time of the gas molecules is on the order of seconds, so that the sensor may actually be responding to the "lingering" gas molecules. This would mean that the sensor response time is actually faster than 5 seconds. But in any event it is at least as fast as 5 seconds which is probably sufficient for most power generation facilities control strategies. As a conclusion, the response time for the hollow core waveguide sensor is within several seconds, which is much quicker than other optical waveguide based gas cells based on published data.

4 Sapphire Photonic Crystal Fiber

4.1 Bundled sapphire photonic crystal fiber fabrication

A sapphire photonic crystal fiber concept was proposed and an initial test was performed prior to the start of this project phase. Sapphire fibers with an outer diameter of approximately 70 μm, were cleaved into 7 pieces approximately 15 cm each. A schematic of the fiber placement is shown in Figure 4-1.

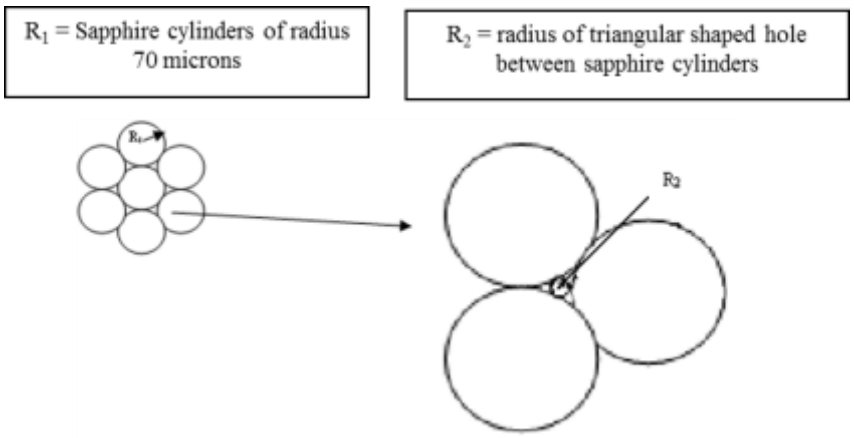

Figure 4-1: Schematic of sapphire fiber structure.

The fibers were grown with the C-axis of the crystal extending along the optical axis of the fiber (along the length of the fiber). Since single crystal sapphire has a hexagonal crystal structure, the two axes perpendicular to the c-axis are equivalent and are referred to as the a-axis. So the cross-section of the fiber shown is taken perpendicular to the c-axis of each of the fibers. Initial analysis of the sapphire photonic crystal fiber indicated that the structure improved the light guiding properties and showed suitability for development as a high temperature gas sensing structure

Fabrication of the first sapphire photonic crystal fiber began with individual single crystal sapphire fibers with an outer diameter of approximately 70 μm. These fibers were cleaved into seven pieces approximately 15 cm each. The fibers were cleaned in a series of steps which included rinsing in alcohol, distilled water, acetone, and diluted phosphoric acid. The fibers were assembled in a pattern that consisted of a central fiber surrounded by six outer fibers, forming a symmetric ring around the central fiber.

The fibers were held in place with platinum wire ties. The platinum wire was wound around the fibers in such a manner as to preserve the ordered arrangement of the fibers and was wound around the fiber at several locations along the entire length of the fibers. An example of this process can be seen in Figure 4-2below. After the process was completed, the fibers were cleaned again. The fiber bundle was then placed on a porous high purity alumina plate (Micromass, from Porvair Advanced Materials) and then inserted into a Deltech furnace. Fibers were heated at 1600°C for 12 hours and then removed from the furnace and allowed to cool to room temperature. Polishing of the fibers was performed with diamond polishing paper of various grits. In order to accomplish this, the fibers were mounted in a polishing fixture and bonded to it with a thermoplastic adhesive.

Figure 4-2: Image of the platinum wire holding the fiber in the correct arrangement

One of the key steps in the design of longer lengths of the 7-rod single crystal sapphire fiber bundle was the fabrication of the fiber bundle itself. The sapphire rods were made by Micromaterials Inc. and grown with the c-axis of the crystal extending along the length of the fiber. Fabrication of the first 50 cm long and 1 meter long sapphire photonic crystal fibers began with individual single crystal sapphire fibers with an outer diameter of approximately 70 μm. As in the 15 cm long structure, the longer length fibers were cleaned in a series of steps which included rinsing in alcohol, distilled water, acetone, and diluted phosphoric acid. The fibers were assembled in a pattern that consisted of a central fiber surrounded by 6 outer fibers, forming a symmetric ring around the central fiber.

The fiber bundle consists of seven fibers arranged in a hexagonal shape with one of the fibers directly in the center of the bundle. This creates an "artificial" cladding that will maintain all of the chemical and physical property characteristics that an individual sapphire fiber would with the added benefit of core protection. The orientation of the fibers in a hexagonal shape was accomplished by threading the seven single crystal sapphire rods inside a fiber funnel with the correct inner diameter. The single crystal sapphire fibers have an outer diameter (OD) of 70 μm so the desired inner diameter of the silica funnel to produce the correct hexagonal arrangement would be three fiber OD's across. This was accomplished by polishing the tapered end of the silica funnel until an uncoated individual silica test fiber with an OD of 210 μm could barely fit through.

Each sapphire fiber was then added to the funnel with the correct inner diameter (ID) so that the only shape it could make was the hexagonal shape with one fiber directly in the center. Next the fibers were adjusted so that they were all the same length at the end face. Then a knot was carefully tied using platinum wire to secure the fiber bundle just outside of the glass funnel to keep the bundle in the correct hexagonal arrangement across the entire length of the entire fiber bundle. A mechanical tweezers arm was used to aid in the fiber tying process. This bundling process can be seen in Figure 4-3 below. The fiber bundle was then pulled approximately 0.5 inches through the funnel and the process was repeated until the entire 50 cm or 1 m of fibers were in the correct arrangement. After bundling, the fibers were cleaned in a series of steps which included rinsing in alcohol, distilled water, and acetone to remove any contaminants from the bundling process.

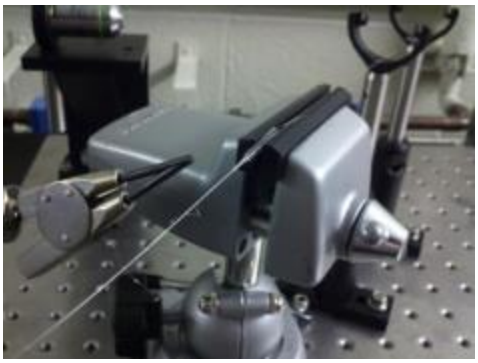

Figure 4-3: Bundling process using the greater than 210 μm ID fiber funnel at the tapered end to form the correct hexagonal structure

Various optical characterization techniques require fibers to be fusion spliced to lead-in or lead-out fibers in order the measure reflections off of certain materials. White light interferometry requires that a lead-in fiber be used in order to have only one reflection point. In order to fabricate a bundled fiber that is fusion spliced to a lead-in fiber, a cautious fabrication had to be used. A 50 cm long, 70 μm diameter single crystal sapphire fiber was first fusion spliced to a 100 μm core, 140 μm cladding graded index multimode silica fiber. This fiber was then placed next to six 45 cm long 70 μm diameter single crystal sapphire fibers and adjusted so that they were all the same length at the sapphire end face. The 50 cm long 70 μm diameter single crystal sapphire fiber that was fusion spliced to the 100 μm core/ 140 μm cladding graded index multimode silica fiber was then adjusted so that when all 7 sapphire rods were pushed through the silica fiber funnel, the fusion spliced fiber would be in the central core location. This was checked by aligning the silica end of the 100 μm core/ 140 μm cladding graded index multimode silica fiber to a 632.8 nm HeNe laser using a 3D stage as seen in Figure 4-4 below.

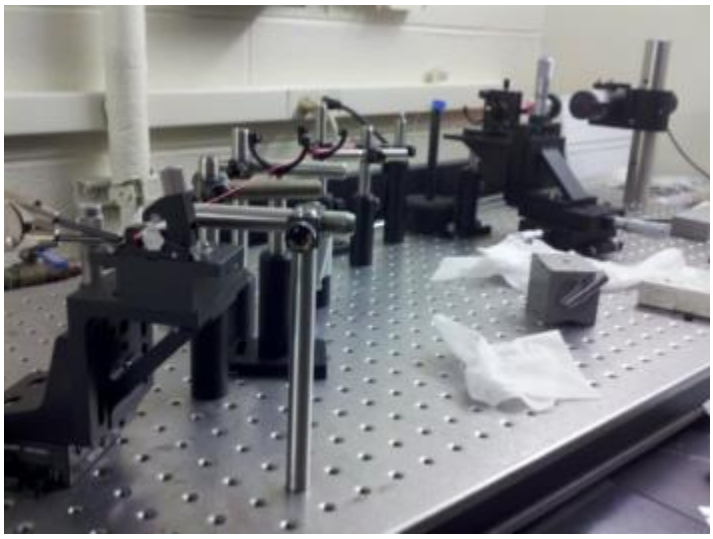

Figure 4-4: HeNe laser connection to determine if the fusion-spliced rod of sapphire is in the central core position of the fiber bundle

An adjustable microscope was then placed at the fiber funnel end of the sapphire fibers while the 632.8 nm HeNe laser was turned on. This confirmed that the fusion-spliced rod was in the correct central core location when illuminated. As in the previous fiber tying stages, a knot was carefully tied using platinum wire to secure the fiber bundle just outside of the glass funnel to keep the bundle in the correct hexagonal arrangement across the entire length of the fiber bundle.

Single crystal sapphire is a very hard material with a Knoop hardness of 2100 and a 9 on the Mohs scale. It is very difficult to polish due to its high mechanical strength. The easiest way to polish single crystal sapphire is through a variety of diamond lapping films starting with coarse grit and working towards fine grit. In all of the above fiber bundle lengths, the fiber bundle must be housed inside an array of protective silica tubes to give stability to the fiber bundle. The array is held together by heating phenyl salicylate wax until it is liquid and then coating the inside of each array tube until the wax solidifies. When the wax solidifies, the fiber bundle will be fixed into place. It is also important to note that the bundle end face must remain as close to perpendicular as possible to get the best results during polishing. This is possible by using a level that is can accurately measure the angle of the fiber polisher. The silica tube array is then mounted in a metal v-shaped groove and is adhered into place using Crystalbond. Once hardened, the Crystalbond maintains the integrity of the entire bundle and the array of tubes. This ensures that the bundles' end face will remain perpendicular to the diamond lapping film.

The rotating plate of the fiber polisher first gets a few drops of water and then the 30 μm grit diamond film is placed on top. Decreasing the polishing grits from 30 μm to 9 μm to 3 μm and then finishing with 0.5 μm grit is the standard procedure to achieve the optimal fiber polish. The fiber bundle is cleaned with methyl alcohol to remove any polishing debris and then checked on an optical microscope before progressing to the next finer grit size to check the bundle's progress. The larger grit sizes generally require more time for optimal polishing compared to the fine diamond grit papers. Figure 4-5 shows a 7-rod sapphire fiber in the early stages of polishing. The wax and Crystalbond is later removed by a series of cleaning steps involving alcohol, distilled water, and acetone to remove any contaminants from the polishing process.

Figure 4-5: Optical micrograph of a single crystal sapphire bundle during an early polishing stage.

4.1.1 Characterization

The polished end-face of one of the fibers produced is shown in Figure 4-6. The sample was mounted in Crystal Bond thermoplastic adhesive for polishing and some of the Crystal Bond can still be seen on the edges of the fibers. The micrograph was taken in reflected light to highlight the structural aspects of the fiber.

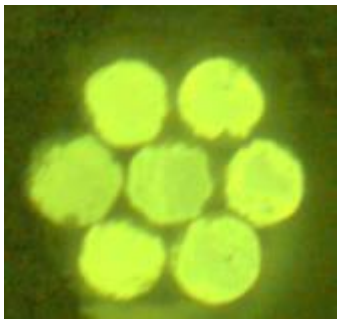

Figure 4-6: Optical micrograph of fiber end-face (reflected light image) with the diameter of the sapphire elements shown as 70 µm

Figure 4-7 shows an optical micrograph of the fiber taken in transmitted light under white light illumination from the transmission of the fiber.

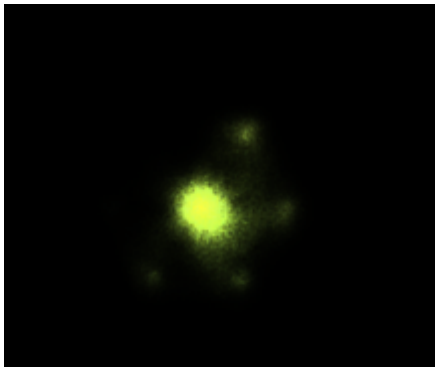

Figure 4-7: Optical micrograph of the photonic crystal sapphire fiber with the diameter of the sapphire elements shown as 70 µm (transmission mode image)

As can be seen in this photo, a significant amount of the light is propagating in the central "core" fiber, which would be consistent with confinement in the core due to the lowering of the average effective refractive index by the holes in the PCF structure. This has been discussed extensively in the literature for silica based PCF's, but we believe this is the first time that this has been demonstrated in a sapphire PCF structure as shown in Pfeiffenberger et. al[4]. The bright region in the center of the micrograph is coincident with the central sapphire cylinder. Very faint light spots can be seen surrounding the central fiber. These correspond to the center positions of the sapphire cylinders surrounding the central "core" sapphire cylinder. The sapphire PCF shown was heated to successively higher temperature up to 1600 °C, demonstrating the extremely high temperature capability of these fibers. Single crystal sapphire in general is known to have excellent high temperature performance and excellent corrosion resistance, both of which were expected to be inherited by the sapphire PCF's.

4.1.2 Initial Sapphire Fiber Bonding Trials

It is desireable to modify the sapphire bundles through a bonding process that joins all of the sapphire bundles together in a way that will be able to allow for the removal of the expensive platinum ties in the fabrication process and one that will operate at high temperature. A variety of high-temperature pastes and mortars used in sensor applications have been unable to perform as desired in this application. As a result, a new sinter-based bonding method is being developed using colloidal alumina. Due largely to the extremely small size of the alumina nanoparticles, sintering can occur at slightly lower temperatures than seen in bulk alumina. Successful bonding was achieved previously using dry and colloidal silica and silicon carbide; alumina would provide the ideal bonding material, as optical, physical, and chemical properties of the sapphire components would remain largely unaffected.

Colloidal alumina has successfully created a firm bond between sapphire plates through sintering. Trials were conducted to confirm the efficacy of colloidal alumina in sinter-bonding sapphire optical fibers. A three-fiber bundle of 70μm-diameter sapphire optical fibers was created, using platinum wire to hold the bundle firmly in place through sintering.

One drop of colloidal alumina was placed on one end of the bundle, and a drop of a slightly more concentrated (~20% reduction in water by weight) colloidal alumina was placed on the other end. The fiber bundle was placed on a sapphire plate and inserted into an alumina tube furnace. The sample was heated to 1600 °C at a ramp rate of 1.5 °C/min. After a 24-hour dwell time, the temperature was ramped back down to room temperature at the same rate.

After sintering, the bundle was removed from the furnace and observed. The three fibers comprising the bundle were tightly bonded and portions of the fiber would fracture before breaking of the bond occurred. Optical micrographs were obtained; Figure 4-8 below verifies the presence of sintered alumina on the fiber bundle.

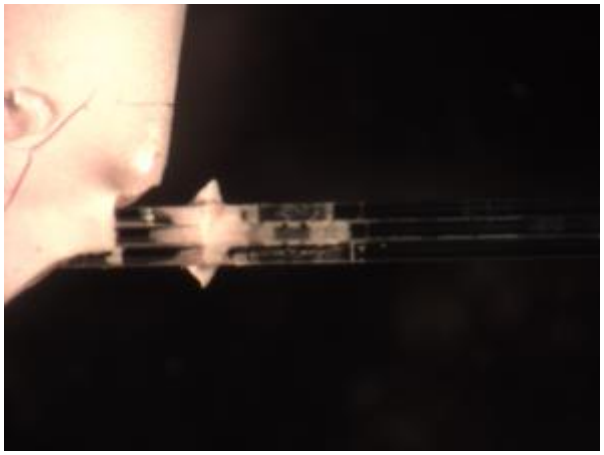

Figure 4-8: Excess Sintered Alumina Visible Around Fiber Bundle

The colloidal alumina successfully bonded the sapphire fibers after sintering. However, there is a significant amount of excess alumina present on the exterior of the fibers, which could interfere with designed optical properties. Ideally, the bonding layer thickness would approach that of a monolayer, and the crystal structure would be oriented in the same direction as the single-crystal sapphire instead of forming polycrystalline alumina. The presence of polycrystalline alumina as a bonding agent as opposed to mortar substances containing silica,

chromia, and other metal oxides is still preferred, as diffusion of the reduced metals at elevated temperatures can rapidly affect the physical and optical properties of the sensor components. Therefore, a thin, single-crystal alumina layer would produce the ideal bond.

4.1.3 Bond Selection Sapphire Bonding Trials

Commercially available colloidal dispersions of silica and alumina were obtained, and a silicon carbide dispersion was created through sonication of dry silicon carbide powder and water. While silica and silicon carbide can cause bonding at relatively low temperatures, high-temperature sintering of alumina may promote diffusion-controlled recrystallization, ideally growing a single grain in the crystal direction of the sapphire plates or fibers, essentially rendering a single crystal bond. Thus, similar experiments were carried out at high temperatures in hopes of inducing the desired effects.

In addition to testing the effect of higher sinter temperature, the percent solids of the colloidal alumina was increased to provide a higher concentration of alumina particles on the bonding surfaces. The as-received colloidal alumina solution contains a reported 10wt% alumina; water was evaporated from the solution on a hotplate at 110^{o}C until the solids content increased to around 15-16wt% alumina; the increase in viscosity was notable. Additionally, it was supposed that diluting the colloidal alumina with a low surface tension solvent could increase surface coverage upon evaporation while decreasing particle bulk, so varying dilutions with ethanol were also tested, with bonding of a sapphire three-fiber bundle tested on some compositions as well.

Small sapphire plates (~1cm x 1cm) were cut and cleaned in an ethanol sonication bath. These plates were subsequently placed on a sapphire sample holder, and one drop of each solution reported in Table 4-1 below was sandwiched between the plates. Three sapphire optical fibers were bundled with platinum wire before addition of colloidal solutions in a similar manner. Subsequently, these samples were sintered at the noted temperature with a ramp rate of 1.5^{o}C/min and a 24 hour dwell time.

Table 4-1: Compilation of Experimental Compositions

Composition	Percent Solids (by weight) in Water$_a$ or Water+Ethanol$_b$	Sinter/Bond Temperature (^{o}C)	Test Substrate Geometry (Sapphire)
Silicon Carbide	10$_a$	1600	Plate
Silica	20$_a$	1600	Plate
Alumina	10$_a$	1600	Plate/3-fiber bundle
Alumina	5$_b$	1600	Plate/3-fiber bundle
Alumina	4$_b$	1600	Plate
Alumina	2.5$_b$	1600	Plate
Alumina	1$_b$	1600	Plate
Alumina	10$_a$	1600 and 1800	Plate
Alumina	15-16$_a$	1600 and 1800	Plate

Sapphire plates were well bonded by solutions of silicon carbide as seen in Figure 4-9 and colloidal silica shown in Figure 4-10 and fired at 1600^{o}C. Interesting microstructures can be seen at higher magnifications (right). The silicon carbide formed a relatively tight grain size distribution at the reported temperature and dwell time. Surprisingly, the colloidal silica appears

to have melted and solidified into an amorphous bonding layer. Both materials formed a strong, durable bond by hand.

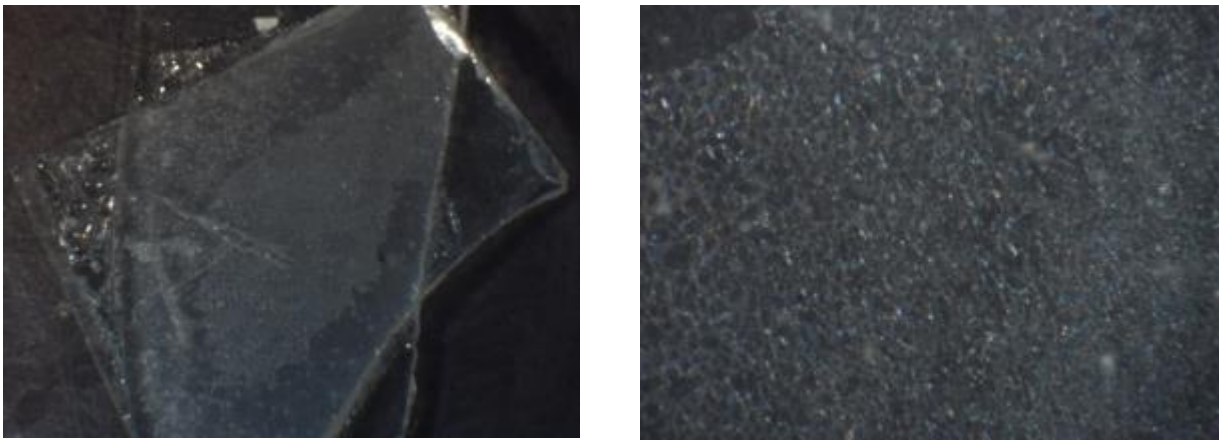

Figure 4-9: Sapphire Plates Firmly Bonded by Silicon Carbide Solution

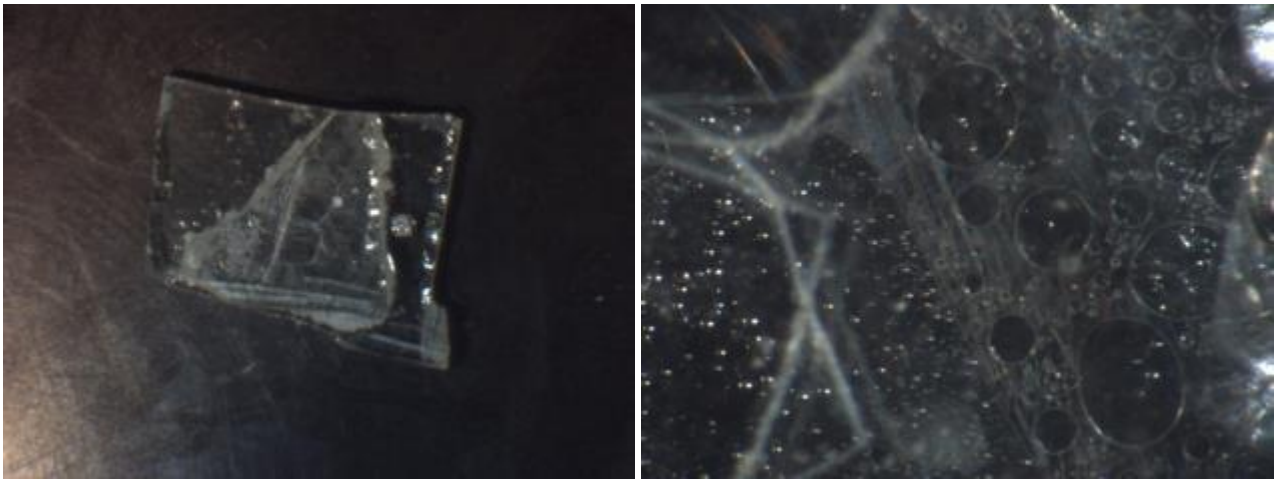

Figure 4-10: Sapphire Plates Firmly Bonded by Colloidal Silica

Colloidal alumina solutions at as-received or slightly diluted concentrations formed relatively weak bonds as shown in Figure 4-11, though more effort was required to separate plates bonded using the as-received solution. Plate coverage clearly became minimal as alumina concentration decreased, as the alumina particles appeared to aggregate rather than smoothly disperse upon drying.

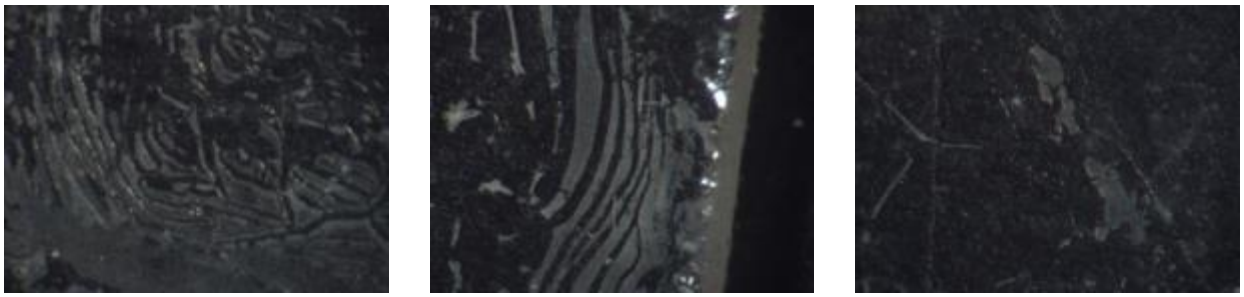

Figure 4-11: Colloidal Alumina Coverage Becomes Scarce at More Dilute Concentrations (Concentration Decreases Left to Right)

Bonding of a sapphire 3-fiber bundle was achieved using the as-received (10wt% alumina) and one of the diluted colloidal alumina dispersions (5wt% alumina), as seen in Figure 4-12. The leftmost column images the as-received 10wt% alumina colloid bond. The top left image illustrates the surface coverage of the alumina particles on the 3-fiber bundle. The bottom left image demonstrates the strength of the bond; upon flexing the individual fibers away from each other near the bond location, the sapphire fibers themselves fractured before the bond was severed (notice that the three fibers are still bonded at the lower left of the image, with fractured fibers laying nearby, originating from the other side of the bond). While the diluted colloidal alumina enabled bonding (top right), upon flexing this bond was severed (bottom right).

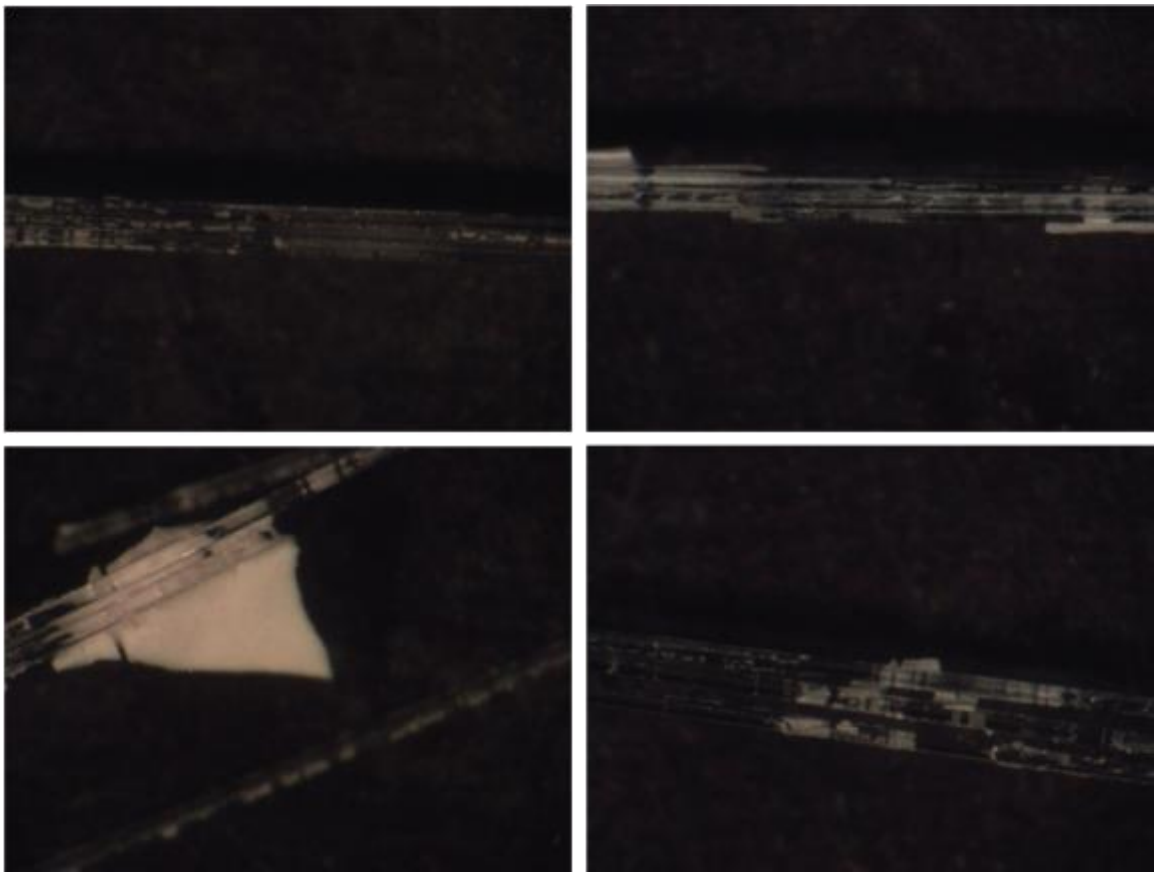

Figure 4-12: 10wt% Colloidal Alumina (Left Column) Forms Strong Bond, While 5wt% Colloidal Alumina (Right Column) Forms Weaker Bond

Subsequent to the above experiments, as-received and concentrated colloidal alumina dispersions were placed between sapphire plates and fired at a higher temperature of 1800^{o}C to promote recrystallization and growth and perhaps achieve stronger bonding or even single-grain growth.

Surprisingly, the colloidal alumina solution did not form a bond, though previous experiments using the same solution on both sapphire plates and sapphire fibers at 1600^{o}C formed strong bonds. The increased-concentration solution did seem to provide more complete coverage of the bonding surfaces, however, as seen in Figure 4-13 below.

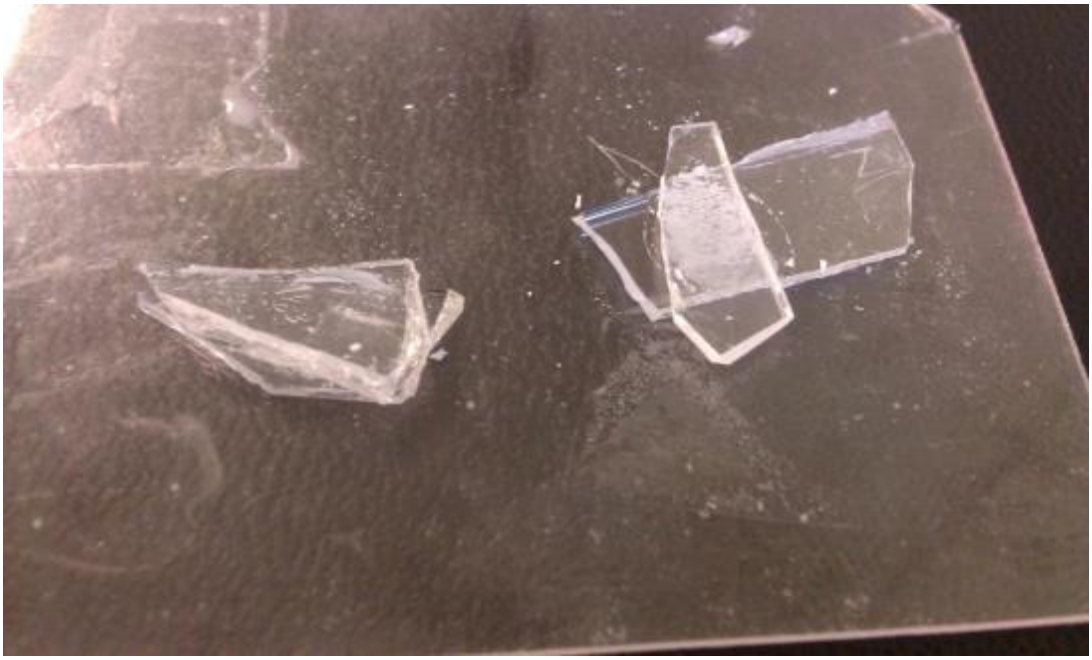

Figure 4-13: Increased Solids% Alumina Solution (right) Increases Coverage of Bonding Surfaces

Since bonding was repeatedly achieved in previous experiments at 1600^{o}C, the experiment was repeated using the as-received and increased solids% solutions at 1600^{o}C, but again, bonding was not observed. After verification that the furnace was indeed reaching and maintaining the target temperature, it was determined that the only variable between this experiment and its predecessors was the alumina tube housing the samples within the furnace; the alumina tube was replaced immediately before the higher-temperature experiment, and though the previous tube appeared to be "clean", several materials had been present within the tube at various points of its lifetime, including chromium, chromia, and magnesia, which are seen to contribute to rapid recrystallization and growth of polycrystalline alumina; apparently the slight amounts of incidental contamination present in the previous tube were enough to contribute significantly to the sintering and bonding behavior of the colloidal alumina. A more concise compilation of the experimental results is found below in Table 4-2.

Table 4-2: Compilation of Experimental Results

Composition	Percent Solids (by weight) in Water$_a$ or Water+Ethanol$_b$	Sinter/Bond Temperature (^{o}C)	Test Substrate Geometry (Sapphire)	Bond Behavior
Silicon Carbide	10_a	1600	Plate	Strong
Silica	20_a	1600	Plate	Strong
Alumina	10_a	1600	Plate/3-fiber bundle	Moderate/Strong
Alumina	5_b	1600	Plate/3-fiber bundle	Weak/Weak
Alumina	4_b	1600	Plate	Weak
Alumina	2.5_b	1600	Plate	Weak
Alumina	1_b	1600	Plate	None
Alumina$_c$	10_a	1600 and 1800	Plate	None
Alumina$_c$	$15\text{-}16_a$	1600 and 1800	Plate	None

$_c$ Firing conducted in brand new alumina tube

4.1.4 Verification of Colloidal Bonding Trials

A 10wt% silicon carbide solution in water was created, using sonication to ensure dispersion. A solution of colloidal silica (Snowtex-40, Nissan Chemical) was also tested. Three sapphire optical fibers were bundled and secured using platinum wire before the bundle was placed on sapphire plates along with one drop of SiC solution on one end and one drop of colloidal silica solution on the other. The samples were then placed in a furnace reaching 1600^{o}C with a 24 hour dwell time and ramp rate of 1.5^{o}C/min.

In an effort to determine the factors contributing to successful sapphire bonding using colloidal alumina, small sapphire plates (~1cm x 1cm) were cut and cleaned in an ethanol sonication bath. One drop of colloidal alumina (Aluminasol-100, Nissan Chemical) was sandwiched between the plates and the samples placed on a shard of polycrystalline alumina with minute amounts of chromium present to replicate the previous conditions. These samples were then heated to 1600^{o}C with a ramp rate of 1.5 ^{o}C/min and a 24 hour dwell time. Other samples were created with identical preparation, but fired separately with chromium absent as detailed in Table 4-3.

Table 4-3: Compilation of Experimental Compositions

Composition	Percent Solids (by weight) in Water	Sinter/Bond Temperature (^{o}C)	Test Substrate Geometry (Sapphire)
Silicon Carbide	10	1600	3-fiber bundle
Silica	20	1600	3-fiber bundle
Alumina	10	1600	Plate
Alumina in presence of chromium	10	1600	Plate

Sapphire fibers were well-bonded by solutions of both silicon carbide as seen in Figure 4-14 and colloidal silica as seen in Figure 4-15. The silicon carbide solution provided a strong bond without a large amount of excess material present after firing. The colloidal silica also bonded the bundle firmly, but a substantial amount of excess silica was present around the bonding site. Perhaps further dilution of the colloid would prevent this agglomeration. Sapphire

plates with colloidal alumina fired in the presence of chromium formed a secure bond, while similar samples with chromium absent did not. Images of the interface between the plates that were fired in the presence of chromium as shown in Figure 4-16 and those fired in the absence of chromium as shown in Figure 4-17 demonstrate different morphologies.

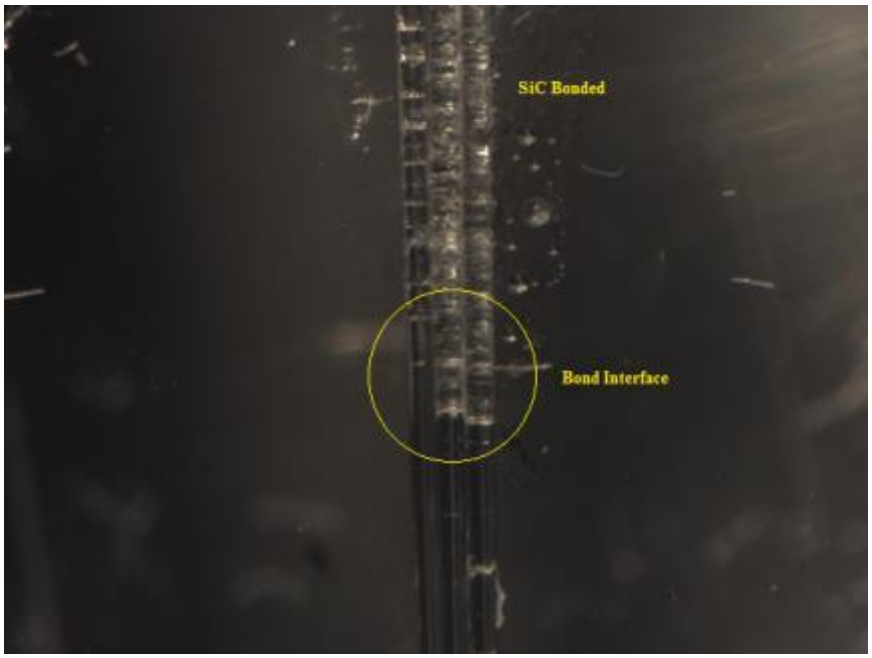

Figure 4-14: Three-fiber bundle is well-bonded by SiC solution

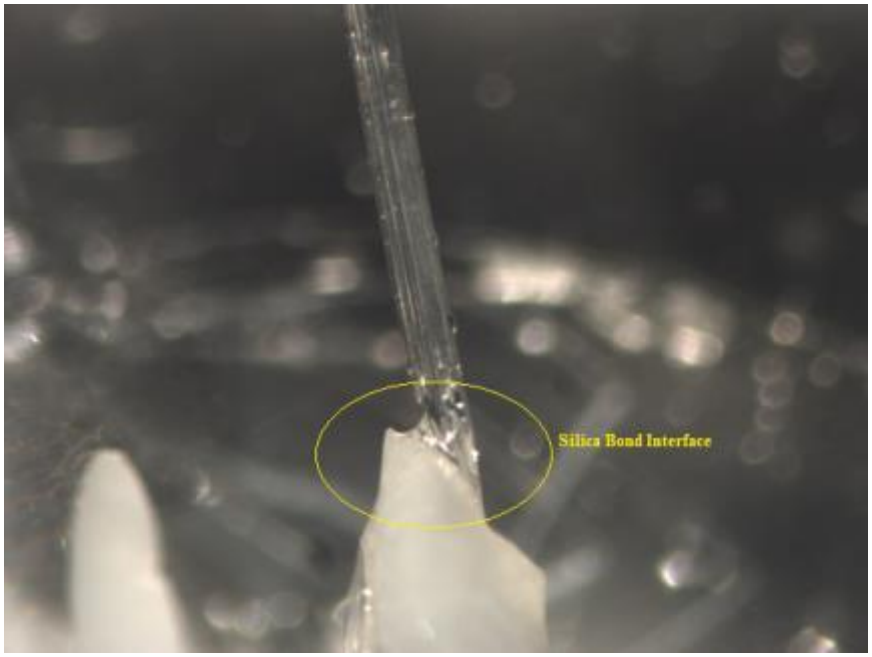

Figure 4-15: Three-bundle sapphire fiber bonded using colloidal silica solution

.

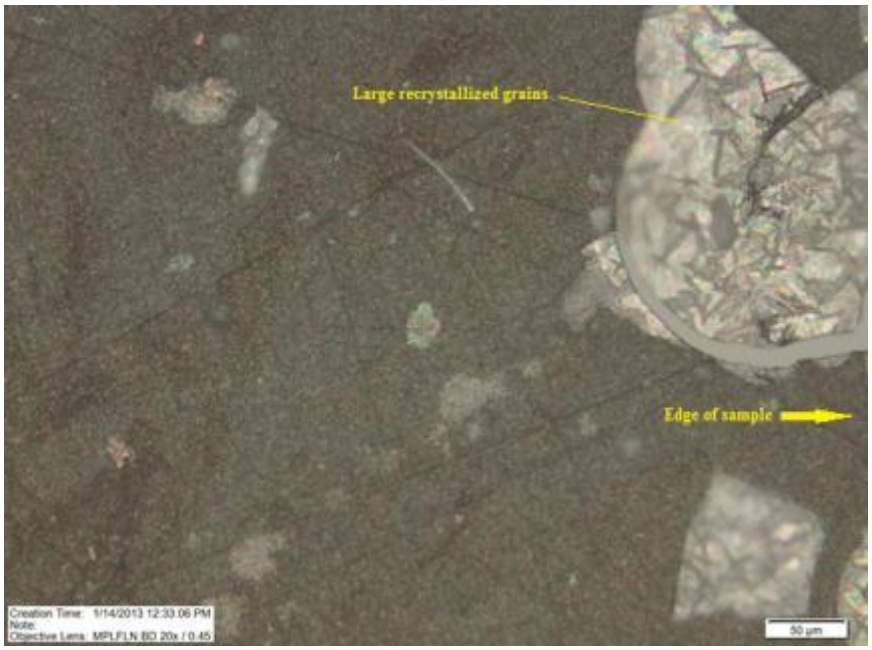

Figure 4-16: Bond interface of colloidal alumina fired in the presence of chromium suggests some recrystallization occurs

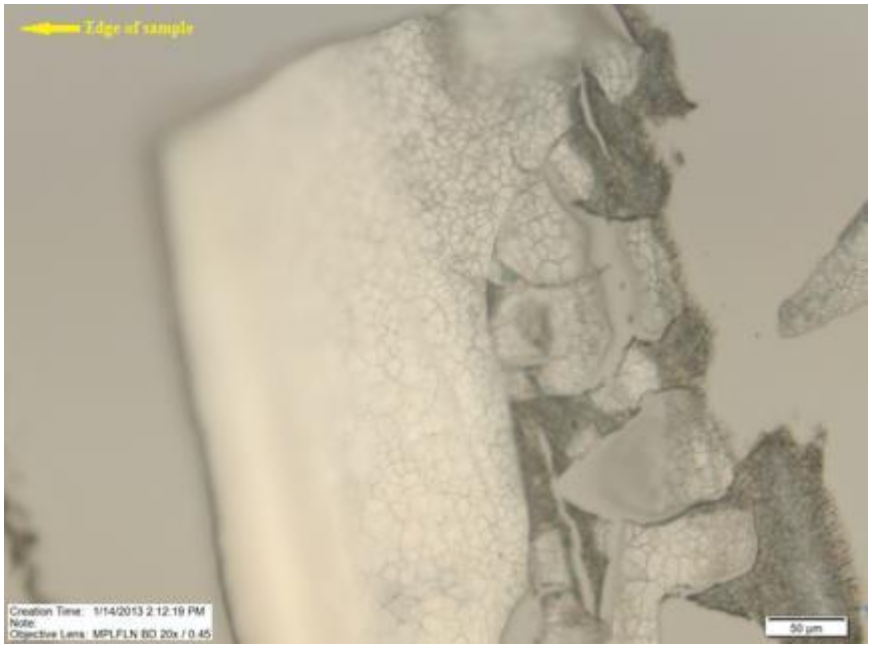

Figure 4-17: Plate interface without chromium (unbonded) does not show recrystallization of the same phase

Interestingly, the samples fired in the presence of chromium had much greater coverage of colloidal alumina at the plate interface than samples fired with chromium absent. While both demonstrated grain growth towards the edges of the sample, those fired in the presence of chromium contained grains that appear to be composed of a different phase; it is reported that

chromium promotes the growth of α-alumina (sapphire) phase as opposed to other alumina polymorphs. Perhaps these recrystallized grains of a different phase are critical to successful bonding; converting all of the colloidal alumina present at the interface into this phase may yield even stronger bonds. Table 4-4 contains a summary of the reported results.

Table 4-4: Compilation of Experimental Results

Composition	Percent Solids (by weight) in Water	Sinter/Bond Temperature (°C)	Test Substrate Geometry (Sapphire)	Bond Behavior
Silicon Carbide	10	1600	3-fiber bundle	Strong
Silica	20	1600	3-fiber bundle	Strong
Alumina	10	1600	Plate	None
Alumina in presence of chromium	10	1600	Plate	Moderate

4.1.5 Chromium Effects on Colloidal Alumina Bonding

Efforts were sought to develop a suitable sapphire bonding agent for optical applications, as commercially available options are limited both in variety and efficacy. To evaluate the effect of chromium on polycrystalline alumina bonding of sapphire, varying concentrations of water-soluble chromium(VI) oxide (Aldrich) were mixed into colloidal alumina (Aluminasol-100, Nissan Chemical) through magnetic stirring. Upon full mixing, one droplet of each solution was placed between two sapphire plates measuring around 1.5cm x 1.5cm. These samples were then elevated to 1600°C at a 1.5°C/min ramp rate with a dwell time of 24 hours. It was discovered that the varying chromium oxide concentration had a large effect on bond strength and crystal morphology, as elaborated below in the following figures and tables.

Table 4-5: Chromium oxide concentration in colloidal alumina causes variation in bond strength and grain morphology

Chromium Oxide Concentration	**Bond Strength**	**Notable Morphology Characteristics**
1ppm	None	Almost entirely polycrystalline, particulate
10ppm	Weak	Polycrystalline/single phase grain mixture
50ppm	Moderate	Similar to 10ppm structure, but more even distribution of morphology characteristics
100ppm	Weak	Majority of grains appear to be of one phase, grains are largest

As identified in Table 4-5, sapphire plates fired with colloidal alumina and 1ppm chromium oxide did not bond, similar to plates fired with colloidal alumina alone. A significant but relatively weak bond was achieved when the chromium oxide concentration reached 10ppm, and the bond was strong once the concentration reached 50ppm. The bond strength diminished when the concentration increased to 100ppm; it could be that a threshold for effective bonding was reached, though definitive statements will be reserved for the next reporting period, when a greater number of samples can be produced and studied.

The plates were separated by force and then studied under optical microscopy to evaluate the grain structure and crystallinity. As with the bond strength, chromium oxide concentration had a large effect on the physical characteristics of the polycrystalline alumina bonding solution.

These differences were obvious at all optical magnifications, as seen in Figure 4-18, Figure 4-19, and Figure 4-20 .

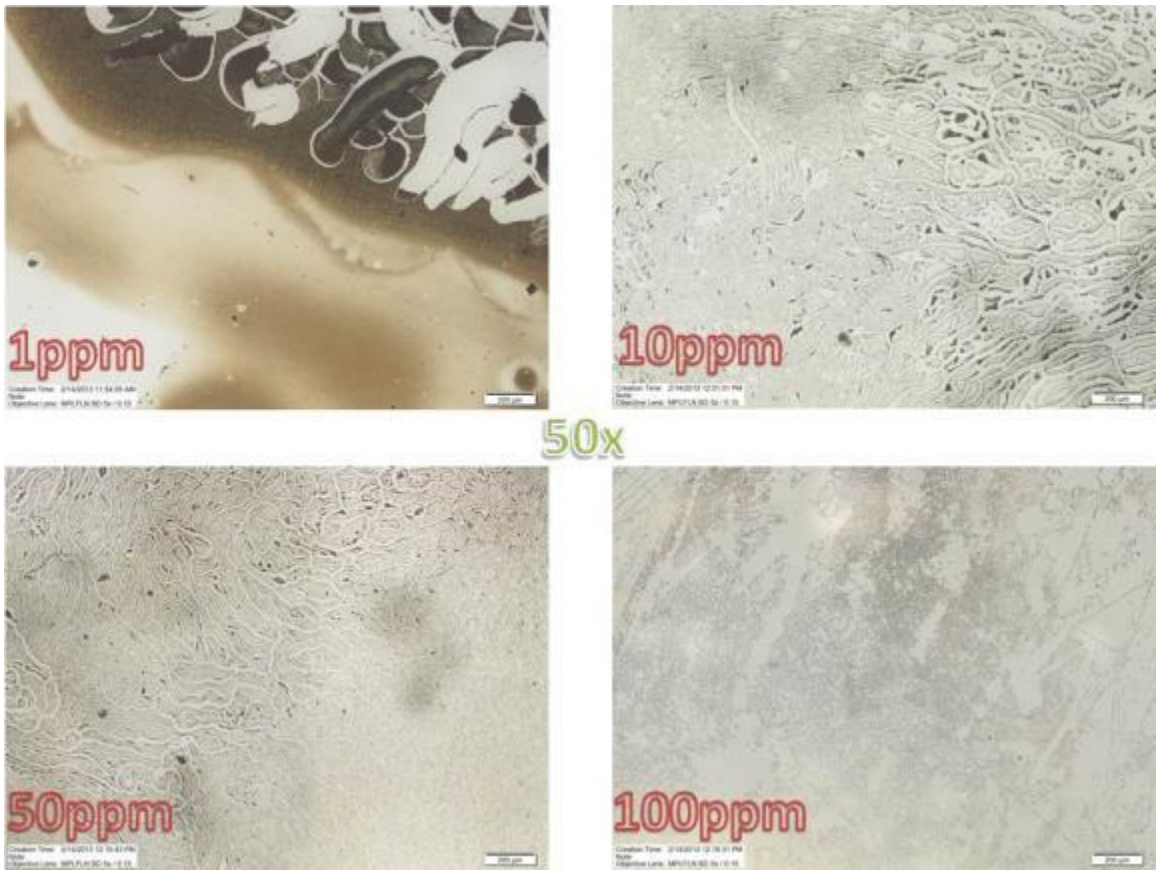

Figure 4-18: Morphology differences are obvious at 50x optical magnification (scale bar is 200µm)

At 50x magnification (Figure 4-18), the unbounded surface of the 1ppm chromium oxide solution is much different in appearance than the remaining concentrations, which did form bonds of varying strength. While the colloidal alumina particles appear to have agglomerated into grain-like structures, these structures are clearly composed of polycrystalline particles, whereas different phases seem to be present in other concentrations. Upon deeper exploration at higher magnification (Figure 4-19, Figure 4-20), these morphology differences are better understood.

Higher magnifications confirm that the colloidal alumina particles with only 1ppm chromium oxide remain distinct, though some sintering behavior may be occurring. In the 10ppm and 50ppm chromium oxide concentrations, small grains appear to be forming among the agglomerations, though the grains are of varied phases. At 100ppm chromium oxide, large grains of one apparent orientation are prevalent (these grains appear optically transparent, but the outlines are distinguishable).

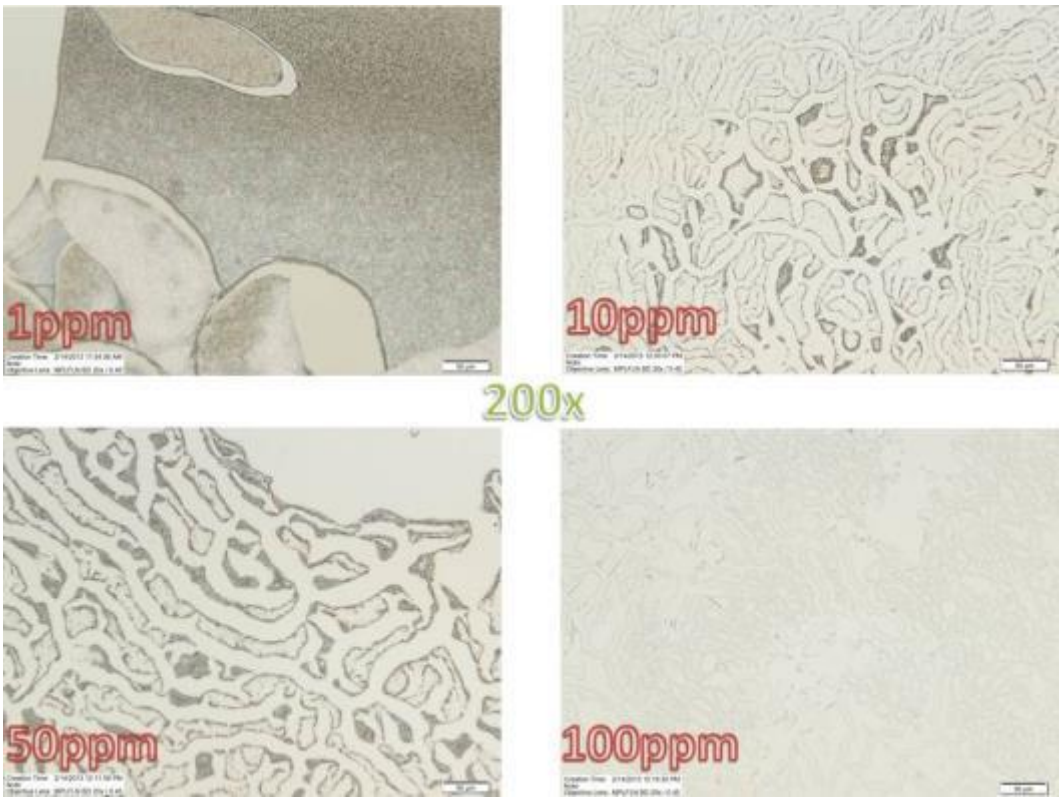

Figure 4-19: Microstructural differences are distinguishable at 200x magnification (scale bar is 50µm)

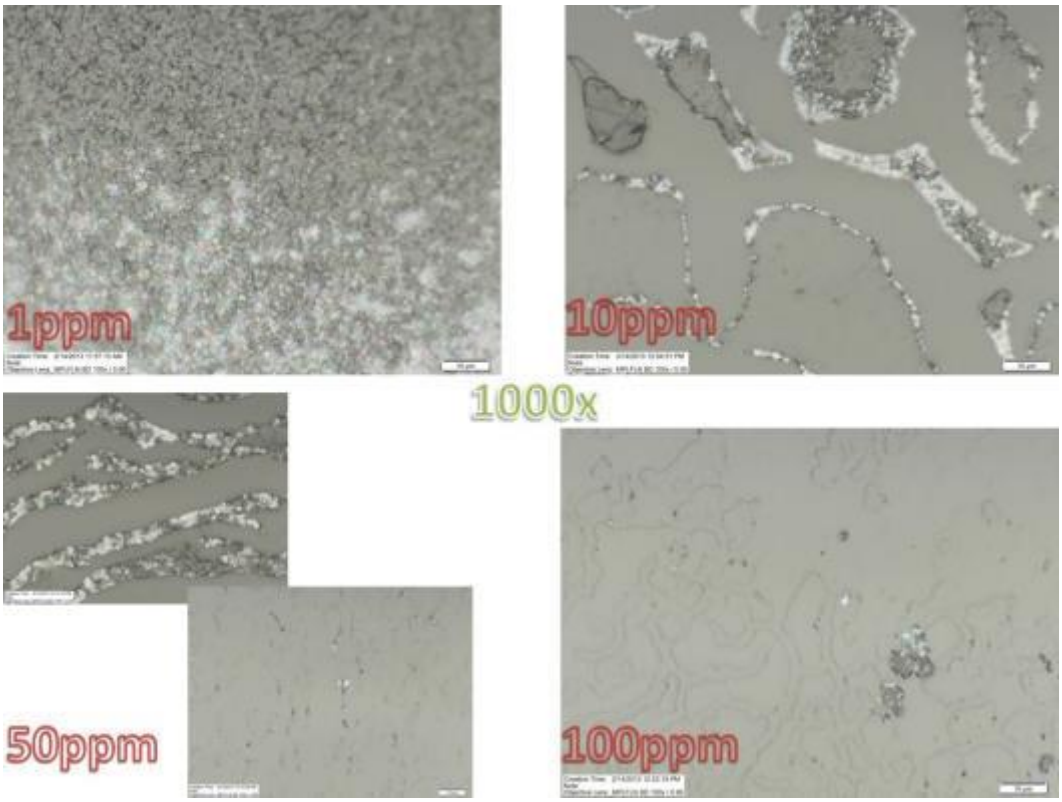

Figure 4-20: Grain and phase structures are discernible at 1000x magnification (scale bar is 10µm)

4.1.6 Bonding of 7-rod Sapphire Fiber Bundles

With the feasibility of bonding sapphire fibers using silica, alumina, and silicon carbide dispersions established adaptation to bonding of the fiber bundles was undertaken. Sapphire fiber bundles containing the 7-rod geometry have the potential to increase gas sensing capability; several 7-rod sapphire fiber bundles measuring 9cm in length were tied using platinum wire before being coated at 1cm intervals with 20wt% colloidal silica (Snowtex-20L, Nissan Chemical) or 10wt% silicon carbide in water (bonding with colloidal alumina will follow pending complete evaluation of ideal chromium oxide concentration). These fiber bundles were then heated to 1600°C with a 24 hour dwell time and ramp rate of 1.5°C/min.

Strong bonds appear to have been made using both silica and silicon carbide solutions, as verified by severing the platinum wire ties and verifying the bond integrity and through optical microscopy (Figure 4-21).

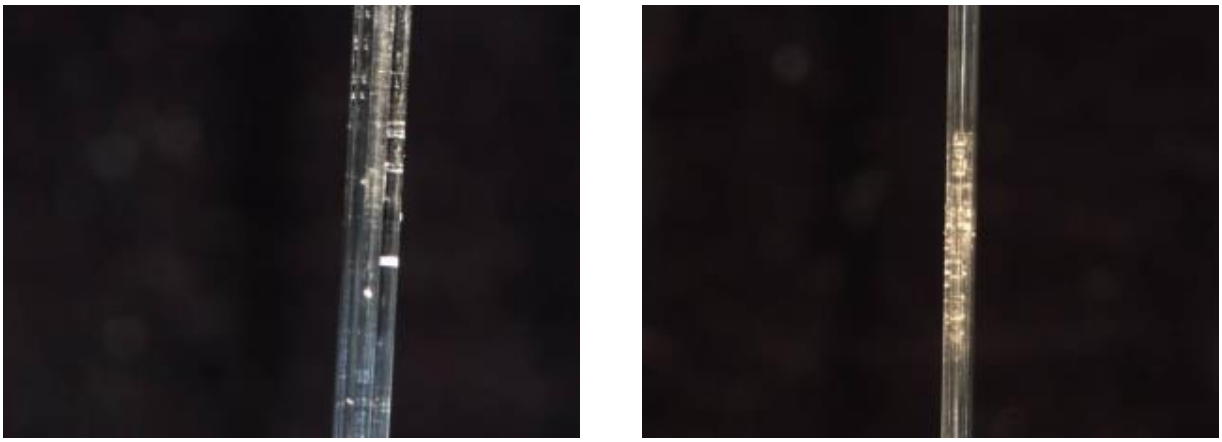

Figure 4-21: Areas of bonded silicon carbide (left) and silica (right) adjacent to bare sapphire fiber

The optical microscopy images verify the presence of the bonding agents as well as the preserved 7-rod geometry (the top three fibers in the 7-fiber bundle are visible).

Optical quality and gas sensing capability of the fabricated 7-rod structures will be evaluated in the near future. In preparation, the fiber bundles were cleaned, cleaved, and mounted to a polishing holder inside a small glass tube using phenyl salicylate (Figure 4-22). The bundled end was then slowly polished using 5μm diamond film, then 0.5μm diamond film until the end face was optically smooth (Figure 4-23). Afterwards, the other end of the bundle is polished using the same method to create smooth, parallel faces.

Figure 4-22: 7-rod bundle in fiber polishing holder

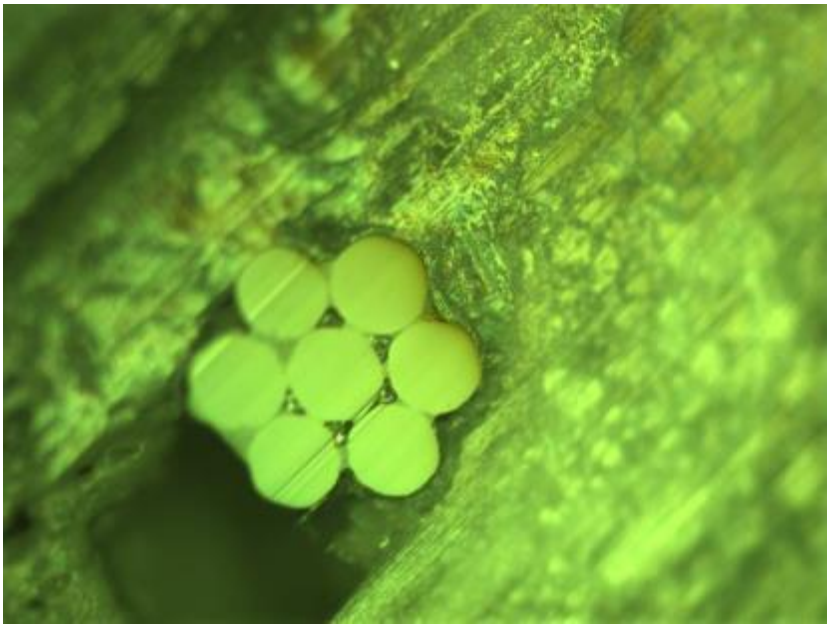

Figure 4-23: 7-rod bundle near finish of polishing process

4.1.7 SEM Analysis of Bonded Sapphire

SEM and EDS work verified the presence of bonding material between fibers within the bundle as well as demonstrating a tight interface, lending credence to the ability of these materials to bond sapphire fibers. At right in Figure 4-24, areas with strong aluminum signatures (corresponding to the alumina composition of the sapphire fibers) appear in red, while areas with

strong silicon signatures (corresponding to the silica content of the bonding agent) appear in blue. The elemental analysis confirms strong infiltration of the colloidal SiO_2 between interior and exterior fibers.

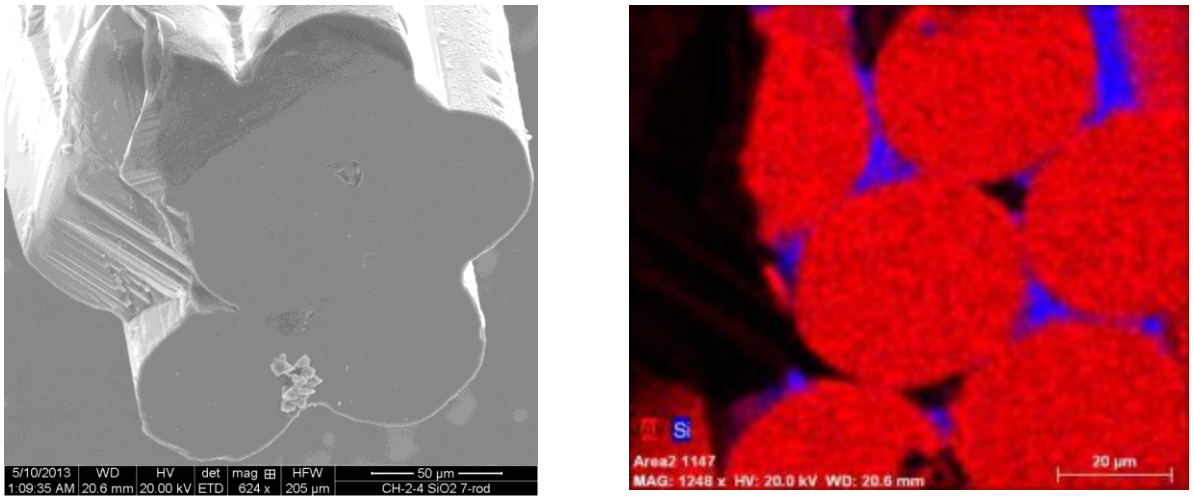

Figure 4-24: EDS mapping suggests ample infiltration of SiO_2

The infiltration of SiC within the bundle is less obvious. As seen in Figure 4-25, spots containing higher concentrations of silicon (in blue) are present throughout the sample, but whether or not bonding has occurred is difficult to determine.

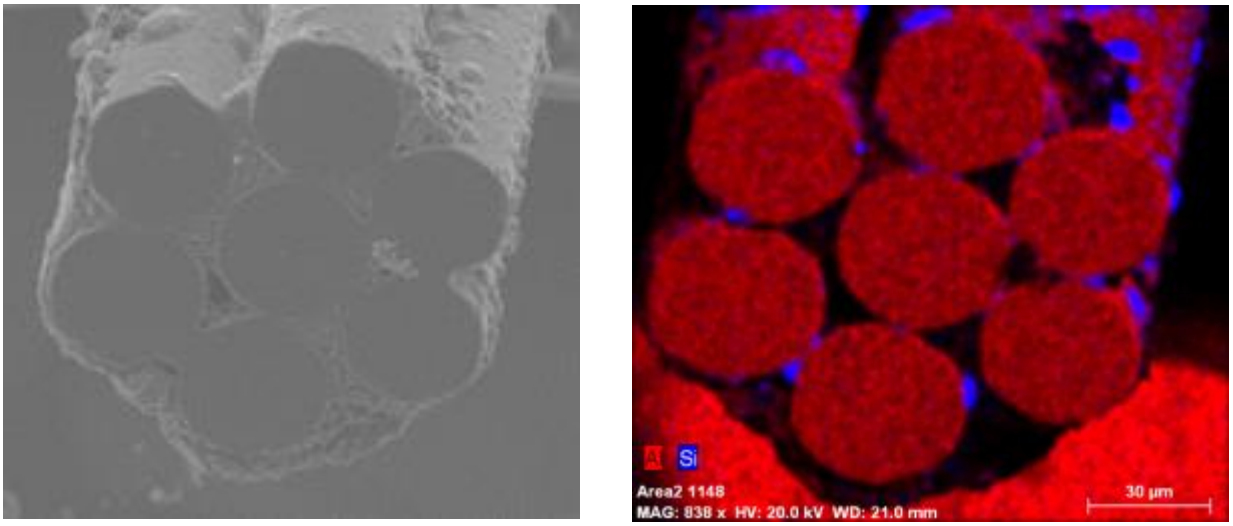

Figure 4-25: EDS mapping shows concentrated areas of SiC presence

Figure 4-26, which contains an overlay of the mapping data with the secondary electron image, provides a clearer picture of the bundle end-face. It remains a challenge to definitively determine whether areas of bonding are present, but areas where bonding seems likely are indicated.

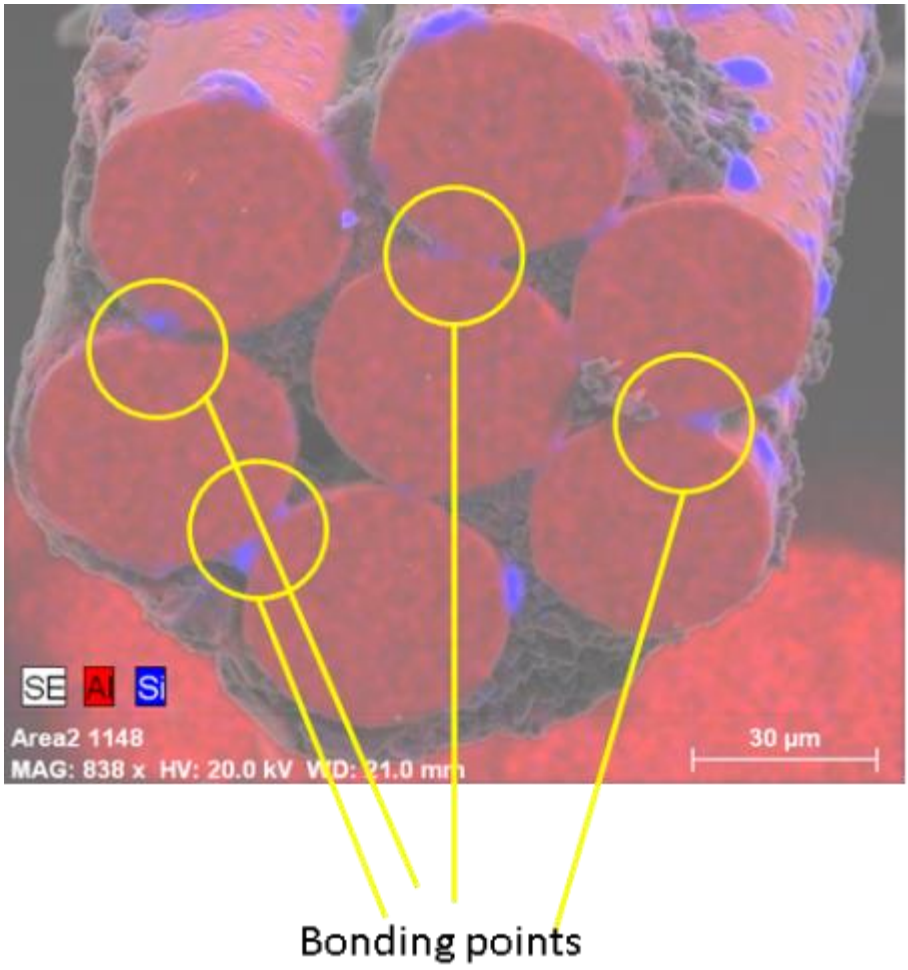

Figure 4-26: Potential bond sites are indicated

4.1.8 Polishing of Bonded 7-Rod Bundles

Bundles were polished until the surfaces were optically smooth with the allowance of minor defects. The SiC and SiO_2-bonded bundles remained well bonded throughout the polishing process, but after polishing the fibers within the $Cr+Al_2O_3$-bonded bundle began to separate. As previously mentioned, it is believed that higher temperature/time in the fabrication process will increase the bond efficacy of this method; verification of this hypothesis will be found in a subsequent report. One of the SiC-bonded bundle ends is seen in Figure 4-27 below, and areas of SiC infiltration and probable bonding are visible. A SiO_2-polished end is visible in Figure 4-28, along with areas of probable SiO_2 bonding.

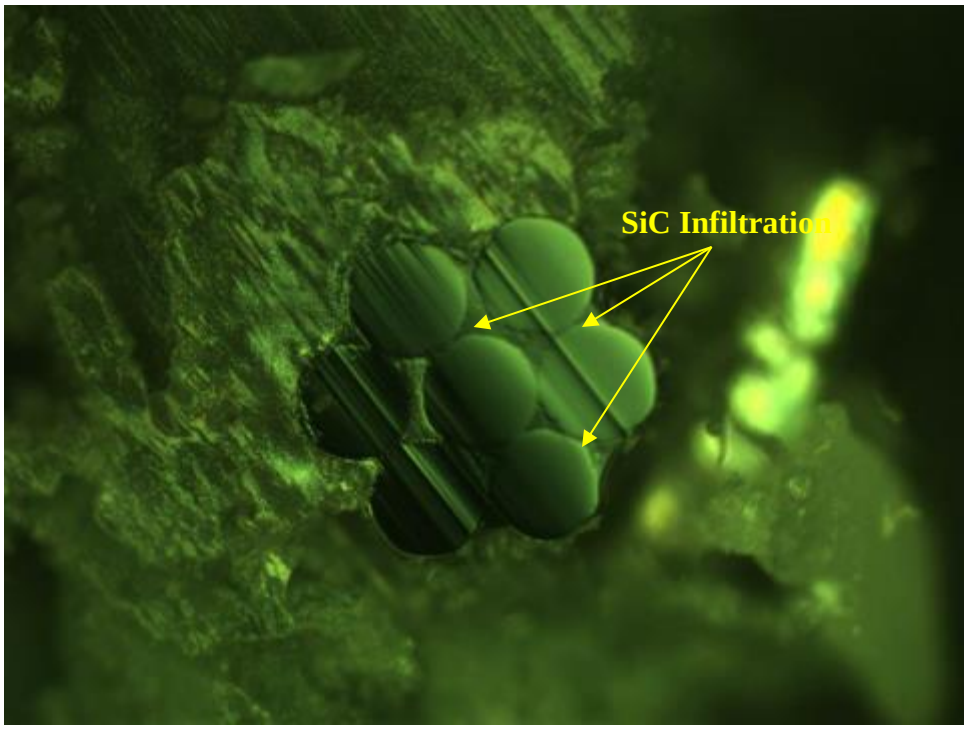

Figure 4-27 : Polished end of SiC-bonded sapphire bundle

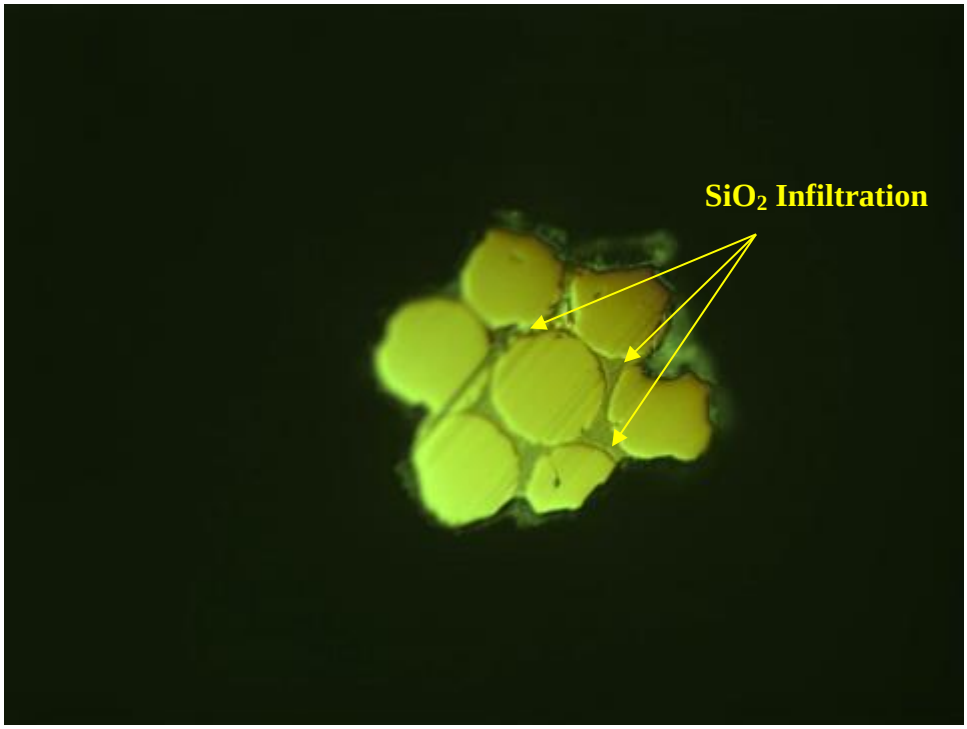

Figure 4-28: Polished end of SiO_2-bonded sapphire bundle

4.1.9 Summary of Bonding Techniques

The advantages and disadvantages of each bonding technique have been compiled and analyzed through iterative experimentation. This information has been compiled in Table 4-6. Many successful tests bonding sapphire plates and fibers have been conducted using colloidal silica. Thorough infiltration of the bonding agent is observed both around and between bundled fibers. Bonding of plates and fibers has been observed to be strong. Silicon carbide provides "spotty" coverage of the fibers and plates. The SiC agglomerates into distinct patches upon heating, which may be advantageous when thorough infiltration is not desired. Bonding of plates is very strong, and bonding of fibers has been observed.

Table 4-6: Compilation of Properties of Viable Sapphire Bonding Techniques

Bonding Material	Advantages	Disadvantages
Colloidal SiO_2	Thorough coating and infiltration of bond agent	Potential for scattering of not applied precisely
	Strong apparent bond	Diffusion could eventually change optical properties
	Easy application, non-toxic	
	Many successful test iterations	
SiC powder	"Spotty" coverage could be advantageous	As with SiO_2, potential for contamination and diffusion
	Strong bonding observed	"Spotty" coverage can be hard to control
	Easy application	Fiber bond efficacy inconclusive
	Strongly bonds plates	
Colloidal Al_2O_3+Cr	Less introduction of reactive elements	Potential for Cr diffusion in other areas of sensor
	Formation of sapphire is theoretically possible	(would not detrimentally affect sensing ability
	Optical properties of sensor should be preserved	but could cause inaccuracy if not properly calibrated)
	Strong fiber bonding observed	Bond efficacy has been difficult to quantify
		Requires precise mixing of chromium oxide compound
		Chromium oxide compound is toxic, though little
		danger is presented at working concentrations

Bonding using colloidal alumina is thought to be ideal, as no foreign element is introduced to the system. This type of bonding has been achieved at high temperatures and pressures, but the fragility of sensor components does not allow for use of high pressures. Small amounts of chromium (on a ppm scale) have been observed to encourage α-alumina growth within the bonding material, which could theoretically produce an extremely strong bond over time. Testing has shown that strong bonding of both plates and fibers is possible although often inconsistent; the conditions required for producing strong bonding are very sensitive. Each of these techniques can find use for various applications in component assembly.

4.1.10 Bond Mechanism Studies

Previous experiments established that bonding of plates and fibers was possible using water-soluble chromium (VI) oxide as a source of chromium dispersed in colloidal alumina with a CrO_3 concentration in the range of 1-100ppm by weight relative to the alumina content. However, the ideal ratio must be determined, as too much CrO_3 will add unnecessary contaminants to the system, potentially increasing the risk of diffusion and therefore altering of sensor properties at service temperatures.

Based on previous successful testing, chromium (VI) oxide was added to 20wt% colloidal alumina (Aluminasol-100, Nissan Chemical) at concentrations by weight relative to alumina content of 5ppm, 50ppm, and 100ppm. The solution was stirred for 2 hours at room temperature to ensure even mixing, and $1cm^2$x1mm sapphire plates were cut and cleaned in an ethanol sonication bath for 15 minutes. One drop of each solution was placed on a sapphire plate and then another plate was placed on top. These samples were placed in a furnace and elevated to 1650°C with a 72-hour dwell and a ramp rate of 1.5°C/min.

Upon extraction of the samples, only light bonding was achieved, and sapphire plates were easily separated. However, the lack of bonding was attributed to the relatively high amount of bonding solution used, resulting in a thick layer of powder; at the time frame utilized for bonding, diffusion could not possibly occur quickly enough through the thickness of the powder layer to successfully bond both plates across the media layer. Therefore, another experiment is currently underway, using the same solutions but applied as a much more "thinned-out" version, having been diluted to 10% by weight in ethanol.

Aluminasol-100 is a colloidal dispersion of amorphous alumina nanoparticles. Based on the diffusion rate of chromium at the temperatures utilized, chromium diffusion and therefore initiation of α-alumina phase nucleation across the colloidal media should be possible. As aforementioned, only very small amounts of chromium are required for α-alumina nucleation; bonding of sapphire components through the nanoparticle interface should be achievable given the proper test conditions.

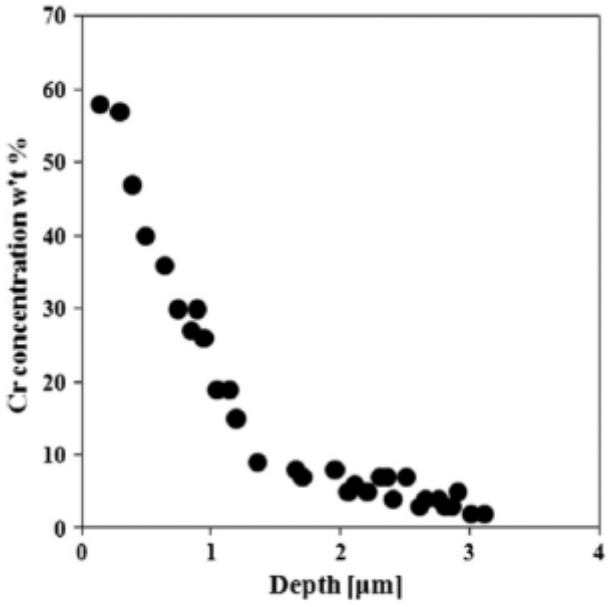

Fig. 3. Concentration profile of Cr in sapphire after annealing at 1873 K for 200 h under oxidation; a Gaussian-type dependence is evident.

Figure 4-29: Chromium Diffusion at Experiment Temperatures Sufficient to Promote Bonding (Data from Journal of Crystal Growth 326 (2011) 45-49)

$Cr+Al_2O_3$ Bonding

Sapphire plates with dimensions of roughly 1cm x 1cm x 1mm were cut and cleaned in ethanol under sonication. Varying amounts of water-soluble chromium (VI) oxide were

dissolved in the colloidal alumina dispersion (Aluminasol-100, Nissan Chemical) as indicated by **Error! Reference source not found.** below. One drop of the proper dispersion was sandwiched etween the plates before heating to 1600°C with a ramp rate of 1.5°C/min and 72 hour dwell at temperature. It was further determined that the technique produced sufficiently inconsistent results as to warrant discontinuation of this investigation. While previous iterations attempted under less tightly-controlled conditions yielded some bonding (though not as strong as the SiO_2 and SiC methods), none of the recent experiments using colloidal alumina and soluble chromium oxide have produced strong bonding as seen in Table 4-7.

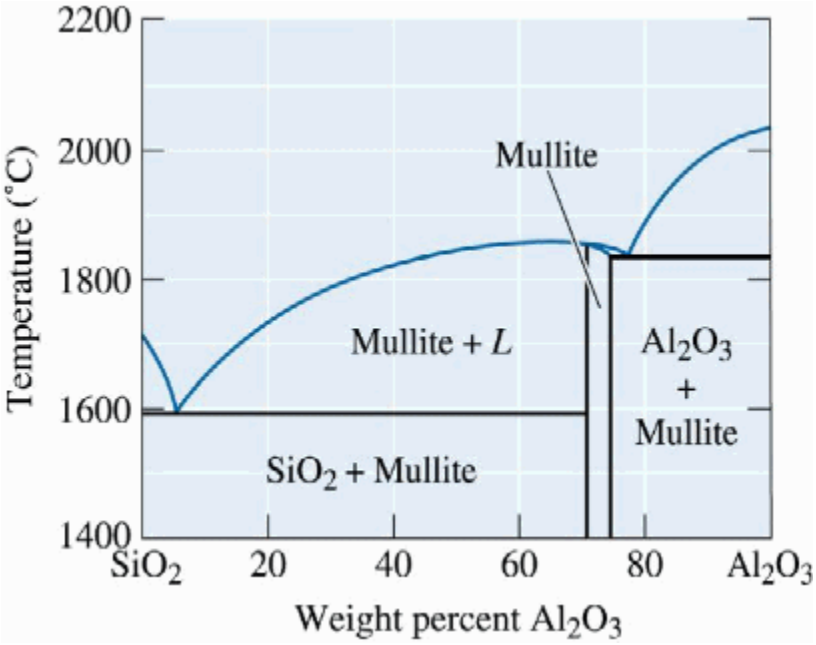

Figure 4-30: Mullite Phase Enables High Temperature Bond Capability

Table 4-7: Cr+Al2O3 Bonding Trials Unsuccessful

Sample	**CrO_3 Concentration (by wt vs Al_2O_3)**	**Result**
CH-2-10A	10ppm	No bond
CH-2-10B	50ppm	No bond
CH-2-10C	100ppm	No bond
CH-2-10D	10ppm (entire solution 1:10 dilution in ethanol)	No bond
CH-2-10E	50ppm (entire solution 1:10 dilution in ethanol)	No bond
CH-2-10F	100pm (entire solution 1:10 dilution in ethanol)	No bond

None of the iterations successfully bonded the sapphire plates. The first attempt (samples CH-2-10A, B, C) contained too high of a solids %, leaving too much distance between the sapphire plates. Diluting the solutions to 10% by volume with ethanol allowed for a much thinner layer to be applied but with similar result, though the undiluted samples contained a large amount of powder between the plates after heating, while the diluted samples did not.The separated, unbonded surfaces will be analyzed via optical microscopy to determine what (if any) microstructural changes took place. It may be that longer time at temperature is simply needed to

produce the desired result, and microstructural cues will provide a basis for continued testing. In conclusion, it was determined it would be most beneficial to spend time and resources on more fully evaluating the SiO_2 and SiC methods.

4.2 Modeling of the Sapphire Photonic Crystal Fiber Optical Properties

4.2.1 Single Crystal Sapphire

Single crystal sapphire has been chosen as the best choice for making high temperature pressure and temperature sensors for a variety of reasons. These consist of a continuous crystal lattice with no grain boundaries, a high melting temperature of 2053°C, a transparent operation range from 0.24 – 4.0μm with respective refractive indices of 1.785 – 1.674, low theoretical loss minimum of $3.4x10^{-3}$dB/km at 1.78μm, and the ability to remain chemically inert[5]. The drawback of using single crystal sapphire fibers is the fact it has no high temperature cladding and this induces a number of difficulties in sensor fabrication and use. Fabrication methods used to make single crystal sapphire fibers do not allow drawing of a cladding with the core, as is done with silica optical fibers. Convective currents in molten zone destroy the structure of the source rod in both the edge-defined film fed growth method[6] (EFG) and the laser heated pedestal growth method[7,8,9,10,11,12] (LHPG). This makes the formation of an *in-situ* cladding layer very difficult.

4.2.2 Single Crystal Sapphire Fiber Cladding

The cladding layer on a single crystal sapphire fiber must meet certain criteria. The fiber cladding must be stable at high temperatures, remain chemically inert, and must have a similar coefficient of thermal expansion to single crystal sapphire[13]. Some of the current materials examined for a post fabrication single crystal sapphire fiber cladding include[14] silicon oxynitride, magnesium silicates, polycrystalline alumina, silicon carbide, zirconia, and niobium.

4.2.3 Fiber Bundling

In order to create a fiber that can survive high temperature/harsh environments a new type of cladding design must first be created. For single crystal sapphire fibers, this problem has been solved[15] by bundling sapphire fibers around the sapphire fiber core, essentially serving as an external cladding. This design having the same material for both the cladding and the core allows for stability at high temperatures, a cladding that remains chemically inert, and has no coefficient of thermal expansion mismatches to that of single crystal sapphire. This type of fiber can potentially be used for pressure, temperature, and gas sensors.

4.2.4 Reduction of Modes in Bundled Fibers

Bundling the sapphire fibers together gives the added value of fiber protection in harsh/high temperature environments, limiting loss of intensity (attenuation), and decreasing the core/cladding effective refractive index difference. This reduction in the effective refractive index difference reduces the number of modes that will propagate in the fiber. This also allows the fibers to eventually approach single mode guidance. In some cases single mode guidance could provide significant benefits of these fibers as it significantly reduces alignment issues to both input and output fibers since the lower order modes are more greatly confined to the core region, whereas higher order modes propagate further into the cladding layers. In other cases such as gas sensing, the modal structure which provides the optimum gas sensing properties may in fact be a multimode structure. Modeling of the fibers can provide information as to the optical

power density in different regions of the fiber and can be used to guide the fiber design to optimize gas sensing performance.

4.2.5 Fiber Optic Modeling

The fiber optic modeling in this work consists of using Comsol Multiphysics 4.2a. Comsol Multiphysics is a very powerful commercial software package for analyzing losses and examining different modes present in a fiber. The objective of the modeling work is to examine how a fiber design will perform optically without having to build the fiber since there are many possible designs. Comsol Multiphysics 4.2a requires the user to first select the geometry and axes of the fiber in question. During this step, the size and shape of the core and cladding layers are chosen. In this model the properties of the fiber are as follows. The central core rod is set to a diameter of 50μm with 5 rods surrounding the central rod with diameters of 70μm each. An image of this fiber can be seen in at left in Figure 4-31. A 50μm diameter single crystal sapphire fiber with an air cladding has also been modeled as seen at right in Figure 4-31.

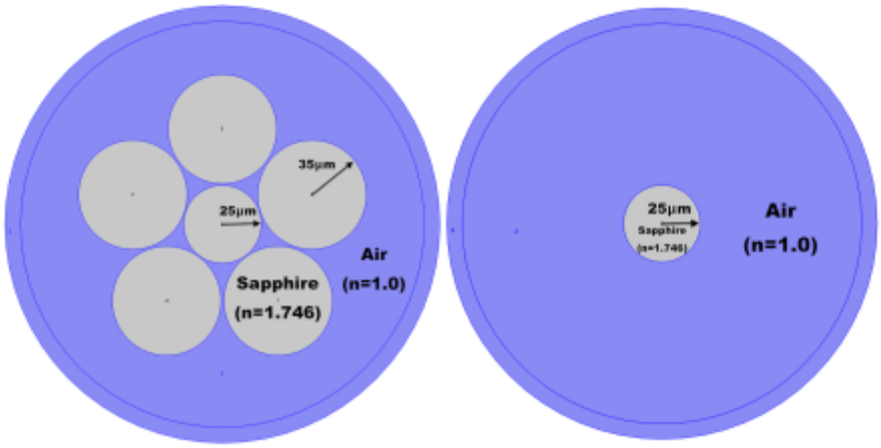

Figure 4-31: Geometry of 6-rod bundled single crystal sapphire fiber (left) and a single rod of single crystal sapphire in air (right) with respective refractive indices. The air (blue) region is set to n = 1.0 and sapphire (grey) (α-Al2O3) is set to n =

Next, the material properties of the fiber are chosen. The main variables include the refractive index (both real and the imaginary part), electric conductivity, relative permittivity, and relative permeability values for the core and cladding. The air (blue) region is set to n = 1.0 and sapphire (grey) (α-Al_2O_3) is set to n = 1.74618. The boundary conditions for each fiber must then be setup. A perfect electrical conductor setting was used for the outer edge, while continuity was set inside the cylindrical perfectly matched layer (PML). The outer diameter of both fibers in **Error! Reference source not found.** was set as a perfectly matched layer (PML). The outer iameter for the PML layer was set to 280μm with an inner PML diameter of 260μm for both fibers. The PML utilizes a reflectionless outer layer used to absorb all outgoing waves. The PML is reflectionless for any frequency, thus absorbing all outgoing radiation. No modes are expected in this outer air layer. A PML region also gives the added benefit of saving valuable memory space on a computationally intensive model such as this. Maxwell's equations for a vector wave having an anisotropic PML can be obtained from the uniformity of the electric field[16] as in Equation (3-1).

$$\nabla \times ([S]^{-1}\nabla \times E) - k_0^2 n^2 [S]E = 0 \qquad (3\text{-}1)$$

In Equation (1) $\boldsymbol{S}$ is the Poynting vector, $\boldsymbol{E}$ is the electric field, $\boldsymbol{k_0}$ is the propagation constant, and $\boldsymbol{n}$ is the refractive index of the medium that contains the PML. The electromagnetic wave heading is chosen for this RF mode and the modal analysis then presumes the wave will propagate in the z-direction. This allows the user to select the perpendicular hybrid mode wave using transversal fields, which will give the modal solutions. The electric field of this wave is given in Equation (3-2).[17]

$$\mathbf{E}(x,y,z,t) = \mathbf{E}(x,y) \exp\left[j(\omega t - \beta z)\right] \tag{3-2}$$

With ω being the angular frequency and β being the propagation constant. The boundary condition on the outside of the cladding layer is set to $n \times \mathbf{E} = \mathbf{0}$. Now using the Helmholtz equation, an eigenvalue equation in terms of the electric field can be written as Equation (3-3).

$$\nabla \times (n^{-2}\nabla \times \mathbf{E}) - k_0^2 \mathbf{E} = \mathbf{0}. \tag{3-3}$$

Equation (3) is solved for the effective refractive index value $n_{eff} = \beta/k_0$, which gives the eigenvalue, with k_0 being the wavenumber. Before these equations are computed, the mesh of the fiber's geometry must be designed. Here a precise mesh using a triangular grid is necessary due to the complicated fiber designs to obtain optimal accuracy. A mesh was developed for the 6-rod case with 38704 elements with an average element quality of 0.9559 as seen at left in Figure 4-32. The mesh for the single rod case had 24812 elements with an average element quality of 0.9775 as seen at left in Figure 4-32. The difference in mesh quality and number of elements stems from Comsol's difficulty to render the multiple fiber rods that are close to touching for the 6-rod case.

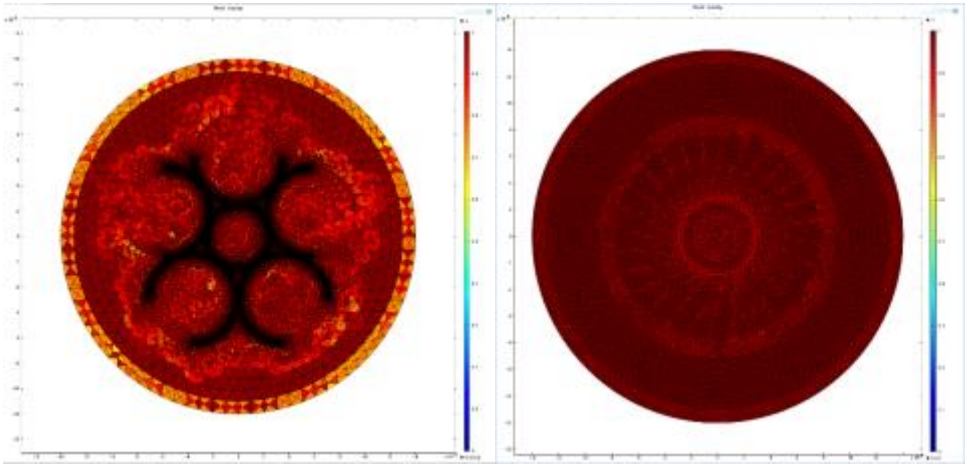

Figure 4-32: 2-D mesh structure for the 6-rod bundled single crystal sapphire fiber with 38704 elements and an average element quality of 0.9559 (left) and for the single rod case with 24812 elements and an average element quality of 0.9775 (right).

After the mesh is chosen, the modal analysis of the fiber begins. The user specifies the desired number of modes to search for and which effective index to look around after specifying the free space wavelength (which is the wavelength at which the modes propagating in the fiber are being tested). Comsol Multiphysics then uses a direct linear system solver (UMFPACK) to

complete its modal analysis by solving near the effective mode index of the single crystal sapphire (1.74618 at a free space wavelength of 1.55μm). The 6-rod case solves for 338941 degrees of freedom while the single rod case solves for 174317 degrees of freedom. In both cases, this is done through a number of iterations until a solution converges that meets a defined error limit.

Confinement loss, L_c, is a commonly used metric for measuring how an optically modeled fiber will perform under optimal operating conditions. It is directly related to the imaginary portion of the propagation constant[18], γ through Equation (3-4).

$$L_c = 8.686*\alpha \tag{3-4}$$

Where α is the attenuation constant. This equation gives the loss[19] in units of dB/m. The propagation constant is defined as Equation (3-5).

$$\gamma = \alpha + j\beta \tag{3-5}$$

Where β is the phase constant and *j* is the imaginary coefficient.

4.3 Modal Analysis

After the solution is computed for a discrete number of modes, the models undergo post processing. Figure 4-33 below is the resultant fundamental hybrid mode for the 6-rod single crystal sapphire fiber showing both polarizations of the electric field. Figure 4-34 below is the resultant fundamental hybrid mode for the single rod case of single crystal sapphire fiber showing both polarizations of the electric field. This is as expected for the optical power to be concentrated directly in the center of the core of both the single rod case and central rod of the 6-rod fiber. The fibers in Figure 4-33 and Figure 4-34 are highly multimode due to the large refractive index contrast between the core and cladding layers. The 6-rod case has an effective mode index of 1.74602 for both polarizations with corresponding confinement losses of L_c= 6.97051e-9 dB/km and L_c= 1.1817e-8 dB/km respectively. The single rod case has an effective mode index for both polarizations of its fundamental mode at 1.74602 with corresponding confinement losses L_c= 2.8976e-8 dB/km and L_c= 2.4770e-8 dB/km respectively.

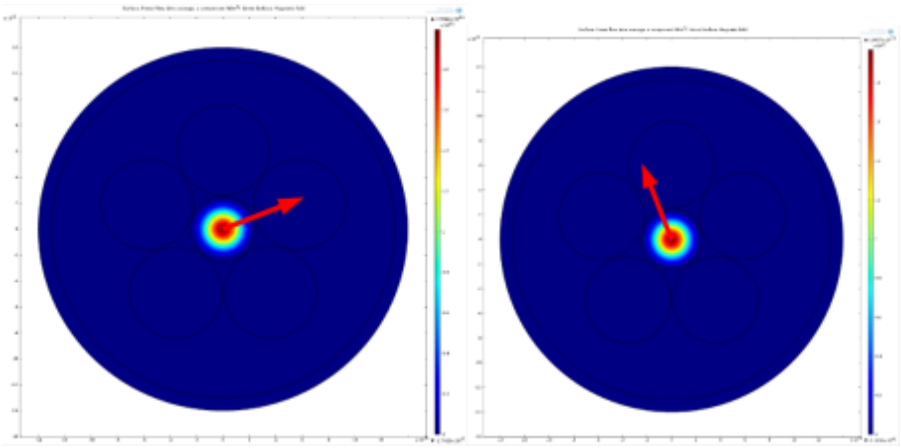

Figure 4-33: Linearly polarized LP_{01}–like modes for the 6-rod bundled single crystal sapphire fiber. The red arrow represents the electric field polarization for the fundamental mode (left and right).

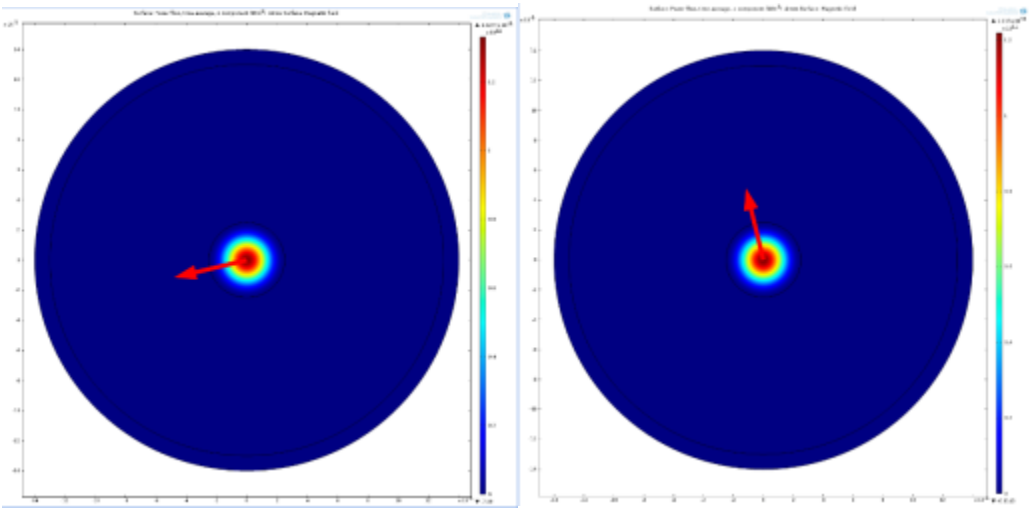

Figure 4-34: Linearly polarized LP_{01}–like modes for the single rod bundled single crystal sapphire fiber. The red arrow represents the electric field polarization for the fundamental mode (left and right).

4.3.1 Mode Number Calculations

The number of modes that propagate in the core region of both fibers is then calculated[20]. This process consists of searching for a desired number of modes between the refractive indices of the core and cladding materials. Both of the fibers being analyzed are highly multimode thus a large number of modes need to be calculated. The power flow time average in the z direction, which is based on the Poynting vector, is calculated for the core in both fibers. This metric removes surface or leaky modes from the results and give a more accurate representation of the actual number of that will propagate in these fibers. The calculated number of modes is determined by both the power flow time average in the z-direction and the propagation constant.

4.3.2 Mode Number Results

Comsol Multiphysics 4.2a has been used to examine confinement loss vs. effective refractive index for both the single rod and 6-rod single crystal sapphire cases. Using this data also allows for the measurement of how many modes will propagate in each of these fibers. As seen in the Figure 4-35 below, the single rod case shows upwards of 4208 modes whereas the 6-rod bundle of single crystal sapphire has approximately 3496 modes. This is a modal reduction percent difference of 18.48% from Equation (3-6) below.

$$\text{Percent Difference} = (4208-3496)/((4208+3496)/2) \tag{3-6}$$

The effective refractive index is plotted versus confinement loss in Figure 4-35 and Figure 4-36 below, which demonstrates the predicted lossy regions with the effective refractive index value at which the mode was recorded. Large bands of high loss can be seen in both Figure 4-35 and Figure 4-36 but are more distinct in the single rod case. The 6-rod bundled case shows smaller bands of high loss, which is most likely due to the greater confinement to the core rod. It is important to note that the loss in the 6-rod bundle is on average less than the single rod case

over the entire effective refractive index range. The lowest order modes have the lowest confinement loss in both fibers. This is especially prevalent in the 6-rod case. As the higher order modes approach a lower effective refractive index value, the modes tend to propagate in more than one rod in the 6-rod structure. This in turn, increases confinement loss. When compared to similar structures that have been modeled for harsh, high temperature environments, we see that other fiber designs offer superior modal reductions in single crystal sapphire.

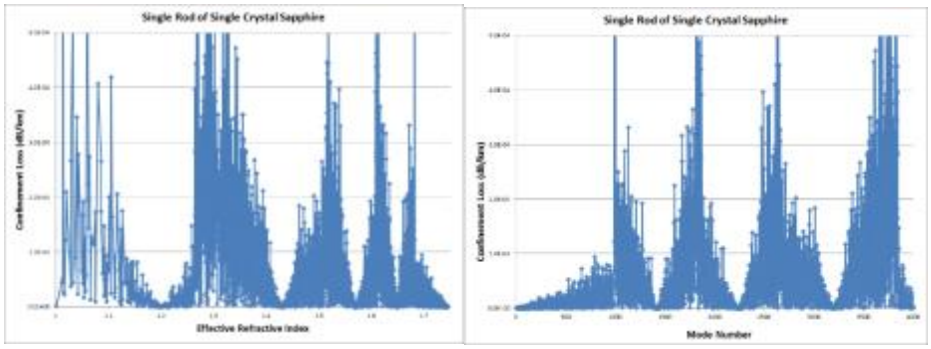

Figure 4-35: Confinement loss vs. effective refractive index (left) and mode number (right) for single crystal sapphire fiber consisting of 1 rod.

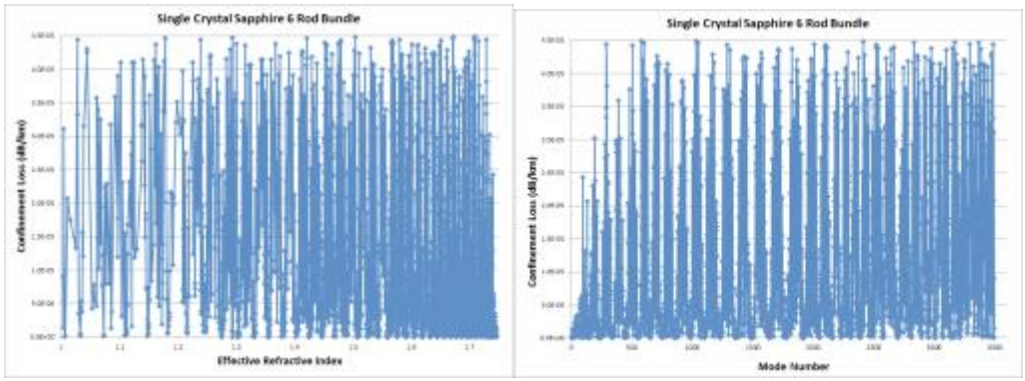

Figure 4-36: Confinement loss vs. effective refractive index (left) and mode number (right) for the 6-rod bundle of single crystal sapphire.

Comsol Multiphysics 4.2a was used to examine both a single rod of single crystal sapphire with a core diameter of 50μm and also a 6-rod structure consisting of 5 rods, with diameters of 70μm, surrounding a central rod with a diameter of 50μm all made of single crystal sapphire fiber. This work enables alternate fiber designs to be tested without having to fabricate the fibers, saving time and money. Fiber designs such as this will continue to be examined due to a large need for temperature and pressure fiber optic sensors that can operate in harsh high temperature environments. The 6-rod case shows a modal reduction percent difference of 18.48% from the single rod of single crystal sapphire fiber. A reduction in the number of modes in these fibers increases the ease of alignment and allows for a more useful fiber.

4.3.3 FEM ANALYSIS OF 6-ROD STRUCTURE

4.3.3.1 Modal Analysis

After the solution is computed for a discrete number of modes, the models undergo post processing. Figure 4-37 below is the resultant fundamental hybrid mode for the 6-rod single crystal sapphire fiber showing both polarizations of the electric field. Figure 4-38 below is the resultant fundamental hybrid mode for the single rod case of single crystal sapphire fiber showing both polarizations of the electric field. This is as expected for the optical power to be concentrated directly in the center of the core of both the single rod case and central rod of the 6-rod fiber. The fibers in Figure 4-37 and Figure 4-38 are highly multimode due to the large refractive index contrast between the core and cladding layers. The 6-rod case has an effective mode index of 1.74602 for both polarizations with corresponding confinement losses of L_c= 6.97051e-9 dB/km and L_c= 1.1817e-8 dB/km respectively. The single rod case has an effective mode index for both polarizations of its fundamental mode at 1.74602 with corresponding confinement losses L_c= 2.8976e-8 dB/km and L_c= 2.4770e-8 dB/km respectively.

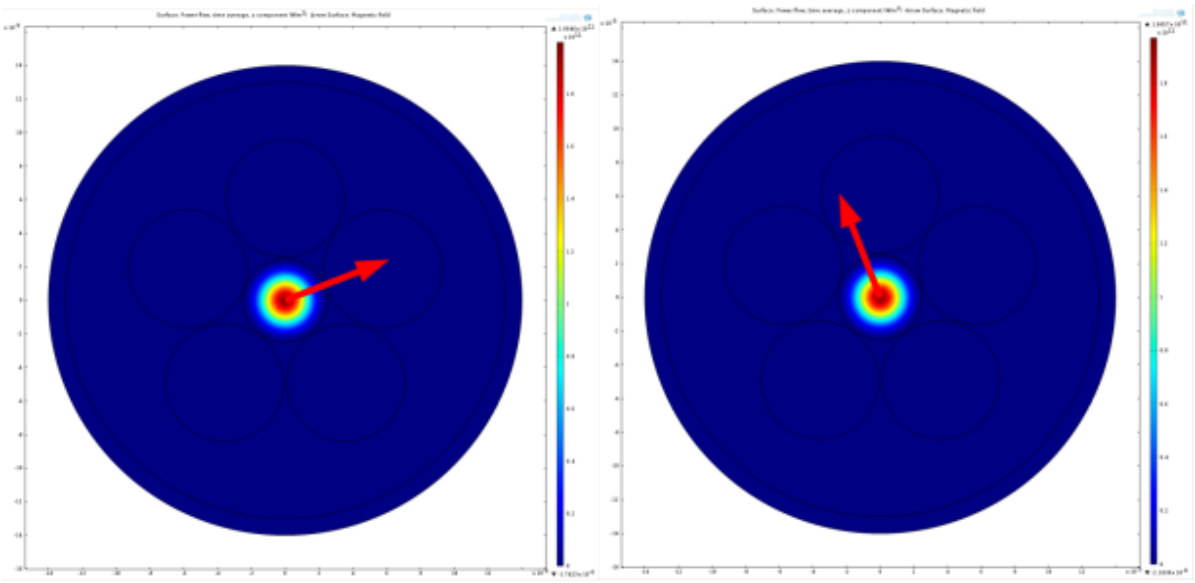

Figure 4-37: Linearly polarized LP_{01}–like modes for the 6-rod bundled single crystal sapphire fiber. The red arrow represents the electric field polarization for the fundamental mode (left and right).

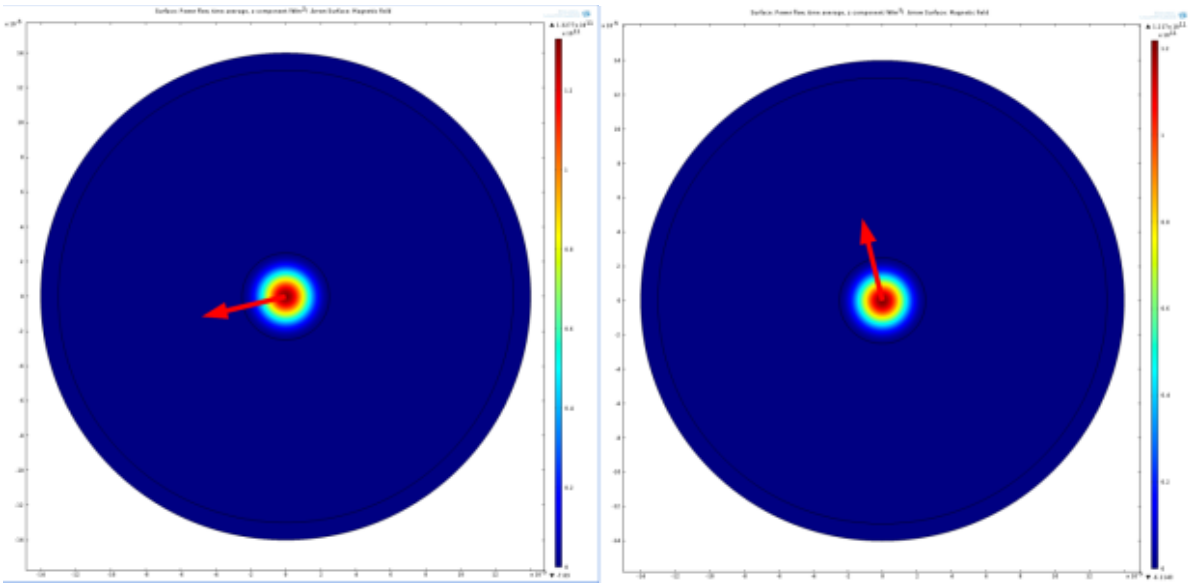

Figure 4-38: Linearly polarized LP_{01}–like modes for the single rod bundled single crystal sapphire fiber. The red arrow represents the electric field polarization for the fundamental mode (left and right).

4.3.3.2 Mode Number Calculations

The number of modes that propagate in the core region of both fibers is then calculated[21]. This process consists of searching for a desired number of modes between the refractive indices of the core and cladding materials. Both of the fibers being analyzed are highly multimode thus a large number of modes need to be calculated. The power flow time average in the z direction, which is based on the Poynting vector, is calculated for the core in both fibers. This metric removes surface or leaky modes from the results and give a more accurate representation of the actual number of that will propagate in these fibers. The calculated number of modes is determined by both the power flow time average in the z-direction and the propagation constant.

4.3.3.3 Mode Number Results

Comsol Multiphysics 4.2a has been used to examine confinement loss vs. effective refractive index for both the single rod and 6-rod single crystal sapphire cases. Using this data also allows for the measurement of how many modes will propagate in each of these fibers. As seen in the Figure 5 below, the single rod case shows upwards of 4208 modes whereas the 6-rod bundle of single crystal sapphire has approximately 3496 modes. This is a modal reduction percent difference of 18.48% from Equation (3-7) below.

$$\text{Percent Difference} = (4208-3496)/((4208+3496)/2) \qquad (3\text{-}7)$$

The effective refractive index is plotted versus confinement loss in Figure 4-39 and Figure 4-40 below, which demonstrates the predicted lossy regions with the effective refractive index value at which the mode was recorded. Large bands of high loss can be seen in both Figure 4-39 and Figure 4-40 but are more distinct in the single rod case. The 6-rod bundled case shows smaller bands of high loss, which is most likely due to the greater confinement to the core rod. It is important to note that the loss in the 6-rod bundle is on average less than the single rod case over the entire effective refractive index range. The lowest order modes have the lowest confinement

loss in both fibers. This is especially prevalent in the 6-rod case. As the higher order modes approach a lower effective refractive index value, the modes tend to propagate in more than one rod in the 6-rod structure. This in turn, increases confinement loss. When compared to similar structures that have been modeled for harsh, high temperature environments, we see that other fiber designs[20] offer superior modal reductions in single crystal sapphire.

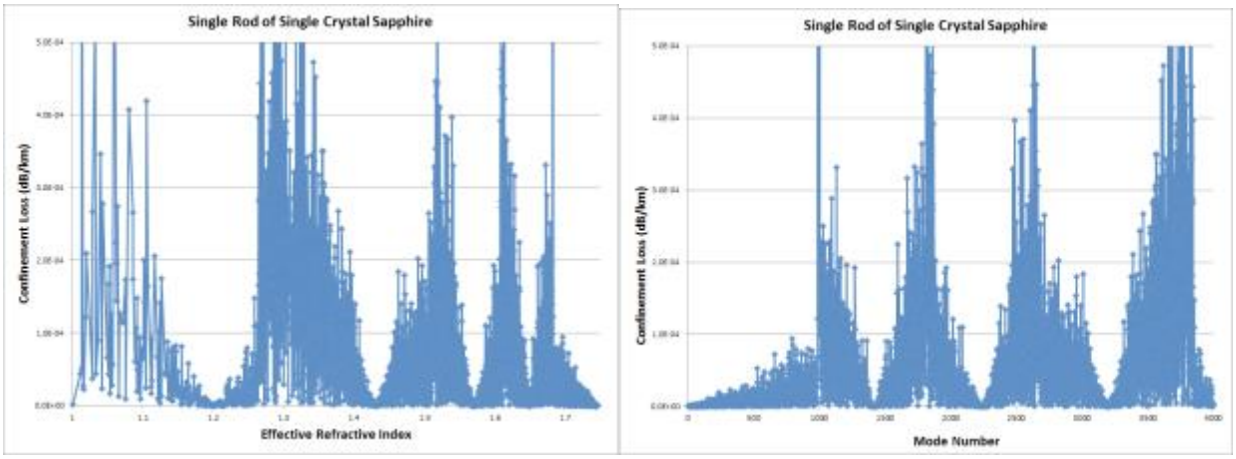

Figure 4-39: Confinement loss vs. effective refractive index (left) and mode number (right) for single crystal sapphire fiber consisting of 1 rod.

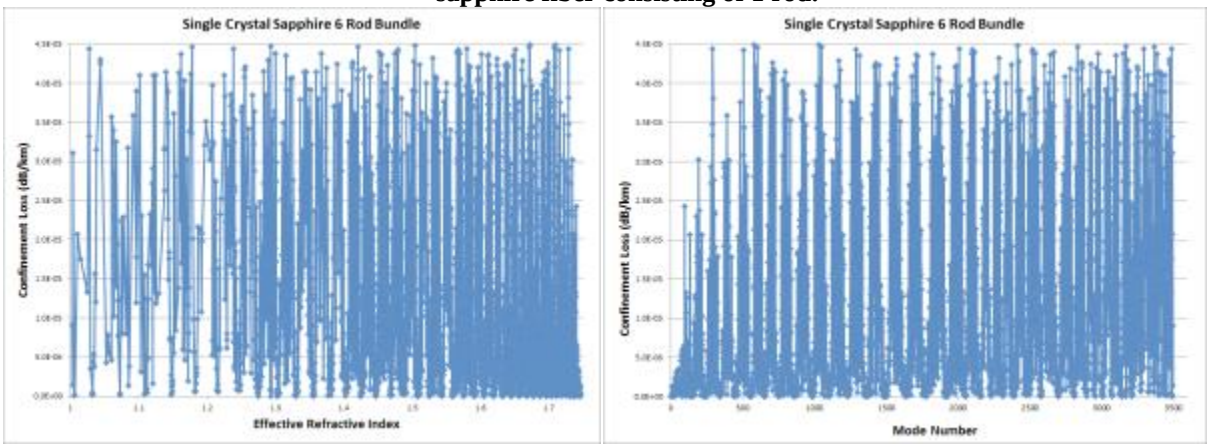

Figure 4-40: Confinement loss vs. effective refractive index (left) and mode number (right) for the 6-rod bundle of single crystal sapphire.

4.3.4 Modal Analysis Conclusions for 6-Rod Structure

Comsol Multiphysics 4.2a was used to examine both a single rod of single crystal sapphire with a core diameter of 50μm and also a 6-rod structure consisting of 5 rods, with diameters of 70μm, surrounding a central rod with a diameter of 50μm all made of single crystal sapphire fiber. This work enables alternate fiber designs to be tested without having to fabricate the fibers, saving time and money. Fiber designs such as this will continue to be examined due to a large need for temperature and pressure fiber optic sensors that can operate in harsh high temperature environments. The 6-rod case shows a modal reduction percent difference of 18.48% from the single rod of single crystal sapphire fiber. A reduction in the number of modes in these fibers increases the ease of alignment and allows for a more useful fiber.

4.4 FEM ANALYSIS OF 7 ROD STRUCTURES

4.4.1 FEM ANALYSIS

The fibers in the following sections are composed of a single crystal sapphire rod surrounded by a ring of 6 other single crystal sapphire rods, all of which are either 70µm (left) or 50µm (right) in diameter as seen in Figure 4-41 below. The air regions, as seen in blue in Figure 4-41, have a refractive index of n=1.0 while the gray region has a refractive index of n=1.74618. The process for creating this type of fiber experimentally has been outlined in previous papers.

The sapphire rods in this study were examined along the C-axis of the crystal extending along the length of the fiber (z-direction). The hexagonal crystal structure of single crystal sapphire has two axes perpendicular to the c-axis, referred to as the a-axes. Finite element analysis can be a very useful tool for fiber optic design. The program used in this paper, Comsol Multiphysics, uses high-order vectorial elements composed of both an automatic and iterative grid refinement calculator. This allows for optimum error estimation during the solving process. Both models in this paper require a complex mesh to render the large air-sapphire regions with high accuracy. These types of RF modal propagation problems are generally solved with a linear solver so that Maxwell's equations in the FEM discretization can be computed without error. Comsol Multiphysics 4.2 also features the Multifrontal Massively Parallel sparse direct **S**olver (MUMPS) solver, which allows for parallel computing on a quad core computer to decrease computation time.

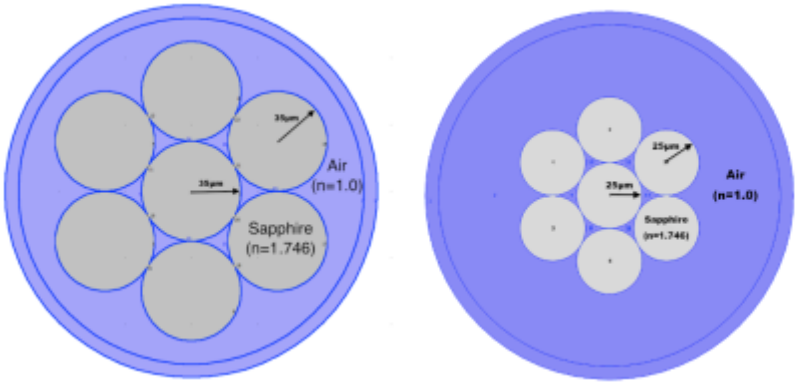

Figure 4-41: Schematic of fibers used in FEM. At left, the bundle composed of 7 (70µm) rods of single crystal sapphire (in gray) surrounded by air (blue region). At right, the bundle composed of 7 (50µm) rods of single crystal sapphire (in gray) surrounded by air (blue region).

The first step in the modeling process is the materials selection. As described above in Figure 4-41, two fibers, a bundled fiber with 70µm diameter rods and a bundled fiber with 50µm diameter rods are to be examined. The dimensions of the rods and the material properties are then adjusted so that the rods of single crystal sapphire (α-Al_2O_3 in gray) have a refractive index of n = 1.74618 and are surrounded by air (blue region), where n=1.0. All models in this paper are solved for using a free space wavelength of 1.55µm, as this is a standard telecommunications wavelength. The outer region of the fibers in Figure 4-41 is set as a perfectly matched layer (PML). The outer diameter for the PML layer is set to 280µm with an inner PML diameter of 260µm. This PML is defined as a reflectionless outer layer, which is used in FEM to absorb all outgoing waves. The PML absorbs all outgoing radiation[22] and is reflectionless for any frequency. Since no modes of interest are expected in this outer air layer, the PML region also saves valuable memory space and decreases computation time.

Confinement loss, L_c, is a commonly used term for measuring loss under optimal operating conditions in FEM modeling. It is directly related to the imaginary portion of the propagation constant[23], γ through the equation:

$$L_c = 8.686*\alpha \tag{3-8}$$

Where α is the attenuation constant. This equation gives the loss[24] in units of dB/m. The propagation constant is defined as:

$$\gamma = \alpha + j\beta \tag{3-9}$$

where β is the phase constant. Another important metric that Comsol Multiphysics can calculate for a given mode is the power flow time average, Po*i*av.

$$\text{Po}i\text{av} = \tfrac{1}{2}*\text{Re}(\mathbf{E}\times\mathbf{H}^*)i \tag{3-10}$$

Which gives us the z_i component in the direction of propagation (into the fiber). This shows that at any point in an electromagnetic field, the vector in Equation (8) can be interpreted in terms of power flow in a specific direction.

The boundary conditions governing each fiber rod in the bundle is then determined. A perfect electrical conductor (PEC) setting was selected for the inner ring surrounding the fiber bundle. A PEC is a surface where the tangential component of the electric field vector ($\vec{E}_t$) is removed. The regions inside of the PEC where set to a continuity boundary condition. As discussed previously, a cylindrical PML was set for the region surrounding the PEC. Comsol is then solved using a direct linear equation solver (UMFPACK) in combination with the MUMPS solver, which allows for the use of multiple cores, near the effective mode index of the single crystal sapphire (1.74602 at 1.55µm).

The next step in the Comsol Multiphysics modeling process is the mesh refinement. The accuracy of the output data is a direct correlation to how precise the mesh is for each fiber structure. The mesh is limited by the memory of the computer as the degrees of freedom increase with a decrease in mesh size. The models for this paper were computed on a 12Gb Macintosh I7 running Comsol 4.2 with a solution time near 7200 seconds for 500 modes. Figure 4-42 below shows a mesh consisting of 64240 elements for the bundled fiber with 70µm diameter rods and 88864 elements for the bundled fiber with 50µm diameter rods.

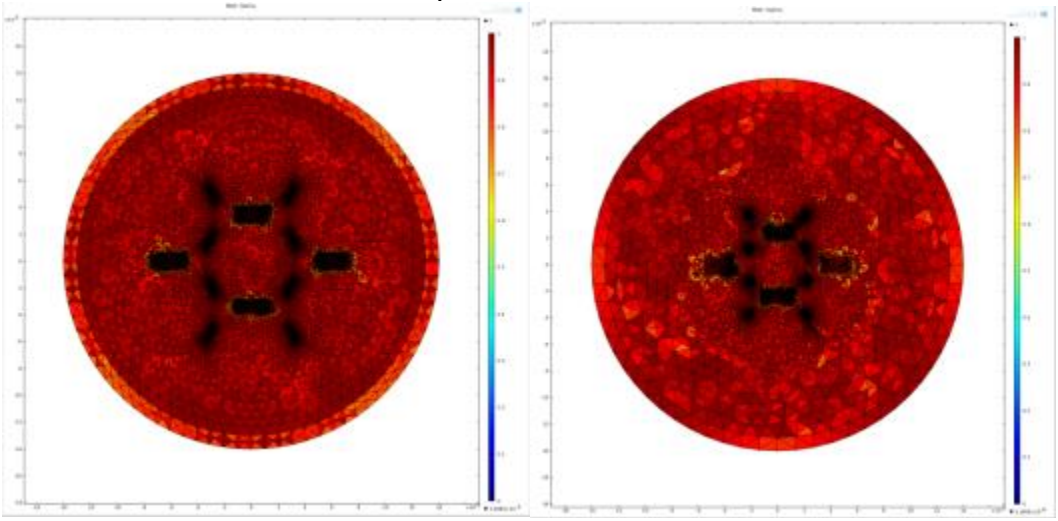

Figure 4-42: 2-D Comsol meshes of both the bundled fiber with 70µm diameter rods (left) and the bundled fiber with 50µm diameter rods (right).

Figure 4-43 below is the resultant fundamental-like hybrid mode for the bundled fiber with 70µm diameter rods solved at a free space wavelength of 1.55µm with 416663 degrees of freedom. Figure 10 below is the resultant fundamental-like hybrid mode for the bundled fiber with 50µm diameter rods solved at a free space wavelength of 1.55µm with 622176 degrees of freedom. In both Figure 4-43 and Figure 4-44, the electric field polarization can be seen by the red arrows. The polarizations of these modes are 90 degrees from each other for a given *LP* mode. The optical power is expected to be concentrated directly in the center of the core of central rod in both fibers due to the coupling from the outer ring of rods in both cases. The 70µm diameter rods case has an effective mode index of 1.74602 with a corresponding confinement loss L_c= 2.0166e-8 dB/km. The 50µm diameter rods case has an effective mode index of 1.74602 with a larger corresponding confinement loss L_c= 1.92e-9 dB/km.

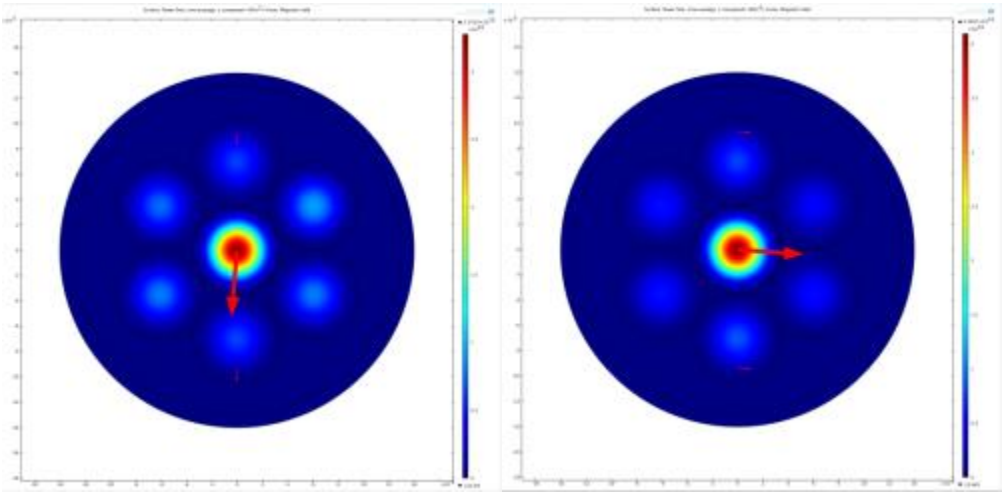

Figure 4-43: Fundamental LP_{01}–like modes for the bundled fiber with 70µm diameter rods showing both electric field polarizations with red arrows.

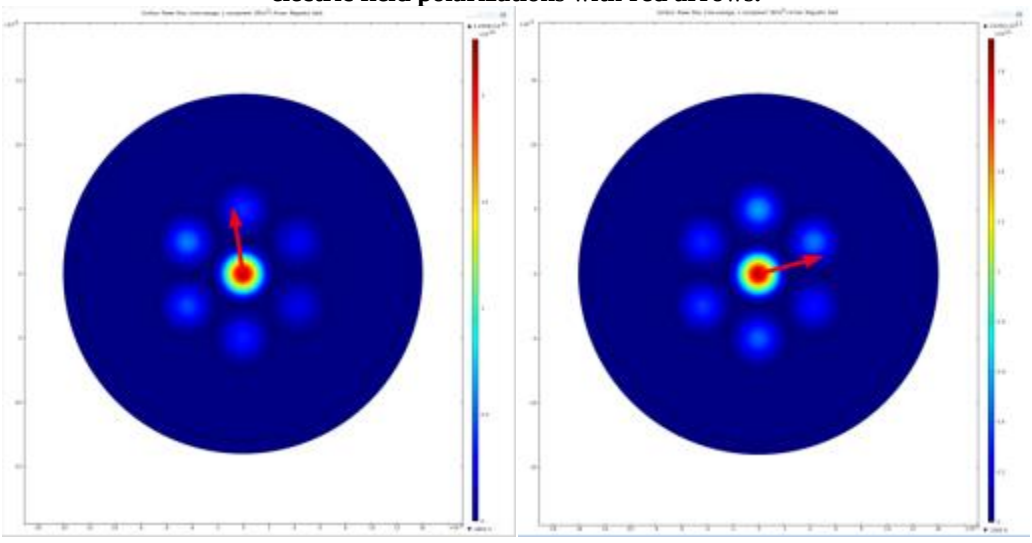

Figure 4-44: Fundamental LP_{01}–like modes for the bundled fiber with 50µm diameter rods showing both electric field polarizations with red arrows.

Comsol Multiphysics also allows us to calculate the number of modes that will propagate in both fibers. By solving for all of the eigenmodes at a free space wavelength of 1.55µm we find that the bundled fiber with 70µm diameter rods holds approximately 38000 modes with 5429 of these modes being confined to the central 70µm diameter core rod. The bundled fiber with 50µm diameter rods holds approximately 22058 modes with 2844 of these modes being confined to the central 50µm diameter core rod. This gives us a modal reduction of 62.49% from the bundled fiber with 70µm diameter rods to the bundled fiber with 50µm diameter rods. Figure 4-45 shows the effective refractive index vs. confinement loss for the bundled fiber with 70µm diameter rods. Figure 4-46 shows the mode number vs. confinement loss (right) for the bundled fiber with 70µm diameter rods.

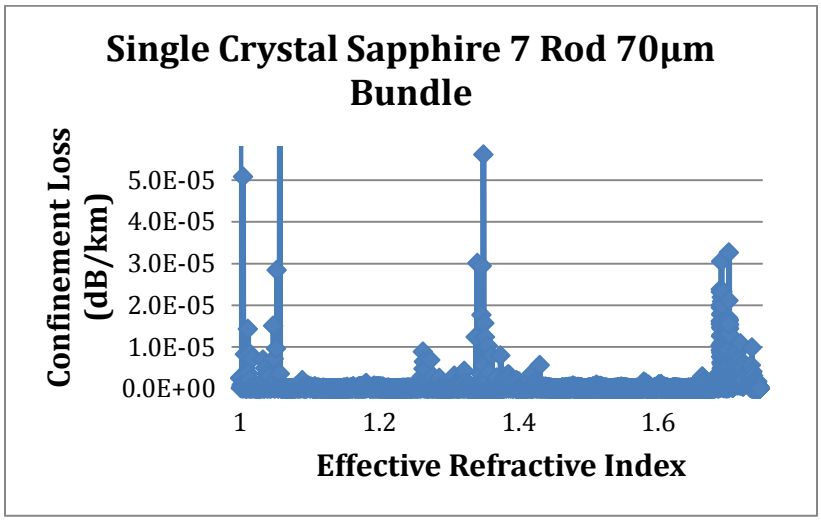

Figure 4-45: Effective Refractive Index vs. Confinement Loss (dB/km) for the bundled fiber with 70µm diameter rods.

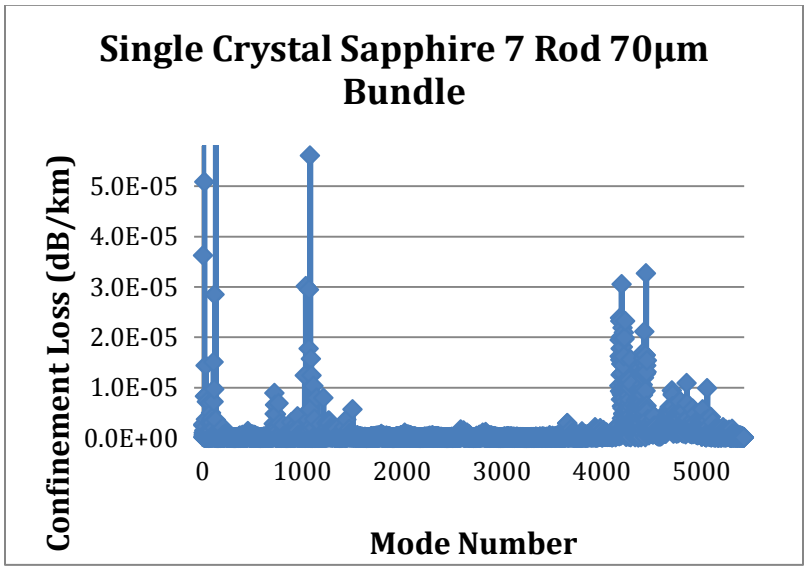

Figure 4-46: Mode Number vs. Confinement Loss (dB/km) for the bundled fiber with 70µm diameter rods.

Figure 4-47 shows the effective refractive index vs. confinement loss for the bundled fiber with 50µm diameter rods. Figure 4-48 shows the mode number vs. confinement loss (right) for the bundled fiber with 50µm diameter rods. The data shows that the confinement loss for the bundled fiber with 50µm diameter rods is much less than that of the bundled fiber with 70µm diameter rods. This is mainly due to the reduction of modes in the 50µm diameter rod case.

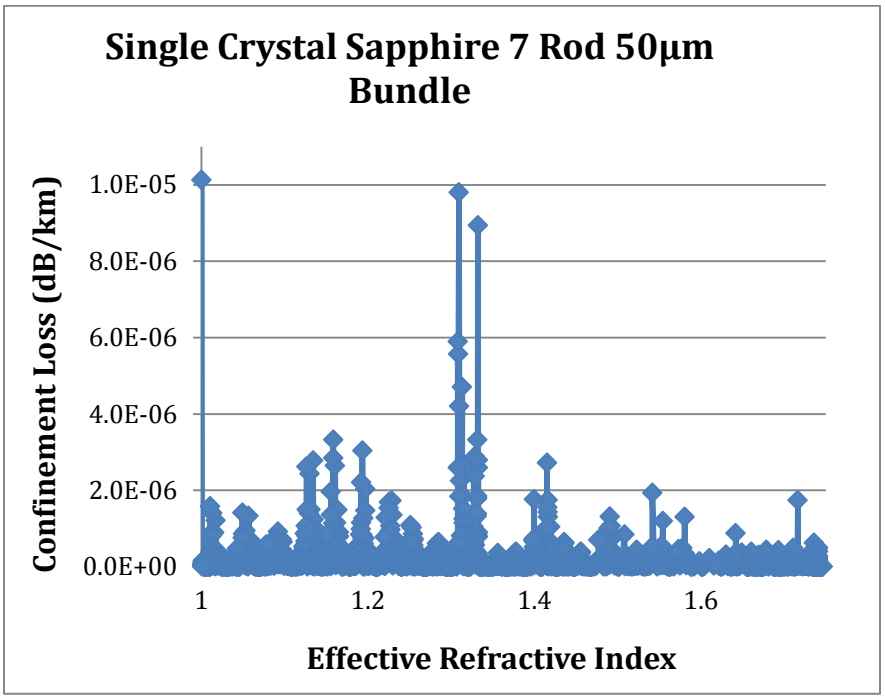

Figure 4-47: Effective Refractive Index vs. Confinement Loss (dB/km) for the bundled fiber with 50µm diameter rods.

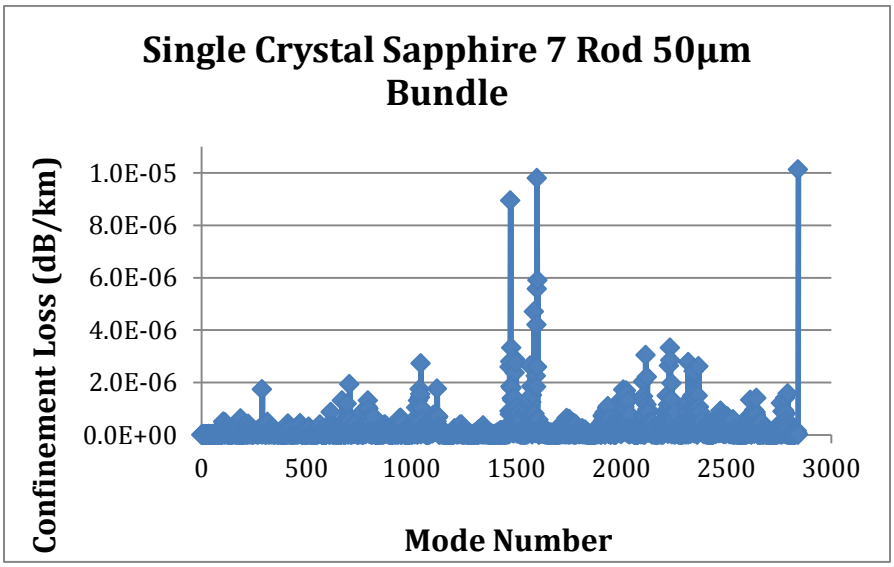

Figure 4-48: Mode Number vs. Confinement Loss (dB/km) for the bundled fiber with 50µm diameter rods.

4.4.1.1 Conclusion of 7-Rod Structures

Two sapphire photonic crystal fiber bundles have been modeled using a multi-physics FEM modeling program. Other single crystal sapphire fiber bundles with this type of structure have been previously modeled but this is the first attempt at optimization by reducing the diameter of the core and surrounding fibers. The bundled fiber with 70μm diameter rods and the bundled fiber with 50μm diameter rods were modeled at a free space wavelength of 1.55μm with the rods all being composed of single crystal sapphire while surrounded by air. This was modeled to see if resulting changes in optical characteristics of each fiber could be determined. This process allows for easy modification of the current size and spacing of the fiber rods in order to further analyze what effect this will have on properties including confinement loss and power flow. The results also show that the confinement loss is directly related to which mode is propagating through the fiber.

4.4.2 Conclusion of 6-Rod and 7-Rod Structures

As seen in the previous pages, the 7-rod bundled structure more efficiently reduces the number of modes compared to that of a 6-rod structure. We believe this is due to the higher order modes traveling out of the core rod and into the air/sapphire region where the outer ring of fibers acts to reflect the would be "lost" modes back into the core region. This theory has been proven more recently with a high temperature all silica fiber. The data for the all silica bundled 7-rod fiber was analyzed and compiled into a journal article. This phenomenon was first realized using the sapphire fibers during NA experiments. The difference in optical intensity with the same input is dramatically higher (3-4x) in the bundled case vs. the single rod case. Fringe visibility experiments were then performed with a bare silica rod about 80um in diameter. First, a bare rod of silica was fusion spliced to a 62.5 MMF, which was then fusion spliced to a 100/140 MMF, which was connected to an 850nm LED. The fringe visibility tests were performed using a sapphire wafer glued to the end of an alumina tube in order to align the fiber to the space where there would be nothing behind the sapphire wafer. Si photodetector measurements where then performed using this setup as well. The photodetector in the single rod case at 60dB gain showed a voltage average of 1.665V and in the dark showed a voltage average of -0.1777V. A photodetector test was then performed with the 850nm LED fusion spliced to the 100/140 MMF fusion spliced to the 62.5MMF and the voltage was saturated at 60 dB so the gain was changed to 50db and an average voltage of 8.5986V was recorded. The single rod of silica was then bundled using 6 rods with a similar diameter as to that of the core (about 80um bare silica) around the central fusion spliced fiber and both the white light interferometry and the photodetector measurements were repeated. There was almost no change in fringe visibility, but the intensity of the bundled fiber was about 3x that of the single rod that was fusion spliced. (The bundled fiber had an integration time of 15s in order to overlap with the single rod which had an integration time of 43ms.) The photodetector measurements of the bundled fiber showed an average voltage of 8.0909V at 60dB gain which is near a 4x improvement in intensity.

4.4.3 Photonic Band Gap Modeling

The MIT Photonic Bands program (MPB) allows users to compute the eigenstates and eigenvalues of Maxwell's equations for plane waves in the frequency domain. The goal with this program is to successfully predict the feasibility of creating a photonic band gap with a 7-rod

single crystal sapphire fiber bundle in air. If this is not possible, new designs will be analyzed to determine where a photonic band gap would exist if the structure can be fabricated.

The MBP program begins with setting the number of bands for each **k** point. For the models in this section the number of bands is chosen to be 8, which is a common number of eigenstates for a hexagonal lattice structure. Next, the **k** points, often called Bloch wavevectors, at which the bands will be solved are set as the corners of the irreducible Brillouin zone. The basis size is chosen in order to maintain a hexagonal structure. Thus we have a basis of ($2/\sqrt{3}$, 0.5), ($2/\sqrt{3}$, -0.5) with the z direction being zero due to this being modeled as a 2D structure. Next the **k** points are linearly interpolated and the lattice directions are chosen. The geometry, grid size, and spacing of the rods in the fiber are then selected as functions of *a* since Maxwell's equations are scale invariant, where *a* is the spacing between rods or air holes, also called the lattice parameter. The radius of the rods or air holes, *r*, is scaled with *a* so that the correct 7-rod structure can be obtained. For the case of a 7-rod structure with all of the rods touching in a hexagonal shape, $r = 0.35$ with $a = 1$ giving an equivalent structure to a fiber having a hexagonal arrangement with all rods touching with each rod being 70 μm in diameter. MPB uses a dielectric constant for the materials in the model and thus the dielectric constant for air $\varepsilon_{air} = 1.0$ and the dielectric constant for single crystal sapphire parallel to the c-axis taken from Kyocera[25] is $\varepsilon_{sapphire} = 11.5$. The image of the resultant fiber structure can be seen in Figure 4-49 below.

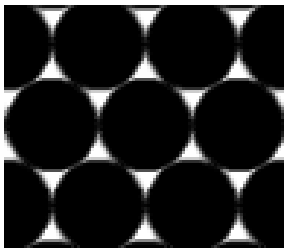

Figure 4-49: Output image from MPB code for the 7-rod structure of single crystal sapphire rods (black region) in a background matrix of air (white region) with r/a =0.5

The TE and TM polarized modes can now be solved to output the band structure for the given fiber geometry. Figure 4-50 below shows the resultant TE modes while Figure 4-51 shows the TM polarized modes for the given structure in Figure 4-49 above.

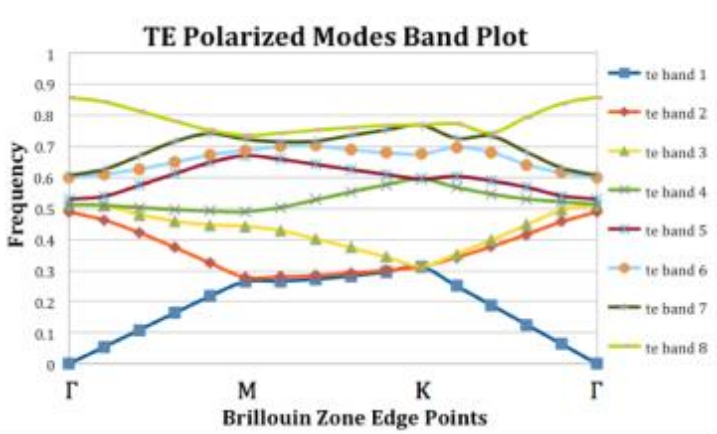

Figure 4-50: TE band gap plot of the frequency (in units of ωa/2πc) versus the Brillouin zone edge points (M, K, and Γ) for the 7-rod structure of single crystal sapphire as seen in Figure 4-49

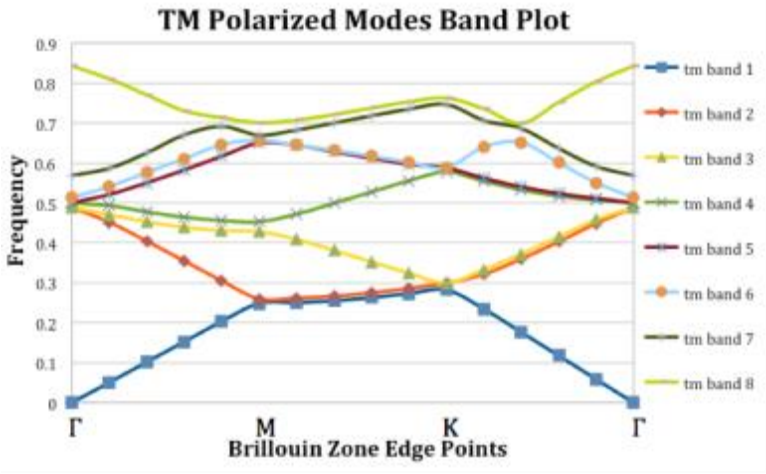

Figure 4-51: TM band gap plot of the frequency (in units of ωa/2πc) versus the Brillouin zone edge points (M, K, and Γ) for the 7-rod structure of single crystal sapphire as seen in Figure 4-49 above

The edges of the Brillouin zone are denoted by the points *M*, *K*, and *Γ*. From here we see that no band gap exists in either the TE or TM mode polarizations. This is due to the very small air fill fraction that is created when the sapphire rods are all touching in a hexagonal arrangement. This is typical for a rod type structure with a high dielectric contrast in a hexagonal arrangement. Analysis of similar structures with a slightly different dielectric contrast as in the MIT MPB tutorial[26] shows that for a hexagonal array of high-index dielectric rods, a photonic band gap open between the first (dielectric) band and the second (air) band for the TM modes but not for the TE modes when the spacing in between the high index rods is increased. This results from the lowest TM mode being localized in the high dielectric regions while most of the electromagnetic power of the air band is found in the lower dielectric regions of the air voids. This in turn increases the air fill fraction of the structure.

Now that the 7-rod bundled fiber made of all single crystal sapphire has been modeled, it is important to find what fiber designs will enable us to have a partial or even a full TE and TM band gap. In order to do this, two distinct fiber designs were analyzed. The first was similar to our previous design of a 7-rod structure of sapphire rods in air, only with the radius and the spacing in between the rods changing in order to find a band gap. The second case is air holes in a background dielectric matrix of single crystal sapphire. This lattice of a high dielectric material is designed so that an almost isolated yet also connected structure consisting of triangular high ε-spots will be connected by narrow veins. A photonic band gap fiber using alumina as a background material with air holes in a hexagonal lattice orientation has already been demonstrated, so this design using single crystal sapphire should also produce a full band gap due to the similarity of dielectric constant between that of single crystal sapphire and alumina.

The first case examined has a 7-rod structure of sapphire rods in air, with the rod size changing from $r = 0.1$ with a respective basis size of $a = 0.2$ to a rod size of $r = 10$ with a respective basis size of $a = 20$. Maintaining the ratio $r/a = 0.5$ allows us to see various rod sizes when all of the 7 rods are touching one another. The ratio r/a is often called the air fill fraction when one of the dielectric constants is defined as air. Scaling of the rod size for five of the ratios analyzed can be seen in Figure 4-52 below. As in previous models, the dielectric constant for air is set to $\varepsilon_{air} = 1.0$ and the dielectric constant for single crystal sapphire parallel to the c-axis is $\varepsilon_{sapphire} = 11.5$.

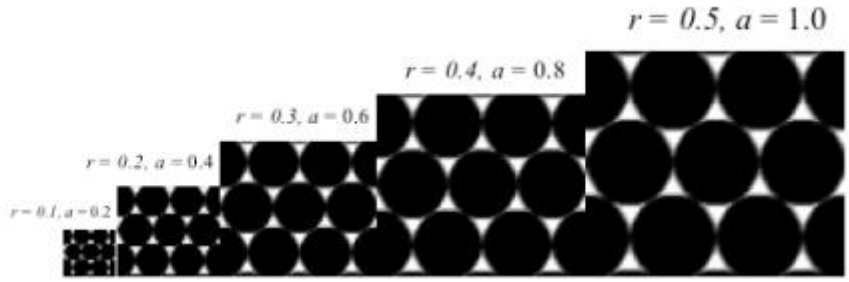

Figure 4-52: Images of five of the varied rod sizes analyzed with r/a = 0.5

Changing the rod radius and the lattice parameter with r/a = 0.5, we see that no band gaps exist for both TE and TM polarizations. This is mainly due to the large amount of sapphire and the minimal amount of air in this structure.

The next case examined has a 7-rod structure of sapphire rods in air, with the rod size kept constant at r = 0.35 while modifying the basis size from a = 0.1 to a = 10. By holding the rod size constant at r = 0.35, the ratio r/a scales the spacing between the rods. Scaling the rod spacing for five of the examined ratios can be seen in Figure 4-53 below. As in previous models, the dielectric constant for air is set to ε_{air} = 1.0 and the dielectric constant for single crystal sapphire parallel to the c-axis is $\varepsilon_{sapphire}$ = 11.5.

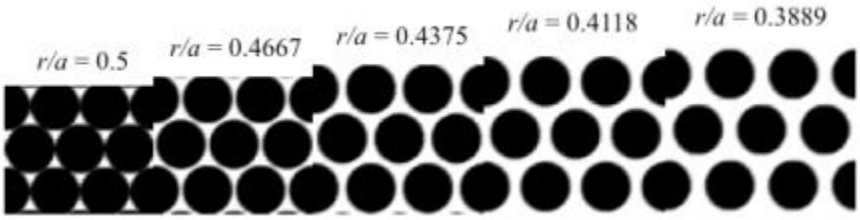

Figure 4-53: Images of five of the varied rod spacing's with r = 0.35

Changing the rod spacing we see that as the r/a ratio decreases, more TM band gaps open up. This directly correlates in a greater air fill fraction, which enables the large dielectric contrast between sapphire and air to produce a photonic band gap in one polarization. In this structure we see that the TM bands dominate in bands 1-2, 3-4, and 6-7, while small TE bands can be found from band 1-2 and band 4-5. This structure contains no full band gap. The TE band data over the entire data range can be seen in Figure 4-54 and the TM is shown in Figure 4-55 respectively.

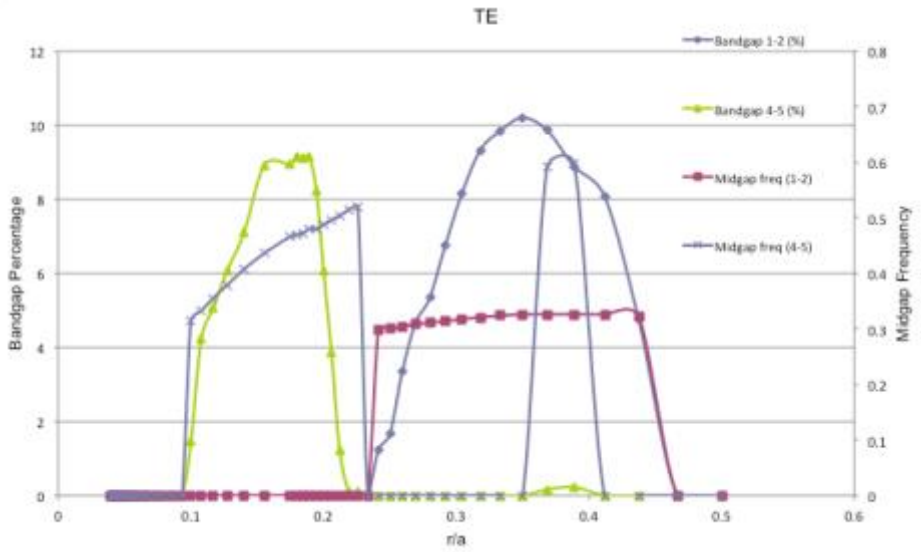

Figure 4-54: TE band profile for a structure with various rod spacing's while r is kept constant at r = 0.35

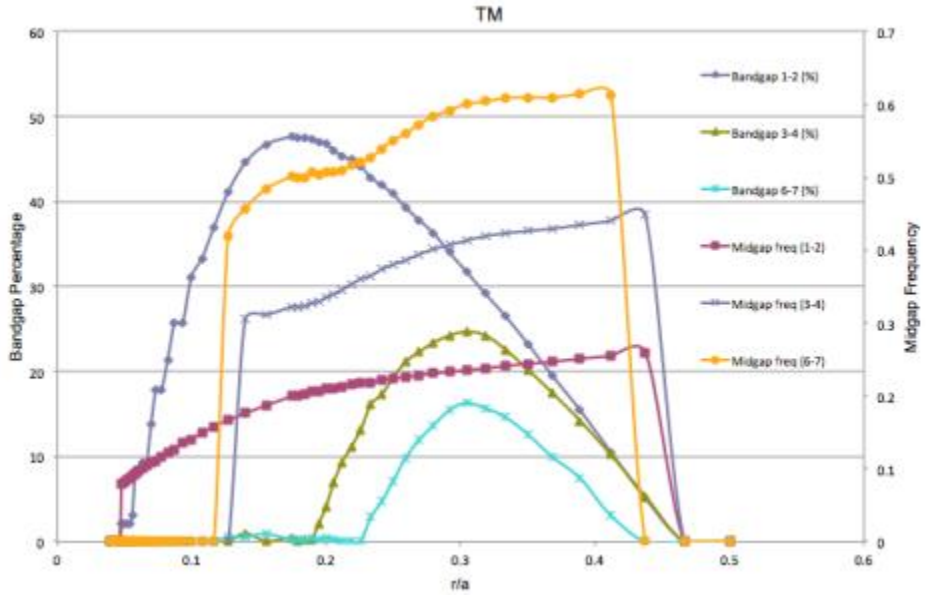

Figure 4-55: TM band profile for a structure with various rod spacing's while r is kept constant at r = 0.35

The next case examined has a 7-rod structure of sapphire rods in air, with the basis size *a* kept constant at $a = 1.00$ while modifying the rod radius from $r = 0.1$ to $r = 0.5$. By holding the basis size constant at $a = 1.00$, the ratio r/a scales the rod radius for a given spacing. Scaling the rod radius for five of the analyzed ratios can be seen in Figure 4-56 below. As in previous models, the dielectric constant for air is set to $\varepsilon_{air} = 1.0$ and the dielectric constant for single crystal sapphire parallel to the c-axis is $\varepsilon_{sapphire} = 11.5$.

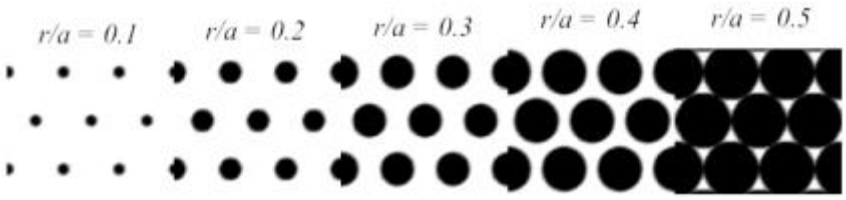

Figure 4-56: Images of five of the varied rod radius's with a = 1.00

Changing the rod spacing, we see that as the *r/a* ratio decreases, more TM band gaps open up. This directly correlates in a greater air fill fraction, which enables the large dielectric contrast between sapphire and air to produce a photonic band gap in one polarization. In this structure we see that the TM bands dominate in bands 1-2, 3-4, and 6-7, while small TE bands can be found from band 1-2 and band 4-5. This structure also contains no full band gap. The TE band data over the entire data range can be seen in Figure 4-57 and the TM is shown in Figure 4-58 respectively.

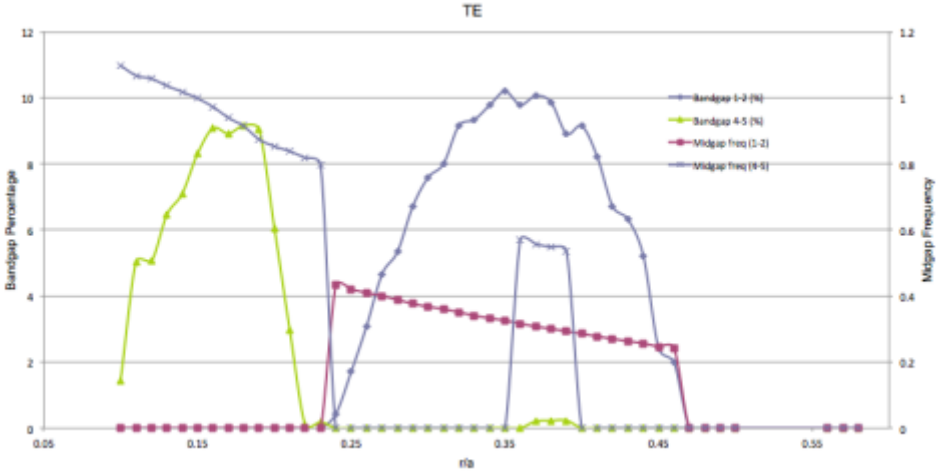

Figure 4-57: TE band profile for a structure with various rod radius's while a is kept constant at a = 1.00

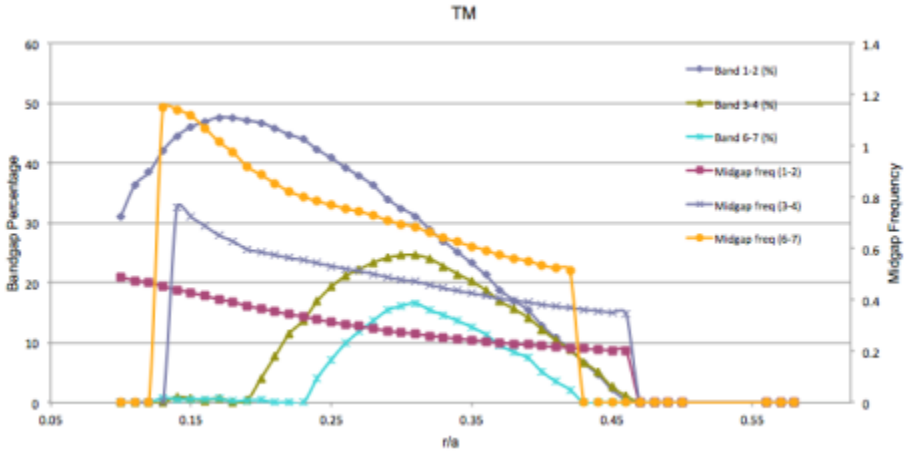

Figure 4-58: TM band profile for a structure with various rod radius's while a is kept constant at a = 1.00

The next case examined has a hexagonal structure of air holes surrounded in a background sapphire matrix. In this case the hole size changes from r = 0.1 with a respective basis size of a = 0.2 to a hole size of r = 10 with a respective basis size of a = 20. Maintaining the ratio r/a = 0.5 allows us to see various hole sizes when all of the 7 holes are touching one another. Scaling the hole size for the first five ratios can be seen in Figure 4-59 below. As in previous models, the dielectric constant for air is set to $\varepsilon_{air} = 1.0$ and the dielectric constant for single crystal sapphire parallel to the c-axis is $\varepsilon_{sapphire} = 11.5$.

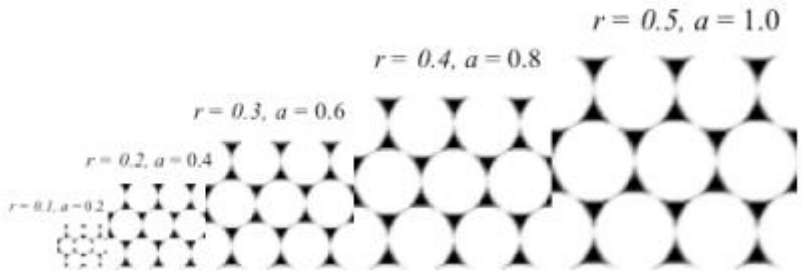

Figure 4-59: Images of five of the varied hole sizes with an r/a = 0.5

Changing the hole radius, we see that with a structure where all of the rods are touching (r/a = 0.5) we find that both TE and TM band gaps exists as well as a full band gap. This is mainly due to the high air fill fraction of the structure, which enables the large dielectric contrast between sapphire and air to produce a photonic band gap. The TE band data over the entire data range can be seen in Figure 4-60 and the TM is shown in Figure 4-61 respectively.

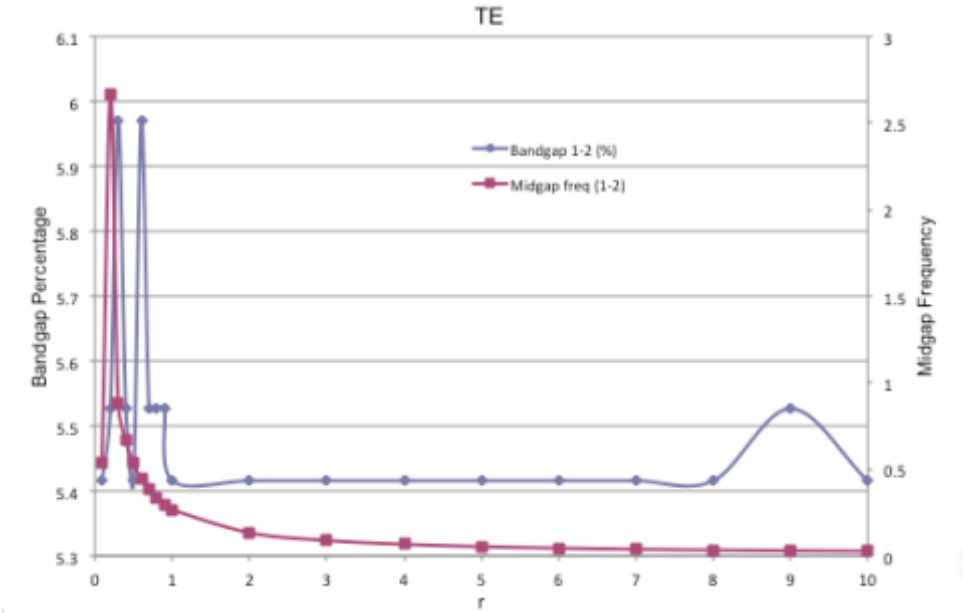

Figure 4-60: TE band profile for a structure with various hole sizes while maintaining the r/a = 0.5 ratio

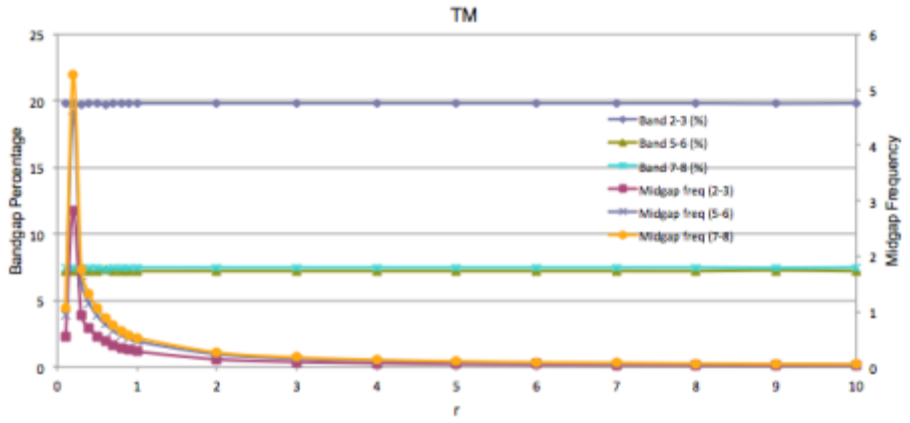

Figure 4-61: TM band profile for a structure with various hole sizes while maintaining the r/a = 0.5 ratio

This data shows the maximum full band gap resides between the TE-1 and TE-2 bands at r = 0.3 and a = 0.6 with a band gap percentage of 5.97% as seen in Figure 4-62 below. In order to convert the band gap frequency along the y-axis into a distinct wavelength one needs to simply multiply by a wavelength value which will determine the value of the lattice parameter a. The value of r can then be determined by the r/a ratio.

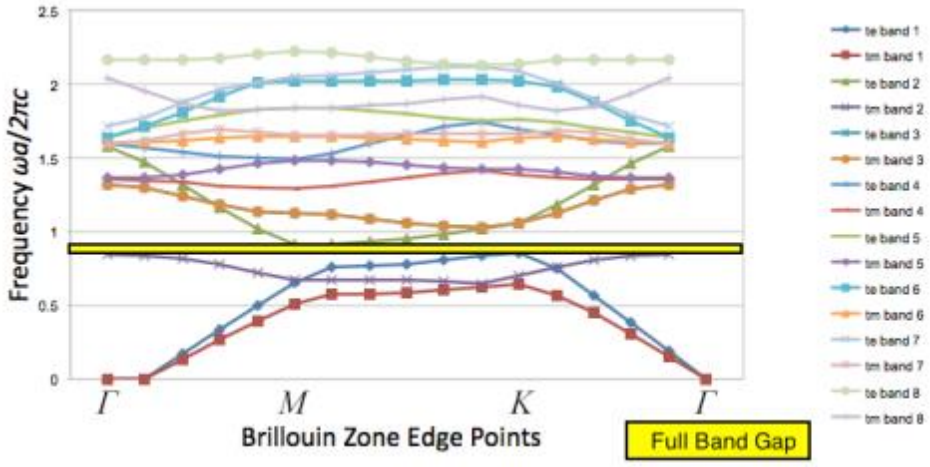

Figure 4-62: TE and TE full band gap profile for a structure with r = 0.3 and a = 0.6

The next case examined has a hexagonal hole structure of air holes surrounded in a background sapphire matrix. In the case the radius of the holes was kept constant with r = 0.35 while the basis size was modified from a = 0.1 to a = 10. By holding the hole size constant at r = 0.35, the ratio r/a scales the spacing between the holes. Scaling the hole spacing for the first five ratios can be seen in Figure 4-63 below. As in previous models, the dielectric constant for air is set to ε_{air} = 1.0 and the dielectric constant for single crystal sapphire parallel to the c-axis is $\varepsilon_{sapphire}$ = 11.5.

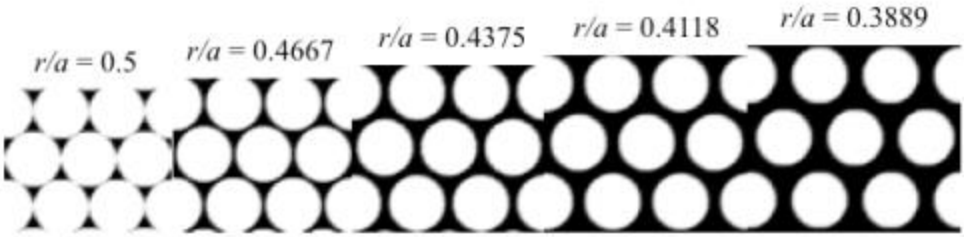

Figure 4-63: Images of five of the varied hole spacing's with r = 0.35

Changing the rod spacing we see that as the *r/a* ratio decreases more TM band gaps disappear. This directly correlates in a greater air fill fraction, which enables the large dielectric contrast between sapphire and air to produce a photonic band gap in one polarization. This test shows a much larger TE gap in band 1-2, with a smaller gap in band 7-8. The TM gaps are present, but are much smaller than the TE polarization and occur mainly between bands 2-3, 5-6, and 7-8. The TE band data over the entire data range can be seen in Figure 4-64 and the TM is shown in Figure 4-65 respectively.

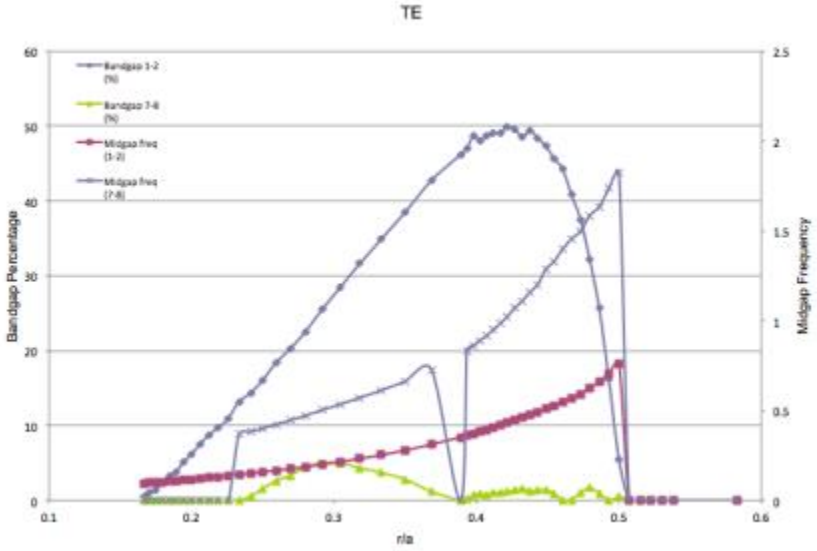

Figure 4-64: TE band profile for a structure with various rod spacing's while r is kept constant at r = 0.35

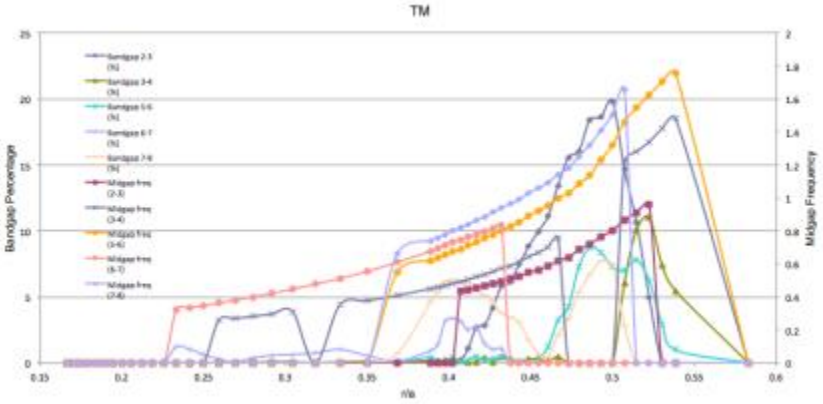

Figure 4-65: TM band profile for a structure with various rod spacing's while r is kept constant at r = 0.35

This data shows the maximum full band gap resides between the TM-2 and TM-3 bands at r = 0.35 and a = 0.74 with a band gap percentage of 15.551% as seen in Figure 4-66 below.

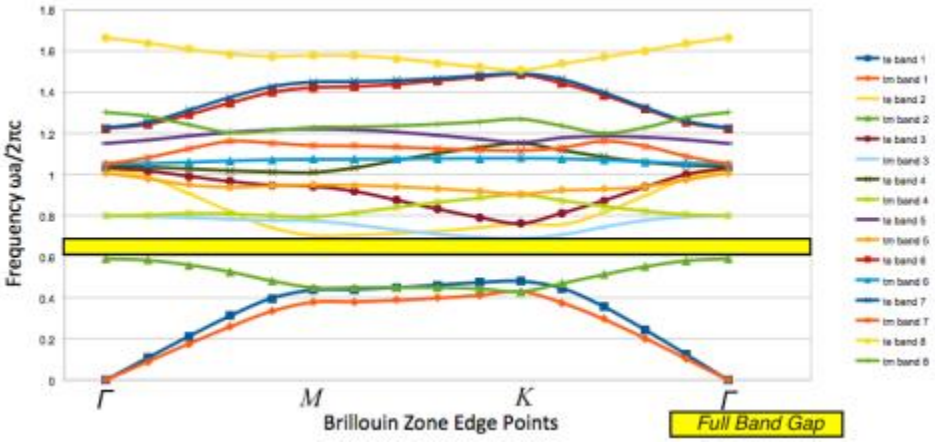

Figure 4-66: TE and TE full band gap profile for a structure with r = 0.35 and a = 0.74

The final case examined has a hexagonal hole structure of air holes surrounded in a background sapphire matrix with the basis size a kept constant at a = 1.00 while modifying the hole radius from r = 0.1 to r = 0.5. By holding the basis size constant at a = 1.00, the ratio r/a scales the hole radius for a given spacing. Scaling the hole radius for five of the analyzed ratios can be seen in Figure 4-67 below. As in previous models, the dielectric constant for air is set to ε_{air} = 1.0 and the dielectric constant for single crystal sapphire parallel to the c-axis is $\varepsilon_{sapphire}$ = 11.5.

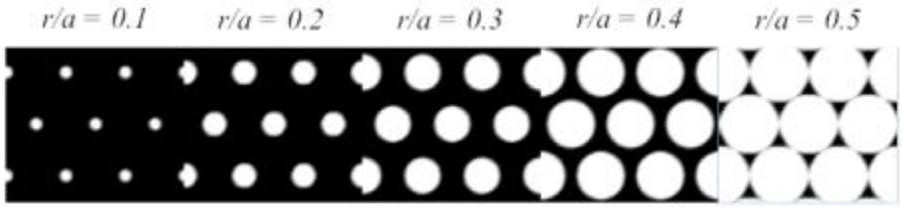

Figure 4-67: Images of five of the varied hole radius's from to r = 0.1 to 0.5 with a = 1.0

Changing the hole radius we see that as in the last two tests the TE polarization dominates. A large TE polarization gap can be seen between bands 1-2 with a smaller gap between bands 7-8. The TM polarization has the majority of its gaps opening up in the r/a >0.4 region with gaps seen between bands 2-3, 5-6, 6-7, and 7-8. The TE band data over the entire data range can be seen in Figure 4-68 and the TM is shown in Figure 4-69 respectively.

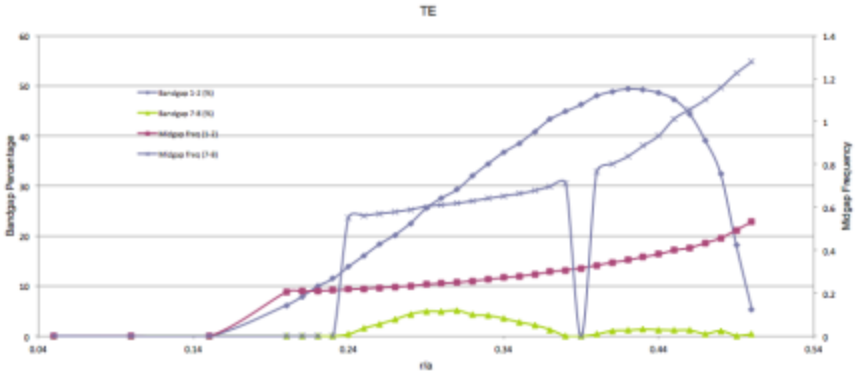

Figure 4-68: TE band profile for a structure with various hole radius while a is kept constant at a = 1.0

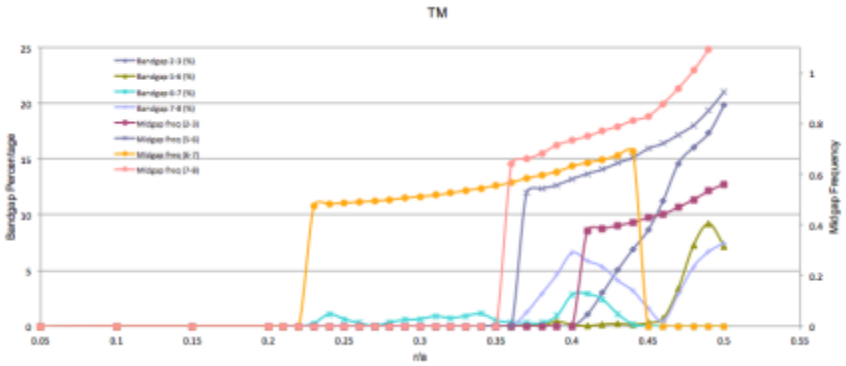

Figure 4-69: TM band profile for a structure with various hole radius while a is kept constant at a = 1.0

This data shows the maximum full band gap resides between the TE-2 and TM-2 bands at r = 0.49 and a = 1.00 with a band gap percentage of 17.5% as seen in Figure 4-70 below. This is the maximum band gap structure possible for air holes in a background matrix of single crystal sapphire.

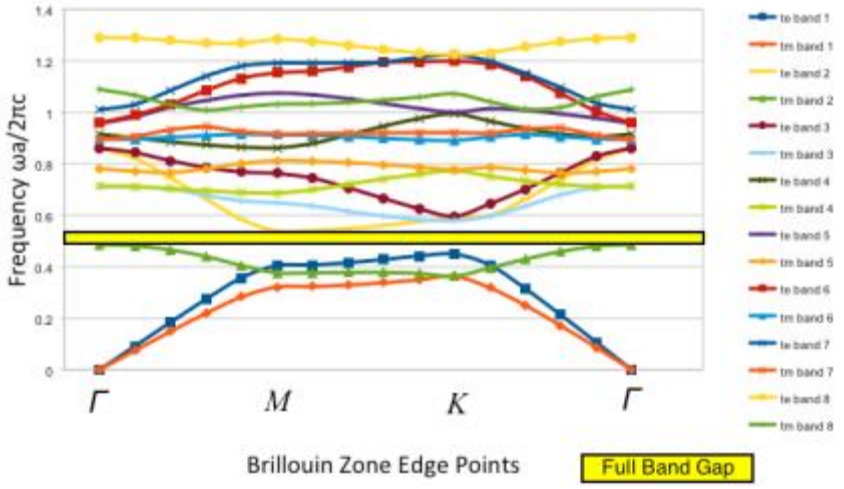

Figure 4-70: TE and TE full band gap profile for a structure with at r = 0.49 and a = 1.00

4.5 Fabrication of the Optimized Sapphire Photonic Crystal Fiber Structures

4.5.1 Fabrication Improvements

One of objectives of this project was the development of a gas sensing system using sapphire fiber for high temperature environments. One of the ideas to improve gas detection in the sapphire bundle was to create an air cavity between two core sapphire fibers in the bundle as shown in Figure 4-71.

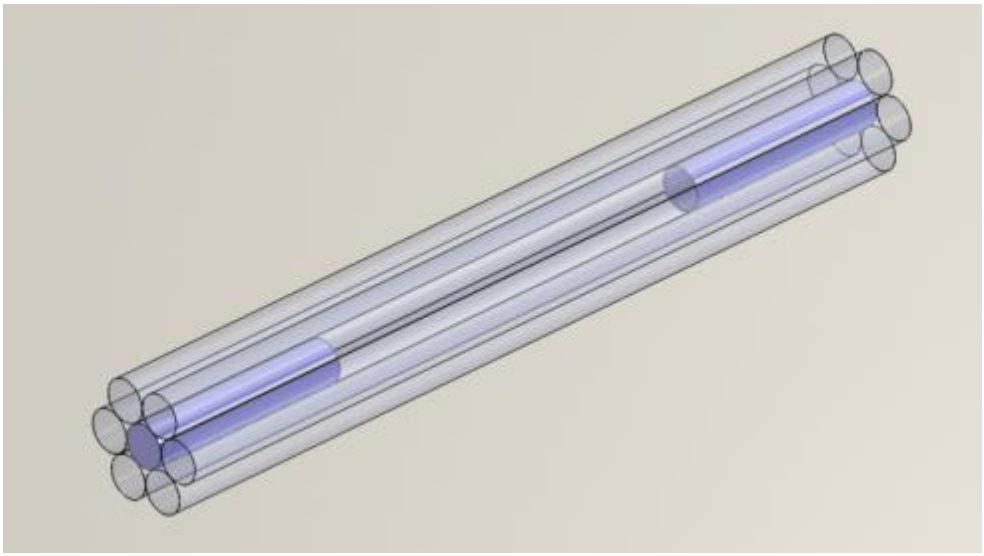

Figure 4-71: New structure for 7-rod Sapphire bundle

Difficulty in the sapphire bundle fabrication process arises from the bonding process. During fabrication of the bundle, contamination from the bonding process sometimes occurs around the core sapphire fiber. This bonding material on the core is shown in Figure 4-72 and contributes to transmission loss in addition making the splicing of the lead-in and lead-out fibers inefficient and of low quality.

Figure 4-72: Bonding material on the surface of Sapphire fiber

Breakage of the bundle after annealing of the bundle bonded with SiO_2 at 1600°C was also encountered. The breakage causes significant loss in the transmission of the bundle and was the main reason that the transmission of sapphire bundle was difficult to detect. As shown in Figure 4-73, there was significant light leakage out of the sapphire bundle due to the breakage of the

bundle. Figure 4-74 shows the transmission of the sapphire bundle when maximum gain was used in a trans-impedance amplifier.

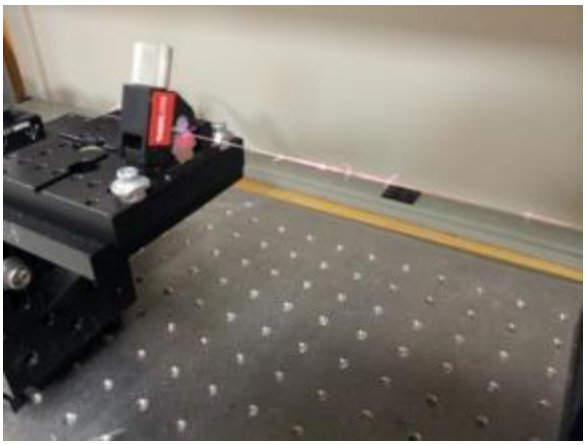

Figure 4-73: Transmission loss due to breakages in the bundle

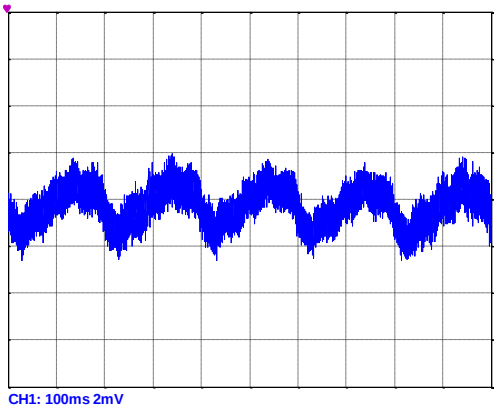

Figure 4-74: Transmission of Sapphire bundle with maximum gain in amp.

After analyzing the problems with the fabrication of the sapphire bundle, several fabrication methods were proposed and analyzed as detailed in this section.

Figure 4-75 shows one of the proposed fabrication methods. One difficulty with this structure is that there is insufficient space to adjust each rod when the bundle is fabricated. Some modifications were needed to eliminate this issue in the fabrication process. Figure 4-76 shows the second fabrication set-up using a funnel tube. The funnel tube was cut in half to ensure that space that the fabrication requires existed. Two 3-axis stages are used to control the position of the each guide funnel tube to ensure that the shape of the 7-rod bundle was maintained. Two additional 3-axis stages controlled the alignment of the two sapphire fibers in the bundle that were to become the core of the SPCF bundle. Controlling the size of funnel tube, while fabricating the tube posed significant difficulty along with alignment between two funnel tubes.

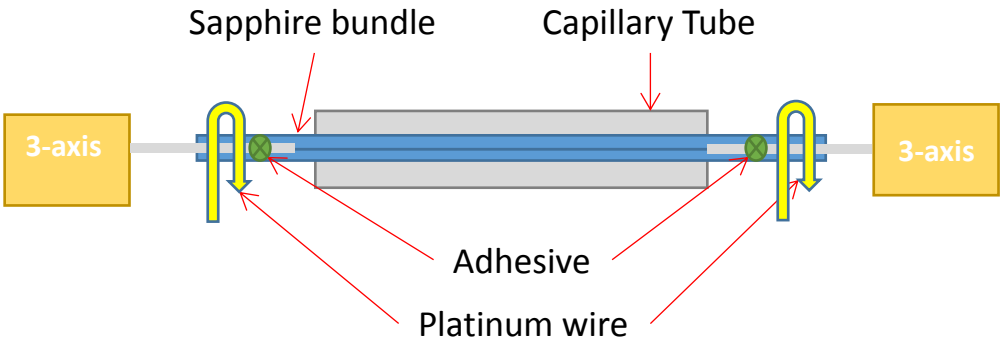

Figure 4-75: Proposed fabrication method

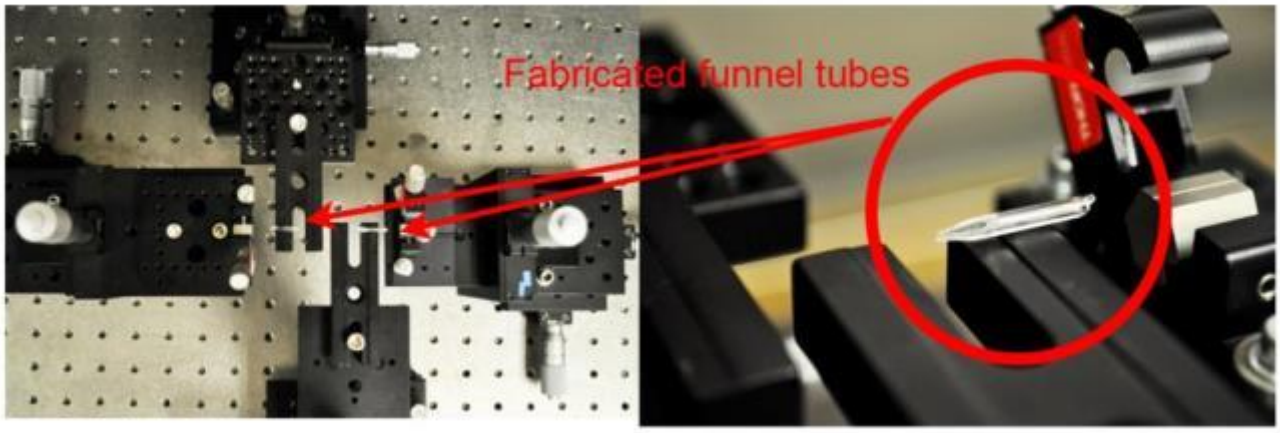

Figure 4-76: Modified fabrication method using funnel tube

In order to eliminate these problems, a third fabrication method was devised and constructed. In this method, a capillary tube with an I.D. of 230µm was polished down in cross section as shown in Figure 4-77. This fabricated capillary tube guided the structure while the sapphire bundle was fabricated in the translation stages. Two sapphire fibers were placed at the bottom of the fabricated capillary tube and two lead-in and lead-out core sapphire fibers were optically aligned to form the core air cavity. The other 4 Sapphire fibers were placed on top of the assembly. Fabrication of the Sapphire bundle was successful. However, the structure and fiber orientation could not be maintained while the platinum wire or adhesive was applied to the bundle.

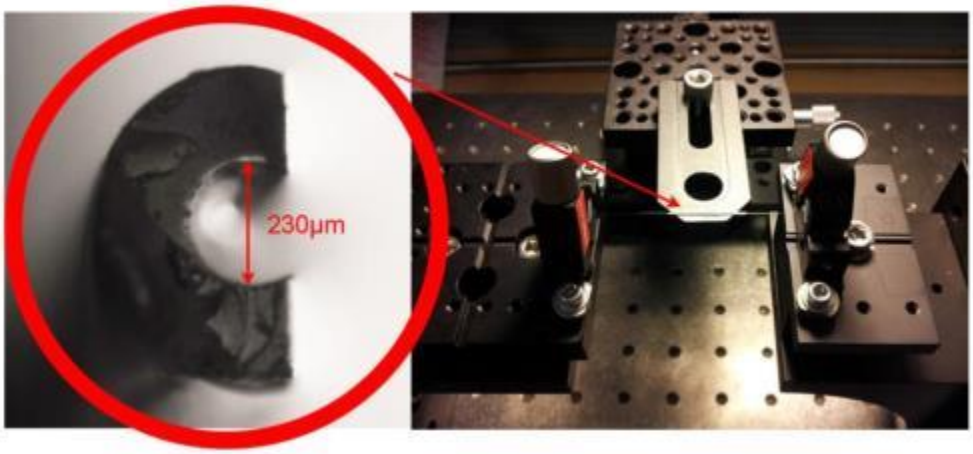

Figure 4-77: Modified fabrication method using capillary tube

In order to help in the assembling of the whole bundle together, a final fabrication method of sapphire bundle was proposed and constructed. Figure 4-78 shows the fabrication set-up using a funnel tube. One of the methods to assemble the bundle with this structure is to use a different center fiber than the outer fiber. By making a longer center rod in the structure, the center rod could be easily extracted after the bundle was fabricated. Platinum wire was applied first to guide the structure and alumina based adhesive was applied after tying with wire to hold the structure. After curing the adhesive for 2 hours, the center rod was extracted from the part where the adhesive was applied. A total of four ties and adhesive was applied on 5cm long sapphire bundle 1.25cm apart. Figure 4-79 shows the successful assembly of Sapphire bundle with an extracting center rod out of 7-rod bundle to make a 6-rod Sapphire tube. This 6-rod bundle was made with 70µm diameter of Sapphire fibers and the hollow hole in the bundle should be sufficient enough to insert 50µm diameter of sapphire fiber as the center fiber. In addition, an LED source with spectrometer will be employed in our sensor system in order to eliminate modal noise from the sapphire fiber.

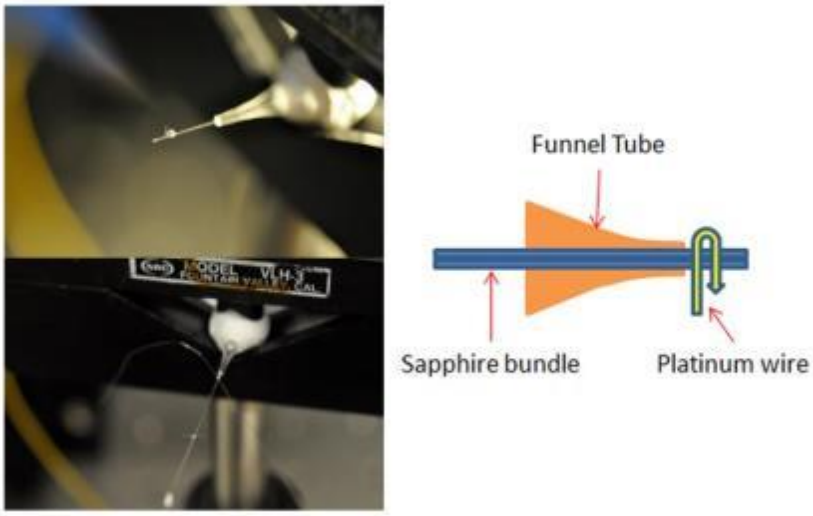

Figure 4-78: Final fabrication method using funnel tube

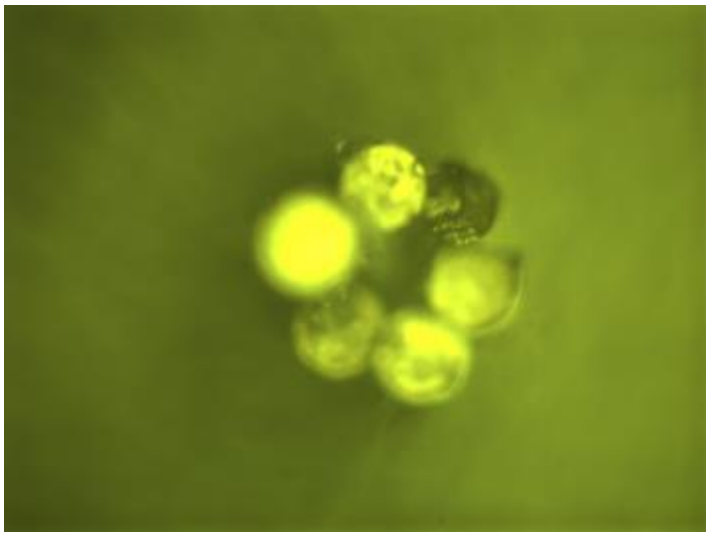

Figure 4-79: Cross section of successful assembly of 6-rod Sapphire bundle

4.5.2 Final Sensor Fabrication

The center-gapped sensor fabrication process was refined. In the initial assembly, platinum wire was used to secure the fiber bundle and preserve the center gap until more permanent bonding agents can be applied. Colloidal silica was used to bond the sensor, adding a drop at 1cm intervals along the sensor while omitting any bonding agent in the center gap region, then heat-treating the sample at 1600°C for 12 hours to encourage diffusion bonding between sapphire components. A second sensor using 70μm fiber was assembled and was bonded using the SiC dispersion for comparison.

In preparation of the center-gapped sensor construction, 70μm-diameter sapphire fiber was sectioned into six 2" long segments to form the outer hexagonal ring and two 4" long segments for the lead in and lead out fibers that form the center gap. Both ends of the lead in/out fibers were polished using 5μm and then 0.1μm diamond polish film to ensure parallel and optically smooth faces. Once the fiber segments were prepared, sensor fabrication was started. For construction using 70μm fibers, a glass funnel with a final inner diameter of ~220μm (Figure 4-80) was used to hold the bundled fiber and maintain the preferred geometry until the bundle can be secured. The funnel was mounted using a clamp (Figure 4-81), and five of the six outer ring fibers were inserted from the open end of the glass funnel. The first polished lead in/out fiber was inserted and pulled into position (the tip of the lead in/out fibers were colored with red marker to more easily distinguish from the outer fibers and ensure proper placement). At this point, a stereoscope was used to view the bundle at the funnel tip, and very fine tweezers push the lead in/out fiber into position at the center of the bundle. The final outer ring fiber was then slid in place from the narrow end of the funnel using the stereoscope and fine tweezers to ensure the geometry remained intact.

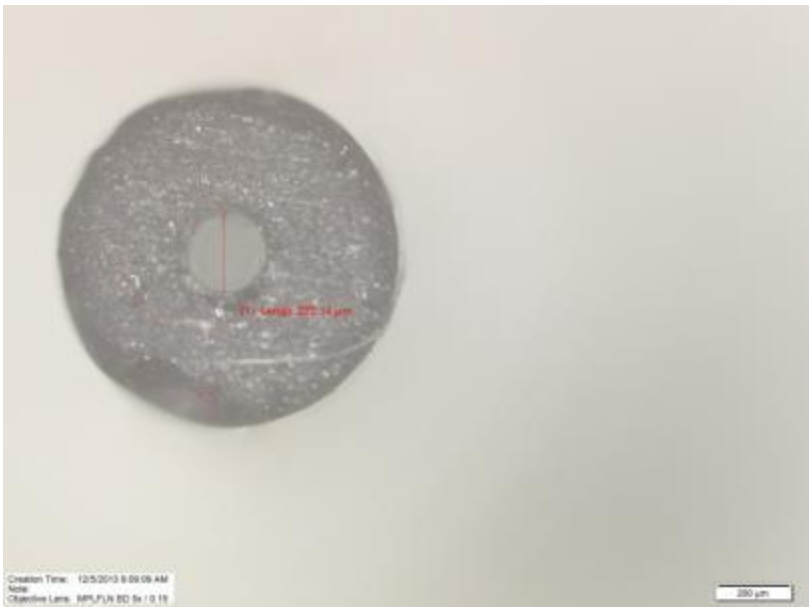

Figure 4-80: Glass Funnel with ~220µm Inner Diameter Maintains Bundle Geometry

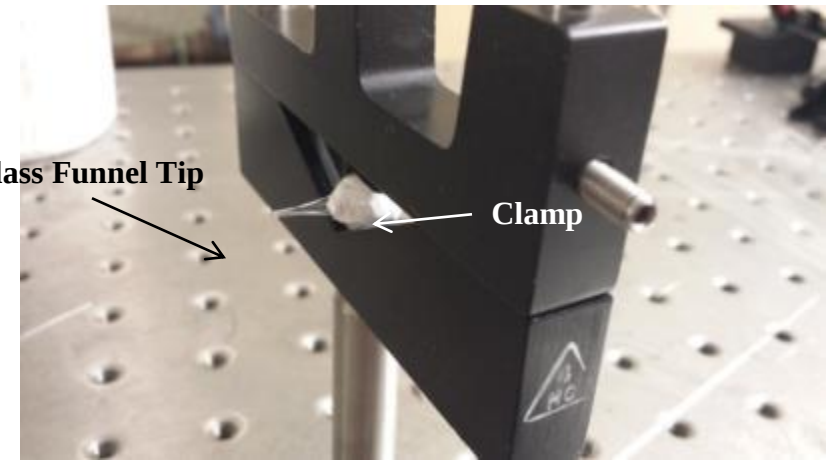

Figure 4-81: Glass Funnel and Clamp Hold Fiber Bundle during Assembly

Once the bundle was fabricated with the first lead-in/out fiber in place, the assembly was secured using fine gauge platinum wire (Figure 4-82 and Figure 4-83). A platinum wire tie was prepared around the tip of the glass funnel before fastening around the bundle to minimize danger to the fragile bundle during the tying (Figure 4-86). These ties were repeated approximately every half-centimeter from the bundle end to the center gap.

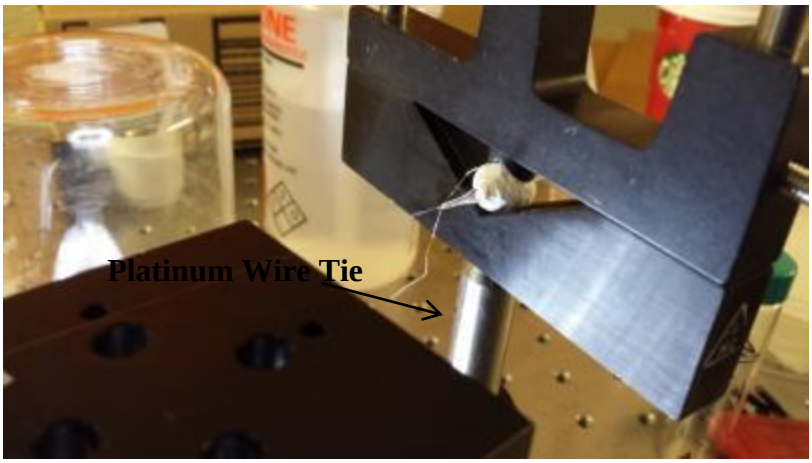

Figure 4-82: Macro View of Sensor Assembly with First Platinum Wire Tie

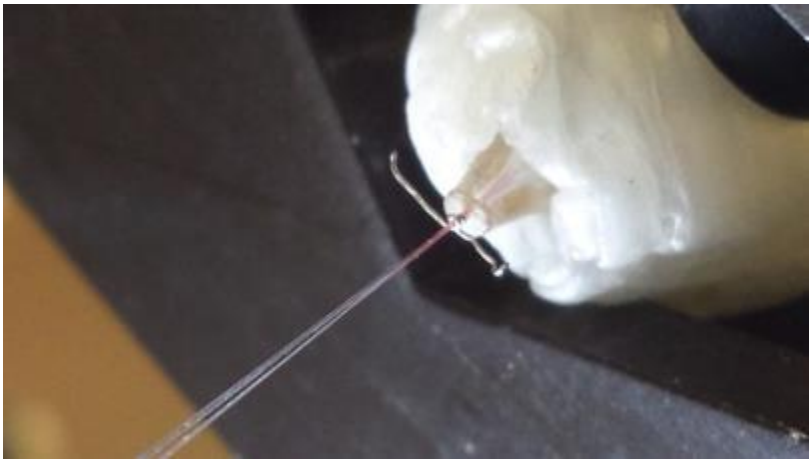

Figure 4-83: Zoomed View of First Tie (red color is marked tip of center fiber)

Once the first half of the sensor was fully secured, the bundle was further pulled through the funnel until it is in position for the insertion of the second lead in/out fiber, then attached to a stage to prevent movement (Figure 4-84). The second lead-in/out fiber was inserted from the wide funnel end and its position was checked using the stereoscope; this step was repeated until it was determined that the fiber was in the center position. Once the position of the final lead in/out fiber was verified, the bundle was secured using platinum wire in a similar manner. When all ties were made (Figure 4-85), the sensor was removed from the funnel and washed with acetone to remove the red marking, then stored in a glass tube to minimize movement before permanent bonding can take place. Permanent bonding on the first sensor was completed by placing a drop of colloidal silica along the length of the sensor at 1cm intervals, omitting the center gap region. Heat treatment at 1600°C for 12 hours encourages diffusion of the SiO_2 and Al_2O_3, creating a strong bond between sapphire components. At this point the sensor was ready for optical testing to verify alignment, correct transmission, and gas sensing ability.

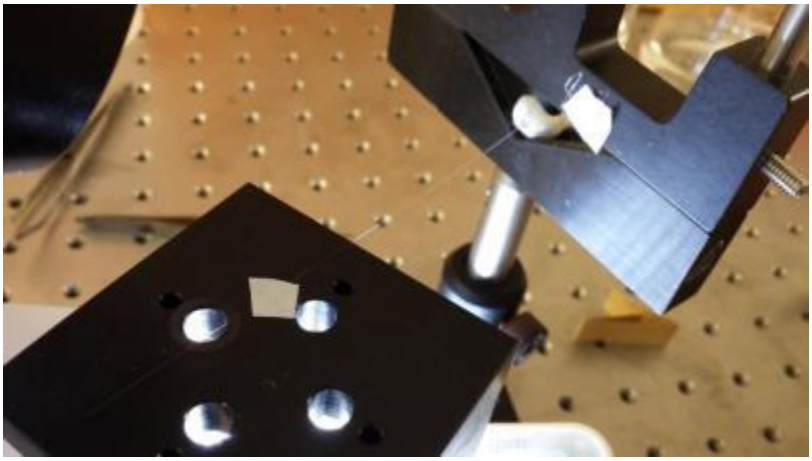

Figure 4-84: Sensor Assembly Ready for Second Lead in/out Fiber Insertion

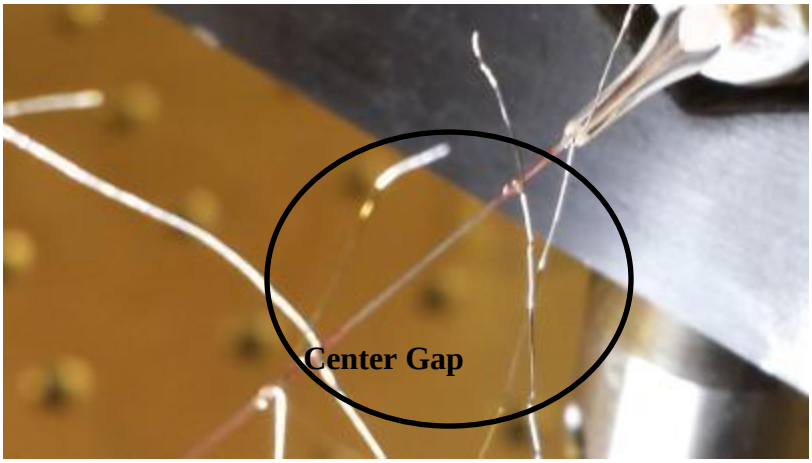

Figure 4-85: Completed Sensor Assembly with Center Gap in View

Figure 4-86: Sensor Assembly through Stereoscope for Scaled Reference

4.5.3 Analysis on 6-rod Center Gap Sapphire Bundle

After fabrication of the 6-rod sapphire bundle, 50μm diameter lead-in and lead-out sapphire fibers were polished and spliced with SM and MM fibers. These fibers were inserted into the 6-rod sapphire bundle using 3-axis stages leaving a center gap between the lead-in and lead-out fibers. Figure 4-87 shows the 6-rod bundle with fabricated center gap between the lead-in and lead-out fibers. After careful adjustment with the 3-axis stages between lead-in and lead-out fiber, the output signal from 6-rod bundle was optimized and a basic transmission and gas absorption test was performed.

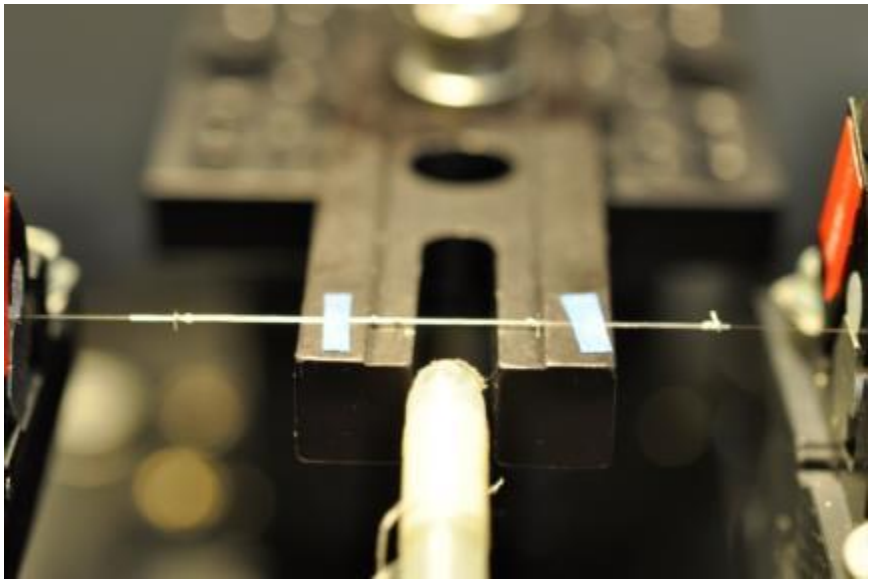

Figure 4-87. 6-rod sapphire bundle with lead-in and lead-out fiber

4.5.4 Analysis on 6-rod sapphire bundle with CTS

Figure 4-88 shows the schematic of sapphire bundle structure using a CTS and oscilloscope. A trans-impendence amplifier was also used with a photo diode. Figure 4-89 show the gas absorption spectrum from the 6-rod sapphire bundle with an air cavity of 1cm. Figure 4-90 show the gas absorption spectrum from the 6-rod sapphire bundle with air cavity of 3cm. From both figures, gas absorption was clearly observed from wavelength 1520nm to 1545nm. This gas absorption spectrum can be improved by averaging data from the scope and eliminating modal noise from the structure. Improvement on signal processing and modal noise will be demonstrated in the next section.

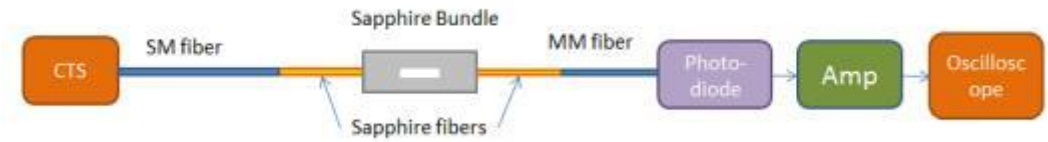

Figure 4-88. Schematic of gas sensing structure using white CTS and oscilloscope

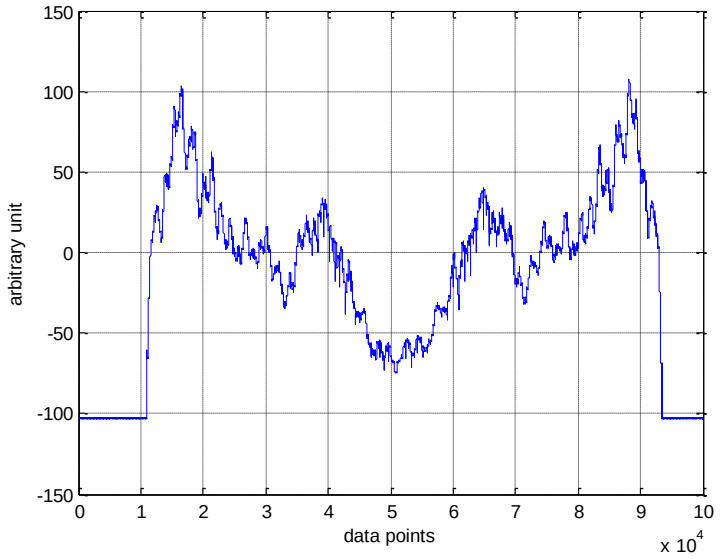

Figure 4-89. Gas absorption test of 6-rod sapphire bundle (air cavity=1cm) with Acetylene gas

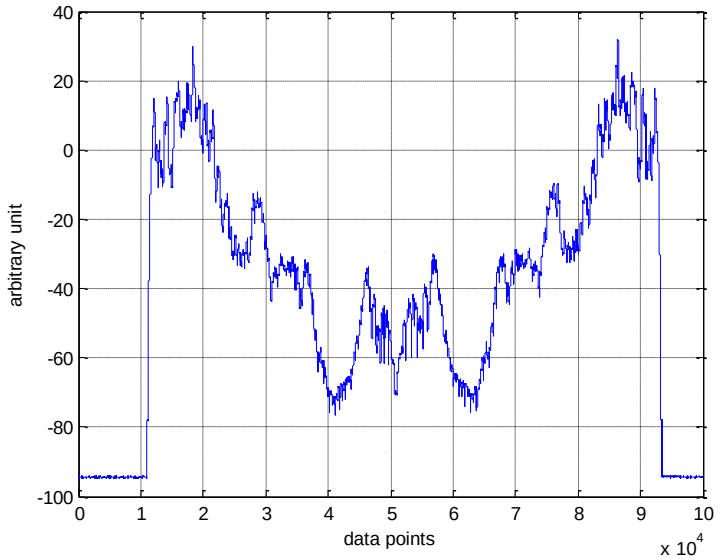

Figure 4-90. Gas absorption test of 6-rod sapphire bundle (air cavity=3cm) with Acetylene gas

4.5.5 Analysis on 6-rod Sapphire Bundle with White Light Source

Analysis of the center gap sapphire bundle with the CTS shows that the system experienced significant modal noise from the coherent light source of the CTS. The problem is almost exclusively confined to the use of laser sources with narrow linewidth and a long coherence length. On the other hand, LEDs or white light sources are highly incoherent light sources with broad spectra. In this section, the CTS was replaced with a white light source to

reduce the modal noise as shown in Figure 4-91. First, an Ando OSA was used as the spectrometer to measure the output of the sensor structure.

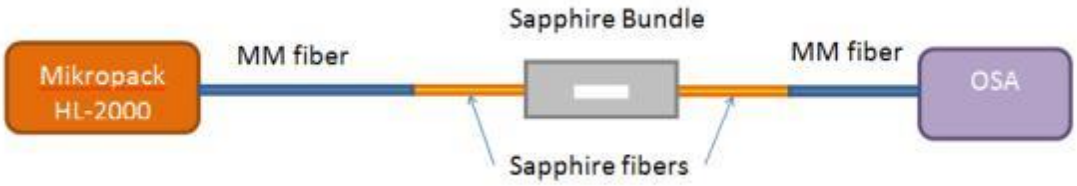

Figure 4-91. Schematic of gas sensing structure using white light source with OSA

Figure 4-92 shows the output spectrum from the Ando OSA between the wavelengths of 1510nm to 1540nm where acetylene gas should have the most gas absorption peaks. As shown in Figure 14, gas absorption peaks could not be clearly observed due to the resolution of the OSA. The highest resolution of the OSA is 50pm while the width of each gas absorption peak is around 100pm. Due to insufficient data points in OSA, meaningful gas absorption could not be observed.

Figure 4-92. Output spectrum using white light source and Ando OSA

4.5.6 Analysis of power losses on fiber pigtails(SM/MM to sapphire fiber)

When the center gap sapphire bundle sensor was tested with a white light source and the OSA, more than 25dB of losses due to the lead-in and lead-out fibers were observed. This was observed by aligning two pigtails together with smallest possible air cavity between them. In this research period, analysis of the power losses on these pigtails was performed. First, surface quality of sapphire fibers was evaluated by microscope. There were several defects and contamination on the sapphire fibers as shown in Figure 4-93. In order to remove these defects from sapphire fiber, sapphire fibers were placed in 5% and 35% hydrochloric acid for more than 24 hours. Unfortunately, these defects and contamination remained on the sapphire fiber after

treating with hydrochloric acid. The manufacturer of these sapphire fibers was contacted and did not provide sufficient information about the fibers. The thinnest fiber they have transmission data on is 100 um. They claimed that for a 100 cm length it's 60% or better at 633 nm with an input NA of less than 0.10.

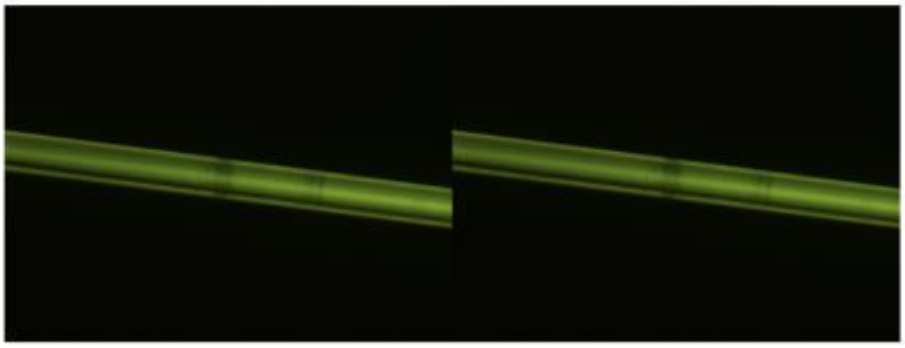

Figure 4-93. Defects and contaminations on sapphire fibers

Secondly, the splicing point between the sapphire fiber and pigtail fiber needed to be investigated since high losses were observed when a visible red laser was employed with the sapphire bundle sensor to observe possible leaks of the input source. In order to investigate the power losses on the splicing point, new lead-in and lead-out fibers were fabricated and their power monitored in each step of the fabrication. Figure 4-94 show a schematic of the monitoring method while fusion spicing between the fiber pigtails and sapphire fibers. As described in the previous report, GRID MM fiber was used as a binding material between set index SM or MM fiber pigtails and the sapphire fiber. Even though 50~60µm long GRID MM fiber usually used as binding material, a total of 310µm of GRID MM fiber was used. A length of 260µm of GRID MM fiber was used as quarter-pitch collimator to improve transmission between fiber pigtails and sapphire fibers.

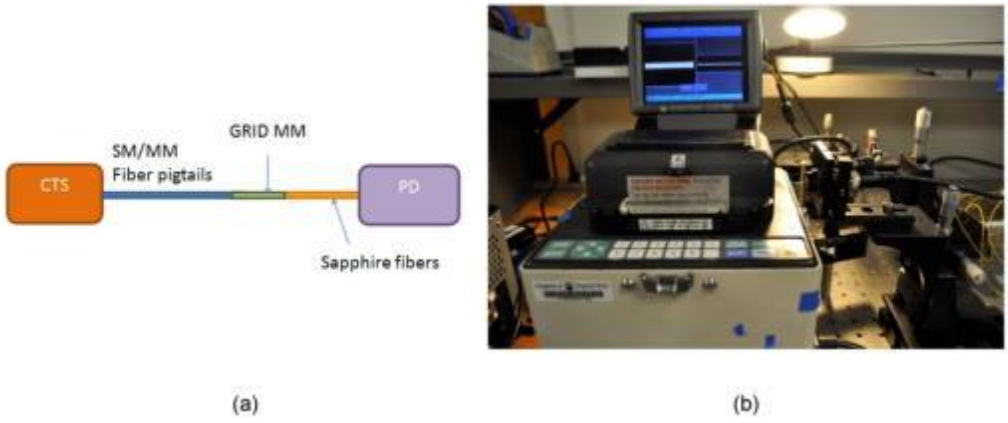

Figure 4-94. (a) Schematic and (b) set-up of monitoring method on fusion splicing method between fiber pigtails and sapphire fiber

Figure 4-95 shows the output power observed in each step of the fabrication between the SM and sapphire fibers. SM fiber (red line), SM fiber spliced with 310µm long GRID MM fiber (blue line), before splicing them with sapphire fiber (green line) and after splicing (black line) were measured. The splicing losses can be estimated around 3dB loss in this case. Larger loss was observed during fusion splicing. Angular displacement between the two fibers could be a cause of such large loss during the fabrication. It was important to monitor the power losses during this fabrication and to produce an optimized splicing condition.

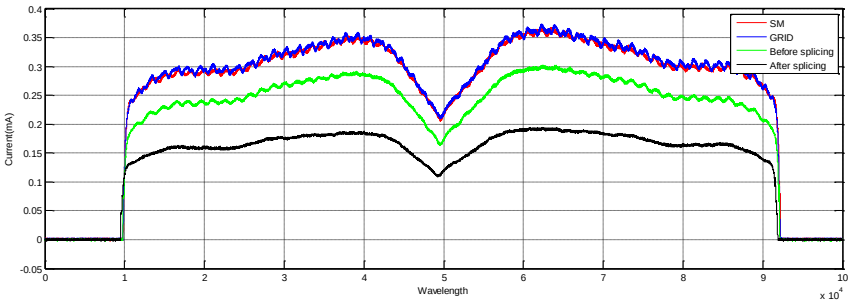

Figure 4-95. Measurements of SM fiber (red line), SM fiber spliced with 310µm long GRID MM fiber (blue line), before splicing them with sapphire fiber (green line) and after splicing (black line).

Figure 4-96 shows the output power observed in each steps of fabrication between the MM and sapphire fibers. Step index MM fiber (red line), MM fiber spliced with 310µm long GRID MM fiber (blue line), before splicing them with sapphire fiber (green line) and after splicing (black line) were measured. The splicing losses can be estimated around 1dB loss in this case.

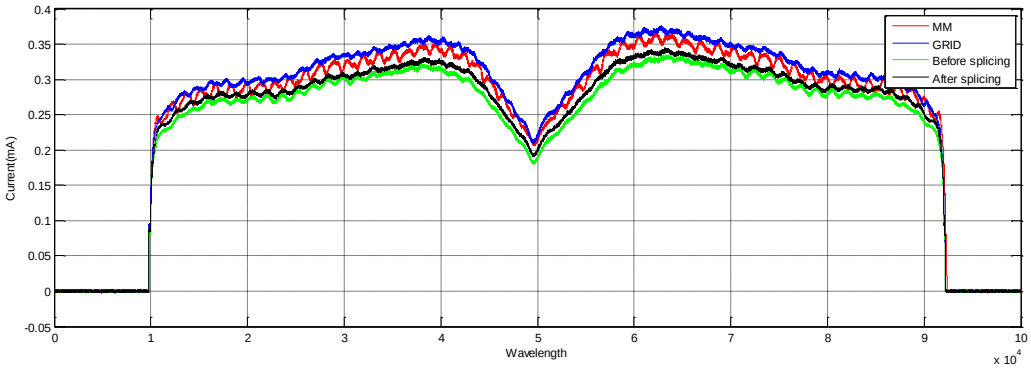

Figure 4-96. Measurements of MM fiber (red line), MM fiber spliced with 310µm long GRID MM fiber (blue line), before splicing them with sapphire fiber (green line) and after splicing (black line).

Finally, newly fabricated lead-in and lead-out fibers were aligned together and the output power was measure to compare with previous measurements that showed a 25dB loss. A 15dB loss was observed by using the newly fabricated pigtails, showing a 10dB improvement in the pigtails by using quarter-pitch collimator and monitoring the splicing process.

4.5.7 Fabrication of Sapphire Bundle Sensor and Gas Chamber

After successfully improving 10dB on in the fabrication of the lead-in and lead-out fibers connections, the center gap sapphire bundle sensor was fabricated with new lead-in and lead-out fibers. Figure 4-97 shows the set-up to fabricate sensor with precision alignment of the center sapphire fiber spliced with pigtails. After alignment of the two center sapphire fibers, high temperature adhesive was applied to maintain the alignment and position.

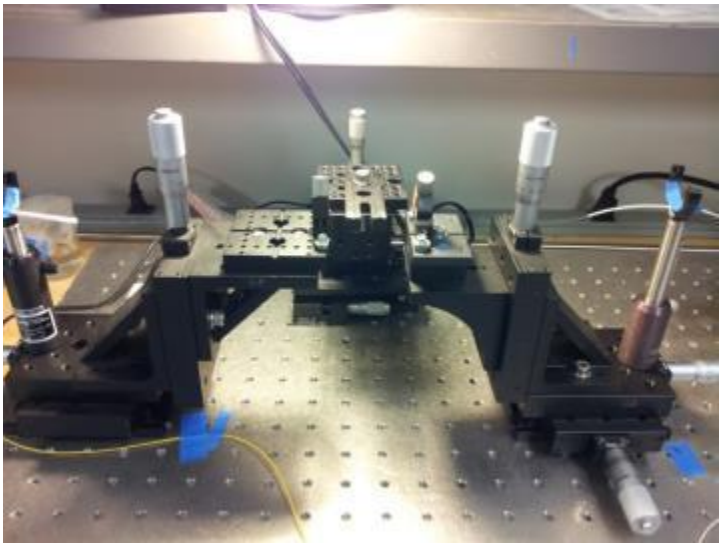

Figure 4-97. Fabrication of sapphire bundle sensor with precision alignment of center sapphire fiber

The fabricated sapphire bundle sensor was placed in a fiber holder for a gas chamber. Figure 4-98 shows the final assembly of the gas chamber and the sapphire sensor. One of outlets on each side was used to insert the fiber pigtails and other outlets were used for introducing gases. A vacuum pump was used to evacuate the gas chamber prior to gas insertion. In this experiment, an unknown concentration of acetylene gas was used to show the gas detection ability of center gap sapphire bundle sensor.

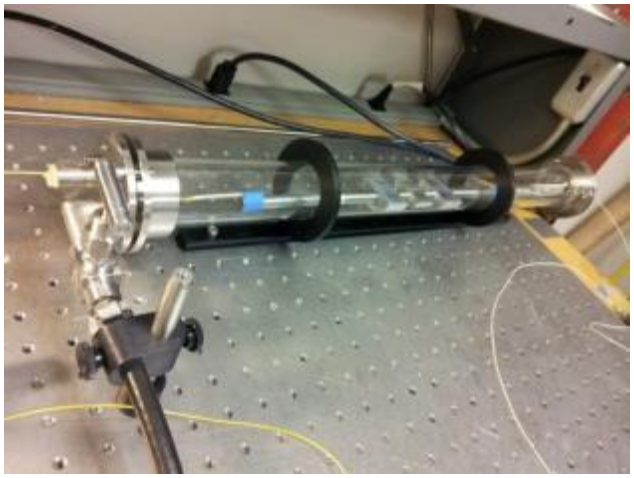

Figure 4-98. Final assembly of gas chamber and sapphire bundle sensor in it

Figure 4-99 shows the gas absorption peaks between the wavelengths of 1530nm and 1540nm. The gas absorption peaks are relatively sharper than the previous measurement data. The main reason in the improvement of signal quality is the use of gas chamber to eliminate noise from the environment and to provide a consistent concentration of the gas.

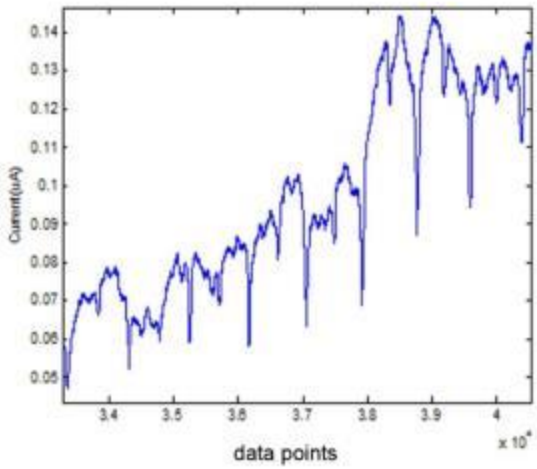

Figure 4-99. Absorption peaks between 1530nm to 1540nm

After signal processing, including low pass filtering and averaging the data, the noise could be further reduced as shown in Figure 4-100. This single gas absorption line at 1532nm should be good enough to calculate the concentration of gas.

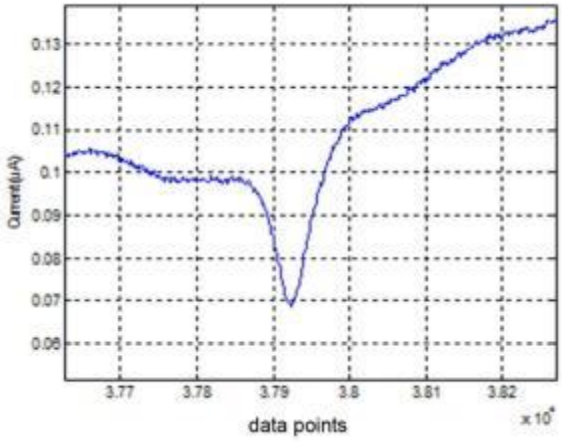

Figure 4-100. Gas absorption peak at 1532nm

In addition to the gas detection test, the wave guiding effect of the sapphire bundle was measured and compared with free space transmission (air cavity=1cm). Figure 4-101 shows the transmission test through sapphire bundle (blue line) and free space (red line). As shown in the figure, the sapphire bundle gives an approximately 20dB improvement on transmission.

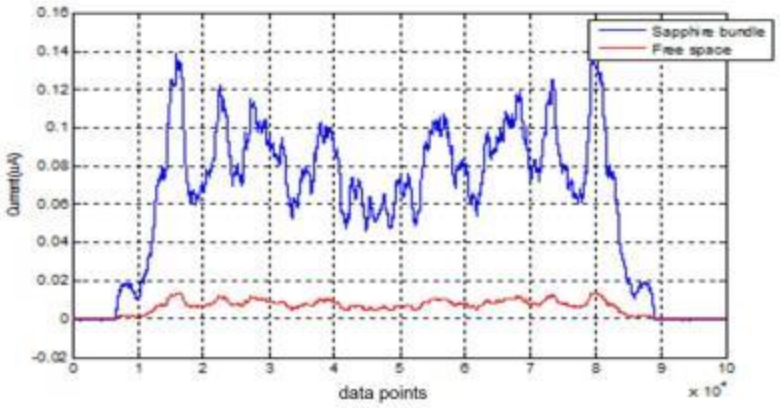

Figure 4-101. Transmission test through sapphire bundle (blue line) and free space (red line)

4.5.8 Modification to Gap Sensor Fabrication

Figure 4-102 shows the fabrication set-up that uses a funnel tub. This fabrication method requires distinguishing a center rod from others. By making a longer center fiber in the structure, the center rod can be extracted after the outer bundle was fabricated. Platinum wire was applied first to guide the structure and an alumina based adhesive (Aremco ceramabond 671) was applied to hold the structure. After curing the adhesive for 2 hours, the center rod was extracted from the portion where the adhesive was applied. A total of four ties and adhesives application 1.25cm apart were completed along the 5cm sapphire bundle length. This 6-rod bundle was made with 70µm diameter of sapphire fibers and hollow hole in the bundle is sufficient to insert a 50µm diameter of sapphire fiber as the center fiber.

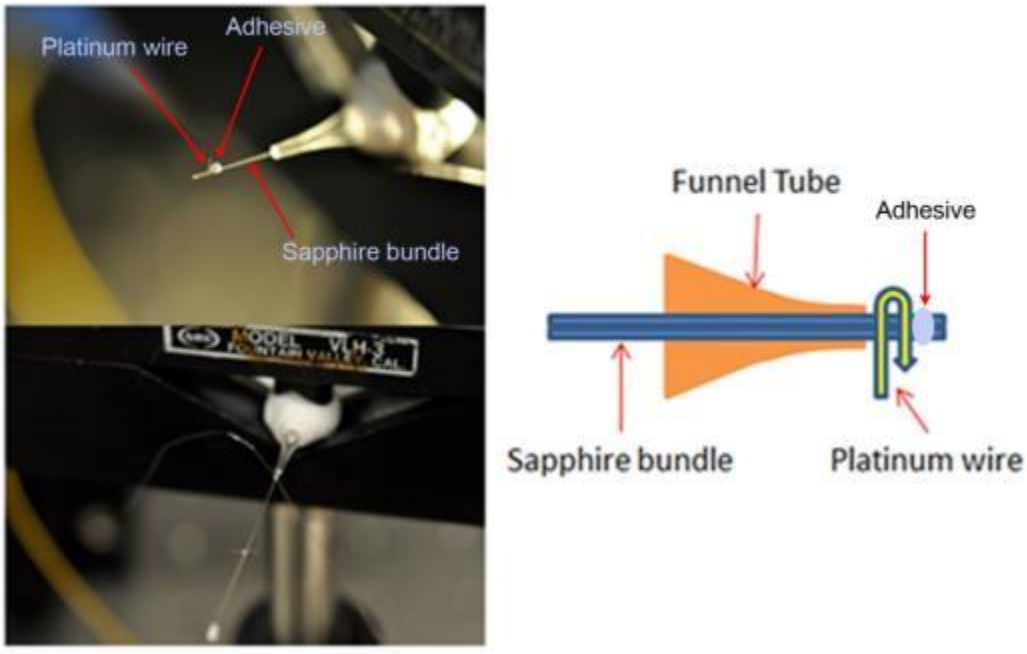

Figure 4-102: Fabrication method using funnel tube

4.5.9 Analysis of Sapphire Bundle in Wavelength of 1520nm to 1570nm

Figure 4-103 shows the schematic of a sapphire bundle sensor structure using a CTS and oscilloscope. A trans-impendence amplifier was used with a photo diode to amplify the output spectrum. Figure 4-104 show the gas absorption spectrum from 7-rod sapphire bundle with an air cavity of 1cm. As shown in Figure 4-104, gas absorption of acetylene was observed in the wavelength range from 1520nm to 1545nm. This gas absorption spectrum can be improved by taking average data from the scope and eliminating modal noise from the structure.

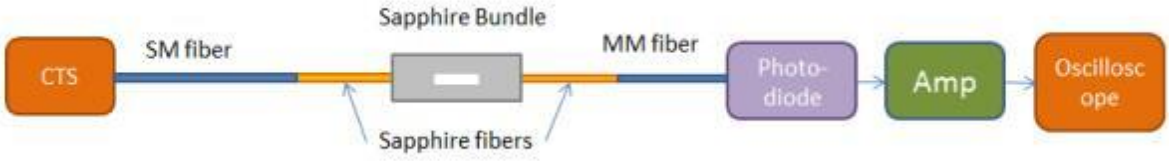

Figure 4-103: Schematic of gas sensing structure using white CTS and oscilloscope

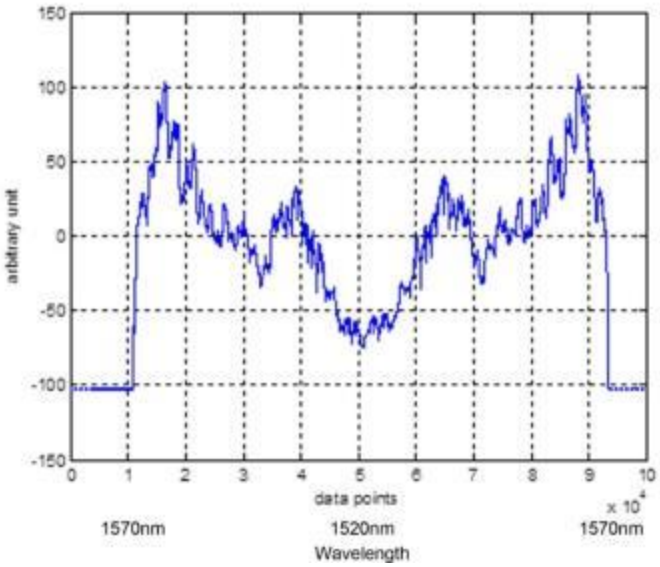

Figure 4-104: Gas absorption test of 7-rod sapphire gap sensor (air cavity=1cm) with acetylene gas

Figure 4-105 shows the gas absorption of the sapphire gap sensor at different gas concentrations. The gas absorption spectrum in this figure was measured without any signal processing. The background is fairly smooth and the gas absorption peaks are sharper than previous measurements. Gas sensing ability and the lowest gas concentration detectable can be improved by optimizing the air cavity length of the sensor.

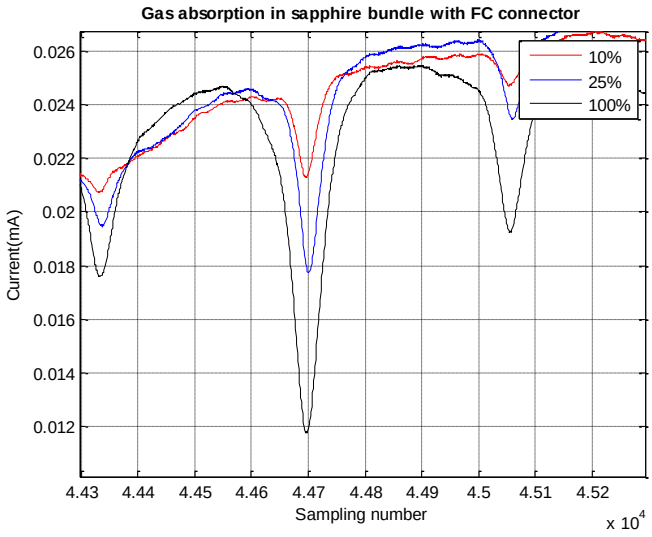

Figure 4-105: Gas absorption of sapphire bundle at different gas concentrations.

4.6 Development of Long Wavelength Fiber Interrogation Instrumentation

4.6.1 Tunable Quantum Cascade Laser (QCL)

Quantum cascade lasers (QCL) are a semiconductor laser which utilizes quantum wells to usually emit mid-infrared light. The laser operation of the QCL is not between different electronic bands but between states within a given quantum well. Figure 4-106 shows a simple schematic of the gain region of a quantum cascade laser. An electron that enters in the gain region undergoes a transition between two sublevels of that quantum well (blue arrow), then undergoes a transition to the lowest sublevel. The transition to the lowest sublevel is non-radiative (red arrow). The electron then tunnels into the upper level of the next quantum well (gray arrow). A QCL can achieve a higher optical gain and multiple photons per electron by employing several quantum wells in a series.

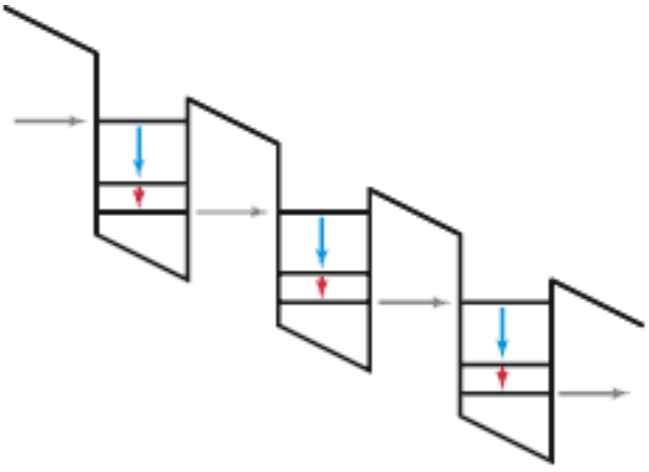

Figure 4-106: Schematic of the gain region of a quantum cascade laser [http://www.rp-photonics.com]

Tunability of a QCL laser can be quite broad. There are two methods used to tune a QCL, either by using distributed feedback (DFB) or an external cavity. The DFB is limited to a few wavenumbers while an external cavity QCL can be tuned to a few hundreds of wavenumbers.

Figure 4-107 shows a wavelength tunable external grating cavity quantum cascade laser system consisting of one QCL. The system provides wavelength coverage from 3.9μm to 4.2 μm. The QCL is operated in a quasi-CW mode with 200~500 ns pulses with a repetition rate of 500 kHz~2 MHz and a duty cycle of 50%. Figure 4-108 shows the specs of the QCL laser we purchased for use in the long wavelength detection system for milestone 5.

Figure 4-107: MonoLux-42 Laser Head

Figure 4-108: Specs of MonoLux-42 QCL laser

Tunable Quantum Cascade Laser	
Operation	• QCW operation with the laser head at room temperature (50 ns-500 ns micropulses at a micropulse repetition rate of 1 MHz-2 MHz) • Square wave macropulse modulation up to 10 kHz for lock-in detection • CW operation by selecting 100% duty cycle (optional)
Wavelength	• User specified center wavelength (AA) • Available center wavelengths are 3.8 μm, 4.1 μm. 4.5 μm, 4.8 μm, 6.3 μm, 6.8 μm, 7.3 μm, 8.5 μm, 9.5 μm and 10.2 μm.
Output spectrum	• Tunable over the gain bandwidth of the QCL
Tuning Speed	• 100 ms for entire tuning range for the laser
Tuning mode	• Continuous and repeated scans over the entire tuning range • Step and scan to any wavelength within the tuning range of the QCL (selected in the operating program on a laptop computer) • Scan over selected tuning range with selected step size and selected scan speed
Power output	• Average power output of 500 mW at the center of each QCL tuning curve for a duty cycle of ~ 50% (wavelength dependent)
Power Output Stability	• ±3% pulse-to-pulse; ±2 % average power over hours
Pulse trigger	• Internal or external; In external mode any pulse repetition sequence can be generated within 50% maximum duty cycle
Output linewidth	• < 2 nm (<0.3 cm^{-1}) when operated in QCW mode
Output beam	• Collimated with beam divergence of < 5 mrad
Output beam quality	• Nearly diffraction limited (TEM_{00})
Wavelength Accuracy	• Better than 0.3 cm^{-1}
Wavelength repeatability	• ± 0.3 cm^{-1} unidirectional
Cooling	• Passively cooled
Guiding beam	• Red 640nm, 4mW laser aligned with IR beams to assist optical arrangement (optional)
Physical Details	• Size: 12 cm (W), 4.5 cm (H), 13 cm (D) • Weight: < 0.5 kg
Computer Interface	• USB
Computer Requirements	• Windows XP or later computer with USB 2.0 port • Software controls laser operation and allows user to select scan mode for as well as enable/disable the laser

4.7 Long Wavelength Gas Detection System Designs

Based around the MonoLux-42 laser with a nominal wavelength at 4.15μm, a number of designs were proposed and specified for the long wavelength gas detection system. These designs are classified by their particular combination of coupling and detection. The coupling is either free-space or fiber-based, while the detection is either transmission or reflection. The naming convention for the proposed systems is shown in **Error! Reference source not found.**.

Table 4-8 : Naming convections for long wavelength fiber interrogation system designs

	Naming Convention for Proposed Long Wavelength System Designs	
Detection →	Transmission	Reflection
Coupling ↓		
Fiber-Based	FB-T	FB-R
Free-Space	FS-T	n/a

A common requirement of these designs is to focus light from the free-space laser into mid-IR single mode fiber, a porous silica tube, or a sapphire bundle. This requirement is met by using a compact, ultra-stable micropositioner in the form of a custom-built fiberport which is shown in Figure 4-109: Fiberport for coupling QCL output into optical fiber components. The fiberport enables five degrees of freedom plus rotational adjustment. Inside the fiberport is an infrared lens at whose focal point resides an FC/APC connection hub. The lens is a geltech aspheric lens with 11mm focal length and numerical aperture (NA) of 0.18. The 11mm focal length defines the separation distance between the lens and connector hub inside the fiberport.

To maximize coupling, the lens NA was chosen to be slightly less than the NA of the mid-infrared (MIR) single-mode fiber (SMF) given for ZrF_4-based fiber as 0.2. This NA is lower than that expected for either the porous silica tube or sapphire bundle. Therefore, the lens automatically satisfies focusing constraints for coupling into the porous silica tube and sapphire bundle.

Figure 4-109: Fiberport for coupling QCL output into optical fiber components

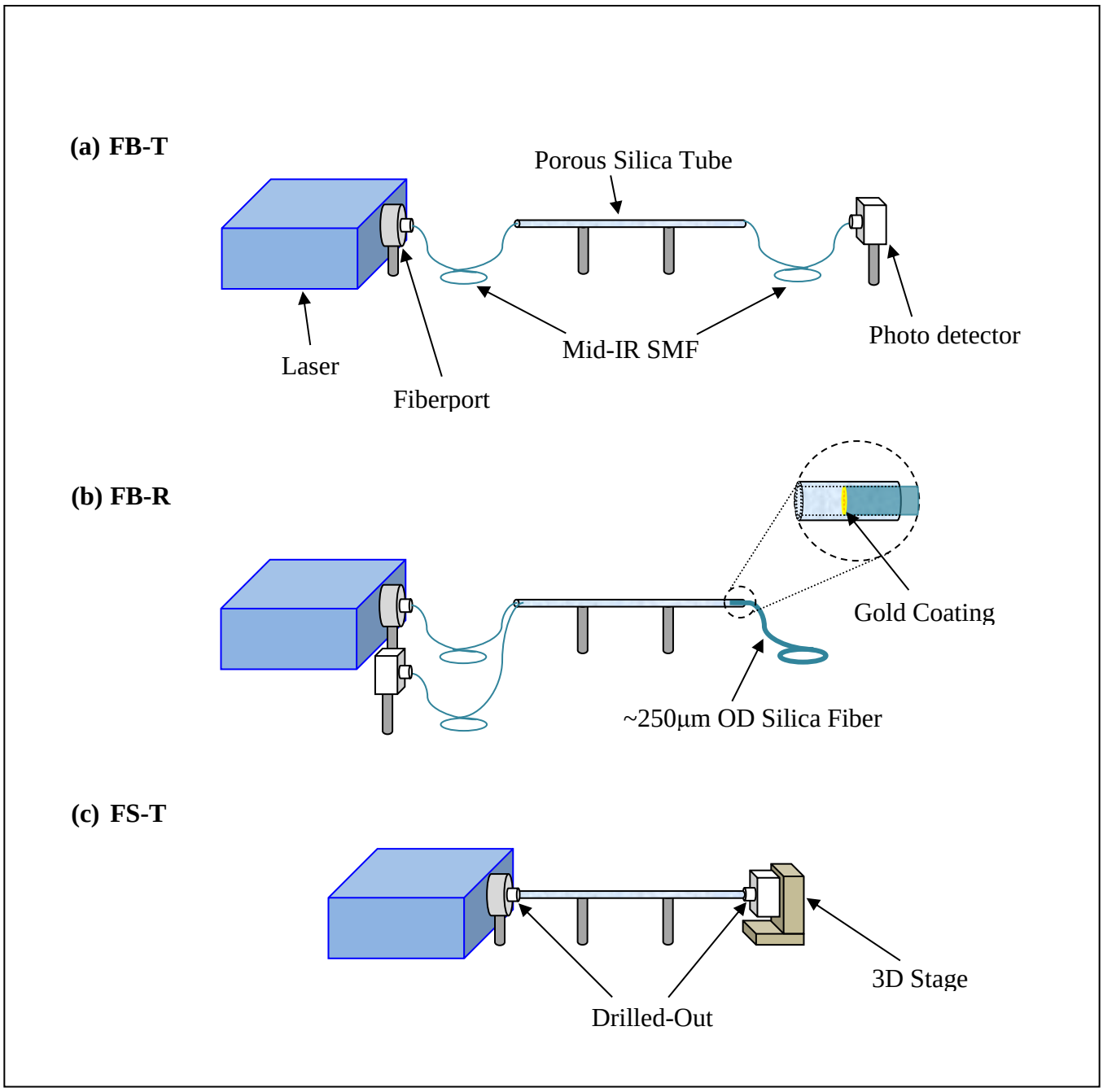

Figure 4-110: Diagrams of the long wavelength fiber interrogation system designs

The fiber-based designs of the long wavelength gas detection use the bare end of an MIR SMF pigtail leading out from the fiberport to excite the porous silica tube or the sapphire bundle. In the transmission design shown in Figure 4-110, another MIR SMF pigtail collects light at the opposite end of the tube or bundle and connects to an adapter at the face of the photo detector (PD). In the reflection design in Figure 4-110, the light collection pigtail is changed to the same side as the excitation and a reflector is introduced at the far end of the tube or bundle. The reflector comprises a large diameter silica fiber, with an outer diameter (OD) of ~250µm that is cleaved and coated with gold. Using a reflection-mode, fiber-coupled system is attractive

because the optical path length through the gas is doubled, thus, the potential gas absorption signal is also doubled.

The free-space transmission design in Figure 6.c of the long wavelength fiber interrogation system does not use SMF fibers for coupling. Instead, the design proposes drilling out the steel ferrule of two FC/APC connectors to a diameter that will accommodate either the porous silica tube or sapphire bundle. These hollowed connectors can be fitted to the fiberport and adapter-mounted PD, such that the tube or bundle can be situated between them in a line-of-site geometry of the laser and PD. The PD may be seated on a 3D stage to maximize coupling alignment. The designs of the fiber integration system that have been developed and are shown in Figure 4-110 are based around the QCL that was purchased and will be deployed as best suits the demands of the optical sensor used.

4.7.1 Long Wavelength System & Signal Processing

The AC-coupled detector is designed to detect transient optical signals. This design eliminates many unwanted slowly-varying noise components from interfering with the desired signal. This is achieved by modulating the input laser light using a chopper, a device with fan blades that rotate at a precise rate to "chop" or periodically interrupt the laser light. This chopping action is said to modulate the laser input. The effect of this modulation is equivalent to rapidly turning the laser on and off. This strobe action increases the speed at which signal fluctuations occur since the fluctuations are proportional to the laser intensity at any given time. So, the increased rate of signal variation separates them from unwanted slowly-varying noise components.

The chopper creates a periodic output signal whose amplitude is proportional to the incident light. A dependable algorithm had to be made to estimate the peak-to-peak amplitude of the photodetector output. Certain approaches that did not work included using the magnitude of the analytic signal, low-pass filtering the power signal, integration of the power signal, and one-sided amplitude retrievals. In hindsight, these techniques all may all have been adversely affected by the positive offset of the photodetector output. Despite their poor initial performance, these techniques may be worth revisiting when trying to reduce acquisition time.

Once a consistent output was established, full bandwidth sweeps were performed (Figure 4-111) and compared versus the tuning characteristic supplied by the manufacturer (Figure 4-112). From Figure 4-111, in blue, the output demonstrated highly oscillatory but periodic behavior.

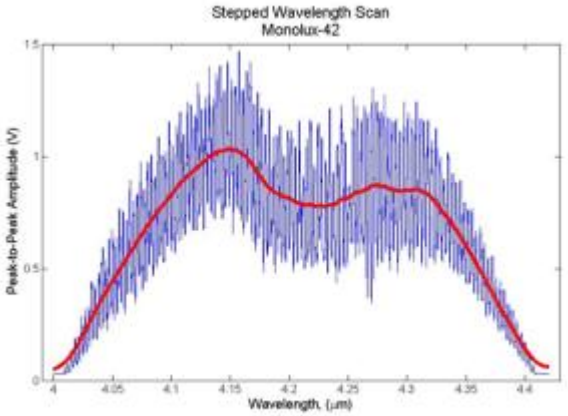

Figure 4-111. Measured laser tuning characteristic: Peak-to-Peak Amplitude vs Wavelength

After running the data through a low-pass filter, the tuning characteristic demonstrated from the manufacturer was recovered as shown in red. This indicated that an optical component in the system was creating etalon. The fringes cycled about every 3.3nm. The fringes actually stemmed from the reflection filter, which does not have anti-reflection coating on the back side. The fringe period is approximated by the formula, $\frac{\lambda_o^2}{2nd} = \frac{(4200nm)^2}{(2 \cdot 2.3 \cdot 10^6 nm)} = 3.84nm.$

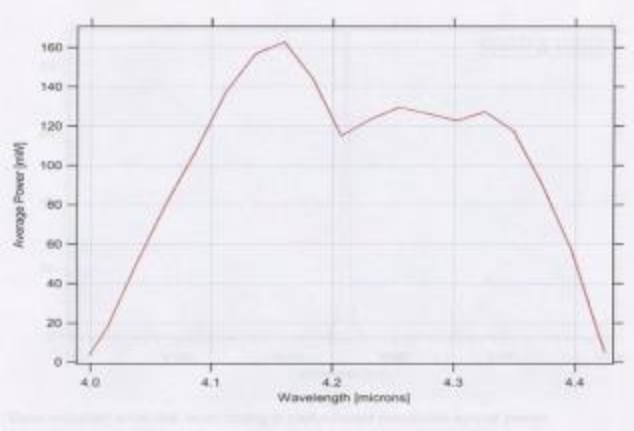

Figure 4-112. Manufacturer's tuning characteristic: Average Power vs Wavelength

Here *n* and *d* is the refractive index and thickness respectively of the filter. The filter as the fringe source was confirmed by rearranging the setup using a 50mm prism to reflect a portion of the beam toward the detector. The updated result, in Figure 4-113 on the next page, shows the effect of removing the filter. The fast oscillation fringe with period 3.3nm is gone. More importantly, however, there is the first observation of absorption lines from CO_2 occurring between 4.2-4.35μm. The lines correspond well specifically with proprietary data from Panalytica and generally with HITRAN database records. There is no doubt about the correspondence of these absorption lines to the gas of interest. Since CO_2 is approximately 500ppm in the atmosphere, the advantage of this spectral window for gas detection is clearly demonstrated by the depth of these absorption lines.

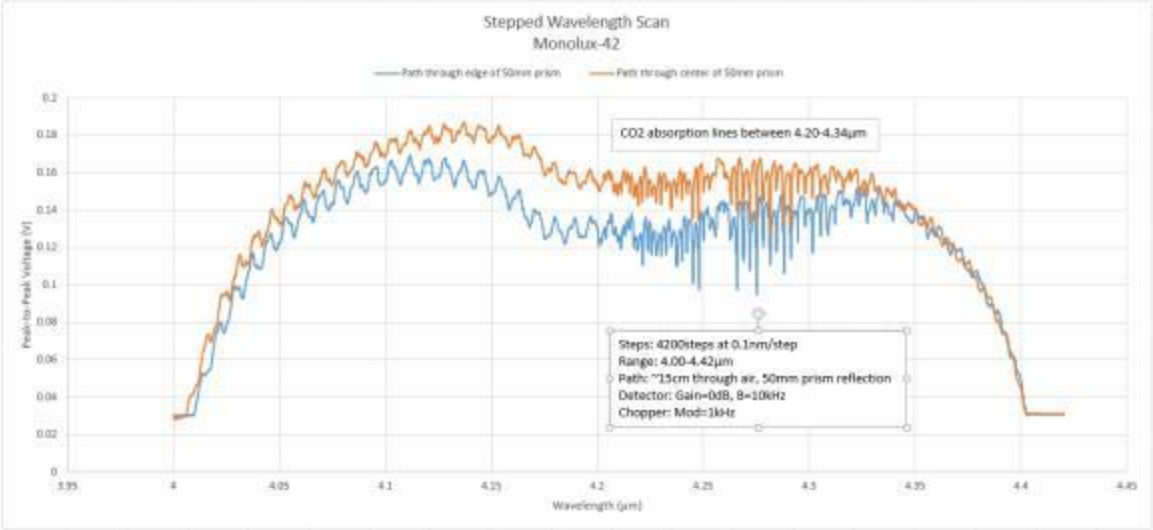

Figure 4-113. Wavelength spectrum showing CO2 absorption lines between 4.20-4.34 microns

Moving forward, another wider fringe is still apparent with a period of 8.3nm that must also be removed. Calculations indicated that his fringe likely stems from reflections between the detector window backing and the detector chip face. The window cannot be removed without disrupting the cooling system of the photodiode, so the entire system was immersed in nitrogen gas to observe the effect of only the background signal. By placing the long wavelength system, including the laser, chopper, prism, and detector inside a sealed chamber (Figure 4-114); N_2 could replace the ambient air for testing.

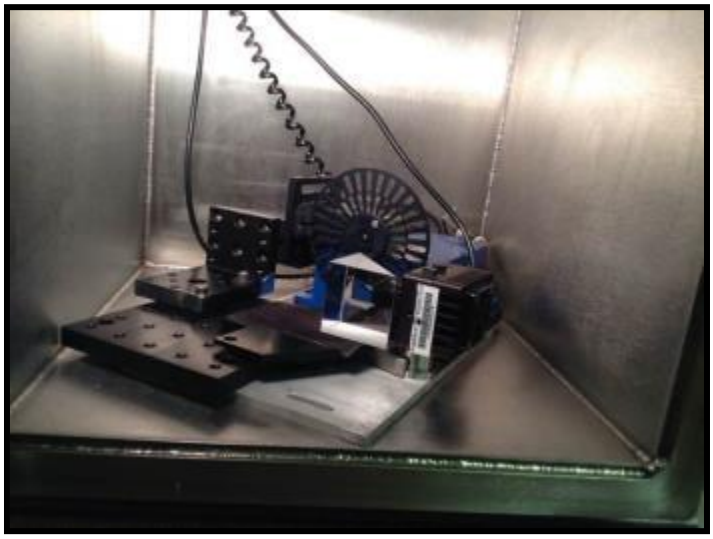

Figure 4-114. Compacted long wavelength system inside chamber for background isolation test

As the tank slowly filled the chamber, CO_2 absorption lines were seen to decrease in strength until finally nearly all air was evacuated and the absorption lines were negligible. Shown in Figure 4-115, are the wavelength spectra representing the system in air (blue) and in nitrogen (orange). The background signal representing the baseline system measurement is given by the curve plotted in orange above. The background signal is a superposition of the laser tuning characteristic and optical system etalons that inscribe sinusoidal variations across the spectrum. Signal processing in the frequency domain (Figure 4-116) using a Fourier transform helps separate any other subtle, less obvious etalons. Two peaks in the frequency spectra indicated not just one, but two optical etalons in the system. The larger peak is from the 8.3nm fringe (Fringe 1) discussed earlier, while the smaller peak, subtler oscillation is a 21.7nm fringe (Fringe 2). Since these are both system derived, they must be calibrated out with further processing. First the oscillations are isolated by filtering and performing a reverse Fourier transformation to observe their individual effects (Figure 4-117 & Figure 4-118).

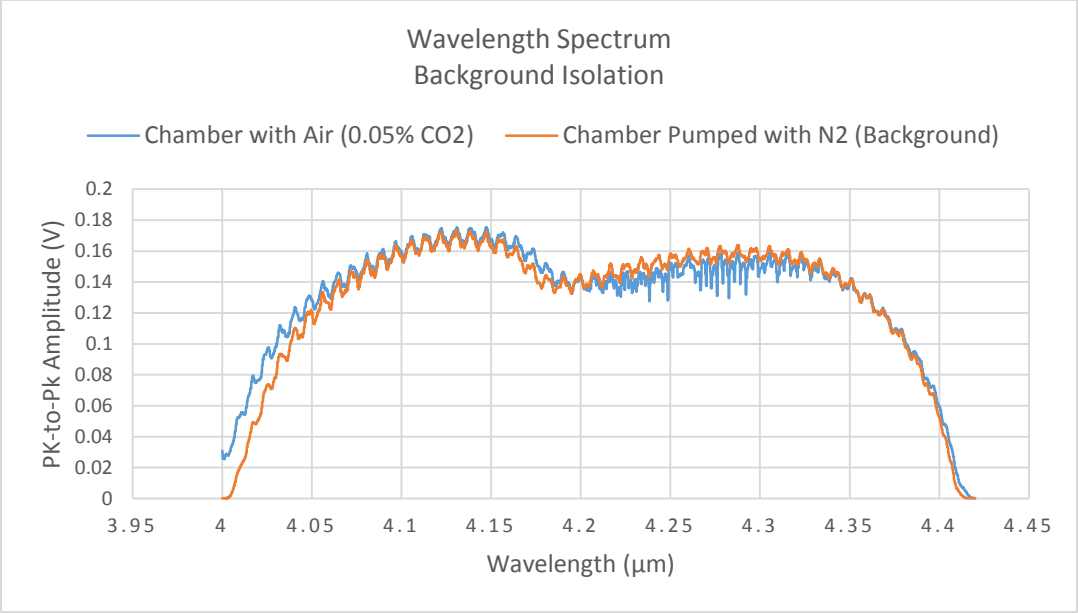

Figure 4-115. Wavelength spectrum in air (0.05% CO2) and in nitrogen (background)

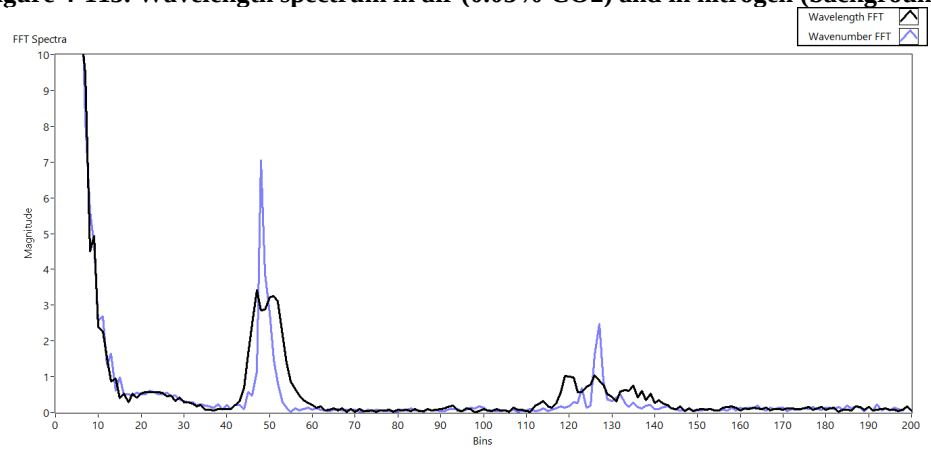

Figure 4-116. Two peaks in frequency spectra indicate two optical etalons – one large and one small

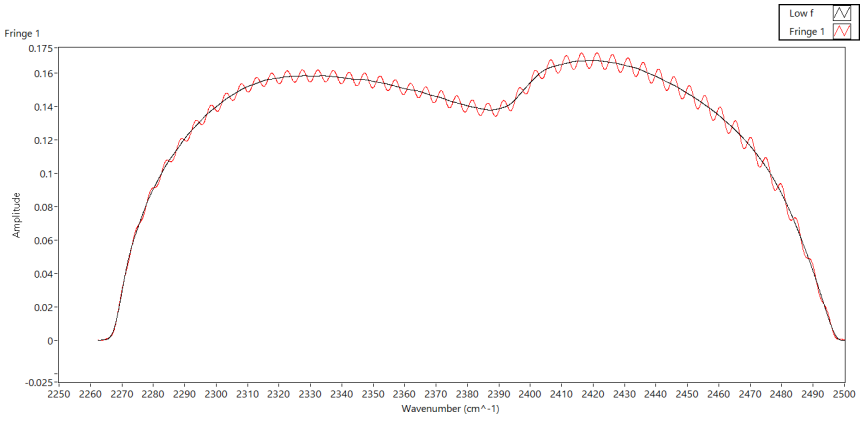

Figure 4-117. Background contribution from Fringe 1

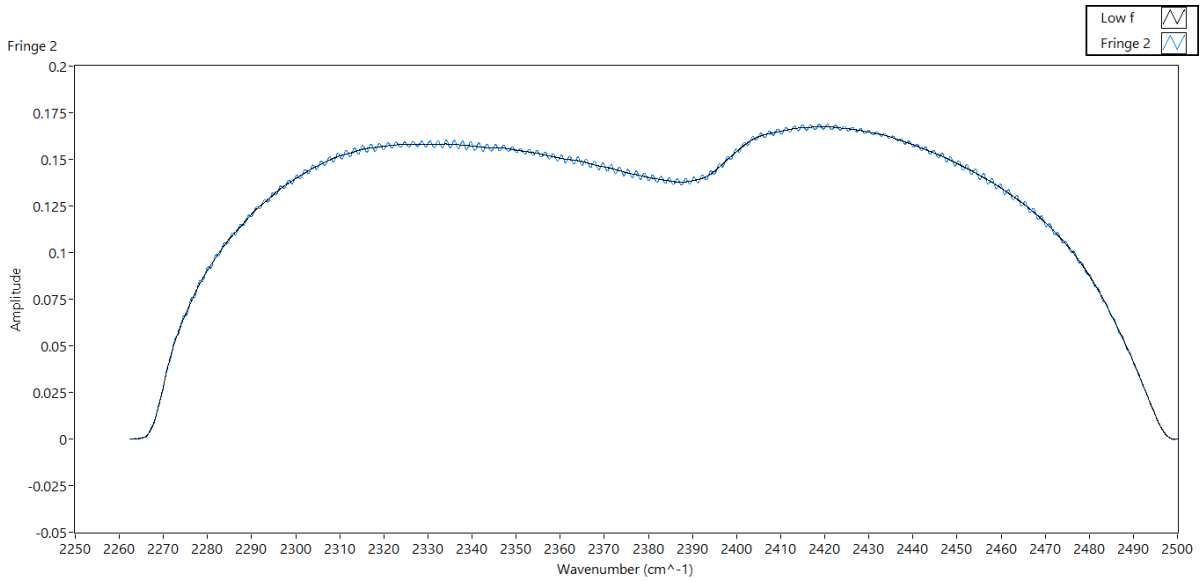

Figure 4-118. Background contribution from Fringe 2

The identified fringes are targeted for removal to complete the background calibration. By adjusting the amplitudes and phases of modeled fringes to recorded wavelength spectra, their combined contribution (Figure 4-119) can be calibrated out to retrieve accurate gas concentration levels.

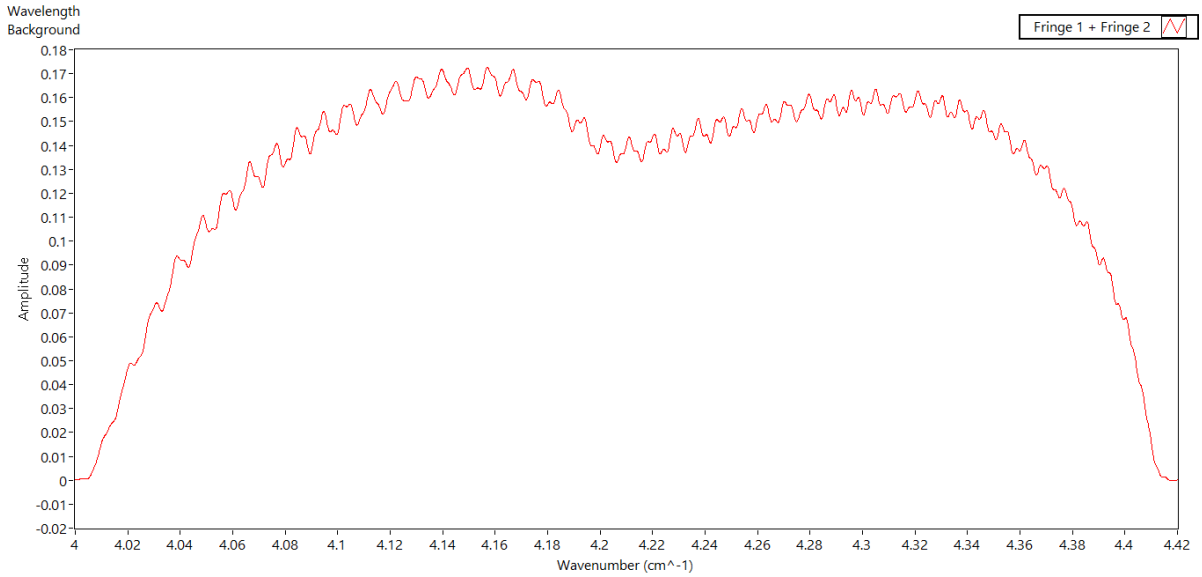

Figure 4-119. Combined contribution from Fringe 1 and 2

4.8 Set-up to Test the Gas Sensing Capabilities of the Sapphire Bundle in High Temperature

When the sapphire sensor was tested with the long wavelength QCL laser, the output spectrum experienced strong loss and half of the spectrum vanished due to the high loss of that wavelength region. Several different lengths of sapphire fiber was tested to determine the most

effective length of sapphire sensor. The length of the sapphire bundle with lead-in and lead-out fibers should be shorter than 30cm to obtain full spectrum output from the sapphire bundle sensor.

Figure 4-120 shows the schematic of the set up used to test the gas sensing capabilities at high temperature in IR region. QCL laser with wavelength range from 4µm to 4.4µm was used as our input source and a photo detector with amplifier was used as our detector. The chopper was used with the photo detector and a DAQ card was used to process the data to computer. A fiber port was used with the laser to couple the output IR light into the 50µm sapphire lead-in fiber. The gas chamber was constructed with laboratory constructed furnace and a thermocouple was used to monitor the temperature inside of the furnace. The gas chamber was connected to a pressure gauge that monitored the pressure inside of the chamber. Both the vacuum pump and premixed gas were connected to the chamber as well. Figure 4-121 shows the corresponding set-up of the gas sensing test at high temperature.

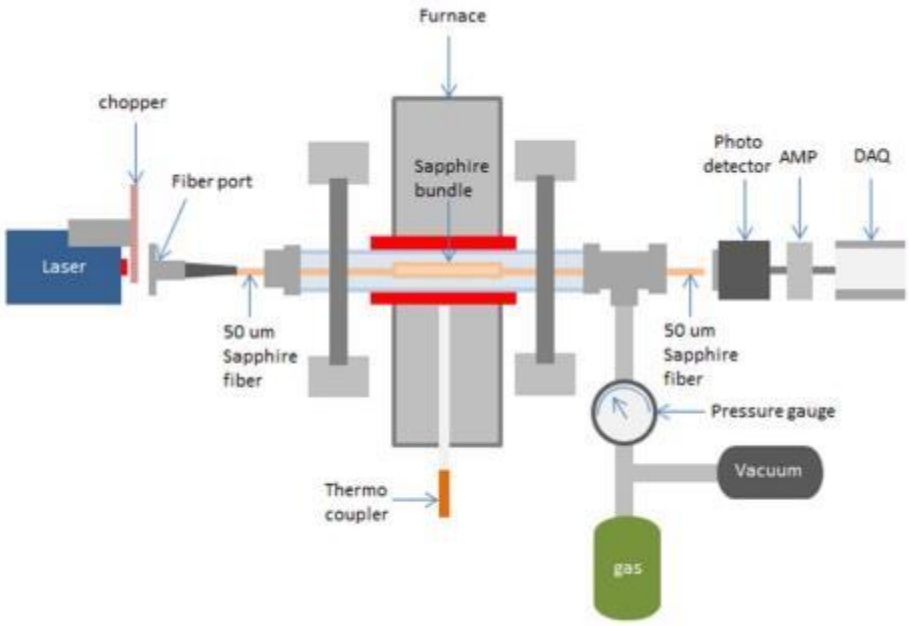

Figure 4-120: Schematic of the set up to test gas sensing capabilities in high temperature in IR region

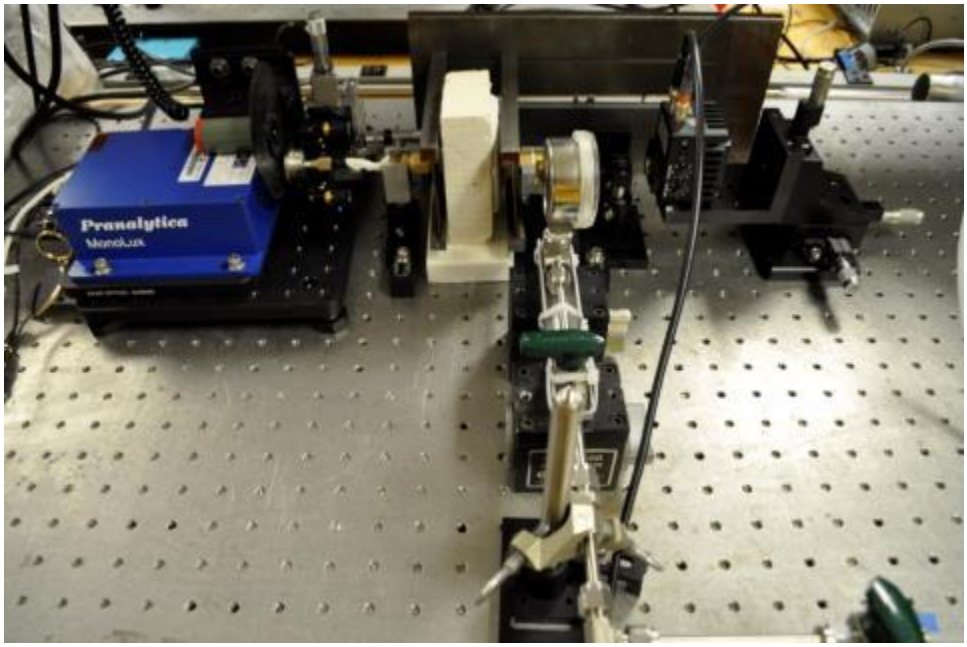

Figure 4-121: Set-up of the gas sensor testing at high temperature

4.9 Testing of the Sapphire Photonic Crystal Fiber Gas Sensing Capabilities

4.9.1 Signal Processing on the Sapphire Bundle

One of the problems with averaging the signal with a CTS and oscilloscope is synchronization between these two devices. Since the CTS does not have any external trigger that can be synchronized with an oscilloscope, the output signal from sapphire bundle does not trigger the oscilloscope to read the sapphire bundle output in time with CTS input. Figure 4-122 shows output signal that does not synchronized each other.

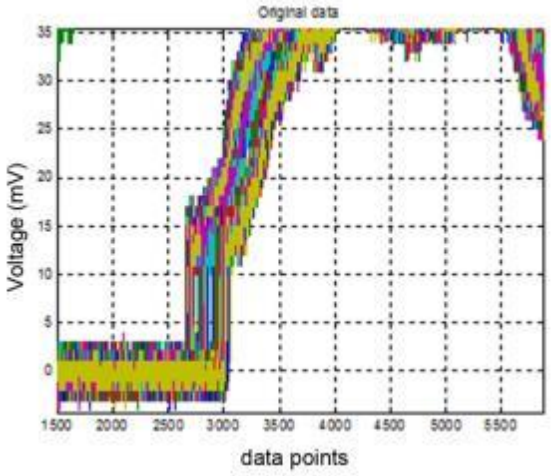

Figure 4-122.Triggering issue on averaging output signal

In order to make the signal to be synchronized each other, manual shifting was executed in Matlab. Figure 4-123 shows the output signal before and after manual shifting in Matlab.

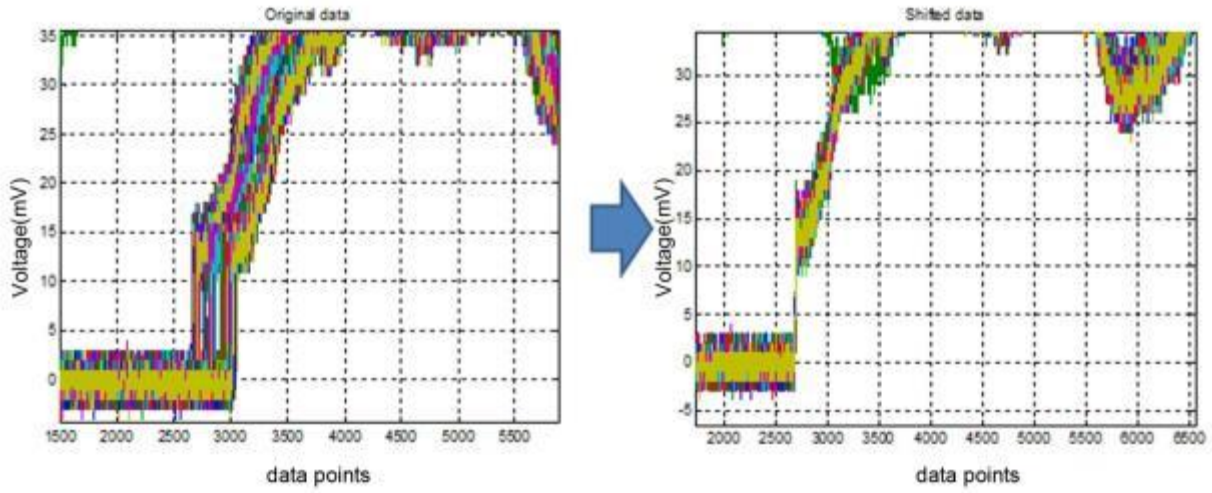

Figure 4-123. Output signal before (a) and after (b) manual shifting

After executing manual shifting of each averaged data and normalization of the background, gas absorption peaks were significantly improved. Figure 4-124 shows the difference between normal averaging and manual shifted averaging at a wavelength of 1530.4nm.

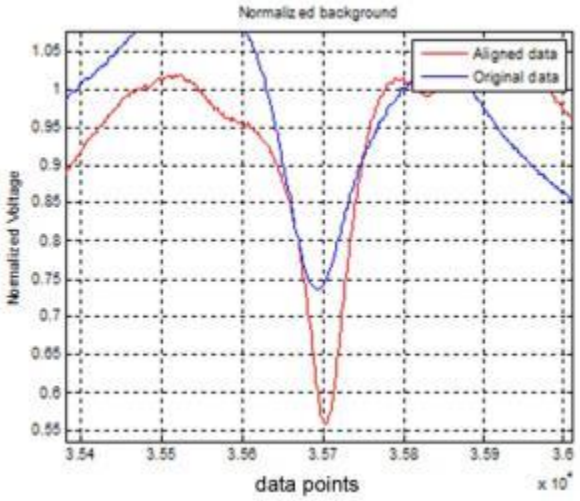

Figure 4-124. The difference between normal averaging and manual shifted averaging at wavelength of 1530.4nm.

After successfully improving signal quality by manual shifting, the sapphire bundle sensor was tested with different gas concentrations. Figure 4-125 shows the gas absorption peaks of acetylene gas at 1530.4nm. These absorption peaks are smoother than before the signal processing. Normalization and averaging with shifted data is not practical in real sensor system environment.

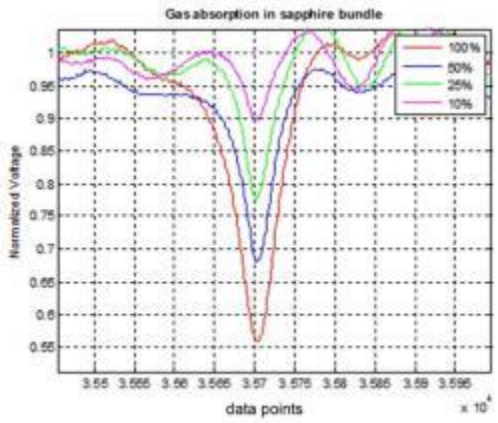

Figure 4-125. Gas absorption peaks with different concentrations of acetylene gas at 1530.4nm.

4.10 Software Development

To anticipate the different wavelength range and power normalization of absorption spectra in the mid-infrared, software solutions are now being developed using a combination of LabVIEW and MATLAB. This implementation offers the flexible control of LabVIEW and powerful analysis tools of MATLAB. LabVIEW provides robust synchronization of laser scanning and data acquisition, along with a front panel that serves as an intuitive GUI. MATLAB contributes sparse matrix manipulation and a concise text-based mathematical toolset for advanced signal processing of mid-infrared spectra.

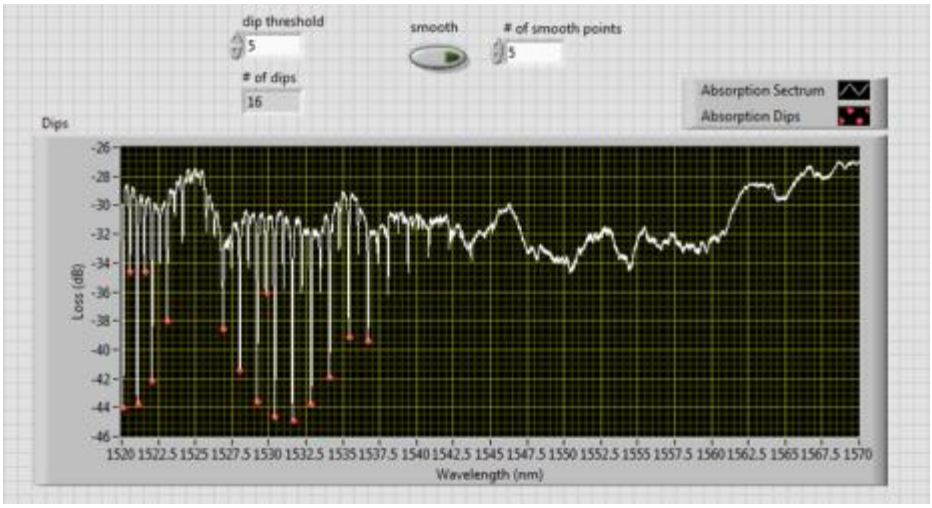

Figure 4-126: Absorption dip threshold detection and smoothing

The following presents preliminary work on the software development. A front panel GUI is an inherent benefit of using LabVIEW. The partial screenshot in Figure 4-126 gives the result of absorption dip threshold detection, in this case for a 6cm porous silica sensor exposed to acetylene gas. The GUI is interactive and modifiable, so that the user can update parameters as the testing procedures are matured for different sensor configurations.

4.10.1 Background Cancelation and Fitting for Individual Absorption Dips

Below, Figure 4-127 exemplifies one means for background cancellation and Lorentzian modeling of an absorption dip. This method identifies the so-called "shoulders" of the dip shown in red in the top plot. A polynomial fit shown in green estimates the background distortion. The background is subtracted from the absorption dip. A fit of the dip, shown in red in the bottom plot, is made with a Lorentzian model. A nonlinear Levenberg-Marquardt algorithm was used to perform the fitting.

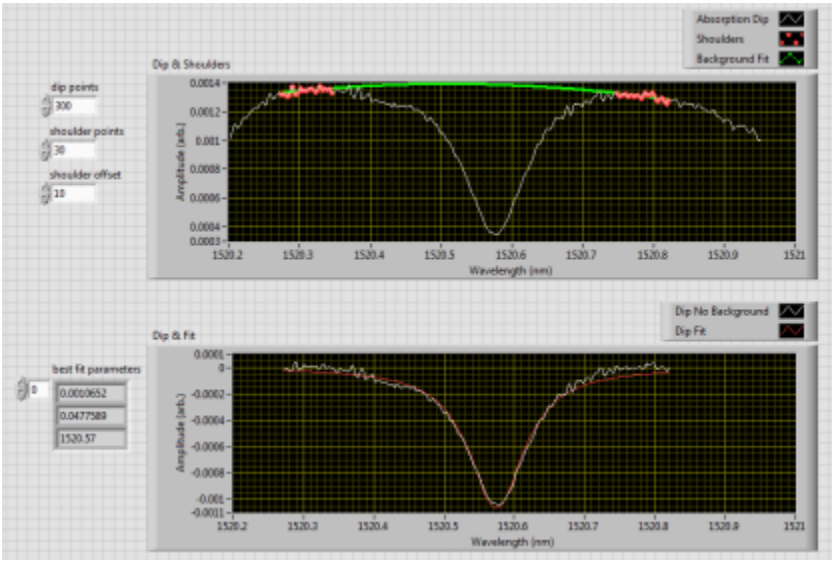

Figure 4-127: Individual absorption dip background cancelation and fitting

4.10.2 Background Cancelation for Fuller Spectrum

These signal processing techniques for individual dips work well when the absorption background is relatively constant over the width of the dip, but can be challenged by more severe distortion. For this reason, spectrum background estimation was pursued using an asymmetric least squares technique. A first result, shown below in Figure 4-128, was achieved in MATLAB.

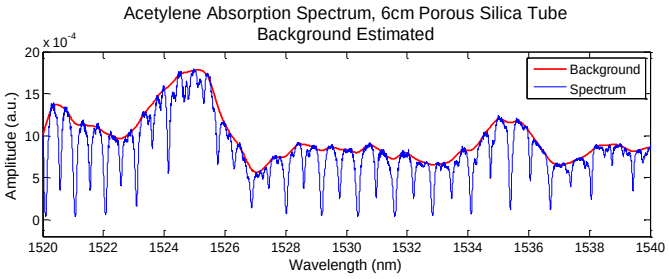

Figure 4-128: Spectrum background estimation by asymmetric least squares

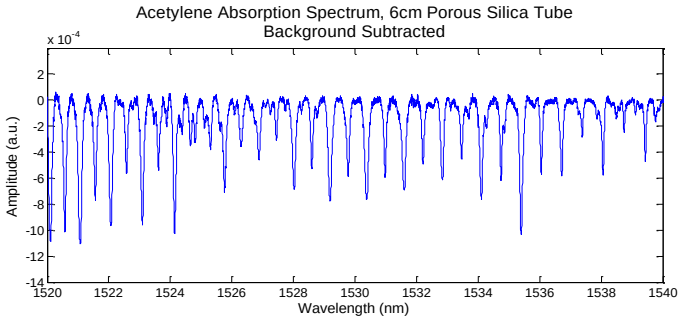

Figure 4-129: Spectrum after background subtraction

After background subtraction, the spectrum appears as shown above in Figure 4-129. Absorption dips occurs as negative deviations from a flat baseline at zero amplitude. Pursuing a background estimation using the entire spectrum is more robust than when considering individual dips especially for variable backgrounds. This example of background cancelation was done in MATLAB and the following gives results displayed to the LabVIEW front panel.

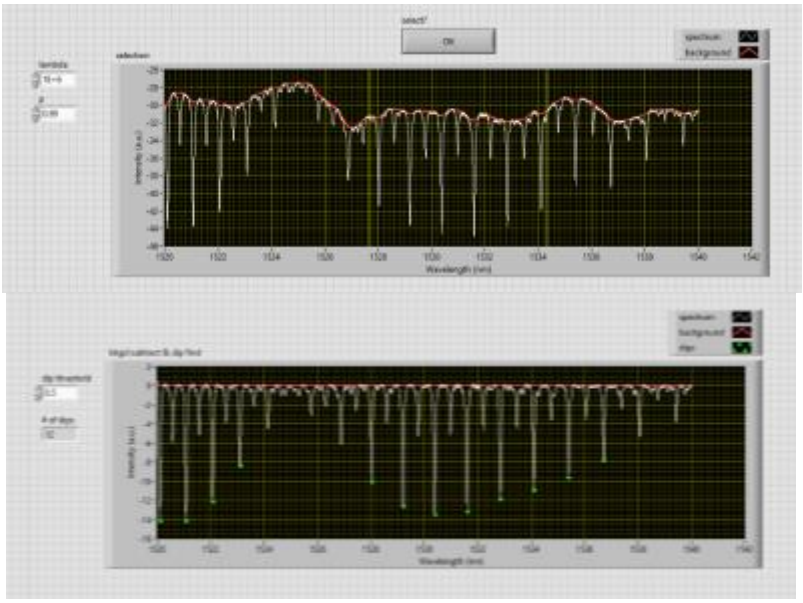

Figure 4-130: Background cancelation shown in LabVIEW front panel

4.10.3 Analysis of sapphire bundle with bending of the MM fiber

In order to understand the background noise in the sapphire gap bundle sensor structure, the lead-in and lead-out fiber were bent to demonstrate the performance of the sensor in a real environment. The diameter of the bend on the MM fiber was 2cm as shown in Figure 4-131. In order to generate dramatic changes in the sapphire bundle sensor, the MM fiber was selected to be fiber that was bent.

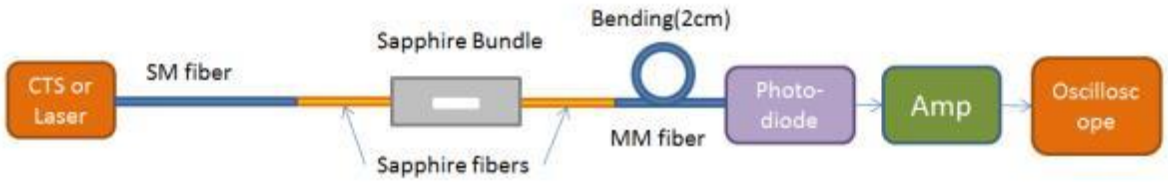

Figure 4-131. Schematic of sapphire bundle with bending in MM fiber

Figure 4-132 show the comparison of gas absorption peaks with and without bending on the MM lead-out fiber in sapphire bundle sensor system. As indicated in the figure, the magnitude of the gas absorption peaks from the background signal remains almost same between the two measurements. Modal noise is expected to be random when a MM fiber is bent. Several measurements were made to confirm the random effect from modal noise but all the measurement showed similar results as described in the Figure 4-132. Therefore, it seems that the background noise of the output signal is not affected by modal noise in MM fiber.

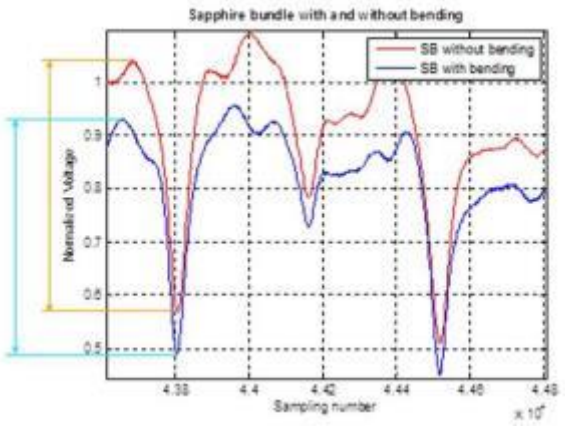

Figure 4-132. Gas absorption of sapphire bundle sensor with and without bending on MM fiber (Wavelength near 1525nm)

4.10.4 Modal Scrambler

A modal scrambler was employed in an effort to eliminate the modal noise from the sapphire bundle sensor optical system. Figure 4-133 the laboratory fabricated modal scrambler and it should generate sufficient magnitude of the vibration on MM fiber to scramble the modal noise in the system.

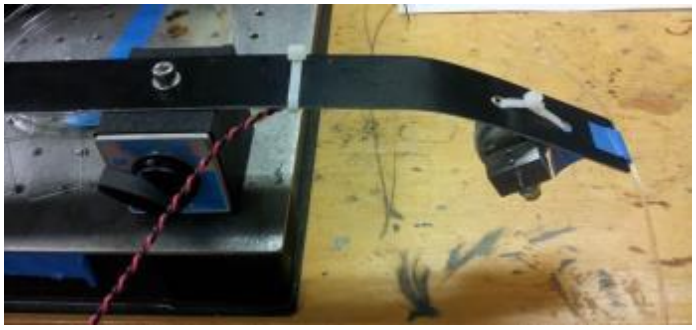

Figure 4-133. Modal scrambler with 15m of MM fiber attached

In Figure 4-134, two different points that modal scrambler was placed are indicated. A 15 m length of MM fiber was used with modal scrambler and the modal scrambler was placed on a different optical table to eliminate the vibrational impact on the sapphire bundle sensor. Unfortunately, no meaningful effect was observed in this experiment. The only thing observed from the experiment was small fluctuations in the background signal and no improvement of the background signal was observed.

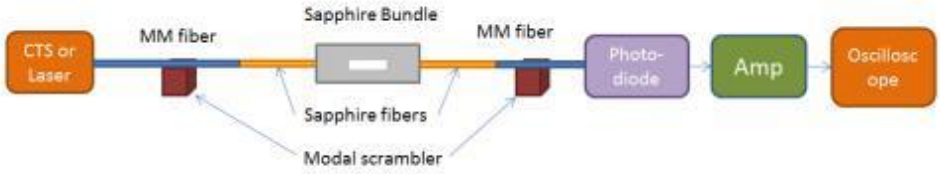

Figure 4-134. Schematic of sapphire bundle sensor with modal scrambler

In order to observe any effect from the scrambler, a simple test was performed with the CTS as shown in Figure 4-135. 15m of MM fiber with a modal scrambler was directly connected to the CTS in order to generate modal noise. As expected, a huge modal noise was observed in the output signal and tested with the scrambler. Unfortunately, there was almost no effect on the signal when modal scrambler was turned on. This confirms that modal scrambler could not help to eliminate modal noise in sapphire bundle sensor. This might be due to high speed scanning rate of the CTS input source. When the modal scrambler generates the vibration, it should give sufficient magnitude but the frequency of the generated vibration may not be sufficient to scramble the modal noise from the CTS.

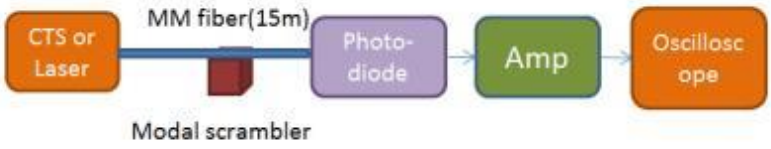

Figure 4-135. Schematic of the simple test with modal scrambler

4.11 New sapphire bundle with FC connector

In previous experiments, a splicing technique between the sapphire and SM/MM fibers was used when sapphire bundle sensor was fabricated. The loss of the spicing point was studied and demonstrated and some improvements on splicing techniques were made but the splicing point still generated significant loss in our system. In order to eliminate as much loss as possible in our system, FC connectors with a 50 μm sapphire fiber were fabricated and assembled with newly fabricated sapphire bundle. Figure 4-136 shows the schematic and set-up of sapphire bundle sensor with FC/FC connectors at the lead-in and lead-out fiber connections. Some improvement in power loss and signal quality was expected in this set-up.

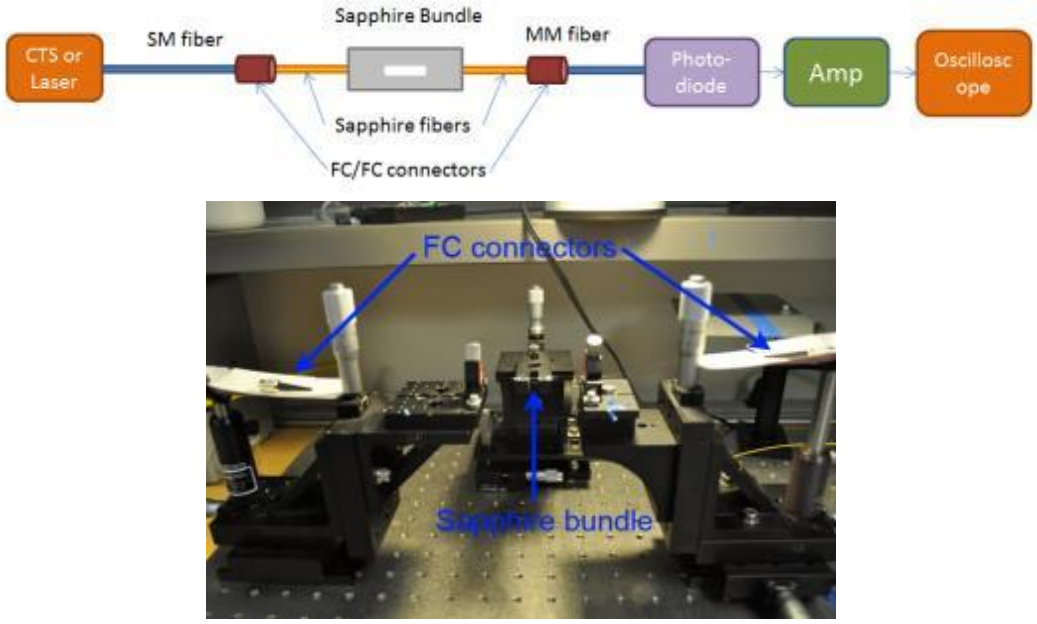

Figure 4-136. Schematic and set up of sapphire bundle with FC/FC connectors

Figure 4-137 shows the transmission spectrum from the sapphire bundle sensor with different lengths of air cavity. Red lines represent the output spectrum from averaging with manual shifting and while the blue lines represent the original averaging data. Measurements were performed with 1mm, 5mm, 10mm and 20mm air cavity in the 50μm center sapphire fiber. As shown in the figure, background fluctuation change as the air cavity length increases.

Several different experiments were performed to study the background signal including adjusting angle, position and length of the air cavity of center sapphire fiber and bending of the MM fiber. The background signal was fairly random when the angle, position and length of the air cavity of center sapphire fiber were changed. However, low frequency fluctuation was maintained when the MM fiber was bent. These experiments indicated that most of the low frequency fluctuation s of the signal depends on the light propagation in the air cavity.

Figure 4-138 shows the comparison between a sapphire bundle with FC connectors and with splicing points between the sapphire and the SM/MM fiber. As expected, transmitted power of the sapphire bundle with FC connector was two orders of magnitude stronger than one with the splicing point. The output spectrum of the sapphire bundle with FC connectors was smoother than the ones with a splicing point. This leads to the conclusion that splicing the sapphire and SM/MM fibers generates a huge loss in the system and also contributes a significant portion of the modal noise in the system.

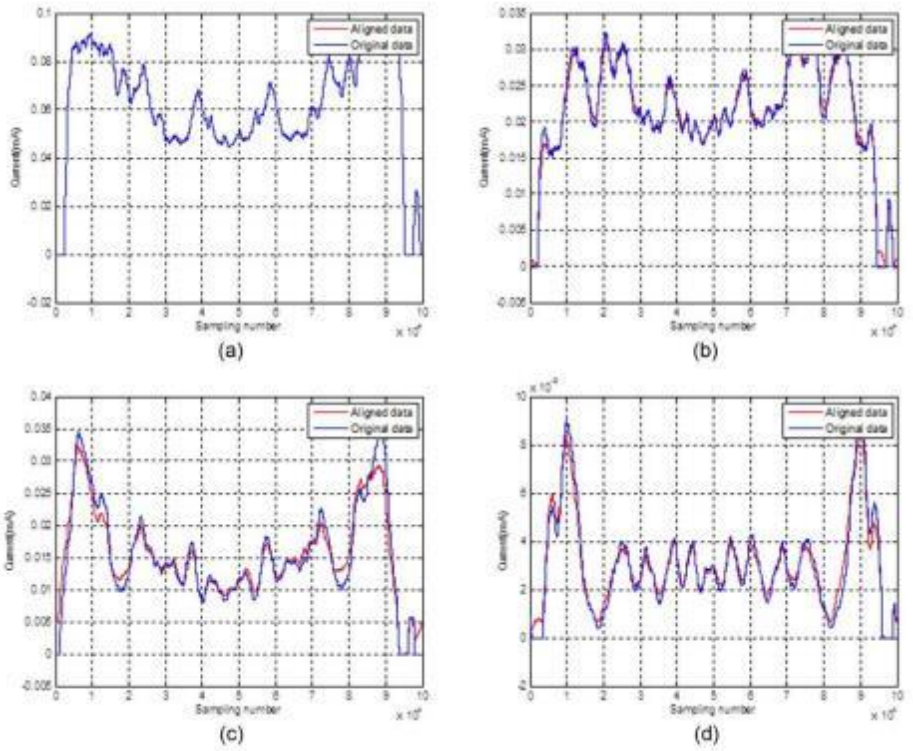

Figure 4-137. Transmission signal from sapphire bundle sensor with (a)1mm, (b)5mm, (c)10mm and (d)20mm air cavity

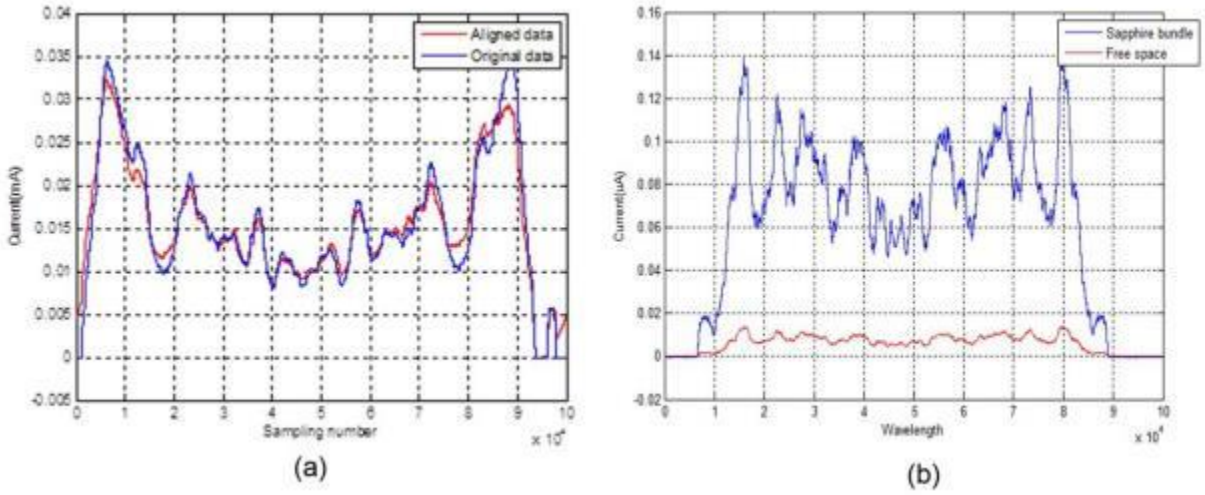

Figure 4-138. Transmission output from sapphire bundle sensor with (a) FC connectors and (b) splicing points between sapphire and SM/MM fibers(Air cavity=1cm)

4.11.1 6-rod Sapphire Bundle with FC Connector vs. Splicing Point

The gas absorption of the sapphire bundle with FC connectors was compared with one with splicing points. After aligning the center fiber with a 20mm of air cavity with a three axis stage, alumina based adhesive was applied to maintain the sensor structure. Following fabrication of the sapphire bundle sensor with a 20mm air cavity, the sensor holder and fitting for the gas chamber was fabricated and assemble the with gas chamber as shown in Figure 4-139.

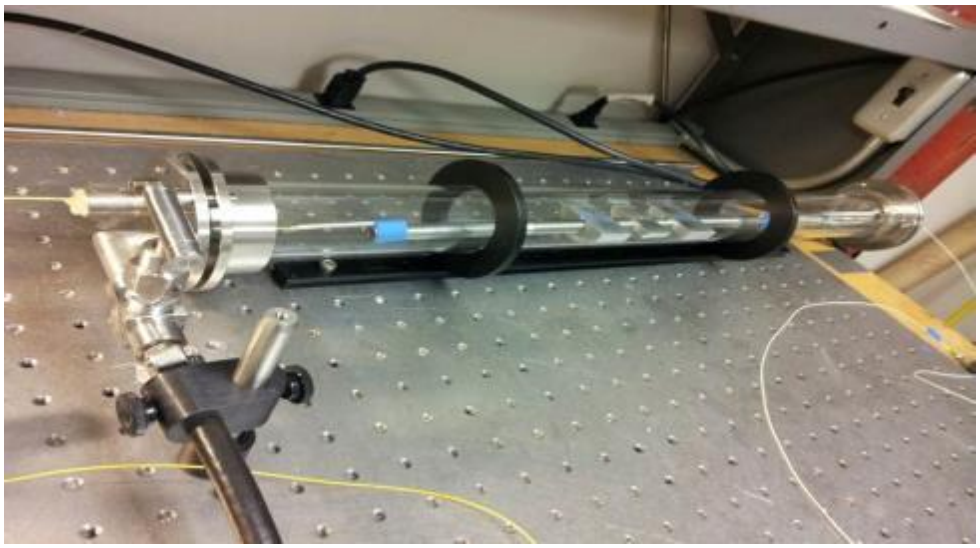

Figure 4-139. Gas chamber with sapphire bundle

Figure 4-140 show the gas absorption peaks of sapphire bundle with FC connectors. As reported in the previous report, averaging data with manual shifting was applied to measure the gas absorption. One can easily observe the improvement of the gas absorption spectrum with FC connector from the figure. It has significantly reduced noise over a bundle connected with splicing points.

Figure 4-141 and Figure 4-142 shows the comparison of the gas absorption between sapphire bundles using FC connectors or splicing points. The output spectrums were normalized with the background signal. As shown in Figure 4-141, the background of the sapphire bundle with the FC connectors has less noise than the sapphire bundle with splicing points. It also has a stronger and smoother absorption peak as shown in Figure 4-142.

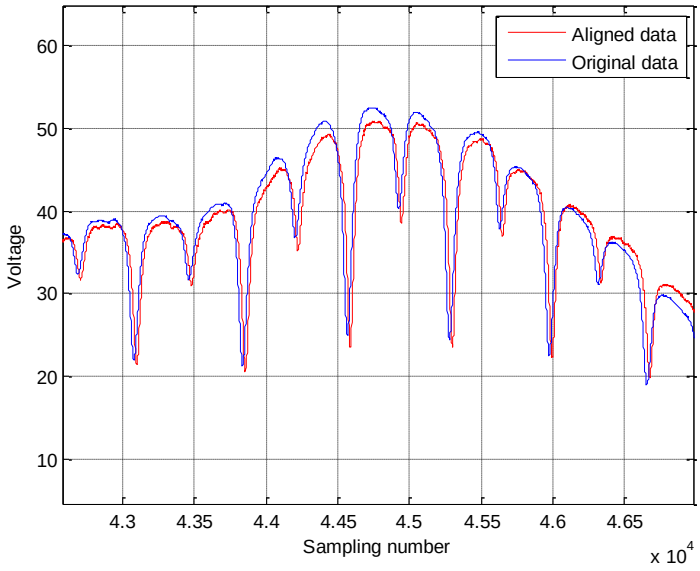

Figure 4-140. Gas absorption of sapphire bundle sensor

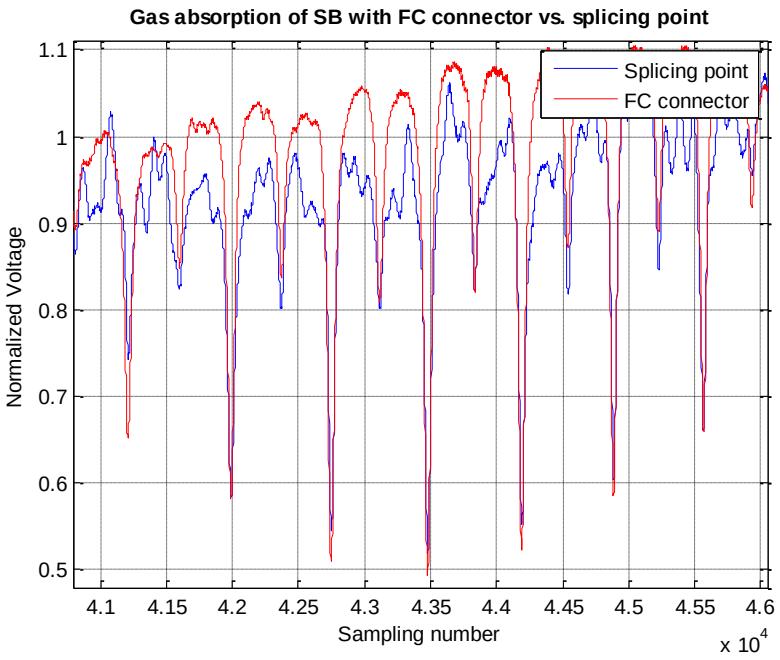

Figure 4-141. Gas absorption peaks of sapphire bundle with FC connector vs. splicing point

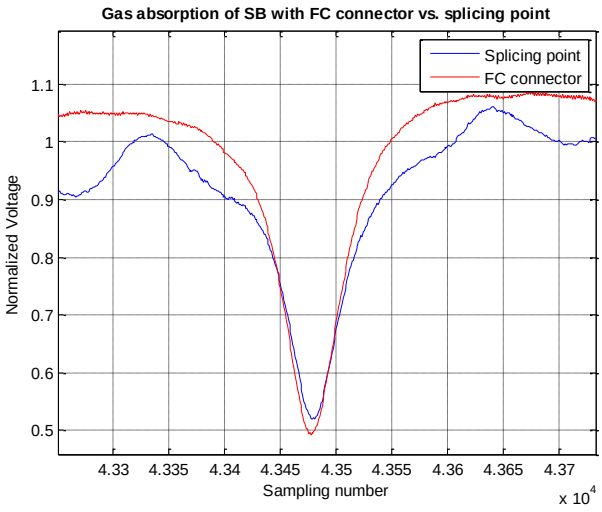

Figure 4-142. Gas absorption peak at 1530.4nm

4.11.2 Gas concentration test on 6-fiber sapphire bundle with FC connectors

Figure 4-143 show the gas absorption of a sapphire bundle with FC connector in 100% acetylene gas. As demonstrated in a previous report, the background of the signal has less high frequency noise than one with splicing points. Low frequency noise and some of the background noise will be reduced in the next section of this report.

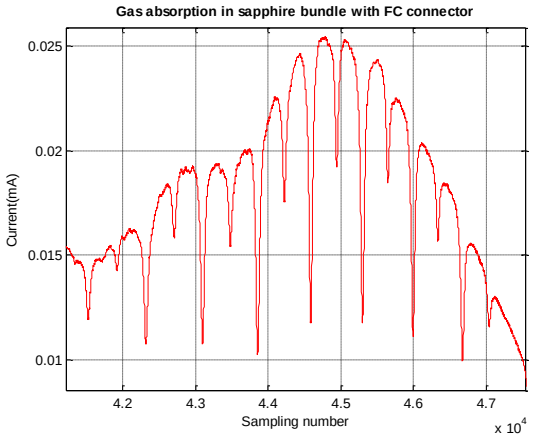

Figure 4-143. Gas absorption of sapphire bundle with FC connector in 100% Acetylene gas

In order to compare the capability of the gas absorption between the sapphire bundle with FC connectors and spicing points, different gas concentrations were backfilled into the gas chamber to measure. Figure 4-144 shows the gas absorption of sapphire bundle with FC connectors at different gas concentrations and Figure 4-145 shows the gas absorption of a sapphire bundle with spicing points from the previous report. Please note that the signal in Figure 4-144 was measured without any signal processing while the signal in Figure 4-145 was normalized with the background signal. Without any signal processing, the gas absorption peaks in FC connectors are much better than ones with splicing points. The background is much smoother and the gas absorption peaks are sharper than the one with splicing points.

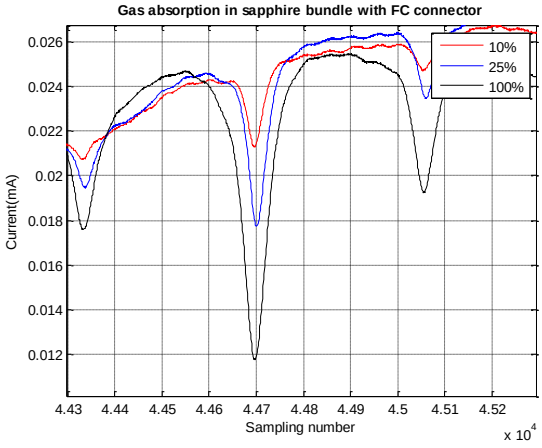

Figure 4-144. Gas absorption of sapphire bundle with FC connector in different gas concentrations.

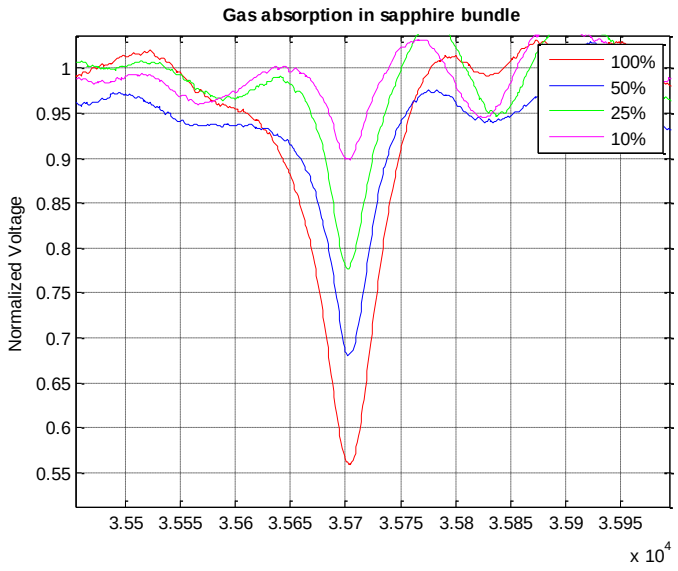

Figure 4-145. Gas absorption of sapphire bundle with splicing point in different gas concentrations.

Figure 4-146 shows the signal processing method used to reduce the low frequency noise out of the gas absorption signal. The green signal represents the original gas absorption signal and red represent the signal out of a low-pass filter. After carefully designing the low-pass filter, the gas absorption signal was normalized with the low-pass filtered signal. Figure 4-147 show the final result of the signal processing. The low frequency noise in the signal was successfully reduced and overall signal quality was improved from one with spicing points.

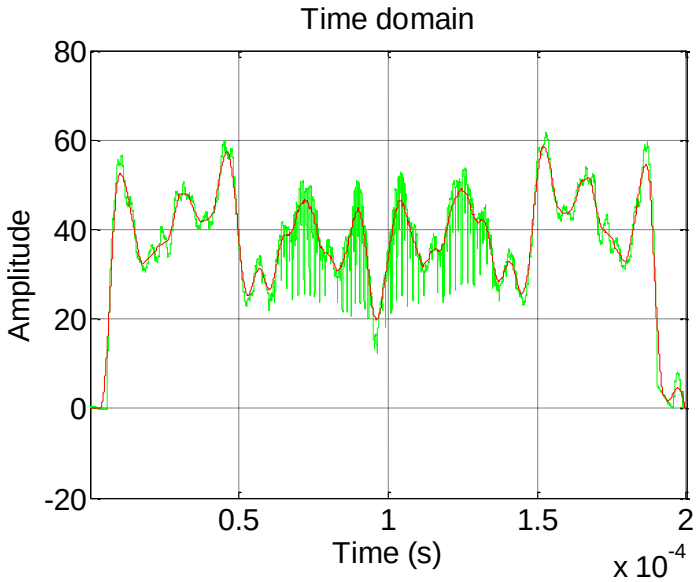

Figure 4-146. Signal processing method used to reduce the low frequency noise out of the gas absorption signal.

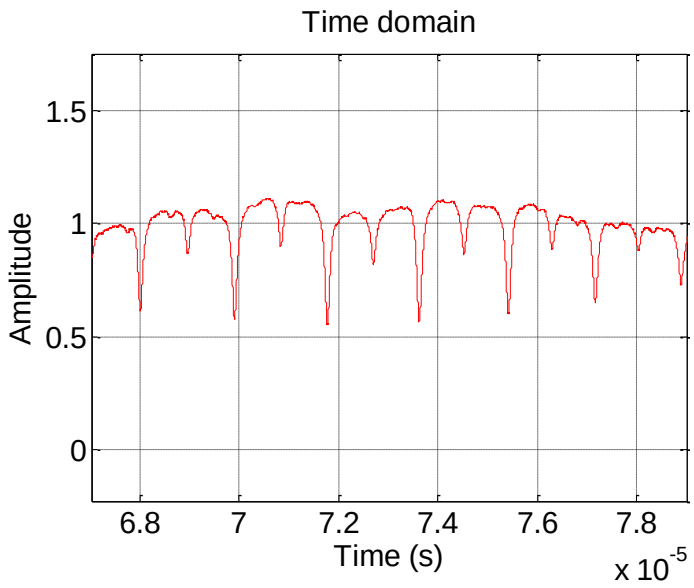

Figure 4-147. Normalized gas absorption signal with low-pass filter

4.11.3 Temperature Test on Sapphire Bundle with Splicing Point.

In order to demonstrate gas sensing capability of the sapphire bundle in high temperature, the sapphire bundle sensor was heated up to 1000°C to test the sensor structure survivability at elevated temperatures. Prior to the temperature test, a ceramic tube with ID of 2.5mm and OD of 5mm was prepared and preheat treated in a laboratory built tube furnace. Figure 4-148 shows the ceramic tube and tube furnace used in this process. The ceramic tube was heated to 1000°C for more than 24 hours to eliminate any possible contamination during the temperature test with sapphire bundle.

Figure 4-148. Ceramic tube and homemade tube furnace that preheated the tube

Figure 4-149 shows the final set up used to perform the temperature test on the sapphire bundle sensor. The sapphire bundle was inserted into the ceramic tube and the assembly was

carefully inserted to MTI GLS 1500X tube furnace. The sapphire bundle was gradually heated up to 1000°C and stayed at temperature for 30 min.

Figure 4-150 shows the transmitted signal out of the sapphire bundle before (blue) and after (red) the temperature test. There was little change in the transmitted signal during the temperature test. These changes could be due to changes in the alignment of the sapphire bundle and is most likely due to sintering of the high temperature adhesive used in the bundle. However, maintaining the alignment of two centered sapphire fiber in sapphire bundle sensor could be confirmed from the test. After the temperature test, the sapphire bundle sensor lead-in fiber was broken while it was being removed from the tube furnace. The broken fiber was a regular SM fiber and it is well known fact that normal SS or MM fiber weakens when they are heated to high temperature. In future temperature tests, longer sapphire fiber will be used inside of the tube furnace.

Figure 4-149. Final set up to perform temperature test on sapphire bundle

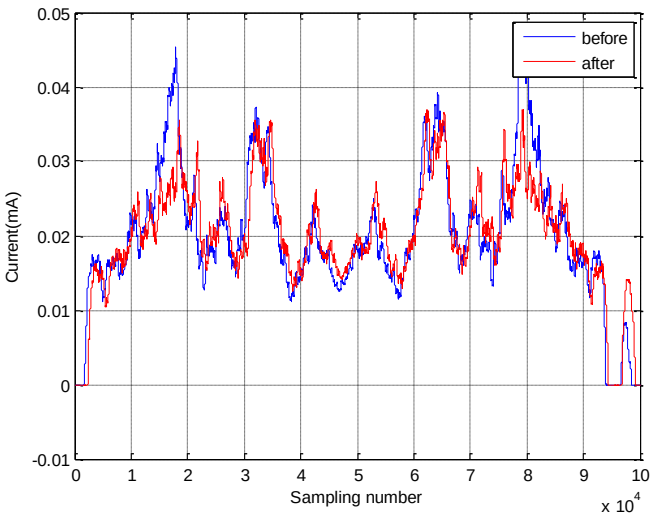

Figure 4-150. Transmitted signal of the sapphire bundle before and after the temperature test

4.11.4 Preparation for Simultaneous Measurement of Temperature and Gas Absorption Test

In order to demonstrate gas sensing capability of the sapphire bundle at high temperature, the gas chamber and sapphire bundle sensor need to be modified. Figure 4-151 shows the overall schematic of the gas chamber and sapphire bundle to demonstrate the gas absorption test at high temperature. The lead-in and lead-out sapphire fibers should be long enough to cover the length of the gas chamber and FC connectors will be placed outside of the chamber. A ceramic tube will be used to protect the sapphire bundle sensor.

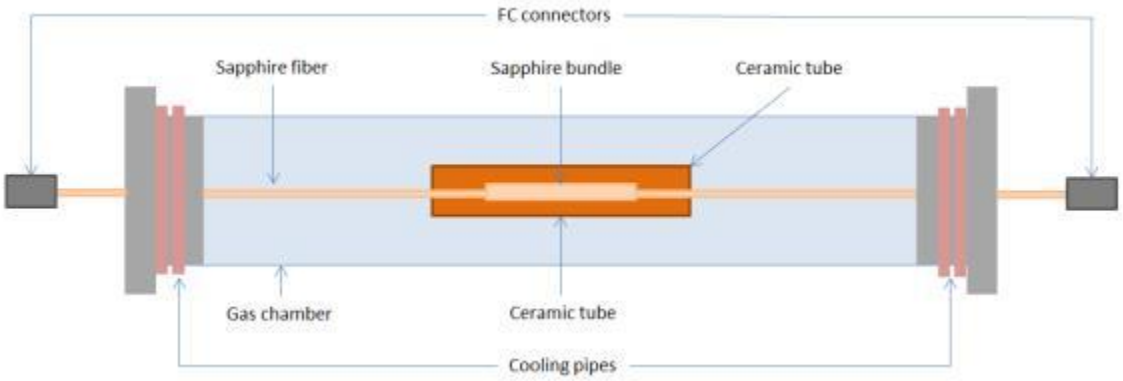

Figure 4-151. Schematic of the gas chamber for gas absorption test at high temperature.

Since our sapphire bundle sensor is expected to be operated up to 1000°C, the gas chamber should be modified to operate at that temperature. One of the issues with the gas chamber at that temperature is the rubber parts inside of the gas sealing fittings located at the tube ends. The manufacturer of the gas chamber suggested that a cooling system be used at the sealing points as shown in Figure 4-151. The cooling system at the sealing was fabricated around the fittings by using heat pipes. Figure 4-152 shows the rubber sealing gaskets used in the fitting and fabrication of the cooling system around the fitting as the manufacturer suggested.

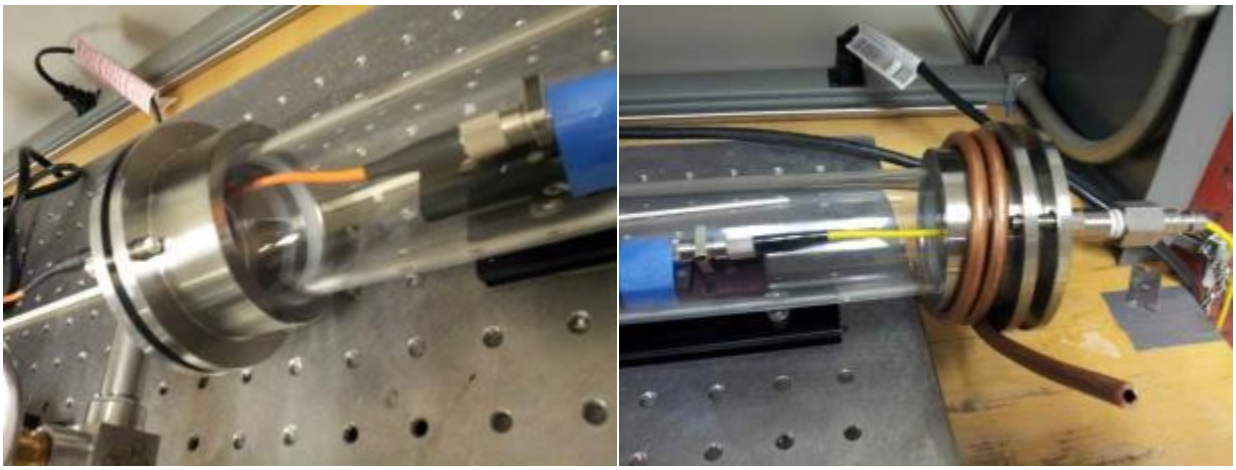

Figure 4-152. Rubber sealing and heat pipes to cool down the sealing

4.11.1 Detection of CO_2 Using LWS and Sapphire Photonic Crystal Fiber gap sensor

Gas detection was accomplished using the setup described in the previous section and allowed for data to be collected at room temperature up to a temperature of 1000°C. Prior to collecting data, the gas chamber was evacuated and a background spectrum was collected. While the gas chamber is airtight and capable of having the CO_2 removed, at the laser prior to coupling into the fiber and at the lead-out fiber and photodetector the system is exposed to atmosphere. As a result of these 2 locations in the optical system being exposed to atmosphere, CO_2 absorption peaks are still present when the system is under vacuum. This problem also limits the detection threshold to the concentration of CO_2 in atmosphere which is estimated between 400-600ppm. Two different premixed concentrations of CO_2 in nitrogen were used as well as diluted concentration of the 5% premix to obtain more data points. The two premix gases used are 5% and 0.1% concentrations. Dilution of 5% with ultra-high purity nitrogen was done to obtain concentrations of 2.5%, 1.25%, and 0.625%. Spectra were collected for these 5 concentrations at room temperature and 750C. The spectra collected at room temperature are shown below in Figure 4-153.

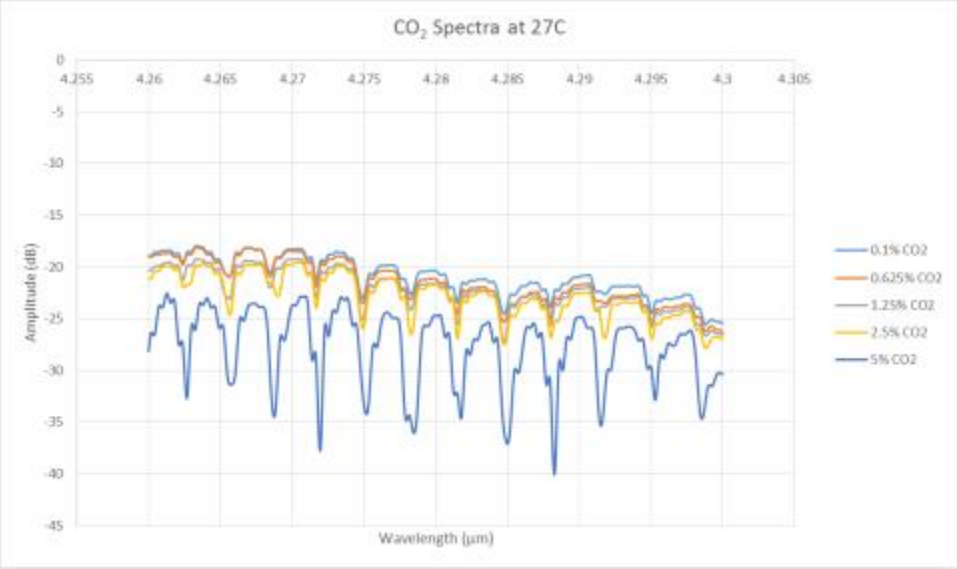

Figure 4-153: Spectra from Sapphire Photonic Crystal Fiber at Room Temperature.

The system was then slowly heated at a rate around 10°C/min stopping at both 250°C and 500°C to take a test spectra to ensure that the signal had not been lost. At 750°C, data was collected at all the concentration data points. The spectra collected at 750°C is displayed in Figure 4-154.

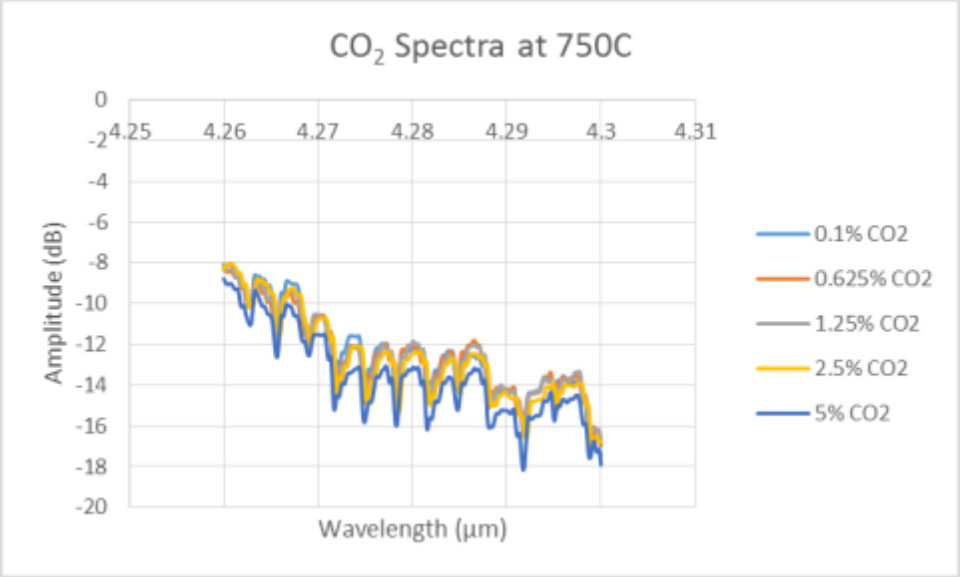

Figure 4-154: Spectra from Sapphire Photonic Crystal Fiber at 750°C.

The primary difference observed between the signal at room temperature and at 750°C is significantly higher intensity across the entire spectrum range. This increase in intensity is due to the blackbody radiation. Two different methods were used to measure the concentration of the gas using the sapphire sensors. The results of the analysis at both temperatures using the parametric slope algorithm are shown below in Figure 4-155.

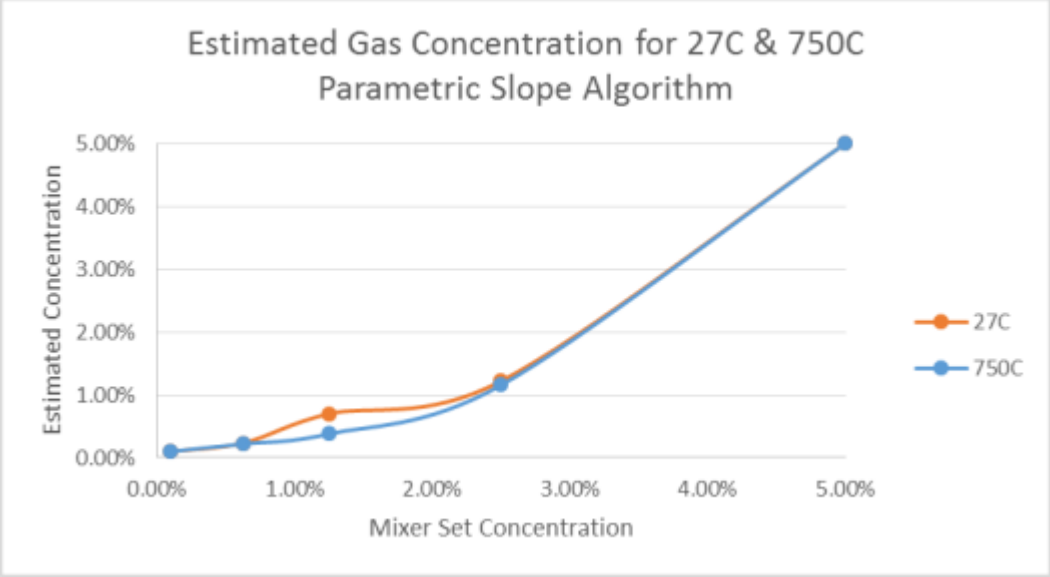

Figure 4-155: Results from Parametric Slope Algorithm for both room temperature and 750°C.

The data, when graphed, shows a linear behavior across the concentration range, though the data points for the 3 mixed points do not correspond exactly to the target concentrations. As both lines are overlapping it indicates that the gas mixer mixes consistently but does not necessarily produce the desired concentration. The points from the graph show the concentration to be approximately half the target values. Figure 4-156 below shows the same results using the

area ratio method. The data from the area ratio algorithm shows trends and estimates the gas concentration to be approximately half of the target values.

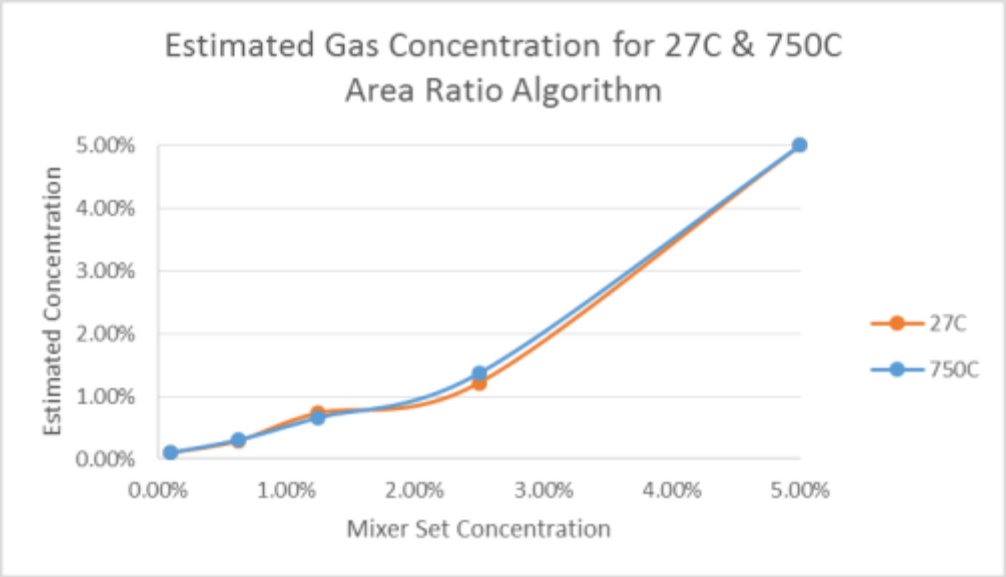

Figure 4-156: Results from Area Ratio Algorithm on CO2 Spectra at room temperature and 750°C.

After testing was completed at 750°C, the furnace was ramped to 1000°C to test the sensor. In the process of reaching 1000°C the seals on the gas chamber were destroyed and it became impossible to control the environment within the gas chamber. Data was still collected and the spectrum is shown below in Figure 4-157. Absorption peaks are still present and indicate that the sensor is capable of functions in 1000°C environment and detecting concentrations of CO_2 present in atmosphere.

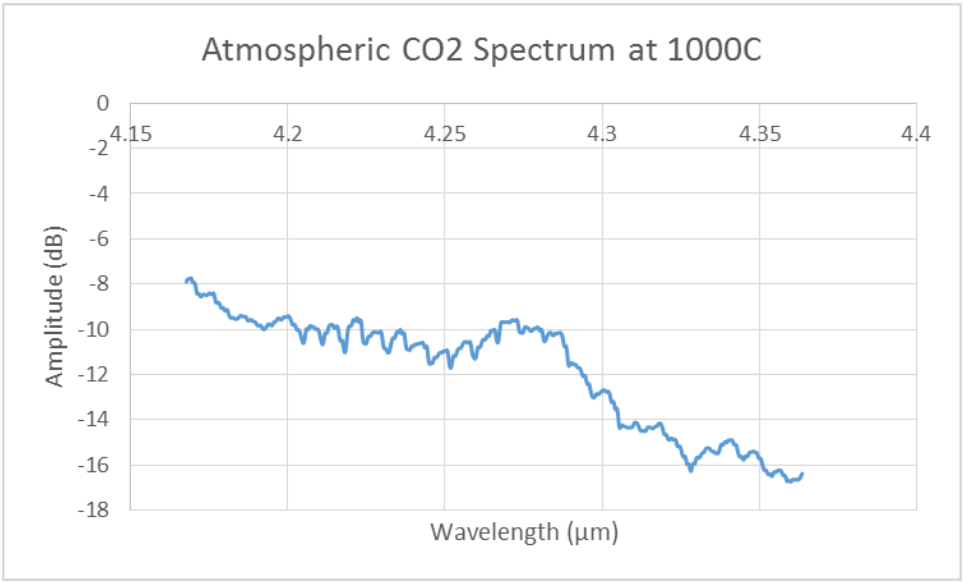

Figure 4-157: Spectrum Collected at 1000°C using Sapphire Photonic Crystal fiber.

4.12 Optical Property Testing and Characterization of the Sapphire Photonic Crystal Fibers

4.12.1 Analysis on Sapphire Photonic Crystal Fiber

One of the gas sensing structures proposed in this project is an optical gas sensor based on a sapphire photonic crystal fiber (SPCF). The advantages of using sapphire fiber in the construction of an optical gas sensor for high temperature application is that sapphire fiber is fully functional to 1600ºC. Sapphire photonic crystal fibers constructed of 7-rod and 3-rod bundles were fabricated with platinum wires that secured the bundled fibers together. The end faces of the SPCF were polished after bundling. A set-up to test the 7-rod and 3-rod SPCF was constructed with a single mode (SM) lead-in fiber and a multimode (MM) lead-out fiber. One possible improvement to the SPCF is to deposit nano-particles into the bundled structure to increase the gas interaction with the injected signal from scattering light at the core-air hole boundary due to the deposited particles. Sapphire photonic crystal fibers with deposited nano-particles in the air holes of 7-rod and 3-rod structures are presented. Additional improvements to the gas detection capability of the Sapphire bundle are also proposed in this report.

Figure 4-158(a) and (b) show the 7-rod and 3-rod SPCF that were fabricated with platinum wires respectively. As shown in Figure 4-158(c), the platinum wire was wound around the circumference of the fiber bundle to maintain the arrangement of the fibers. Both ends of the bundles were carefully polished to reduce the refraction from the ends. After polishing, a set up with a lead-in(SM) fiber, lead-out (MM) fiber, CTS (input source), photo diode with amplifier and oscilloscope was constructed. As in previous experiments, an average was made out of 50 output spectrums to achieve accurate measurements. Figure 4-159(a) shows the output spectrum of our experimental set up with the 3-rod SPCF. An 8.5 cm long 3-rod SPCF was used in this experiment. As shown in Figure 4-159(b) small gas absorption peaks were observed. . However, the signal contains a fair amount of noise and the system itself was not stable when the gas was applied on the SPCF. In Figure 4-159, the horizontal axis shows the output from the SPCF from the oscilloscope in a time scale from the CTS input of a wavelength scan from 1520nm to 1570nm. This time scale on the abscissa can easily be converted to wavelength scale and the beginning and ending wavelengths are superimposed on the abscissa. The beginning of the output signal corresponds to 1520nm of wavelength and middle of the signal corresponds to 1570nm of wavelength. Then it will scan back to 1520nm of wavelength.

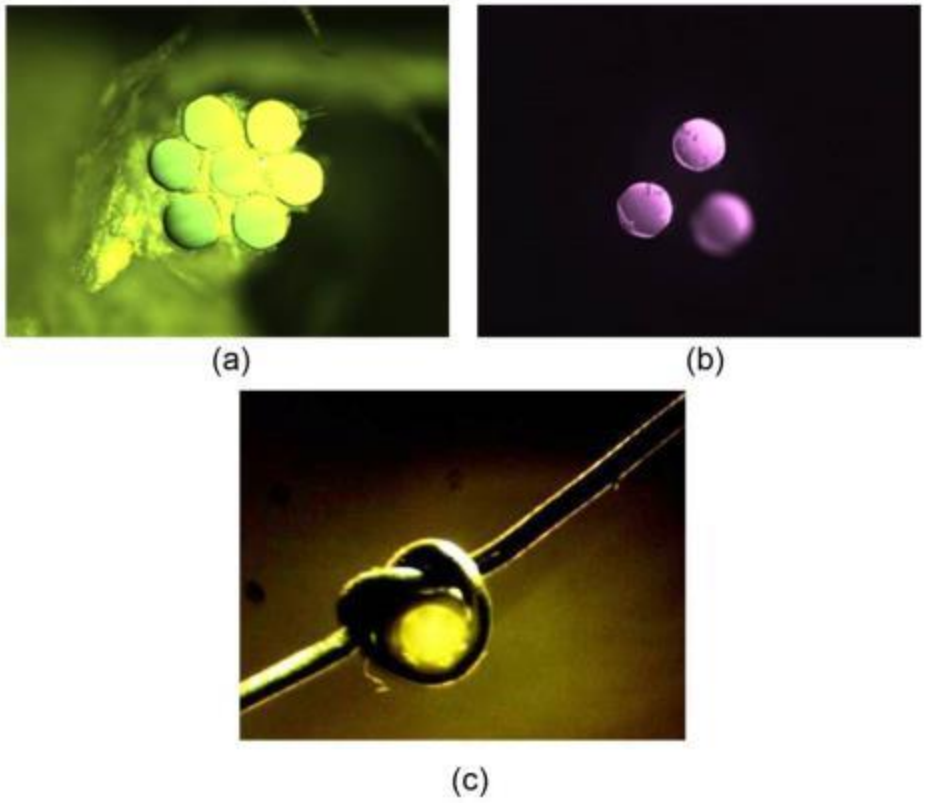

Figure 4-158. Polished ends of 7-rod (a) and 3-rod (b) Sapphire bundles and platinum wire (c) holding the fiber bundle

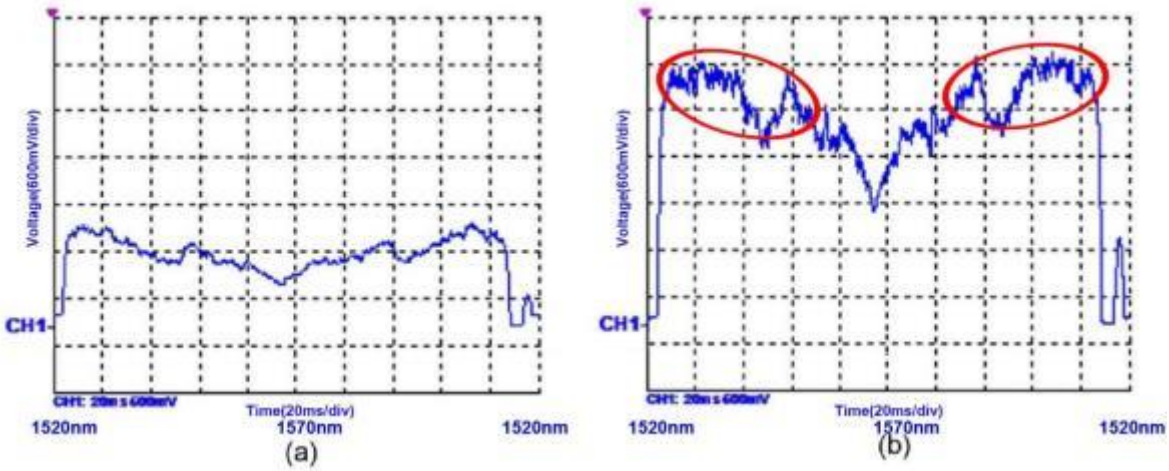

Figure 4-159. Spectrum of the 3-rod Sapphire bundles (a) without gas and (b) with gas

Figure 4-160(a) shows the output spectrum of the 3-rod bundle SPCF with deposited nano-sized alumina particles. The same 8.5cm long 3-rod SPCF from the previous experiment was used in this experiment. As shown in Figure 4-160(b), a slight improvement in the gas

absorption peaks was observed when compared to the 3-rod Sapphire bundle without the nano-particles. However, it still consisted of some noise and the system itself was not stable when the gas was applied to the SPCF. Both gas absorption spectrums of the 3-rod SPCF have weak absorption peaks when compared with free space gas absorption spectrum.

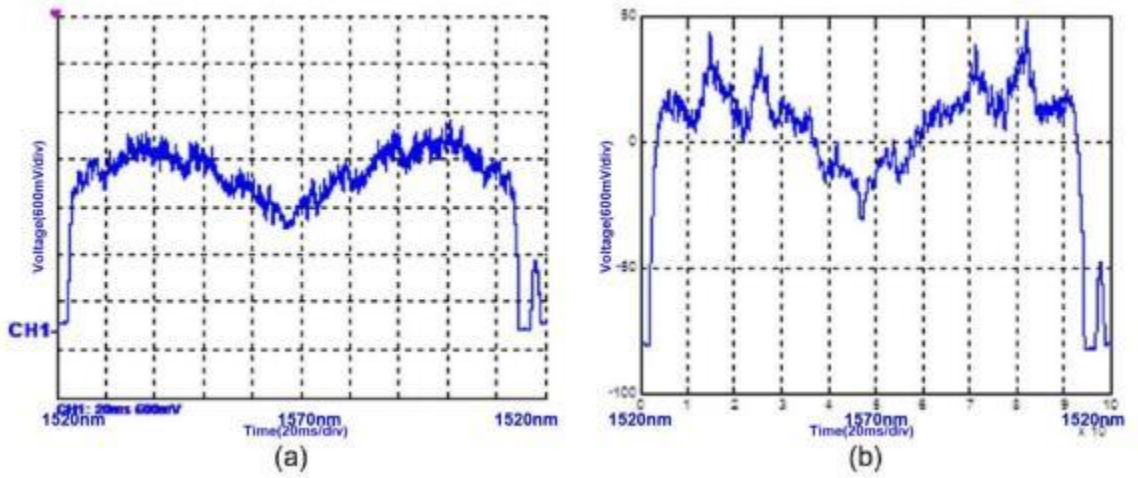

Figure 4-160. Spectrum of the 3-rod Sapphire bundles (a) without gas and (b) with gas

Figure 4-161(a) shows the output spectrum of our experimental set up with a 7-rod SPCF. A 5.5cm long 7-rod SPCF was used in this experiment. As shown in Figure 4-161(b), the gas absorption peak was not well observed with the 7-rod SPCF. Since light is transmitted through the center fiber of the 7-rod SPCF bundle, it has less chance to interact with gas than the 3-rod fiber where the light is transmitted through the air hole between the 3 sapphire fibers.

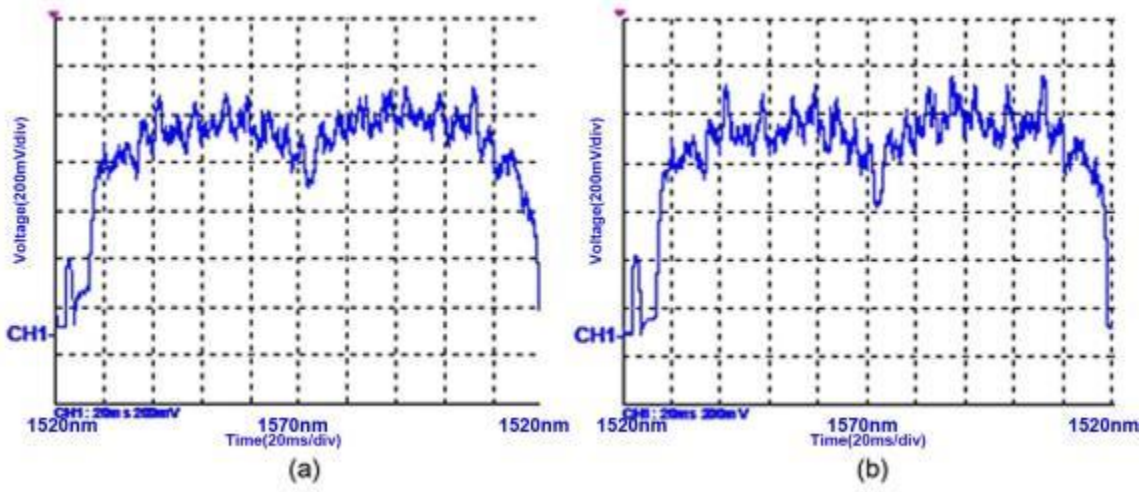

Figure 4-161. Spectrum of the 7-rod Sapphire bundles (a) without gas and (b) with gas

Figure 4-162(a) shows the output spectrum of 7-rod sapphire bundle with nano-sized alumina particles deposited in the air holes. The same 5.5cm long 7-rod SPCF from the previous experiment was used. As shown in Figure 4-162(b), a significant difference between the 7-rod bundle with and without the nano-particles could not be observed.

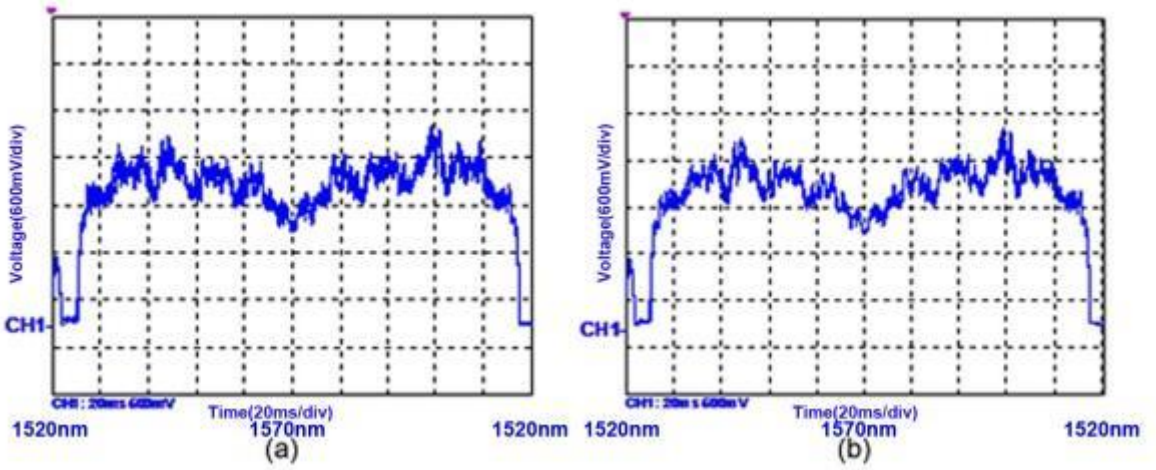

Figure 4-162. Spectrum of the 7-rod Sapphire bundles (a) without gas and (b) with gas

4.13 Investigation of variation in our fiber alignment

For many purposes, fiber alignment is needed throughout our experiments to achieve better light coupling into various optical materials. In this section, the accuracy of alignment was investigated and analyzed for future measurements. A 30mm long Sapphire fiber was placed between two SM fibers and the transmission using a CTS was measured. 10 measurements were performed to measure the accuracy on alignment procedure on two coupling points in and out of the sapphire fiber. Table 4-9 shows the actual transmission measurements out of the sapphire fiber with lead-in and lead-out fibers from the CTS. Each measurement was done with reconstruction of the set-up and alignment. **Error! Reference source not found.** summarized verage transmission loss from each measurement. Average transmission is -10.16 dB and standard deviation of our alignment is 0.94dB.

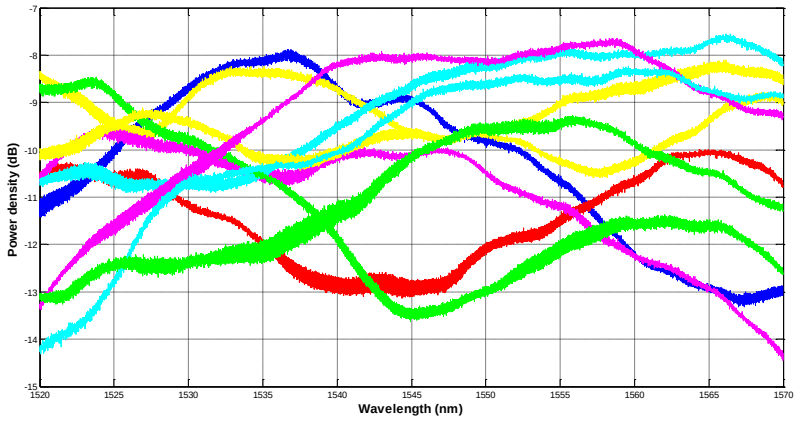

Figure 4-163: Measurements of transmission out of Sapphire fiber

Table 4-9: Summary of transmission loss of 10 measurements with new alignment

Measurement	Transmission loss(dB)
1	-10.22
2	-11.42
3	-8.93
4	-10.95
5	-9.12
6	-11.33
7	-9.78
8	-9.15
9	-9.86
10	-10.88
AVG	-10.16
STD	0.94

4.13.1 Preliminary Experiments on Sapphire Fiber

When the sapphire sensor is integrated into the optical system, single-mode and multi-mode fibers are used as the lead-in and lead-out fibers. Baseline measurements on this system need to be performed to verify the gas measurement when the sapphire sensor is employed in the system. Verification began with characterizing free space spectroscopy between lead-in and lead-out fibers, followed by determination of gas sensing capability of a single sapphire fiber and then components of a SPCF with a gap in the core. In the first experiment the distance between the SM and MM fiber was 3cm. Figure 4-164 shows the transmission spectra of the free space spectroscopy between the SM and MM fiber using a CTS as the source and a photodiode as a detector. Figure 4-164(a) is the spectra without gas being applied to the system, while Figure 4-164(b) is the spectra with the gas applied. As shown in Figure 4-164(c), gas absorption can be easily achieved by subtracting no-gas transmission spectrum from gas applied transmission spectrum.

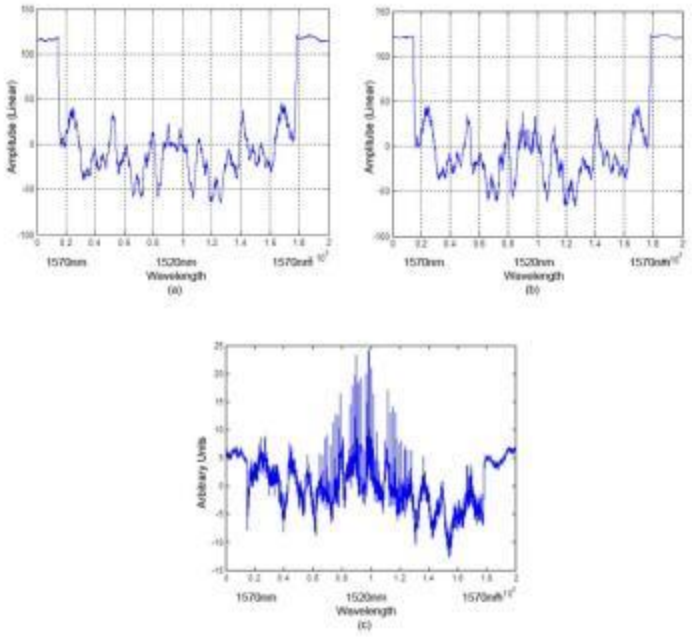

Figure 4-164: Measurements on SM and MM fibers without gas (a), with gas (b) and (c) difference

Following the free space spectroscopy test, a 3cm long polished sapphire fiber was placed between the SM and MM fibers and the transmission was measured with and without gas being applied. Figure 4-165 shows the individual transmission spectra of the sapphire fiber between the SM and MM fiber. Figure 4-165(c) shows the difference between the transmission spectra where gas absorption peaks are not observed.

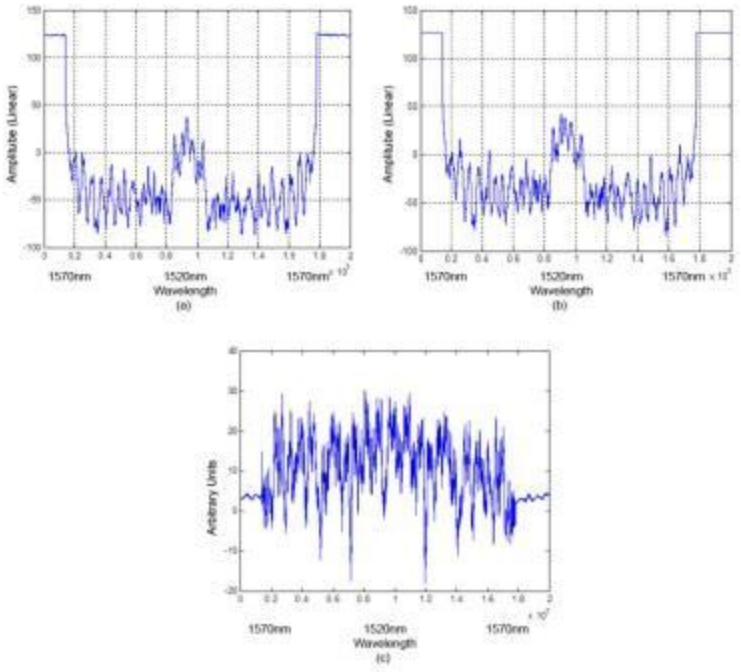

Figure 4-165: Measurements on Sapphire fiber between SM and MM fibers without gas (a), with gas (b) and (c) difference

4.13.2 Gold Nanoparticles on Sapphire Fibers

Gold plating has additional been attempted on sapphire fibers in an attempt to provide a gold film with which to form nanoparticles. The goal has been to plate a thin film of gold on the surface and then using a thermal annealing treatment to form gold nanoparticles to act as scattering centers on the surface of the sapphire tube. It is also hoped that this will allow for some surface plasmon interactions to occur and provide useful information using these phenomena. Plating was done on a small section of 50μm diameter sapphire fiber with unpolished ends to determine viability of plating technique. The plating was done using the recommended times from the manufacturer for plating on glass. This consisted of dipping the fiber into the sensitizing solution for 30 seconds, then a rinse in DI water for 30 seconds. The fiber is then dipped into the plating solution for ~30 minutes to allow for full plating of the gold film on the surface.

After successful plating was achieved, a second sample was plated using the same conditions with the addition of a mask on the end being dipped in the plating to prevent gold from contacting the polished surface. The fiber used in this test was still a 50μm diameter fiber and was approximately 5cm long with both ends polished for optical transmission. The mask

used was quick drying clear coat nail polish. This was used because it dissolves completely in acetone and is easily removed from surfaces.

After plating, the sapphire fibers were annealed in the furnace to convert the thin gold film into nanoparticles on the surface. This process is readily used to form nanoparticles for semiconductor nanowire synthesis using annealing temperatures in the range of 500-600°C. Previously on glass tubes that were plated prior to phase separation and then phase separated a distinct color and film change was observed. This change is believed to have been caused by the formation of particle shapes at the cost of the uniform film formed prior to annealing. The furnace treatment used, based on our observed film changes in tests with glass, is that of 575°C for 1 hour to form the particles. This was done in a regular box furnace with no atmosphere controls. Initial furnace treatment failed to alter the film and research has shown that significantly higher temperatures are needed to form nanoparticles from a thin gold film on sapphire substrates. The new furnace conditions determined from research are 925°C for 15 minutes.

Gold plating on sapphire has been successfully done on two samples, one unpolished and one polished with a mask on the end. Optical micrographs of these two fibers are shown below in Figure 4-166. Both of these tubes were easily plated and clearly shown a bright gold color present on the surface. The fiber on the right is the polished fiber that was left in the plating solution longer due to an unforeseen problem and shows some excess gold flakes stuck on the surface. Most of this residue was easily washed away using ethanol. For the protection of the polished ends a mask was applied to the end of the fiber inserted into the plating solution while the other end was carefully kept out of all of the solutions. Figure 4-167 below shows the mask with plating and the fiber after removal of the mask. The mask is shown as a blob of nail polish on the fiber that was also plated during the process which was expected. The mask was removed after soaking in acetone for 5 minutes and slightly agitating the fiber by moving it. The image on the right shows the clean surface after removal of the mask. No residue or gold plating was visible on the end of the fiber. The mask was successful in protecting the end surface from plating.

Figure 4-166: Gold plated Sapphire Fibers

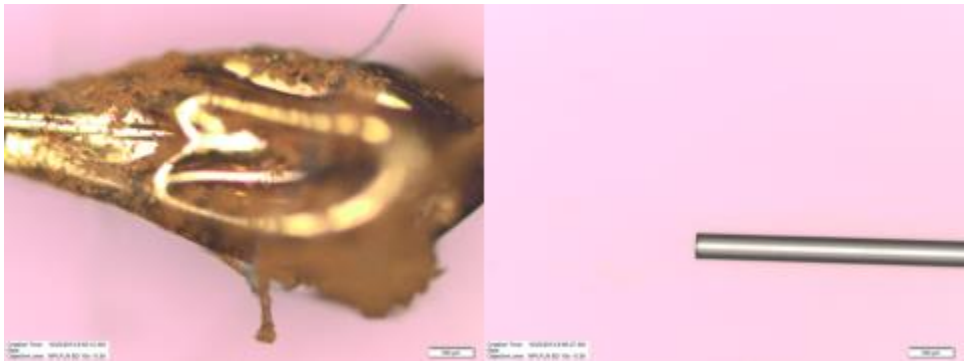

Figure 4-167: Mask on Sapphire (Left) and Sapphire after mask removal (Right).

Both the polished and unpolished fibers were heat treated at 575°C for 1 hour in a box furnace. The fibers were placed on an alumina plate in the center of the furnace for the test. Both fibers exhibited the same color and texture change previously observed. The optical microscope was not able to achieve a clean picture of the film showing the changes. The furnace treatment at 925°C was successful in causing an observable change to the film with the naked eye. The 50µm plated fiber was unfortunately damaged in process and was not able to be processed at the higher temperature. Optical results are currently pending on the plated 70µm fiber.

Gold nanoparticles were applied on a sapphire fiber to help scattering of the light out of the sapphire fiber. Figure 4-168 shows the transmission spectra of the gold nanoparticle coated sapphire fiber between the SM and MM fiber. Figure 4-168(c) shows the difference between transmission spectra where gas absorption peaks are not observed.

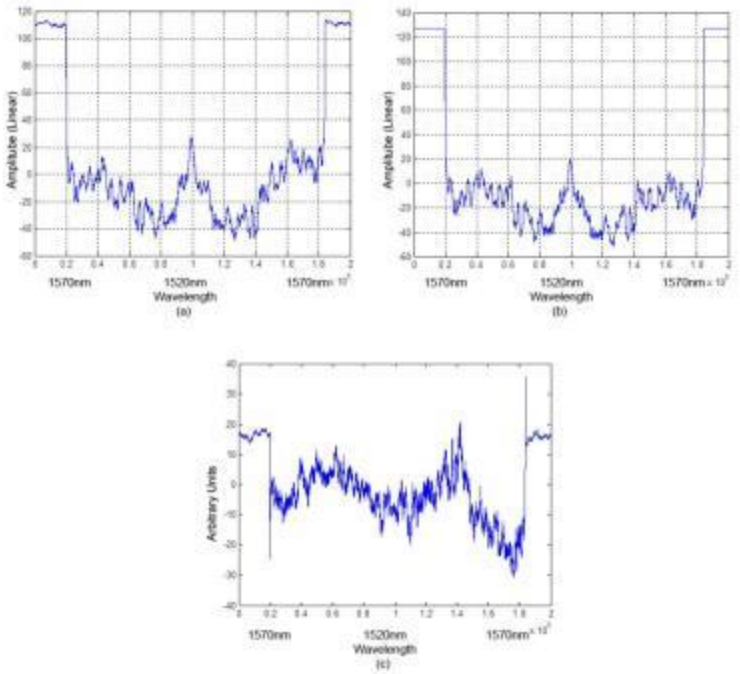

Figure 4-168: Measurements on Sapphire fiber between SM and MM fibers without gas (a), with gas (b) and (c) difference

4.13.3 Preliminary Experiments on 7-rod Sapphire Bundle

When Sapphire bundle is constructed into our system, single-mode and multi-mode fibers are used as our lead-in and lead-out fibers. The sapphire fiber needed to be spliced with MM fiber. Figure 4-169 shows the splicing condition between the MM and sapphire fiber using a 60µm long GRID MM fiber. One of the benefits of using a GRID MM fiber between the MM and sapphire fiber is that the core region of the GRID MM fiber melts faster than the cladding region of the fiber, ensuring the alignment of two fiber when during splicing.

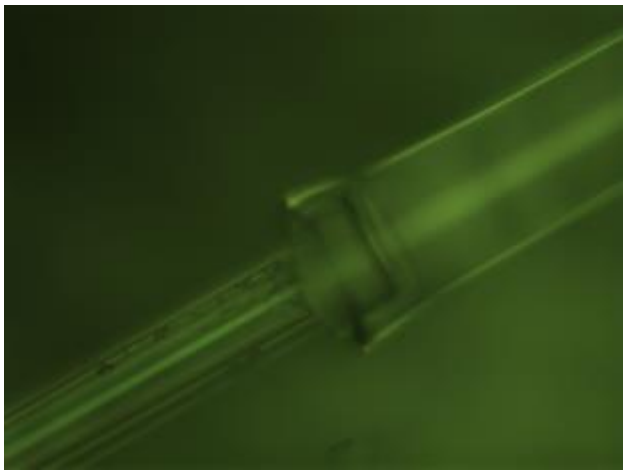

Figure 4-169: Splicing between MM and Sapphire fiber with GRID MM fiber

After splicing the MM fiber with the sapphire fiber, the lead-in SM fiber was aligned with another sapphire fiber and placed with the MM fiber spliced sapphire fiber in individual 3-axis stages. A CTS and photodiode with trans-impedance amplifier was used as the input source and detector respectively in the system as shown in Figure 4-170. An air cavity was created with a length of 10mm and 30mm and the alignment between the fibers was precisely adjusted in each measurement to ensure maximum transmission for each measurement. Gas absorption peaks were successfully measured in each case. Figure 4-171 and Figure 4-172 show the measurements with 10mm and 30mm of cavity respectively. Due to the limitations of the translation stages, a longer cavity could not be measured.

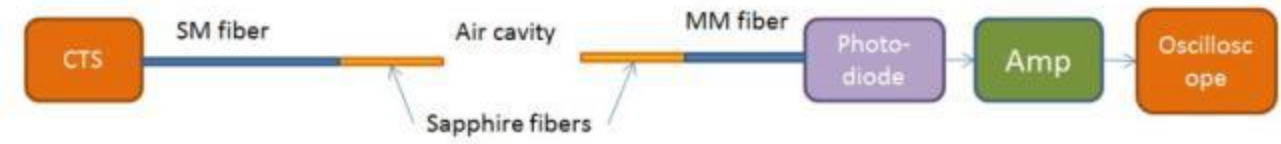

Figure 4-170: Schematic of preliminary experiment on Sapphire bundle

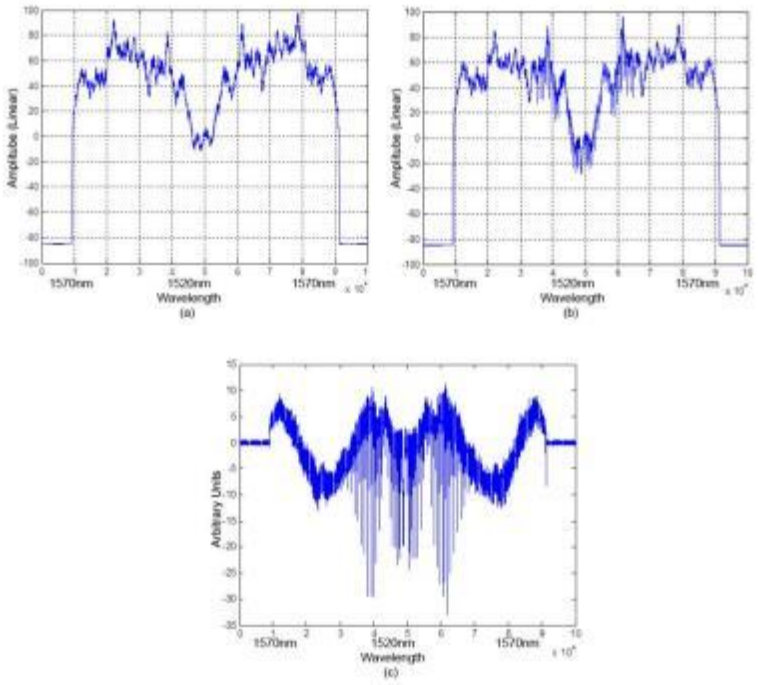

Figure 4-171: Measurements on 10mm of cavity between two Sapphire fibers without gas (a), with gas (b) and their difference(c)

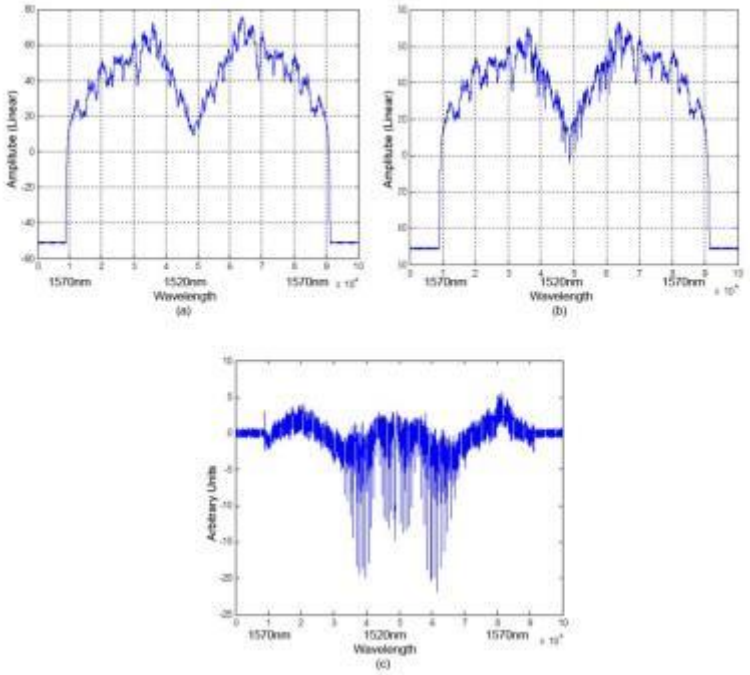

Figure 4-172: Measurements on 30mm of cavity between two Sapphire fibers without gas (a), with gas (b) and their difference(c)

5 Porous Glass Gas Sensor Development

5.1 Development of Suitable Joining Technologies Between the Sensor and the Standard Lead-in/Lead-out Fibers

5.1.1 Cleaning Procedure for Green Glass Tubes

The green non-phase separated glass tubes used to produce the porous glass fiber were found to be dirty and have a residue present that affected draw characteristics. A test matrix was developed to determine the minimum amount of cleaning necessary to remove the residue from the surface of the tubes and improve drawing capability. A bath of Ammonium Bifluoride solution was used to etch the surface of the glass and provide the cleanest surface possible. Solution strengths of 5% and 10% Ammonium Bifluoride were used with three different soak timesTable 5-1 shows the different testing conditions used.

Table 5-1: Test Matrix

Time/Concentration	5% Ammonium Bifluoride	10% Ammonium Bifluoride
5 minutes	2 Samples	2 Samples
10 minutes	2 Samples	2 Samples
20 minutes	2 Samples	2 Samples

The soaking solutions were made to a volume of 2L using Ammonium Bifluoride flakes. The 5% solution was produced with 100g of Ammonium Bifluoride and adding DI water up to 2L. The 10% solution was prepared in the same manner using 200g. All 6 samples for each solution were submerged in the bath horizontally and agitated to remove all bubbles from inside the tubes. The solution was then stirred every 2 minutes. Two samples were removed after 5 minutes and rinsed in a tub of DI water for 2 minutes then rinsed with flowing DI water and allowed to air dry. The process was repeated on 2 samples at 10 minutes and the final 2 at 20 minutes. Figure 5-1 shows the difference between the non-etched samples to those from the 20 minute 10% etch.

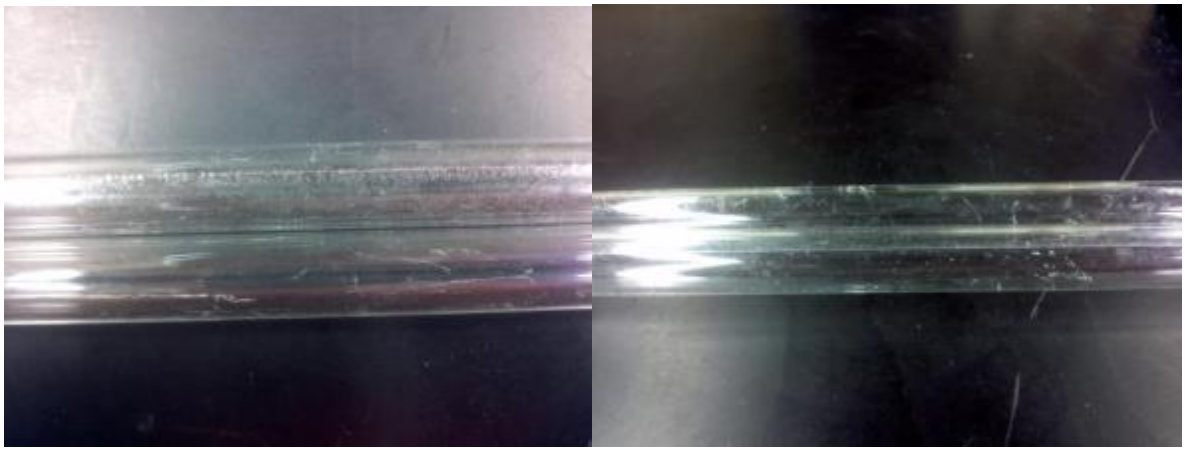

Figure 5-1: Two tubes prior to etching (left) and two tubes after etching 20 minutes in 10% Ammonium Bifluoride solution.

Figure 5-1 shows the residue present on the glass tubes prior to etching as well as white marks and scratches that are present both before and after etching. Figure 5-1 also shows that after the strongest etch that no residue remains on the tubes. The white marks are physical

damage caused by the glass tubes rubbing against each other in storage. These marks were still visible after all etches and are surface imperfections caused by the tubes rubbing and bumping against each other in the container. This residue was also visible on the inside of the tube. Figure 5-2 shows all the samples etched in the 5% solution and the remaining residue present on all the tubes. All samples still show residue present on the surface with the 20 minutes showing the least amount.

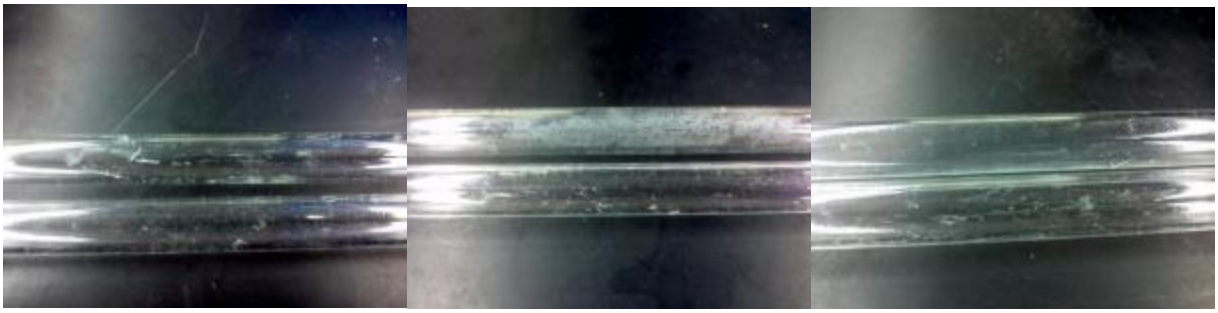

Figure 5-2: Samples shown from all 5% solutions 5 minutes (left), 10 minutes (middle), and 20minutes (right).

Five of the 6 samples etched in the 10% solution showed no noticeable residue. The one sample that showed remaining residue was one of the 2 samples etched for 10 minutes. Figure 5-3 shows the two 10 minute samples with the upper one still having residue remaining. . One sample showed no remaining residue (bottom) while the top sample showed significant residue remaining.

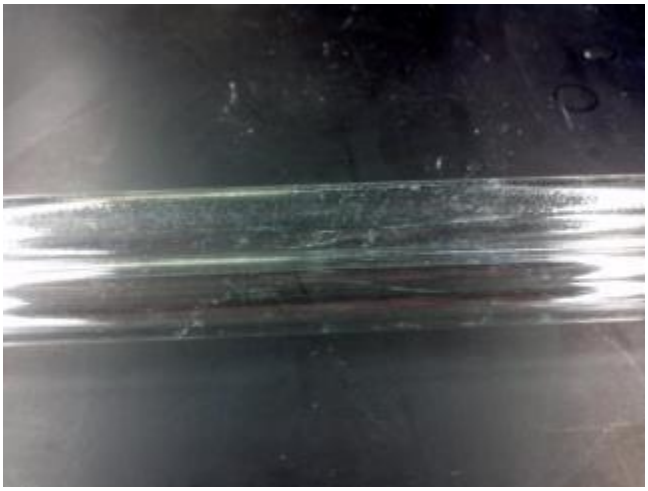

Figure 5-3: Samples etched for 10 minutes in 10% solution

The one sample that had residue remaining may have had thicker residue than other samples. The samples etched for 20 minutes in the 10% solution looked the best of any samples. All of these test samples will be drawn to determine if the remaining residue causes significant drawing problems. Due to the one sample still having residue in the 10 minute test, all samples prepared for sensor will be etched 20 minutes in 10% Ammonium Bifluoride to ensure the cleanest surface possible.

5.1.2 Preform Fabrication

Glass tubes received were cleaned using ammonium bifluoride to ensure the best drawing quality possible. Fibers were drawn from 6 test conditions to determine the cleaning effects on drawing and fiber characteristics. The different cleaning processes are listed in Table 5-2 below.

Table 5-2: Cleaning conditions used.

Condition	Time (minutes)	Concentration NH_4F_2
A	5	5%
B	10	5%
C	20	5%
D	5	10%
E	10	10%
F	20	10%

Fibers drawn from each of these conditions were processed to produce porous qualities. All fibers were 6-9 inches in length to fit in the processing furnace. The procedure is listed below.

1. Fibers heated to 570 °C at a rate of 5 °C/min and held there for 20 hours then cooled to room temperature with the same rate.
2. Fibers were then placed in a test tube for the acid treatments.
3. Surfaces etch of fibers using 5% Ammonium Bifluoride for 5 minutes.
4. Acid drained from tube and replaced with 3N Nitric acid and placed in beaker of water heated to 80C and left to soak overnight (>18 hours).
5. Acid drained from tube and replaced with DI water and left to soak overnight.
6. DI water drained and replaced with 0.5N Sodium Hydroxide for 30 minutes.
7. Sodium hydroxide drained and 3N Nitric acid replaced in tube for 3 hours.
8. Nitric acid drained and replaced with DI water and allowed to soak overnight.
9. DI water drained and fibers allowed to air dry.

All fibers had identical processing save the initial cleaning treatment. Fibers from the unclean samples were not processed due to extremely poor drawing capability and the inability to produce a straight section of fiber of necessary length. Two tubes were cleaned for each condition and were used to draw fibers from. All fibers drawn from condition A had bubbles and were not straight as a result. For conditions B, C, D, and E fibers were of mixed quality. At these conditions straight well drawn fibers were produced from some sections of the source tubes while other suffered the same problem as the minimum cleaning condition. All of the fibers produced from condition F tubes were of excellent quality and suffered no ill effects during drawing. This would indicate that the surface contamination varies in amount tube to tube and even along the length of tubes. This would indicate that the strongest cleaning process should always be used to ensure the best drawing behavior. Sections of each fiber were then cleaved and mounted to stubs and coated with approximately 5nm of gold palladium alloy for pore size analysis in SEM.

Figure 5-4 below shows two images from condition A, that show both the bubble as well as surface residue that is undesirable. In addition to the bubbling pits in the surface that are much larger than the pore size were present.

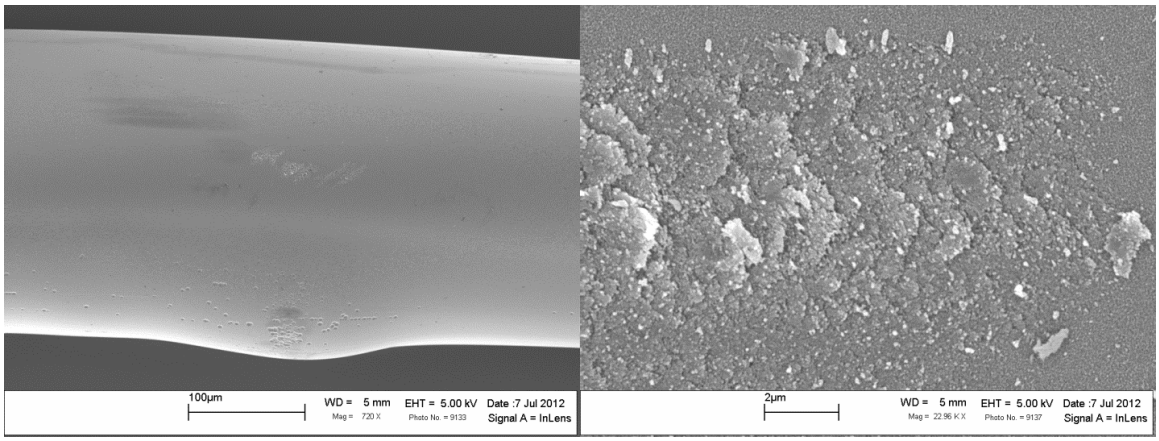

Figure 5-4: Images of condition A samples.

Images were taken of all samples to compare pore sizes. Figure 5-5 below shows all 6 samples at similar magnification next to each other for direct comparison of pore size. The measurements of all pores show that the pore sizes range from 15-30nm across all samples. This strongly indicates that the initial cleaning has no effect on the pore size and only on the drawability of the fiber and the straightness of the fiber. Since there is no effect on pore size and variability of drawing quality was present in all conditions but condition F all future fibers will be cleaned using condition F to ensure optimal drawing and the removal of all residue.

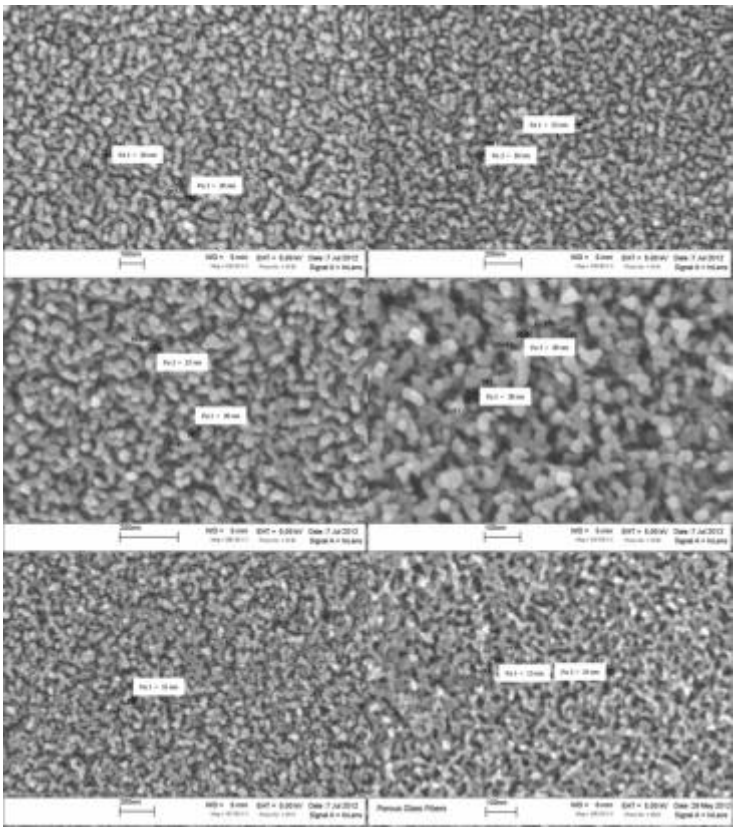

Figure 5-5: Images with measurement of pores for all conditions A (Top Left), B (Top Right), C (Middle Left), D (Middle Right), E (Bottom Left), and F (Bottom Right).

5.1.3 Methods to Improve Mechanical Stability of Porous Fibers

Fibers that have been produced had poor mechanical strength after undergoing the process to produce pores. This weakness is due to the fibers having a hollow core and having very thin walls. This lack of mechanical stability makes the fibers difficult to handle and very prone to damage during most handling. Currently methods to improve the strength of fiber are being investigated. The primary method for improving mechanical strength is to increase the wall thickness of the fibers. This is accomplished by using a torch to collapse the source tubes to smaller size and with thicker walls. This is being done because thick walled tubes tend to provide thick walled fibers while thin walled tubes tend to provide thinner walled fibers. This difficulty in collapsing tubes is to maintain an even round inner diameter. This is the primary problem being encounters as constant inner diameter is needed for the optical properties to be optimal.

5.1.4 Preliminary Bonding Trials

Porous glass based tube possess very good thermal and chemical durability and they are transparent in a wide spectrum range. It makes possibility of using this kind of material as an optical sensor element. In this project, the optical gas sensing system using porous silica based tube will be analyzed and demonstrated.

In order to develop such a system, optical properties and characteristics of the porous tube should be implemented with optical sensor system. In the beginning of development of such systems, the transmission test was performed using component testing system (CTS, Micron Optics Inc., Si-720) as the input source and the output was monitored with a LeCroy oscilloscope. Corning SMF-28 and Thorlab 105/125 MM fiber were used as lead-in and lead-out fibers to the porous glass tube. An InGaAs photodiode (Thorlabs) with transimpedance amplifier were used in conjunction with the LeCroy oscilloscope. Figure 5-6 shows the initial set-up for transmission test of the system.

Development of suitable joining techniques between the gas sensor and a lead-in or lead-out fiber is also required and one of the joining techniques using CO_2 laser bonding was evaluated. The joining technique between porous glass and Corning SMF-28 was implemented using Synrad CO_2 laser as shown in Figure 5-7.

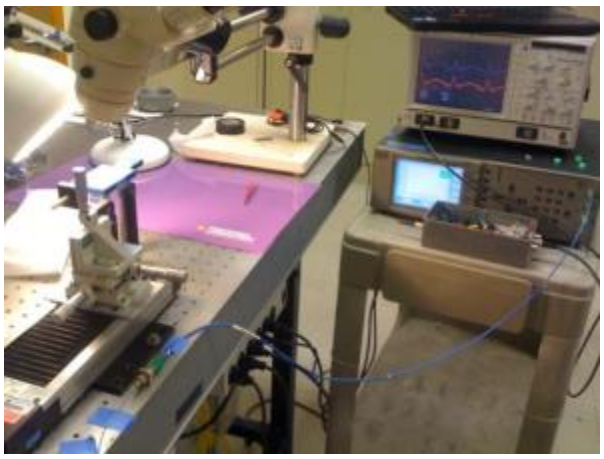

Figure 5-6: Initial set-up with the porous tube for transmission test.

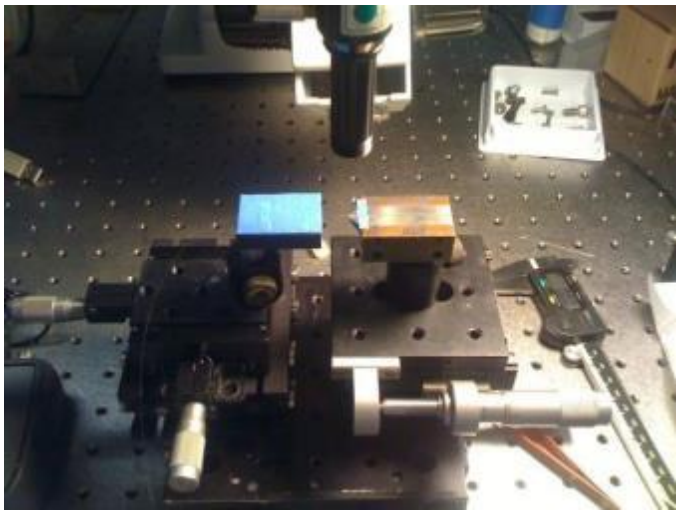

Figure 5-7: Set-up for CO_2 laser bonding between SMF-28 and porous silica tube.

One of the problems in the system was that the I.D. and quality of the porous glass tube. As shown in Figure 5-8, the ID of the tube is much larger than the OD of the lead-in or lead-out fibers. It caused significant problems with transmission loss in the system and joining technique with the CO_2 laser. I.D. of the tube should be in tolerance of ~10μm with O.D. of the fiber to improve transmission loss and joining technique with CO_2 laser bonding. The output signal of the system contained some saturation problems in the Thorlab InGaAs photodiode with transimpedance amplifier. It can probably be improved with matching the I.D. of the tube with O.D. of the fiber.

Improving I.D. of the porous silica tube will give significant benefits to the system. We will attempt to achieve an I.D. of the tube in tolerance of few microns with O.D. of the fiber and improve quality of the tube as well. The fiber drawing tower in CPT should give us improvements on these aspects. Suitable joining techniques between the tube and the fiber will be continue to investigated with using the CO_2 laser, electrical arc fusion splicer and high temperature adhesives. Transmission loss and bonding conditions will be monitored in different techniques and optimizing technique will be proposed based on the experimental data.

Analysis and demonstration of system response with 8cm long silica based porous tube. Figure 5-8 shows the lead-in and lead-out fibers with the 8cm long silica based porous tube. The size of the tube is not uniformed and ID of the tube is much larger than OD of the fibers. It dramatically reduced our output signal and the signal's quality. Figure 5-9 shows the input and output signals of the system. The gains of the transimpedance amplifier were 10^5 and 10^7 for input and output signals. The signal quality and noise can probably be improved by using well matched ID of the tube with the OD of the standard fibers.

As shown in Figure 5-9, the noises were observed in input and output signals in our system. In order to verify whether the system has system noise or interference noise, we used a SMF cable with TIA and oscilloscope configuration to measure the baseline transmission and did average the output signals at a stabilized condition. The system noise could be removed by averaging the signals as shown in Figure 5-10.

Figure 5-8: Lead- in and lead –out fibers with porous tube

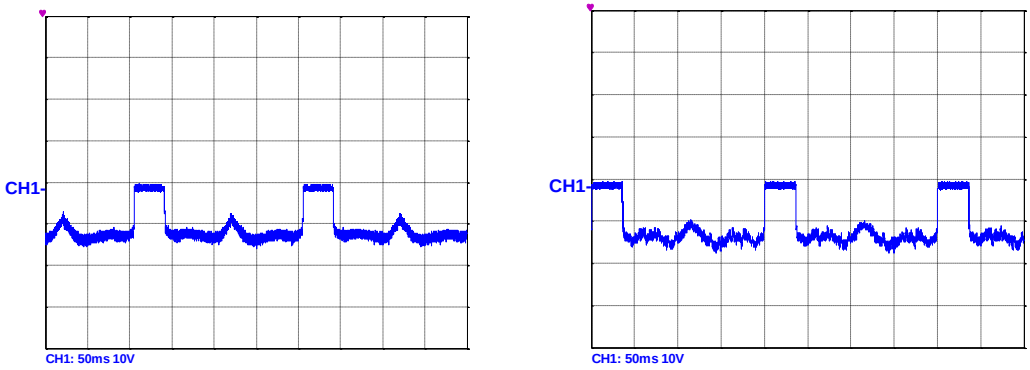

Figure 5-9: Input (left) and output (right) signals of the system with 8cm long porous tube.

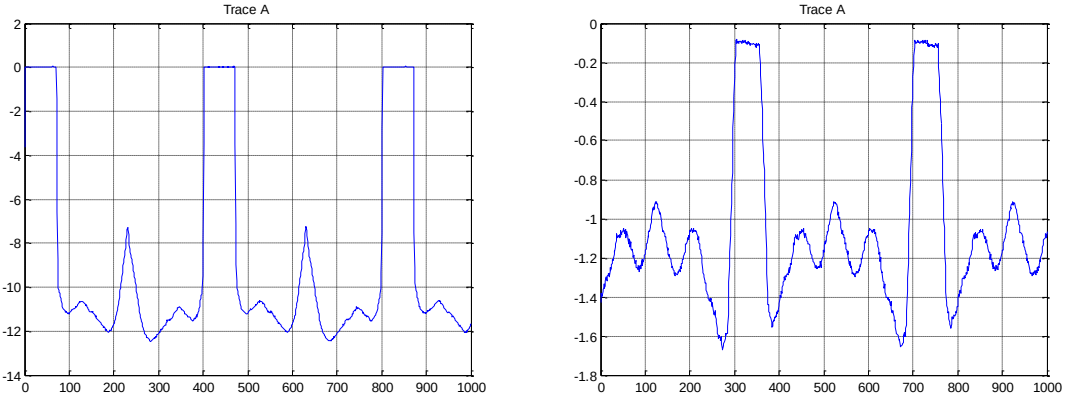

Figure 5-10: Averaged input (left) and output (right) signals of the system with 8cm long porous tube.

Analysis on the CO_2 laser bonding technique between standard fiber and silica based porous tube. **Error! Reference source not found.** shows CO_2 laser bonding between fibers and he porous tube with different laser powers. We could not observe any changes on the tube with laser power below 1.5W. With 2 W and 2.5 W, it shows pretty good shrinkage of the tube and a weak bonding effect between the tube and the fiber. Any power above 3W contributed a burned spot on the tube and made some bending on the tube instead of shrinking or bonding it. We also

observed different shrinkage and bonding effects with different thickness of the tube. A thinner tube has better shrinkage and bonding effects than thicker tubes.

After analysis on laser power, CO_2 laser bonding with 2.5 W applied around the tube. Figure 5-11 shows the CO_2 laser bonding around the porous silica tube by rotating the tube. As shown in Figure 5-11, the porous tube totally collapsed on the fiber after applying CO_2 laser 5 times around the tube. It had pretty strong bonding force between the tube and the fiber but it created the transmission loss of 2.15dB.

In order to test the consistency of the CO_2 laser bonding, several attempts were made around the tube. Unfortunately, we experienced huge transmission loss (more than 25dB) on other attempts. Table 5-3 shows the results of other attempts that we had to apply CO_2 laser more than 10 times to achieve reasonable bonding effects between the porous tube and the fiber. It created micro bending or sharp bending on the fiber and resulted huge transmission loss in the system.

The CO_2 laser bonding can be improved by using a matched ID of the porous tube with the fiber. It can be improved if a 120 degree mirror assembly is used to apply CO_2 laser bonding around the tube. It should give us better uniformly melting points around porous silica tube.

Table 5-3: CO2 laser bonding between standard fiber and porous tube with different laser powers.

CO_2 laser power	Duration	Result	Observation
1.5W	7 sec.		Did not observe any changes. No shrinkage or bonding
2W	7 sec.		Observed shrinkage and weak bonding effects.
2.5W	5 sec.		Observed shrinkage and weak bonding effects.
3W	5 sec.		Observed a burned spot on the tube and it bended the tube instead of shrinkage

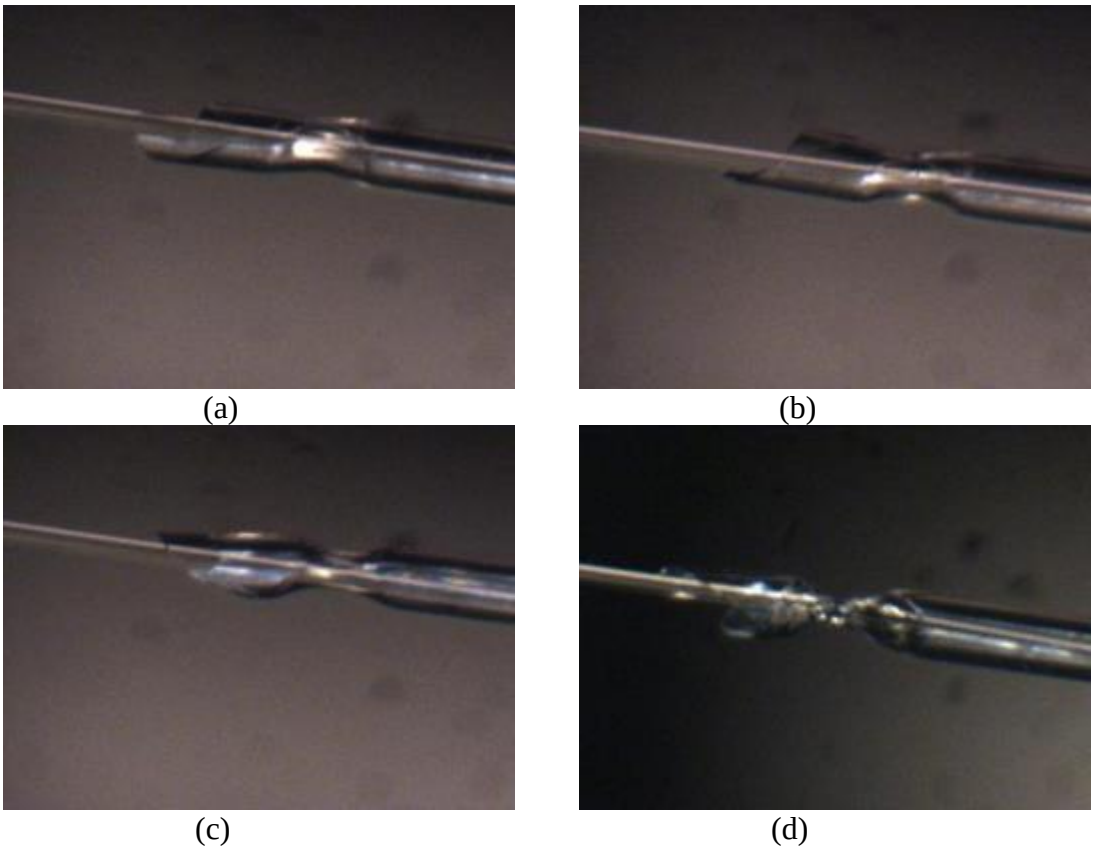

Figure 5-11: CO_2 laser bonding around the porous tube

Figure 5-12: CO_2 laser bonding around the porous tube with applying laser more than 10 times

5.1.5 Additional Bonding Techniques

One of the goals of this project was the research and development of the optical gas sensing system using porous silica based tubes and photonic sapphire fiber structure. Porous silica based tubes possess very good thermal and chemical durability and they are transparent in a wide of spectrum range. This makes it possible to o use this kind of material as an optical sensor element. Progress was made in development of suitable joining techniques between a porous silica tube and Corning SMF-28 using CO_2 laser and electrical arc fusion splicer. Figure 5-13 shows the Synrad CO_2 laser and the Sumitomo optical fiber fusion splicer that were used in

the development of the joining techniques. In a part of development such joining technique, a joining techniques between Glass tube and capillary tube was also evaluated and demonstrated prior to leeching process. If the sensor structure can be employed with a capillary tube, it should give an advantage on assembling the sensor and alignment of the fiber. Transmission test between lead-in and lead-out fibers with porous tube was performed with these bonding techniques.

The system with a mirror surface at the end of a porous tube was investigated to determine if it would perform better than having lead in and lead out fiber. In order to achieve a mirror surface, gold platting was applied at the end face of Corning SMF-28. Reflective signals from the mirror surface were measured with different cavity lengths.

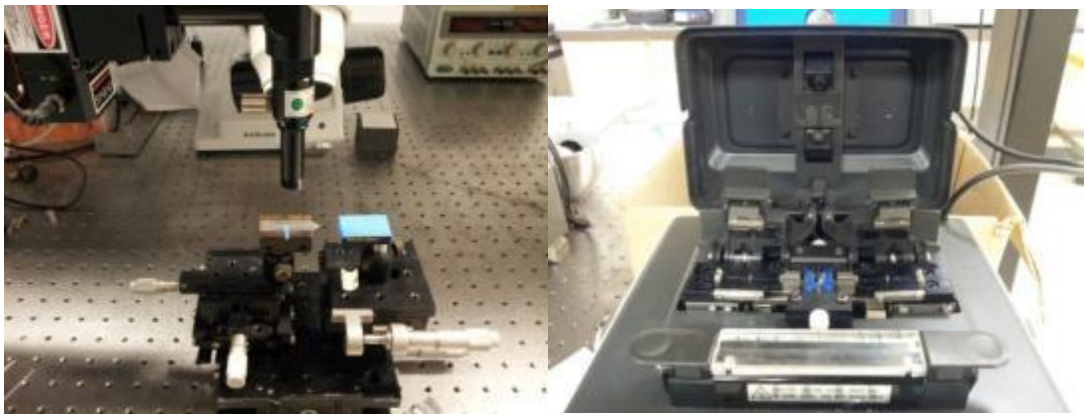

Figure 5-13: Set-up for CO_2 laser (Left) and electrical arc fusion splicer (Right) bonding between SMF-28 and porous silica tube.

5.1.6 Joining Techniques Between Porous Tube and SMF-28 Using CO_2 Laser and Fusion Splicer.

Table 5-4 shows CO_2 laser bonding between SMF-28 and the porous tube with different laser powers. O.D. of the porous tube is around 850 microns and the I.D. of the porous tube is around 135 microns. There was no shrinkage or bonding effects on the porous tube with any laser powers below 1.5W. With 2W of laser power, it started to show some shrinkage and a weak bonding effect on the porous tube. Finally, with 2.5W of laser power, it showed a stronger bonding effect between the porous tube and the SMF-28. The bonding conditions with different laser powers are highly dependent on the thickness of the porous tube. The required laser powers could be achieved throughout several trails with different sizes of porous tubes. The summary of the laser powers and durations that were required for performing proper bonding between the porous tube and the SMF-28 are shown in Table 5-5.

The first attempts to bond SMF-28 with the porous tube using fusion splicing resulted in many failures. Through analysis of these failures and by conducting several trials, a successful bond of the sensor and fiber using fusion splicing was achieved. One of the main problems encountered was the size of the porous tube. Since there are limited diameters of tube that can be used in the fusion splicing machine, the O.D. of the porous tube needed to be reduced. However, it should not be too small to properly handle the tube. After achieving the required diameter of the tube, the proper condition of the fusion splicing needed to be optimized. After several trails, approximately 500 micron O.D. of porous tube was employed in the fusion splicing machine. The condition of the fusion splicing machine was found after a few trails. Table 5-6 is the set up for the fusion splicing.

Table 5-4: CO2 laser bonding between SMF-28 and porous tube with different laser powers.

CO_2 laser power	Duration	Result	Observation
1.5W	7 sec.		Did not observe any changes. No bonding
2W	7 sec.	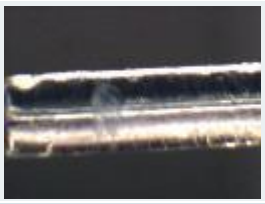	No shrinkage, weak bonding.
2.5W	7 sec.		Observed shrinkage and strong bonding.

Table 5-5: Required CO2 laser power to achieve strong bonding with different wall thickness of the porous tubes.

Wall Thickness of porous tube	CO_2 laser power	Duration	Observation
200~400 microns	**1.5W**	7 sec.	Did not observe any changes. No bonding
400~600 microns	**2.5W**	7 sec.	No shrinkage, weak bonding.
600~800 microns	**3W**	7 sec.	Observed shrinkage and strong bonding.

Table 5-6: Fusion Splicer Settings

Arc duration	00.40
Prefusion	00.20
Arc Gap	00.00
Overlap	10.00
Arc Power	0003

Finally, a strong bonding force between the fiber and the porous tube was achieved and Figure 5-14 shows the actual bonding using fusion splicing. The desired O.D of the porous to be used in fusion splicing bonding should be between 400 microns to 700 microns.

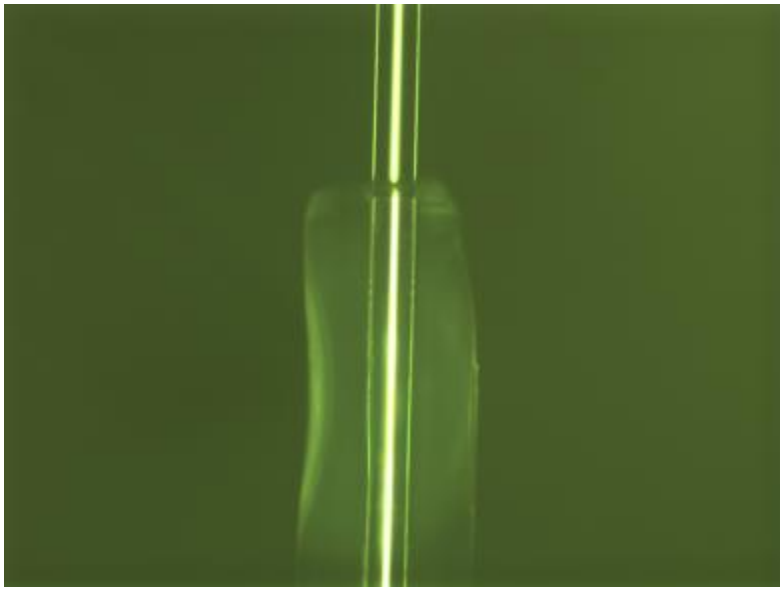

Figure 5-14: Bonding between porous tube and SMF-28 using fusion splicing

5.1.7 Transmission Test Between Lead-in and Lead-out Fibers with Porous Tube.

Error! Reference source not found. shows the first attempt of a transmission test using porous tube and a capillary tube. The result shows some experimental error in the measurement. As shown in Table 5-7, the transmission loss decreased on both the porous tube and the capillary tube when the cavity length increased from 22.41mm to 27.64mm. These measurements show some experimental error and we believed the error comes from the porous particles that are generated during the insertion process.

Table 5-7: Transmission loss measurement on porous tube and capillary tube

Cavity	Porous Tube	Capillary Tube
13.58mm	-30dB	-20dB
127.46mm	-31dB	-28dB
22.41mm	-32dB	-29dB
27.64mm	-27.5dB	-24dB

A second set of measurements was performed due to these potential errors. Table 5-8shows the second set of measurement results. While the lead-in and lead-out fibers were inserted into the porous tube, it made some porous particles inside of the tube due to the friction between the fiber and the porous tube. These particles make a contribution to the transmission loss. Very careful alignments were performed to reduce the porous particle inside of the tube. These measurements show reasonable values with different cavity lengths.

Table 5-8: Second transmission loss measurement on porous tube and capillary tube

Cavity	Porous Tube	Capillary Tube
13.58mm	-32dB	-15.5dB
127.46mm	-36dB	-17dB
22.41mm	-39dB	-20dB
27.64mm		-24dB

Both measurements show an unexpected signal improvement when CO_2 laser was applied on the porous tube during the bonding process. On the first attempt, signal improvement from -30dB to -19dB was observed. On the second measurement a similar improvement was observed and the transmission loss decreased from -32dB to -20dB. We believe that this improvement is due to consolidation of the porous particles inside of tube. When the CO_2 laser is applied to the porous tube, it melts down the porous particles on the end face of the fiber and it improves the signal quality due to reduction of the scattering effects of the particles. **Error! Reference ource not found.** shows the actual measurements before and after the CO_2 laser was applied on the porous tube. In order to verify the repeatability of the phenomenon a second measurement was performed as shown in Table 5-9.

Table 5-9: Output signals before and after CO2 laser applied

	Before CO_2 laser bonding	After CO_2 laser bonding
1st Measurement	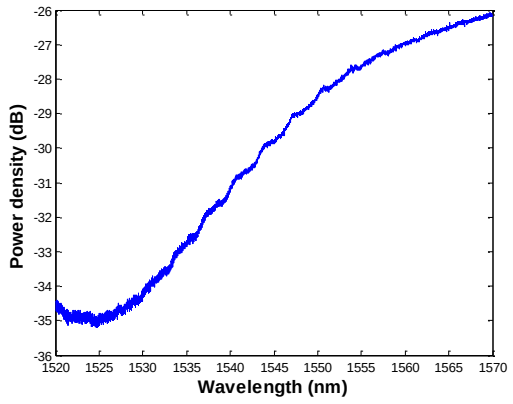	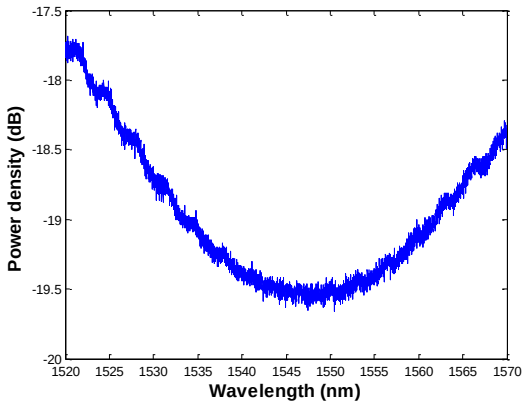

2nd Measurement	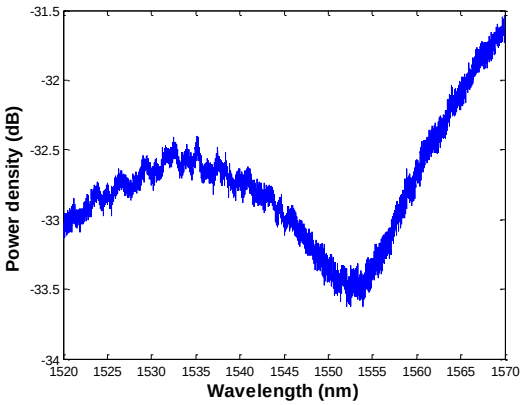	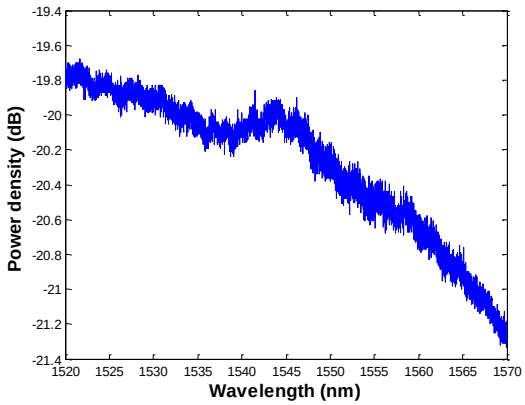

5.1.8 CO2 Bonding Trials Between Glass Tubes and 127µm Fused Silica Capillary Tube Prior to Leeching Process.

In order to investigate the possibility of using a solid silica capillary tube in our sensor design, CO_2 bonding trails were performed. A length of the silica capillary tube is inserted into a porous capillary tube and bonded. The bonding between these two components could be done at any stage in the process of making the sensor structure porous. The advantage that this approach confers is in the ease of bonding with the optical system fibers with reduced concern for bonding power used in the final assembly of the gas sensor system. These should give us an advantage on assembling the sensor and alignment of the fiber. If our sensor structure can employ a capillary tube, it will make easier to insert the fiber into the porous tube. Figure 5-15 shows two samples of the porous glass tube. Sample B in the figure has an ID and OD that is too large while sample A has a well matched I.D. with the O.D. of the capillary tube.

Table 5-10 shows the CO_2 laser bonding results on sample A and B with a solid silica capillary tube. Both samples had successful CO_2 laser bonding with different laser powers. Due to the non-uniform sizes of the tube, limited CO_2 bonding trails could be performed. Only a few sections of the tube were used in this experiment. Bonding conditions were highly dependent on the wall thickness of the tube.

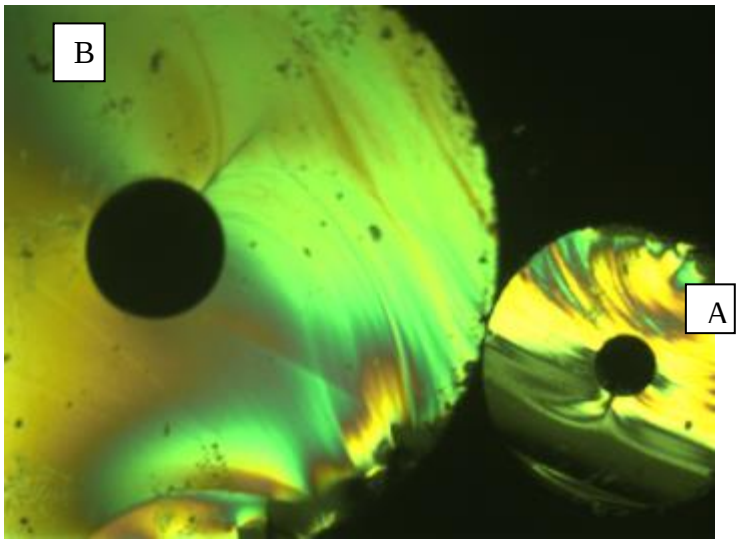

Figure 5-15: Samples of Glass tube

Table 5-10: CO2 bonding between Glass tube and capillary tube with different laser power

Power/Duration	Sample A	Observation	Sample B	observation
2.5W/ 10sec	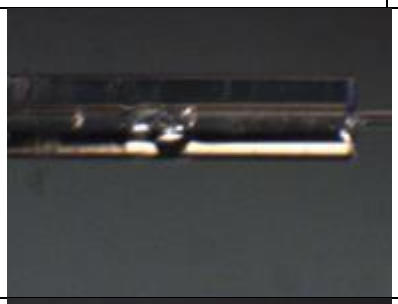	**Weak bonding**	**N/A**	**N/A**
3W/ 10sec	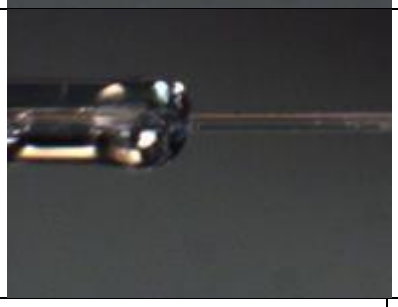	**Strong bonding**	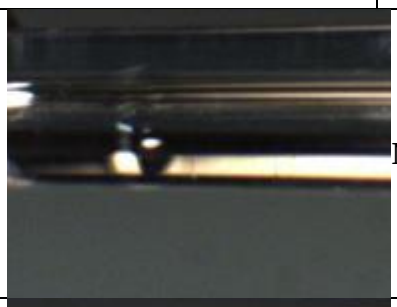	**No bonding**
3.5W/ 10sec	**N/A**	**N/A**	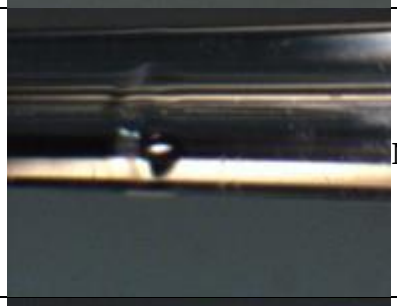	**No bonding**
4W/ 15sec	**N/A**	**N/A**	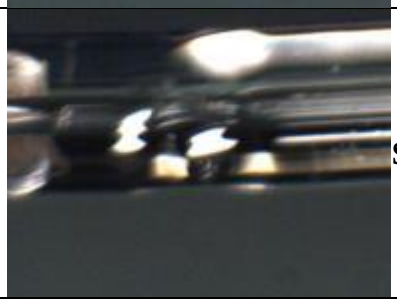	**Strong bonding**

5.1.9 Waveguide of the Porous Tube

The longest porous tube that is typically available is 14.5cm. Output spectrums of the gas sensor were measured with different distances between lead-in and lead-out fibers. As shown in Figure 5-16, the range is from 1cm to 13cm and gas absorption spectrums were also measured. The I.D. and O.D. of porous tube are 150μm and 390μm. The I.D. and O.D. of capillary tube are 127μm and 147μm. Table 5-11 shows the transmission losses of the porous tube and the capillary tube with different distances between the lead-in and lead-out fibers. Transmission loss of the porous tube gradually decreased from -22dB to -36dB when the cavity changed from 1cm to 13cm. The average decrement is 1.07dB/cm. It clearly shows that porous tube has a waveguide effect but not as confined as a silica based capillary tube.

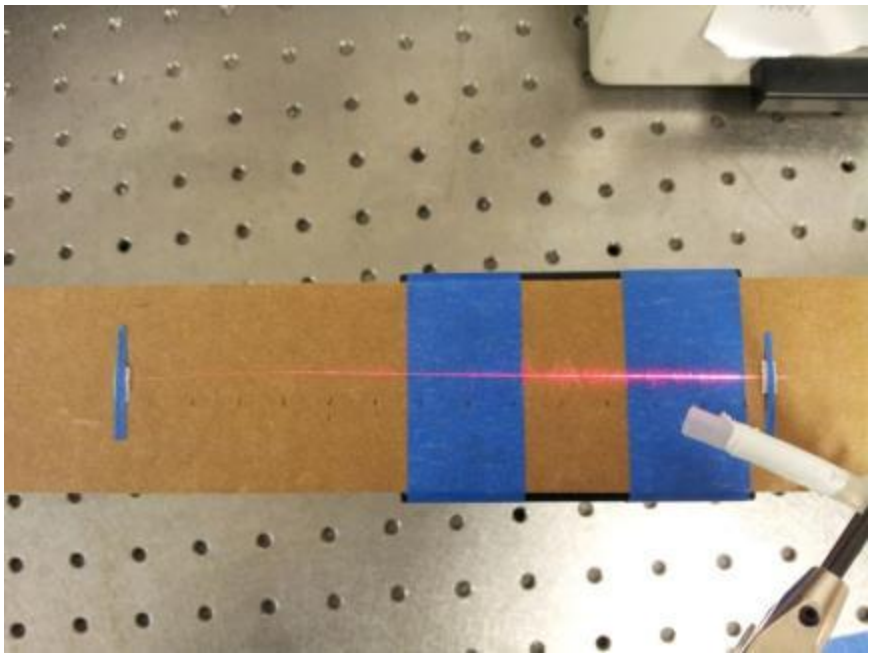

Figure 5-16: Set up for waveguide of porous tube

Table 5-11: Transmission losses in porous tube vs. capillary tube

Distance	Porous Tube(dB)	Capillary Tube(dB)
1cm	-22.15	-14.89
2cm	-23.70	-15.26
3cm	-24.68	-15.94
4cm	-25.82	-16.48
5cm	-26.71	-17.21
6cm	-27.14	-17.95
7cm	-28.78	-18.74
8cm	-29.46	-19.28
9cm	-31.55	-19.98
10cm	-32.24	-20.89
11cm	-33.75	-21.14
12cm	-34.98	-21.93
13cm	-36.12	-22.22

The gas absorption spectrum of the porous tube was also measured for each distance which was easily obtained for each distance by directly blowing the Acetylene gas on the porous tube as shown in Figure 5-16. Figure 5-17 shows the absorption spectrum with 13cm of the cavity between lead-in and lead-out fibers. Gas absorption peaks were easily observed from 1520nm to 1545nm.

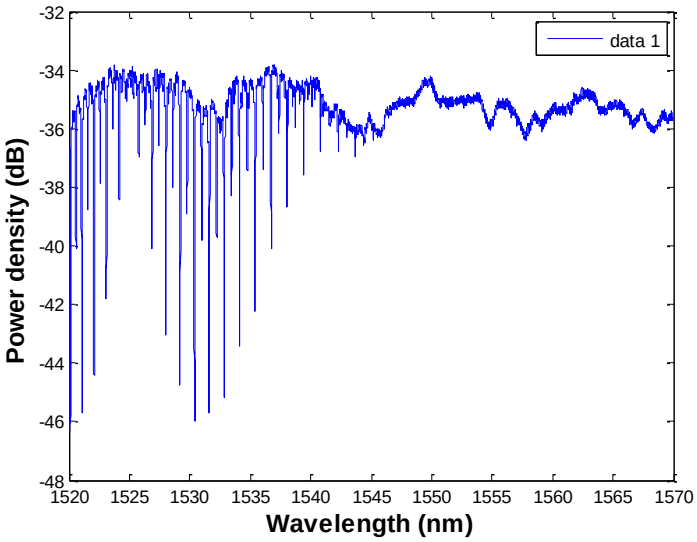

Figure 5-17: Absorption spectrum of C2H2 at 13cm of cavity

5.1.10 Suitable location for the Bonding Technique

Before the analysis of the bonding technique a suitable location of bonding site was investigated. Figure 5-18 shows the possible locations of bonding sites. 5 samples were prepared for each location to find the proper location to bond. We used a CO_2 laser and a fusion splicer to perform this experiment. The porous tube had an I.D. of 150µm and O.D. of 390µm with a distance between two the fibers of 5cm. Table 5-12 shows the results of the 5 samples for each location after bonding. At the end of fiber bonding, 3 of the 5 samples experienced a significant loss due to misalignment and bending of the fiber. When the bonding location was at the end of the porous tube, breakages were experienced at the end of the porous tube. It makes the bond fragile if the bonding is done at the end of porous tube. The proper location of the bond should be in the middle of these two ends which gives an average transmission is -36.24dB.

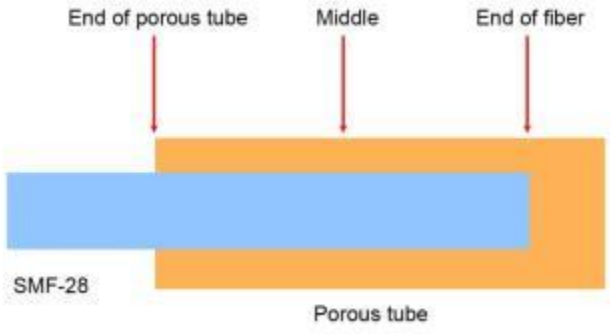

Figure 5-18: Possible locations of bonding techniques

Table 5-12: Transmission loss for each location after bonding

Sample	End of porous tube	middle	End of fiber
1	-38.15	-36.57	>-60
2	-41.22	-34.19	-48.21
3	-39.47	-37.08	>-60
4	-34.21	-39.25	>-60
5	-39.57	-34.11	-43.51

5.1.11 Bonding Technique Using High Temperature Adhesives.

In order to investigate the possibility of using a high temperature adhesive in our sensor design, adhesive bonding trails were also conducted. Selection of an adhesive that will minimize any issues is very important. The main criteria used for selecting an adhesive are chemical compatibility, similar thermal properties, and ability to serve over the necessary temperature range. Using this criteria the adhesive selected is a silica based adhesive available from Aremco, type 618N. This adhesive has temperature range that well exceeds that of the necessary 500 °C. Upon curing, the adhesive is nearly pure silica and will have similar thermal properties as the glasses it is bonded to. It closely matches that of the fused silica optical fiber but differs from the porous glass. It is the closest match that is commercially available.

The potential advantage is the ease of assembling the sensor and alignment of the fiber. Ceramabond 618-N and Ultra Hi-temp Ceramic Adhesive (904 Zirconia) were used in our experiments. Ceramabond 618-N should be cured at steps of room temperature, 200°F, 500°F and 700°F and it should be cured for two hours at each step. 904 Zirconia could be cured at room temperature for 24 hours. We prepared two samples for each adhesive and Figure 5-19 shows one of the samples where we applied the adhesive between the porous tube and the fiber. The porous tube had an I.D. of 150μm and O.D. of 390μm and distance between the two fibers was 5cm.

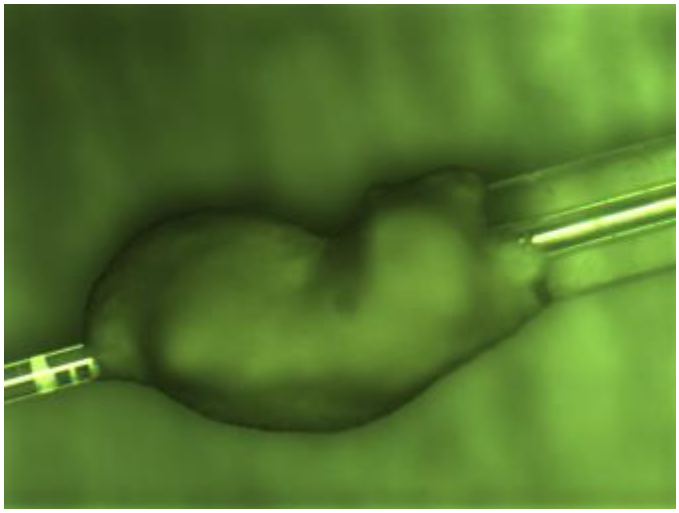

Figure 5-19: Bonding using high temperature adhesive between the fiber and porous tube

After constructing two samples with each adhesive, a thermal cycle test was performed to verify any possible thermal shock or thermal expansion differences in our sensor design. Figure

5-20 shows the set-up for the thermal cycles tests where a MTI GSL-1500X tube furnace was used in the experiment. Samples with 904 Zirconia were tested up to 500 °C at rate of 5 °C/min and samples with Ceramabond 618-N were tested up to 700 °C at rate of 5 °C/min. As shown in Figure 5-20, the sensors were monitored and measured during the thermal cycle test. We could observe fluctuations in the transmission loss during the test and the transmission loss gradually decreased as the temperature increased. After cooling down, the sensors experienced a significant transmission loss. Table 5-13 shows the result after thermal cycle test on each sample. Average transmission loss of sensor with Ceramabond 618-N is -15.15dB and Average transmission loss of sensor with 904 Zirconia is -14.37dB.

Figure 5-20: Bonding using high temperature adhesive between the fiber and porous tube

Table 5-13: Transmission losses on samples after thermal cycle test

Ceramabond 618-N

Sample	Before	After	Difference
1	-30.36	-47.23	-16.87
2	-32.84	-46.27	-13.43
Avg.	-31.6	-46.75	-15.15

Ultra Hi-temp Ceramic Adhesive (904 Zirconia)

Sample	Before	After	Difference
1	-34.25	-48.19	-13.94
2	-32.44	-47.24	-14.8
Avg.	-33.345	-47.715	-14.37

5.1.12 Summary of bonding techniques.

5.1.12.1 CO2 Laser Bonding

Figure 5-21 shows an example of the CO_2 laser bonding between a porous tube and a fiber. 3.5W of the CO_2 laser power was used for 10 seconds on the junction in Figure 5-21(b). As shown in Figure 5-21(a), it does not give uniformed bonding around the tube and it may cause some bending of the lead-in or lead–out fibers. This bending causes transmission loss or misalignment between lead-in and lead-out fibers. We prepared 10 samples to test the repeatability of the fabrication using CO_2 laser. The porous tube has I.D. of 150μm and O.D. of 390μm and the distance between two fibers is 5cm.

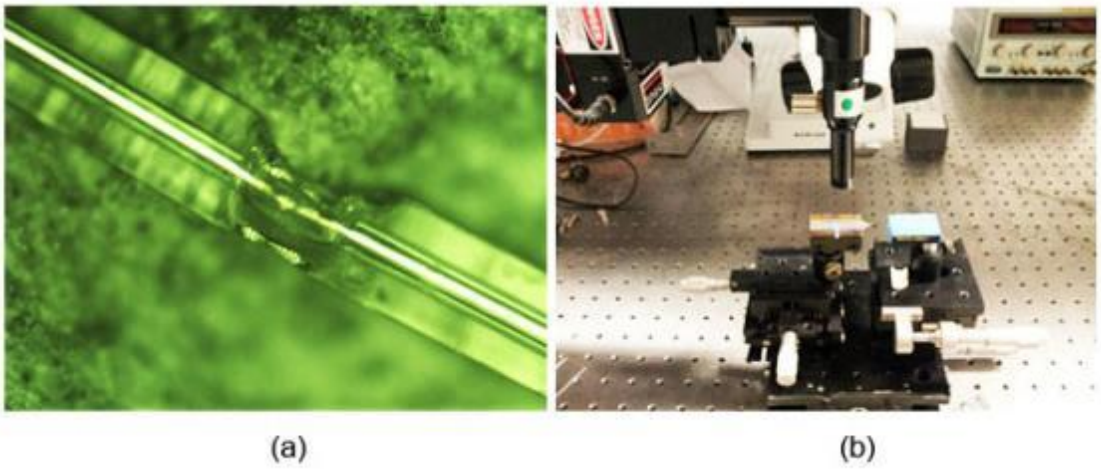

Figure 5-21: Bonding sample (a) and set-up (b) using CO2 laser between the fiber and porous tube

Table 5-14 shows 10 transmission losses of the 10 samples before and after CO_2 laser bonding. The average transmission loss of CO_2 laser bonding is around -2.5dB with a standard deviation of the transmission loss of 0.98. One of the advantages using CO2 laser bonding is that it can easily and precisely adjust the alignment of the two fibers with translation stages before the bonding. The other advantage is ease of fabrication compared to bonding with the fusion splicer.

Table 5-14: Transmission losses of 10 samples before and after CO2 laser bonding

Sample	Before	After	Difference
1	-36.11	-40.48	-4.37
2	-39.45	-41.31	-1.86
3	-32.19	-35.12	-2.93
4	-35.48	-38.45	-2.97
5	-37.84	-39.18	-1.34
6	-34.67	-36.27	-1.6
7	-32.51	-36.1	-3.59
8	-33.47	-36.13	-2.66
9	-32.87	-35.55	-2.68
10	-32.97	-34.05	-1.08
Avg	-34.756	-37.264	-2.508

5.1.12.2 Bonding with Fusion Splicer

Figure 5-22 shows bonding between a porous tube and fiber using a fusion splicer. We used a Sumitomo optical fiber fusion splicer and following is the setting of the splicer in Figure 5-22(b). Arc duration=0.8, prefusion=0.1, overlap=10 and arc power=25. As shown in Figure 5-22(a), it gives uniformed bonding around the tube. We prepared 10 samples to test the repeatability of the fabrication using CO2 laser. The porous tube has I.D. of 150μm and O.D. of 390μm and distance between two fibers is 5cm.

Table 5-15 shows 10 transmission losses of the 10 samples before and after fusion splicer bonding. The average transmission loss of fusion splicer bonding is around -3.16dB and a standard deviation of the transmission loss is 1.57. One of the possible reasons that the fusion splicer bonding has more transmission loss than CO_2 laser bonding is the limited access on the alignment of the two fibers. Bonding with the fusion splicer has a limitation when used with a porous tube. If O.D. of porous tube is larger than 970μm, the fusion splicer can't be used to make a bonding due to the limitation of the fusion splicer machine.

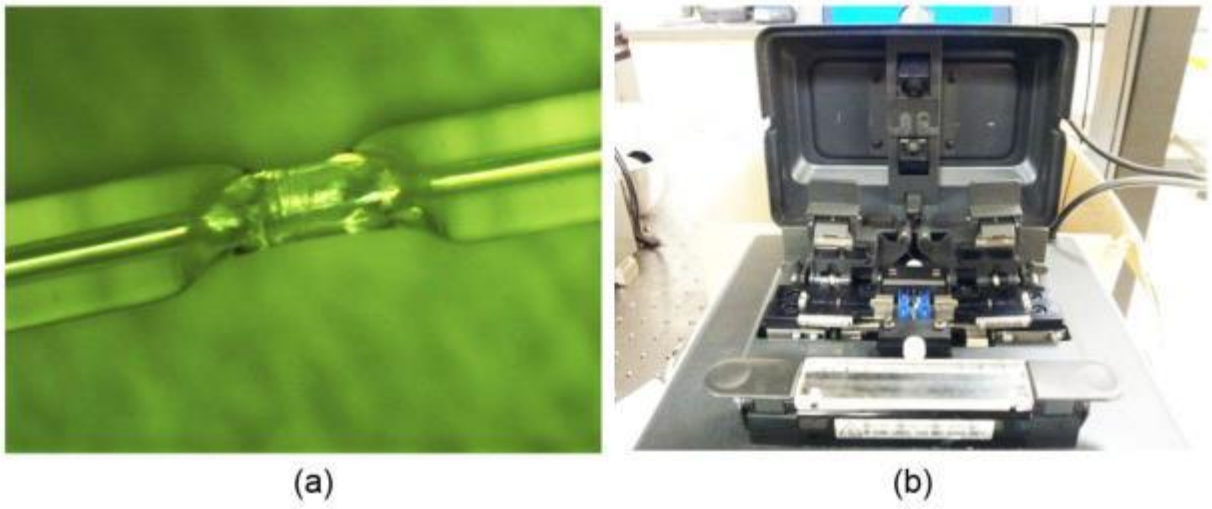

Figure 5-22: Bonding sample (a) and set-up (b) using fusion splicer between the fiber and porous tube

Table 5-15: Transmission losses of 10 samples before and after fusion splicer bonding

Sample	Before	After	Difference
1	-36.19	-42.71	-6.52
2	-33.12	-37.2	-4.08
3	-34.2	-36.27	-2.07
4	-38.48	-40.24	-1.76
5	-35.18	-37.21	-2.03
6	-33.35	-35.91	-2.56
7	-32.72	-37.89	-5.17
8	-36.08	-39.73	-3.65
9	-34.62	-36.34	-1.72
10	-35.49	-37.54	-2.05
Avg	-34.943	-38.104	-3.161

5.1.12.3 Durability of the Gas Sensor

In order to investigate the durability of the gas sensor using a porous tube, we constructed a simple set-up as shown in Figure 5-23. One side of the sensor was fixed and the other side of the sensor was attached with weight. The weight was gradually increased until breakage of the sensor structure occurred. Three samples for each bonding techniques were tested in this experiment. The porous tube had an I.D. of 150μm and O.D. of 390μm and distance between the two fibers was 5cm. Table 5-16 shows the result of the test for each bonding technique. The average strain of the CO_2 laser bonding can survive is 1362 με and the average strain the fusion splicer bonding can survive is 1283 με.

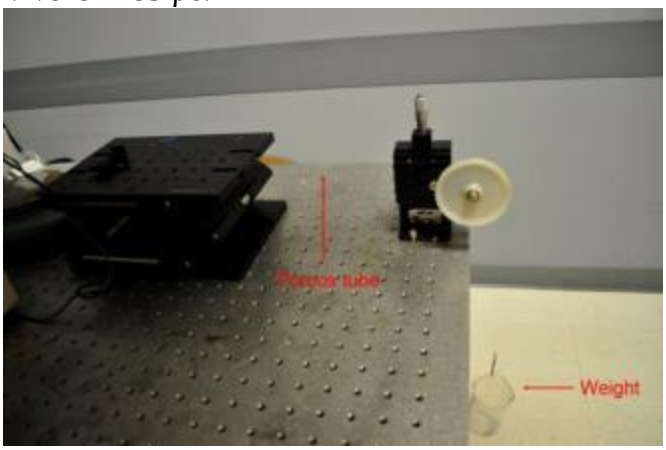

Figure 5-23: Simple set-up to test durability of sensor structure

Table 5-16: Durability test on each bonding techniques

CO_2 Bonding

Sample	Weight(g)	Break Point	Strain(με)
1	134.51	Tube	1493
2	118.34	Bonding	1314
3	115.16	Bonding	1278
Avg	122.67		1362

Fusion Splicer

Sample	Weight(g)	Break Point	Strain(με)
1	121.05	Bonding	1334
2	110.15	Bonding	1223
3	116.41	Bonding	1293
Avg	115.87		1283

5.2 Improving Mechanical Strength of Porous Fibers

The initial set of fibers produced had wall thicknesses in the range of 50 microns in thickness. After these thin walled tubes were made porous they became very fragile and would break under normal handling conditions. The thin wall nature is predominately a result of the initial size of the green glass preform that the tubes are drawn. All starting preforms available for use are the same size with a starting outer diameter of 12.8mm and inner diameter of 10mm.

The relatively thin wall of the preform tubes limits the wall thickness of any capillary tube that is drawn off this starting preform. In order to alter the wall thickness of the preforms and thus the drawn capillary tubes, the preform tubes were collapse to fabricate a thicker walled preform. Using an oxy-hydrogen torch and glass lathe these initial preforms were collapsed to make preforms with thicker walls and also a smaller initial starting outer diameter. These smaller outer diameters were desired to help transition drawing from the lathe to the mini draw tower. The new preforms are approximately 8mm outer diameter and 1-2mm in inner diameter. These thicker walled preforms allowed for tubes to be produced with the desired inner diameter of 130 microns with a 300-400 micron wall thickness.

5.2.1 Methods to Improve Uniformity of Green Glass Tubes

All tubes produced in the previous quarter were drawn using a horizontal glass lathe with an oxy-hydrogen torch as a heat source. The lathe has significant limitations on drawing capabilities and quantity of tubes produced. This has been the primary push for the use of a draw tower in production of green glass tubes that are the basis of the porous capillary gas sensor structure. The mini draw tower located in the Center for Photonics Technology was used for it benefits in drawing. The primary difference between the draw tower and the glass lathe is that the draw tower draws vertically and allows for continuous draws, while the modified glass lathe draws horizontally over short distances. The major capabilities of both the lathe and draw tower are listed in Table 5-17 below..

Table 5-17: Capabilities of Lathe and Draw Tower

	Draw Length	Draw Speed	Preform Limitations (Max OD)	Heat Source	Diameter Uniformity
Lathe	1m maximum	Up to 5m/min	Torch- none Furnace- 17 mm	Torch, Tube Furnace	50 microns total length
Draw Tower	Continuous for preform	>50m/min	Laser-7.9mm Furnace-17mm	Laser, Tube Furnace	<10 microns

The main issue with tubes pulled on the lathe is the lack of uniformity. This leads to very short lengths of tube being useful for further tests. Tubes produced on the lathe also suffered from very poor repeatability. The draw tower provides much tighter control on diameter of the tubes and over much longer lengths. The transition to the draw tower required smaller preforms to fit in the laser assembly. Tubes collapsed to have a small enough outer diameter to use the laser heat source had very small inner diameters. These preforms resulted in tubes that were too large of an outer diameter for bonding tests. Etching of the outer diameter was done in an attempt to provide a small enough outer diameter to fit the laser assembly while still having a big enough inner diameter to be useful. The fibers were etched using 48% hydrofluoric acid. This provided etch rates in the range of 500-600 microns/min. The etching process was successful in making the preforms small enough, however it induced a significant amount of stress in the preforms. This caused thermal shocking when the fibers were then heated in the pulling process. This shock could be eliminated by adding an additional thermal annealing step in the box furnace. The laser heating also had problems providing equal heat to the preform, so furnace heating was chosen for all future pulls. The use of the tube furnace provided good control of the temperature

and accommodates a wide range of preforms. Figure 5-24 below shows the draw tower as well as the tube furnace used.

The tube furnace used was made on-site and consists of resistive heating element in a porous ceramic brick powered by a variable voltage transformer. Temperature is monitored by using a type K thermocouple. The draw tower makes continuous pulling possible due to the drum that pulls the fiber and also spools it as it is drawn. The draw tower also allows for continuous measurement of the outer diameter of the fiber by using a laser micrometer. Using mathematical calculations the needed outer diameter can be found for a desired inner diameter based on the size of the preform. Since the diameter is continually monitored it allows us to change drawing conditions to reach and maintain the exact tube size desired. The draw tower allows for a wide range of tubes to be produced by allowing control of the temperature, draw speed, and feed speed of the preform. The temperature is set on the furnace at approximately 700°C. At this temperature gravity begins to pull the tube from the preform. When the tube reaches the drum it is attached with a piece of tape and the motor is started. The draw speed is increased until the desired diameter is reached as measured by the laser micrometer. The feed speed is then increased to maintain a constant amount of glass being pulled and to maintain fiber diameter.

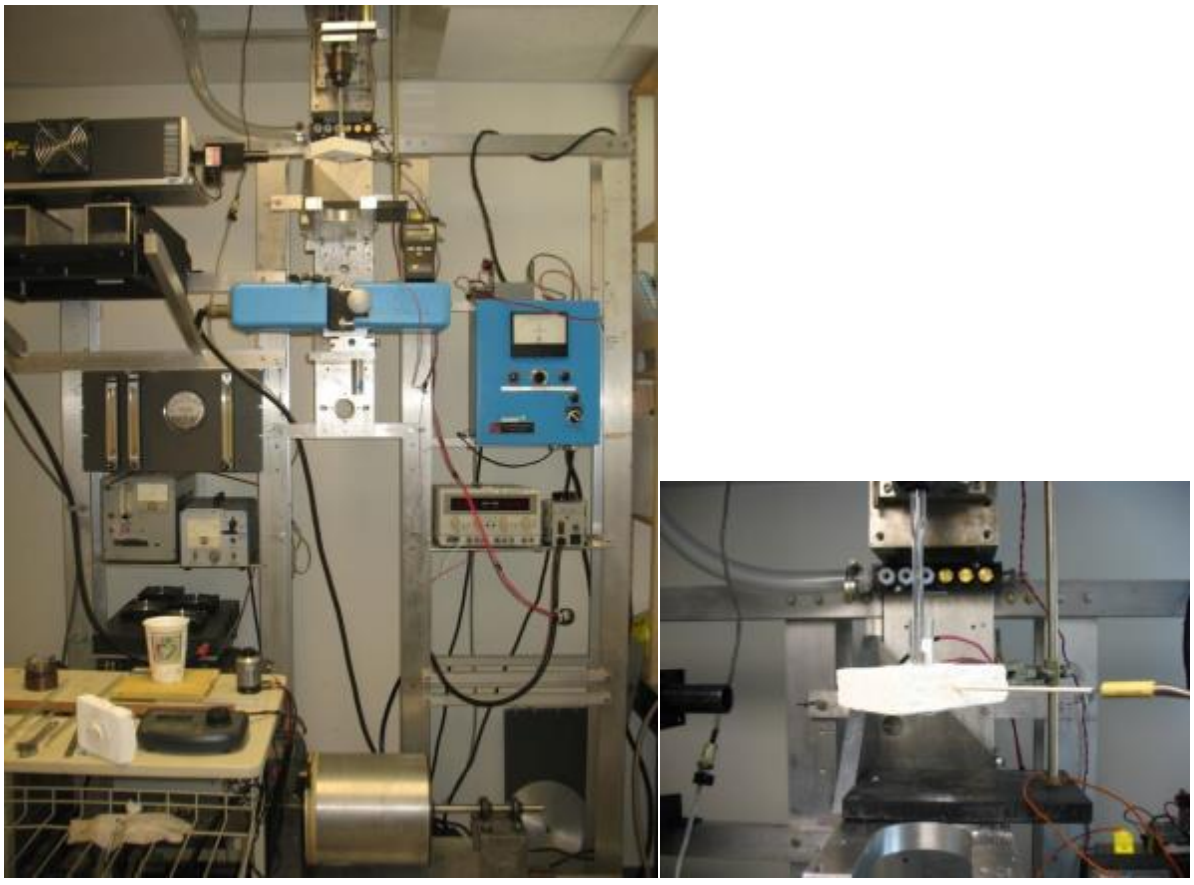

Figure 5-24: Complete draw tower (Left) and tube furnace used (right).

5.2.2 Characterization of Drawing Process

The use of the mini draw tower for the production of all tubes being used in this project leads to a greater need for understanding the drawing capabilities of the draw tower. The

capabilities are limited by three controllable factors: draw speed, feed speed, and temperature. These factors combined with the initial preform size control the final pulled tube size. Understanding the effects of these factors is necessary to allow for repeatability and prediction of the final tube size.

The controls present on the mini draw tower are limited to the electric controls for the motors. Temperature is controlled by using a variable voltage transformer and monitored using a type K thermocouple. Feed and pull speeds are controlled by adjusting the voltage to the electric motors. In order to develop a good understanding of the draw down characteristics these voltage settings have to be converted to more useful units of velocity. These velocities were observed and measured. Since preform dimensions vary, draw conditions are changed to give the desired final inner diameter. The limitations of mini draw tower system allow for only measuring the outer diameter of the drawn tube. Since a target inner diameter is needed this allows for a wide variety of final diameters. The wide range of final diameters makes it very difficult to relate to drawing conditions or to translate to other preforms. To be able to use this information on different preforms a draw down ratio is much more useful information. Trials across a wide range of conditions will provide draw down ratios for those conditions and provide a map for future draws on any preform.

The exact velocities of the draw tower were calculated first. The draw speed was calculated by first measuring the diameter of the drum and figuring the circumference. The circumference of the drum was found to be 842.889mm. The speed was then measured by the number of rotations as measured by the counter on the machine and timed using a stop watch. The feed speed was then measured again using a stop watch and caliper to measure distance traveled. The ranges of speeds capable are summarized in Table 5-18 below.

Table 5-18: Summary of Feed and Draw Speed Ranges

	Minimum Speed (mm/min)	Maximum Speed (mm/min)
Feed Speed	2.02	47.38
Draw Speed	962.75	24645.89

The controls for both speeds are smooth adjustments and allow for any speed over the possible range. In addition to governing the draw speed the drum size is the main factor in controlling the maximum size of the pulled tube. This limitation is caused by the radius of curvature of the drum and the specific glass being pulled at the time. The larger the outer diameter of the tube the less it can be bent before fracture occurs. The maximum size for a continuous draw of the green glass and the current drum size is approximately 650-700 microns. The range is given due to imperfections in the glass. Tubes in the range of 700-800 microns can be produced in short lengths approximately 2 rotations of the drum before breaking. The draw speed has the largest effect on tube size and due to this the trials are run using a constant temperature and feed speed. Several trials have been completed so far and data is continually being added as tubes are produced. Data has been collected in certain regions based on the preform sizes currently available. The draw down ratios from the 3 trials is shown below in Figure 5-25.

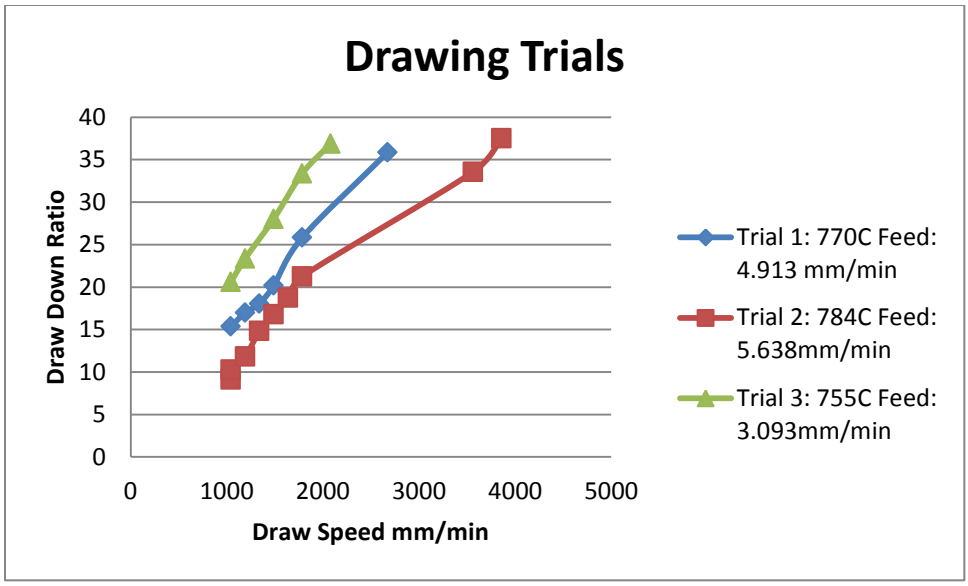

Figure 5-25: Draw down ratios versus draw speed.

Each of these trials was done at a constant temperature and constant feed speed. The draw speed was then varied to get different draw down ratios. The draw down ratio is calculated off of the outer diameter alone since that is actively measured during the process. The outer diameter is measured by use of a laser micrometer. It was discovered during these trials that there is an error present in the measurement of the outer diameter. This was found to be constant and present in all measurements and was +15 microns. Since the error was constant and present in all measurements it allows for us to factor it out. The constant factors of each of these trials are listed below in Table 5-19.

Table 5-19: Constants from Draw Trials

	Preform OD (mm)	Preform ID (mm)	Temperature (C)	Feed Speed (mm/min)
Trial 1	8.2	2.8	770	4.913
Trial 2	8.1	1.9	784	5.638
Trial 3	8.9	4	755	3.093

All of the preforms used were made by collapsing tubes using oxy-hydrogen torch on a glass lathe. Each of these trials have a very similar draw down ratios achieved at different draw speeds. All of the trials exhibited linear behavior with the exception part of trial 2. In trial 2, lower draw down ratios were used to get thicker final tubes. Higher draw speeds were used at the end and those don't appear to be on the same trend as the other data points. While all of these conditions is able to yield similar draw down ratios for the outer diameter they have differing effects on the inner diameter. After draws were completed, selected pieces were examined and measured under optical microscopy to determine the inner diameter. In trial 3 at a temperature of 755 °C the draw down ratios for the inner diameter are nearly the same as that of the outer diameter. This is ideal for most draws. In both trial 1 and 2, at the higher temperatures of 770 °C and 784 °C respectively, the draw down ratios for the inner diameter are significantly higher than that of the outer diameter. This is due to the higher temperature causing the tube to collapse as drawing is occurring. The higher temperatures were desired to help accommodate

higher feed speeds. In trial 2 based on the observed draw down of the outer diameter the expected inner diameter should range from approximately 240-100 microns. Measurement of the inner diameters in the microscope showed that the actual inner diameter ranged from 90-10microns. This significant collapse eliminates any of these tubes from being useful in gas cells but still aid in the characterization of the draw tower.

Characterization of the mini draw tower is an ongoing process that will continue to gain more data points as more conditions are tested. The final goal of this characterization is to provide a chart that will allow a user to set conditions for a preform based on the needed tube size. Similar draw down ratios are possible across a wide range of conditions that yield very different results. Data from these trials has yielded the maximum tube size that can be continuously pulled of 650-700 microns, this limitation comes largely from the size of the drum used to pull the fiber and curvature it puts in the fiber. The temperature where collapse becomes a significant part of drawing is also better understood for the system. The temperature for trial 1 and 2 was initially increased to provide enough heat for the higher feed rates. These trials yielded tubes that had inner diameters that were too small but also indicate that it is possible to collapse a tube as it is being drawn and possibly eliminate the need for a separate collapsing step on the lathe.

5.2.3 Method to Improve Fiber Insertion in Tube

Insertion of the fused silica fiber in the end of the porous glass tubes was difficult due to the close tolerances of the inner diameter to the fiber size. To eliminate this difficulty and to ensure good bonding with the lead in fiber bonding of a silica capillary tube to the green glass tube before being made porous was done. The fused silica capillary tube was a commercially available capillary tube with 127 micron inner diameter and a 200 micron outer diameter. Since the fused silica tube is not being made porous this makes it easier to insert the lead in fiber. Bonding trials of the fused silica tube to the porous glass tubes are being run. Initial tests were successful in bonding a green glass tube to the fused silica capillary tube using the CO_2 laser. These bonded tubes were then subjected to the phase separation and leaching process as normal. Three samples were made and processed, all of these samples survived. The bonding to the fused silica capillary tubes was able to survive the leaching process; however, the tubes became very fragile and broke during handling after processing. All of the tubes broke in the same location, at the end of the fused silica capillary tube. Failure at this location occurred because it provided a cleaving point for the porous glass tube. This, in combination with a thinner wall of approximately 75 microns, led to them being very fragile. Increasing the wall thickness should provide necessary strength for the tubes to not break during handling.

5.3 Sensor System Sensitivity Improvement

Various methods of optical gas detection were investigated in this report. These methods are detection using a porous plate with a CO_2 laser, fiber taper within a porous tube, and Whispering Gallery Mode (WGM) with a porous material. Preliminary research and tests of these methods were investigated and are presented. Gas sensing ability of each method was performed and their basic transmission characteristics were measured.

5.3.1 Gas Detection Using Porous Plate with CO_2 Laser

Figure 5-26(a) shows the application of a CO_2 laser to a porous plate to create structural changes in the porous material which can be expected to create waveguide effects on porous

material due to these changes. As shown in Figure 5-26(b), two sets of samples were prepared using 0.5W-1.2W CO_2 laser to test the consistency of the experiments. It was observed that it created a "burned" spot on the porous plate if the power of CO_2 laser was increased to over 1.0W. It should be noted that it was critical to use the same focal length of the CO_2 laser when the samples were prepared as the power of a CO_2 laser is highly dependent on the focal length. After preparing two sets of samples, each sample was placed between collimators as shown in Figure 5-27.

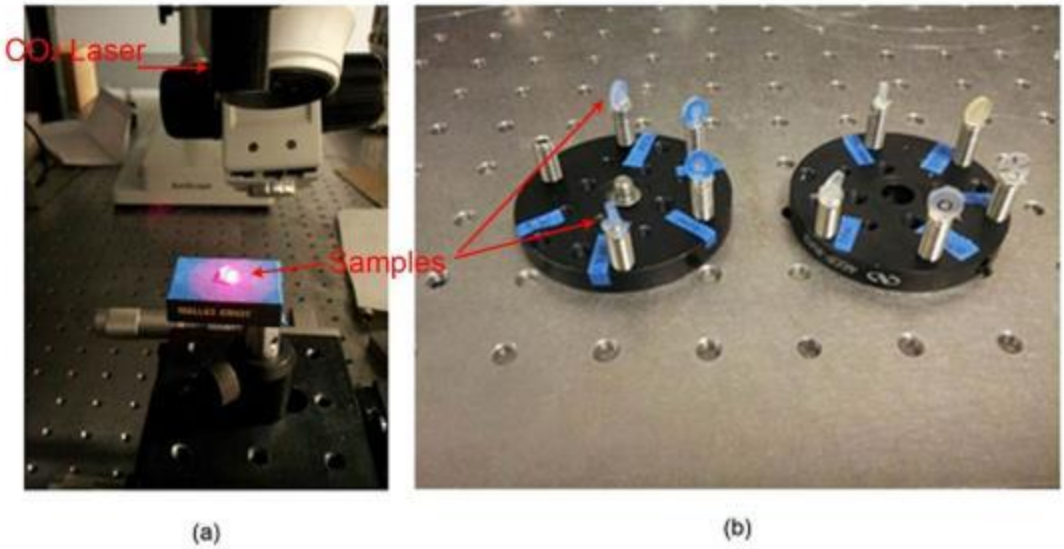

Figure 5-26: Set up to apply CO2 laser on porous samples (a) and prepared samples (b)

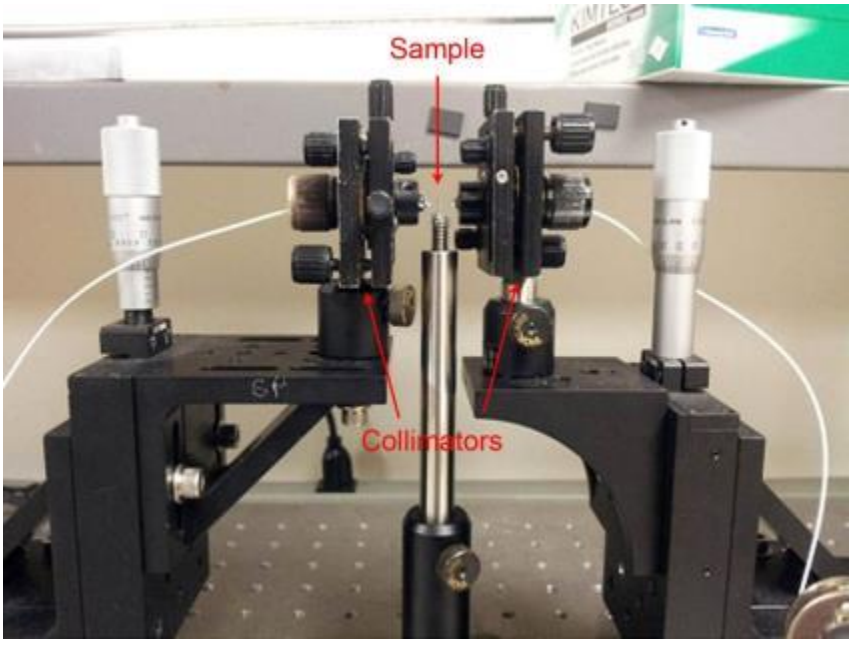

Figure 5-27: Set up for transmission loss and gas sensing on porous plate

Table 5-20 shows the results of the transmission test on the samples that were placed between the two collimators. Since each porous plate has a different thickness, thicker samples were used with a higher power of the CO_2 laser. As can be seen in the table 1.2, both sets of samples show some improvement in the transmission test. When we used more than 1W of CO_2 laser power on the samples, a "burned" spot began to appear and a subsequent decrease in the transmission improvement as shown in 2nd sample set.

Table 5-20: Summary of porous samples

1st sample set		
Power(w)	Thickness(mm)	loss(dB)
0.00	1.64	-34.12
0.50	1.66	-32.22
0.70	1.69	-31.51
1.00	1.74	-28.19
2nd sample set		
0.00	1.61	-34.45
0.80	1.63	-31.32
1.00	1.67	-27.58
1.20	1.70	-29.13

Figure 5-28(a) and (b) shows the gas absorption spectrums of the porous plates when applying 0.5W and 0.7W of CO_2 laser power respectively. The gas absorption peaks can be observed between 1520nm and 1540nm. These wavelength peaks are well matched with reference acetylene gas absorption data. Improvements were observed on both transmission and gas absorption when aCO_2 laser was applied onto a porous plate. The possible reason for transmission improvement can be due to the improvement of surface quality of the porous material and/or structural changes made to the bulk of the porous material. It may create bigger pores in the material that allows the light to react with more gas.

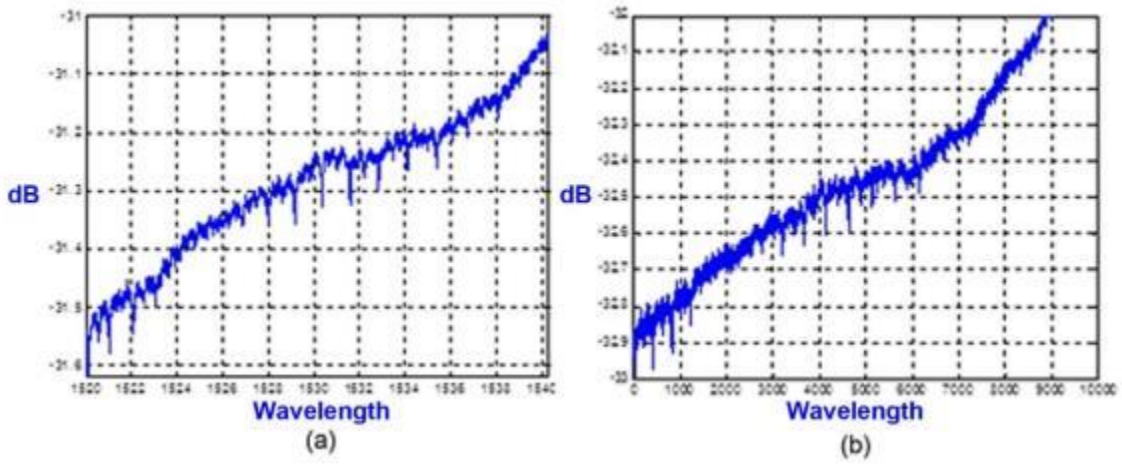

Figure 5-28: Gas absorption spectrum of porous plate with applying 0.5W (a) and 0.7W (b) CO2 laser

5.3.2 Gas Detection Using Fiber Taper

Figure 5-29 shows the set-up to fabricate the fiber taper from a SMF-28. A Propane torch was used to heat the fiber and two translation stages with fiber holders were used to stretch the fiber while the heat was applied with the propane torch. NI Labview was used to control the speed and distance of the translation stages. Three axes stages were also used to locate the tip of the torch and a protective glass tube. Several trails were performed to find the proper settings and it was observed that the temperature from the propane torch and the alignment and speed of the two translation stages is critical to achieve the desired taper diameter of 2μm.

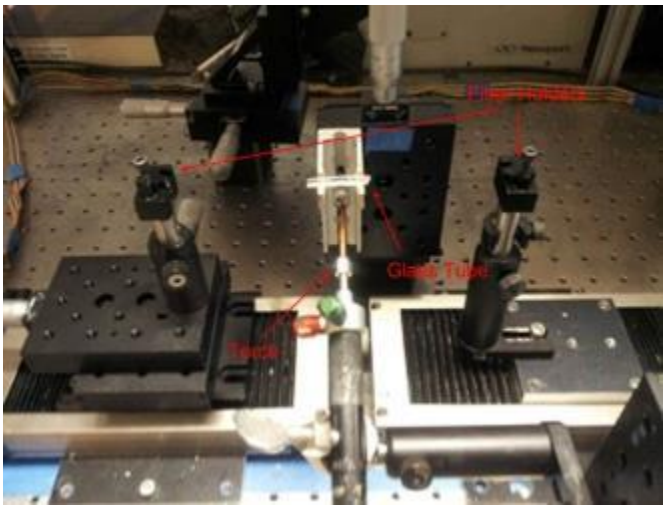

Figure 5-29: Set up to fabricate fiber taper with SMF-28

As the taper was fabricated from the SMF-28, the transmission spectrum was monitored. When the fiber gets stretched out, transmission loss of the taper gradually decreased. Figure 5-30 shows the spectrum of the taper with 2μm diameter with a transmission loss of the taper of around -8.5dB. From several trails of fabrication, it was learned that the alignment of the holder is critical. Bending of the taper was experienced and it produced a higher transmission loss when compared to having a proper alignment between the two fiber holders.

Figure 5-31(a) shows the gas absorption spectrum of the fiber taper with the acetylene gas applied to the system and Figure 5-31(b) shows the difference between the spectrum with gas and without gas. In Figure 5-31(b) the gas absorption spectrums can be observed from 1520nm to 1540nm. One of the advantages of using fiber taper in the porous tube is the minimization of the transmission loss and elimination of the alignment difficulties between the two fibers that was experienced in the previous tests when the porous tube with lead-in and lead-out fibers was used. One of the drawbacks of using fiber taper in the porous tube is a weak gas absorption peak. The low gas absorption peak can probably be improved by fabricating fiber taper thinner than 1μm.

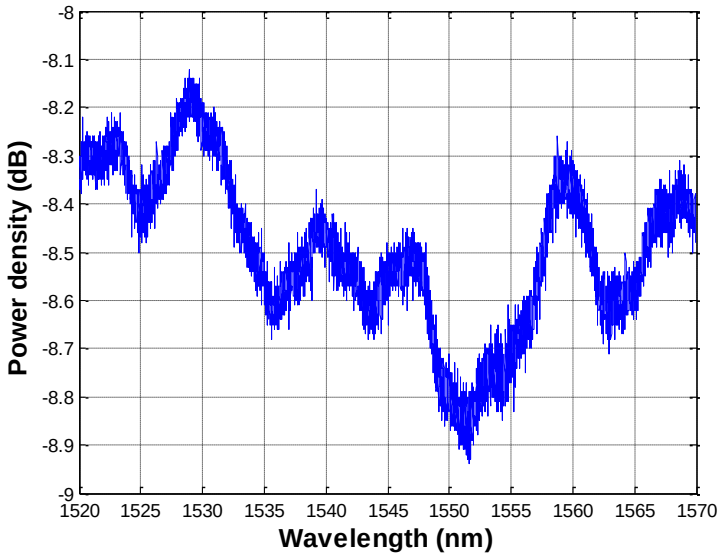

Figure 5-30: Spectrum of 2µm fiber taper

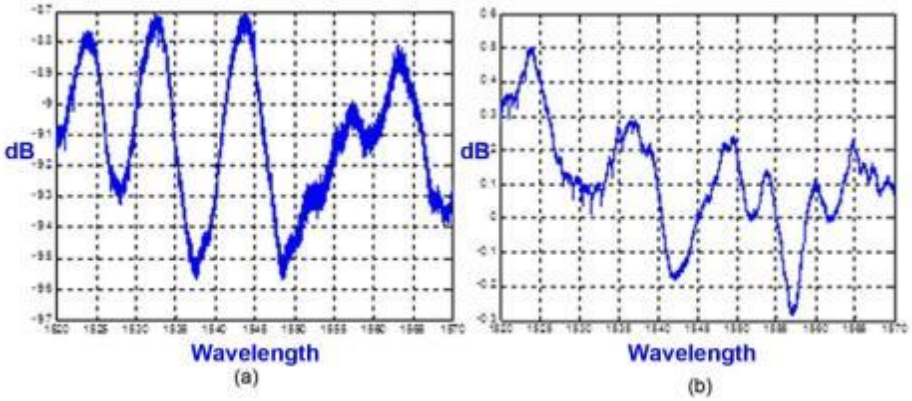

Figure 5-31: Gas absorption spectrum (a) and the difference (b)

5.3.3 Gas Detection Using WGM

After several trials to achieve a proper fiber taper with 2µm diameter, a set-up was constructed to fabricate the WGM with a 125µm fiber and 400µm porous tube as shown in Figure 5-32. After fabrication of the taper with SMF-28, a fiber taper was glued to the glass plate with proper holds as shown in Figure 5-32. A 105/125µm MM fiber and 400µm porous tube were placed in a fiber holder and positioned across to the fiber taper.

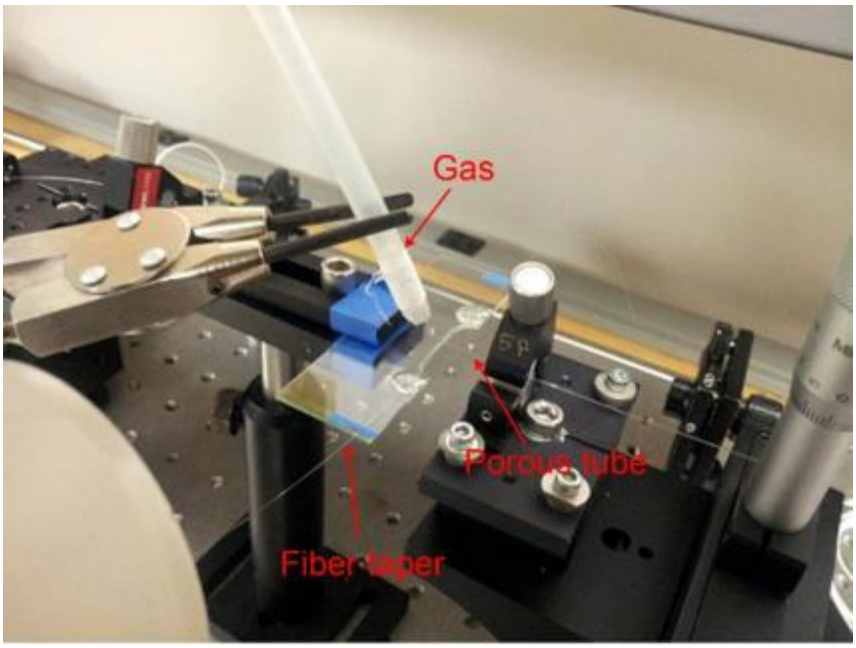

Figure 5-32: Set up to construct WGM with 105/125µm fiber and 400µm porous tube

Figure 5-33(a) shows the output spectrum of the WGM structure with a 105/125µm MM fiber. As soon as the 105/125µm MM fiber was placed across the fiber taper, it produced an absorption spectrum as shown in Figure 5-33(a). Gas absorption spectrum with acetylene gas was performed in WGM structure with 125µm fiber as shown in Figure 5-33(b) and several measurements were performed to get averaged data. Since the output spectrum contains high noise, consistency of gas absorption from this structure could be readily observed.

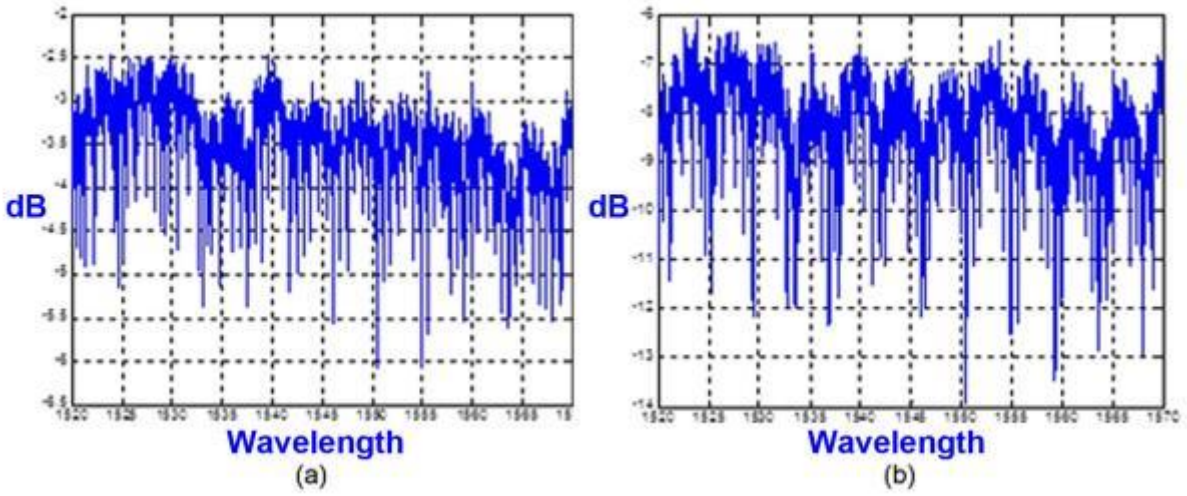

Figure 5-33: Output spectrum (a) of WGM structure with 105/125µm MM fiber and gas absorption spectrum (b)

Figure 5-34(a) shows the output spectrum of the WGM structure with a 400µm porous tube. As soon as the 400µm porous tube was placed across the fiber taper, it produced an absorption spectrum as shown in Figure 5-34(a). When the WGM of the porous tube is compared to the MM fiber, the structure with the porous tube has less noise than the structure with MM

fiber. The gas absorption spectrum with acetylene gas from the WGM structure with a 400µm porous tube is shown in Figure 5-34(b) and represents several measurements that were performed to get averaged data. Figure 5-35 shows the difference between the two spectrums from Figure 5-34. Phase changes in these two spectrums could be observed and these can potentially be used for gas detection.

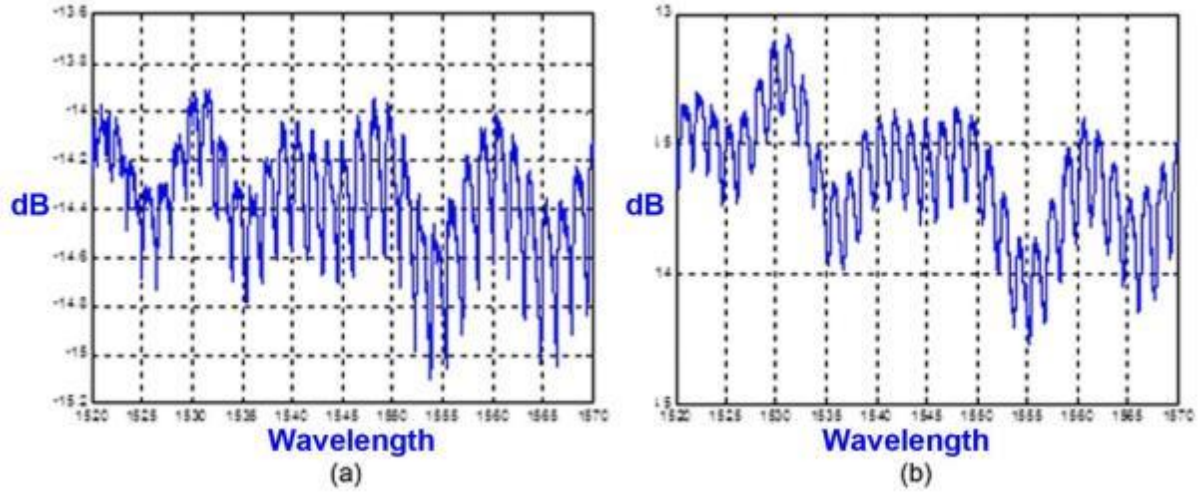

Figure 5-34: Output spectrum (a) of WGM structure with 400µm porous tube and gas absorption spectrum (b)

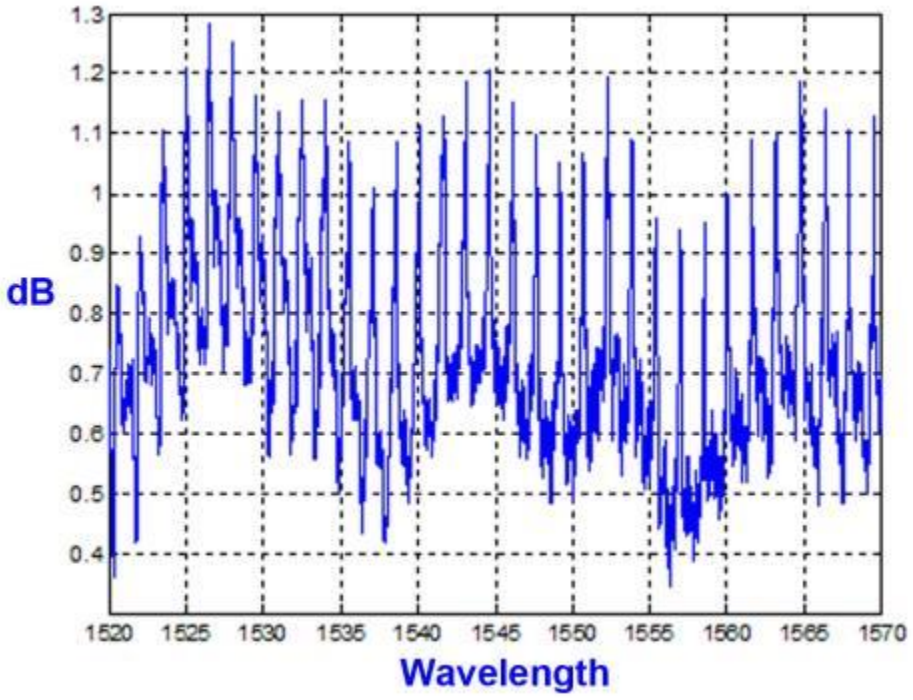

Figure 5-35: The difference between with gas and without gas in the WGM structure with 400µm porous tube

5.3.4 Gas Mixer

In order to test multiple gases over a large concentration range, a gas mixer that utilized flow controllers was utilized to mix gas at desired concentrations for the sensitivity test of the gas sensors. The description of the operating principles for the gas mixer are taken directly from the SmartTrak 100® Series Mass Flow Controller instruction manual.[1] "The operating principle of the SmartTrak instruments mass flow controller is based on heat transfer and the first law of thermodynamics. During operation process gas enters the instrument's flow body and divides into two flow paths, one through the sensor tube, and the other through the laminar flow bypass. As shown in Figure 5-36, the laminar flow bypass which is often called laminar flow element (LFE) generates a pressure drop, P1–P2, forcing a small fraction of the total flow to pass through the sensor tube (m1).

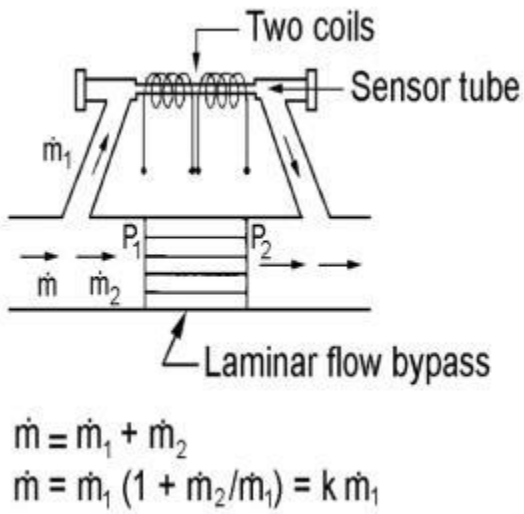

Figure 5-36: Flow Paths through the Instrument

Two resistance temperature detector (RTD) coils around the sensor tube direct a constant amount of heat (H) into the gas stream. During operation, the gas mass flow carries heat from the upstream coil to the downstream coil. The resulting temperature difference (ΔT) is measured by the SmartTrak microprocessor. From this, SmartTrak calculates the output signal. Since the molecules of the gas carry away the heat, the output signal is linearly proportional to gas mass flow.

Figure 5-37(a) and (b) show the mass flow through the sensor tube as inversely proportional to the temperature difference of the coils. The coils are legs of a bridge circuit with an output voltage in direct proportion to the difference in the coils' resistance; the result is the temperature difference (ΔT). Two other parameters, heat input (H) and coefficient of specific heat (C_p) are both constant. Through careful design and attention to these parameters, this output signal is made linear over the transducer's normal operating range as shown in Figure 5-38. As a result, the measured flow through the sensor tube is directly proportional to the gas flow in the main body.

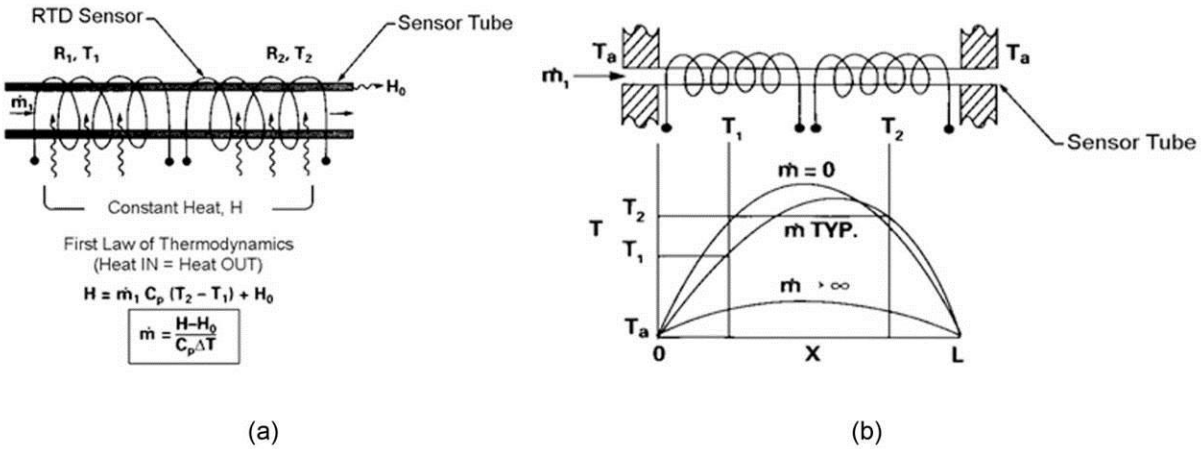

Figure 5-37: Flow Measuring Principle (a) and Sensor Temperature Distribution (b)

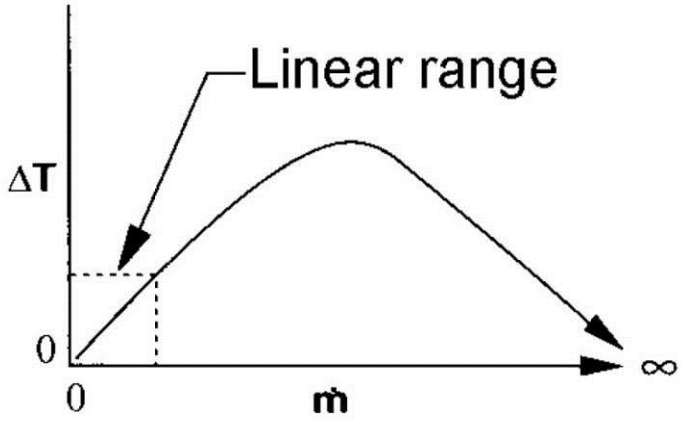

Figure 5-38: Linear Range of the Transducer's Output Signal

In the SmartTrak mass flow controllers, the gas which flows through the monitoring section is precisely regulated by the built-in electromagnetic valve. The normally closed valve is similar to an on/off solenoid valve, except that the current to the valve coil, and hence the magnetic field, is modulated so that the ferromagnetic valve armature, or valve plug, assumes the exact height above the valve's orifice required to maintain the valve's command flow (set point). The result is excellent resolution."

Figure 5-39 shows the layout of our current gas mixer. It consists with 4 inlets and one outlet. The maximum number of gases that can be combined in the mixer is 4 with each inlet connected to a mass flow meter. Each channel has a valve to control input of the gas to that channel. When a single gas is used in multiple inlets, these valves can be opened to flow the same gas to multiple channels at the same time. Each mass flow meter is connected with mass flow controller and a switch to control the mass flow and set point. There is a switch above the mass flow controller and the mass flow meter to be controlled or monitored can be selected from

the mass flow controller. Each mass flow meter is also connected with digital flow box to monitor the real time gas flow of each channel.

The range of mass flow for channel 1 and 2 is 0-1000 standard cubic centimeters per minutes (SCCM). Channel 3 has 0-100 SCCM and channel 4 has 0-10 SCCM. Each mass flow meter has accuracy of $\pm$1% of full scale. Since the gas mixer is equipped with two of high flow meters (0-1000 SCCM), it significantly reduces the accuracy of the gas mixer. From simple calculation, an estimate of the accuracy of the gas mixer is 200ppm range since each mass flow meter has $\pm$1% of full scale. One of the possible ways to improve the gas mixer is to replace the high flow meter with a low flow meter with better accuracy. The use of a gas chamber with vacuum can be also used to improve the accuracy of the gas mixture.

Figure 5-39: Top view and front view of gas mixer

5.3.5 Gas Detection Using Porous Glass Sensor

Gas detection was performed using the porous glass sensors with cavity lengths of 5, 10, and 15cm. This data was collected at room temperature and was done in a gas cell that allowed for control of the atmosphere. The gas cell is shown in Figure 5-40 below. This setup allows for the lead-in and lead-out fibers to be sealed with epoxy at each end and a separate port for gas flow. Vacuum was pulled prior to flowing test gases into the chamber. Test gas was flowed into the gas chamber using a Sierra Instruments Model 954 Digital Flo-Box that metered the gas flow and concentration. This gas mixer allows for up to 4 simultaneous gases to be mixed at one time but for these experiments only 2 gases were mixed, the acetylene test gas and nitrogen as the inert carrier gas. Gas concentration for testing was controlled by varying the flow rates of the gases. In these experiments the nitrogen is kept on the high flow rate source and at a constant flow. The concentration was controlled by varying the acetylene flow rate. The gas mixer's accuracy is determined by each of the independent flow meters, and is given as a percentage of the maximum flow rate for that given meter. The gas mixer's specifications and accuracy is discussed in 5.3.4. The spectra collected for the 5cm sensor is shown in Figure 5-41 below.

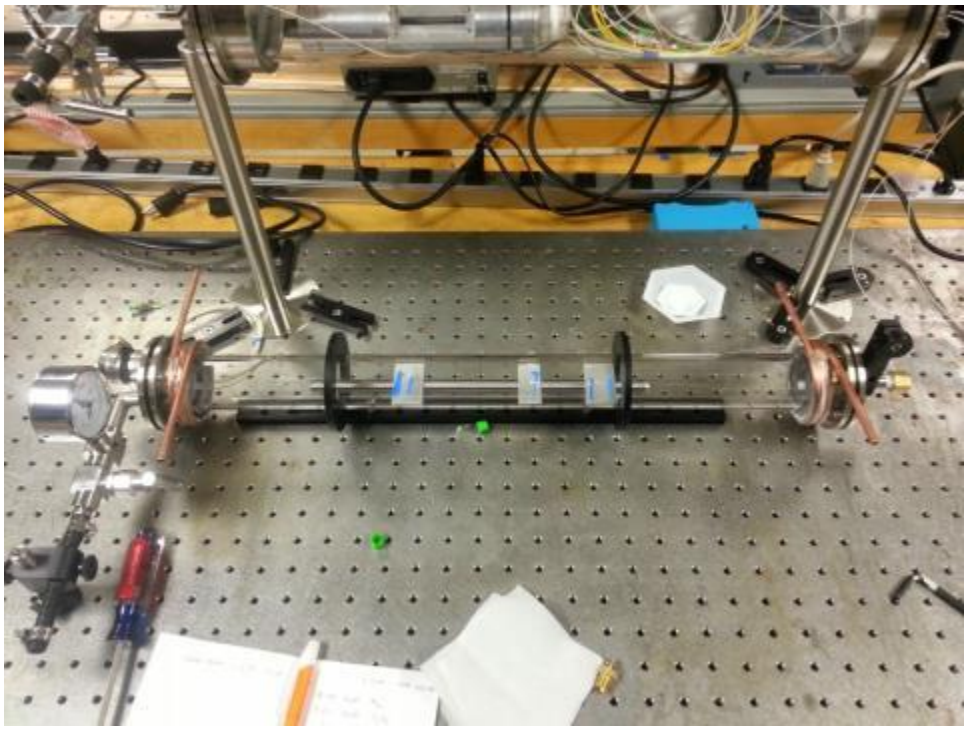

Figure 5-40: Gas Chamber Setup for testing of Porous Glass sensors.

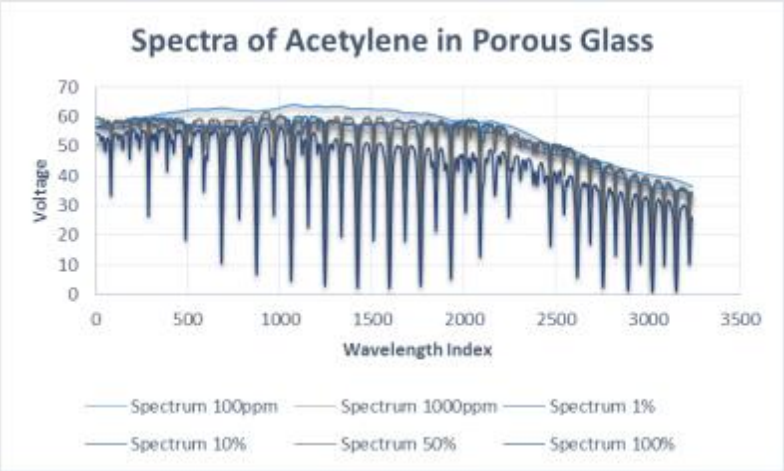

Figure 5-41: Spectra Collected for 5cm Cavity Length for all Concentrations.

The spectra shown above in Figure 5-41 is the spectra as recorded from the oscilloscope and still has the background data present in the signal which makes it more difficult for exact peak to peak comparisons for the concentrations. For data comparisons and analysis between the concentrations the spectra is normalized and has the background removed which also allows for comparison between different cavity lengths. Detection of the spectra in these sensors was done using a photodetector with an amplifier connected to an oscilloscope. In the case of the 5cm cavity the amplifier was set to 10^5 while for the 10 and 15cm cavities it was set to 10^7 which limits our ability to directly compare data between different values. Figure 5-42 below shows the signal from the 5cm cavity with the background removed.

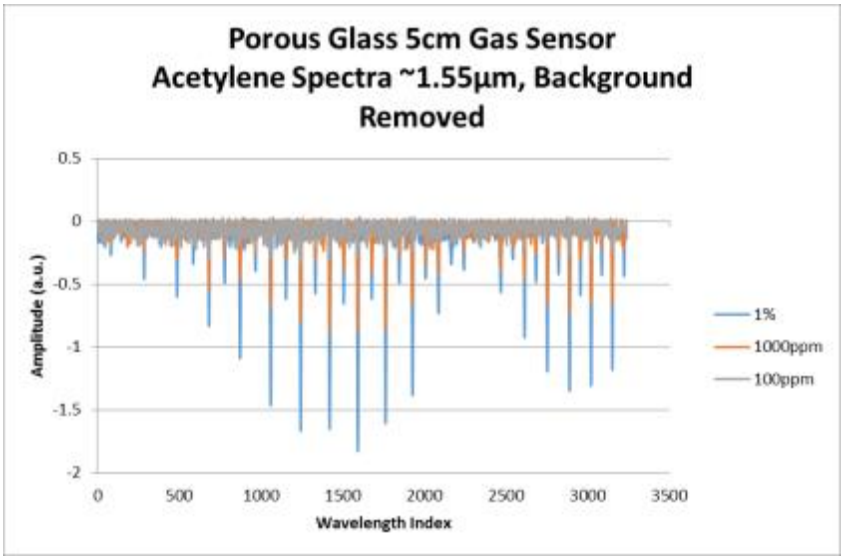

Figure 5-42: Spectra for Acetylene on 5cm Cavity with Background Signal Subtracted.

The spectra collected for the concentrations 1%, 1000ppm, and 100ppm is shown as detection limit is the target of these experiments. After removing the background clear peaks are observed in the 1000ppm and 1%. The peaks are present but difficult to see due to noise in the

signal with the 100ppm spectrum due to the low signal to noise ratio of only 2. This is the lower detection limit for the 5cm cavity with 100ppm being extremely difficult to differentiate from the noise of the signal. The spectra for the same 3 concentrations are shown below in Figure 5-43 for the 10cm cavity length. The signal for the same 3 concentrations for the 15cm cavity is shown in Figure 5-44. Comparing the signal between the three different cavity lengths show all the same peaks with varying intensity. In both the 10cm and 15cm cavity length samples the 100ppm signal was cleaner and had less noise and allowed for the peaks to be more easily identified. The spectra collected from the 15cm cavity showed much higher peaks heights on both the 1000ppm and 100ppm concentrations compared to the height of the 1% peaks. The increase in interaction volume is expected to give stronger peaks.

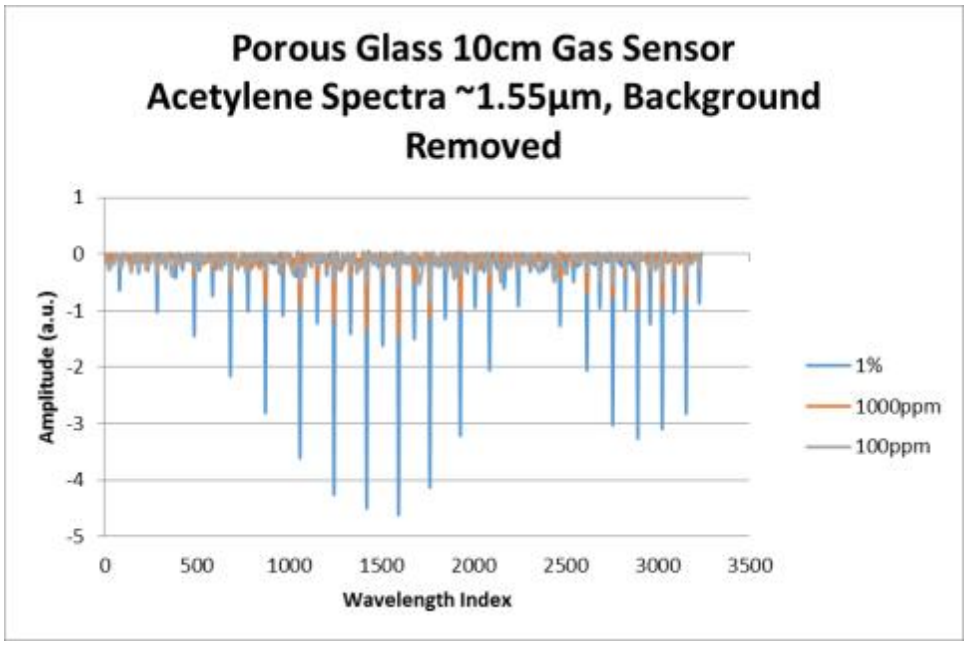

Figure 5-43: Spectra for Acetylene on 10cm Cavity with Background Signal Subtracted.

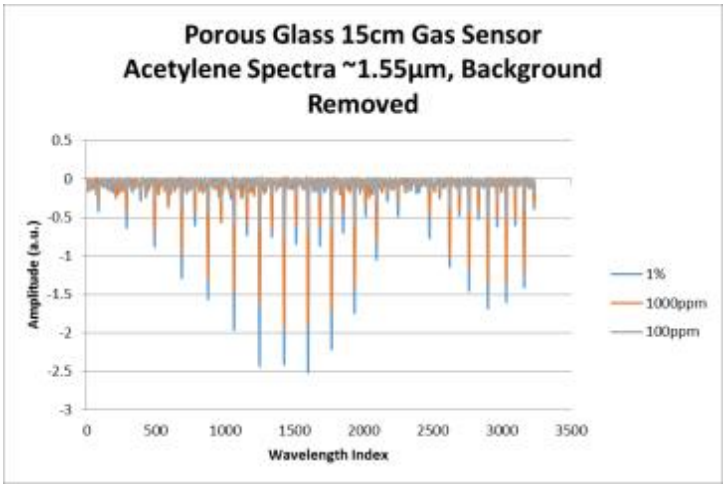

Figure 5-44: Spectra for Acetylene on 15cm Cavity with Background Signal Subtracted.

In the case of all three cavity lengths the signal to noise ratio of the 100ppm samples was 2-3 which limits the minimum concentration that can be detected. The error in the gas mixer also limits detection below this point as the error is approaching 100ppm +/-100ppm. With the error of the gas mixer the minimal detection limit is between 1-200 ppm. A more finite detection limit cannot be stated without a more accurate method to mix the gases or use of a premixed gas.
Using the data collected from measuring these concentrations, estimations of the gas concentration were made using different reference points to best understand how to fit the data and allow for extrapolation of the data to find unknown concentrations. Estimation data from the 5cm cavity was the best fitting and estimated the best of all three cavity lengths. Figure 5-45 below shows the plots of the for different reference point.

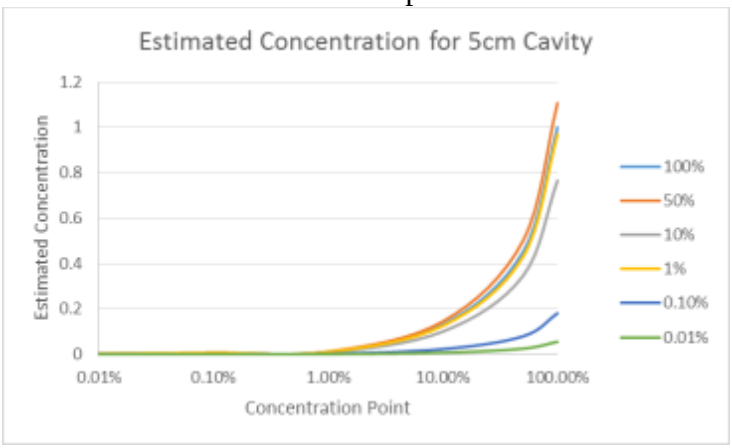

Figure 5-45: Estimation lines for 5cm cavity based on different reference concentration.

The results using a 100% acetylene concentration as the reference point provides the best estimation of concentrations. Figure 5-46 below shows the same graph zoomed in on the lower concentration value range.

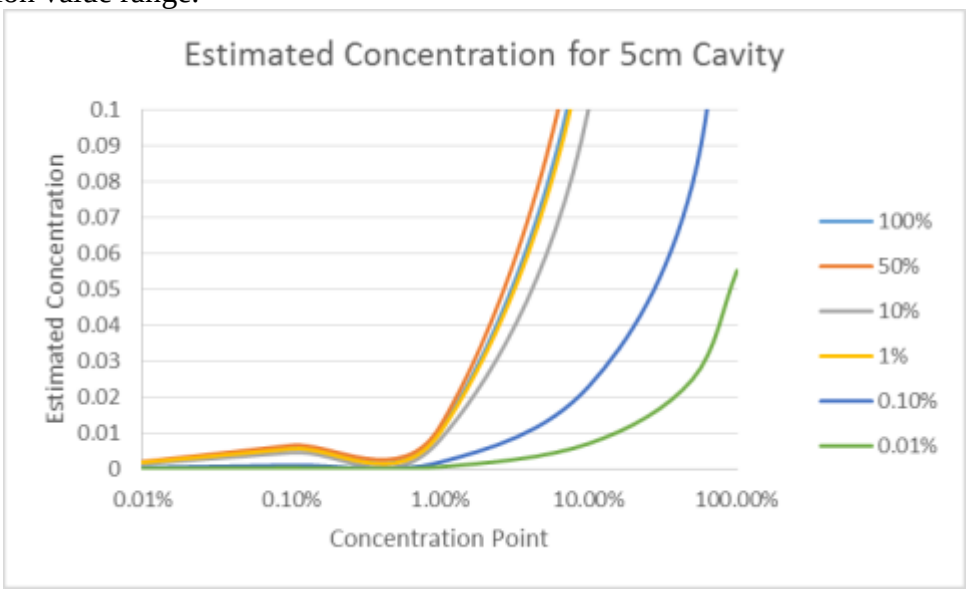

Figure 5-46: Estimation lines for 5cm cavity based on different reference concentrations zoomed.

These lines each represent a different concentration used for the reference point. Use of the dilute 1000ppm and 100ppm concentration as the reference shows a poor fit to the data and does not estimate the pure acetylene. The best fit comes from the use of the pure acetylene as the reference point. The estimates from this fit are shown with their target concentrations below in Table 5-21.

Table 5-21: Concentration Estimate using 100% Reference Point

Target Concentration	Estimated Concentration
100ppm	1800ppm
1000ppm	5600ppm
1%	1%
10%	13%
50%	45%

The data shows good estimation until dilute concentrations and this disagreement can come from the manually fitted background as well as the low signal to noise ratio of the 100ppm signal.

5.3.6 Investigating the System Using Mirror Surface at End of Porous Tube

In order to investigate using a mirror surface to improve the signal quality, gold platting was applied to the end face of a fiber. The fiber with the mirrored surface will be inserted into one end of the porous tube sensor while the other end has a standard optical fiber inserted. The mirrored surface will act as a reflector allowing the optical signal to travel the length of the sensor and back to be collected by the standard fiber. This structure will increase the interaction length between the gas and the injected light while reducing the loss that would be incurred by equivalent increase of the porous sensor due to systemic and alignment losses. Several samples of the fiber were prepared for the gold plating. After plating gold on the end of the fiber, the quality of the gold coating was verified. Figure 5-47 shows gold plating at the end face of SMF-28.

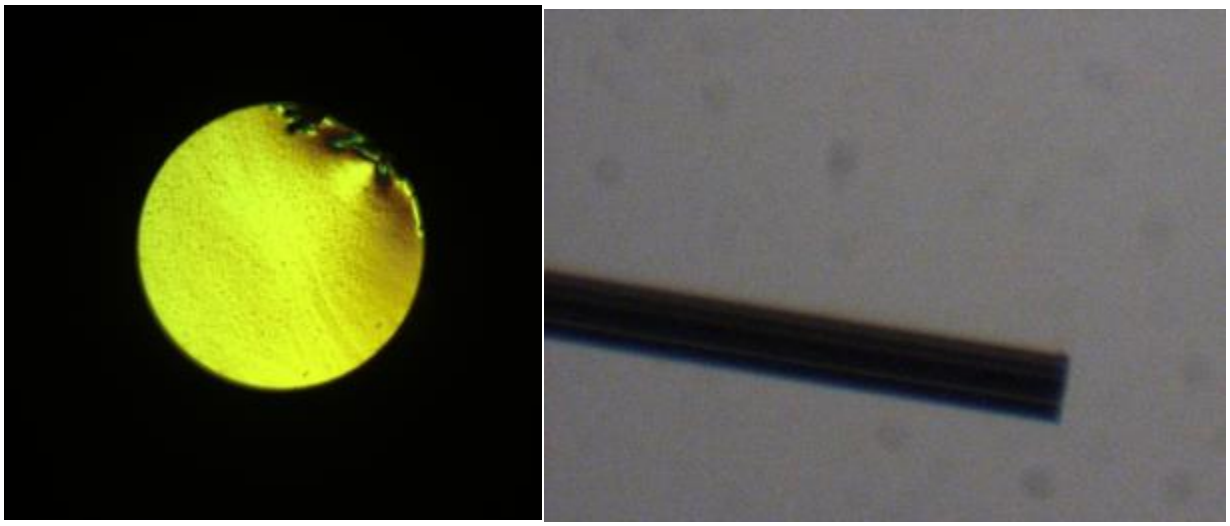

Figure 5-47: Gold plating at the end face of the fiber

After successful coating of the end of the fiber, a new structure with mirror face was constructed as shown in Figure 5-48. Extremely careful cleaning was performed prior to the construction. In order to avoid porous particles during the insertion process, careful alignment using linear stages was performed.

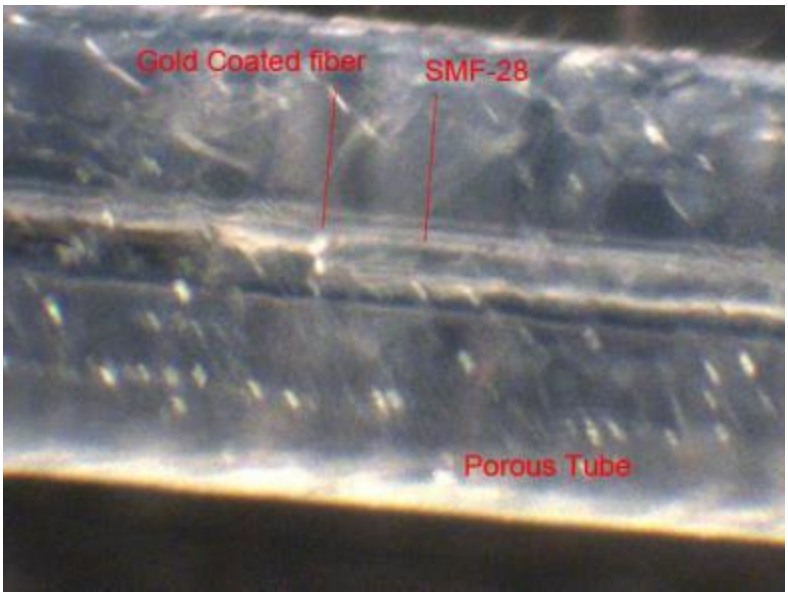

Figure 5-48: Structure with mirror face at the end of fiber

The first measurement was made with around 300 microns of the cavity length between the gold face and the lead in SMF-28. The output spectrum from CTS is shown in Figure 5-49. As Figure 5-49 shows, the gold coated mirror face yields a significant interference signal. This interference signal was observed due to the reflections from the two end faces of the cavity. In order to use the mirror surface in our system, the interference signal should be eliminated. One of the possibilities of the interference signal is the construction of an optical sensor structure that can measure temperature and gas sensing simultaneously at the same point.

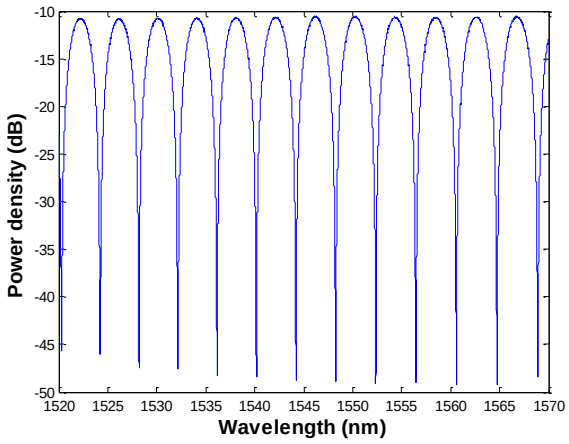

Figure 5-49: Output spectrum with 300microns of cavity length

As we increase the cavity length, the interference is gradually decreased. Figure 5-50 shows the output spectrums with 20mm and 50mm of the cavity lengths.

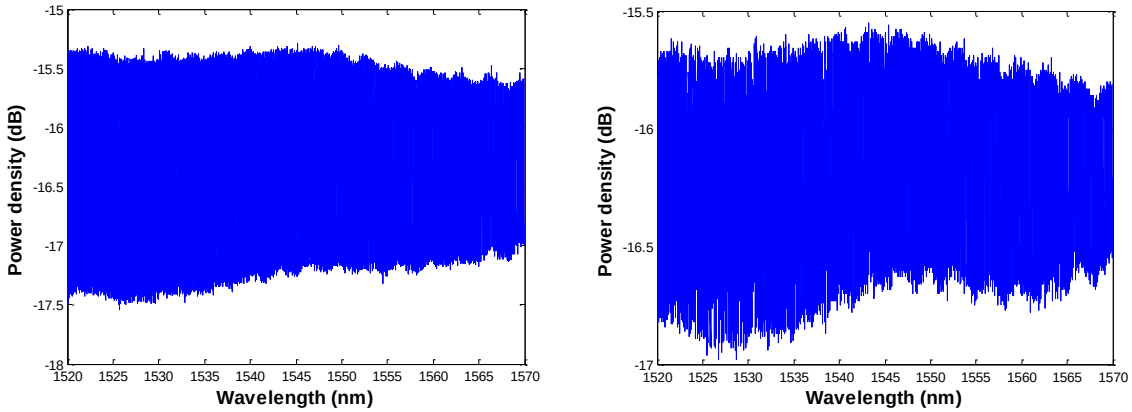

Figure 5-50: Output spectrums with 20mm (left) and 50mm (right) of cavity lengths

The longest sample of porous tube we had was around 75mm long and we could only test our system up to 60mm of cavity length. Figure 5-51 shows the output spectrum with 60mm of the cavity length. It shows a pretty weak interference with 60mm of cavity length which should be equal to 120mm of the total length of travel.

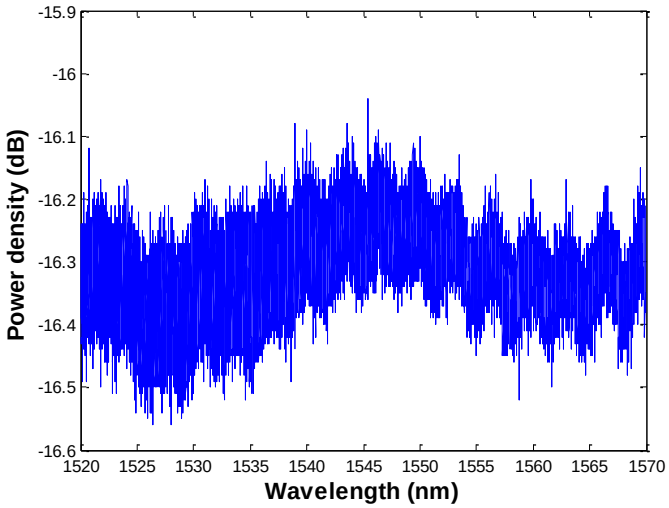

Figure 5-51: Output spectrum with 60mm of cavity length

5.3.7 Mirror Surface Using Dual-Core Fiber

Our previous test using two etched fibers experienced significant loss in the transmission, possibly due to an etched core in the fiber. In order to avoid etching of the core region, two non-etched fibers were used with a larger porous tube in our experiment. The porous tube had a 250μm ID and a 350 μm OD and gold coated fiber with a 125 μm OD. The air cavity between the two fibers and the gold coated reflecting fiber was 20mm. Figure 5-52 shows the result of the gas absorption with acetylene gas. The average of transmission loss of the 20mm cavity was -39.47dB and the strongest gas absorption peak were around 4dB. The regular porous glass sensor structure of our gas sensor using lead-in and lead-out fibers and a 20mm cavity has a -23.70dB loss and a40mm cavity has -25.82 dB of transmission loss. The gas absorption peak is around -6dB~-7dB. One of possible way to improve transmission using a mirror surface is the use of

larger diameter gold coated fiber for the reflecting surface. This will ensure the most of light will be reflected back to the receiving fiber.

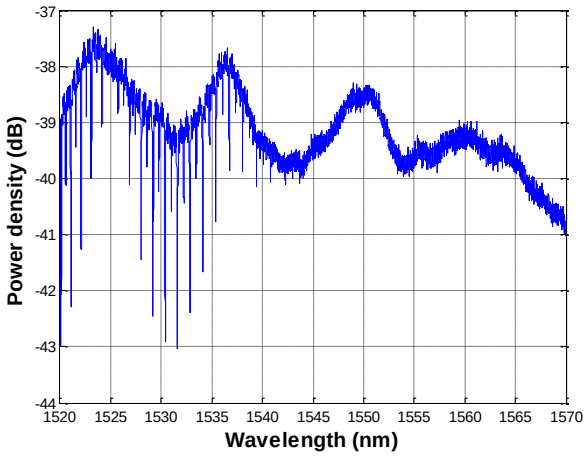

Figure 5-52: Gas absorption test with acetylene gas

As shown in Figure 5-53, a quarter-pitch collimator was fabricated at the end of SM fiber and an optical circulator was used. The measurement was made with around 4cm of the cavity length between the reflective gold surface and the collimator. The output spectrum from the CTS is shown in Figure 5-54. As the figure shows, the gold coated mirror face yields huge interference signal. This large interference signal was observed due to the reflections from the two end faces of the cavity. In order to use a mirror surface in our system, the interference signal needs to be eliminated.

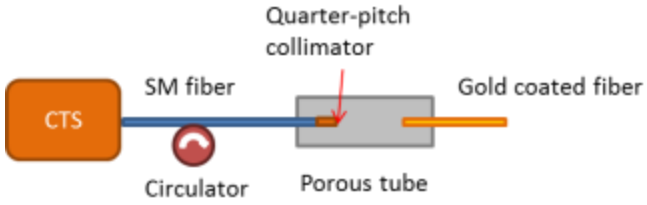

Figure 5-53: Schematic for quarter-pitch collimator with circulator

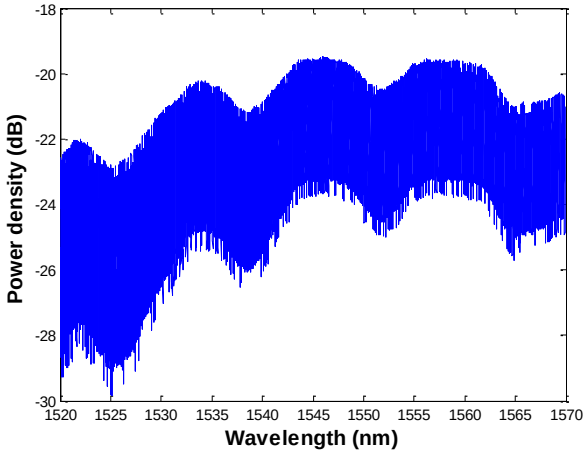

Figure 5-54: Signal output from quarter-pitch collimator with circulator

Figure 5-55 shows an alternative structure using the quarter-pitch collimator that can be employed to improve signal reception from the reflective mirror surface. The measurement was made with around 2cm of the cavity length between the gold face and collimator. The output spectrum from the CTS is shown in Figure 5-56. As the figure shows, interference of previous structure can be eliminated and transmission could be improved when we compared it with two non-etched fibers.

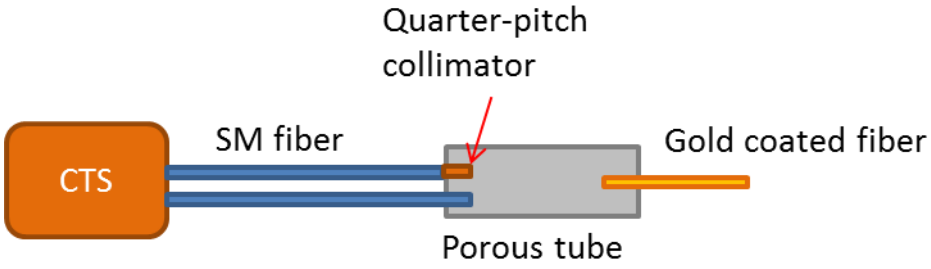

Figure 5-55: Schematic for quarter-pitch collimator as dual-sore fiber structure

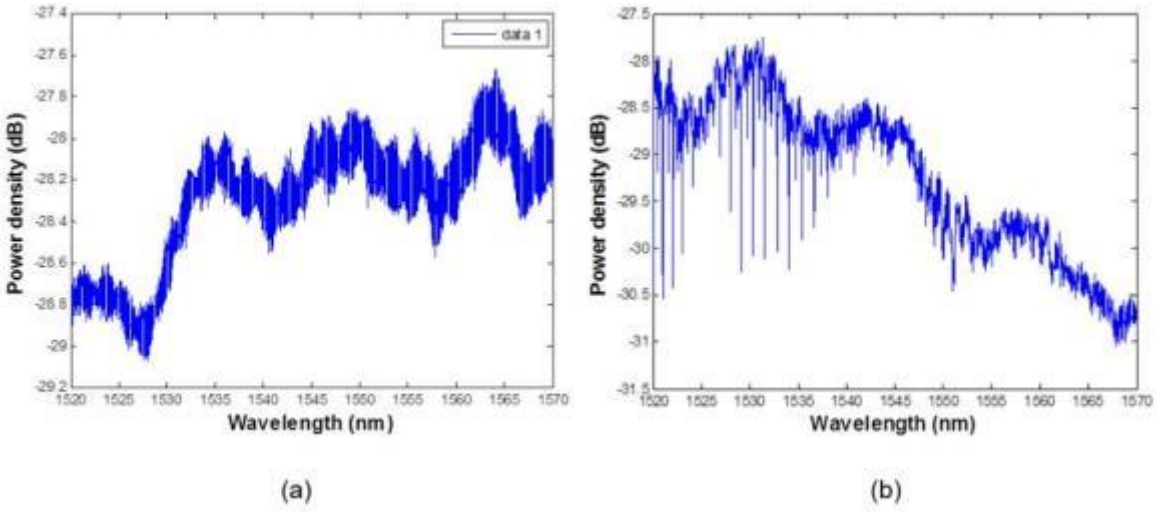

Figure 5-56: Signal output from quarter-pitch collimator with dual core structure (a) without gas and (b) with gas

5.3.8 Method for Improving Signal Loss

Plating a metal on the inside surface of the Glass tubes is being investigated to improve the signal quality of the waveguide. The metal plating will improve the signal transmission through the tube by increasing the reflectivity of the glass surface. Gold is being investigated due to its excellent reflectance of light in the infrared wavelength region, and the thickness needed for good reflectance. Gold plating of glass is well established using electroless plating methods. Electroless plating is done by using auto-catalytic aqueous solutions and requires no outside charge to be applied. The solutions consist of a sensitizing solution to prepare the surface, the plating solution with the metal compound, and a reducing solution to deposit the metal ions. This is the same process used to make traditional mirrors. Poor adherence of metal

films to the glass surface requires the use of the sensitizing solution to prepare the surface. Tin and palladium solutions are the most commonly used sensitizing solutions for glass. These methods are predominately used to coat flat surfaces necessitating the adaptation of the process to coat the inside of a capillary tube. Using the process studied by Takeyasu et al.[1] some results of plating on a capillary tube has been successful. This process was used on green Glass to attempt to plate gold on the inner surface. The glass surface was first sensitized using a solution of trifluoroacetic acid and tin (II) chloride. This should activate the surface and help provide locations for the gold to deposit. The plating solution consisted of a mixture of 0.024M tetra-chloro auric acid, 0.75M sodium hydroxide, and 0.086M sodium chloride. The reducing solution was 0.5 vol% glycerol. The plating solution and reduction agent were mixed together and 4 green Glass tubes were dipped in the mixed solution. Two samples were left in solution for 30 minutes with the other two samples being left for 90 minutes. No gold deposition was present on the first two samples so the other two were left to see if deposition just needed longer to occur. A second trial was done with new solutions made to ensure that the concentrations matched previous work. None of these samples showed any gold deposition present either. The coating may not have been successful due to the glass composition difference from what was tested in previous work. Once a gold coating has been successfully applied to the inner surface of the capillary tube, the film will have to be evaluated. The primary issue will be if the pores can still be opened to allow gas flow. The removal of the glass substrate from behind the thin gold film should be enough to remove the gold over the pores.

5.3.8.1 New Plating Technique

The plating of metal such as gold or silver is desirable for its benefits to improve transmission of signal inside the porous capillary tube. These coatings work to improve the transmission by increasing the reflectance of the surface and minimizing the amount of light lost into the glass. Gold and silver metal films can be very good reflectors even when present at very thin layers. Gold as thin as 60nm can reflect approximately 80% of incident light of the wavelength of 1550nm. The desire for a commercially available coating is of great importance.

Coating of metals especially silver on glass has been widely done in the process of making mirrors. Research was done to find a commercially available coating process for use after trying an experimental process for gold plating that failed to coat on the glass. A commercially available set of chemicals for coating was found from AngelGilding.com. This company provides both silver and gold coating kits for making mirrors at home. Both the silver and gold coatings will be evaluated on green glass tubes. The coatings then must be evaluated based on adhesion to the surface and whether gas can still be sensed once made porous. Initial coating attempts were done simply by using capillary action to pull plating solution into the tube. This process had problems with clogging deposition on the inner surface of the tube at the tube end and required a setup that better facilitated solution to the inside of the tube.

The chemicals needed for both silver and gold coating were obtained. The plating process for both silver and gold involves sensitizing the surface with a tin chloride solution to aid adherence of the metal ions to the glass. The plating bath in both cases consists of a metal ion solution, an activating solution, and a reducing agent. These chemicals are mixed in equal parts to begin the plating process. The plating process was done per the manufacturer's directions given with each plating kit. The silver plating process takes approximately 5 minutes to complete while the gold plating occurs at a much slower rate taking 30 minutes to complete. In both plating cases 3 types of samples were tested: a piece of fused silica, a piece of green glass,

and the green Glass capillary tubes. In both the silver and gold plating tests, metal was successfully plated on all samples. The samples were all cleaned using a 5% ammonium bifluoride solution and then rinsed in deionized water prior to starting the plating. They were then dipped in the sensitizing solution for 1 minute then rinsed and then placed directly in the mixed plating solutions. The pieces of both fused silica and green glass rested in the bottom of the solution completely submerged in solution. The capillary tubes were standing in the solution while resting on the side of the beaker with a small bit of capillary tube extending out of solution. Figure 5-57 below shows several capillary tubes that have been coated with gold as well as a magnified region of the film.

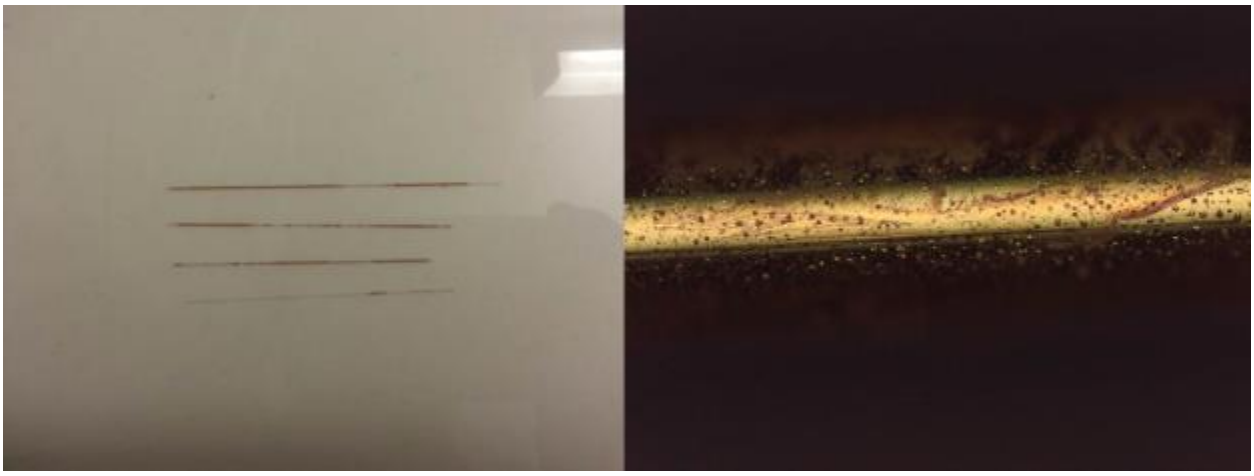

Figure 5-57: Capillary Tubes plated in gold (left) and magnified section of gold film (right).

The gold plating exhibited better adhesion on the green glass versus the silver. Both plating samples could be wiped off with a finger while still wet but adhere well after drying. In both cases the tubes had significant plating on the outside of the tubes with little to no observable coating on the inside of the tubes. This was caused by the limited amount of solution present inside the capillary tube. Based on information from the manufacturer on how much glass the solution can plate was determined. The plating solution is capable of plating 2064 mm^2/mL. The volume and inner surface of the tested capillary tubes were then calculated. The height used in the calculation was determined from an estimated height of liquid based on capillary pressure. Based on a 170 micron diameter capillary tube, the height of the liquid was estimated to be 87.05mm. This leads to an inner surface area of 46.49mm^2 and a volume of liquid of 0.00198mL. This volume of liquid is only enough to plate 4.079mm^2, approximately 10% of the surface present. Exchange of new solution is expected to be very small with no agitation of the liquid, which agrees with the experimental results. Another factor contributing to poor coating of the inside surface was clogging of the hole by deposited metal. Figure 5-58 below shows a sample from the silver coating trial that was clogged at the end. The picture doesn't show enough detail to see the clog. The dark region that is present at the end indicated by the arrow is the end of the capillary tube that was at the bottom of the plating solution. The hole was almost completely blocked off by metal and sediment from the solution collecting at the tip. This problem was significantly worse in the silver coating than in the gold coating.

Figure 5-58: End of capillary tube clogged with plating solution.

In order to better control the plating process a system was developed to limit the coating to the inside of the tube. The system uses a vacuum to pull the solutions through the capillary tube thus eliminating undesired coating on the outside of the tube as well as providing fresh solution to fully coat the inside of the tube. The setup is shown below in Figure 5-59.

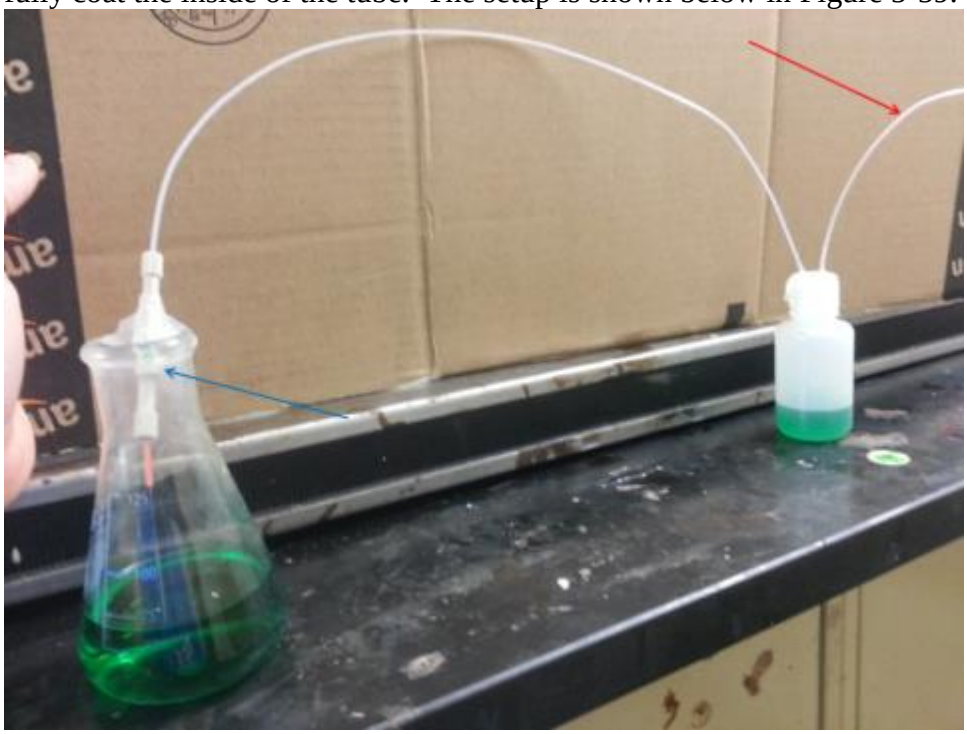

Figure 5-59: Vacuum Setup for capillary tube pumping.

The red arrow on the right of the figure shows the tube leaving the liquid trap and going to the vacuum pump which is not pictured. The simple system is comprised of a vacuum pump with a bottle to collect solution in the line to the capillary tube. The blue arrow indicates the

connector used to join the plastic tubing to a glass capillary tube. A reasonably air tight connection is needed for this system to successfully pull liquid through the tube. Fittings were obtained from IDEX Health and Science to connect to glass capillary tubes. The system uses a polymer sleeve to fit snugly around the glass tube then a standard compression fitting to connect to joints. A wide variety of sizes are readily available allowing for various capillary tube sizes. Figure 5-60 below shows a close up of the joining fitting used in the setup.

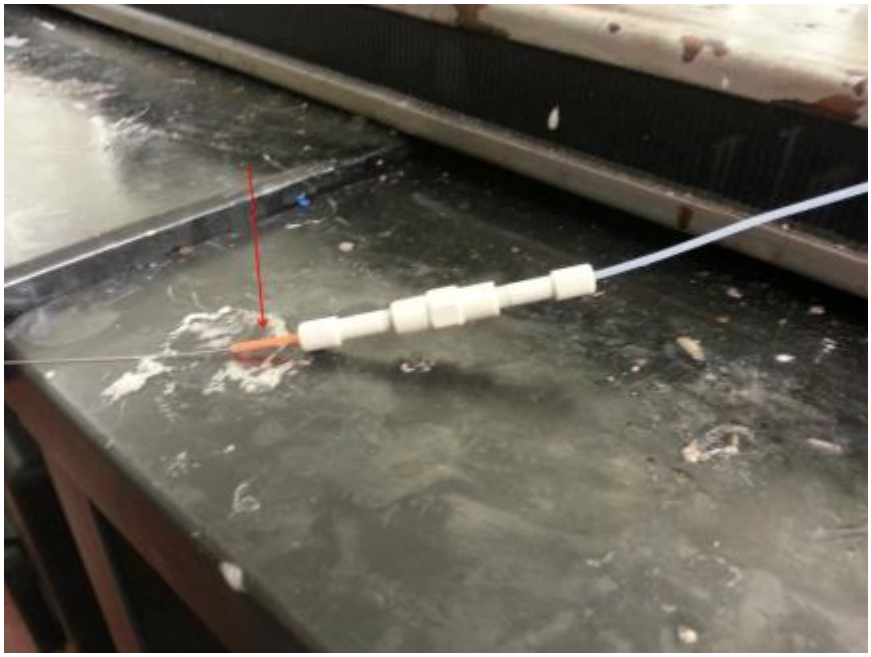

Figure 5-60: Connector assembly connecting glass capillary tube to standard plastic tubing.

The arrow in Figure 5-60 shows the polymer sleeve that is covering the glass capillary tube. Test liquid has been successfully pulled through the system currently as shown in Figure 5-59. The flow rate through the capillary tube is currently very slow and has to be improved before running the plating solution through. Inadequate sealing on the capillary tube is the main cause for the poor flow rate.

5.3.8.2 Improvements to Vacuum Plating System

The investigation of metal plating has continued with the use of a vacuum based system to flow plating solution through the capillary tubes. This system has been developed using a vacuum pump with a trap for the liquid. The initial setup suffered from poor flow and was capable of plating one tube at a time. Improvements made have been the switching to a glass flask as a trap instead of plastic trap as well as additional tubes to allow for simultaneous plating of 3 tubes at a time. Gold plating has shown very promising results using this system. Plating silver has not shown good results due to its fast deposition rate. Even with an increase in flow rate through the glass tube the silver plating still collects at the tip and clogs the tube preventing any additional flow. The setup for plating is shown below in Figure 5-61.

Figure 5-61: Vacuum setup with glass trap.

Initial plating trials were carried out on green glass and were very successful. After the successful plating the tubes were then processed as normal. The phase separation treatment resulted in changes in the gold film. This change caused the film to be lost during the leaching process. The plating process was then attempted on phase separated glass to eliminate any changes to the gold film. The deposited gold film did not behave any differently on the phase separated than on the green glass samples. The leaching process still resulted in a change to the film and is shown below in Figure 5-62.

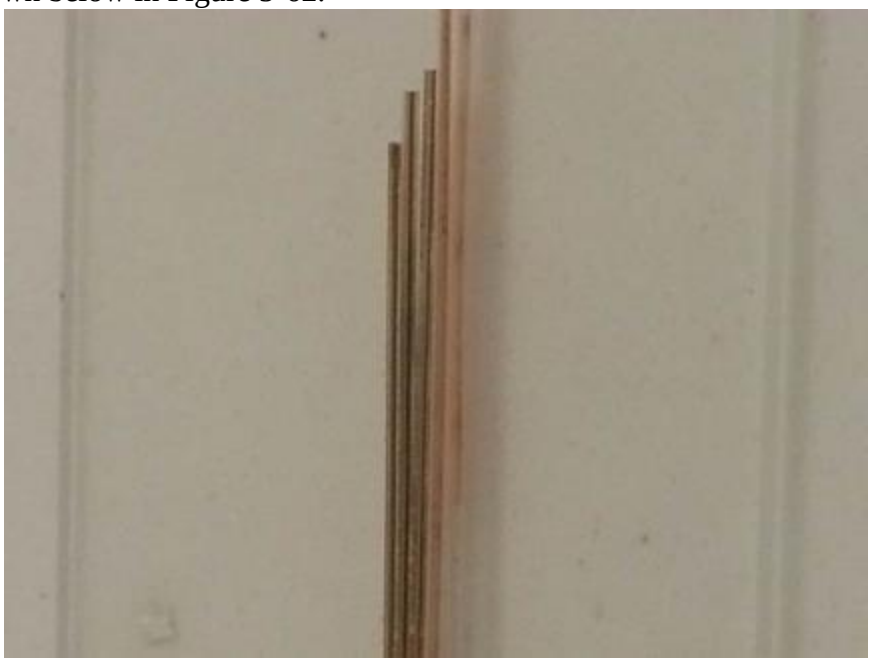

Figure 5-62: Gold Plated Glass Tubes

The three tubes on the left are plating on phase separated glass while the two on the right are after the leaching process. The gold plating prior to leaching appears with a bright yellow gold luster while after leaching the coating appears to have a much stronger red hue present. This difference is shown below in Figure 5-63.

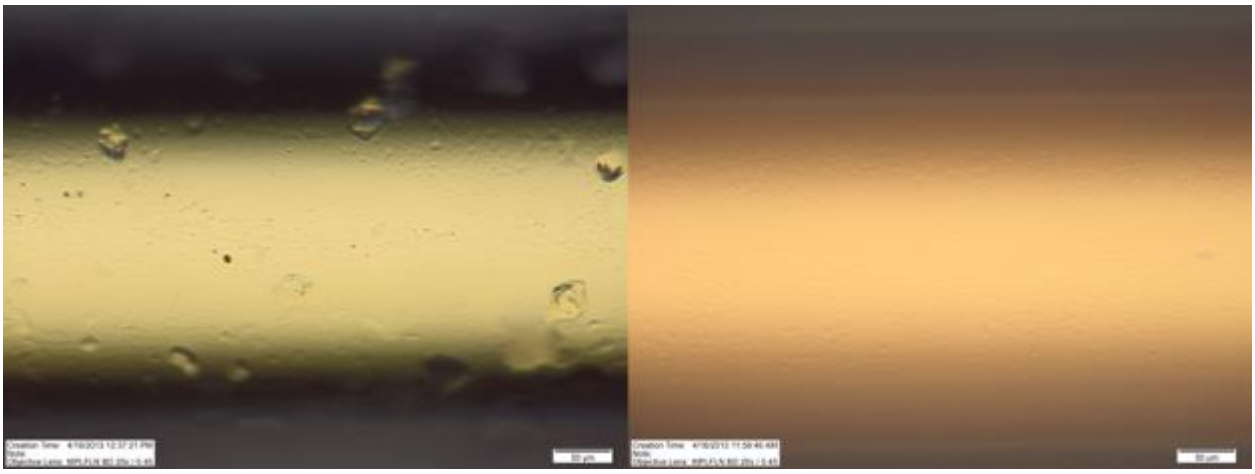

Figure 5-63: Comparison Gold plating on Phase Separated (left) and Porous Glass (right).

These images were taken on the optical microscope at the same magnification. In both cases the focus is done on the top glass surface of the tube, this allows us to see the glass surface as well as a strong color from the gold film behind it. The gold film is initially bright yellow gold and after the leaching process changes both how much light it reflects as well as the color. The film on the porous tube has a distinct red hue in comparison to the solid tube. The glass surface is also much smoother and should be noted that the porous tube in Figure 5-63 is a larger tube than the phase separated one. Changes in the film are also easily seen by the use of Polarized Light Microscopy, this is done by the addition of polarizer and analyzer in the optical path. Figure 5-64 below shows a direct comparison between both a phase separated and porous tube when observed under bright field and then under polarized light.

Figure 5-64 shows the gold plating on a phase separated tube and the gold plating on leached porous tube under two different microscopy techniques. The plated tubes observed are different sizes with the visible gold region being in the core in both cases. The field of focus is on the gold surface and looking through the surface of the glass tube. The curved nature of the tube limits the amount in focus area. Under bright field the gold coating on the phase separated tube (Top Left of Figure 5-64) appears as a bright yellow coating that reflects most of the light, while after leaching the porous tube (Top Right of Figure 5-64) the coating appears to be more translucent and have a red hue. Use of Polarized Light Microscopy further accentuates the differences in the two coatings. In the case of the phase separated tube (Bottom Left of Figure 5-64) the gold becomes very faint and the gold traces appear on the outer surface of the tube. Polarized light on the plated porous glass tube (Bottom Right of Figure 5-64) causes the coating to exhibit a very bright red gold appearance and to appear more opaque.

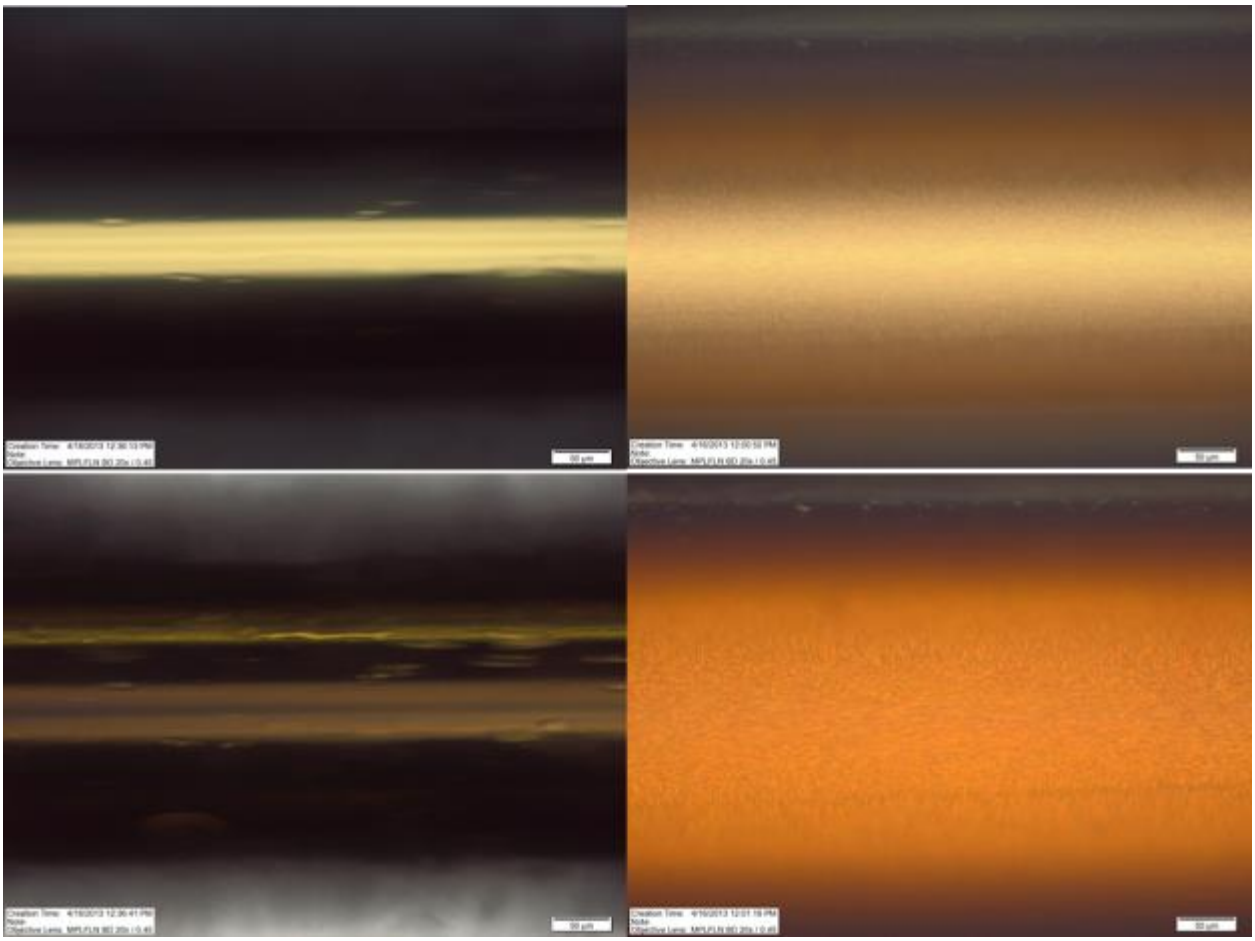

Figure 5-64: Comparison of Gold Plated Phase Separated Glass under Bright Field (Top Left), Phase Separated Glass under Polarized Light (Bottom Left), Porous Glass under Bright Field (Top Right), and Porous Glass under Polarized Light (Bottom Right).

The interior of the glass tubes that are used as the porous glass tube component of the gas sensors have been successfully Gold coated. During this quarter the analysis of the gold plated tubes has been done as well as improvements to the plating process have been completed. Initially plating was done by using a vacuum pump to simultaneously pull plating solution through the tubes. This process was successful in plating tubes but suffered from poor repeatability and also had a large amount of wasted plating solution. Using pressure to push plating solution through the tubes instead of pulling through with vacuum has been investigated. The use of pressure to push fluid was originally investigated in an attempt to plate gold directly onto porous glass, both within the pore structure and within the tube ID. Several attempts at plating on porous glass failed. Plating attempts failed due to a reaction of the plating solution with residual sensitizing solution in the pore structure. The plating process consists of 3 main steps: flow sensitizing solution, rinse with DI water, and then flow with plating solution. Fluids flowing through the porous tubes are predominately through the length of the tube, but over time filling of the pores occurs. Rinsing of the porous glass with DI water to remove the sensitizing solution was unsuccessful. This is evidenced by the sensitizing solution rapidly reacting with the plating solution and driving all of the gold particles out of solution and preventing successful plating of gold. During the plating process, this reaction would occur causing the precipitation of

the gold from solution turning the porous tube black. Decreasing the time of the sensitizing solution by half and increasing rinse time by a factor of 4 still did not remove all of the solution from the pore structure. This problem has prevented any successful plating directly on porous glass.

Pressure plating was then applied to the still solid, phase separated glass that was previously plated successfully using the vacuum setup. A setup consisting of 3 syringes with each of the 3 main steps of the plating process was used. Luer lock 60mL syringes were used with plastic tubing attached to the end using epoxy. The plastic tubing was connected using the same connectors from IDEX that were used in the vacuum setup to connect the syringes to the glass tubes. The pressure plating was very successful in plating the solid phase separated glass tubes. This process has shown many advantages over the vacuum system such as the increased throughput and material usage and improved coating repeatability. Plating was done on heat treated green glass tubes, which were then processed as normal to make the glass porous.

SEM analysis of the gold films both before and after the leaching process has been done as well as some preliminary optical transmission and gas sensing tests. SEM was done using a FESEM with EDS for chemical data. Figure 5-65 is a lower mag SEM image that shows the gold film both before and after the leaching process.

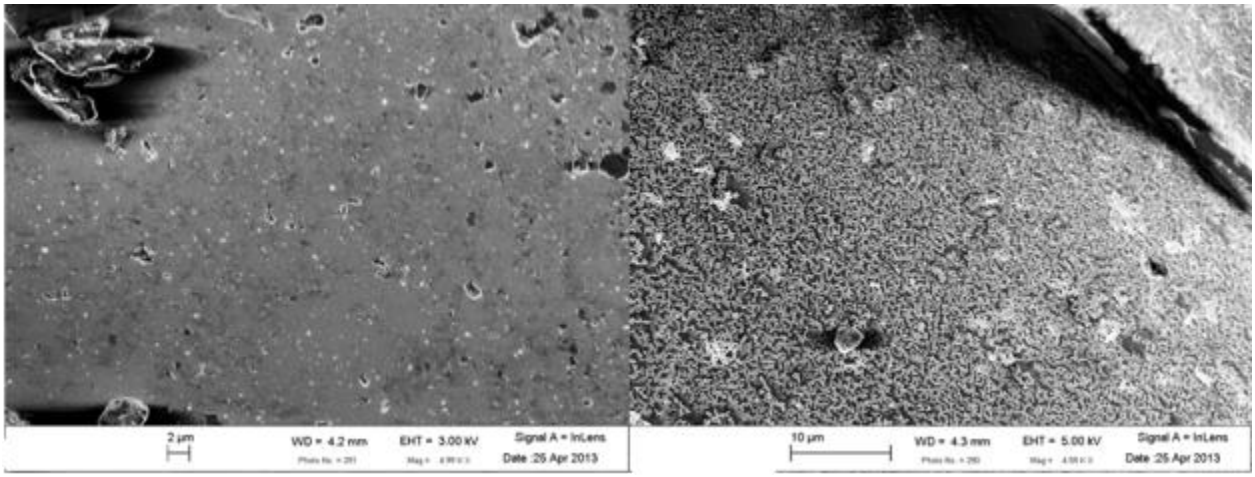

Figure 5-65: SEM of gold film on phase separated glass (left) and after leaching process making it porous (right).

The SEM images were taken on the inside surface of a glass tube. Samples were prepared by taking a tube, both leached and unleached, with plating and breaking it to expose the inside surface for analysis. This also showed how well the plating adhered to the glass as it did not come off during the fracturing of the glass. The gold film prior to leaching appeared very smooth and uniform with some defects present. The film after leaching on the other hand appears to have a very porous structure with interconnected gold ligaments. In addition to the SEM taken on the inside surface of the tube, SEM images were taken of the end of tube to look at the interface between the film and glass surface. The glass-gold film interface is shown in Figure 5-66.

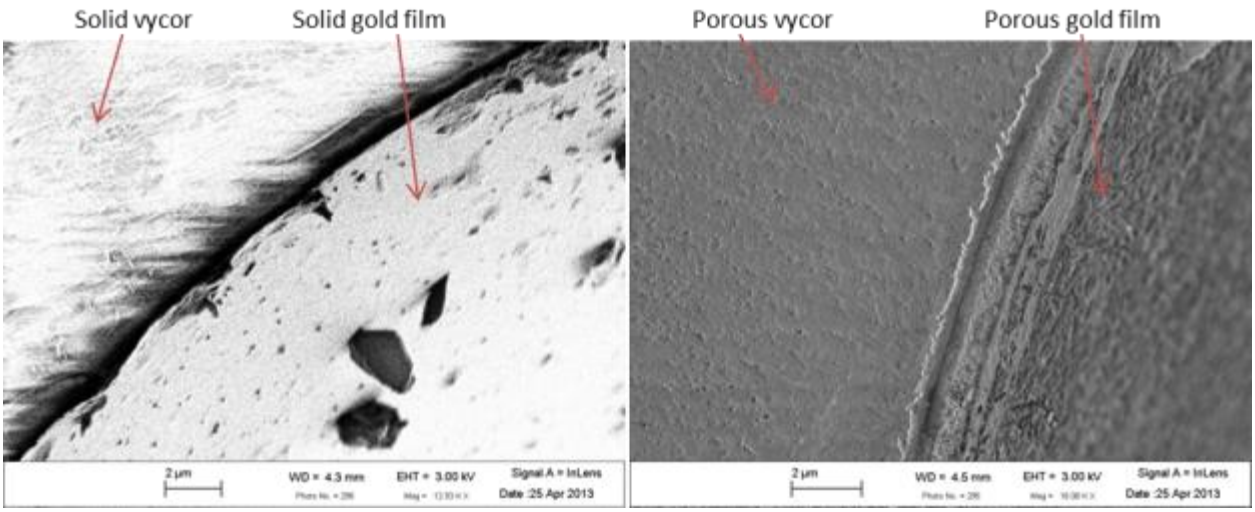

Figure 5-66: SEM of end face showing interface between gold film and glass.

The interface prior to leaching shows a gap between a very continuous gold film and the glass surface. This differs from the interface seen on the porous sample which appears to be completely smooth and against the glass. While only a few samples have been examined it is thought that the thicker layer of gold on the solid tube makes it easier for separation of the film during sample prep. This resulted in the film separation on the solid glass tube while it's not seen on the porous glass sample. Closer examination of the gold film shown in Figure 5-67 indicates that the glass is indeed porous with pores sizes typical of a non-coated sample.

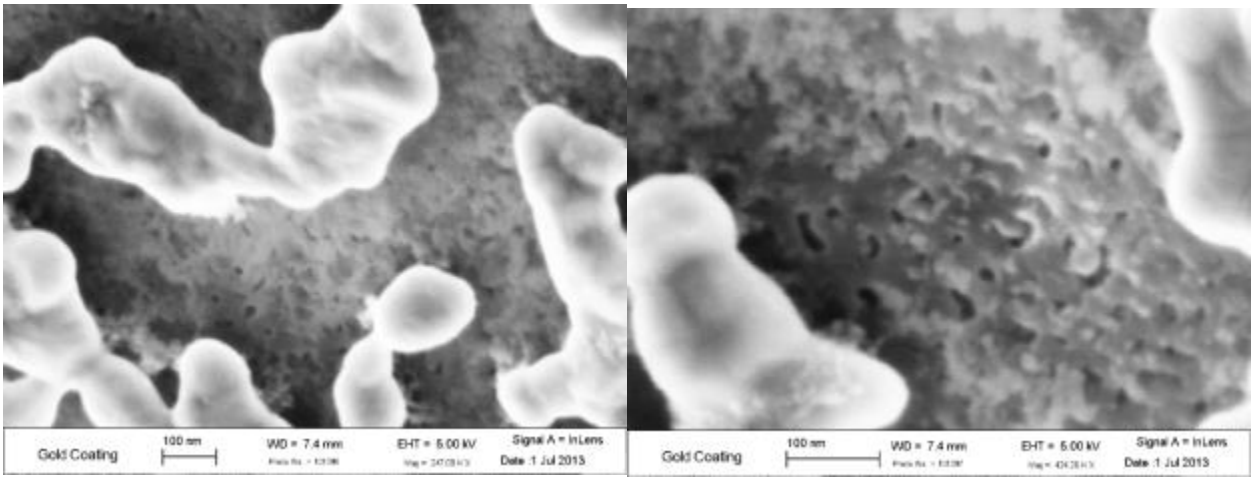

Figure 5-67: SEM of porous gold film on porous glass.

The porous gold film is found to be composed of approximately 100nm ligaments in an interconnected network while the glass has approximately10nm pores. In addition to the imaging of the gold film, EDS was used to collect chemical information on the gold film. Figure 5-68 shows 2 points where EDS spectra were collected. In both cases, silica glass and gold in addition to carbon from the graphite coating was seen to be present. Gold was present in both spectra due to the spot size of EDS of 1µm, which picked up gold from the adjacent ligaments when positioned in glass region. This agrees with the results of picking up considerably less gold when

not position directly on the ligament. The EDS results also showed that no other elements were detected in the deposited gold which is desired. Composition results from the spectra are summarized below in Table 5-22.

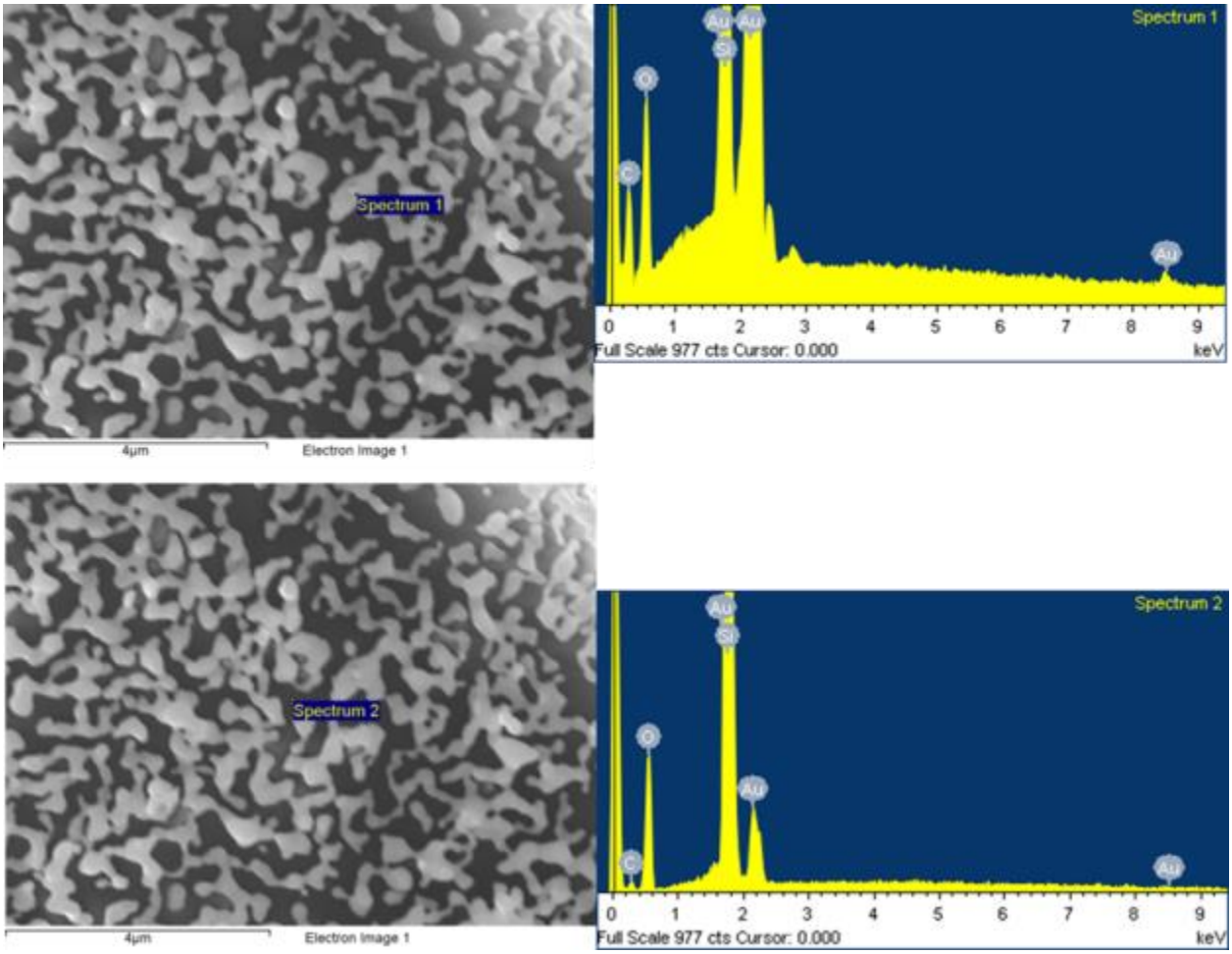

Figure 5-68: EDS of gold film Spectrum 1(top) was from a gold ligament while Spectrum 2 (bottom) was from the glass region.

Table 5-22: Composition results from EDS on gold film.

Summary At. %	Carbon	Silicon	Oxygen	Gold
Spectrum 1	37.30	34.93	11.46	16.31
Spectrum 2	13.16	41.24	44.00	1.61

.

In addition to material characterization of the gold films preliminary optical tests have been done using a porous gold coated tube. Transmission tests have been done on both gold

coated glass tubes before and after leaching. Figure 5-69 shows the results of the transmission loss tests.

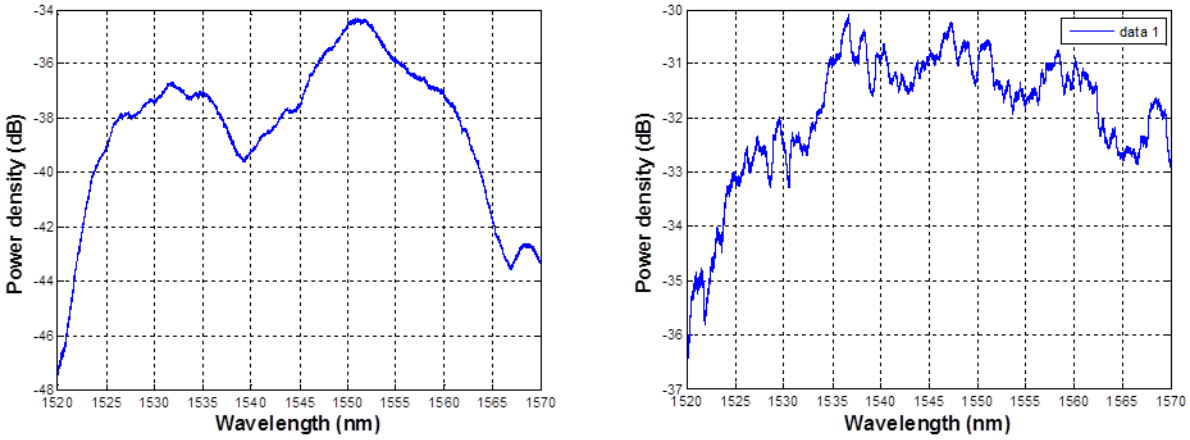

Figure 5-69: Transmission spectra for gold coated glass before leaching (left) and after leaching (right).

The spectra exhibited a change after the leaching process that is similar in shape to the spectra before leaching. The loss experienced by the signal also decreased between 5-10dB after leaching. While, these transmission tests were done using a similar sized tube with a 5cm cavity a firm conclusion on the improvement of the sensor signal due the gold coating can‘t be made.. A gas sensing test was also done to determine if the presence of the film affected the ability to sense gas. Figure 5-70 below shows the results from the gas sensing test using acetylene gas.

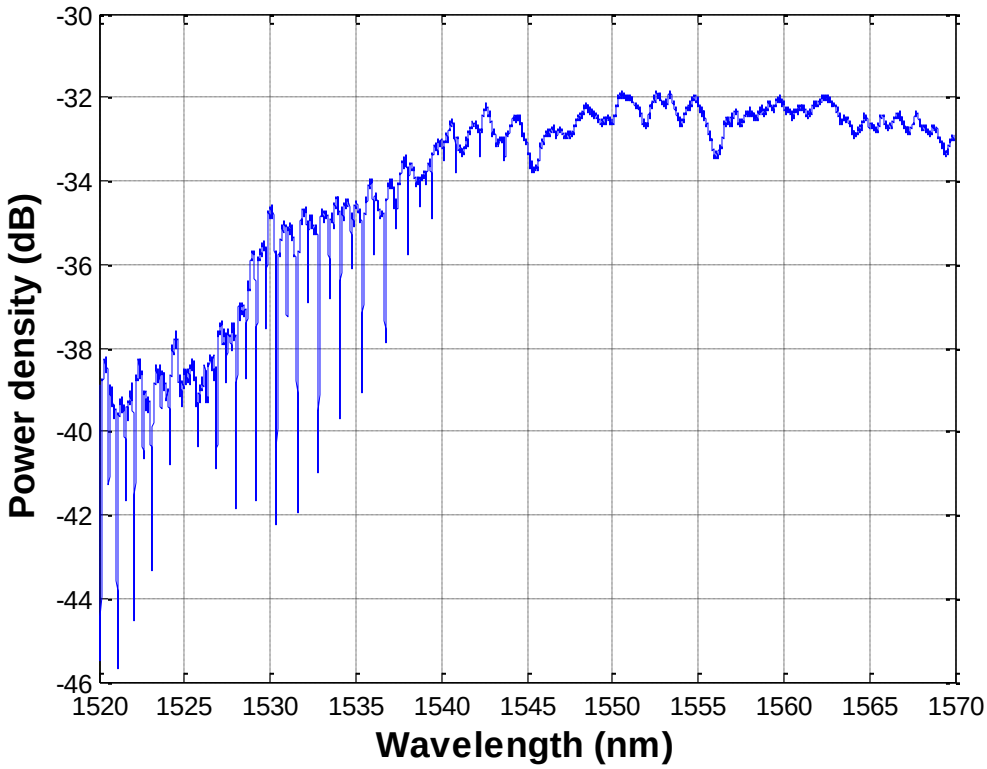

Figure 5-70: Absorption spectra of acetylene gas using gold coated glass tube.

The spectra shows several absorption peaks for acetylene as expected and very successfully detected the gas. This shows that the gold film does not prohibit gas detection. Testing on several more samples is necessary to determine if the gold coating provides a benefit for decreasing loss of signal.

5.3.9 Trials to Vary Film Thickness

Production of gold coated glass tubes has continued. The plating process is now fully being done using pressure to push the plating solution through the tubes to eliminate variability found in using the vacuum process. All tubes that are being used in plating trials are 9 inches in length which is the limiting length of the box furnace used for phase separation. The tubes inner diameters have not been tightly controlled in initial trials and tubes have been selected with an inner diameter in the range of 130-200µm. This has not been controlled to make sure the plating process works on a wide variety of tube sizes and to also develop the plating conditions. Preliminary results have shown that transmission of a solid coated glass tube to be lower than an uncoated porous tube. Transmission on a coated porous glass tube showed similar transmission to an uncoated porous tube and additional data is needed to understand the behavior of the coating. The pressure based system allows for the quantity of plating solution and pressure to be held constant and use only plating time to control the amount of gold plating. Plating conditions for time trials are shown in Table 5-23.

Table 5-23: Plating conditions for plating time trials

Sensitizing Time	Rinse Time	Plating Solution quantity	Applied Pressure	Plating time
30 seconds	30 seconds	6mL	60mL	5,10,15 minutes and full plating

The applied pressure is measured by the mark that the plunger on the syringe was depressed to and held at during the plating. Full plating is the amount of time for all plating solution to pass through the tube. The total time for plating takes approximately 22 minutes. To allow for direct comparison between plating conditions and also to improve repeatability of optical measurements the inner diameters are measured prior to plating. A target inner diameter of 170µm with a tolerance of +/- 5µm is being used for all tubes in the plating times trials. The tubes will be plated then measured for optical transmission then leached and optical transmission measured again.

Tubes plated to the full time have recently shown what appears to be some flaking of the gold plating from the glass surface. This is expected to be caused by a thicker coating and disappears during the leaching process. Small gold flakes have been observed in the waste leaching solutions indicating that some excess gold is removed from the tubes but uniform coating is still observed in most of the tube. These samples also have not changed color as much during the leaching process as previous samples, indicating that a thicker coating is being applied. As a gold film thickens its reflectivity increases starting in the IR region and moving into visible light range, indicating that the more yellow gold it appears the thicker the coating. This also means that thinner gold films will tend to have a more red hue. Plating trials have been completed on samples for both the 5 and 10 minute conditions of plating. Samples have exhibited odd behavior in plating with uneven deposition of gold along the length of the tube. This has not been observed before in the plating of the gold when using pressure in the plating process. Plating on the tube was observed to be more gold and exhibit more plating at both ends

of the tube. After the difference in plating was observed the same batch of solution was used to plate a sample until all the plating solution was used with the same difference in plating behavior being observed. The only difference between these plating trials and previous trials was the amount of activated gold solution prepared for the test. Previously 20mL of solution has always been prepared for testing; these trials had 30mL of solution prepared. The activated gold solution was prepared by mixing equal parts of gold and activator solution and should not behave differently as long as the ratio is the same. This is currently being investigated as a cause for the change in plating behavior. Other possible causes could be based on a time effect of using the same container for storing the activated solution since it leaves a small residue behind. The container is cleaned in between each test and dried before making a new solution. While uneven plating was observed in all the samples a clear difference in color was observed between the 5 and 10 minute samples indicating a different thickness of gold present. Trials were repeated with the original chemical quantities to determine if that was the cause of the uniformity problems and was found to have no improvement of the problem. Additionally switching the storage container for the activated chemicals from a polypropylene bottle to a glass vial had no effect on the uniformity.

5.3.10 Investigation of Plating Uniformity Problem

Eliminating the quantity of plating solution used as a cause of the uniformity problems increased the need for experiments to determine and eliminate the problem. The change was assumed to be caused by a minor change in the plating conditions. The non-uniformity was observed in all the different plating times that were tested, indicating either a problem with the glass or the solution. The sensitizing and rinse times had been unchanged in all trials both before and after the problem occurred. These trials were done at the same pressure as previous trials though the tubes were slightly different sizes. This indicates that a possible change in flow rate may be the cause of the changes in uniformity. Two experiments were conducted to determine the exact effects that flow rates of plating solution have on uniformity. Both trials were set up to test three different flow rates while holding other conditions steady. These trials used tubes of the same length and batch of glass that was used in the plating time trials were the uniformity problems were first encountered. The plating trial conditions are listed below in Table 5-24.

`

Table 5-24: Flow Rate Trial A Conditions

	Plating solution quantity (mL)	Plating time (min)	Flow Rate (drops/ 10 seconds)
Trial 1	6	25	10
Trial 2	6	~15	20
Trial 3	6	~5	30

Plating in the first experiment was done using constant amounts of plating solution and plated until solution was gone so each sample experienced different amounts of plating. The flow rate measurement used in these experiments was done by counting the number of drops out of the end of the tube over a 10 second window. Tubes in the first trial showed minimal plating at high flow rates due to the limited plating time with such little solution. The second experiment was carried out to ensure that limited plating did not affect the outcome. The second experiments conditions are listed in Table 5-25 below.

Table 5-25: Flow Rate Trial B Conditions

	Plating solution quantity (mL)	Plating time (min)	Flow Rate (drops/ 10 seconds)
Trial 1	6	25	10
Trial 2	9	25	20
Trial 3	12	25	30

The second trial was done to ensure that all tubes were able to plate for the same amount of time and allow for the only effect to be that of flow rate. In both experiments the sensitizing and rinse times were held constant. The tubes used in these trials were selected with IDs ranging from 125-200 microns due to the necessary flow rates needed. Applied pressure was uncontrolled except as needed to achieve the desired flow rates.

These two tests were successful in showing a variety of flow rates and plating times resulting in different film qualities. It however did not eliminate the uniformity problems that were being observed. Figure 5-71 below shows the results from Trial A that consisted of constant plating solution.

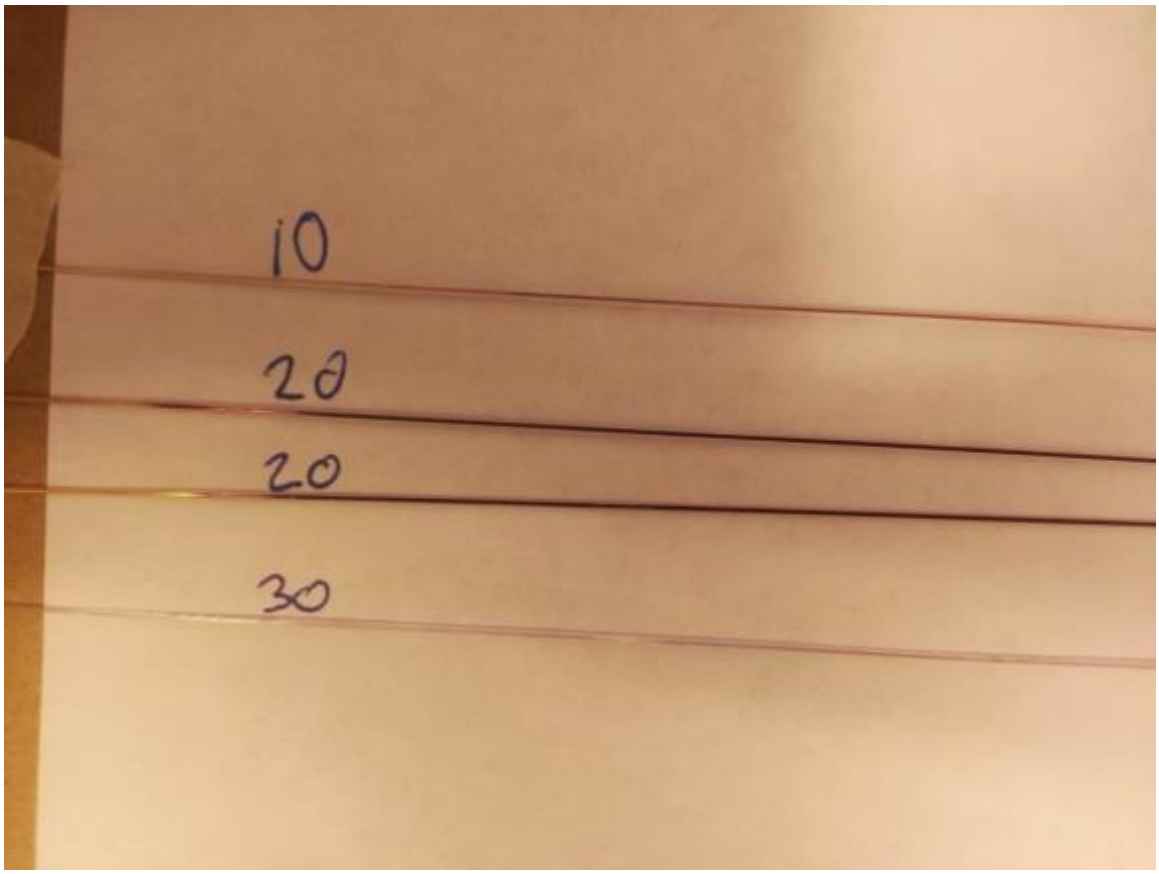

Figure 5-71: Samples from Trial A Measuring Effects of Flow Rate.

In Trial A, 3 velocities were tested where the slowest velocity showed gold coating along the entire length, the middle velocity showed regions of gold and dark purple, while the fastest velocity experienced very little plating due to running out of solution. Trial B was done with the

same velocities but with enough solution to allow for equal plating times for all conditions. Figure 5-72 shows the results of Trial B.

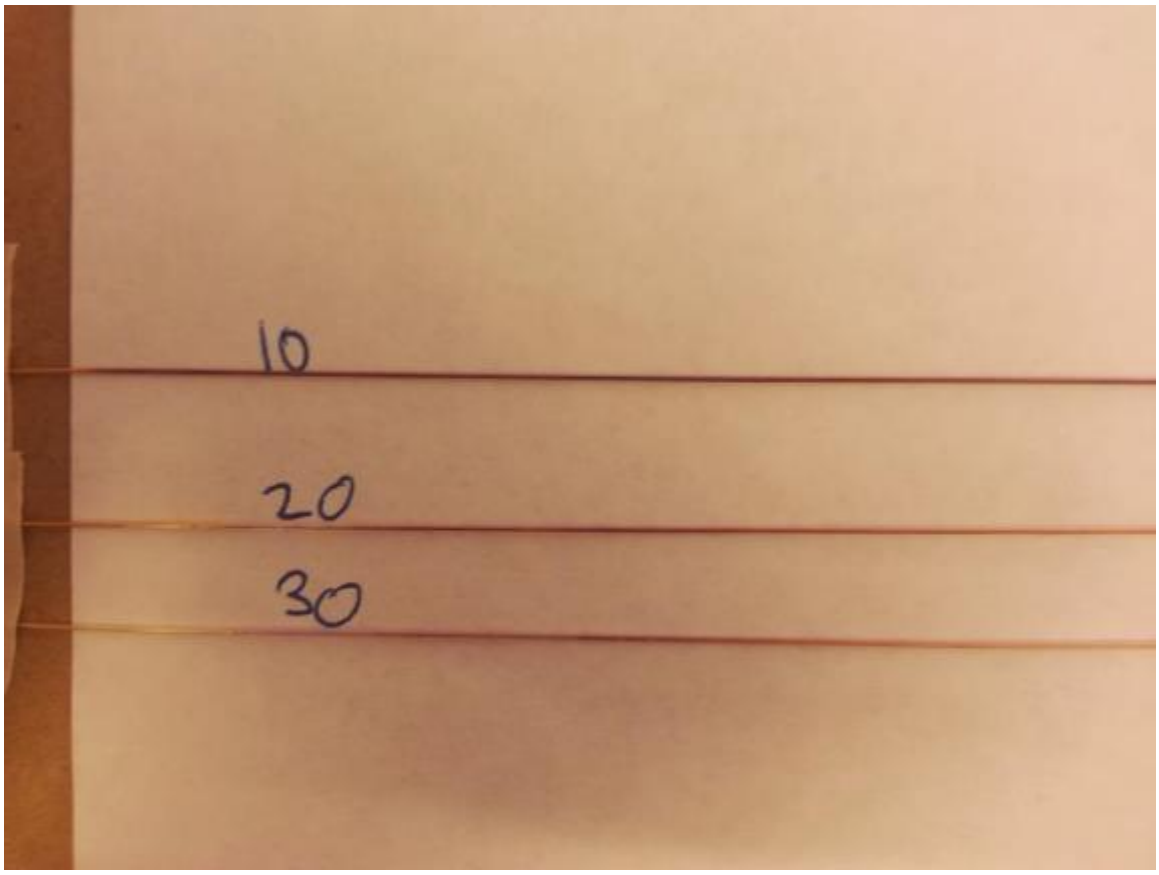

Figure 5-72: Samples from Trial B Measuring Effects of Flow Rate.

The samples from Trial B showed much better plating overall with gold observed on all samples. The uniformity problem was still present and looked similar in all conditions. A bright yellow gold color was present at both ends with a red hue present in the middle of the tubes. The results from these trials have shown that over a range of flow rates uniformity is not affected as originally believed. This eliminates flow rate of plating solution as the cause of the uniformity problems. It also showed that with adequate solutions higher flow rates help improve uniformity but due not create a perfectly uniform film. All tubes produced in these trials are being optically characterized at different locations and lengths to determine benefits and properties of different colors of gold films. The darker areas also still seem to be capable of reflecting longer wavelengths of light better based on its appearance under different lighting conditions. Higher flow rate samples showed less variation in the colors of the different regions but still were distinctly different along the length. These trials have eliminated flow rate as being the primary cause of the uniformity problems. Continuing to look for the causes of the uniformity problems led to testing of the flow rate of the sensitizing and rinse solutions since the times were constant in all trials. The test conditions in Table 5-26 below for testing the flow rates of the sensitizing solution and rinse. This trial was designed to look at the extremes of these and consisted of just changing the flow rate between a low rate of ~5drops/10sec and a high rate of ~30drops/10sec.

Table 5-26: Sensitizing and Rinse Flow Rate Conditions

	Sensitizing Solution Flow	Rinse Flow
Trial 1	Low	Low
Trial 2	Low	High
Trial 3	High	Low
Trial 4	High	High

The results did not show a lot of variation between the samples but the uniformity problem existed on all samples though to varying degrees. Figure 5-73 shows the results of Trial 1 and Trial 4. The lower flow rates did show better performance than the higher flow rates for these solutions possibly indicating more sensitizing of the glass occurring but not capable of eliminating the uniformity problems observed. Another possible cause of the uniformity problems investigated was that of dirt or contamination from the open tubes over time. Tubes were cleaned using a 6 Normal HCl acid treatment but this did not show any change to plating samples

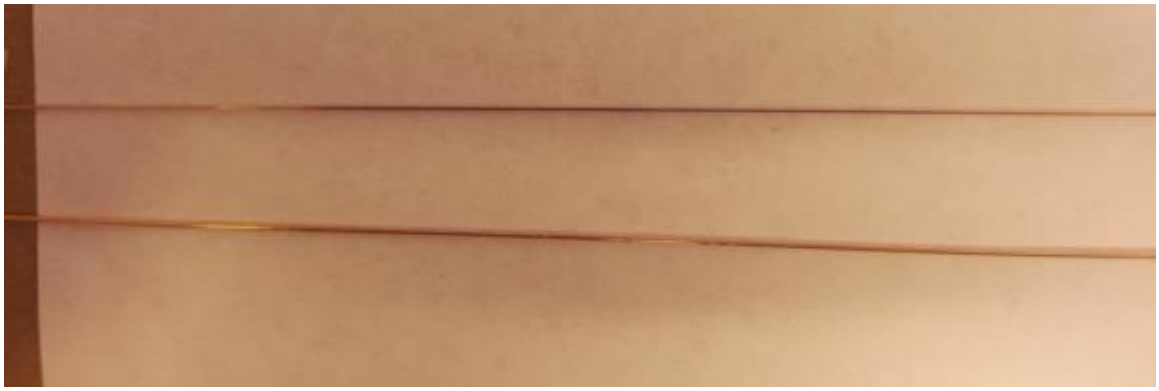

Figure 5-73: Sensitizing and Rinse Trial 1 (Bottom) and Trial 4(Top).

.

5.3.11 Evaluation of Gold Films Using SEM

To better understand the issues causing the uniformity problems, SEM analysis was done of the films plated during the flow rate trials. This analysis was done on sections from the ends and middle of all samples to look at film thickness and develop an understanding of the color of film versus thickness and also film adhesion to the glass. This analysis was carried out using the FEI Quanta 600 FEG ESEM in back scatter detection mode to provide Z-contrast. The Z-contrast will allow us to easily identify the glass from the gold film and measure the film thickness while avoiding noise normally encountered at edges of samples by secondary electrons. Figure 5-74 below shows low mag SEM images of 3 different samples each from an end and middle section of the tube.

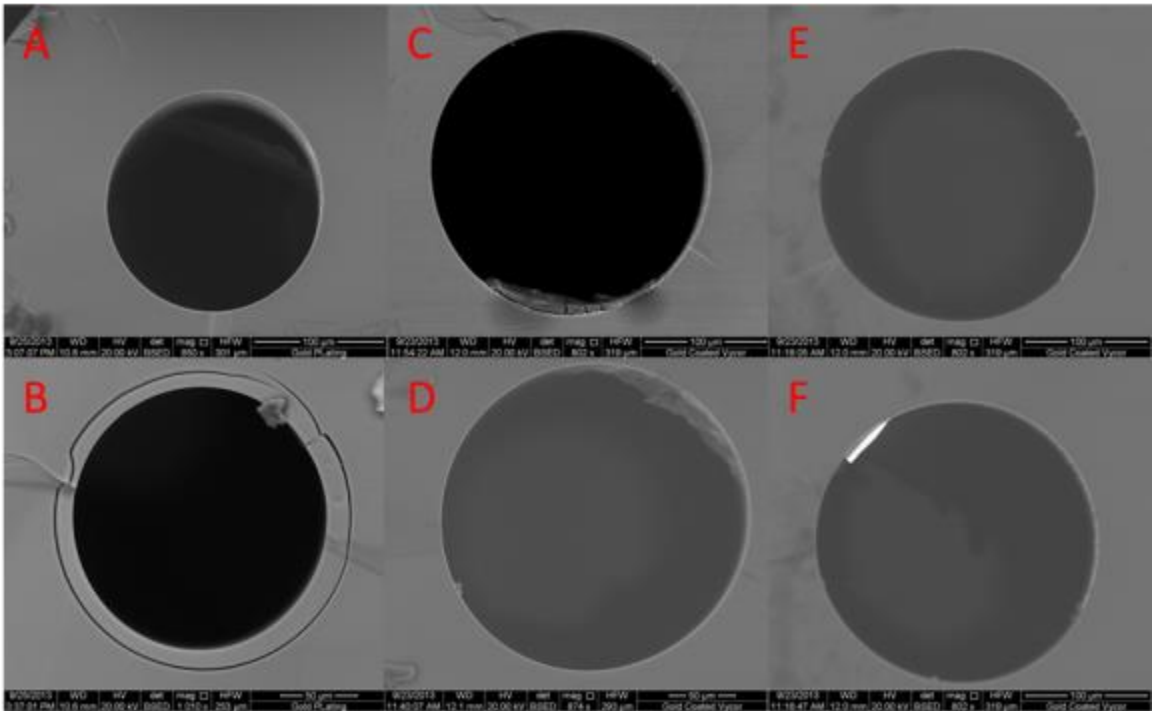

Figure 5-74: Low Magnification SEM of A) Trial 1-1 Yellow Region, B) Trial 1-1 Red Gold Region, C) Trial 2-1 Yellow Region, D) Trial 2-1 Purple Hue Region, E) Trial 2-3 Yellow Region, F) Trial 2-3 Red Region

Figure 5-74 shows that a thin gold film is present on all samples though not uniformly around the diameter. The primary difference in these comes from the thicker region around those from the middle of the tubes (Bottom Row of Figure 5-74). The coating appeared the same whether at the middle or end of tube with variations in thickness that was not related to color. Figure 5-75 below shows several of the observed film thicknesses in the end of regions of the gold. The observed film thicknesses in these regions range from 40nm on one sample, 80nm on a second, and 160nm on third sample. All of these tubes were plated with different flow rates but all appeared bright yellow gold color to the naked eye. Figure 5-76 below shows some of the measurements taken from the middle of tubes.

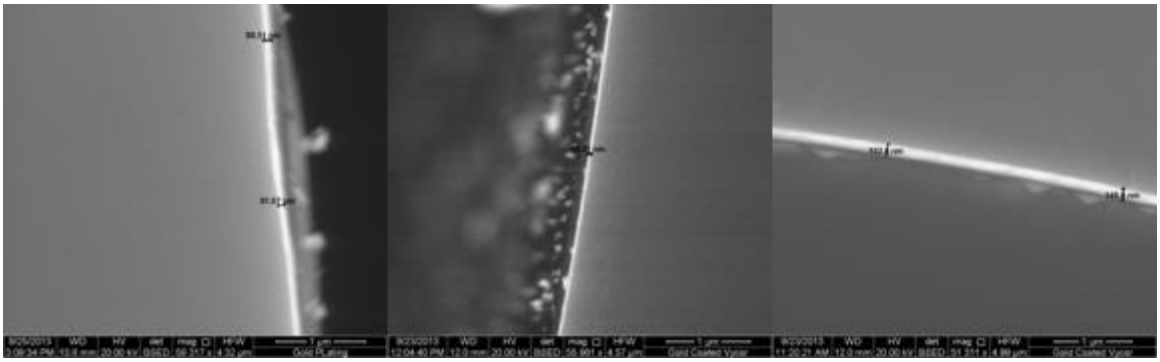

Figure 5-75: SEM with measurements from end of tube regions.

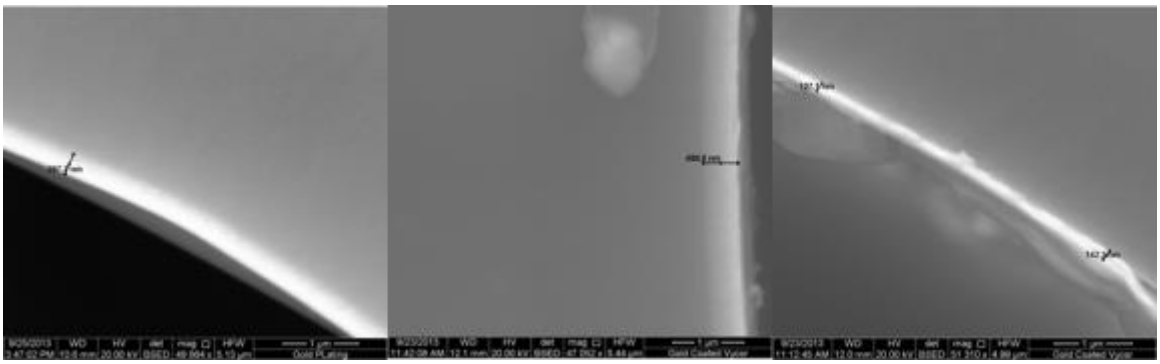

Figure 5-76: SEM with measurements from middle of tube regions.

The films in this region were thicker than those found at the end of the tubes and ranged from 120-400nm in thickness. The color in these regions appeared darker with an almost purple hue though was still reflective to light. There is some overlap on the ranges indicating that the thickness is not the primary cause of the color difference and the observed odd region is likely the primary cause of the observed difference.The SEM identified a thin region ~10 microns in the middle of the tubes that appeared to be a different phase of glass than the rest of the tube. Figure 5-77 below shows this region.in detail.

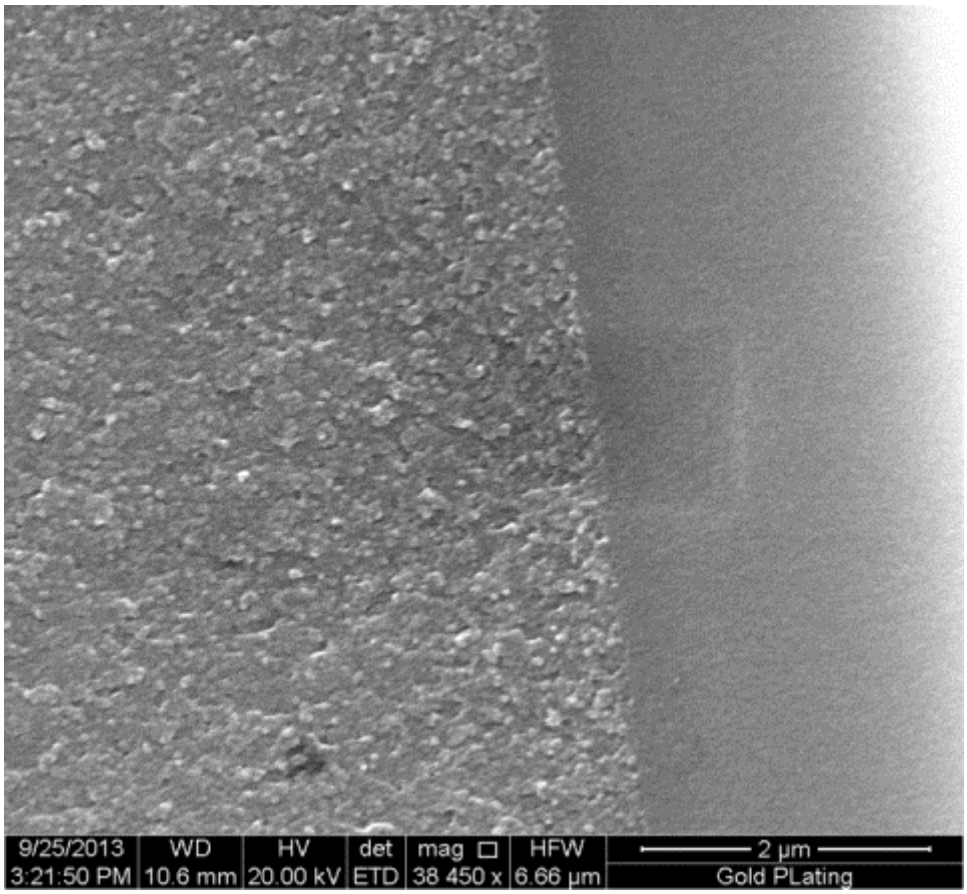

Figure 5-77: Two phase region from near tube inner surface.

Figure 5-77 shows the two phase region present with the left side being closer to the hole of the tube. This region was found to be in of all of the tubes in the middle regions. The region closer to the inner surface appears almost porous in comparison to the rest of the glass. This was not observed in any of the regions examined at the ends. In addition to this two phase region, cracking of the tubes was present in these regions. Figure 5-78 below shows several of the tubes experiencing this cracking.

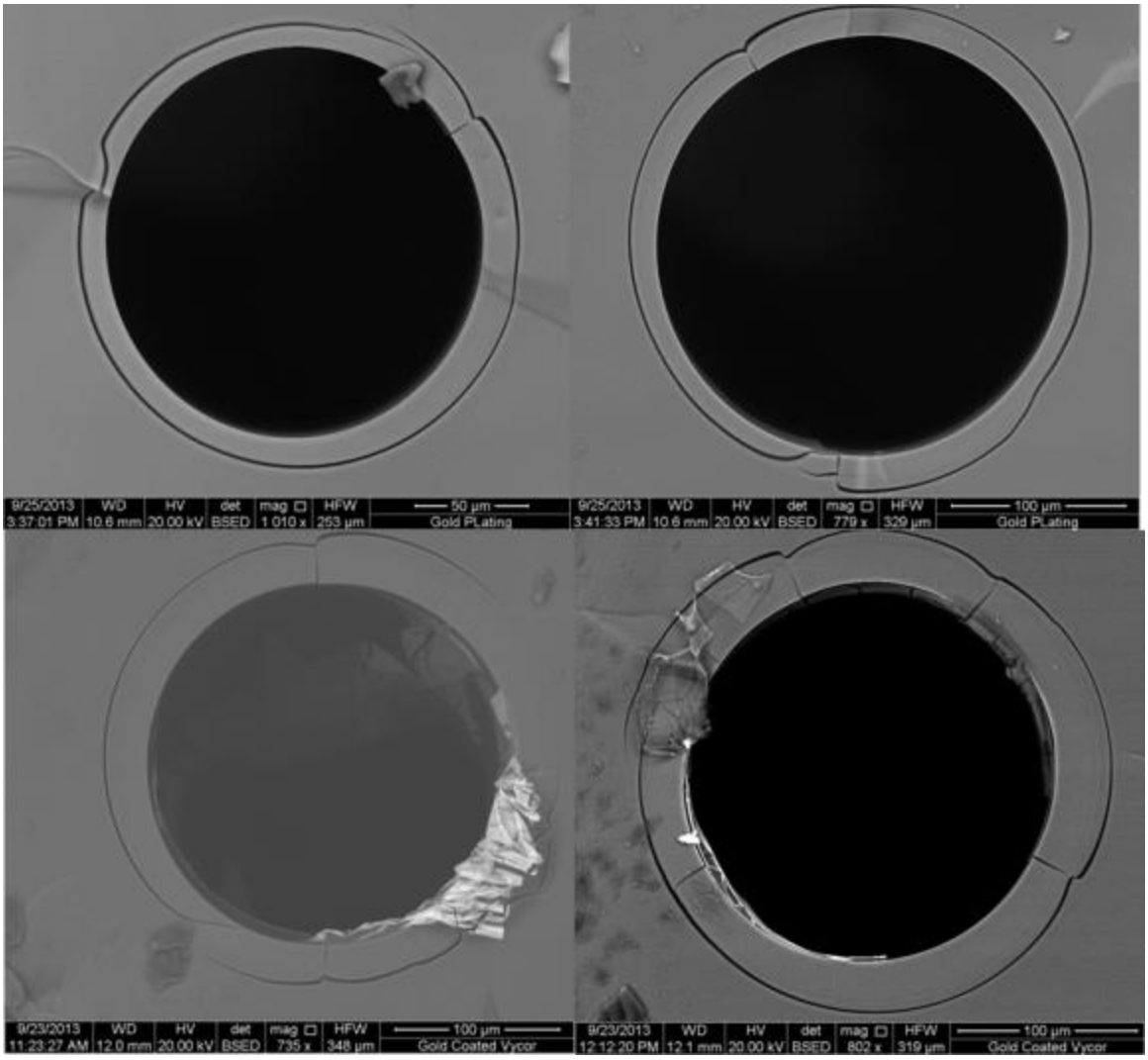

Figure 5-78: SEM images from middle of tubes showing cracking in two phase region.

EDS analysis was done on several of the two phases regions to determine if there was a compositional change in these regions. Table 5-27 shows the results in weight percent of 2 different 2 phase regions. The two rows shaded indicate the spectra collected from the odd region present near the inner surface of the tubes and only in the middle of the tubes. These regions were found to have Higher Silicon and aluminum content with significantly lower Sodium content was found in these regions indicating that soda in the glass was leached out during the plating process. This would suggest that the phase separation was uneven along the length of the

tube or the glass composition has changed. This confirms the results that were indicated in the flow rate trials; that the uniformity problems are not being caused by the plating solution.

Table 5-27: EDS Analysis of Two Phase Regions

Element	O	Na	Al	Si
GP1-wt%	52.24	1.44	3.28	43.04
GP3-wt%	53.1	3.87	3.11	39.93
GP4-wt%	50.17	3.18	3.48	43.17
GP5-wt%	58.9	4.62	2.49	33.99

Since this problem was not previously encountered in plating trials, it is thought that a change in glass composition or the phase separation treatment is the cause of the uniformity problems being observed. Phase separation is dependent on both the time and temperature of the treatment and small variations in the temperature can cause different phase separation results leading to different glass behavior. To confirm that glass behavior along length was different, confirmation trials removing 1 or both end of the tubes prior to plating was done. This allowed for the removal of the potentially non-uniform parts of the tube from along the length.

The glass used was drawn from several source tubes and had not been well tracked or separated. To eliminate the problems encountered, all remaining glass drawn for plating trials was scrapped and new glass was drawn. A temperature profile of the length of the furnace was taken at 3 times over the 20 hour treatment to look for any variations in the temperature that could have caused uneven phase separation. The temperature remained even except for the final inch of the furnace near the door. At this location it took approximately 7 hours longer to reach the temperature which would explain the behavior being different at one end. The other end of the furnace was not well profiled due to difficulties in locating a thermocouple there, but it does not appear to show any significant temperature differences. In addition, newly produced and phase separated tubes do not appear to have the uniformity problems. The most likely cause of uniformity was a problem the occurred in the furnace during that specific phase separation treatment and has been eliminated from future plating trials.

After the determination of the cause of the uniformity problems and the inability to control it, trials to vary film thickness have resumed. Using information gained during investigation of the uniformity problems, minor changes were made to the plating process. Increasing the flow rate of the plating solution, and decreasing the rinse time to only 5 seconds after the sensitizing solution has been used are the two adjustments made to all plating trials. The reduced rinse time is done to increase the amount of sensitizing solution left on the surface and also due to changes in the manufacturer's published directions. Additional changes specific to thickness trials are the times targeted for stopping the plating. The three times being initially tested for varying thicknesses are 13, 15, and 17 minutes. Additional changes post plating to improve ability to insert fibers is to use a furnace treatment to dry the tubes prior to any processing to ensure a nice stable film. The furnace treatment used was 110°C for 2 hours to remove all moisture from the tubes.

Preliminary Optical testing has been carried out on solid, gold plated glass tubes to determine any improvements in signal and to provide a baseline measurement prior to leaching of the tubes. Three tubes were measured using a tunable laser source with 25mW power setting.

The signal was measured using an optical power measurement and measured in dBm. A SMF was used for the lead in fiber while MMF was used for the lead out fiber to provide the highest collection of signal. This measurement differs from previous measurements which were carried out using CTS. The CTS was done at much lower powers using a light source output power of 0.2mW. Signal in those tests was also collected and measured in dBm. The signals in both cases were converted back to mW and measured as a percentage of the input power to provide a direct comparison.

Plating of tubes has continued with the uniformity issues appearing periodically. All tubes whether uniformity problems exist or not are processed through the leeching process. The success rate currently is very low for the gold plating surviving the leeching process. The coating is lost approximately on half of the tubes entirely while the other half loses some of its plating. Figure 5-79 shows a batch of gold tubes plated under identical conditions and the same batch of plating solution. Uniformity problems are clearly visible in the tubes 1, 2, 6, and 7 starting at the top numbering down. The other tubes showed slight variations in color but were uniform in color along the length of the tube.

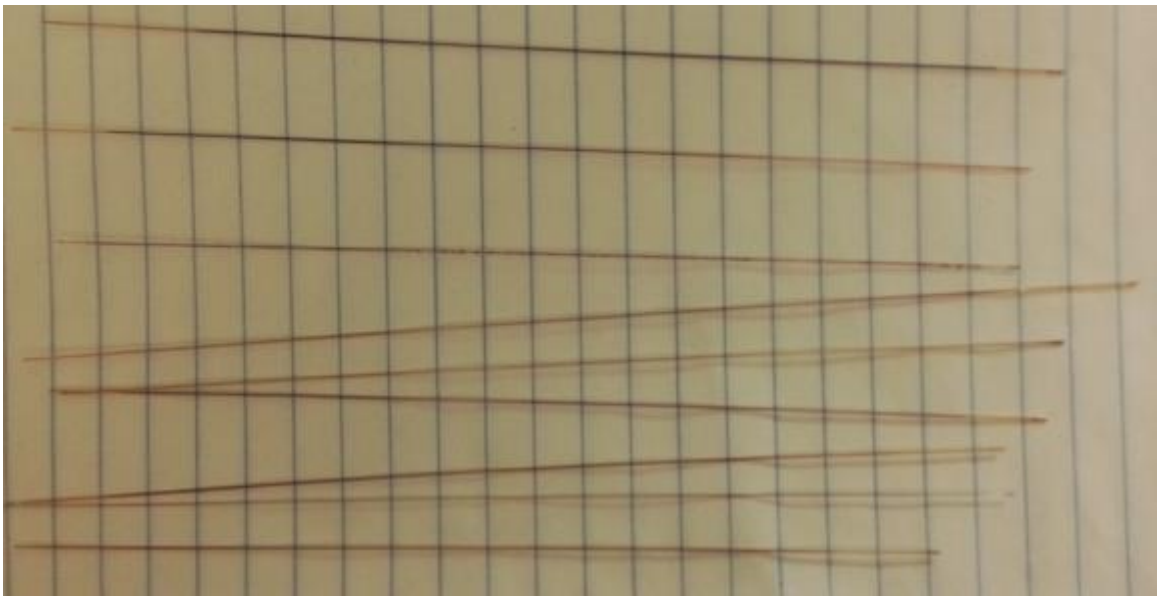

Figure 5-79: Batch of Gold Plated tubes showing Uniformity problems

This uniformity problem is observed in approximately 30-40% of tubes in a given batch. Optical testing was done on 3 of the best looking of the tubes out of the batch to get a baseline for comparison to those after leeching. Table 5-28 below shows the results of the preliminary optical testing. It summarizes both the observed output power and its percentage of the input power for comparison to previous tests that used a different light source. The results from these tests show wide variation across samples and even across cavity lengths. Sample 1 had the largest inner diameter while 3 had the smallest inner diameter. During the setup for these optical tests, no control over the alignment of the lead fibers in the tubes was used. The signal was found to be very depending on slight variation in the fiber angle on the magnitude of 5-10dB. Previous tests on the original gold plated tubes were tested on the CTS. The percent of input power that was transmitted down the tube was measured to be approximately 0.00158%. These values were significantly better than those results. Most of the tests previously done on the porous glass

showed values of approximately 0.5% power for a 5cm cavity length which is significantly less than the new plated tubes. The true comparison won't happen until the tubes are made porous and measured again. All three tubes were processed together and unfortunately none of them survived, most of the gold plating came off during the nitric acid step and upon drying the tubes curved, cracked and nearly disintegrated. More plated tubes are being leached currently. Previous tubes have been successfully made porous without losing the gold coating and seem to be very dependent on the composition of the glass. The non-uniformity appears to have no effect on the ability to transmit as sample 3 in this test had very good transmission and was non-uniform. Due to the variable nature of successes in the leeching process results are still pending for tubes after leeching. The three tubes that were tested did not have gold coating that completely survived with only coating remaining on small sections of the tubes.

Table 5-28: Preliminary Transmission Loss Results from Gold Coated Green Glass

Cavity Length (cm)	Gold 1(dB)	% Input Power	Gold 2(dB)	% Input Power	Gold 3 (dB)	% Input Power
1		X	12.81	76.40	-47.90	X
2		X	4.72	11.86	-0.15	3.864
3	-11.30	0.296	3.05	8.08	-2.90	2.052
4	-16.25	0.0948	-0.25	3.776	-5.21	1.204
5	-25.35	0.0116	0.20	4.2	-4.80	1.32
6	-27.75	0.00672	-1.10	3.10	-5.42	1..148
7	-32.30	0.00236	-1.98	2.536	-6.34	0.928
8	-34.12	0.00156	-3.80	1.668	-6.34	0.928
9	-37.27	3.04E-5	-5.06	1.248	-6.54	0.888
10	-49.03	5E-5	-7.45	0.72	-6.54	0.888
11			-5.25	1.20	-7.00	0.8
12			-6.50	0.896	-6.95	0.808
13			-10.14	0.388	-5.28	1.184
14			-10.20	0.38	-4.75	1.34

Gold plating trials continued on green glass tubes in an effort to improve transmission characteristics of the porous tubes. Samples for optical testing have been very limited due to extremely poor success rates of plating surviving the leeching process. The plating process results in varied qualities and adhesion of the gold to the glass surface. Efforts to improve this with the sensitizing solution times and flow rates were not successful.

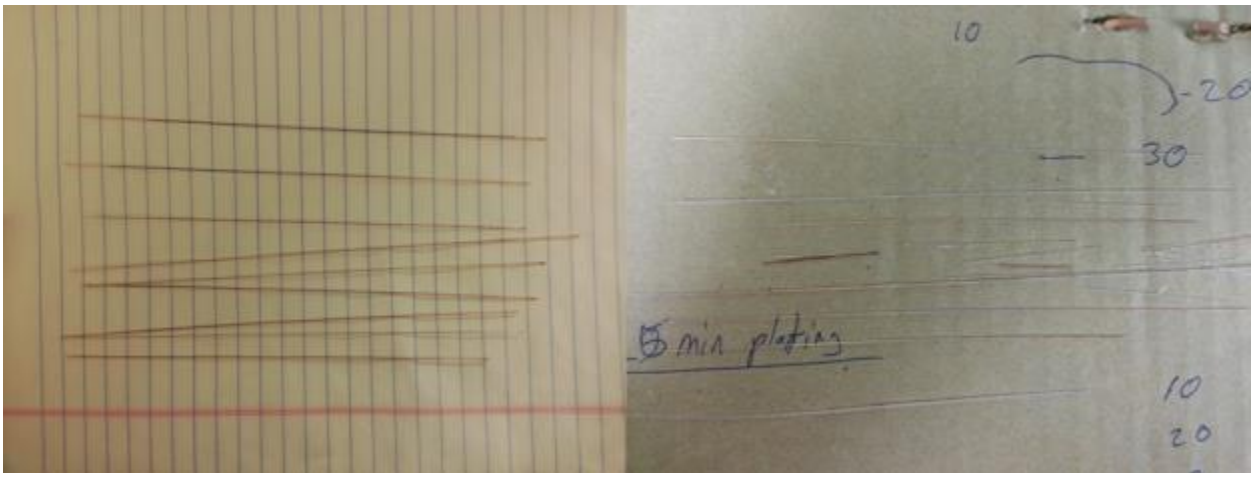

Figure 5-80. Plated Fibers before (Left) and After (Right) Leeching Treatment.

Of the 9 tubes shown above only 3 exhibited any coating after the leeching process. Optical results have still been unreliable due to flakes of gold coating or problems resulting from curvature of the tube obstructing the optical path. Additional testing was done to determine if the inner diameter has a direct effect on the adhesion. Testing was done on tubes of 2 size ranges: 140-160 microns and 210-230 microns. The larger size was chosen based on successful plating from initial testing. Four samples of each size were plated using identical conditions. Two of the samples, 1 from each of the test pools, encountered flow rate problems and did not have any plating visible. The remaining six samples are shown below in Figure 5-81.

Figure 5-81: Gold Plated Tubes testing the effects of inner Diameter on Film Quality.

All samples showed uniform plating over the length of the tubes. The 3 samples of smaller diameter appeared to have more of purplish red hue still present rather than the bright yellow gold that is observed during full plating. Additionally the smaller tubes clogged during plating and did not experience the full length of plating that the larger tubes did. High pressure rinsing was not able to clear the clog and only passing a fiber through the tube was able to clear it. This also removed nearly all of the gold coating. Passing a fiber through the large diameter tubes did not damage or remove the gold coating however.

While larger tubes and higher flow rates tend to provide the best adhered gold film on the solid phase separated glass tubes, the ability for the coating to survive the leeching process is not

well understood. Coatings plated at identical conditions have been observed to have varying results of surviving the leeching process. This variation leads to the hypothesis that the coating is very dependent on minute changes in composition. The green glass used to produce these tubes was provided as cullet from Corning's commercially production just prior to the shutdown of the line. Drawing behavior from preform to preform has been observed to vary significantly as well as a contamination issue that has been observed to varying degrees that is removed with an ammonium bifluoride etch prior to drawing. The changes in drawing behavior clearly tell us that our preforms have compositional issues and these compositional variations are the primary culprit for the variation observed in testing.

Several small lengths of porous gold coated fiber were successfully made from the large diameter tubes for optical testing. The starting length of coated tubes put into the leeching process were 16-25 cm. Lengths with continual gold coating still present at the end of the leeching treatment ranged from 4-10cm of tubes indicating significant film loss. These tubes were tested for transmission and gas detection of acetylene.

5.3.12 Transmission Tests of Gold Coated Porous Glass

Transmission spectra were collected on multiple gold tubes and at a variety of cavity length on each sample. The spectra were collected using a CTS as both the light source and detector. In these tests SMF was used for both the lead in and lead out fibers. Test setup consists of three 3D stages with the gold coated sensor positioned on the middle stage which also had tilt control as well as xyz control. Lead-in and lead-out fibers were fixed to stages at each end of the sensor. Lead fibers were inserted until touching while the stages were at maximum travel toward the sensor. This position allows for the fibers to be separated up to a distance of 5cm. The setup is shown below in Figure 5-82.

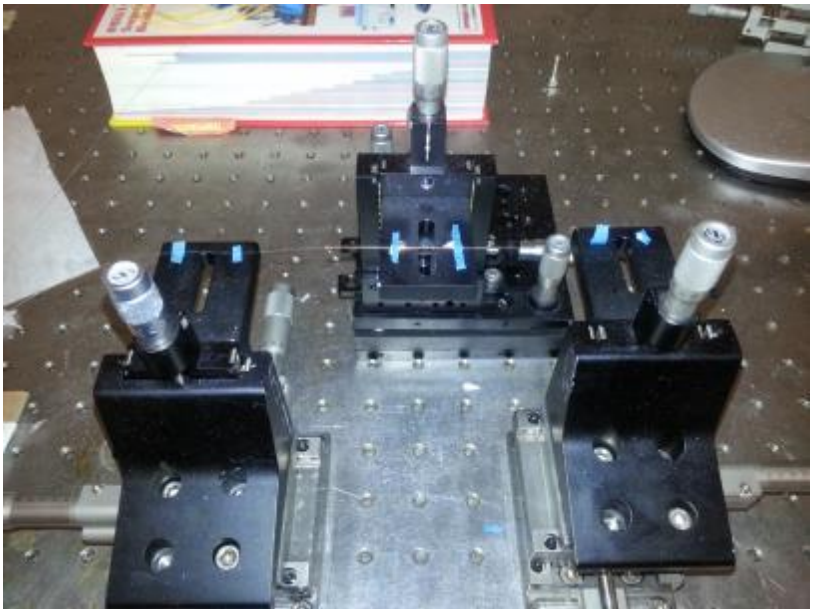

Figure 5-82: Test Setup for Transmission Test of Gold Coated Glass Tubes.

Spectra were collected on both solid green glass with gold plating as well as porous glass with gold plating. This data was collected to understand how the film characteristics change during the leaching process and to understand any benefits the gold film may provide. Fiber

alignment was adjusted until the maximum transmission power was achieved prior to recording the data. The alignment was readjusted each time after the cavity length was increased. In the case of the porous gold glass samples the optimal alignment was achieved by positioning the tube above the lead-in and lead-out fibers which induced a slight bend in the sample. The presence of the bend in the sample is believed to increase signal intensity due to both reflection due to the gold coating as well as improved alignment. Successfully plated gold tubes have only been possible on larger tubes with inner diameters in the 200-230 micron range. This larger inner diameter makes alignment extremely difficult and is aided by the bending holding the lead fibers against the outer surface of the tube. Due to the variability of the gold coating process and the difficulty in maintaining the coating through the leaching process, cavity lengths for this test were very small for most samples. Figure 5-83 below shows the spectra collected from 2 gold coated solid green glass tubes with a 3cm cavity length.

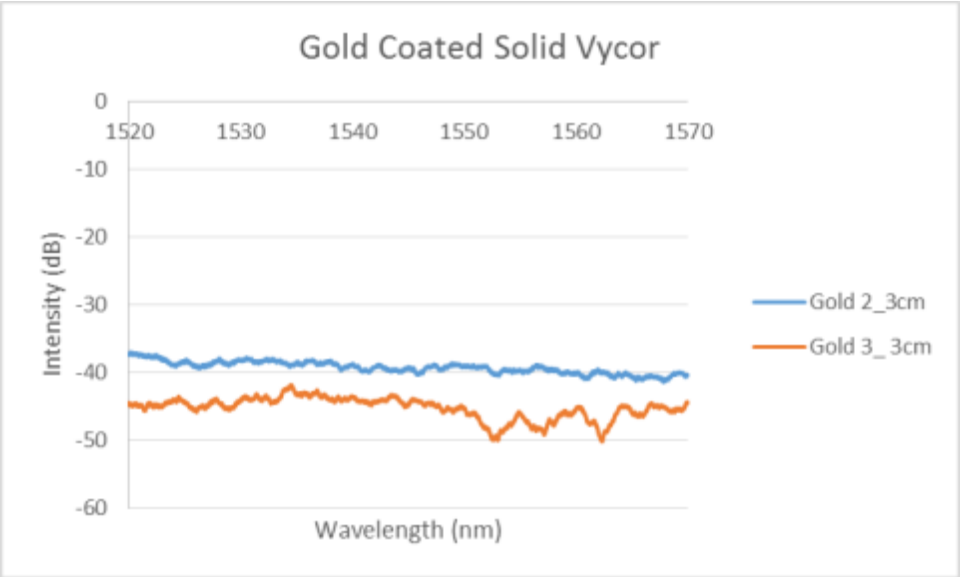

Figure 5-83: Transmission Spectra from 2 Gold Coated Solid Glass Tubes with same cavity length.

The spectra collected showed variation between the sensors but appeared similar for the 2 sensors. Spectra were collected varying cavity length and are shown in Figure 5-84. Increasing cavity length showed a steady decrease in transmission with increasing cavity length. Major drops in signal strength occurred at with the initial increase in cavity length and then had a much slower rate of decrease after that point. The signal became less uniform with increasing cavity length as well. Spectra collected from gold coated porous glass from 3 tubes with a constant cavity length are shown in Figure 5-85.

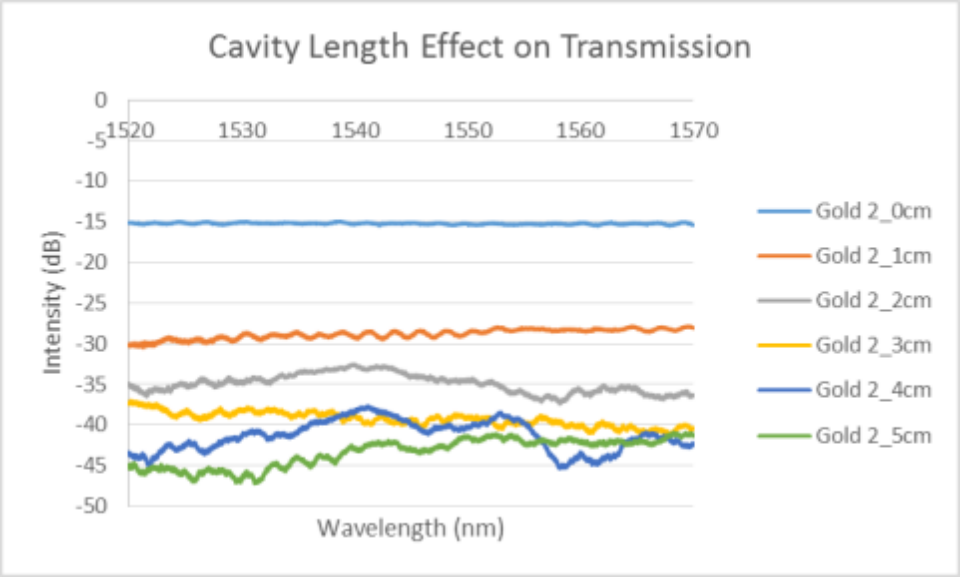

Figure 5-84: Transmission Spectra from Gold Coated Solid Glass Tube Varying Cavity Length.

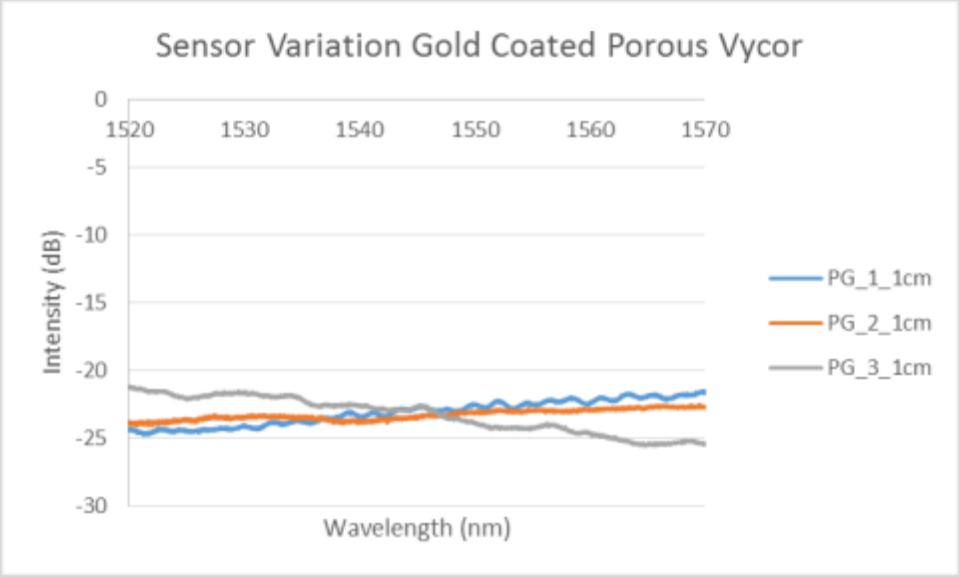

Figure 5-85: Spectra from Gold Coated Porous Glass Tubes with same Cavity Length.

Spectra from the 3 tubes with cavity length of 1cm show similar signal across sensors with similar signal strength. Spectra were then collected to a maximum cavity length possible of each sensor. Variation of the signal was shown below in Figure 5-86.

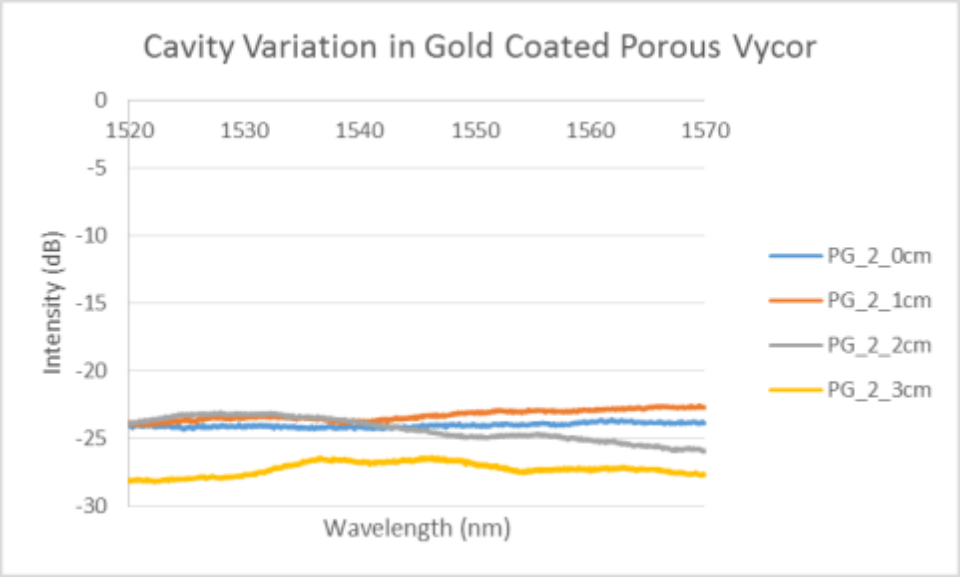

Figure 5-86: Spectra from Gold Coated Porous Glass Tube with varying cavity Length.

Spectra collected on the gold coated porous glass tubes showed significantly different behavior than the signal behavior on gold coated solid glass. In the case of the solid glass samples increase in cavity length showed a steady decrease in signal strength. This behavior is expected and corresponds with behavior of just increasing the distance between 2 fibers in free space. Signal strength in the porous samples was found to be significantly higher (5-10dB) for the same cavity length. In addition loss with increasing cavity length up to 3cm was minimal and indicating the gold coating is providing some reflection and assisting to minimize loss.

5.3.13 Gas Detection of Gold Coated Porous Glass

Detection of Acetylene was done using a gold plated porous glass tube to determine the effects of the gold coating on gas detection. The setting is similar to the setup for transmission tests with the CTS being used as the light source and using a SMF as lead-in but differs in that a MMF is used for lead out and an oscilloscope attached to a photodetector for detection. The three stage setup from Figure 5-82 is used to align the fibers at a cavity length nearly 4cm long. This is the longest possible cavity from the available gold coated porous tube. After alignment the lead fibers were attached using a silica based ceramic adhesive to fix the alignment. The sensor was then inserted in the gas cell as shown in Figure 5-87 for testing.

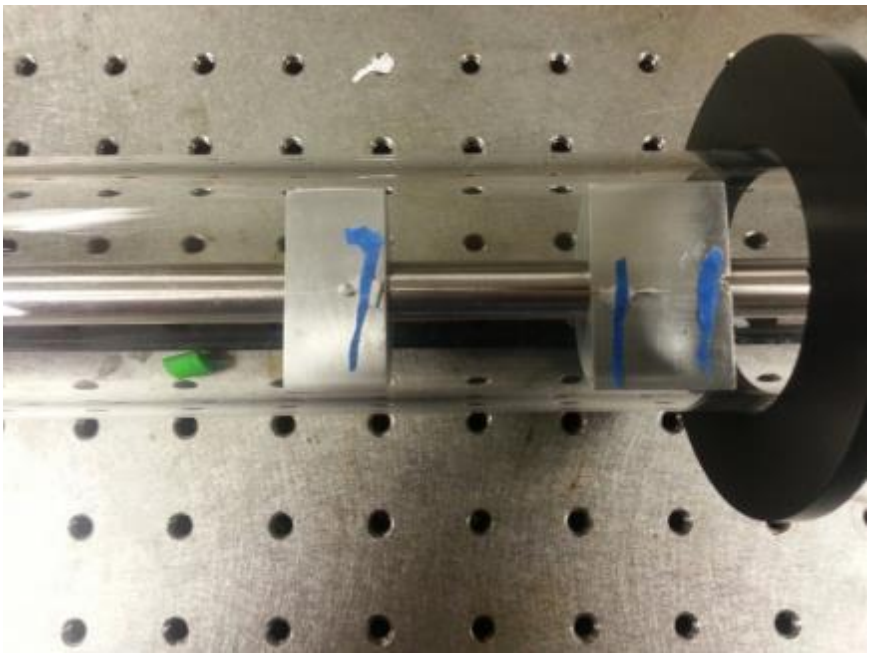

Figure 5-87: Gas Cell Setup for Testing of Gold Plated Porous Glass Sensor.

Gas concentrations tested were based on the results from the testing of the porous glass sensor testing. These tests were done using the same test conditions that the regular porous glass. Concentrations values for comparison were chosen to be 10% and lower, since trace concentrations are the desired detection point. Based on the results of the 10% test, additional concentrations were tested at 1% and 0.1% acetylene. The data from these tests was compared to the 5cm porous glass sensor tested as this was the closest cavity length possible for comparison. The other difference in this test comes from the use of a photodetector and oscilloscope for detection. In this detection method an amplifier is used to increase the signal going to the oscilloscope. The amplifier is capable of providing amplification from 10^4-10^9 gain. In the case of the 5cm porous glass sensor the amplifier was set at 10^5 while the amplifier was set at 10^6 for the gold coated porous glass sensor. Figure 5-88 shows the raw spectra collected at the 10% acetylene concentration for both sensors.

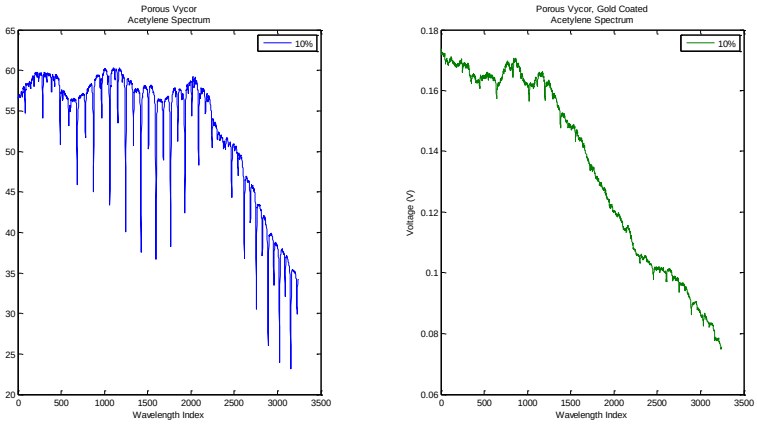

Figure 5-88: Spectra collected from 10% Acetylene on Porous Glass (Left) and Gold Plated Porous Glass (Right).

This data represents amplitudes of the peaks in voltage plotted against wavelength index. The wavelength index is an integer representation of the wavelength range of 1520-1570nm. The most noticeable difference in the spectra is seen in the amplitude of the absorption peaks, which are much higher on the regular porous glass sensor. The overall signal strength is also significantly different with the signal maxing out at 60V for the porous glass while maxing out at 0.18V for the gold coated porous glass. This significant signal strength loss in the gold coated tube is further magnified by the 10x higher setting on the amplifier. This trend is also observed at the lower concentrations and is shown below in Figure 5-89 for both sensors at 0.1%.

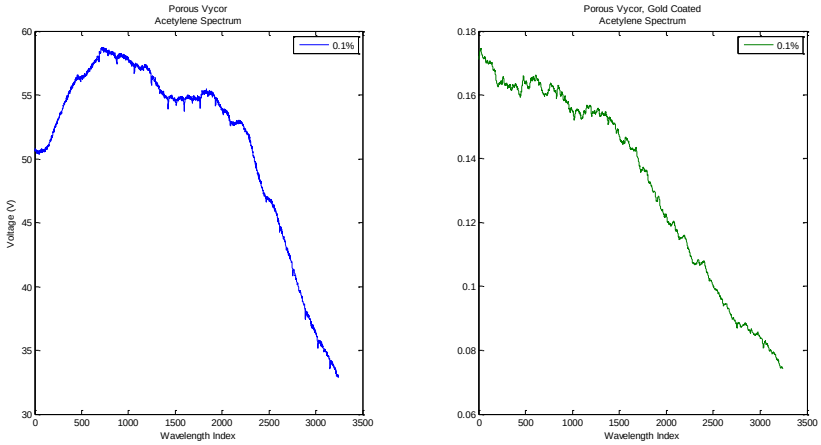

Figure 5-89: Spectra collected from 0.1% Acetylene on Porous Glass (Left) and Gold Plated Porous Glass (Right).

The same trends are observed at lower concentrations as at higher concentrations. In addition the absorption lines are difficult to observe in the gold coated samples at all and the algorithms are barely capable of detecting their presence after the background is removed. This indicates the minimum concentration detectable for a gold coated porous glass to be at or above 1000ppm for acetylene while the minimum detectable concentration for a regular porous glass sensor is at or below 100ppm. There is no data to suggest any impact on the absorption peaks of the gas simply just on the output power of the laser source. Transmission tests on the gold coated porous tubes indicate that the presence of the gold allows for additional reflection and improved signal based on minimal loss with increasing cavity. The poor performance in gas detection is caused due to the lower transmission power of the signal and potentially caused by poor alignment due to the larger inner diameter of the gold coated tubes. Early work on joining techniques showed that fibers bonded with ceramic adhesive to the porous glass had significantly worse performance at holding alignment and signal strength than those bonded with the CO_2 laser. The presence of the gold coating currently prohibits the use of the laser for bonding. While the gold coating shows some improvement in transmission quality, further work is warranted in understanding why this is not translated to improved system sensitivity.

Additionally solution gold plating has been used to produce a gold mirror surface on the end of 240 micron multimode fiber. This mirror surface was produced for insertion into the end of a porous glass tube. This mirror is being used to provide the mirror surface discussed in previous reports where the lead in and lead out fibers are inserted into the same end of the porous glass tube. This design is done to increase sensitivity by doubling the interaction volume. These

mirror surfaces were plated by being submersed in the plating solutions as per the manufacturer's directions for plating. Figure 5-90 below shows a fiber after being plated with gold. The plating surface was observed to be mostly uniform with all of the fibers exhibiting some minor amounts of coating missing. Optical tests are currently pending using these mirrors inserted into the end of the glass tubes.

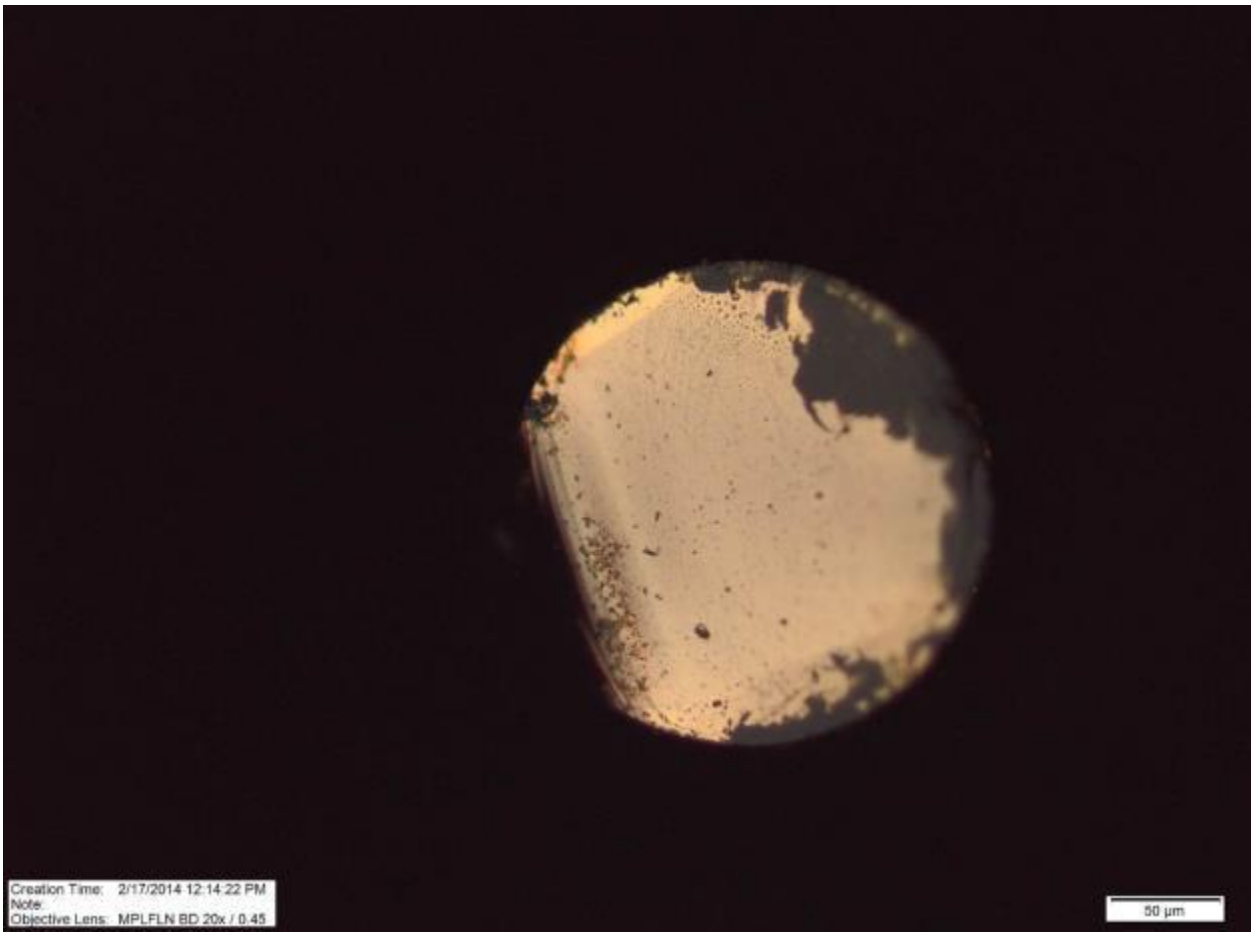

Figure 5-90. Gold mirror formed by plating on the end surface of MMF.

5.4 Signal Processing Improvement

5.4.1 Signal Demodulation of Gas Detection

The software development will focus first on acquisition and detection. For initial testing, sample data from a porous silica tube 6 cm in length filled by acetylene gas was used. The progression of the software is illustrated with the aid of plotted figures. Consider Figure 5-91, in blue is the acquired transmission spectrum. Notice however that the spectrum shows power fluctuations across the wavelength band. These fluctuations, due to the gas cell material, geometry, and bonding, comprise a unique background signal. The background must be compensated before continuing with detection. To compensate the background signal, peak finding and interpolation is used to approximate the fluctuations. Figure 5-91 shows the approximated background signal in red.

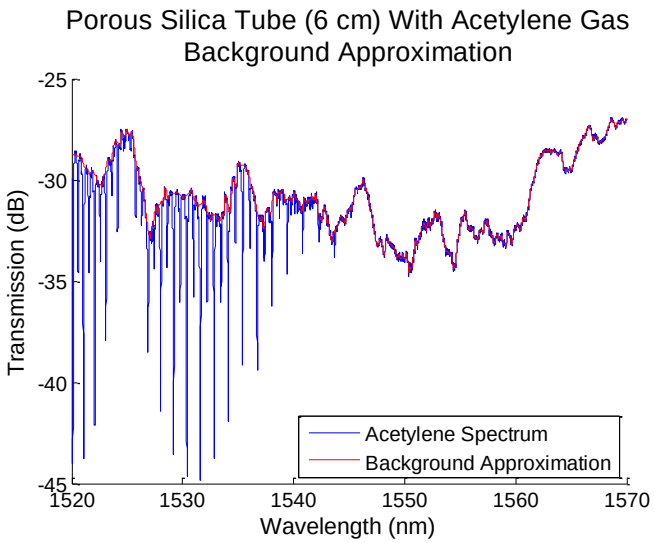

Figure 5-91: Background Approximation

The transmission spectrum is processed in linear units and the effect of the background is removed by division. Now appearing flipped, the normalized result yields ready comparison against established reference data in Figure 5-92. In blue is the measured, background-compensated, acetylene spectrum. In green is the corresponding reference information. The overall shape and significant peaks marked in red confirms detection for the target gas acetylene.

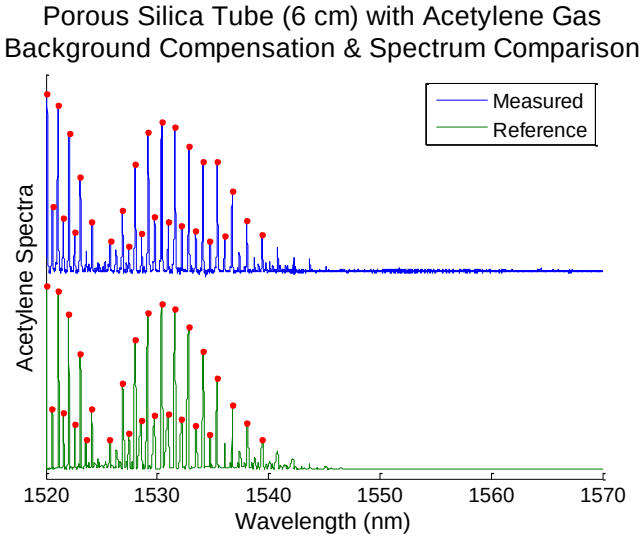

Figure 5-92: Background Compensation & Estimation

In Figure 5-91 and Figure 5-92, acquisition and detection have been demonstrated for acetylene. In the programmed software, flexible data structures are used so that other gases can be tested. For various gases of interest, especially hydrocarbons, a reference detection library is being built over the appropriate measurement range for detection verification. Estimation procedures are also being explored to accurately determine the concentration of target gases. The task of estimation is the most technical and important aspect of the software. Ultimate performance will depend on its proper implementation in association with good measurement

practices. We recognize according to Beer-Lambert's Law that there is a linear relationship between absorption line strength and the concentration of a gas. Figure 5-93 gives a close-up view of an absorption peak for acetylene between 1528.9 nm and 1529.5 nm. The absorption peak is mathematically fitted using a model Lorentzian distribution shown in red. Beer-Lambert's Law describes direct proportionality between the absorption peak height and the gas concentration.

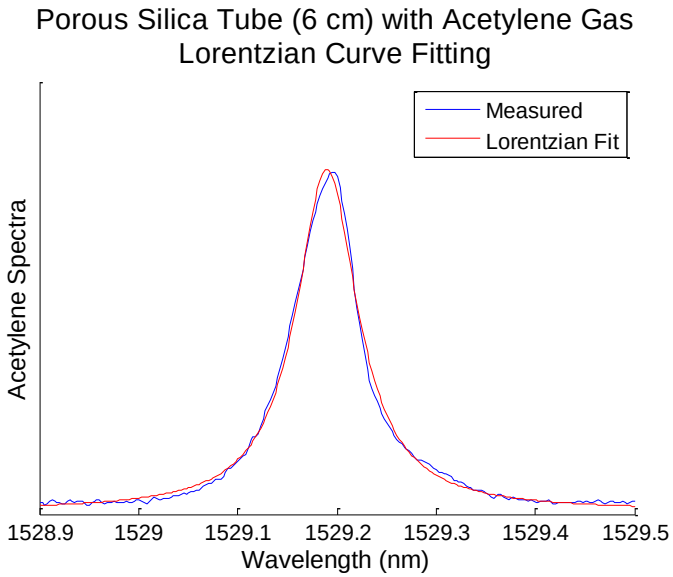

Figure 5-93: Lorentzian Curve Fitting

By calibrating spectrum measurements against records for gases of a known fractional volume, the concentration of a target gas can be found as a simple ratio of peak heights or integral areas. Measurement accuracy will be dependent on a number of factors including measurement resolution, the number of independent samples, electronic system noise, and particularly the accuracy of calibration data. Quantitative indicators to assess the function and performance of the sensor will be supplied as calibration data is recorded and the signal processing software matures.

In order to investigate the gas sensing ability of the porous tube gas sensor, an initial set up was constructed as shown in Figure 5-94. The CTS was used as the input and output source and SMF-28 was used as the lead in and lead out fibers to the porous tube gas sensor. The CTS scans the wavelength between 1520nm to 1570nm. The length of the overall porous tube was 7.5cm with a cavity length between the lead-in and lead-out fibers of 5cm. The porous tube had an I.D. of 150µm and O.D. of 390µm.

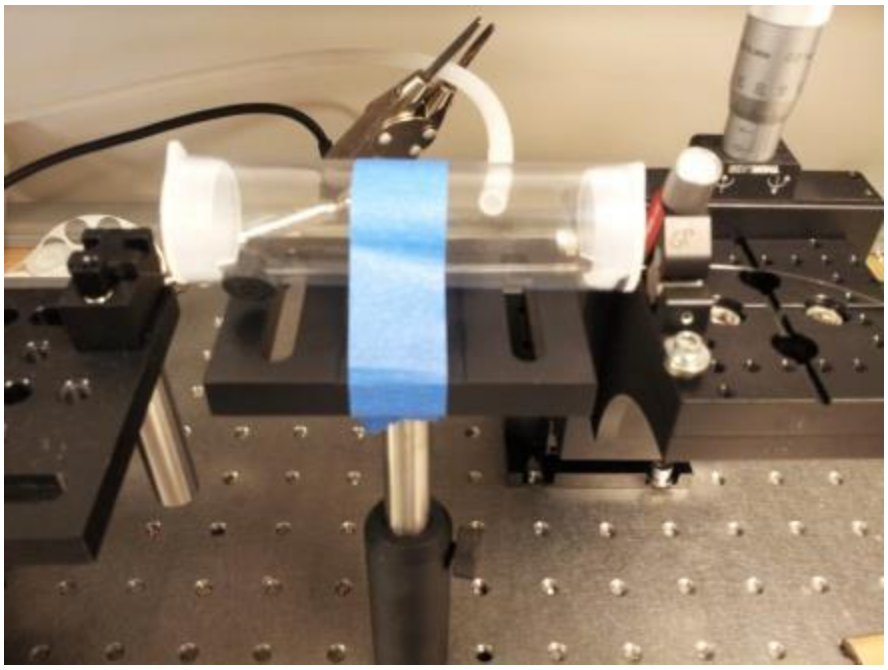

Figure 5-94: Gas sensor with gas cell

After employing the gas cell in our system, the absorption peaks were successfully observed by the CTS. It started showing some absorption peaks immediately after applying acetylene gas into the gas cell. Figure 5-95 shows the output spectrum of the gas sensor around 10 seconds after applying acetylene gas into gas cell. We could clearly observe the increase of the absorption peaks as an increase in the amount of acetylene gas. For reference, Figure 5-96 shows the absorption spectrum for acetylene gas from HITRAN database for corresponding wavelengths.

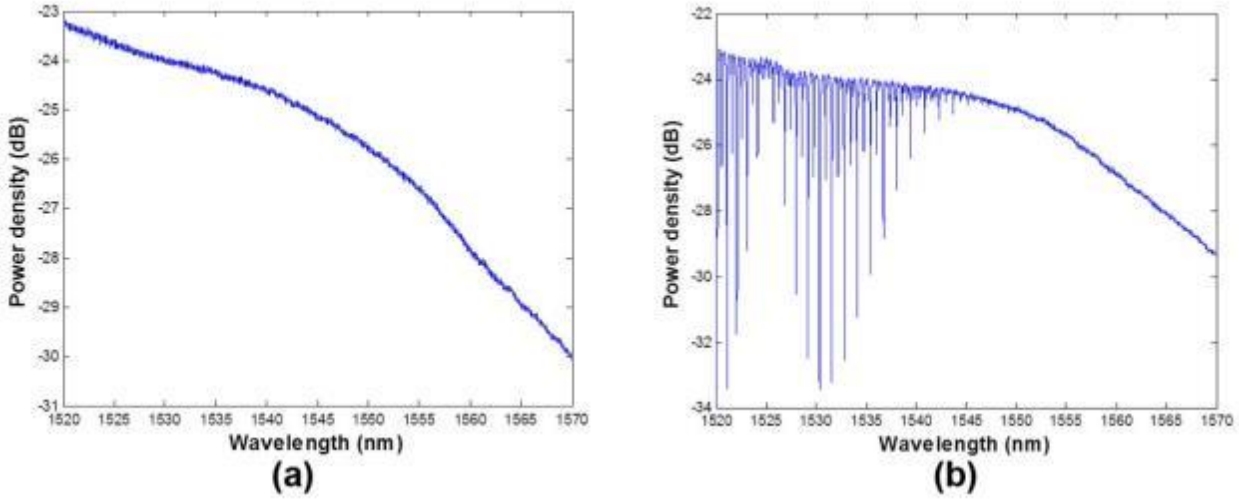

Figure 5-95: Output spectrum without acetylene gas (a) and with acetylene gas (b)

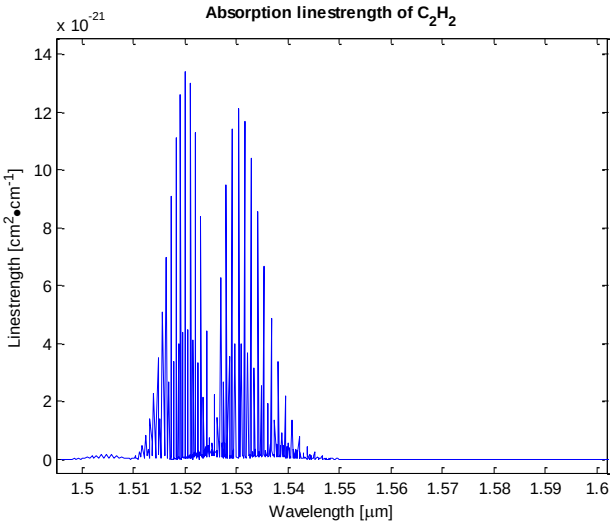

Figure 5-96: Absorption spectrum of C2H2 from HITRAN database

5.4.2 Data Acquisition Software for Long Wavelength System

Data acquisition software for the long wavelength system was written in LabVIEW to collect transmission spectra from the sapphire bundle. Measurements were performed by sweeping the Monolux-42 laser source over wavelengths from 4.0 to 4.42 microns and recording the transmission spectrum. The software was designed to synchronize the wavelength sweep, amplitude determination, and spectrum recording. Figure 5-97 shows the "Wavelength Sweep" tab of the data acquisition software. The panel depicts spectrum measurements with point by point amplitude and state machine timing updates. Figure 5-98 shows the "DAQ & Amplitude Settings" tab of the data acquisition software. Inputs on this panel control triggering and peak-to-peak amplitude demodulation from the AC-coupled photodetector.

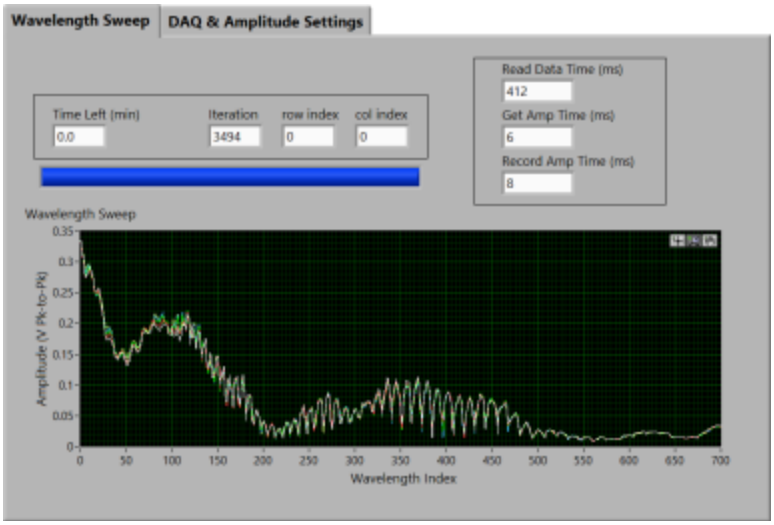

Figure 5-97 "Wavelength Sweep" tab of data acquisition software for long wavelength system

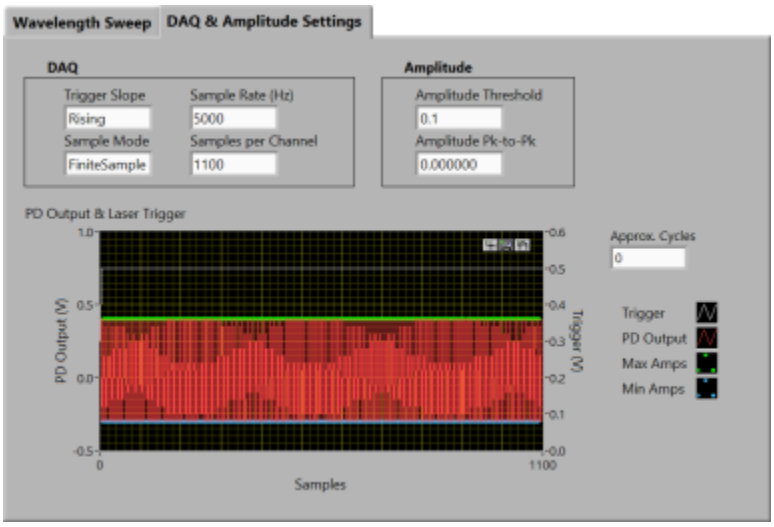

Figure 5-98 "DAQ & Amplitude Settings" tab of data acquisition software for long wavelength system

5.4.3 Signal Processing Software

Signal processing software was written using LabVIEW and MATLAB to estimate gas concentration. The software's physical basis is Beer-Lambert's law, which predicts direct proportionality between concentration and optical absorbance. The implementation compares absorption measurements of an unknown concentration level and a known reference concentration level. Signal processing sifts through raw transmission spectra and occurs in three main stages: background cancellation, absorption dip identification, and concentration estimation. The three stages are reflected in the three visible tabs of the software front panel. Examples screenshots capture execution of each stage for the porous glass gas sensor in 5.4.4 and the sapphire bundle gas sensor in 5.4.5. During background fitting and cancellation, fluctuations in average value are compensated. The "Fit Background" tab shows raw spectra in white and fitted backgrounds in red (Figure 5-99, Figure 5-102). The top plot is the presumed reference concentration spectrum and the bottom plot is the unknown comparison concentration spectrum. The "Find Dips" tab shows use of local threshold values to identify common absorption dips of significance in the reference and comparison spectra.

5.4.4 Porous Glass Gas Sensor

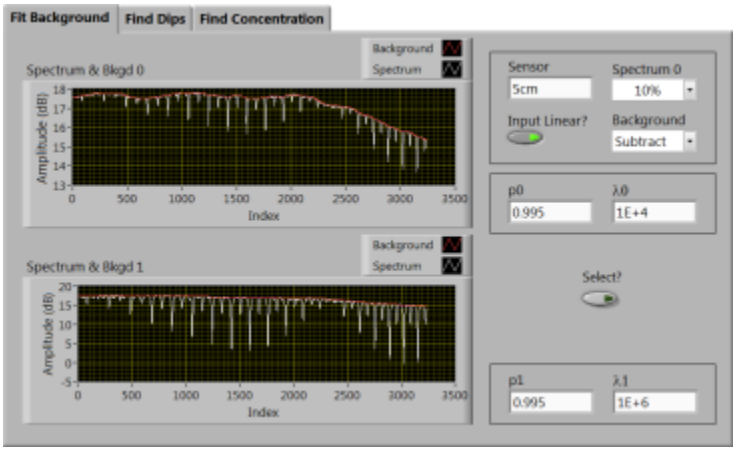

Figure 5-99 "Fit Background" tab of concentration estimator for porous glass sensor

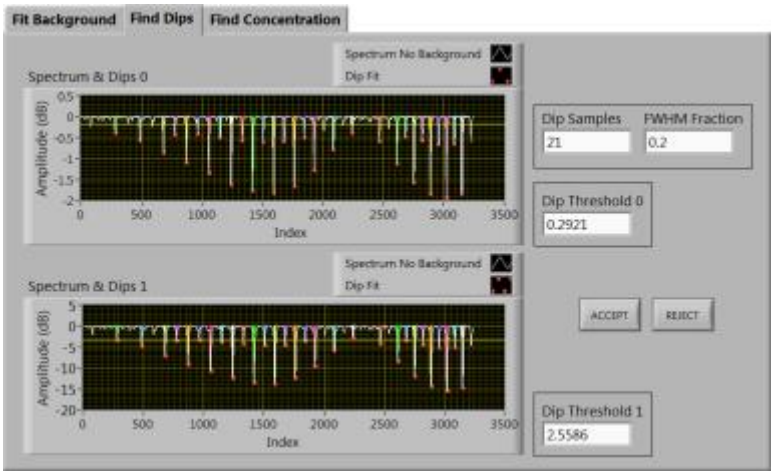

Figure 5-100 "Find Dips" tab of concentration estimator for porous glass gas sensor

After identifying common absorption dips in reference and comparison spectrum, the concentration can be estimated. The "Find Concentration" tab demonstrates the process. Corresponding dips from the reference and comparison are windowed by a width-controlled unity-height Gaussian profile and plotted parametrically. A linear fit of the parametric plot yields a slope for each dip that is logged (Figure 5-101, Figure 5-104, top right). The average slope from all dips parameterizes the concentration ratio of the unknown over the reference. The final concentration estimate of the unknown is found by multiplying the slope by the reference concentration.

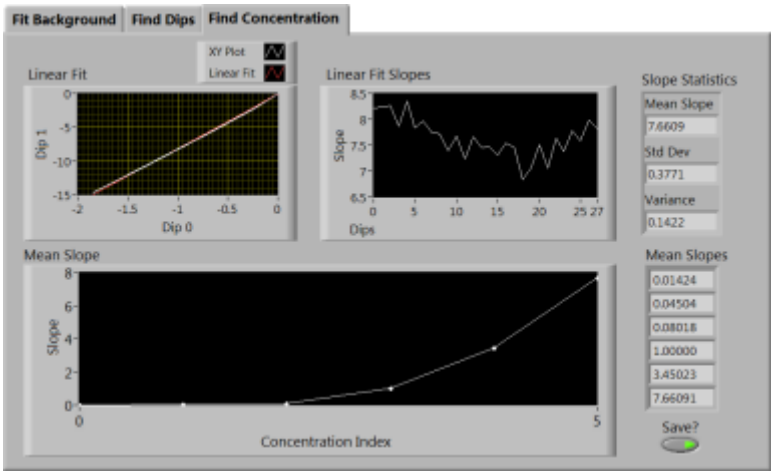

Figure 5-101 "Find Concentration" tab of concentration estimator for porous glass gas sensor

5.4.5 Sapphire Bundle Gas Sensor

The three stages of concentration estimation for the sapphire bundle gas sensor are identical to the discussion for the porous glass gas sensor. However, the high sensitivity carbon dioxide in the mid infrared calls for a procedural change compared to what was done for acetylene at 1550nm. The change is made for background fitting and cancellation, whereby the

background for lowest concentration measurement is chosen for all spectra instead of a unique background for each spectrum. This constant background is shown in red in Figure 5-102 for both the reference and unknown. Having an invariant background common to all measurements attempts to offset shifts due to either temperature ramping or saturation effects.

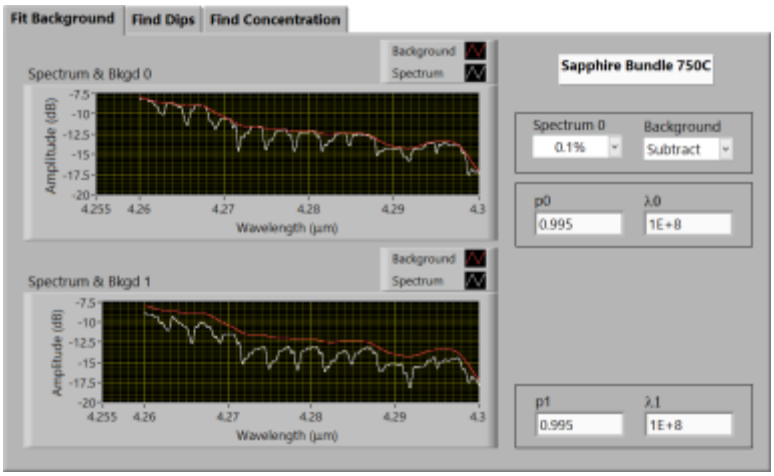

Figure 5-102 "Find Background" tab of concentration estimator for sapphire bundle gas sensor

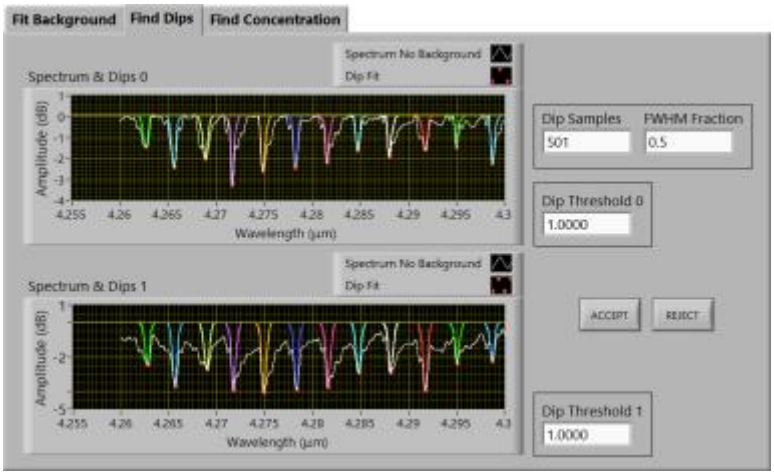

Figure 5-103 "Find Dips" tab of concentration estimator for sapphire bundle gas sensor

Figure 5-103 depicts the dip finding for the sapphire bundle gas sensor and how dips are measured with respect to the common background. For concentration estimation using the sapphire bundle, Figure 5-104 indicates the parametric slope algorithm. An alternative concentration ratio to the parametric slope is also available as the ratio of dip areas from the unknown over the reference.

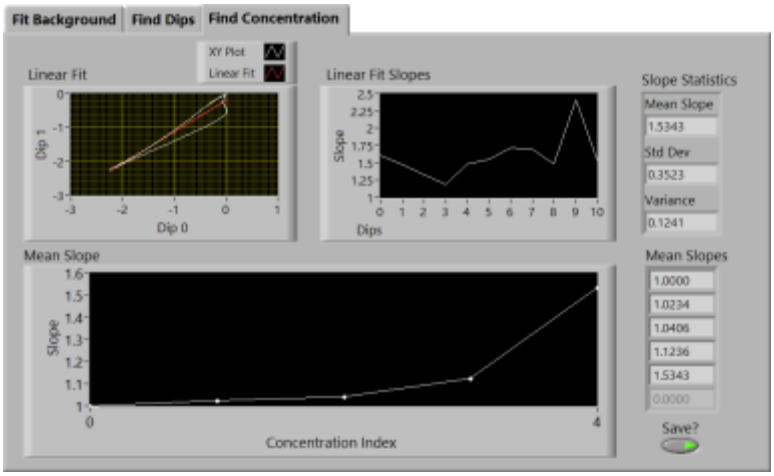

Figure 5-104 "Find Concentration" tab of concentration estimator for sapphire bundle gas sensor

5.5 Investigation of Pore Size and Fiber Geometry on the Observed Optical Properties

5.5.1 Pore Characteristic Tests

The need for the optimum sensor requires that a variety of pore sizes be tested. This has led to the need to modify the pore structure of the glass. Previous work has shown that pore sizes smaller than the currently used process will not sense gas, so the focus will be on using methods to increase the pore size. To increase the pore size annealing trials will be used to consolidate pores and provide a new pore structure. The selected annealing trials that have been selected and produced are listed below in Table 5-29.

Table 5-29: Annealing Trials Tested

	Temperature (°C)	Time (min)
Trial 1	600	25
Trial 2	700	25
Trial 3	800	25

Based on previous research these conditions should provide consistent pore modification and an increase in size without full consolidation. These conditions will be tested in the gas cell and evaluated based on gas detection, detection time, sensitivity, effects on bonding, mechanical strength, and transmission loss. Additional temperatures will be tested as needed if any of these conditions fail to detect gas.

Alteration of pore structure has been studied using annealing to manipulate the size, volume and surface area of the pores. Three initial conditions were selected and then an additional two were added. These conditions were analyzed using SEM to observe any changes. Rough estimations of the percent porosity was made using ImageJ to calculate the number pixels in each pore. These conditions were then tested for transmission loss, gas absorption, gas detection time, and mechanical strength. The results from these tests were presented earlier in Section 1.2.4-6. All samples for the annealing trials were prepared using the normal glass processing conditions. After these tubes were prepared they were annealed in a Thermolyne 1500

box furnace. All annealing conditions were done for a constant time of 25 minutes. Test conditions are detailed in Table 5-30.

Table 5-30: Annealing Conditions tested to change pore size.

Trial	Temperature (°C)	Time (min)
1	No anneal	0
2	600	25
3	650	25
4	700	25
5	750	25
6	800	25

SEM was performed on multiple samples for each condition. The SEM images showed a discernible difference between the conditions as expected based on previous research. A characteristic image for each condition is shown below in Figure 5-105.

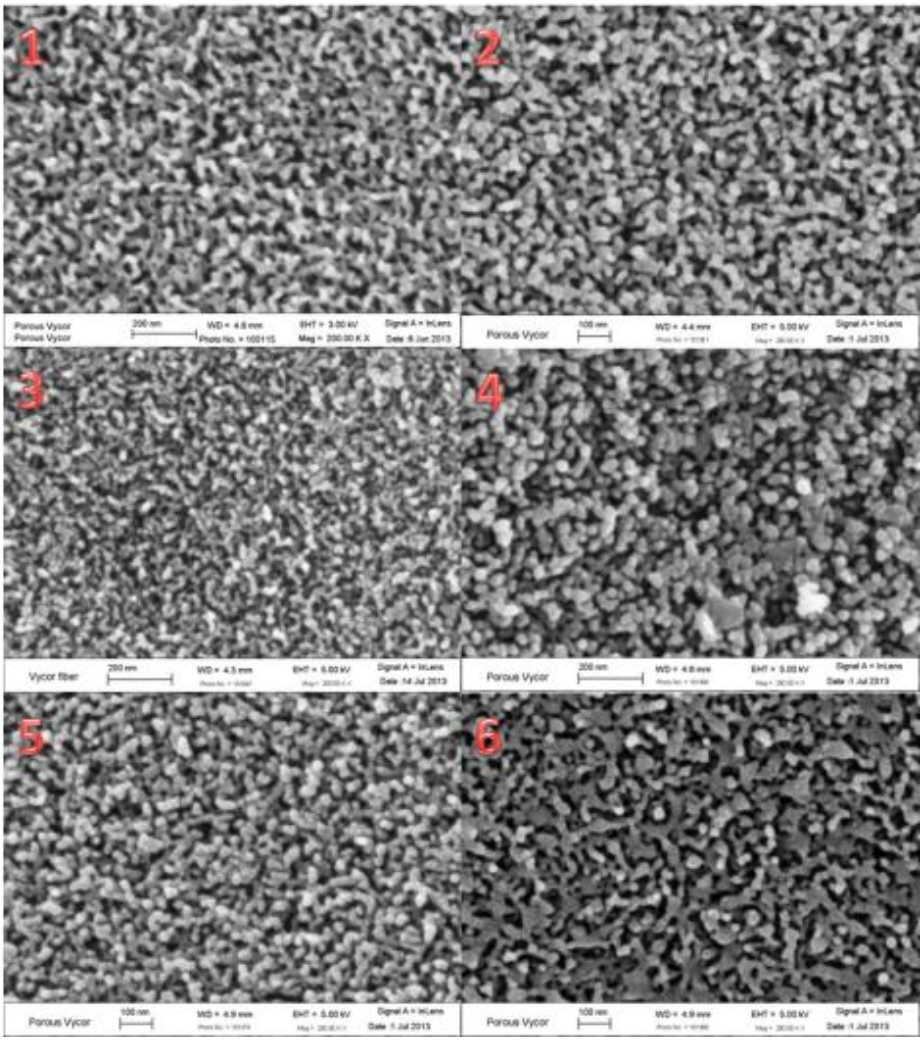

Figure 5-105: Characteristic SEM image of each condition, numbers correspond to the conditions listed in Table 5.

Pore sizes and shapes are noticeably different in each of the annealing conditions. Images were taken from 8 samples in each condition for analysis using ImageJ. The threshold value was set individually on each image before calculating porosity due to differing levels of contrast image to image. Thresholding of the image allows for the separation of regions with significant differences in contrast, such as displayed in the SEM images where the silica skeleton and the pores are very different. The built in pore calculation in ImageJ was then used to calculate the average size of the pores and the pore area percentage. These values were then averaged across the samples in each condition and plotted below in Figure 5-106.

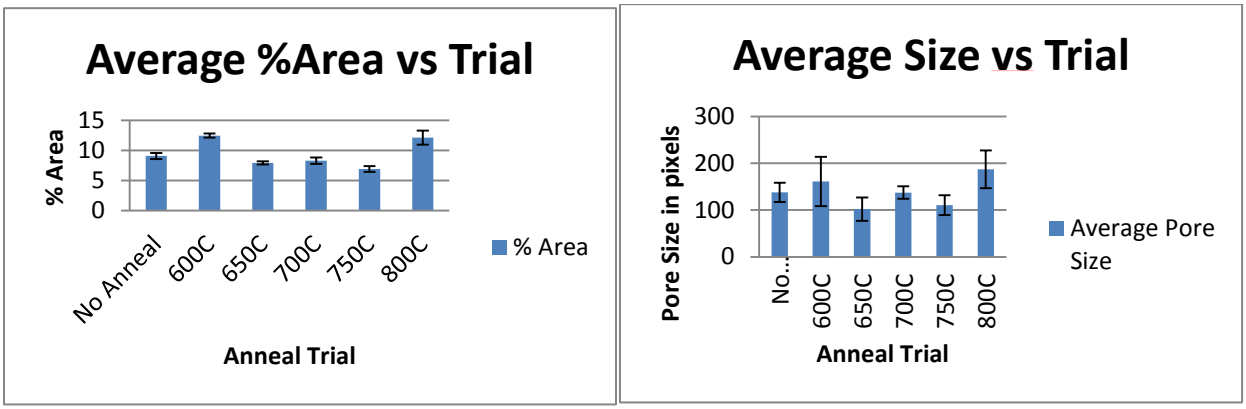

Figure 5-106: Plot of Average %Area and Average Pore size with error bars at 1 standard deviation.

The percent area for all samples had very tight standard deviation. The 600°C samples showed an increase in area percentage which would be expected representing the smaller pores consolidating into larger pores. At the higher annealing temperatures this would correspond to the pores then condensing and becoming smaller. The increase in the percent area at the 800°C condition is not expected but these samples also had a much larger variation in pore size and also exhibited a variation in curvature of fibers. The increased curvature in the 800°C samples made it very difficult to get samples that have an adequate length. All SEM samples were taken from the ends of the tubes used in the optical and gas sensing tests. The decrease in porosity agrees well with the observed decrease in transmission loss as well as the decrease in gas detection time, with the exception of the 800°C samples. The analysis of the samples in the 800°C is confused by the significant change in the pore shape. A more complete characterization using porosimetry would like yield a reduction in the pore size and percent area at 800°C as has been shown in bulk glass samples previously investigated in this project. Porosimetry was not utilized due to the inability to produce a sufficient sample weight necessary for analysis. In addition, it is likely that the pore connectivity is disrupted as the pores consolidate to form the structure seen in the 800°C samples, thereby restricting the flow of gas into sensor.

5.5.2 Transmission Test of Porous Gas Sensors with Different Annealing Conditions

Figure 5-107 shows the set-up used to investigate the optical properties of porous gas sensors that underwent different thermal annealing conditions. In order to analyze the optical properties of each sample, identical conditions should be applied to each of them. As shown in Figure 5-107, three-axis translation stages were used to duplicate conditions for each sample. The annealing process should produce differences in the pore structure resulting in a change in

the optical characteristics and these differences were optically analyzed. The annealing conditions are 600ºC for 25 min., 700ºC for 25 min. and 800ºC for 25 min and non-annealed samples used a control.

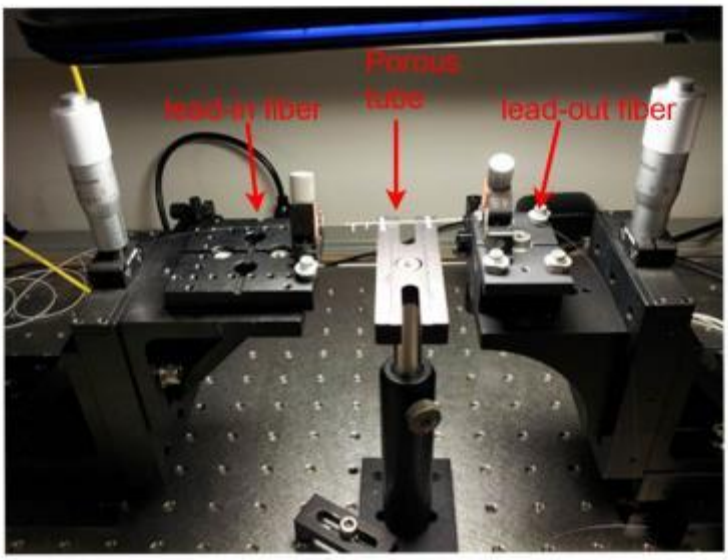

Figure 5-107. Set up to measure transmission loss in each annealing condition

Transmission losses of the porous gas sensors was measured across samples with different cavity lengths between the lead-in and lead-out fibers for each sample set of thermal annealing conditions. Cavity lengths from 1 to 10cm were measured in each sample. Table 5-31 show the average of the transmission loss for each annealing condition with different cavity lengths. In order to obtain consistent data, 8 samples in each annealing condition were measured. Transmission in porous gas sensors was improved as the temperature of the annealing condition increased.

Table 5-31: Average transmission losses with different cavity lengths

	Annealing condition(ºC)					
Cavity(cm)	**25**	**600**	**650**	**700**	**750**	**800**
1	23.80	22.93	22.59	22.65	21.47	21.47
2	25.17	24.28	23.81	23.20	22.69	22.69
3	25.99	25.38	24.89	24.50	23.75	23.75
4	27.84	26.71	26.20	25.13	24.70	24.70
5	28.39	27.87	27.40	27.20	25.59	25.59
6	29.57	29.01	28.19	28.18	26.85	26.85
7	30.13	29.57	28.92	28.96	27.96	27.96
8	30.93	30.47	29.63	30.00	28.73	28.73
9	32.41	31.99	31.51	30.88	29.63	29.63
10	33.63	33.11	32.28	31.72	31.00	31.00

Cavity in cm Transmission loss in dB

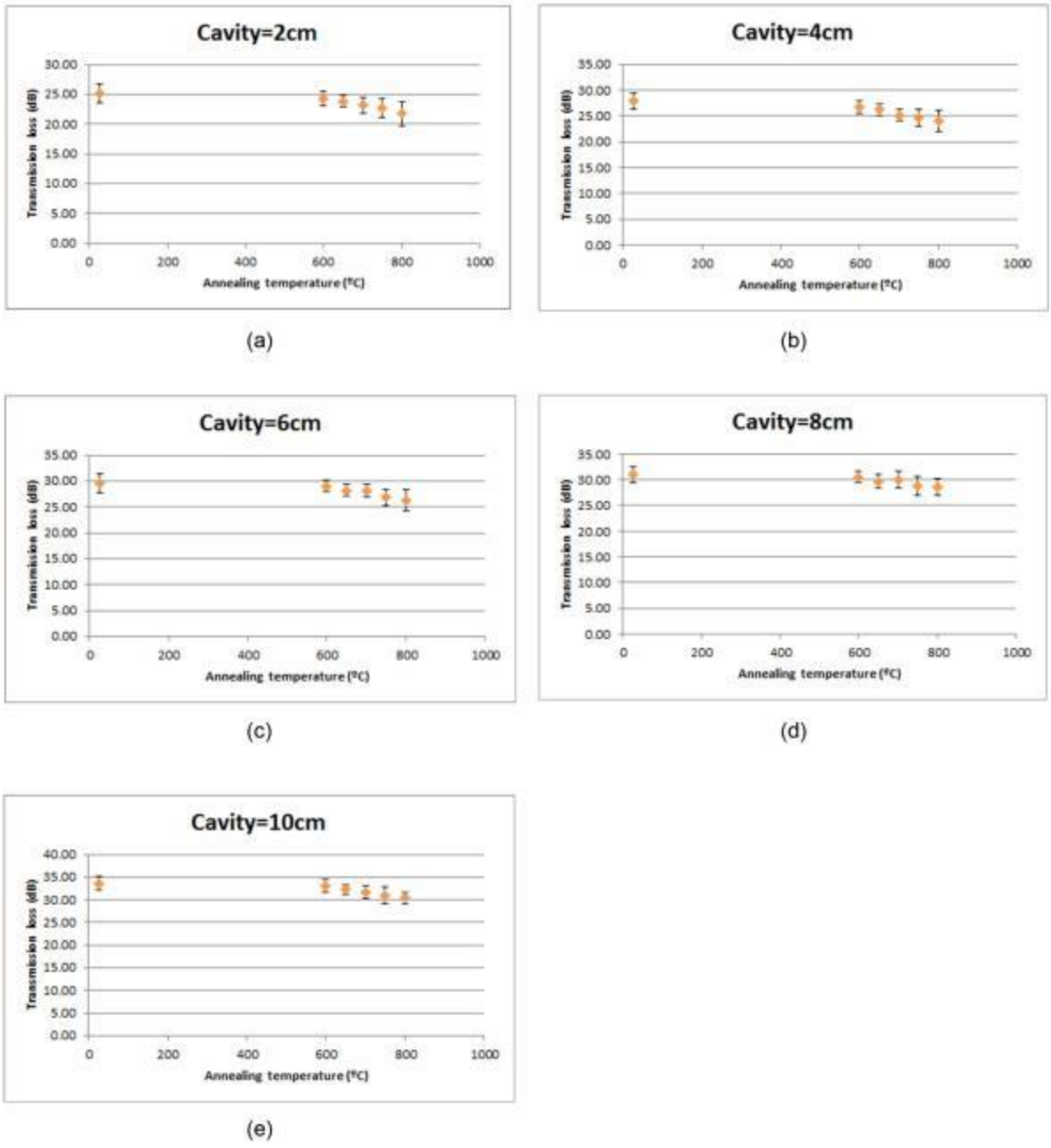

Figure 5-108. Transmission losses vs. temperatures of annealing conditions with cavity of (a)2cm, (b)4cm, (c)6cm, (d)8cm, and (e)10cm

Transmission losses vs. annealing temperatures are plotted in Figure 5-108 for each of the annealing condition groups along with the standard deviation for different cavity lengths. The graph shows a general improvement in the transmission of the gas sensor with some degree of deviation as the annealing temperature increases. Annealing at the elevated temperatures should

alter the pore structure of the porous tube component of the sensor resulting in the observed transmission improvement. It should be noted that the there is significant difficulty in producing identical conditions during testing within and across groups. Alignment of the lead-in and lead-out fibers, the exact cavity length, and variation in the inner diameters of the porous tubes contribute to the variation in the optical properties while equipment setup and environment potentially contribute to the measurement variation. In general, at this stage of the evaluation of the optical properties of the porous gas sensor, the optical properties shows a relationship trend where the property changes with changes in the annealing conditions of the fiber.

5.5.3 Gas Absorption and Gas Detection Tests

Figure 5-109 shows the results of the gas sensing test of the sensors that were subjected to different annealing conditions. As the temperature of the annealing process increased, the overall intensities of the gas absorption decreased while the overall transmission improved. Sensitivities of gas absorption as defined by the peak depth decreased as the annealing temperature increased. This leads to an increase in the detection time of the gas absorption peak that will be shown in next section.

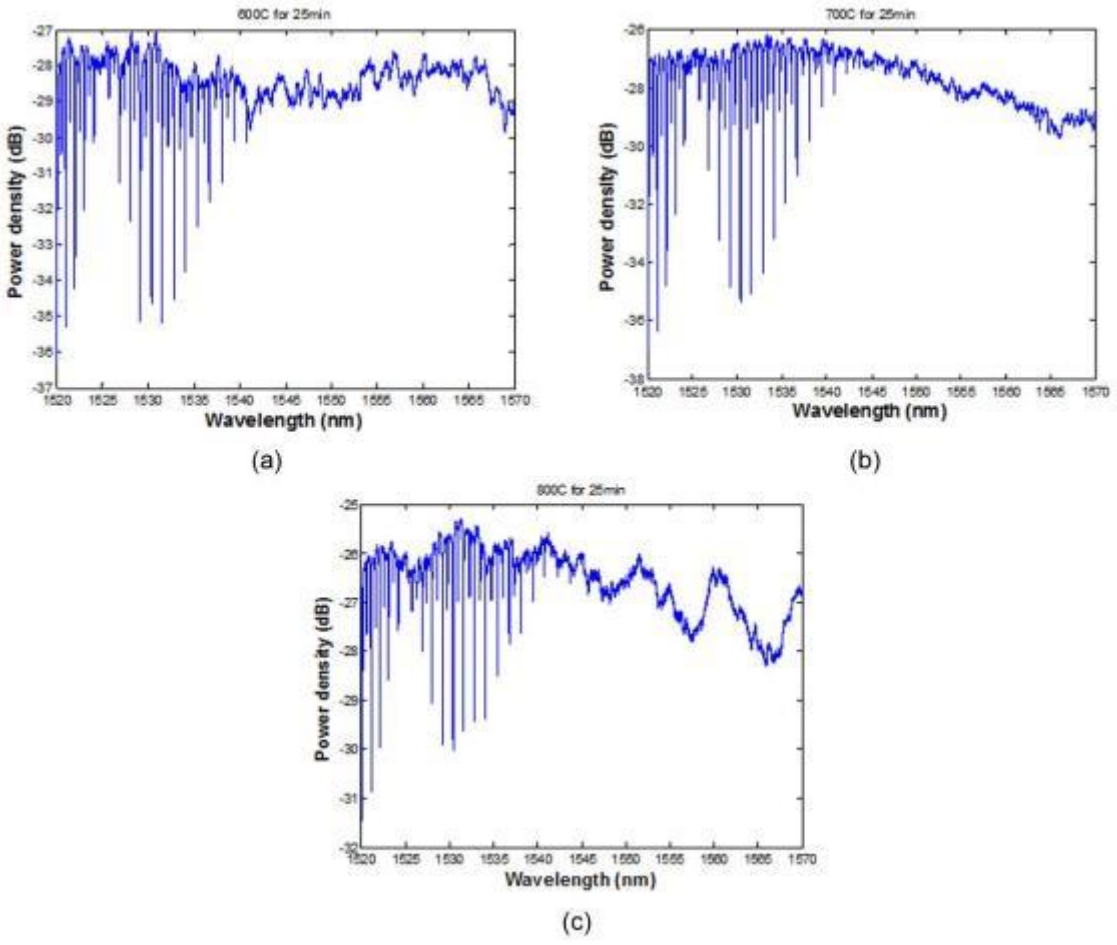

Figure 5-109. Gas absorption spectra of sensor with anneal temperatures of: (a) 600ºC, (b) 700ºC and (c) 800ºC

Gas detection time was also measured in our experiment. In order to measure the detection time, one of the absorption peaks at 1521nm was selected and time it took the peak to reach 2dB of this particular wavelength was measured for each annealing condition. Figure 5-110 shows an example of gas absorption with an annealing condition of 600ºC for 25 min. As indicated in Figure 5-110, time for the absorption peak at 1521nm to drop by 2dB was measure for each sample.

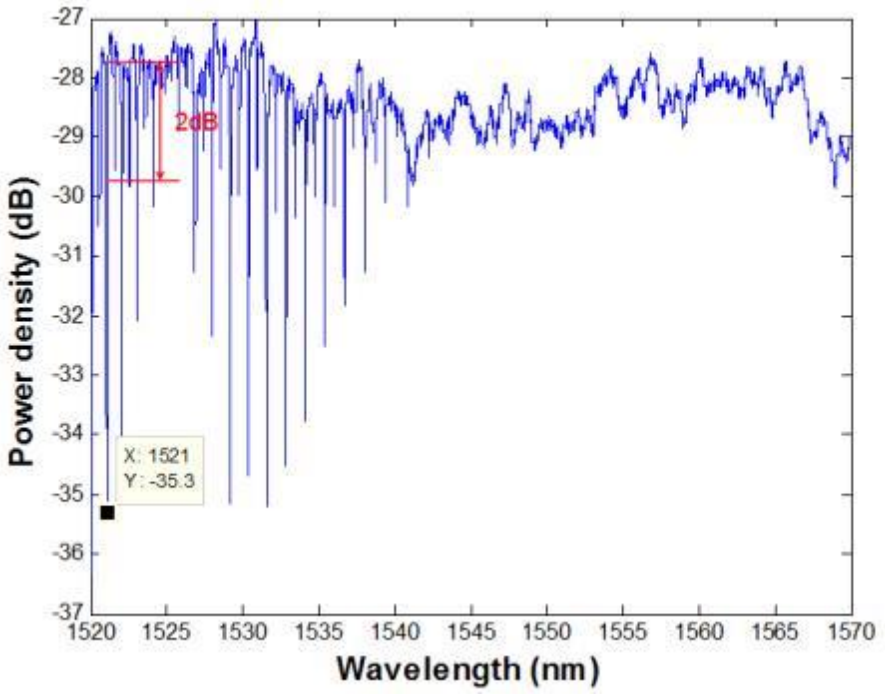

Figure 5-110. Example of gas absorption detection time spectra for sensor annealed at 600 ºC for 25min.

Figure 5-111 shows the graphical relationships of detection time and annealing temperature for sensors with a 5cm cavity length. The graphs show an increase in the detection time as the annealing temperature increases. Table 5-32 shows the average times of gas absorption to reach 2dB point at 1521nm. 8 samples at each annealing condition were measured in this experiment. Gas detection times gradually increases as the temperature of annealing increases. It is a reasonable result when we consider the result of the transmission test. Due to the alteration of the pore structure at the higher temperature of the annealing process, the transmission in gas sensor is improved while the gas detection time of the sensor is increased. The average increment of gas detection time is 0.41sec. per 50^{O}C.

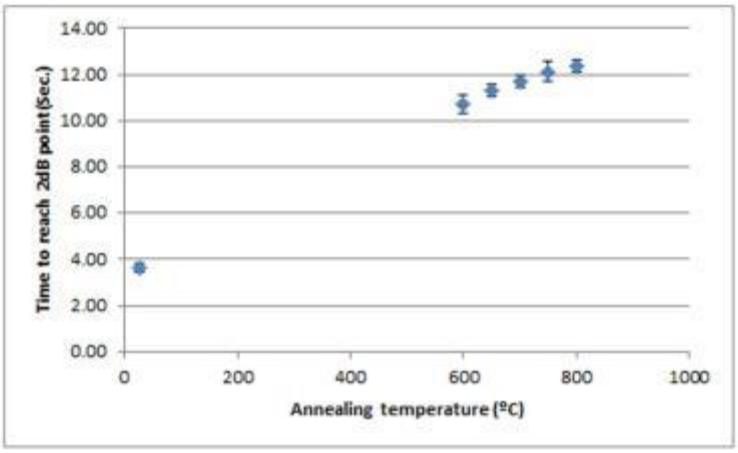

Figure 5-111. Detection time vs. temperatures of annealing conditions with 5cm of cavity length

Table 5-32: Average time of gas absorption to reach 2dB point at 1521nm

	Annealing condition(ºC)					
	25	**600**	**650**	**700**	**750**	**800**
avg time(sec.)	3.64	10.72	11.30	11.73	12.12	12.38
Std(sec.)	0.22	0.41	0.26	0.26	0.42	0.27

5.5.4 Mechanical strength of Porous Tube with Different Annealing Conditions

In order to investigate mechanical strength of the porous tube, we constructed a simple set-up as shown in Figure 5-112 where the sensor assembly was tested. One side of the sensor was fixed and the other side of the sensor was attached with weight. The weight was gradually increased until breakage of the sensor structure occurred. The average porous tube has I.D. of 145μm and O.D. of 350μm and distance between two fibers is 5cm.

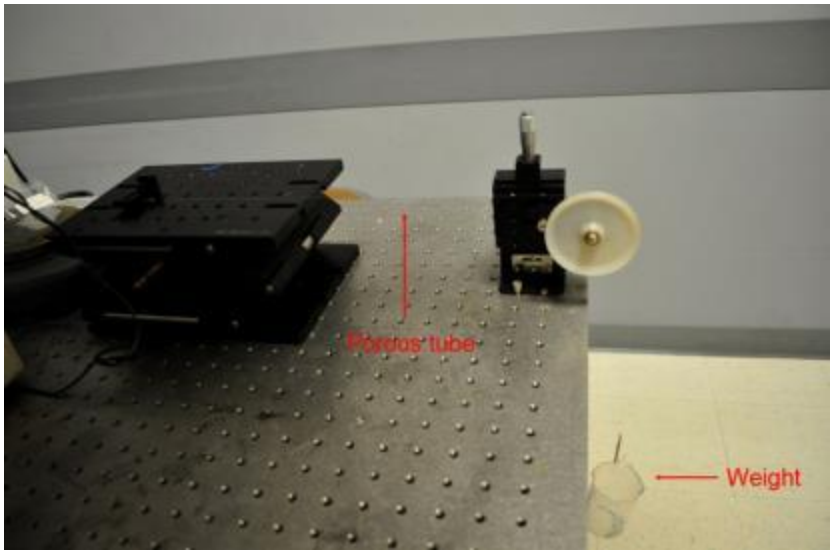

Figure 5-112. Set-up to test mechanical strength of porous tube

Figure 5-113 shows the mechanical strength as the relationship between the weight (gram) applied and the annealing temperatures of sensor assemblies with a 5cm cavity length. The graph shows decrement of the mechanical strength with some degree of deviation as the temperature of the annealing condition increase. Table 5-33 shows the average mechanical strength of the porous tube with different annealing conditions. 8 samples at each annealing condition were measured in this experiment and average standard deviation of the mechanical strength is 1.09g. Mechanical strength gradually decreases as temperature of annealing process increases. The average decrement of mechanical strength is 2.33g per 50^{o}C.

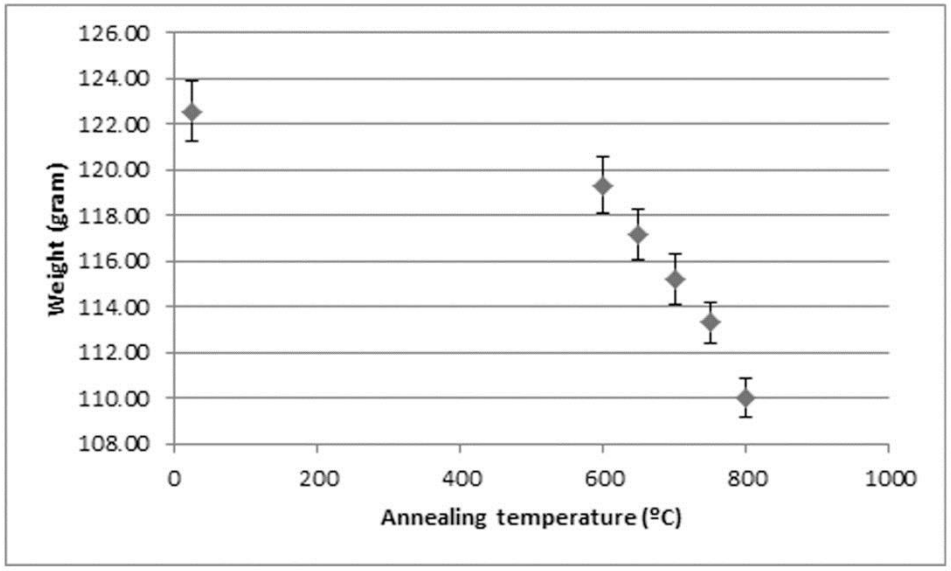

Figure 5-113. Mechanical strength vs. temperatures of annealing conditions with 5cm of cavity length

Table 5-33: Average mechanical strength of porous tube with different annealing conditions

	Annealing condition(ºC)					
	25	**600**	**650**	**700**	**750**	**800**
Avg(g)	122.57	119.33	117.17	115.24	113.32	110.01
Std(g)	1.31	1.23	1.12	1.13	0.89	0.85

5.5.5 Different Geometry Evaluation in Porous Glass

Current sensor design utilizes tests a single porous tube to guide the light. Preliminary tests have been done to look at the possibility of making a photonic crystal fiber structure using porous glass. An ideal structure would be precisely arranged in a hexagonal shape. Several techniques have been attempted to form the hexagonal shape and been unsuccessful. These techniques involved stacking the tubes in flat layers to make the hexagonal tube assembly and then attempting to stack the layers inside an outer tube. These attempts have led to the design of a mold that is currently being machined to hold the tubes during assembly and while the tube assembly is being inserted in the outer tube in order to maintain tube orientation. While waiting for a mold, a random bundled tube arrangement was produced as a preliminary preform in order to get a feel for the drawing conditions of a stacked tube array. Pulling conditions for this preform has required much higher heat and draw speeds than drawing of the sensor tubes. This

preform also exhibited significantly different drawing behavior. Figure 5-114 below shows the results of the initial draw with random tube arrangement.

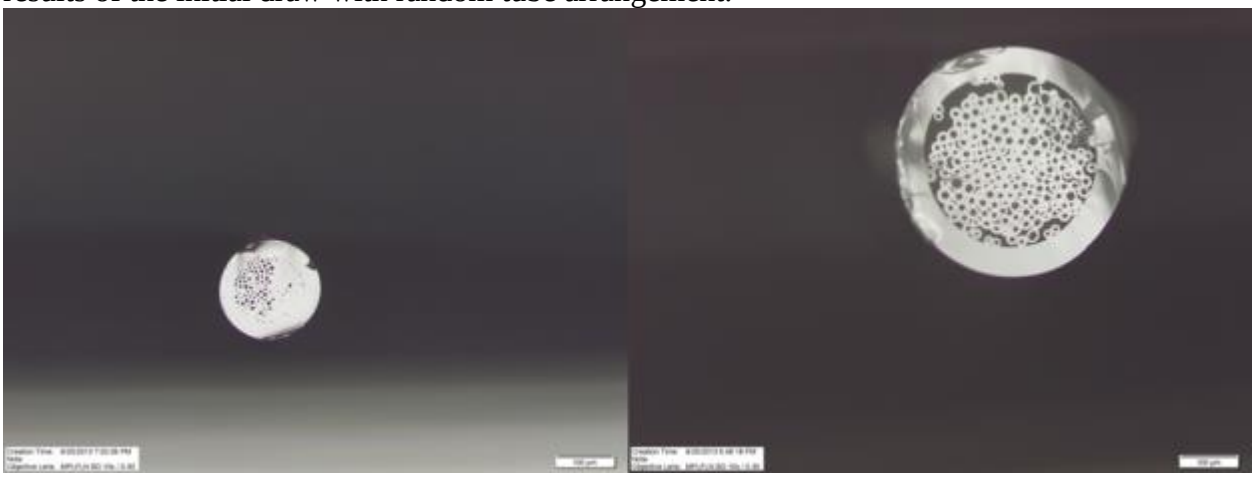

Figure 5-114: Random Arrangement fibers pulled on mini draw tower.

The two different samples were taken from the same preform just at different point in the draw corresponding to different draw speeds and sizes. The sample on the left was drawn at higher speeds and eliminated much of the void space around the edge seen on the sample on the right. It also had about half the tubes collapsed solid. This uneven collapse is caused by variation in the heat profile in the draw furnace. Rotation is being investigated as a way to compensate for the heat variations. The preliminary trial was unsuccessful in producing the bundled tube arrangement of the preform. However, this random arrangement allows for investigation and characterization of the draw process using an easily produced preform that can be used to illicit the parameters ranges where a successful fiber draw may reside. This allows for development of the process before using the much more difficult made preform from the mold.

5.5.5.1 Ordered Stacked Tube Preforms

In the previous quarter, random arrays of stacked tubes were loaded into a preform and drawn as the first step in moving towards a porous PCF based fiber. The random arrangement does not provide any useful optical purposes but serves to develop an understanding of the draw process and to help develop the drawing conditions for an ordered array. Previously the outer tube of the preform was planned to be an ID:7mm with an OD:10mm Glass tube to help limit the number of stacked tubes. Use of the smaller Glass tubes rather than the normal ID:10mm/ OD:12mm tubes used for preforms have run into several problems. The smaller tubes suffer from thermal shock that is not experienced in the larger tubes. Annealing these tubes prior to drawing has allowed for this problem to be minimized, however it has also been found to have a different draw behavior at the same temperature as tubes from the larger preforms. This has made drawing very difficult to the point of making it impossible to use for the stacked tube preforms. The larger outer tubes requires significantly more tubes for each stack and becomes harder to handle making production slower. To produce the ordered array of tubes a mold was needed to hold the arrangement. 3D printing was investigated as a method for producing a mold of the necessary dimensions but none of the available printers at Virginia Tech could provide the needed resolution for the mold without becoming prohibitively expensive. Therefore, a mold was milled out of a polypropylene block using a tapered end mill with a 30° taper. This allows for the

necessary shape to be made. Figure 5-115 shows the mold as well as the tubes stacked in arrangement.

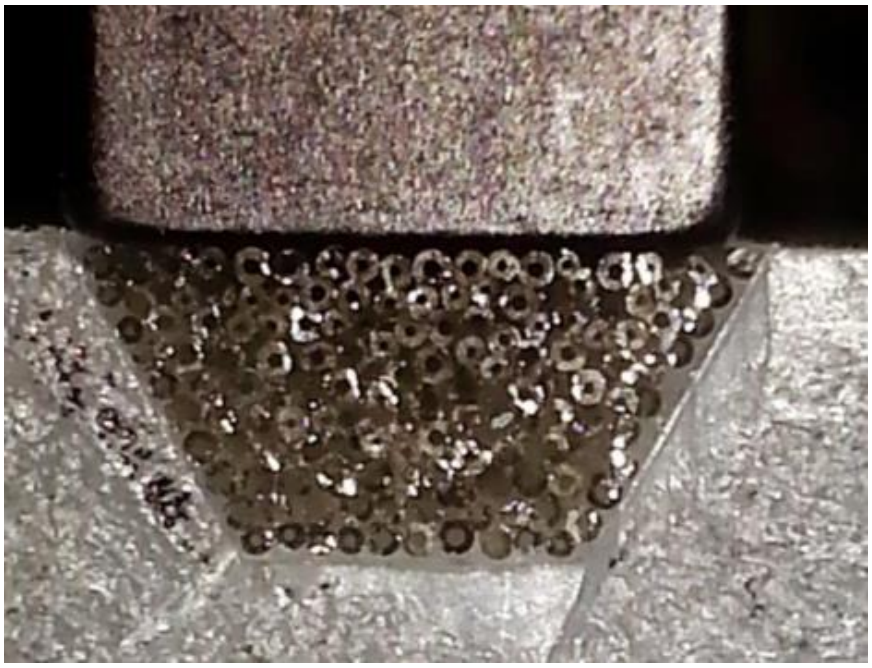

Figure 5-115: Milled Mold with Stacked tubes for Preform

The mold allows for easy stacking up to the halfway point though problems have occurred in holding the arrangement of the tubes stacked up above the halfway point. The length of the preform that is able to be produced has been severely limited to a length of only approximately 4" due to curvature in the drawn tubes. Currently the two halves of the stack have been produced and the inserted next to each other in the outer tube. Fibers so far have been of poor quality due to separation of these halves as well as trapped gas that deforms the fiber during drawing. Each of the halves had been fused at both ends to hold the arrangement but this caused blow out of the expanding air in the tubes during drawing and made very poor fibers. Figure 5-116 below show a fiber produced that has the halves separated.

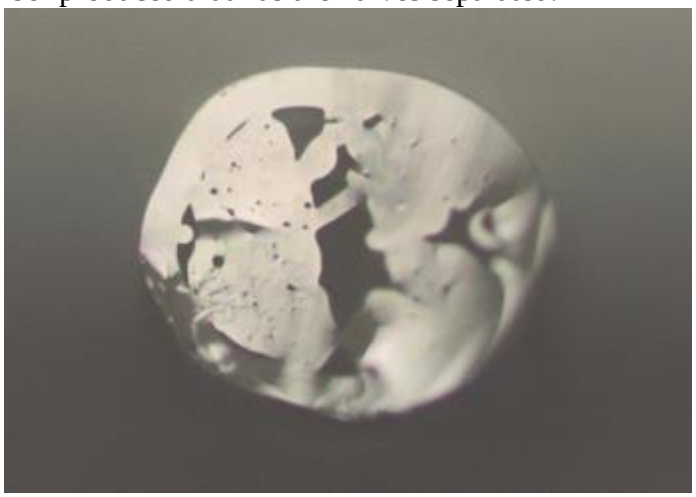

Figure 5-116: Ordered Stacked Tube Fiber Suffering from Collapse and Separation of Halves.

Modifications to the mold have been made to allow the entire stack to be made at one time, thereby eliminating the separation of halves previously encountered. A method of holding the tubes together without trapping air is still being investigated.

Another method for producing an ordered tube preform being investigated is 3D printing of the preform out of the desired glass powder. This method is just being investigated now and a successful design has been made that is within the capabilities of the 3D printing technologies available. Determining the necessary powder size and producing enough powder are the current steps needed before being able to produce a preform using this method. Figure 5-117 shows 2 designs that have been made for 3D printing with holes of 1 and 2mm being possible.

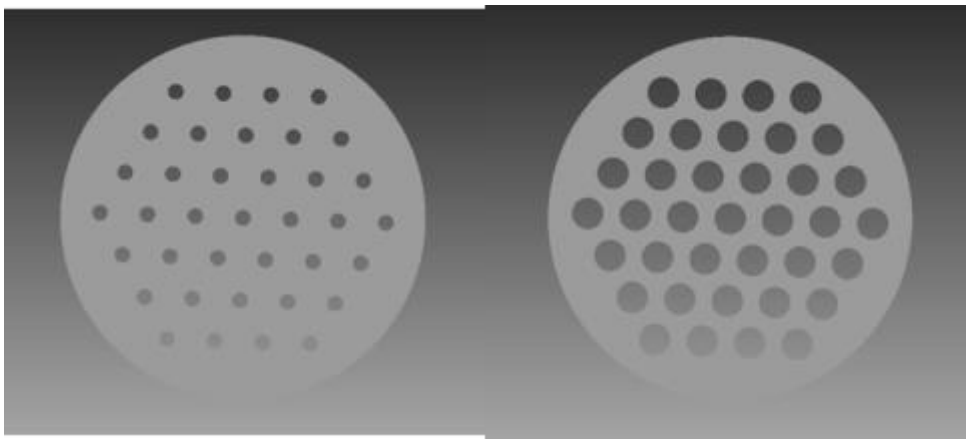

Figure 5-117: PCF CAD Model for 3D Printing of Preform.

5.5.6 Photonic Crystal Fiber Production

Fabrication of a PCF structure using green glass has been ongoing. Several techniques have been attempted and found to be unsuccessful. The use of the mold greatly increased the ability to hold shape but limited ways to hold the tubes after removing from the mold. Adhesives were tested but always wicked down the tubes in the stack and contaminated them and made drawing impossible. Moving to a butane torch to fuse the ends of the tubes has been successful in holding the shape but can only be used at one end of the tubes to prevent sealing the tubes and causing blow out from the trapped air during heating. The mold was initially used to hold the bottom half of the stack and the stack the tubes freely for the second half, this was unsuccessful as the tubes do not allow for enough surface to hold the layer above them. Attempts to assemble two halves and then place them in the preform were also unsuccessful as this cause the fiber to draw into two split halves with the two stacks not fusing together. As a result the mold has been modified to allow for the entire stack to be constrained in the mold prior to fusing the end together using the butane torch. The mold is mobile and allows for tapping in multiple directions to aid in settling the tubes to their needed arrangement. These improvements are being applied to all preforms being produced from here on. The only limitation currently limiting PCF production and testing is the large quantity of similar tubes needed to form a stack. For the available outer tubes size of 10mm and the size of the tubes ~500 microns in diameter the number of tubes needed ranges from 271 for tubes 526 microns in diameter up to 331 for tubes 476 microns in diameter. The length of the stack has been limited to ~4” to allow for tubes to be straight enough to not disrupt stacking order as well as to help limit the lengths of tubes needed.

Approximately 100ft of tube is needed with similar size to make just one stack. Producing and sorting the sizes greatly slows down the production of these preforms.

5.5.6.1 Experimental Results

Fabrication of PCF fibers encountered several setbacks due to furnace issues over the last months. Both the primary furnace and its backup failed. The primary was able to have a new heating element placed in it while the backup catastrophically failed. The new heating element was sealed with alumina adhesive instead of the normally used castable alumina. This change apparently causes a very different heat profile in the furnace. It also resulted in different voltage settings than needed previously in the furnaces. This allowed for successful pulling of tubes but when attempting to draw a PCF draw it failed due to the much higher voltage needed to attempt to achieve the necessary temperature. Two new furnaces have now been manufactured with the original castable alumina ceramic and are now in place for use. This has allowed for a successful draw of a PCF fiber without destruction of the furnace. Figure 5-118 below shows the mold in its current configuration with a stack of tubes present.

Figure 5-118: PCF Stack in two different lighting conditions

Figure 5-118 shows that the mold is capable of holding and forming stacked tubes of the desired shape. The preform shown above is not ideal and contains tubes with too large of a range of outer diameters and wall thicknesses. Ideally the preform will contain only thick or thin walled tube with a range of diameters of 30 microns. This will be necessary for the PCF fiber to function as desired. This preform will be used to better hone drawing conditions and allow for understanding the draw process. Additional preforms are continually being produced as fibers become available. Figure 5-119 below shows the preform after fusing the end and preparing to insert it into the outer tube.

Figure 5-119: Fused Tube Stack

Preforms will continue to be produced to allow for more PCF fiber to be made but are limited by the time necessary to sort and measure the tubes for the stack.

PCF fiber has been produced but at a very slow rate due to the time consuming nature of measuring and binning enough tubes of the correct size to stack for a preform. Most recent preforms were successful in drawing though suffered from regions of collapse and shifting of the tube stack. Figure 5-120 below shows sample fibers from the draw.

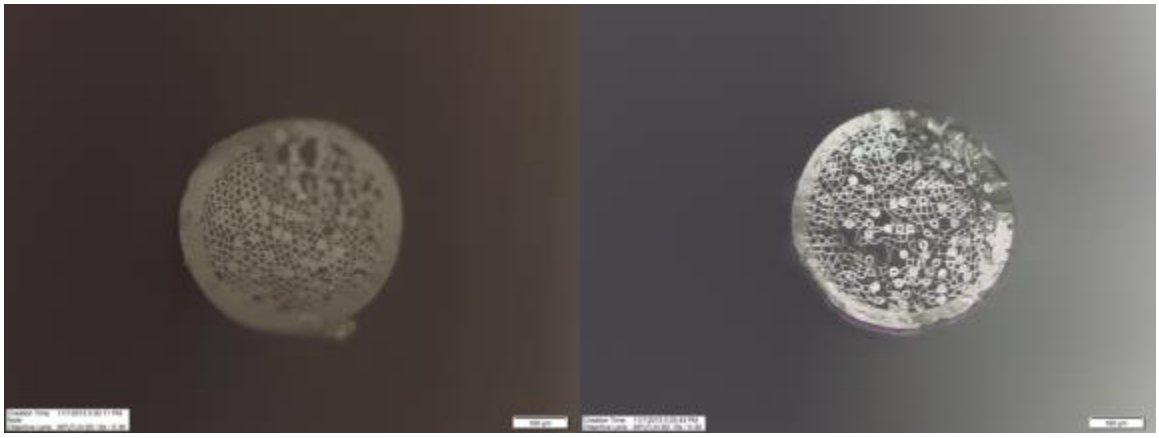

Figure 5-120: PCF Fibers

Thick walled tubes present through the matrix collapsed solid before the thin walled neighbors while the thin walled tube held their shape worse and moved during drawing. The further away from the joint at the end of the preform the worse order was held.

Attempts to produce this structure are done using stacks of previously drawn glass tubes prior to any processing. The arrangement of the tubes is held by stacking the tubes inside a polypropylene mold. Previous attempts have involved using the same tubes as fibers are drawn from as the outer tube for the tube stack. This size of preform has required over 300 tubes of similar size to be stacked into the 10mm mold and then drawn. This number of tubes makes it very difficult to draw the array and hold the arrangement as well as extremely time intensive to form a single preform.

To improve draw characteristics and improve throughput of preforms a smaller mold was produced at the smallest size possible at 6.35mm to reduce the number of tubes needed down to approximately hundred tubes. This also requires that the outer tubes be collapsed to similar size to hold the stack arrangement. This approach has greatly improved the ability to hold the arrangement during drawing. Figure 5-121 below shows 2 PCF fibers that have successfully held their arrangement during drawing.

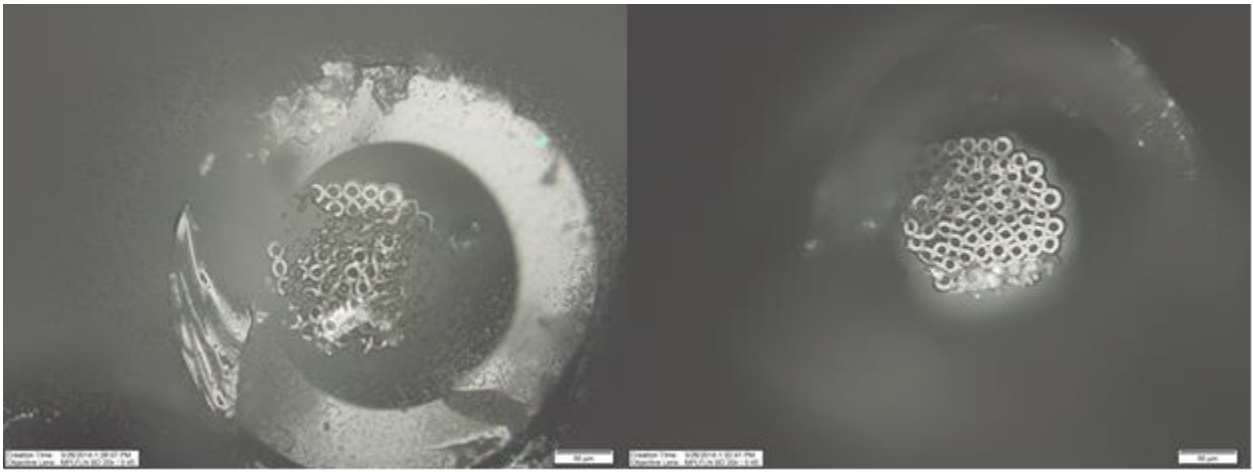

Figure 5-121. Glass PCF Structure using smaller tube Stack.

These tubes held their arrangement but separated from the outer tube and did not draw down as a whole fiber structure. This problem as well has warping of the tube shapes is indicative of uneven heat profile. Problems in the heat profile of the furnace arise due to air flow that occurs during drawing and alignment issues. Efforts to improve the furnace characteristics are being done by the creation of an iris system for the furnaces used on the mini draw tower.

Production of a glass photonic crystal fiber has continued with improvements to the drawing process. Previous results showed that an uneven heat profile existed within in the drawing furnace which resulted in uneven collapse of tubes in the stacked assembly used for PCF fabrication. An iris assembly for the furnace was produced to provide a more even heat profile and to improve the draw characteristics. The iris assembly, which was made from made of 1018 steel, was designed to be manually operated. The completed iris assembly is shown below in Figure 5-122.

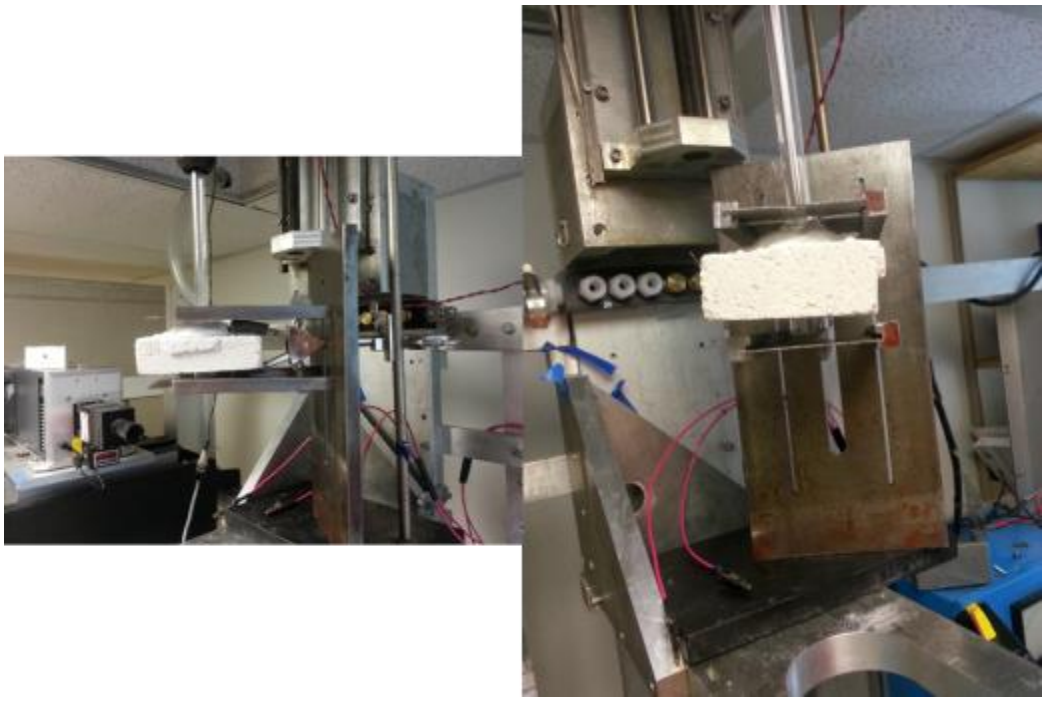

Figure 5-122: Iris Assembly Attached to draw tower Side View (Left) and Front (Right).

The iris assembly closes off the furnace during drawing to reduce air flow induce cooling of the preform. This was an apparent performance improvement as a significant reduction furnace voltage needed from the variac power source for a given temperature. The upper iris is closed during heat up around the desired preform, while the lower iris is close after the bait has been pulled down from the preform. This closes the opening to just barely larger than the fiber size. Drawing is then carried out using normal drawing procedures to reach a desired fiber size.
PCFs produced while using the iris system have shown significant improvements compared to non-iris equipped furnace drawn fibers. Figure 5-123 shows sections from 2 fibers pulled after the installation of the iris system.

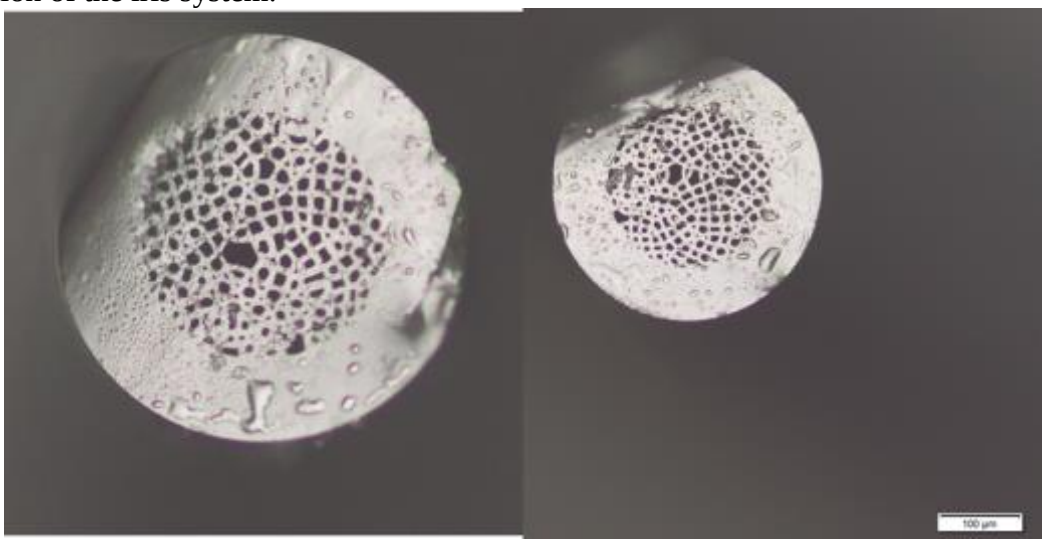

Figure 5-123: PCF Produced on Draw Tower with Iris System

The fibers produced with the use of the iris system were completely free of the problem of uneven collapse of the tube stack. Previously drawn fibers were prone to being solid for half of the stack while large holes present in the other half. These fibers shown Figure 5-123 still shows deformation of the initial tube stack but tube sizes are observed to be significantly more uniform across the entire fiber.

In addition to the iris assembly, reduction of preform size was done to drastically lower the amount of tubes used in the stack in an effort to hold the arrangement during drawing. This change reduced the number of tubes in the stack to approximately 100 from over the 300 previously needed. This change yielded some improvement but still varied along the length of the preform. It has been observed from looking at fibers along the length of the draw that fibers from the beginning of the preform tended to be more collapse and have very poor geometries. Fibers produced later were found to have better arrangement and better collapse characteristics than fibers from the beginning draw process. This behavior tends to indicate that PCF drawing requires time to reach a uniform drawing condition to produce useful fibers. This trend agrees with commercially produced PCF in other glass systems that require over a third of the preform to be drawn before reaching a steady drawing state. This does not pose a problem for commercially produced PCF that are drawn from preforms approximately 3 feet in length where losing a foot of preform is feasible and still allowing for preform for useful fiber to be drawn. Due to the limitation of preform size in our experiments being approximately 5 inches for a tube stack our ability to produce a PCF fiber with the desired structure is problematic. This limitation of preform length is the most likely culprit for not being able to produce a PCF fiber that has the needed geometry.

5.6 Development and Fabrication of Prototype Optical Fiber Sensor Package

5.6.1 Preliminary Packaging Design for Porous Glass Gas Sensor

A basic design was completed for packaging of a test sensor for possible applications at high temperature and environments. The basic design for the packaging was done for two possible designs, depending on lead in and lead out fiber design for the sensor. Figure 5-124 show these tow designs. This design is based on using an outer porous metal tube with ID 1/8” and OD ¼” to provide the main protection for the sensor. Steel tubes will then be used to protect lead in and lead out fibers. The material for the porous metal tube will be titanium or an available Hastelloy composition depending on CTE matching the system and a prospective environment. A ceramic adhesive will be used to seal the ends of the tube and chosen based on matching the CTE of the porous metal tube. Adhesives are available from Aremco that have the needed thermal ranges and CTE match. A ceramic spacer is desired for use to hold the porous glass gas sensor in the center of the metal tube.

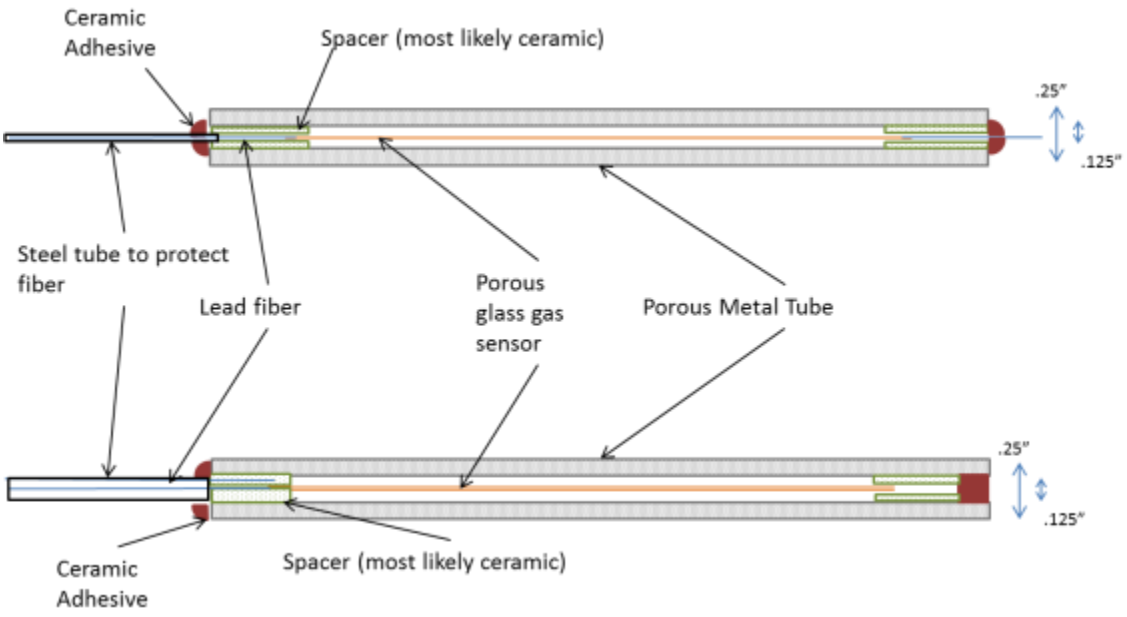

Figure 5-124: Basic Packaging Design

5.6.1.1 Materials Packaging Design

In the previous quarters preliminary design for a field testable package for a porous glass gas sensor was shown. That design has been improved and is shown below in Figure 5-125 for the 2 possible designs.

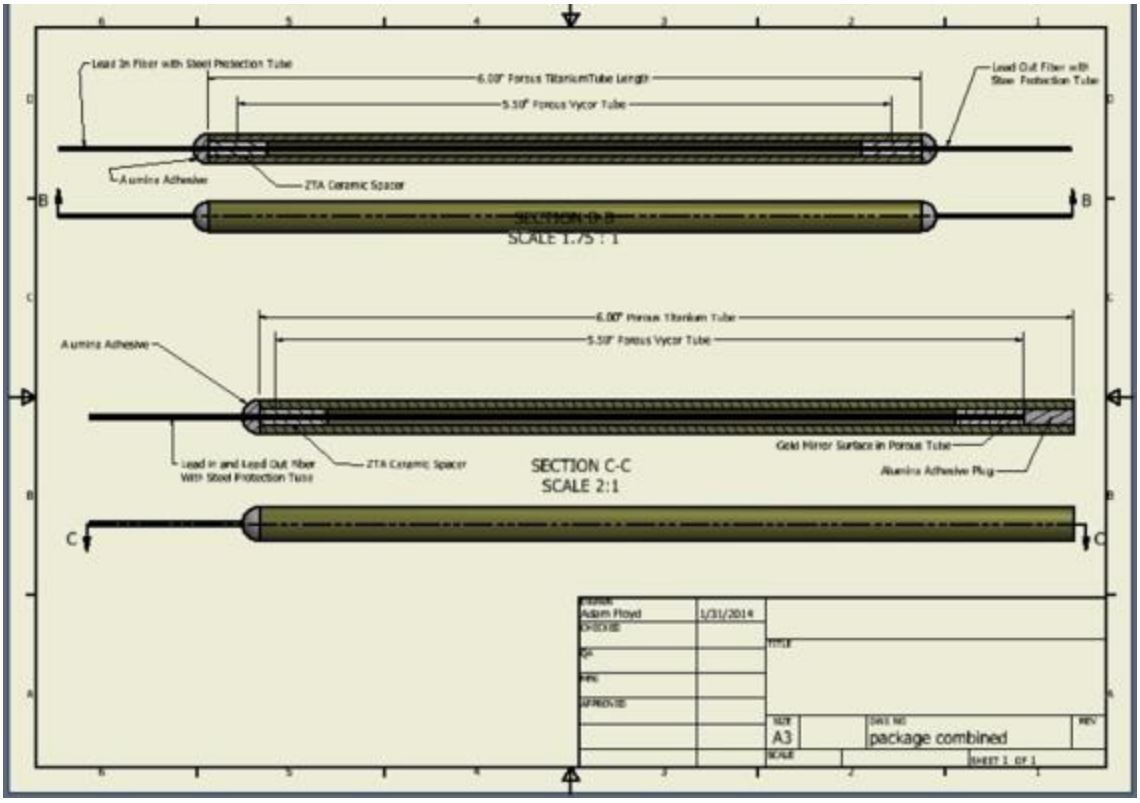

Figure 5-125. Schematic Drawing of 2 Possible Packages for Porous Glass Gas Sensor.

These designs show the two possible designs for the package as well as cutaway views. In addition to the designs this package is being developed and demonstrated for testing. A mock assembly of the package is shown below in Figure 5-126.

Figure 5-126. Package Mockup for Glass Gas Sensor

Fabrication of prototype sensor assembly has been completed based on the design above with some minor changes to provide additional packaging protection. This minor change involved the addition of a steel mono coil tube to provide the protection of the optical lead-in and lead-out fibers. These tubes are threaded on the end and connect directly to the porous metal tube. This addition also allows for the removal of the ceramic adhesive to close the end of the metal tubes. A cutaway of the prototype sensor is shown below in Figure 5-127.

Figure 5-127: Cutaway of Prototype Porous Glass Gas Sensor Package.

Figure 5-128 below is a magnified view of the sensor showing the porous sensor and the glass ferrules.

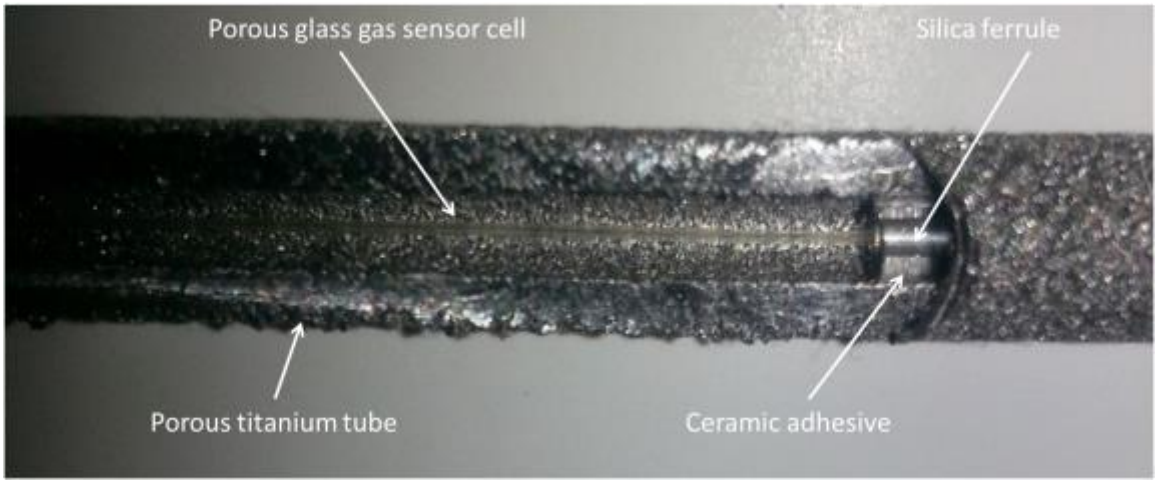

Figure 5-128: Close up of Porous Glass Gas Sensor.

The prototype sensor was fabricated using a porous glass gas sensor with SMF lead in and MMF lead out bonded with the CO_2 laser as previously tested. Fused silica glass ferules hold the porous glass sensor in the center of the metal tube. The metal tube is a porous titanium tube which gives a maximum service temperature of this prototype is by the upper limit of the porous glass at a temperature of 500°C. Figure 5-129 details the fully constructed and laboratory test ready prototype sensor.

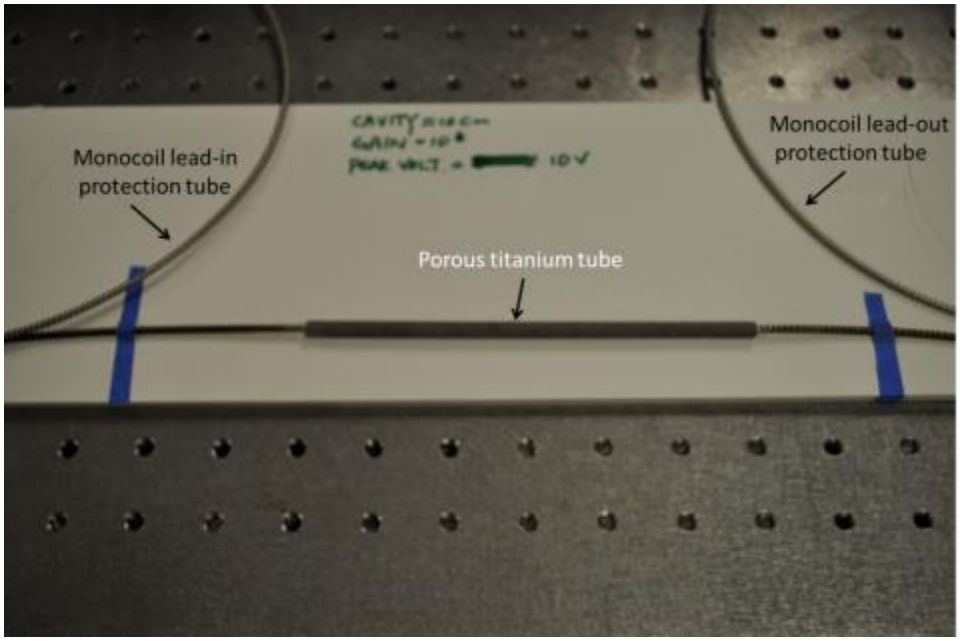

Figure 5-129: Lab test ready porous glass sensor prototype

6 Conclusion

An optical fiber with a porous cladding and solid core has been made using a phase separable glass for the cladding region of the fiber. The porosity in the cladding region is derived from a spinodal phase separable composition that produces a 3 dimensionally interconnected pore structure. This pore structure allows for a gas species to diffuse quickly into the core region of the fiber depending on the pore size and the gas type. The optical fiber works through an evanescent wave interaction with the gas and with a response time on the order of seconds. A range of processing conditions has been investigated in order to be able to optimize the fiber structure for a particular application. The optical fiber should be robust in higher temperature environments up to 600˚C as there is little alteration in the pore structure below this temperature. Pore structures do evolve at higher temperatures with some average pore sizes increasing. This process was used to modify the pore structure of the fibers.

Optical testing of the porous clad structure and the hollow core porous fiber showed that porous hollow-core waveguide is capable of simultaneous detection of acetylene and carbon monoxide while the porous clad optical fiber was tested for high temperature gas sensing with operation up to 500 ˚C being demonstrated. Porous clad fibers were characterized and gas sensing tested for fiber samples which have been exposed to different heat conditions. The samples survived heat treatments up to 800℃ and demonstrated good sensitivity for acetylene The porous hollow-core tubing waveguide was used for the high temperature detection of carbon monoxide. We used multimode-fiber as the lead-out fiber to effectively suppress the modal interference and for SNR enhancement. A specially designed stainless steel tubing system with a built-in furnace was used as the high-temperature gas chamber. The porous fiber sample can be heated to any temperature from room temperature up to more than 500°C. With an improved signal processing method, noises could be maximally suppressed with distinct absorption lines observed.

Work on fabrication and bonding of the sapphire photonic crystal fiber, modeling of sapphire photonic crystal fibers, investigation of joining technologies of the porous glass gas sensors and fabrication of the porous glass sensors was completed. Progress has included work on modeling of sapphire photonic crystal fibers, a new concept which was invented under this program. The modeling was done on a 6-rod sapphire photonic crystal fiber to investigate the optical properties of the change from a single rod optical fiber and a 7-rod structure. The 7-rod bundled structure more efficiently reduces the number of modes compared to that of a 6-rod structure. Analysis of the fiber structure shows a modal reduction of 18.48% percent from that of the single rod of single crystal sapphire fiber. The modeling was done to investigate the presence of a photonic band gap in a sapphire photonic crystal fiber. No complete band gaps were found in the bundled rod case, however complete band gaps were found in the holey sapphire photonic crystal fiber structure. Joining of the porous glass gas sensor with a lead-in optical fiber has been demonstrated to be possible with the use of a CO_2 laser. 3-rod and 7-rod sapphire bundles did not provide sufficient gas absorption peaks to be detected.

Sapphire photonic crystal fibers have been fabricated using a bundle and tie method. Feasibility of bonding the fibers has been demonstrated with the use of a colloidal alumina application along with a sintering heat treatment. Feasibility of high temperature bonding the sapphire components has been demonstrated with the use of silicon carbide and colloidal alumina along with a sintering heat treatment. The ability of colloidal alumina to bond sapphire fibers has been demonstrated. Sapphire bonding characteristics of colloidal alumina in the presence of chromium were explored and verified. It was discovered that chromium oxide

concentrations of 50ppm produced the strongest bond and that single-phase grains were produced as the chromium concentration was increased7-rod sapphire bundles were created and bonded using colloidal silica and silicon carbide dispersions.

7-rod sapphire bundles were created and bonded using colloidal silica, silicon carbide, and chromium oxide/colloidal alumina dispersions. Additional samples were analyzed via SEM and EDS for topographical and elemental verification of bond characteristics, finding that SiO_2 and SiC dispersions may induce a sufficiently strong bond, but the $Cr+Al_2O_3$ dispersion does not likely produce a strong bond under these preparation conditions. Iterative experimentation has resulted in a significant amount of information regarding bond efficacies of the various techniques. The advantages and disadvantages of these bonding techniques were catalogued and analyzed. Each of the three techniques listed are viable and may have distinct uses. It has also concluded that the Al_2O_3+Cr sapphire bonding method is too unreliable to consider as a useful method at this point. Colloidal silica has been successfully used to bond a center-gap sapphire fiber sensor, and silicon carbide will be used to bond a second assembled sensor.

Gold plating has also been done on sapphire fibers in an attempt to provide a film that can be transformed into nanoparticles to scatter the light out of the fiber and allow for more interaction with the glass. Gold has been successfully plated onto the sapphire using a mask to protect the polished ends that can be cleanly removed with acetone without damaging the gold film. A successful furnace treatment has also been found that transforms the film in particles.

Successfully demonstrate of the fabrication of a 6-rod sapphire bundle with a hollow core was completed. The newly fabricated 6-rod Sapphire bundle with a hollow core should provide a significant improvement in the gas detection of the 7-rod sapphire bundle. The improvement on splicing point between sapphire and SM/MM fibers has been successfully demonstrated and signal processing has been performed to enhance gas absorption peaks. The fabrication of the 6 rod SPCF gap bundle (diameter of 70μm) with hollow core was successfully constructed with lead-in and lead-out 50μm diameter fiber along with transmission and gas detection testing. Testing of the sapphire photonic crystal fiber sensor capabilities with the developed long wavelength optical system showed the ability to detect CO_2 at or below 1000ppm at temperatures up to 1000°C

A routine for background estimation routine completed in MATLAB was incorporated into LabVIEW. Data acquisition using the Lecroy LT342 oscilloscope was replaced by the MCC DAQ 1608-FS Plus. Voltage measurements for triggered acquisition were modified and incorporated into a larger programming demonstration for stepped sweeping the Monolux-42 laser. Acquisition timing was made adjustable so laser power stabilization occurred between steps. More than half a dozen approaches were taken for demodulating the signal amplitude from the photodetector output. An average max/min difference calculation was settled upon for the measurement. Optical etalons in the long wavelength system were addressed by angling, reorienting, and switching out components. A demonstration of a full wavelength scan of the laser was completed, with evidence of CO_2 absorptions lines in the correct part of the spectrum. Optical etalons manifesting as fringes in the signal background were isolated and identified by immersing the system in inert nitrogen gas. The fringes are targeted for removal to complete the background calibration.

Analysis of practical aspect of the signal processing has been investigated and demonstrated. In order to analyze the modal noise on sapphire bundle sensor, MM fiber was bent with a diameter of 2cm and compared with a normal sapphire bundle sensor. Another effort to eliminate the modal noise from the system was made with a modal scrambler. A sapphire bundle

using FC connectors between the sapphire fiber and SM/MM fibers was fabricated and demonstrated an improvement in the signal quality and output power. After successful construction of the gas chamber with the sapphire bundle sensor, different gas concentrations were applied to compare gas sensing ability with previous sapphire bundle. The signal process technique using band pass and low pass filter were performed to improve signal quality..

A sapphire photonic crystal fiber sensor was successfully analyzed using a long wavelength system. In order to optimize the sapphire bundle structure, several analyses have been performed with a longer wavelength system. Gas sensing capabilities of the sapphire sensor at high temperature up to 1000ºC have been determined with different gas concentration of CO_2. Gas was detected at concentrations as low as atmospheric CO_2 which is estimated between 400-600ppm. In future research, there are significant amount of improvements that can be made in longer wavelength system including increasing coupling efficiency of QCL laser into the system, increasing air cavity of the sapphire bundle and improving signal processing technique. These should improve the overall aspects of the sensor performance, including sensitivity and the lowest detectable gas concentration.

In order to develop an optical gas sensor using a porous glass capillary tube, joining technique between the porous tube and Corning SMF-28 were developed. Three possible bonding techniques were investigated and analyzed. These bonding techniques include the bonding using CO_2 laser, fusion splicer and high temperature adhesive. Three bonding techniques were analyzed for their repeatability, transmission characteristics, fabrication process, gas sensing ability and durability. The work on the joining technologies consisted of the investigation on the use of CO_2 laser bonding of the porous glass sensor to an optical fiber and a silica capillary tube. Joining of the porous glass capillary tube and the optical fiber was accomplished along with an initial transmission assessment of the bonding technique. Investigation into arc fusion splicing was begun as an alternative approach to joining the optical components. The high temperature adhesive experienced a 14~-15dB loss due to thermal expansion difference and misalignment between lead-in and lead-out fibers. To demonstrate such transmission loss, a thermal cycle test was performed with several samples. One of the possible reasons that fusion splicer bonding has more transmission loss than CO_2 laser bonding is the limited access in the alignment of two fibers. The bonding with fusion splicer has a limitation with the use of the porous tube. If the O.D. of the porous tube is larger than 970μm, the fusion splicer can't be used for bonding due to size limitation of the fusion splicer.

Improvement of bonding techniques can be accomplished by employing refractive mirror during CO_2 laser bonding. It should provide uniform bonding around the porous tube and improve bending issue in transmission loss. Improvement of the control during the insertion of the fiber into porous tube by employing multi translation stages during the assembly may also help. From our analysis and experiments, bonding technique using CO_2 laser is most suitable technique for our gas sensing purpose.

Initial characterization of the mini draw tower was completed. The final goal of this characterization is to provide a chart that will allow a user to set conditions for a preform based on the needed tube size. Similar draw down ratios are possible across a wide range of conditions that yield very different results. Draw down ratios also exhibited linear behavior based on increasing the pull speed with constant temperature and feed speed. Data from these trials has yielded the maximum tube size that can be continuously pulled of 650-700 microns, this limitation comes largely from the size of the drum used to pull the fiber and curvature it puts in the fiber. The temperature where collapse becomes a significant part of drawing is also better

understood for the system. Three different conditions have been found that allow for thick walled tubes to be produced from preforms without the need for a collapse step. This allows for easier production of the tubes in addition to greater uniformity during fabrication.

Gold and silver plating are being evaluated for improving transmission in porous capillary tubes. Using commercially available plating solutions trials have shown that both gold and silver can readily be plated on green glass. Gold plating of tubes has been very successful at plating both green glass and phase separated glass tubes using a vacuum based system to flow the plating solution. The system has been improved to allow for plating of three tubes simultaneously. Gold plating was lost on green glass tubes after going through the phase separation and leaching process. Gold plating on phase separated tubes underwent a change during the leaching process but was still present on the tubes. The use of a vacuum system to plate gold directly on a porous tube was unsuccessful. A new system was developed to use pressure to flow liquid through a porous tube.

The gold coating was produced on a phase separated glass and shown to form a clean and uniform coating on only the inside surface of the tube. The tubes were then subjected to the normal leaching process to make the glass porous and the gold film was observed to also be porous and exhibited an approximately 100nm ligament structure that was continuous across the surface. ED's measurements detected no contamination in the gold film and the film was thin enough to still detect the glass below it. Initial tests showed the transmission currently is on par with non-coated tubes and actually possibly less loss on the porous gold than the solid gold film. Gas detection was also possible on a coated tube. Further tests are necessary to determine the improvement of transmission over no coating. Possible gas sensing structures using a porous plate with a CO_2 laser, fiber taper with a porous tube, and Whispering Gallery Mode (WGM) with the porous material was demonstrated.

The absorption spectrum of a gas mixture can be analyzed to list and quantify the mixture's gaseous components. This analysis is most easily executed in software, in this case using MATLAB. The software's development has been described in terms of three pieces: acquisition, detection, and estimation. These pieces naturally divide the programming routine and pace the development of future work. Acquisition and detection have been concretely demonstrated using a porous silica tube gas cell of 6 cm in length and acetylene as the test gas. Lorentzian curve fitting was exemplified as a beginning step in the estimation procedure. Various estimation techniques are under consideration as the software evolves. Certain features of the mature software will include simultaneous inspection of multiple absorption peaks across a single spectrum measurement and temporal averaging of subsequent measurements to reduce noise fluctuations.

Software development was described for data acquisition and signal processing. Data acquisition programming was shown to synchronize the wavelength sweep, amplitude determination, and spectrum recording. Signal processing software was explained as a three stage procedure stepping through background cancellation, absorption dip identification, and concentration estimation. The discussion of the software covered both the porous silica gas sensor and sapphire bundle gas sensor. The implementation compares absorption measurements of an unknown concentration level and a known reference concentration level. There are automation improvements suggested to future editions of the data acquisition and signal processing software. Automated trigger synchronization could be enforced by simultaneously monitoring data reading and wavelength stepping. Automated selection of background fitting parameters and absorption dip thresholds would expedite processing of new data sets.

Pore sizes were manipulated using annealing treatments to change the pore structure of the samples. In addition to no annealing, 5 annealing trials were done and compared using SEM, gas detection, detection time, mechanical strength, and transmission loss. ImageJ was used on SEM images to estimate the pore size and percentage of pore area. Increasing the annealing temperature was shown to decrease transmission loss while increasing detection time for gas detection. Analysis of images showed an increase in the pore area percentage at both the 600 and 800°C conditions and a decrease at the other conditions. The increase at 600°C is explained by the smaller pore consolidating to form larger ones. The 800°C samples had extremely high amounts of variation and curvature present and were difficult to get long enough samples that were straight. The significant change in the pore shape complicated the pore size and area analysis when compared to the other samples. Further investigation of the change in the pore structure would be warranted if the optical properties of the porous tube become useful in the sensor design.

Optical properties of the porous gas sensor with different annealing temperature was investigated and analyzed in this report. Analysis and demonstration include transmission test with different cavity lengths, gas sensing ability, gas detection time and mechanical strength of porous tube. The transmission loss of the sensors improved as the annealing temperatures increased, but the gas detection time increased and the mechanical strength decreased with an increase in annealing temperature. Improvement in the understanding the porous material was achieved from these experiments and possible improvement can be made when gas chamber with gas mixer and furnace can be used in our future experiments. Significant improvement of accurate measurement including sensitivity, lowest concentration of the detectable gas and detection time can be achieved in next research period.

Initial draw test have completed on random tube arrangement preforms in the green glass in an effort to move towards producing a photonic crystal fiber structure in the porous glass. The fabricated fibers suffered from incomplete forming of the stacked tube array or full or partial consolidation of the tubes. Stacked tube preforms are much more sensitive to heat profile variations and require higher temperature and draw speeds to prevent excess voids being present. A mold has been produced and is aiding in the production of an ordered tube preform and has greatly improved alignment though it has led to an increase in the number of tubes needed do to larger outer tubes being required. Optimizing the stack and drawing conditions is the primary focus from now on to allow for the stack to be drawn to fiber size. Investigation of 3D printing a PCF preform is also being done and is promising provided enough glass of the correct size can be produced. A preliminary packaging design for the porous glass sensor has also been proposed based on design using a porous metal shield tube.

Improvements in the drawing process and the addition of an iris assembly to the drawing furnace to provide an even heat profile were successful in significantly improving the quality of the drawn fibers, although a true PCF was not realized. The inability to produce these fibers has been determined to be the limited preform size. Current process limits the length of preform that can be made to around 5” in length and is insufficient to allow for ideal drawing conditions to be reached. Improvements to the preform process and tube stacks to increase length would allow for this to be successfully produced.

Porous glass based sensor was used in a variety of configurations to detect acetylene to determine the best sensor setup for detecting gas. The minimum detectable concentration was estimated and problems with the current test were evaluated. The current minimum measured detectable level was determine to be in the range 100-200ppm though due to the accuracy of the

gas mixer, this cannot be more precisely stated. At this concentration, the signal to noise ratio was found to be very low nearing the detection limit. Gold coating on the inner surface was evaluated for improving the transmission characteristics. Transmission test data indicates that the gold coating increases the reflectivity of the inner surface and has the potential to improve the signal. Gas testing on gold coated samples yielded significantly poorer results than the uncoated counterparts though this problem is attributed to poor alignment and joining technology that was used to make the gold coated tube. The presence of the film did not prevent gas detection but its effects are not well understood without further study.

A complete materials package was designed and produced for the porous glass sensors and is capable of being operated at the upper limit of the porous glass sensors of 500°C. This package was produced using a porous titanium metal tube with fused silica ferrules to hold the sensor. Lead fibers were protected by metal monocoil.

7 References

[1] D. Gaskel, Introduction to metallurgical thermodynamics, 2nd ed., New york: McGraw-Hill, 1981.

[2] W. Kingery, H. K. Bowen and D. R. Uhlmann, Introduction to Cermaics, 2nd ed., New York: John Wiley and Sons, 1976.

[3] R. Swalin, Thermodynamics of solids, 2nd ed., New York: John Wiley and Sons, 1972.

[4] Neal Pfeiffenberger; Gary Pickrell "Finite Element Modeling of Sapphire Photonic Crystal Fibers" Virginia Tech. MS&T, Houston, TX October 21, 2010.

[4] Neal Pfeiffenberger; Gary Pickrell "Finite Element Modeling of Sapphire Photonic Crystal Fibers" Virginia Tech. MS&T, Houston, TX October 21, 2010.

[5] Nubling, R. K., and Harrington, J. A., "Optical properties of single-crystal sapphire fibers," Appl. Opt. 36:5934-5940. (1997).

[6] LaBelle, H. E., Jr., "EFG, the invention and application to sapphire growth," J. Cryst. Growth 50, 8–17 (1980).

[7] Jundt, D. H., Fejer, M. M., and Byer, R. L., "Characterization of single-crystal sapphire fibers for optical power delivery systems," Appl. Phys. Lett. 55, 2170–2172 (1989).

[8] Feigelson, R. S., "Pulling optical fibers," J. Cryst. Growth 79, 669–680 (1986).

[9] Chang, R. S. F., Sengupta, S., Dixon, G. J., Shaw, L. B., and Djeu, N., "Growth of small laser crystals for study of energy kinetics and spectroscopy," Growth, Characterization, and Applications of Laser Host and Nonlinear Crystals, T. J. Lin, ed., SPIE 1104, 244–250 (1989).

[10] Chang, R. S. F., Phomsakha, V., and Djeu, N., "Recent advances in sapphire fibers," Biomedical Optoelectronic Instrumentation, Katzir, A., Harrington, J. A., and Harris, D. M., eds., SPIE 2396, 48–53 (1995).
[11] Merberg G. N., and Harrington, J. A., "Optical and mechanical properties of single-crystal sapphire optical fibers," Appl. Opt. 32, 3201–3209 (1993).
[12] Nubling, R. K., Kozodoy, R. L., and Harrington, J. A., "Optical properties of clad and unclad sapphire fiber," Biomedical Fiber Optic Instrumentation, Katzir, A., Harrington, J. A., and Harris, D. M., and Milanovich, F. P., eds., SPIE 2131, 56–61 (1994).
[13] Pedrazzani, J. R., "Sapphire Optical Fibers," [Specialty optical fibers handbook], Elsevier Academic Press, Burlington, MA, USA. 651-670 (2007).
[14] Desu, S. B. et. al., "High temperature sapphire optical sensor fiber coatings," SPIE Int. Soc. Opt. Eng. Proc. SPIE Int. Soc. Opt. Eng. 1307: 2-9 (1990).
[15] Pfeiffenberger, N. T., Pickrell, G., Kokal, K., and Wang, A., "Sapphire photonic crystal fibers," Opt. Eng. 49, 090501; doi:10.1117/1.3483908 (2010).
[16] Pfeiffenberger, N. T., Pickrell, G., "Finite Element Modeling of Sapphire Photonic Crystal Fibers," Proc. MS&T, Houston, TX (2010).
[17] Comsol Multiphysics manual, version 4.2a, (2011).
[18] Saitoh K., and Koshiba, M., "Full-vectorial imaginary-distance beam propagation method based on finite element scheme: Application to photonic crystal fibers," IEEE J. Quantum Electron. 38, 927-933 (2002).
[19] Saitoh K., and Koshiba, M., "Leakage loss and group velocity dispersion in air-core photonic bandgap fibers," Opt. Express 11, 3100-3109 (2003).
[20] Pfeiffenberger, N. T., Pickrell, G., "Finite Element Modeling for Mode Reduction in Bundled Sapphire Photonic Crystal Fibers," Proc. MS&T, Columbus, OH (2011).
[21]Pfeiffenberger, N. T., Pickrell, G., "Finite Element Modeling for Mode Reduction in Bundled Sapphire Photonic Crystal Fibers," Proc. MS&T, Columbus, OH (2011).
[22] Jianming Jin, "The Finite Element Method in Electromagnetics," Second Edition, John Wiley & Sons, Inc, New York 2002.
[23] K. Saitoh and M. Koshiba, "Full-vectorial imaginary-distance beam propagation method based on finite element scheme: Application to photonic crystal fibers," IEEE J. Quantum Electron. **38**, 927-933 (2002).
[24] Kunimasa Saitoh and Masanori Koshiba, "Leakage loss and group velocity dispersion in air-core photonic bandgap fibers," Opt. Express **11**, 3100-3109 (2003)
[25] http://americas.kyocera.com/kicc/pdf/Kyocera%20Sapphire.pdf

[26] http://ab-initio.mit.edu/wiki/index.php/MPB_Data_Analysis_Tutorial